REFRIGERATION SCIENCE AND TECHNOLOGY PROCEEDINGS

CHINESE ASSOCIATION OF REFRIGERATION (CAR) FOR COOPERATION
WITH THE INTERNATIONAL INSTITUTE OF REFRIGERATION (IIR)

10th IIR Conference on Caloric Cooling and Applications of Caloric Materials

Baotou, China

August 21-24, 2024

INSTITUT INTERNATIONAL DU FROID
INTERNATIONAL INSTITUTE OF REFRIGERATION

ISBN: 978-2-36215-063-0
ISSN: 0151-1637
Code: 2024/4

PROCEEDINGS

REFRIGERATION SCIENCE AND TECHNOLOGY

10th IIR Conference on Caloric Cooling and Applications of Caloric Materials

August 21-24, 2024

Shangri-La Baotou, Baotou, China

Editor

Chinese Association of Refrigeration (CAR)

NO.67 FUCHENG ROAD, HAIDIAN DISTRICT,
BEIJING, CHINA

https://thermag-x.scimeeting.cn

Publisher

International Institute of Refrigeration
177, boulevard Malesherbes
75017 Paris, France

Contents

Conference Chair
Prof. Ercang LUO, CAR Vice President, Technical Institute of Physics and Chemistry

Organizing Committee
Chair
Prof. Qingguo MENG, CAR Executive Vice President

Co-Chair
Mr. Zhengang LIU, Deputy General Manager, Baogang Group
Mr. Mi YAN, President of Baotou Research Institute of Rare Earths
Member
Mr. Didier COULOMB, IIR Director General
Porf. Xianting LI, IIR Commission E1President, Tsinghua University
Prof. Andrej KITANOVSKI, University of Ljubljana
Prof. Reinhard RADERMACHER, University of Maryland
Prof. Xiaohu LI, CAR Vice President and Secretary General
Mr. Jie DING, CAR Vice President, Dalian Bingshan Group
Mr. Qiang WANG, CAR Vice President, Moon Environment Technology
Prof. Xudong TIAN, CAR Vice President, Hefei General Machinery Research Institute
Prof. Changyong LIU, CAR Vice President
Prof. Kexue WEN, CAR Vice President, China Railway Special Cargo Logistics
Prof. Wei XU, CAR Vice President, China Academy of Building Research
Prof. Hong XU, CAR Vice President, China Household Electric Appliance Research Institute
Prof. Jianming TAN, CAR Vice President, Gree Electric Appliances, Inc. of Zhuhai
Mr. Zhihua ZHAO, Chief Engineer of China Northern Rare Earth (Group) High-Tech Co., Ltd.
Mr. Zhiqiang LI, Standing Vice-President of Baotou Research Institute of Rare Earths

Secretary General
Prof. Huaqian JING, CAR Deputy Secretary-General

Programme Committee
Prof. Wei DAI, Technical Institute of Physics and Chemistry
Prof. Fengxia HU, Institute of Physics
Prof. Jiaohong HUANG, Baotou Research Institute of Rare Earths
Prof. Huilong HOU, Beihang University
Prof. Tao JIN, Zhejiang University
Prof. Xianting LI, IIR Commission E1 President, Tsinghua University
Prof. Suxi QIAN, Xi‘an Jiaotong University
Prof. Xiaoshi QIAN, Shanghai Jiaotong University
Prof. Limin QIU, Zhejiang University
Prof. Jun SHEN, Beijing University of Sciences and Technology
Prof. Peijue SUN, Institute of Physics
Prof. Yan WANG, Baotou Research Institute of Rare Earths
Prof. Jianghong WU, Huanan University of Sciences and Technology
Dr. Jingyuan XU, Karlsruhe Institute of Technology
Prof. Peng ZHANG, IIR Section A2 President, Shanghai Jiaotong University
Dr. Biao ZHONG, Technical Institute of Physics and Chemistry, CAS
Associate Prof. Min ZHOU, Technical Institute of Physics and Chemistry
Scientific Committee
Prof. Jader BARBOSA, Federal University of Santa Catarina
Prof. Luana Caron, Bielefeld University
Prof. Alberto CORONAS, IIR Commission E2 President, Rovira i Virgili University
Prof. Wei DAI, Technical Institute of Physics and Chemistry
Prof. Oliver GUTFLEISCH, Technische Universitat, Darmstadt
Prof. Huilong HOU, Beihang University
Prof. Fengxia HU, Institute of Physics
Prof. Jiaohong HUANG, Baotou Research Institute of Rare Earths
Prof. Ji Hwan JEONG, IIR Commission B2 President, Pusan National University
Prof. Tao JIN, Zhejiang University
Prof. Andrej KITANOVSKI, University of Ljubljana

Prof. Xianting LI, IIR Commission E1President , Tsinghua University
Prof. Xavier MOYA, University of Cambridge
Prof. Antoni PLANES, University of Barcelona
Prof. Suxi QIAN, Xi‘an Jiaotong University
Prof. Xiaoshi QIAN, Shanghai Jiaotong University
Prof. Limin QIU, Zhejiang University
Prof. Julie STAUNTON, University of Warwick
Dr. Jingyuan XU, Karlsruhe Institute of Technology
Prof. Peng ZHANG, IIR Section A2 President, Shanghai Jiaotong University
Prof. Qiming ZHANG, Pennsylvania State Universit

Copy right and Disclaimer

International Institute of Refrigeration
Institut International du Froid

IIR/IIF
177 boulevard Malesherbes
75017 Paris
France
e-mail: iif-iir@iifiir.org

DOI: 10.18462/iir.thermag.2024.0001

EFFECT OF TEMPERATURE VARIATION RATE ON THE LIFE OF THERMOELECTRIC DEVICES IN PCR INSTRUMENTS

Junhao Yan[(a)], Zeyu Liu[(a)], Zun Liu[(a)], Limei Shen[(a), (b), *], Junlong Xie[(a)]

[(a)] School of Energy and Power Engineering, Huazhong University of Science and Technology
Wuhan, 430074, China, EP_Shenlimei@hust.edu.cn
[(b)] Shenzhen Huazhong University of Science and Technology Research Institute
Shenzhen, 518057, China

ABSTRACT

Polymerase chain reaction (PCR) is an in vitro molecular cloning technology that is widely used in medical testing, agricultural development and industrial pharmaceuticals. At present, PCR machines mainly use TEC for rapid heating and cooling to create temperature cycles. However, the cycle conditions will cause structural damage and significant performance degradation, causing device failure. This paper proposes a thermoelectric device performance degradation and life prediction model. After verifying the accuracy of the model, the impact of different temperature change rates on the device life is studied. When the average temperature change rate is 2.5℃/s, the lifespan of the device is approximately 28.27 years; when the average temperature change rate is 5℃/s, the lifespan will be dropped to 25.70 years. This article has positive significance for promoting the use of thermoelectric devices and the selection of temperature change rates of traditional PCR instruments.

Keywords: Lifetime prediction, temperature variation rate, PCR instrument, thermoelectric

1. INTRODUCTION

Polymerase chain reaction (PCR) is an in vitro molecular cloning technology (Li et al., 2020) capable of amplifying DNA to a sufficient number of target double-stranded DNA fragments, so that they can be measured by conventional analytical techniques. PCR is the basis for many downstream research and applications, include sequencing, pathogen detection, mutation detection, molecular archeology, cancer research, diagnosis, mutation, drug discovery and genetic engineering (Madadelahi et al., 2024). In order to obtain better amplification results, the temperature of heating and cooling process needs to be precisely controlled (Zhou et al., 2018). PCR amplification has the problem of slow heating/cooling rate, resulting in a long detection time of about 2-3h (Chen et al., 2016). Thermoelectric devices have the characteristics of controllable size, easy integration, low cost, fast response. They have been widely used in PCR instruments to provide solutions to the above problems.

At present, many researchers have further developed PCR instruments that use thermoelectric devices for temperature control, and use methods such as PID, fuzzy PID, linear auto-disturbance rejection algorithm and other methods to optimize the control system (Liu et al., 2023), so as to obtain higher temperature control accuracy to ensure the accuracy of results. Alternatively, thermoelectric devices can be combined with fan cooling, liquid cooling, microchannels, etc. to increase the temperature rise and cooling rate (Ling et al., 2023) and shorten the time required for experiments. However, as the heating and cooling rates increase, the life of the thermoelectric device is difficult to be guaranteed, so it is necessary to analyze.

A PCR instrument needs to go through dozens of thermal cycles for one amplification, which puts the thermoelectric device in a thermal cycle condition for a long time. This will easily cause device performance degradation. What's more, a higher heating and cooling rate will accelerate the performance degradation of the thermoelectric device. The reason is that the thermal cycle causes the internal structure of the devices to be subjected to cyclic alternating thermal stress, which is easy to cause fatigue and creep (Mcpherson, 2010). At the same time, the structural materials in the device have different Young's modulus, and the strain at the interface is different, which causes microscopic damage, cracks and holes (Towashiraporn et al., 2004). These cracks and holes are filled with air, which is a poor conductor of heat and electricity, causing the device resistance to increase and performance indicators such as output power and ZT value to decrease. As the number of cycles

increases, cracks and holes continue to grow and performance gradually degrades, resulting in shortened life. Many researchers have carried out studies on the effects of thermal cycling on the performance and lifetime of thermoelectric devices. In terms of experimental research, Barako et al.(2012) found that after 10,000 thermal cycles, the ZT of the device decreased by 6%, the thermal conductivity increased by about 5.2%, the resistance increased by 5%, and the Seebeck coefficient remained basically unchanged. Hatzikraniotis et al.(2010) found that after 6000 cycles, the output power of the device decreased by 14%, the resistance value increased by 16.1%, the Seebeck coefficient decreased by 3.8%, and the average thermal conductivity decreased by 6.6%. Harish et al.(2021) and Tatarinov et al.(2012) conducted thermal cycle studies on TEGs for vehicles, and also found that the output power of the device decreased significantly after cycling. In terms of simulation, Wang Xue et al.(2022) proposed and studied a new high temperature $CaMnO_3$ base U-type single leg thermoelectric module. Under 6W and 300K, the maximum thermal stress is 3.31GPa and the fatigue life is 41686 cycles. Y.J. Cui et al.(2022) found that thermoelectric modules can increase the output power of photovoltaic cells with small temperature coefficients, but the increase will disappear with the increase of the number of cycles. The ratio between the thickness of the photovoltaic cell and the thickness of the insulation layer between modules has a suitable value that can eliminate the shear stress at the silver paste, thereby increasing the overall device life. Wu Yongjia et al.(2014) conducted numerical analysis of material thickness, thermodynamic and thermal stress properties of thermoelectric modules, and studied the influence of high heat flux on thermal efficiency, power output and thermal stress. The device life can also be improved by reducing thermal stress.

The above researchers used experiment and simulation to study the life of thermoelectric devices, and gave the proportion of device performance, resistance and other indicators decline. However, since the thermoelectric devices in the PCR machine need to alternately perform heating and cooling behaviors, and the single cycle time is relatively short, the conclusions in the above article are difficult to directly apply to the thermoelectric devices in the PCR machine. In terms of research methods, experimental research is too time-consuming and can only obtain the life of a specific device under specific working conditions. Simulation research is difficult to obtain the performance degradation of the device at a specified time. Even if the life can be obtained, it is only for a certain working condition, when the working conditions change, all simulations need to be re-simulated, which will also take a lot of time. Therefore, a performance degradation and life prediction model of thermoelectric devices is proposed in this paper. The influence of temperature change rate on the performance degradation and life of devices in PCR cycle conditions is studied by using this model, and analyzed from the perspective of average temperature change rate, difference between heating rate and cooling rate, and thermal cycle period. This study has a positive significance for promoting the use of thermoelectric devices and the development and selection of temperature variable rate of traditional PCR instrument.

2. LIFE PREDICTION MODEL

Thermoelectric devices are generally composed of dozens to hundreds of thermoelectric units. When the device is operating, the thermo-mechanical behavior of all thermoelectric units is similar, and by discretizing the overall structure, the performance of each thermoelectric unit can be analyzed first, and then the performance of all thermoelectric units can be substituted for the performance of the overall structure. It has been verified that this substitution can meet the engineering accuracy, so it is reasonable to study the temperature distribution and thermal stress distribution of the thermoelectric unit to characterize the performance degradation of the overall device (Wang et al., 2019). Barako et al.(2012) conducted thermal cycling experiments on thermoelectric modules and proved that solder is the most prone to damage in each structure of thermoelectric devices, which is very similar to the situation of solder joints in microelectronics assembly. Therefore, this paper selected Darveaux model, the widely used solder joint failure models, for research and analysis (Wong et al., 2016).

2.1. Mathematical model

According to the degradation of the device, the Darveaux model divides the actual lifetime N into two parts, the initial lifetime N_0 and the propagation lifetime, namely:

$$N = N_0 + \frac{a_0}{da/dN} \quad (N_c > N_0) \qquad \text{Eq. (1)}$$

In the equation, N_0 is the initial life. When the number of cycles $N_c<N_0$ is in the initial life range, the performance of the device is not affected by the number of cycles. There is no crack, and the crack length $a = 0$. When $N_c>N_0$, cracks begin to appear, and the performance of the device decreases. a_0 is the critical crack length, when crack reaches this length, it is considered that the device fails completely. *da/dN* is the growth rate of the crack with cycle. ΔW_{ave} is the average viscoplastic strain energy density of the interface unit per cycle. It represents the energy generated by deformation per cycle. Before complete failure, the relationship between the initial life N_0 and the crack growth rate and ΔW_{ave} conforms to the following function (Darveaux, 2000):

$$N_0=K_1\Delta W_{ave}{}^{K_2} \quad \text{Eq. (2)}$$

$$\frac{da}{dN}=K_3\Delta W_{ave}{}^{K_4} \quad \text{Eq. (3)}$$

In the above equations, K_1, K_2, K_3 and K_4 are all model constants, which are related to the physical properties of the material and the cycle temperature. ΔW_{ave} is related to device geometric parameters and cycle temperature, and cannot be measured through experiments, but it can be directly obtained by simulation. Therefore, in this paper, the combination of simulation and experimental data is used to determine the model constants and ΔW_{ave}. The strength at the interface is usually weaker than the overall strength and is more likely to fail. Thus, it is assumed that the crack length on the interface is *a*, and the distance between two adjacent cracks is *l*. the dimensionless damage parameter is:

$$\omega=\frac{a}{l} \quad \text{Eq. (4)}$$

ω is used to characterize the relative size of the crack on the interface, which increases with the growth of the crack. If $\omega = 0$, it means that the crack is very small relative to the interface, and it can be considered as no damage; if $\omega = 1$, it means that the interface is full of cracks, the device is severely damaged. $0 < \omega < 1$ indicates that the thermal load leaves damaged areas on the interface, which have strong resistance to heat flow and electric current, so it can be considered that the effective conductive area of the interface is reduced. If the initial cross-sectional area of the thermoelectric arm is *A*, then the effective conductive area is $(1-\omega)A$. According to the resistance definition equation, the resistance after the effective conductive area is reduced is:

$$R_a=\frac{\rho l}{(1-\omega)A}=\frac{R_0}{(1-\omega)} \quad (5)$$

Where R_0 is the initial resistance, ρ is the resistivity, ω is between 0 and 1 according to the degree of damage. According to the study of Barako et al.(2013), resistance increases significantly with the cycle, which is the main reason for the decrease of ZT value of the comprehensive evaluation index of thermoelectric devices. Therefore, resistance is taken as the performance degradation evaluation index in this paper. Previous studies have shown that the crack length a of the device increases linearly with the number of cycles (Bhate et al., 2008), that is, *da/dN* in Eq. (1) is a constant. By taking Eq. (1), (2), (3) and (4) into (5), the relationship between resistance R_a and ΔW_{ave} after damage can be obtained:

$$R_a=\frac{R_0 l}{1-K_3\Delta W_{ave}{}^{K_4}\left(N_c-K_1\Delta W_{ave}{}^{K_2}\right)} \quad (N_c>N_0) \quad (6)$$

Where N_c is the number of cycles as an independent variable, R_0 is the initial resistance value. Therefore, as long as the model parameters K_1, K_2, K_3, K_4 and ΔW_{ave} are determined, the resistance value of the device under the corresponding number of cycles can be obtained, so as to evaluate the degree of degradation and performance.

2.2. Margins Simulation model and verification

In order to obtain the average viscoplastic strain energy density of model constants K_1, K_2, K_3 and K_4 and unit cyclic interface elements, the geometric model was established, thermal cycling conditions were set up and finite

element analysis was performed with reference (Barako et al. 2013). The boundary conditions of the model are: the upper and lower ends are fixed; only the heat transfer from the cold source and heat source to the thermoelectric unit is considered, and the heat transfer from the thermoelectric unit to the outside world in other directions is ignored. The thermoelectric unit consists of a substrate, conductor, solder layer, thermoelectric arm and other components, as shown in Fig.1(a). The ceramic substrate, electrode and solder layer are directly made of materials preset by the software, and the material performance parameters are determined by the software's built-in function. The difference between P-type thermoelectric arm and N-type thermoelectric arm is ignored for thermoelectric materials. And the thermophysical and mechanical properties of copper and Bi_2Te_3 are given by reference (Snyder et al., 2008).

Then the grid is divided and the grid independence is verified. By comparing the size of ΔW_{ave} under different grid numbers, we select a partition method of grid number 25175 for calculation. As mentioned above, model constants K_1, K_2, K_3 and K_4 cannot be obtained directly, so simulation calculations are required to obtain model constant values that match the model. Take the following values: K_1=32798.6(cycle/psi^(K_2)), K_2=-1.4, K_3=1.8126(10^{-7}in/cycle/psi^(K_4)), K_4 = 1.12, put the simulation results into Eq.(6) to get the resistance change curve with the number of cycles, and compare it with the experimental data (Barako et al. 2013). As shown in Fig.1(b), it is the experimental resistance data and the model prediction data in this paper. It can be found that the error is small, so the above values are selected as the model constants in this paper.

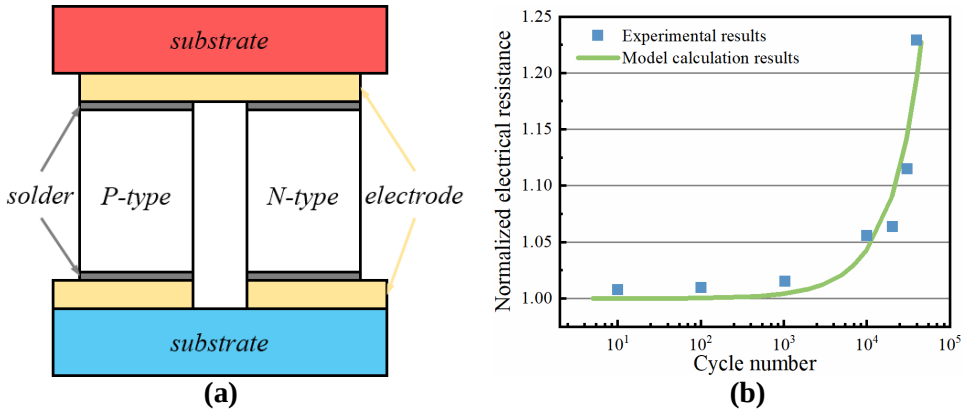

Fig. 1: (a) Structure diagram of thermoelectric unit; (b) Comparison of experimental resistance data and model prediction data in this paper.

3. RESULTS AND DISCUSSION

Based on the above thermoelectric device performance degradation and life prediction model, this article calculates the device life when the heating rate and cooling rate change. The working conditions refer to the PCR temperature change rates given by some manufacturers, as shown in Table 1 (Gao 2020), and are named B, C, D, and E working conditions. Referring to Zhang Fakun's(2018) research, the working conditions of a heating rate of 6℃/s and a cooling rate of 4℃/s are added and named as working condition A. The hot end temperature change curve during simulation is shown in Figure 3:

Table1. PCR instrument performance index

Manufacturer	Heating rate	Cooling rate	Temperature control accuracy	Group
ABI	3.5℃/s	3.5℃/s	±0.25℃	B condition
Roche	4.5℃/s	2.5℃/s	±0.25℃	C condition
TIANLONG	3.5℃/s	3℃/s	±0.3℃	D condition
Bioer	3℃/s	2℃/s	±0.3℃	E condition

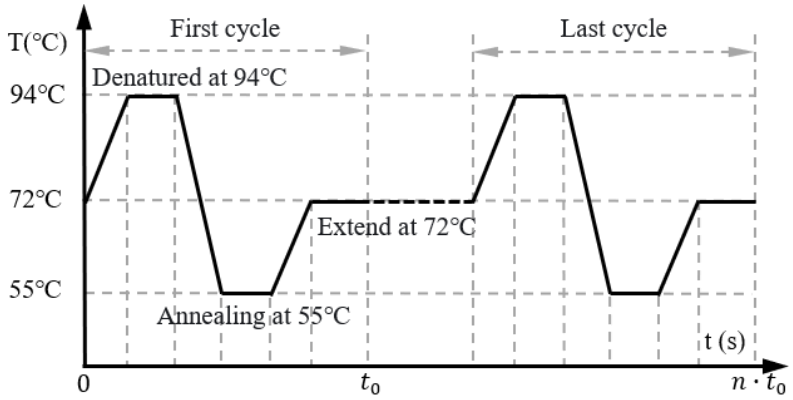

Fig.2 Temperature change curve at the hot end

The simulation model was modified and calculated according to the above working conditions. This study selected the vulnerable point, that is, the point with the largest ΔW_{ave} and the most serious failure, for analysis. The failure standard is 10% resistance change, result is as follows:

3.1. Thermal Cycle Life Analysis

Figure 3(a) shows the simulation results of the life of thermoelectric devices under different thermal cycle conditions. Taking the average value of heating rate and cooling rate as the temperature change rate, the temperature change rate of working condition A is 5℃/s and the lifespan is 25.7 years; the temperature changing rate of working condition B is 3.5℃/s and the lifespan is 26.45 years; the temperature changing rate of working condition C is 3.25℃/s, and the service life is 27.27 years; the temperature change rate of D working condition is 3.5℃/s, and the lifespan is 27.8 years; the temperature change rate of E working condition is 2.5℃/s, and the lifespan is 28.27 years. It can be found that as the temperature change rate decreases, the service life basically shows an upward trend, but D working condition is an exception: the temperature change rates of B working condition and D working condition are both 3.5℃/s, but the latter has a higher lifespan. Out of the former 1.35 years. Therefore, there are factors other than temperature change rate that affect device life. In the second part of this article, the calculation method of life is explained, which is directly affected by the viscoplastic strain energy density ΔW_{ave} and the thermal cycle operating period t_0. Next, the above two factors are analyzed.

The viscoplastic strain energy density ΔW_{ave} is obtained by simulation, and the larger it is, the smaller the number of thermal cycles the device can withstand, so it can be used to characterize the influence of thermal cycle conditions on the device. Figure 3(b) shows the simulation results of viscoplastic strain energy density.

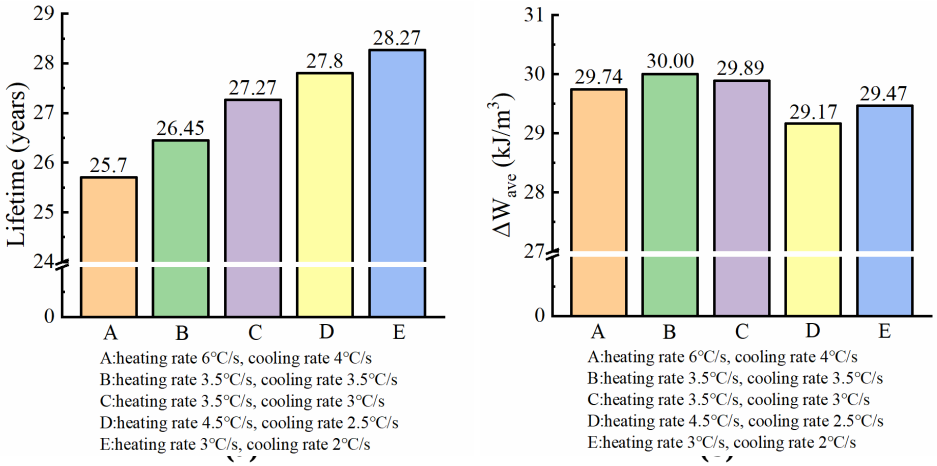

Fig.3 (a)Life of thermoelectric devices under different thermal cycle conditions, (b)Viscoplastic strain energy density of thermoelectric devices under different thermal cycle conditions

From the data under three working conditions B, C, and E, it can be found that ΔW_{ave} dropped from 30.00kJ/m^3 to 29.89kJ/m^3, and then to 29.47kJ/m^3, which decreases as the temperature change rate decreases. Also paying attention to the data under the two working conditions A and D, ΔW_{ave} dropped from 29.74kJ/m^3 to 29.17kJ/m^3, and this conclusion can also be reached. This is because the temperature change rate decreases, the change of thermal stress on the device also slows down, reducing the impact of fatigue damage; creep damage is related to the stage of constant stress, it is basically unchanged. The combined action of the two can reduce the damage of the device, slow down the crack growth, and can withstand longer thermal cycling, which is reflected in the increase of life. Comparing working conditions B, C, and E with working conditions A and D, it can be found that the latter has a higher temperature change rate but a lower ΔW_{ave}. This is due to the large difference between the heating rate and the cooling rate. The smaller cooling rate promotes the release of stress during high temperature stage, thereby reducing the overall stress of a single cycle, that is, the viscoplastic strain energy density.

3.2. Number of thermal cycles of the device

Figure 5 shows the cycle times of the device under different working conditions. Compared with Figure 4, it can be found that the cycle times of the device under D working condition is the largest, which is 4.603×10^6 times, but its life is only 27.8 years, which is not the largest. The cycle times of operating condition B is the smallest, which is 4.461×10^6 times, but its life is 26.45 years, which is not the smallest. This is because the life is calculated from the number of cycles and the thermal cycle period t_0, and the thermal cycle period is also affected by the temperature change rate. In PCR technology, in order to ensure the activity and amplification effect of the enzyme, the temperature must be strictly controlled and the time to maintain the set temperature, so with the decrease of the temperature change rate, the thermal cycle t_0 will increase. Comparing the results under the three working conditions B, C, and E, ΔW_{ave} continues to decrease and the number of cycles increases. At the same time, the period of a single cycle increases from 187s to 192s and 197s, so the number of cycles increases as shown in Figure 6. This is because device lifetime is defined as the period of a single cycle multiplied by the number of cycles, since both increase, device lifetime also increases significantly. Comparing the results of working conditions A and D, the ΔW_{ave} changes are the same as above, the number of cycles also increases, and the cycle increases from 180s to 190.5s, which significantly increases the device life. However, comparing the working conditions B, C, and E with the working conditions A and D, it can be found that the ΔW_{ave} of the A working condition is smaller than the ΔW_{ave} of the B and C working conditions, but the lifespan is lower; the D working condition ΔW_{ave} is smaller than the E working condition ΔW_{ave}, and its lifespan is also lower. This is because the impact of the thermal cycle operating period t_0 on the life at this time exceeds the impact of ΔW_{ave} on the life. Although the cycle number N of groups A and D is larger, the thermal cycle operating periods of the three operating conditions B, C and E The growth of t_0 is more obvious, and the combined effect is reflected in the longer life of the device under the three working conditions of B, C and E.

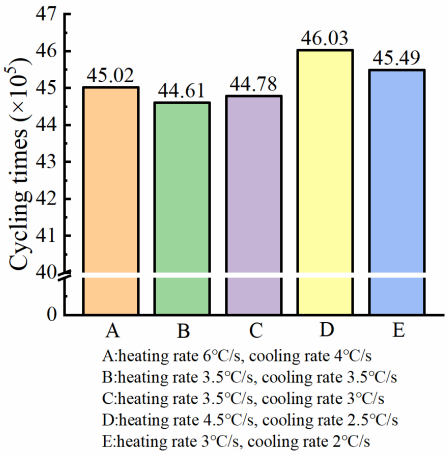

Fig.4 Cycle times of thermoelectric devices under different thermal cycle conditions

4. CONCLUSION

By conducting thermal cycle transient simulations of devices under different heating rates, it is found that the

device life is mainly affected by the temperature change rate and the thermal cycle period. The lower the average temperature change rate and the longer the cycle period, the greater the lifespan. When the average temperature change rate is 5℃/s, the lifespan is 25.7 years; when the average temperature change rate is 2.5℃/s, the lifespan is 28.27 years. When the above parameters are the same, the greater the difference between the heating rate and the cooling rate, the greater the life of the device. The temperature change rates of working conditions B and D are both 3.5℃/s, but the difference between the heating rate and cooling rate of the latter is larger, and its lifespan is 1.35 years longer than the former. This article has positive significance for promoting the use of thermoelectric devices and the development and selection of temperature change rates of traditional PCR instruments.

ACKNOWLEDGEMENTS

This work is jointly supported by National Key Research and Development Program of China (Grant No. 2022YFB3803900), the National Natural Science Foundation of China (Grant No. 52176007), Science, Technology and Innovation Commission of Shenzhen Municipality (Grant No. JCYJ20210324115611030).

NOMENCLATURE

N	Life span	N_0	Initial life
N_c	Cycle number	a	Crack length [mm]
a_0	Critical crack length[mm]	da/dN	Crack growth rate with cycle
ΔW_{ave}	Viscoplastic strain energy density [kJ/m^3]	K_1	Constants of Darveaux model[cycle/psi^(K_2)]
K_2	Constants of Darveaux model	K_3	Constants of Darveaux model[cycle/psi^(K_4)]
K_4	Constants of Darveaux model	l	Distance between two cracks
ω	Relative size of interfacial crack	A	Cross-sectional area of thermoelectric arm[m^2]
R_0	Initial device resistance[Ω]	R_a	Device resistance after damage[Ω]
ρ	Electrical resistivity[Ω · m]	t_0	Thermal cycle [s]

REFERENCES

Ji Li, Shihao Liu, Shilin li, et al., 2020. PCR Instrument Temperature Control System Based on Multimodal control. 2020 Chinese Control And Decision Conference (CCDC).

Masoud Madadelahi, Rahul Agarwal, Sergio O, et al.,2024. A roadmap to high-speed polymerase chain reaction (PCR): COVID-19 as a technology accelerator. Biosensors and Bioelectronics 246, 115830.

X. Zhou, C. Zhang, H. Jiang, et al., 2018. A temperature control system for polymerase chain reaction machine for cell-systematic evolution of ligands by exponential enrichment-based automated screening of nucleic acid aptamers, Nanosci. Nanotech. Let. 10 596–602.

J.J. Chen, I. Hsiang Hsieh, 2016. Using an IR lamp to perform DNA amplifications on an oscillatory thermocycler, Appl. Therm. Eng. 106, 1–12.

Jingjing Qian, Qinming Zhang, Meng Lu, 2023. Integration of on-chip lysis and paper-based sensor for rapid detection of viral and exosomal RNAs. Biosensors and Bioelectronics 226, 115114

Zhilin Liu, Dongfang Sun, Bin Jiang, et al., 2023. Continuous gradient temperature control of microfluidic chip based on thermoelectric cooler. Applied Thermal Engineering 234, 121277

Weisong Ling, Wei Zhou, Jiarong Cui, et al., 2023. Experimental study on the heating/cooling and temperature uniformity performance of the microchannel temperature control device for nucleic acid PCR amplification reaction of COVID-19. Applied Thermal Engineering 226, 120342

Mcpherson J W., 2010. Reliability physics and engineering. Springer, Cham.

Towashiraporn P, Gall. K, Subbarayan G, et al., 2004. Power cycling thermal fatigue of Sn–Pb solder joints on a chip scale package. International Journal of Fatigue 26(5), 497-510.

M. T. Barako, Park. W. Marconnet, A M, et al., 2013. Thermal cycling, mechanical degradation, and the effective figure of merit of a thermoelectric module. Journal of Electronic Materials 42(3), 372-381.

E. Hatzikraniotis, Zorbas, K T, Samaras I, et al., 2010. Efficiency study of a commercial thermoelectric power generator (TEG) under thermal cycling. Journal of Electronic Materials 39(9), 2112-2116

S. Harish, D. Sivaprahasam, B. Jayachandran, 2021. Performance of bismuth telluride modules under thermal cycling in an automotive exhaust thermoelectric generator. Energy Conversion and Management 232, 113900.

Dimitri Tatarinov, Wallig. Daniel, Bastian, Georg., 2012. Optimized characterization of thermoelectric generators for automotive application. Journal of Electronic Materials 41, 1706-1712

Xue Wang, Hongchao Wang, Wenbing Su, et al., 2022. U-type unileg thermoelectric module: A novel structure for hightemperature application with long lifespan. Energy 238, 121771.

Cui, Y J, Wang, B L, Wang, K F, et al., 2022. An analytical model to evaluate the fatigue crack effects on the hybrid photovoltaic-thermoelectric device. Renewable Energy 182, 923-933.

Yongjia Wu, Tingzhen Ming , Xiaohua Li, et al., 2014. Numerical simulations on the temperature gradient and thermal stress of a thermoelectric power generator. Energy Conversion and Management 88, 915-927.

P. Wang, J.E. Li, B.L. Wang, et al., 2019. Lifetime prediction of thermoelectric devices under thermal cycling. Journal of Power Sources 437, 226861.

M. T. Barako, Woosung Park, A. M. Marconnet, et al., 2012. A reliability study with infrared imaging of thermoelectric modules under thermal cycling. 13th InterSociety Conference on Thermal and Thermomechanical Phenomena in Electronic Systems, CA, USA, San Diego, 86-92

E.H. Wong, W. D. Van Driel, A. Dasgupta, et al., 2016. Creep fatigue models of solder joints-A critical review. Microelectronics Reliability 59, 1-12.

Robert Darveaux, 2000. Effect of Simulation Methodology on Solder Joint Crack Growth Correlation. In: 2000 Proceedings. 50th Electronic Components and Technology Conference, IEEE, Las Vegas, 1048-1058.

D. Bhate, D. Chan, G. Subbarayan, 2008. A Nonlinear Fracture Mechanics Approach to Modeling Fatigue Crack Growth in Solder Joints. Journal of Electronic Packaging 130, 021003-1.

Snyder, G Jeffrey; Toberer, Eric S., 2008. Complex thermoelectric materials[J]. Nature Materials 7, 105-114

Zhi-wei Gao, 2020. PCR instrument temperature control system, Xi'an University of Technology, Xi'an, China.

Fakun Zhang, 2018. The Development of Amplification Unit of Real Time Fluorescence Quantitative PCR, Changchun University of Science and Technology, Changchun, China.

DOI: 10.18462/iir.thermag.2024.0002

NAVIGATING THE HEAT MAZE: A SHOWCASE TUTORIAL OF TCCBUILDER SOFTWARE

Katja KLINAR[(a)], Katja VOZEL[(a)], Andrej KITANOVSKI [(a)]

[(a)] University of Ljubljana, Faculty of Mechanical Engineering
Ljubljana, 1000, Slovenia, lahde@fs.uni-lj.si

ABSTRACT

Thermal management, i.e., controlling the temperature, intensity, and direction of heat flow between components in a system, is critical for high energy efficiency, optimized performance, high reliability, and safety.We wanted to take the progress of novel thermal management techniques a step further, which led us to the development of the world‘s first open-source thermal control circuits simulation tool, TCCbuilder. The basis for such a tool is a large database of suitable materials and thermal control elements(thermal switches, thermal diodes, etc.). Using various available TCCbuilder‘s templates or from TCCbuilder‘s library in the library of the TCCbuilder, users can design their own thermal control circuit, test its operation, and evaluate the results. Among other options, there is also the possibility to design a caloric device, which is presented step by step in this presentation.The toolcan also serve as a foundation for knowledge exchange in the field of thermal management.

Keywords: refrigeration, heat pump, energy conversion, heat transfer, thermal management, thermal diode, thermal switch, caloric

1. INTRODUCTION

The limitations of conventional thermal management methods become apparent when trying to meet the complex thermal control requirements of modern systems. Especially for smaller systems with higher power densities, conventional approaches are no longer effective. Effective thermal management that includes control of temperature, intensity and direction of heat flow between components, is critical for high energy efficiency, optimized performance, reliability, and safety, and this can be achieved by using thermal control elements. Thermal control elements, e.g. thermal diodes, thermal switches, thermal regulators, and others (Fig. 1),show potential for advanced and optimized thermal management(Klinar et al., 2021; Klinar & Kitanovski, 2020; Swoboda et al., 2021; Wehmeyer et al., 2017; Wong et al., 2021). Besides experimental evaluation, numerical analysis is also crucial for further development and evaluation. Silva et al. (2018) presented the Heatrapy tool, which was the first tool that enabled simulation of thermal switches.

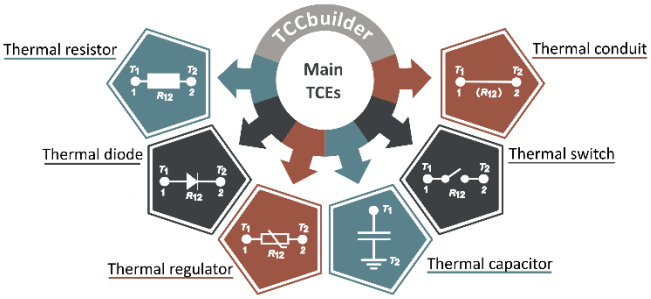

Figure 1: Six main thermal control elements.

In response to theabove-mentioned challenges and broader development of thermal control elements, we have launched a project whose goal is to provide researchers with a tool for developing novel thermal management techniques. And so, we introduce the world's first open-source thermal control circuit simulation tool with graphical user interface, TCCbuilder(Vozel et al., 2024). TCCbuilder is not only a state-of-the-art tool for researchers, but also serves as a foundation for knowledge sharing in the field of thermal management.

This paper describes the step-by-step process of designing thermal control circuits using various elements available in the TCCbuilder. Users can create and test their own thermal control circuits, including the design of caloric devices. Input data (e.g., temperature- and external field-dependent thermal properties) can be found in the TCCbuilder‘s library of materials. However, the user can also enter their own data. The results of simulation (system properties and time evolution of the system with respect to temperature) are exported to a text file in a format that can be imported into standard editors for further analysis.

The tool is based on an comprehensive database of materials and thermal control devices (thermal switches, thermal diodes, etc.) compiled from extensive literature searches and contributions from fellow researchers. The final version is scheduled for release in 2024 and can beaccessed at www.tccbuilder.org. This platform is expected to revolutionize thermal management practices and facilitate innovation in thermal control circuit design and optimization.

TCCbuilder is an open-source simulation tool for building thermal control circuits (TCCs) consisting of various thermal control elements (TCEs, see Figure 1). TCCbuilder has an integrated library of materials and their (thermal) properties that can be used in simulations. The heat transfer model in TCCbuilder is based on Fourier‘s law of heat conduction, discretized with finite volume method and backward-difference scheme.

2. SHOWCASE TUTORIAL

The step-by-step tutorial is based on the analysis published by Klinar et al. (2022). It evaluates, as an example, a caloric embodiment comprising a magnetocaloric material (MCM) gadolinium, sandwiched between two thermal switches, made of a ferrofluid, embodied between a heat source and a heat sink (Fig. 2, left). The simulation is divided into several stages, where each stage corresponds to a process in the Brayton thermodynamic cycle. All four Brayton thermodynamic processes repeat until the quasi-steady-state is reached (Fig. 2, right).To use the software please visit www.tccbuilder.org.

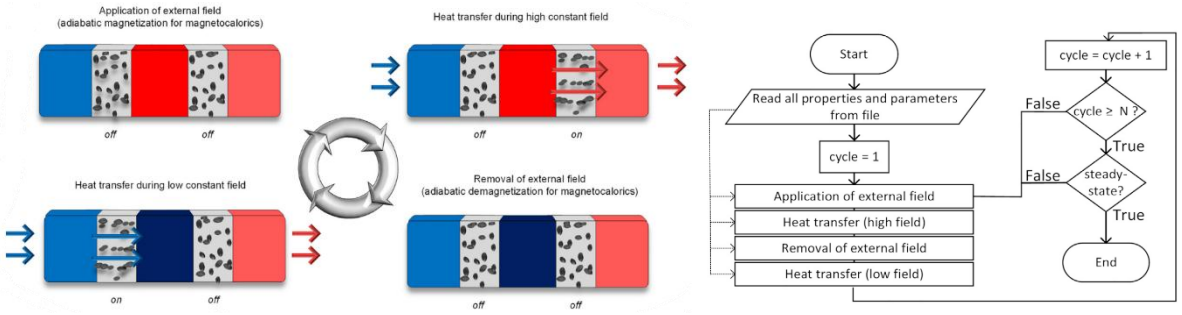

Figure 1: Left) Embodiment of a magnetocaloric device and presentation of the single-stage non-regenerative Brayton thermodynamic cycle. Right) Flowchart of the numerical model for the evaluation of a magnetocaloric device. Adapted from Klinar et al. (2022).

We start by setting the dimensionality of our model to 1D and the scale of 20 microns in the upper right corner (Fig. 3, left). Then we can draw the thermal control elements (TCEs) by selecting them from the “Draw” menu in the upper left corner and clicking and dragging on the canvas (Fig. 3, left).For each drawn TCE, we can open the edit dialog by right-clicking on the element(Fig. 3, right). The following properties can be set: name, index in thermal control circuit (TCC), number of control volumes, color, length, contact resistances and thermal properties. For almost all TCEs, the material the TCE is made of can also be set.

In this tutorial, the TCC is a magnetocaloric cooling device, where the first and the last TCEs are thermal resistors representing a heat source, and a heat sink, respectively. In the middle, there is a thermal capacitor made of a magnetocaloric material (Fig. 4, left). The remaining two TCEs are thermal switches that control the heat flow through the device.

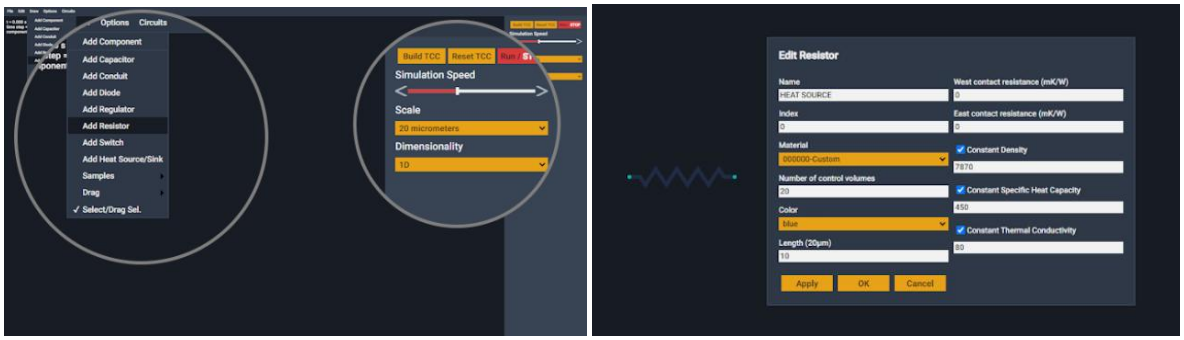

Figure 2: Left) Select the dimensionality of the model and draw TCC. Right) Define properties of each TCE.

The TCEs are named HEAT SOURCE, SWITCH1, MCM, SWITCH 2, and HEAT SINK, respectively.When we have finished drawing the TCC, we can set the simulation parameters by clicking on ―Build TCC" in the upper right corner (fig. 4, right). A startup dialog will open where we can set the time step, start temperature, boundary conditions and cyclic operation of the TCC. In our case, the time step is 0.1 ms, and the ambient temperature is 293 K. There is an adiabatic boundary condition at the left edge and convection at the right edge of the device.

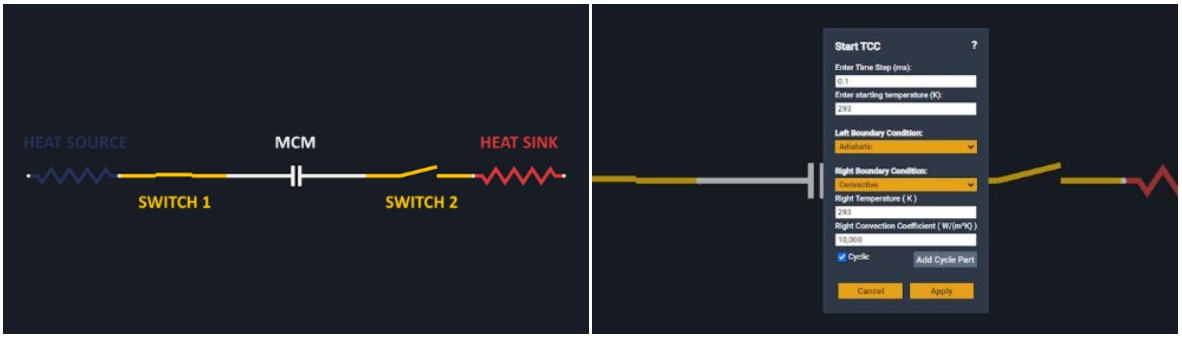

Figure 3: Left) Schematic representation of TCC of magnetocaloric device in TCCbuilder. Right) Setting the boundary conditions.

In cyclic operation, as in the magnetocaloric cooling device, cycle parts must be defined (Fig. 5, left). For each selected cycle part, the components that are affected during that part can be added to the part. In the case of the magnetic field change, we can only add the capacitor named MCM since it is the only magnetocaloric TCE in the TCC. We set the magnetic field strength to 1 T. The cycle parts of our magnetocaloric device include instantaneous on/off switching of the magnetic field, instantaneous switching of the two heat switches, and two heat transfer processes with a duration of 0.02 s (operation at 20 Hz). After all cycle parts have been set and listed in a column in the right part of the canvas (Fig. 5, right), the simulation can be started by clicking the ―Apply" button.

Figure 4: Setting the cyclic operation of the TCC.

During the simulation, we can change the speed in the upper right corner (up to the speed limit of the processor; please note that this does not change the time step) and also pause the simulation by clicking the ―Run/STOP" button. Pausing the simulation when the MCM is magnetized, in our case the left switch must be off and the right switch on, which can be corrected by clicking the switches if necessary.On the other hand, if the simulation is paused when the MCM is demagnetized, in our case the left switch must be on and the right switch must be off. This ensures that the temperature of the heat source decreases over time. In this way, the maximum temperature span of the device at zero cooling power is simulated.

Fig. 6 shows both heat transfer processes: when MCM is heated due to magnetocaloric effect, thermal switch on its left is switched off, while thermal switch on its right is switches on, allowing heat flux from MCM towards the heat sink (Fig. 6, left). The situation is reversed in the heat transfer process when MCM is cooled due to the magnetocaloric effect, where thermal switch on its left is switched on, thus allowing heat flux from the heat source to the MCM (Fig. 6, right). The graph below shows the temperature of all the control volumes in the components.

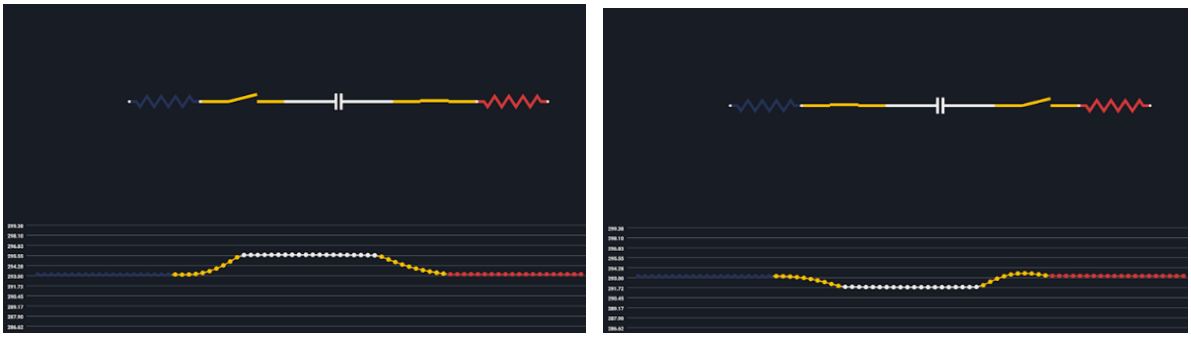

Figure 5: Left) Heat transfer process after the magnetization process (MCM is heated due to the magnetocaloric effect). Right) Heat transfer process after demagnetization (MCM is cooled due to the magnetocaloric effect).

The simulation time is logged in the upper left corner of the canvas. In our case, the steady state, where the temperature at the left edge stops decreasing, is reached after about six seconds. We can stop and export the simulation by selecting one of the options from the —File” menu. If we want to review the temperature evolution of our device in a custom editor (e.g. Notepad or Excel), we select —Save Report As”. The file with the simulation results isready for download in a few seconds.The results file contains information about the TCEs in the TCC and the temperature evolution of all control volumes of the TCC (Fig. 7, right).

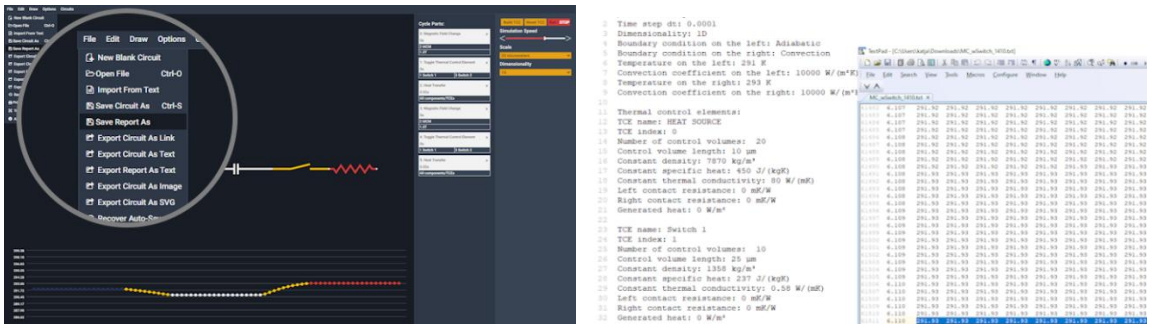

Figure 7: Left) Exporting the results. Right) Exported results file.

3. CONCLUSIONS

In this tutorial, we demonstrated how to utilize the open-source TCCbuilder software for the design of various thermal control circuits using assorted templates for the thermal control elements. This software also includes a comprehensive materials and thermal control elements library with over 100 options suitable for thermal managementapplications. As previously noted in the Introduction, TCCbuilder's use extends beyond (magneto)calorics, facilitating the creation and assessment of diverse thermal control circuits. Over time, we plan to expand the software's capabilities by adding new elements, materials, and features, further enhancing its versatility. We aim to make TCCbuilder an indispensableresource for researchers and students. We encourage those interested in using or contributing to the development of the software and its materials library to contact us.

Figure 6: QR code to access TCCbuilder website.

ACKNOWLEDGEMENTS

The authors also acknowledge the financial support of the Slovenian Research Agency for the research project no. J7-3148: TCCbuilder: An open-source simulation tool for thermal control circuits and the core research program no. P2-0223.

REFERENCES

Klinar, K., & Kitanovski, A. (2020). Thermal control elements for caloric energy conversion. *Renewable and Sustainable Energy Reviews*, *118*, 109571. https://doi.org/10.1016/j.rser.2019.109571

Klinar, K., Swoboda, T., Muñoz Rojo, M., & Kitanovski, A. (2021). Fluidic and Mechanical Thermal Control Devices. *Advanced Electronic Materials*, *7*(3), 2000623. https://doi.org/10.1002/aelm.202000623

Klinar, K., Vozel, K., Swoboda, T., Sojer, T., Muñoz Rojo, M., & Kitanovski, A. (2022). Ferrofluidic thermal switch in a magnetocaloric device. *IScience*, *25*(2), 103779. https://doi.org/10.1016/j.isci.2022.103779

Silva, D. J., Amaral, J. S., & Amaral, V. S. (2018). Heatrapy: A flexible Python framework for computing dynamic heat transfer processes involving caloric effects in 1.5D systems. *SoftwareX*, *7*, 373–382. https://doi.org/10.1016/j.softx.2018.09.007

Swoboda, T., Klinar, K., Yalamarthy, A. S., Kitanovski, A., & Muñoz Rojo, M. (2021). Solid-state thermal control devices. *Advanced Electronic Materials*, *7*(3), 2000625.

Vozel, K., Klinar, K., Petelin, N., & Kitanovski, A. (2024). *Tccbuilder: open source tool for simulation and analysis of thermal control circuits*. https://tccbuilder.org/

Wehmeyer, G., Yabuki, T., Monachon, C., Wu, J., & Dames, C. (2017). Thermal diodes, regulators, and switches: Physical mechanisms and potential applications. *Applied Physics Reviews*, *4*(4). https://doi.org/10.1063/1.5001072

Wong, M. Y., Tso, C. Y., Ho, T. C., & Lee, H. H. (2021). A review of state of the art thermal diodes and their potential applications. *International Journal of Heat and Mass Transfer*, *164*. https://doi.org/10.1016/j.ijheatmasstransfer.2020.120607

DOI: 10.18462/iir.thermag.2024.0003

ELASTOCALORIC SOLID-STATE REFRIGERATION DEVICE BASED ON NATURAL RUBBER: COMPARISON OF MATERIALS ON A SINGLE STAGE SETUP

Marianne SION [(a), (b), (c)], Gildas COATIVY [(d)], Atsuki KOMIYA [(a), (c)], Gaël SEBALD [(a)], Shihe XIN [(b)]

[(a)] ELyTMaX IRL 3757, CNRS, Univ. Lyon, INSA Lyon, Centrale Lyon, Université Claude Bernard Lyon 1, Tohoku University, Sendai, Japan

[(b)] CETHIL UMR5008, F-69621, INSA-Lyon, CNRS, Université Claude Bernard Lyon 1, Villeurbanne, France

[(c)] Institute of Fluid Science, Tohoku University, Sendai, Japan

[(d)] Univ Lyon, INSA Lyon, LGEF, EA682, F69621, Villeurbanne, France

ABSTRACT

This work presents an elastocaloric cooling device, tested with various natural rubber (NR) samples. The device is based on a 4-step process: stretching, contact with the heat sink, un-stretching, and finally contact with the heat source. A comparison of different types of natural rubber films is reported, in order to investigate whether the NR film used has a strong impact on the cooling performances. It was shown that the NR films exact composition has a small impact on the elastocaloric effect exhibited by the rubber, whereas the thickness of the NR films is the main parameter for cooling power and the effectiveness of the heat transfer between NR film and heat exchangers.

Keywords: Natural rubber, Elastocaloric effect, Refrigeration device, Cooling power, Temperature span

1. INTRODUCTION

Compressed gases, such as freons, are the most used technology for refrigeration systems. This raises questions about their toxicity, efficiency and potential environmental impact. The research on alternative refrigeration methods may bring solutions that challenge the current trade-off of vapor compression-based system between performance and above-mentioned drawbacks. One of them is to use caloric materials [Crossley (2015), Moya (2014), Moya (2020)], that present an entropy variation, and so a temperature change, when submitted to respectively a magnetic field [de Oliveira (2010), Pecharsky (1999)], an electric field [Ma (2017), Wang (2020)], a pressure [Mañosa (2010)] or a uniaxial stress [Chauhan (2015), Tušek (2015), Wu (2017), Sion (2024)]. Natural rubber has a high elastocaloric effect and thus caught attention to design an elastocaloric refrigeration device. The elastocaloric effect occurs when the material is mechanically loaded and unloaded [Sion (2024)]. Two types of systems for elastocaloric metals or polymers for refrigeration were studied according to the state of the art: the regenerative systems using solid-liquid heat exchangers [Engelbrecht (2017), Sebald (2020), Tušek (2016)] and single stage systems using solid-solid heat exchangers [Greibich (2021), Ossmer (2015), Ossmer (2016)]. Most works focused on Shape Memory Alloys (SMA), such as Ni-Ti alloys, showing very high elastocaloric effect, leading to devices exhibiting an absolute cooling power being between the Watt to the hundreds of Watt, but also requires very high driving forces [Torello (2022)]. On the contrary, natural rubber require much smaller force, but its very low thermal conductivity can significantly constraint the geometry of the devices [Torello (2022)]. In previous work, a 4-step cooling process experimental setup [Sion (2024)] was proposed and tested under various contact and stretching times. In this work, it is presented a comparison between various rubber compositions using the same device. The cooling performances (temperature span, cooling power) are presented and discussed.

2. EXPERIMENTAL METHOD

2.1. 4-step principle

A 4-step basis experimental setup is shown on Figure 1. First, the NR is stretched to an extension ratio $\lambda = 6$, thus producing an increase in temperature. During the second step, a contact with the Hot Heat Exchanger (HHEX) is

made, leading to a heat transfer from the NR to the HHEX. After a chosen contact (heat transfer) time, the HHEX is moved back. Then the rubber is released until it reaches an extension ratio of λ = 4, leading to a decrease in temperature. Finally, the Cold Heat Exchanger (CHEX) is put in contact to the NR film to transfer the heat from the CHEX to the NR, removing the CHEX after the same contact (heat transfer) time as HHEX. Then the 4-steps cycles are repeated, inducing an increase of the temperature span (ΔT_{span}) between the two exchangers.

2.2. 4-step experimental device description

A single stage experimental setup has been developed (Figure 1). The setup consisted of 2 actuators, which were placed perpendicularly to each other to either stretch the NR or move the HHEX and CHEX in contact with the NR [Sion (2024)]. A metal block with cooling fans constituted the HHEX, which was stabilized at ambient temperature. A thin stainless-steel plate, constituting the CHEX, was thermally insulated on one side using a polystyrene block. Electrical flat resistors attached to CHEX were used to determine the cooling power (PC). Different sensors were implemented to measure the force, displacement, heat flux and various temperatures.

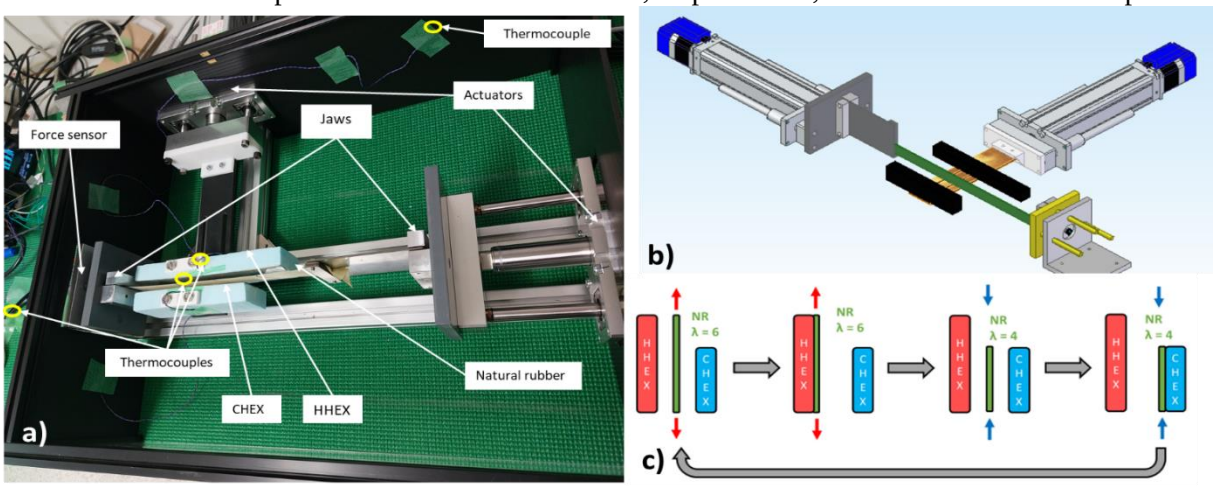

Figure 1: 4-step experimental setup. (a) Complete experimental setup; (b) 3D design of the experimental setup (c) 4-step refrigeration device principle

2.3. NR film characterization

Nine different natural rubber samples were purchased from three different companies (Elanova, Sumitomo and Xinyinte Rubber Products). First, 4 different compositions of natural rubber of thickness 1 mm were prepared and labelled EL2 to EL4. From another supplier, 3 samples with a unique composition (labelled SU) but three different thicknesses (0.5 mm, 1 mm, 2 mm) were prepared. Finally, the last two samples (NR) were prepared in two different thicknesses (0.4 mm and 0.6 mm). The composition of the EL samples is shown in the Table 1, corresponding to custom-made compositions based on state-of-the-art references [Gros (2015), Tosaka (2004), Candau (2014)]. SU samples and NR samples are commercial natural rubber grades, of unknown exact composition.

The experimental crosslink density of the rubber chains, ν has been determined by fitting the experimental mechanical curves with the Eq.1 formula [Candau (2021), Sebald (2023)] with σ the engineering stress, R the gas constant, λ the extension ratio and T the temperature.

$$\sigma = \nu RT \left(\lambda - \frac{1}{\lambda^2}\right) \qquad Eq.1$$

The samples had been cut in a dog-bone shape by a CO_2 laser cutting, in order to ensure a proper and homogeneous stress as well as a firm grip with the fixation jaws. It also minimized the irregularities of the cutting line, prone to initiate cracks.

The adiabatic temperature span ΔT_{adiab} was measured for the different, previously trained, samples. The training of the samples consists of a first series of cycles, such as described in Figure 1 (c), from an extension ratio of 1 to 5,

and then a second series of cycles from 1 to 6.3. After those cycles, the sample is put back to an extension ratio of 1 and, after some waiting time for the sample to get rid of any elastic deformation, the initial length of the material was adjusted, to accommodate for any residual deformation. Following this training, the adiabatic temperature measurement was made using an IR camera (Optris Xi 400). The extension ratio range was from $\lambda = 4$ to $\lambda = 6$ at frequency $f = 0.16$ Hz, using a rectangular waveform. The adiabatic temperature has been given for the EL samples in Table 1.

	Natural Rubber (phr)	***Stearic acid (phr)***	***ZnO (phr)***	***CBS (phr)***	***Sulfur (phr)***	***6PPD (phr)***	***Heating time (min)***	**Curing temperature (°C)**	**ν expected (10^{-4} mol/cm^3)**	**ν experimental (10^{-4} mol/cm^3)**	**Adiabatic temperature (°C)**
EL2	100	2	1	1.5	2.25	-	25	140	1.5	1.56	4.1
EL3	100	2	1	0.75	1.125	-	35	140	1	1.38	4.0
EL4	100	2	1.5	1.9	1.2	1	15	160	1.5	1.31	3.5
EL5	100	2	1.5	1.3	0.8	1	15	160	1	1.04	3.8

Table 1: ELANOVA samples compositions, curing conditions, and resulting crosslink density N.

2.4. Experimental test campaign

The nine different natural rubber samples were tested using the 4-step experimental setup, as a way to design a cooling proof a concept. In the following, the samples will be named according to their composition (EL2 to EL5, SU and NR), followed by the thickness in brackets. The influence of the contact (heat transfer) time was studied in order to establish its impact on the performances of the system. Four contact (heat transfer) times were tested (1 s, 3 s, 5 s and 7 s). The samples were tested using a rectangular waveform. Applying in all cases the same stretching time of 0.3 s, the period of the entire cycle varied from 3.6 s (f=0.3Hz) to 15.6 s (f=0.06 Hz). The system being run until the stabilization of the CHEX temperature for each contact (heat transfer) time, and for each thermal load in the CHEX, each sample was subjected to a total of 330~1350 cycles.

2.5. Methodology for performance calculation

Different sensors implemented in the experimental setup allowed to determine different useful parameters and give a better understanding of the system performances. Details about the sensors and calculations have been given in previous work [Sion (2024)]. The instantaneous mechanical power P_{mech} (Eq.2) in the setup was obtained by the measurement of the force and displacement. The cooling power PC (Eq. 3) was obtained by powering resistors in the CHEX. The COP (Eq.4) was determined by the ratio between PC and P_{mech}. The following formulas were used:

$$P_{mech} = f \int_0^{\frac{1}{f}} F \frac{\partial u}{\partial t} dt \qquad Eq.2$$

F, u, and $\frac{1}{f}$ are respectively the mechanical force of the actuator, the displacement and the period of the cycle, f being the frequency.

$$PC = RI^2 \qquad Eq.3$$

with R and I being the resistance value and the applied DC current

$$COP = \frac{PC}{P_{mech} + P_{actuator\,2}} \qquad Eq.4$$

$P_{actuator\,2}$ being the average power of actuator moving the exchangers, over one cycle. The force between the exchangers and the NR was negligible (<0.1N) as the actuator was only used to put alternatively the HHEX and CHEX in contact with the NR. As a consequence, $P_{actuator\,2}$ has been neglected for the COP calculation.

3. RESULTS

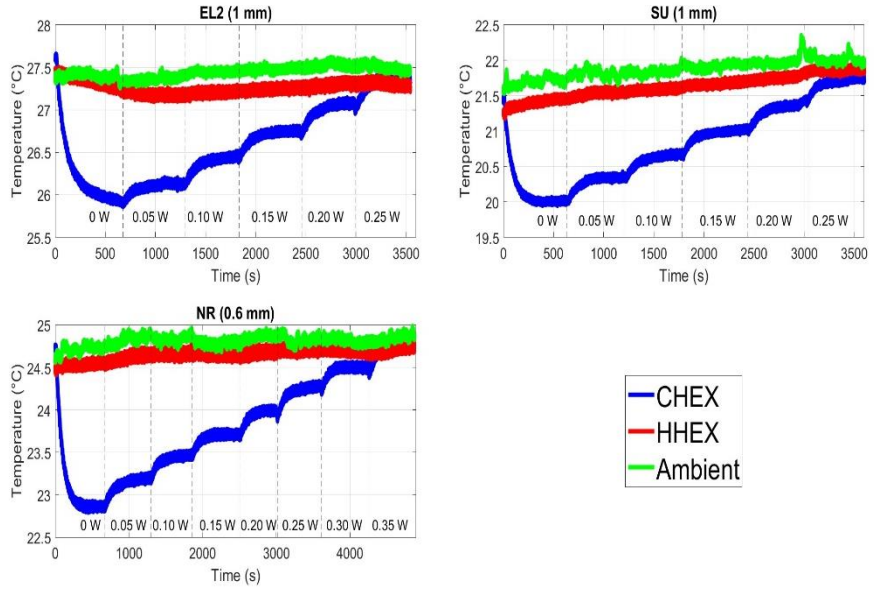

Figure 2: Temperature profile of EL2 (1 mm), SU (1 mm) and NR (0.6 mm) for a 1s contact (heat transfer) time. The plateaus show the increase of injected heating power (50mW) for

Figure 2 presents the temperature profile of three different natural rubber film, EL2 (1 mm) in the top left side, SU (1 mm) in top right side and NR (0.6 mm) at the bottom, under the same condition for a contact (heat transfer) time of 1s. The different graphs show the ambient temperature, the HHEX temperature and the CHEX temperature. The HHEX temperature has been stabilized during the whole experiment by using forced air convection. The temperature of the CHEX decreased until it reached a stabilized plateau. Then the heat source in the CHEX was increased by steps of 50 mW, until the temperature reached back that of HHEX (temperature span cancellation), giving the maximum cooling power (PC_{max}) [Sion (2024)]. The maximum cooling power PC_{max} was found to be 250 mW for both the samples EL2 (1 mm) and SU (1 mm), and 350 mW for NR (0.6 mm).

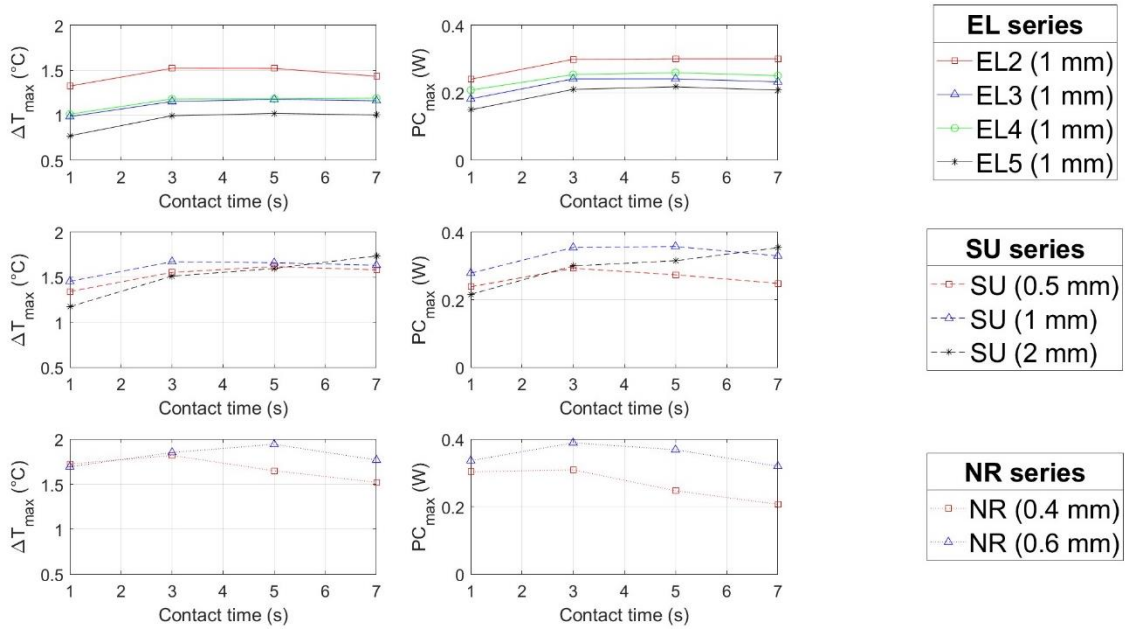

Figure 3: Maximum temperature span ($\Delta T_{span\ max}$) and maximum cooling power (PC_{max}) for different contact (heat transfer) time

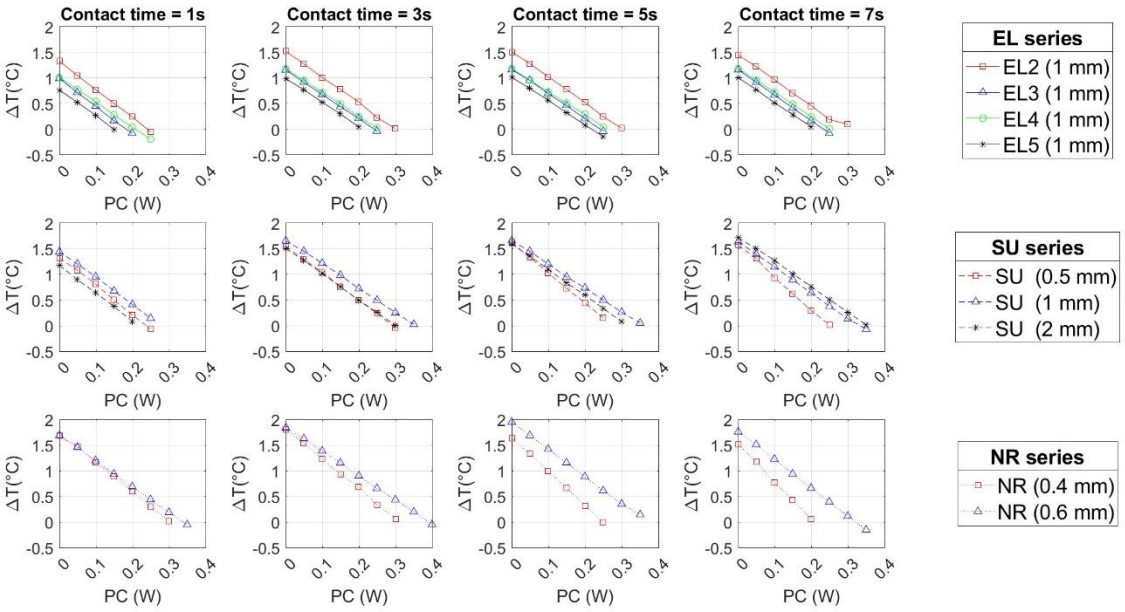

Figure 4: Temperature span (ΔT_{span}) as a function of cooling power (PC) for different contact (heat transfer) time (1, 3, 5, 7s). Each column corresponds to one specific contact (heat transfer) time.

Figure 3 shows the maximum temperature span ($\Delta T_{span\ max}$) on the left side, as well as the maximum cooling power (PC_{max}) on the right side. It can be seen that for all samples, the $\Delta T_{span\ max}$ ranged between 1 and 2°C, whereas the PC_{max} was between 0.2 W and 0.4 W. The EL samples revealed the influence of the network chain density on the $\Delta T_{span\ max}$ and PC_{max}. For the EL2 which has the highest crosslink density (ν=1.56 10-4 mol/cm3) $\Delta T_{span\ max}$=1.5°C and PC_{max}= 0.30W while for EL5 (with the lowest crosslink density ν=1.04 10-4 mol/cm3) $\Delta T_{span\ max}$=1.0°C and PC_{max}= 0.20W. For intermediate cross-linking densities, the values lie between the two. Besides, the contact (heat transfer) time was found to have a limited effect with an optimal value of 3 s for all cases.

Figure 4 shows the ΔT_{span} as a function of PC, for the nine different rubber samples, for all tested contact (heat transfer) times (1, 3, 5, 7s). Each column shows a specific contact (heat transfer) time and each line shows a specific set of NR samples. It can be seen that for rubber samples with the same thickness of 1 mm, the ΔT_{span} ranged from 1 to 1.5°C. These samples had a maximum cooling power of 0.3 to 0.35 W. For the other thickness (0.4, 0.5, 0.6 and 2 mm), similar ΔT_{span} and PC were found, with a maximum of 2°C temperature span and 0.4 W of cooling power for NR (0.6 mm). For all samples, the results were rather similar but it seemed that the slopes of the curves are dependent on the thickness.

4. DISCUSSION

It was shown that for the nine different rubber tested, the obtained ΔT_{span} and PC_{max} remained of similar values. The average ΔT_{span} was 1.5°C with a standard deviation of 0.3°C, whereas the average PC_{max} was 0.3W with a standard deviation of 0.05W. It should be noted however that the optimum contact (heat transfer) time globally increased with the thickness of the tested samples, suggesting a compensation between the absorbed heat at each cycle from CHEX and the cycle period time, leading to similar cooling powers.

The ΔT_{abiab} of the NR samples was around 4°C, whereas the maximum temperature obtained during experiment was limited to 2°C or less, probably because of the thermal losses of the CHEX as well as the generation of a gradient within the NR film. More details can be found in our previous work [Sion (2024)]. Another explanation could be the thermal mass of the different elements composing the exchangers, acting as a heat sink and preventing the generation of a higher ΔT_{span}. Also, the material being continuously in contact with the ambient air, additional thermal losses may decrease the temperature difference between the NR film and the heat exchangers.

There may be two ways to enhance the performances of the experimental setup: decrease the thermal mass of the

exchangers, which seems to be difficult to achieve since the exchangers are as small as possible and insulated, or increase the NR elastocaloric effect. From the state of the art, the elastocaloric effect of polymers (through notably the stress-induced crystallization) might be enhanced, like polymers with higher uniformity in the chain-length [Zhang (2022)], although the adiabatic temperature change is remaining of similar value for natural rubber or even rubber blends [Candau (2023)]. Another idea could be to improve the thermal conductivity of NR, using fillers as for the case of electrocaloric material [Zhang (2015)].

Regarding the cooling power, the values were compared to the ideal cooling power in the absence of thermal losses. A coefficient has been defined in Eq. 5 to check the Heat transfer effectiveness (HT_{eff}) [Sion (2024)], as the ratio between the actual cooling power and the ultimate theorical cooling power. The ultimate cooling power is determined as follows, in the assumption of a full heat transfer between NR and the heat exchangers, and the absence of thermal losses:

$$\boldsymbol{PC_{ult} = {Q_{ult}}/{\frac{1}{f}}} \quad \text{where} \quad \boldsymbol{Q_{ult} = \rho C_p V \Delta T_{adiab}}$$

$$\boldsymbol{HT_{eff} = PC_{max} \,/\, PC_{ult}} \qquad Eq.5$$

With ρ, C_p, ΔT_{adiab} and V are respectively the density of NR, heat capacity, adiabatic temperature change and volume and PC_{max} is the maximum value of cooling power.

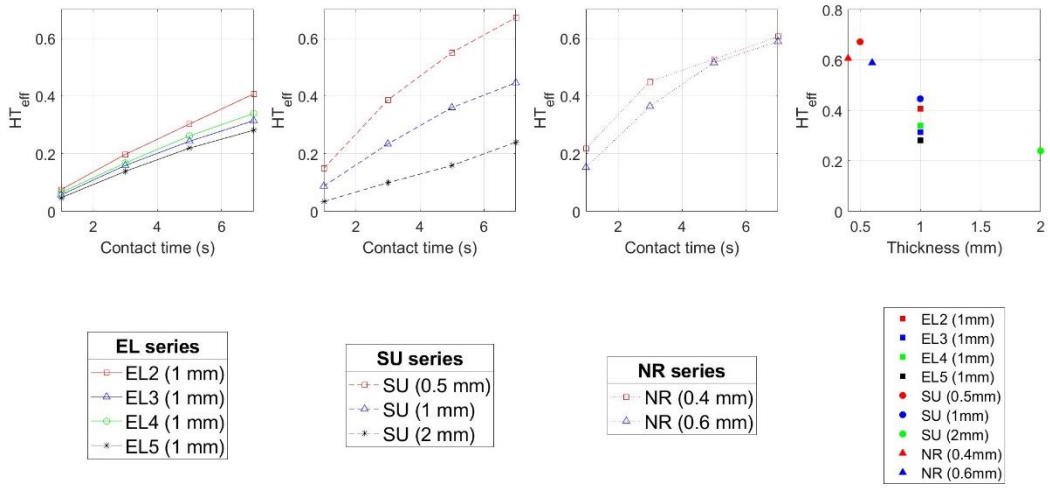

Figure 5: Heat transfer effectiveness (HT_{eff}) as a function of contact (heat transfer) time for all nine kind of NR samples; HT_{eff} as a function of thickness for 7s of contact

Figure 5 presents the Heat transfer effectiveness of the different NR films. For the EL2 to EL5 samples, the maximum HT_{eff} is ranging from 25% to 40%, the results being very similar for all the different compositions. For the SU samples, the maximum HT_{eff} range was much larger, from 20 % to 65%, showing that the thickness indeed had a strong impact on the heat transfer. For the NR samples the maximum HT_{eff} reached almost 60%. On the last graph on the right of Figure 5 is shown the dependence of the heat transfer effectiveness with the thickness, for a contact (heat transfer) time of 7s, confirming a distinct decreasing trend. It was observed that even with such a high contact (heat transfer) time, the heat exchange with the NR samples remained partial. This suggested also that a thinner sample was preferable as it decreased the heat exchange time constant.

The determination of the COP (under the condition of maximal power and $\Delta T_{span} = 0$) has been performed for the different types of NR samples and is given in Table 2. The COP was defined as the ratio between the PC_{max} and the mean mechanical power P_{mech} [Sion (2024)]. The energy released during the unloading of the NR is slightly lower than the energy absorbed during loading, leading to an average mechanical power much lower than the maximum of the peaks values. The peaks appear to have an almost identical value, confirming that the elastic energy get almost fully recovered during the unloading step. The highest COP_{max} was found to range from 5.9 for the sample EL2 (1 mm) to more than 20 for the SU (0.5 mm) sample, revealing significant differences for the mechanical losses.

Contact (heat transfer) time (s)	*1s*	*3s*	*5s*	*7s*	*1s*	*3s*	*5s*	*7s*	*1s*	*3s*	*5s*	*7s*
Name	**COP_{max}**				**PC_{max} (W)**				**$\Delta T_{span\ max}$ (°C)**			
NR (0.4 mm)	9.6	15	13	12	0.30	0.30	0.25	0.20	1.7	1.8	1.6	1.5
SU (0.5 mm)	14	24	15	17	0.25	0.30	0.25	0.25	1.3	1.6	1.6	1.6
NR (0.6mm)	2.5	6.1	7.1	11	0.35	0.40	0.35	0.30	1.7	1.8	2.0	1.8
EL2 (1 mm)	1.1	2.7	3.3	5.9	0.25	0.30	0.30	0.30	1.3	1.5	1.5	1.4
EL3 (1 mm)	1.6	3.8	5.5	8.0	0.20	0.25	0.25	0.25	1.0	1.1	1.2	1.2
EL4 (1 mm)	1.5	3.7	5.4	8.0	0.20	0.25	0.25	0.25	1.0	1.2	1.2	1.2
EL5 (1 mm)	1.1	3.3	6.0	7.3	0.15	0.20	0.20	0.20	0.8	1.0	1.0	1.0
SU (1 mm)	1.1	3.8	5.5	8.7	0.25	0.35	0.35	0.35	1.4	1.7	1.7	1.6
SU (2 mm)	0.4	1.9	2.8	5.1	0.20	0.30	0.30	0.35	1.2	1.5	1.6	1.7

Table 2: COP_{max}, PC_{max} and $\Delta T_{span\ max}$ values for all nine types of NR tested

5. CONCLUSION

This work has shown that for all the nine types of natural rubber, the performances were found to exhibit small differences only. The observed maximum temperature span was typically 1.5°C and the maximum cooling power 0.3 W. The optimum contact (heat transfer) time observed was about 3s for all samples. The maximum COP observed was about 24 for SU (0.5 mm), at a time contact of 3s. The COP varied a lot with the thickness of the NR film, from >20 for 0.5 mm sample, down to 5 for 2 mm. This is in line with the heat transfer effectiveness that degrades also for larger thickness. This may be due to a higher temperature gradient in thick samples thus limiting the heat transfer across the rubber sample itself due to low thermal conductivity and relatively high heat capacity. NR material composition seems to have an impact on the ΔT_{span} whereas the thickness seems to impact the cooling power. The investigation on the diffusivity and specific heat coefficient of material might be a path to explore in improving this refrigeration devices.

ACKNOWLEDGMENTS

This work was made in memory of Professor Jacques JAY, which contributed to it greatly but sadly passed away at the beginning of December 2023. This work was performed within the framework of the International Research Network ELyT Global.

NOMENCLATURE

NR	Natural rubber	COP	Coefficient of Performances	ΔT_{span}	Temperature span	σ	Engineering stress
PC	Cooling power	HT_{eff}	Heat transfer effectiveness	$\Delta T_{span\ max}$	Maximum temperature span	R	Gas constant
PC_{max}	Maximum cooling power	ν	Crosslink density	ΔT_{adiab}	Adiabatic temperature span	λ	Extension ratio

REFERENCES

[Candau (2014)] Candau, N., 2014. Compréhension des mécanismes de cristallisation sous tension des élastomères en conditions quasi-statiques et dynamiques (phdthesis). INSA de Lyon.

[Candau (2021)] Candau, N., Vives, E., Fernández, A., Maspoch, M., 2021. Elastocaloric effect in vulcanized natural rubber and natural/wastes rubber blends. Polymer 236, 124309. https://doi.org/10.1016/j.polymer.2021.124309

[Candau (2023)] Candau, N., Zimny, A., Vives, E., Maspoch, M.L., 2023. Elastocaloric Waste/Natural Rubber Materials with Various Crosslink Densities. Polymers 15, 2566. https://doi.org/10.3390/polym15112566

[Chauhan (2015)] Chauhan, A., Patel, S., Vaish, R., 2015. Elastocaloric effect in ferroelectric ceramics. Appl. Phys. Lett. 106, 172901. *https://doi.org/10.1063/1.4919453*

[Crossley (2015)] Crossley, S., Mathur, N.D., Moya, X., 2015. New developments in caloric materials for cooling applications. AIP Advances 5, 067153. *https://doi.org/10.1063/1.4922871*

[de Oliveira (2010)] de Oliveira, N.A., von Ranke, P.J., 2010. Theoretical aspects of the magnetocaloric effect. Physics Reports 489, 89–159. *https://doi.org/10.1016/j.physrep.2009.12.006*

[Engelbrecht (2017)] Engelbrecht, K., Tušek, Jaka, Eriksen, D., Lei, T., Lee, C.-Y., Tušek, Janez, Pryds, N., 2017. A regenerative elastocaloric device: experimental results. Journal of Physics D: Applied Physics 50, 424006. *https://doi.org/10.1088/1361-6463/aa8656*
[Gros (2015)] Gros, A., Tosaka, M., Huneau, B., Verron, E., Poompradub, S., Senoo, K., 2015. Dominating factor of strain-induced crystallization in natural rubber. Polymer 76, 230–236. https://doi.org/10.1016/j.polymer.2015.08.058
[Greibich (2021)] Greibich, F., Schwödiauer, R., Mao, G., Wirthl, D., Drack, M., Baumgartner, R., Kogler, A., Stadlbauer, J., Bauer, S., Arnold, N., Kaltenbrunner, M., 2021. Elastocaloric heat pump with specific cooling power of 20.9 W g–1 exploiting snap-through instability and strain-induced crystallization. Nat Energy 6, 260–267. *https://doi.org/10.1038/s41560-020-00770-w*
[Ma (2017)] Ma, R., Zhang, Z., Tong, K., Huber, D., Kornbluh, R., Ju, Y.S., Pei, Q., 2017. Highly efficient electrocaloric cooling with electrostatic actuation. Science 357, 1130–1134. *https://doi.org/10.1126/science.aan5980*
[Mañosa (2010)] Mañosa, L., González-Alonso, D., Planes, A., Bonnot, E., Barrio, M., Tamarit, J.-L., Aksoy, S., Acet, M., 2010. Giant solid-state barocaloric effect in the Ni–Mn–In magnetic shape-memory alloy. Nature Mater 9, 478–481. *https://doi.org/10.1038/nmat2731*
[Moya (2014)] Moya, X., Kar-Narayan, S., Mathur, N.D., 2014. Caloric materials near ferroic phase transitions. Nature Mater 13, 439–450. *https://doi.org/10.1038/nmat3951*
[Moya (2020)] Moya, X., Mathur, N.D., 2020. Caloric materials for cooling and heating. Science 370, 797–803. *https://doi.org/10.1126/science.abb0973*
[Ossmer (2015)] Ossmer, H., Miyazaki, S., Kohl, M., 2015. Elastocaloric heat pumping using a shape memory alloy foil device, in: 2015 Transducers - 2015 18th International Conference on Solid-State Sensors, Actuators and Microsystems (TRANSDUCERS). Presented at the 2015 Transducers - 2015 18th International Conference on Solid-State Sensors, Actuators and Microsystems (TRANSDUCERS), pp. 726–729. *https://doi.org/10.1109/TRANSDUCERS.2015.7181026*
[Ossmer (2016)] Ossmer, H., Wendler, F., Gueltig, M., Lambrecht, F., Miyazaki, S., Kohl, M., 2016. Energy-efficient miniature-scale heat pumping based on shape memory alloys. Smart Mater. Struct. 25, 085037. *https://doi.org/10.1088/0964-1726/25/8/085037*
[Pecharsky (1999)] Pecharsky, V.K., Gschneidner Jr, K.A., 1999. Magnetocaloric effect and magnetic refrigeration. Journal of Magnetism and Magnetic Materials 200, 44–56. *https://doi.org/10.1016/S0304-8853(99)00397-2*
[Sebald (2020)] Sebald, G., Komiya, A., Jay, J., Coativy, G., Lebrun, L., 2020. Regenerative cooling using elastocaloric rubber: Analytical model and experiments. Journal of Applied Physics 127, 094903. *https://doi.org/10.1063/1.5132361*
[Sebald (2023)] Sebald, G., Lombardi, G., Coativy, G., Jay, J., Lebrun, L., Komiya, A., 2023. High-performance polymer-based regenerative elastocaloric cooler. Applied Thermal Engineering 223, 120016. https://doi.org/10.1016/j.applthermaleng.2023.120016
[Sion (2024)] Sion, M., Jay, J., Coativy, G., Komiya, A., Sebald, G., 2024. Natural rubber based elastocaloric solid-state refrigeration device: design and performances of a single stage system. J. Phys. Energy 6, 025003. https://doi.org/10.1088/2515-7655/ad20f4
[Torello (2022)] Torello, A., Defay, E., 2022. Maximizing adiabatic temperature change in elastocaloric polymers. Chem 8, 3165–3167. https://doi.org/10.1016/j.chempr.2022.11.017
[Tosaka (2004)] Tosaka, M., Kohjiya, S., Murakami, S., Poompradub, S., Ikeda, Y., Toki, S., Sics, I., Hsiao, B.S., 2004. Effect of Network-Chain Length on Strain-Induced Crystallization of NR and IR Vulcanizates. Rubber Chemistry and Technology 77, 711–723. https://doi.org/10.5254/1.3547846
[Tušek (2015)] Tušek, J., Engelbrecht, K., Mikkelsen, L.P., Pryds, N., 2015. Elastocaloric effect of Ni-Ti wire for application in a cooling device. Journal of Applied Physics 117, 124901. *https://doi.org/10.1063/1.4913878*
[Tušek (2016)] Tušek, Jaka, Engelbrecht, K., Eriksen, D., Dall'Olio, S., Tušek, Janez, Pryds, N., 2016. A regenerative elastocaloric heat pump. Nat Energy 1, 1–6. *https://doi.org/10.1038/nenergy.2016.134*
[Wang (2020)] Wang, Y., Zhang, Z., Usui, T., Benedict, M., Hirose, S., Lee, J., Kalb, J., Schwartz, D., 2020. A high-performance solid-state electrocaloric cooling system. Science 370, 129–133. *https://doi.org/10.1126/science.aba2648*
[Wu (2017)] Wu, Y., Ertekin, E., Sehitoglu, H., 2017. Elastocaloric cooling capacity of shape memory alloys – Role of deformation temperatures, mechanical cycling, stress hysteresis and inhomogeneity of transformation. Acta Materialia 135, 158–176. *https://doi.org/10.1016/j.actamat.2017.06.012*
[Zhang (2015)] Zhang, G., Li, Q., Gu, H., Jiang, S., Han, K., Gadinski, M.R., Haque, M.A., Zhang, Q., Wang, Q., 2015. Ferroelectric Polymer Nanocomposites for Room-Temperature Electrocaloric Refrigeration. Advanced Materials 27, 1450–1454. https://doi.org/10.1002/adma.201404591
[Zhang (2022)] Zhang, S., Yang, Q., Li, C., Fu, Y., Zhang, H., Ye, Z., Zhou, X., Li, Q., Wang, T., Wang, S., Zhang, W., Xiong, C., Wang, Q., 2022. Solid-state cooling by elastocaloric polymer with uniform chain-lengths. Nat Commun 13, 9. https://doi.org/10.1038/s41467-021-27746-y

DOI: 10.18462/iir.thermag.2024.0004

STRUCTURE, MAGNETISM AND MAGNETOCALORIC EFFECT OF PEROVSKITE OXIDES $GD_{1.8}CE_{0.2}NIMNO_6$

Huiqin Yun [a b], Jingshun Liu [a],*, Ze Li [a]

[a] School of Materials Science and Engineering, Inner Mongolia University of Technology

Hohhot 010051, People's Republic of China

[b] School of Physical Science and Technology, Baotou Normal University, Key Laboratory of Magnetism and Magnetic Materials of Inner Mongolia Autonomous Region

Baotou 014030, People's Republic of China

*Email: jingshun_liu@163.com

ABSTRACT

In this work, polycrystalline sample of perovskite oxide $Gd_{1.8}Ce_{0.2}NiMnO_6$ was prepared by the conventional high-temperature solid-phase reaction method, and the magnetic properties of the sample was investigated. $Gd_{1.8}Ce_{0.2}NiMnO_6$ shows Griffiths-like phase in the temperature region of paramagnetic-ferromagnetic phase transition process. The magnetic moment undergoes a process of transformation from disorder to order, which laying the foundation for further research on the magnetothermal effect of this material. $Gd_{1.8}Ce_{0.2}NiMnO_6$ showed a significant magnetic entropy change near the Curie temperature at the magnetic field of 7 T, which reaches 3.13 $J \cdot kg^{-1}K^{-1}$, and its relative cooling power（RCP）reaches 231.1 J/kg. Therefore, the research results of this article prove that Ce doped Gd based powders have good application prospects in the field of magnetic refrigeration.

Keywords: Double perovskite oxide, Magnetocaloric effect, Griffiths-like phase, Phase transition

1. INTRODUCTION

Double perovskite, a widely used functional material,exhibits complex interactions between ions, and unique electromagnetic properties, such as spin-glass behavior, magnetocaloric effects, and Griffiths-like phase appear[0-0], which have led to increasing exploration of rare-earth oxide functional materials and deeper investigation of their electromagnetic properties.

In recent years, the double perovskite oxide La_2NiMnO_6 has received widespread attention for its potential application in magnetic refrigeration technology, because it exhibits simultaneously dielectric effect, magnetocaloric effect[0-0], ferromagnetic-paramagnetic transition0, and superexchange interaction[0,0]. The magnetocaloric effect consists first in magnetizing the magnetic material at constant temperarature, whereby heat released to the outside causes the temperature to rise. Then, during isothermal demagnetization, it absorbs heat from the outside which causes the temperature to decrease. Magnetic refrigeration is a clean technology, with high cycle efficiency, and high stability.

This paper studies the structure, magnetic properties, magnetocaloric effect and magnetic transition modes of the double perovskite oxide $Gd_{1.8}Ce_{0.2}NiMnO_6$ after the Gd_2NiMnO_6 parental sample is doped with rare earth element Ce at the A site. Sample testing was mainly done with XRD and PPMS instruments, and experimental data processing and plotting was performed with Origin software.

2. EXPERIMENT

The samples of $Gd_{1.8}Ce_{0.2}NiMnO_6$ were prepared by the high-temperature and solid-phase reaction method. Gd_2O_3, CeO_2, NiO and MnO_2 powders with purity of 99.99% were weighed accurately, and the weighed samples were ground into a zirconium oxide mortar for 4 h to get the components fully mixed. The ground powders were then put into a sintering furnace, which pre-sintered at 1000 ℃ for 12 h. The samples were then ground for 6 h and calcined at 1200 ℃ for 24 h.

The phase formation of samples was examined by XRD, and their crystal structures were analyzed. The magnetization intensity versus temperature curve (*M-T* curve) was measured at 0.01 T and 10 -320 K using the PPMS. *M-H* curve (*M* is the magnetization intensity, *H* is applied magnetic field) was measured at 0-7 T and 100-230 K. The hysteresis loop was measured with an external field of -7 T to 7 T.

3. MEASUREMENT RESULTS AND ANALYSIST

3.1 Crystal Structure Analysis

The XRD pattern of the $Gd_{1.8}Ce_{0.2}NiMnO_6$ ceramic sample is given at Fig. 1. No impurity peaks are observed in the sample, which indicates that the sample is monophase. The spatial point group obtained by Match software is a monoclinic space group of $P2_1/n$.

3.2 Magnetic Analysis

The relationship between the magnetization intensity (*M*) and temperature (*T*) for sample $Gd_{1.8}Ce_{0.2}NiMnO_6$ when 0.01 T is shown at Fig. 2. The ZFC curve and FC curve of $Gd_{1.8}Ce_{0.2}NiMnO_6$ are nearly straight lines when $T > 128$ K, indicating that the sample exhibits paramagnetic properties when $T > 128$ K. Below 128 K, the two curves gradually separate. The FC curve increases rapidly to a magnetization intensity level, that indicates an increase in ferromagnetism. In the paramagnetic-ferromagnetic transition temperature, T_C corresponds to the minimum value of the dM_{FC}/dT, as shown in the inset of Fig. 20. The paramagnetic-ferromagnetic transition may becaused by Ni^{2+}–O–Mn^{4+} superexchange. And the inset of Fig. 2 shows the curve of the product of magnetization and temperature (χT) versus temperature (*T*) for the $Gd_{1.8}Ce_{0.2}NiMnO_6$ sample at 0.01 T. The greatest value in the curve corresponds to Nair temperature (T_N), and the sample exhibits an antiferromagnetic ordering *when* $T < T_N$0. When *T* is within 123 K to 200 K, the magnetization intensity and χT value increase with decreasing temperature, indicating that the sample is mainly ferromagnetic0. However, the value of χT decreases with temperature decreasing below 123 K, indicating an antiferromagnetism behavior, the T_N of this sample being 123 K. According to Fig. 2, as the temperature decreases, the two curves of ZFC and FC show different tendencies. M_{FC} increases gradually, whereas, M_{ZFC} starts to drop sharply below T_N, indicating that the sample becomes less ferromagnetic and more antiferromagnetic when $T < T_N$, and this is a state of ferromagnetic-antiferromagnetic coexistence[0,0]. In summary, the samples show cluster spin glass behavior, which is mainly due to the ferromagnetic clusters undergoing a process of magnetic moment transformation from disordered to ordered phase under external fields0

The Fig. 3 shows the χ^{-1}-*T* curve (χ is the magnetization rate, *T* is temperature) for the sample $Gd_{1.8}Ce_{0.2}NiMnO_6$ at 0.01 T and the $log(\chi^{-1})$-$log(t_m)$ curve. For temperatures higher than 218 K, the χ^{-1}-*T* curve fits well with the C-W law suggesting that a Griffiths-like phase may be present in this sample[0,0]. However, for $T > T_\theta$, the sample behavior shows a departure from the C-W linear law and a collapse of χ^{-1}.

The χ^{-1}-*T* curve was fitted with the Griffiths phase model $\chi^{-1} \propto (T-T_C)^{1-\lambda}$. The model implies that $log(\chi^{-1})$ is a linear function of $log(t_m)$, where $t_m = (T-T_C)/T_C$; such behavior is observed experimentally for low temperatures, indicating that the sample has the characteristics of the Griffiths-like phase[0,0]. λ is calculated form the slope of the $log(\chi^{-1})$-$log(t_m)$ curve ($\lambda = 0.99896$). We usually define the range T_C to T_G as the Griffiths-like phase region, where T_G is the temperature at which the system is completely in the paramagnetic state, i.e., the Griffiths-like phase temperature point0. The Griffiths-like phase is a state between ferromagnetism and paramagnetism. According to Fig. 3, the sample is in the paramagnetic state at temperatures above T_G0, which indicates a ferromagnetic-paramagnetic coexistence state when $T_C < T < T_G$. The appearance of the Griffiths-like phase is induced by quenching disorder, as the structural deformation and competition between the two phases due to quenching disorder would make the Griffiths-like phase particularly stable0.

The Fig. 4 shows the *M-H* curve of $Gd_{1.8}Ce_{0.2}NiMnO_6$ at 0.01 T. When the temperature reaches approximately 230 K, the *M-H* curve is a quasi straight line, indicating that the samples are in the paramagnetic state at higher temperatures0. Below 190 K, the *M-H* characteristicbecomes gradually curved, indicating a transition from the pure paramagnetic state to paramagnetic-ferromagnetic coexistence state in the region from 200 K to 230 K. When $T < 200$ K, the sample clearly exhibits ferromagnetism. However, with below 7 T, the magnetization intensity of the samples does not gradually saturate, indicating the presence of antiferromagnetic components in this group of samples0.

3.3 Magnetocaloric Effects

The change in magnetic entropy is obtained from thermodynamic theory and the *M-H* curve[0,0]. The Fig. 5 shows the curve of the magnetic entropy changes versus temperature *(-ΔS-T)* for the sample $Gd_{1.8}Ce_{0.2}NiMnO_6$ at an isomagnetic field. The increasing intensity of applied field enhances the magnetic ordering within the system, which in turn changes the Mn-O bond length and Mn-O-Mn bond angle in its crystal structure. This structural phase change causes an increase in the change in magnetization near the critical temperature[0,0]. The $-\Delta S_M \approx 3.12\ J\cdot kg^{-1}K^{-1}$.

From the perspective of refrigeration, the refrigeration efficiency (Refrigeration Cooling Performance, RCP) is an important indicator of the cooling performance of the material. The magnetic refrigeration efficiency is given by equation (1)0.

$$RCP = |-\Delta S_M|(\Delta T_{FWHM}) \quad (1)$$

where ΔT_{FWHM} is the difference between the temperatures corresponding to a magnetic entropy change that is half of the maximum value, i.e., $\Delta T_{FWHM}=T_2-T_1$. The RCP is 231.10 J/kg.

3.4 Phase transition

In 1964, Banerjee0determined phase transition of a sample by analyzing the H/M-M^2 curve. In the Arrott curve, according to Banerjee's criterion, if the curve has an S-shape near T_C then it is a first-order phase transition, otherwise it is a second-order phase transition0. The Fig. 6 shows the H/M-M^2 curves of the $Gd_{1.8}Ce_{0.2}NiMnO_6$. As seen in Fig. 6, the slopes of the Arrott curves are all positive in 100 K to 200 K, indicating that the paramagnetic-ferromagnetic transition of the sample is probably a second-order phase transition in this temperature range.

We use the recalibration curves further determine the transition for this sample. Franco concluded that if all recalibration curves for different magnetic fields coincide, then this sample has undergone a second-order phase transition. The recalibration curves are diffusely distributed when $T<T_C$, then the system has undergone a first-order magnetic phase transition0. The Fig. 7 represents the recalibration curves for this group of samples at 1 T to 7 T. The vertical coordinate is the ratio of ΔS to ΔS_M at the magnetic field, and the horizontal coordinate is θ. That the recalibration curves for the samples mostly coincide with the primary curve at $T<T_C$, indicating that the sample is a second-order magnetic phase transition.

The Fig. 8 shows the loop curves of the $Gd_{1.8}Ce_{0.2}NiMnO_6$ sample at different temperatures. Combining Fig. 8 with the relevant literature[0-0], it can be concluded that the increase of magnetization intensity of this sample at 5 K becomes slow as the field goes from 7 T to -7 T and back to 7 T, but still does not reach saturation, indicating the presence of antiferromagnetic components in this sample. The loop curves at different temperatures (10, 130, 140, and 300 K) all pass through the origin, indicating an absence of hysteresis. As the temperature increases, the magnetization intensity gradually decreases and changes gradually from a curved to a straight line, indicating that the sample is no longer ferromagnetic and becomes paramagnetic. It was observed in the loop curves that there was no hysteresis between the lifting field curves from 5 K to 300 K. Therefore, it was concluded that the sample underwent a second-order phase transition[0,0].

3.5 References

[1]Kundu A K, Nordblad P, Rao C N R. Glassy behaviour of the ferromagnetic and the non-magnetic insulating states of the rare earth manganates $Ln_{0.7}Ba_{0.3}MnO_3$ (Ln= Nd or Gd)[J]. Journal of Physics: Condensed Matter, 2006, 18(20): 4809.

[2]El-Hagary M, Shoker Y A, Emam-Ismail M, et al. Magnetocaloric effect in manganite perovskites $La_{0.77}Sr_{0.23}Mn_{1-x}Cu_xO_3$ ($0.1\leq x\leq 0.3$)[J]. Solid state communications, 2009, 149(5-6): 184-187.

[3]Lazuta A V, Ryzhov V A, Kurbakov A I, et al. Inhomogeneous Magnetic State above the Curie Temperature of the Doped Cobaltite $La_{1-x}Sr_xCoO_3$[J]. Solid State Phenomena, 2011, 168: 457-460.

[4]Retuerto M, Munoz A, Martínez-Lope M J, et al. Magnetic interactions in the double perovskites R_2NiMnO_6 (R= Tb, Ho, Er, Tm) investigated by neutron diffraction[J]. Inorganic Chemistry, 2015, 54(22): 10890-10900.

[5]Chakraborty T, Nhalil H, Yadav R, et al. Magnetocaloric properties of R_2NiMnO_6 (R= Pr, Nd, Tb, Ho and Y) double perovskite family[J]. Journal of Magnetism and Magnetic Materials, 2017, 428: 59-63.

[6]Kakarla D C, Jyothinagaram K M, Das A K, et al. Dielectric and Magnetodielectric Properties of R_2NiMnO_6 (R= Nd, Eu, Gd, Dy, and Y)[J]. Journal of the American Ceramic Society, 2014, 97(9): 2858-2866.

[7]Su L, Zhang X Q, Dong Q Y, et al. Magnetocaloric effect and critical behaviors of R_2NiMnO_6 (R= Eu and Dy) double perovskite oxides[J]. Journal of Alloys and Compounds, 2018, 746: 594-600.

[8]Zhou S M, Guo Y Q, Zhao J Y, et al. Nature of short-range ferromagnetic ordered state above TC in double perovskite La_2NiMnO_6[J]. Applied Physics Letters, 2010, 96(26).

[9]Blasse G. Ferromagnetic interactions in non-metallic perovskites[J]. Journal of physics and Chemistry of Solids, 1965, 26(12): 1969-1971.

[10]Zhou S, Shi L, Yang H, et al. Evidence of short-range magnetic ordering above T_C in the double perovskite La_2NiMnO_6[J]. Applied Physics Letters, 2007, 91(17).

[11]Ye F, Dai H, Wang M, et al. The structural, dielectric, and magnetic properties of $GdMnO_3$ multiferroic ceramics[J]. Journal of Materials Science: Materials in Electronics, 2020, 31: 3590-3597.

[12]Li L, Xu P, Ye S, et al. Magnetic properties and excellent cryogenic magnetocaloric performances in B-site ordered RE_2ZnMnO_6 (RE= Gd, Dy and Ho) perovskites[J]. Acta Materialia, 2020, 194: 354-365.

[13]Liu J, Wang W Q, Wu H Y, et al. Electromagnetic properties of Co-doped chalcogenide manganese oxides $La_{0.8}Sr_{0.2}MnO_3$[J]. Journal of Inorganic Materials, 2018, 33(11): 1237-1247.

[14]Yun H Q, Zheng L, Duan Y M, et al. Magnetic and electrical properties of chalcogenide manganese oxides $La_{1.3-x}Dy_xSr_{1.7}Mn_2O_7$($x$=0.025) [J]. Journal of Low Temperature Physics, 2017, 39(03): 40-43.

[15]Chen C X. Progress in charge ordering in chalcogenide manganese oxides [J]. Journal of Inorganic Materials, 2005, 20(1): 1-12.

[16]Palakkal J P, Raj Sankar C, Varma M R. Multiple magnetic transitions, Griffiths-like phase, and magnetoresistance in La_2CrMnO_6[J]. Journal of Applied Physics, 2017, 122(7).

[17]Pérez N, Casanova F, Bartolomé F, et al. Griffiths-like phase and magnetic correlations at high fields in Gd_5Ge_4 [J]. Physical Review B, 2011, 83(18): 184411.

[18]Wang F, Wan S L, Zhou M, et al. Griffiths-like phase study of Eu-doped layered chalcogenide $Nd_{1.2}Sr_{1.8}Mn_2O_7$ [J]. Journal of Low Temperature Physics, 2016. 38(02): 145-149.

[19]Nair H S, Swain D, Adiga S, et al. Griffiths phase-like behavior and spin-phonon coupling in double perovskite Tb_2NiMnO_6[J]. Journal of applied physics, 2011, 110(12).

[20]Xing R, Wan S L, Wang W Q, et al. Magnetic transition behavior of perovskite manganites $Nd_{0.5}Sr_{0.3}Ca_{0.2}MnO_3$ polycrystalline[J]. Chinese Physics B, 2016, 25(4): 047601.

[21]Liu F, Gao Y, Chang H, et al. Control of magnetic properties and band gap by Co/Mn ordering and oxygen distributions of La_2CoMnO_6[J]. Journal of Magnetism and Magnetic Materials, 2017, 435: 217-222.

[22]Sun X D, Xu B, Wu H Y, et al. Magnetic entropy change and electrical transport properties of Tb-doped bilayer manganese oxides $La_{4/3}Sr_{5/3}Mn_2O_7$. Journal of Physics, 2017, 66(15): 245-252.

[23]Jin X, Xu B, Zhou M, et al. Calculation of magnetic entropy change of chalcogenide manganese oxides $La_{1.2-x}Tb_xSr_{1.8}Mn_2O_7$ (x=0, 0.05) by fitting magnetization curves. Rare Earths, 2017, 38(03): 98-102.

[24]Banerjee B K. On a generalised approach to first and second order magnetic transitions. Physics Letters, 1964, 12(05): 16-17.

[25]Mira J, Rivas J. First-order magnetic phase transitions and colossal magnetoresistance: Joining manganese perovskites and MnAs[J]. Modern Physics Letters B, 2004, 18(15): 725-747.

[26]Yu B, Han H, Lan X, et al. Exploiting Magnetism and Magnetocaloric Effect in $Nd_{0.55}Sr_{0.45}Mn_{0.98}Ga_{0.02}O_3$[J]. Journal of Superconductivity and Novel Magnetism, 2017, 30: 2227-2232.

[27]Hu H B. Analysis of the application of important parameters of hysteresis lines of magnetic materials. Enterprise Technology and Development, 2018, 24(06): 170-174.

[28]Zhang H L, Li Z, Qiao Y F, et al. Study on the martensitic phase transformation of Hassler alloy Ni-Co-Mn-Sn and its magnetothermal effect. Journal of Physics, 2009, 58(11): 7857-7863.

3.6 Tables and Figures

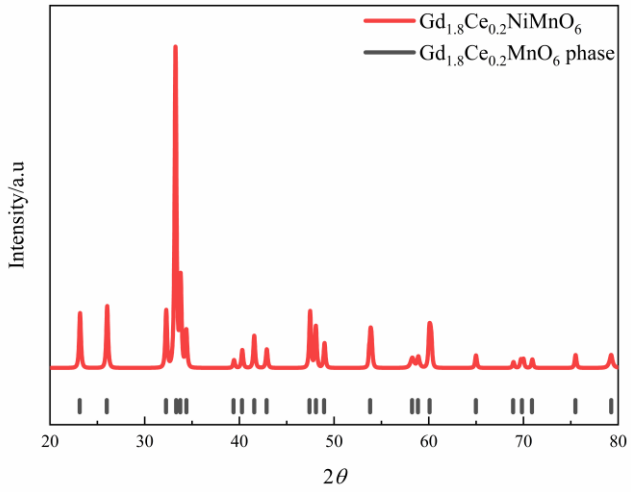

Fig. 1. XRD pattern of $Gd_{1.8}Ce_{0.2}NiMnO_6$ sample.

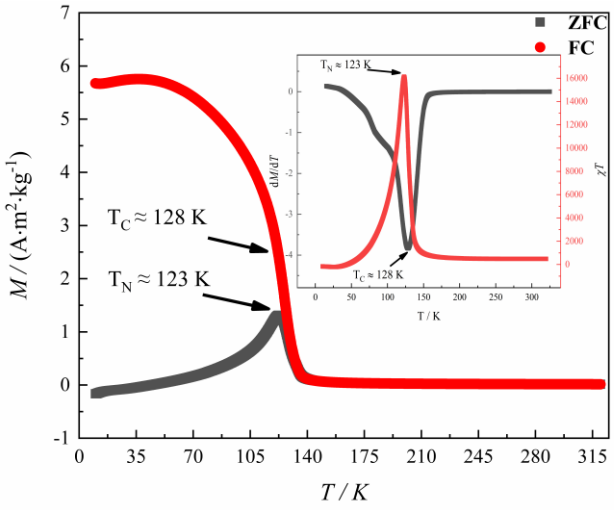

Fig. 2. *M-T*, χT-*T*, d*M*/ d*T* – *T* curve of $Gd_{1.8}Ce_{0.2}NiMnO_6$ sample at 0.01 T.

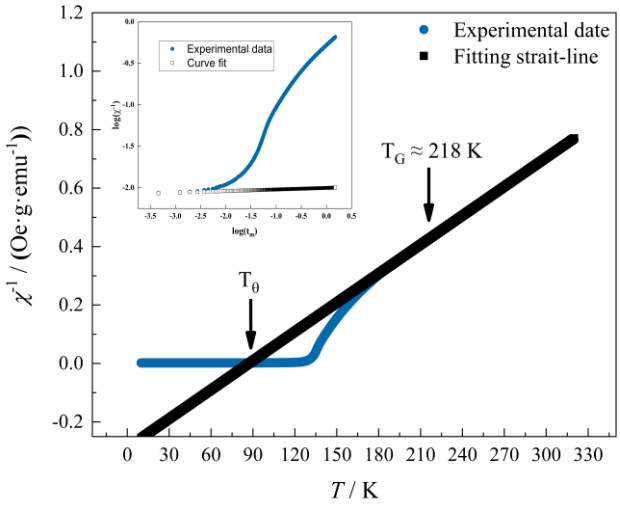

Fig. 3. χ^{-1}-T **curves of** $Gd_{1.8}Ce_{0.2}NiMnO_6$ **sample at 0.1T and** $log(\chi^{-1})$-$log(_{tm})$ **curve.**

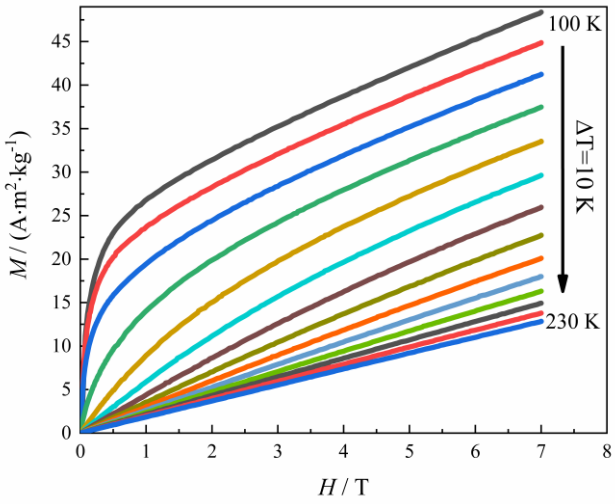

Fig. 4. M-H **curves of the** $Gd_{1.8}Ce_{0.2}NiMnO_6$ **samples at different temperatures.**

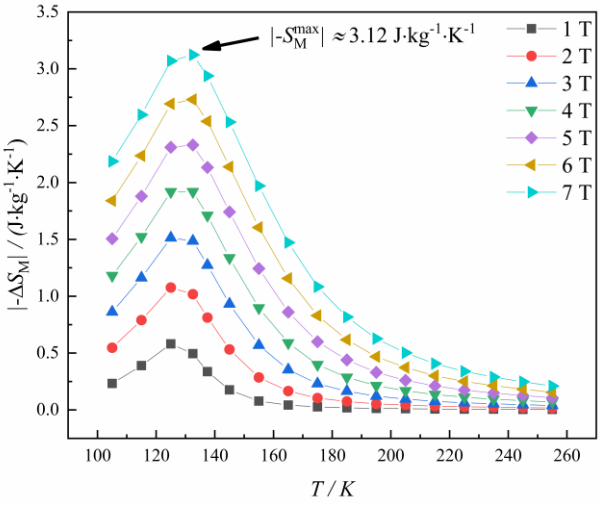

Fig. 5. Curve of magnetic entropy change versus temperature $(-\Delta S$-$T)$ **for** $Gd_{1.8}Ce_{0.2}NiMnO_6$ **sample at isomagnetic field.**

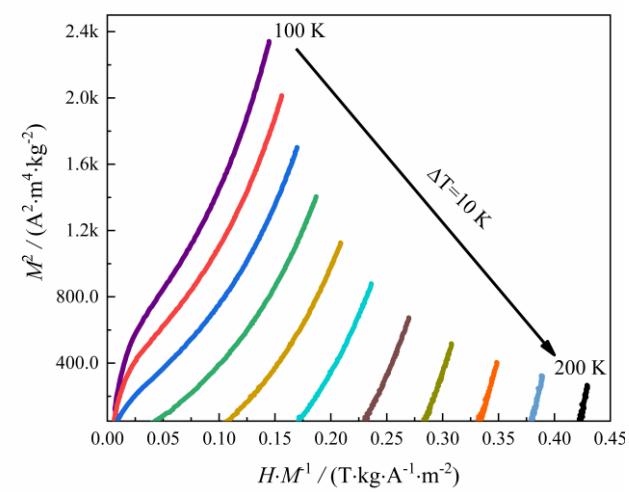

Fig. 6. Arrott curve (H/M-M^2) of $Gd_{1.8}Ce_{0.2}NiMnO_6$ sample from 100 K to 200 K.

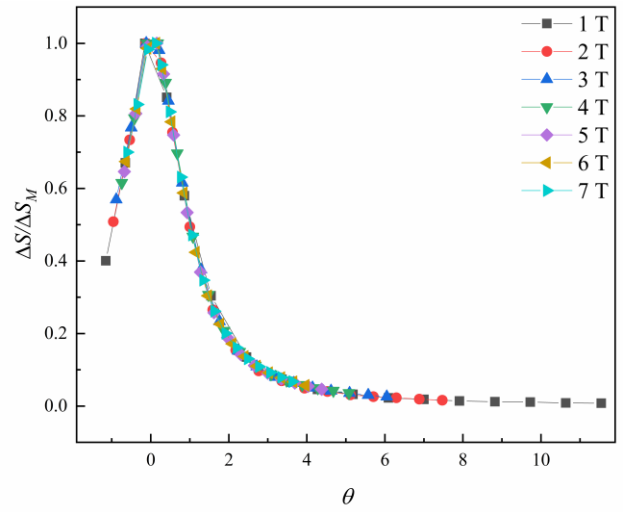

Fig. 7. Recalibration curves of $Gd_{1.8}Ce_{0.2}NiMnO_6$ samples at different magnetic fields.

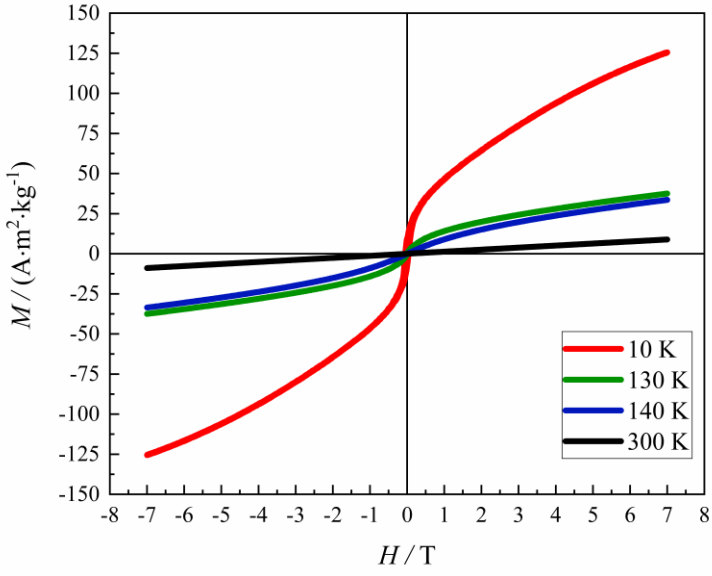

Fig. 8. Loop curves of $Gd_{1.8}Ce_{0.2}NiMnO_6$ samples at different temperatures.

4. CONCLUSIONS [LEVEL 1 HEADING]

In this chapter, the structural and magnetic of $Gd_{1.8}Ce_{0.2}NiMnO_6$ sample were analyzed using data from XRD, *M-T* curves, and *M-H* curves. The main results are as follows. The XRD shows that this polycrystalline sample exhibits good monophasicity with a space group of $P2_1/n$. From the χ^{-1}-*T* curve, we observe a deviation of χ^{-1} from the C-W straight line, before collapsesing when $T > T_\theta$. Subsequently, Curie-Weiss fitting is performed, and the fitting results all satisfy the relationship $\chi^{-1} \propto (T-T_C)^{1-\lambda}$, which proves the existence of a Griffiths-like phase in this sample. The value of T_G is 218 K. Combined with the *M-H* curve, it is concluded that the sample is in the pure paramagnetic state when $T > T_G$. When $T_C < T < T_G$, the sample is in the ferromagnetic-paramagnetic coexistence state. At $T < T_N$, the ferromagnetic state weakens, the antiferromagnetic state strengthens, and the cluster spin-glass behavior appears. The $|-\Delta S_M|$ of the sample is 3.12 $J \cdot kg^{-1}K^{-1}$. Using the magnetic refrigeration efficiency formula, the RCP is 231.10 J/kg. Regarding the Arrott, recalibration and loop curves, the Arrott curve has a positive slope. When $T < T_C$, the recalibration curve does not show a dispersion distribution, and there is no hysteresis, indicating that the sample is a second-order magnetic phase transition.

ACKNOWLEDGEMENTS

This project was supported by the National Natural Science Foundation of China (NSFC) under grant nos.52061035, 51871124, 51561026 and 51401111, Young Leading Talent of ~~"G~~Grassland Talents" Project of Inner Mongolia Autonomous Region, Inner Mongolia Natural Science Cultivating Fund for Distinguished Young Scholars (no. 2020JQ05), Science and Technology Planning Project of Inner Mongolia Autonomous Region (no. 2020GG0267), Program for Innovative Research Team in Universities of Inner Mongolia Autonomous Region (no. NMGIRT2211), Inner Mongolia University of Technology Key Discipline Team Project of Materials Science (no. ZD202012).

DOI: 10.18462/iir.thermag.2024.0005

EFFECTS OF INTERFACIAL COMPOUNDS INDUCING BY AG INTERLAYER ON THE BI_2TE_3-BASED THIN FILMTHERMOELECTRIC COOLER

Zeyu Liu[(a)], Leyao Chu[(a)], Ruiheng Liu[(b)], Limei Shen[(a)*], JunlongXie[(a)]

[(a)] School of Energy and Power Engineering, Huazhong University of Science and Technology
Wuhan, 430070, China, EP_Shenlimei@hust.edu.cn
[(b)]Shenzhen Institute of Advanced Technology Chinese Academy of Sciences
Shenzhen, 518055, China

ABSTRACT

It has been found that interfacial compounds (IFC)$Cu_4Ag_3Te_4$ and Ag_2Te induced by Ag interlayers can greatly optimize electrical contact at interface between Cu electrode and Bi_2Te_3thin film. However, effects of IFC on thin film thermoelectric cooler (TFTEC) cooling performance was unclear.Herein, we developed a TFTEC simulation modelto evaluate influenceofinterfacial compoundson cooling performance.For TFTEC with ZT=1.09,resultsshowed thatinfluence of IFC was twofold. On the one hand, IFC decreasedcontact resistivity, which increased cooling flux and cooling temperature difference. On the other hand, IFC degraded cooling performance of TFTEC due to its lower ZT than Bi_2Te_3thin film.With the same contact resistivity,maximum cooling flux $q_{c,max}$of TFTEC with IFC was 254.3 W/cm^2, which was only 69.36% of that without IFC. And maximum cooling temperature difference ΔT_{max} of TFTEC with IFC was 64.18K, which was only 79.25% of that without IFC.

Keywords: Thermoelectric Cooler, Thin Film, Interfacial Compounds, Cooling Performance

1. INTRODUCTION

Solid-state thin film thermoelectric coolers (TFTEC) have many attractive advantages, e.g., no moving parts,high reliability, quick response and high cooling flux,making it one promising method for thermal management of microchip hotspots(Shi et al., 2020). However, their use has been limited by the relatively highcontact resistance$R_c$at the electrode/TE leg interface, which will greatly degrade its cooling ability(Da Silva and Kaviany, 2005; He et al., 2018).Considering the influence of the electrical contact resistance R_c, the maximum cooling flux$q_{c,max}$and the maximum cooling temperature differenceΔT_{max}can be calculated as Eq. (1)(2)

$$q_{c,max} = \frac{\alpha^2 T_c^2}{2\rho l + 4R_c S} \tag{1}$$

$$\Delta T_{max} = \frac{\alpha^2 T_c^2}{2k\rho + 4kR_c S/l} \tag{2}$$

where α, ρ and $k$are respectively the Seebeck coefficient, the electrical resistivity and the thermal conductivity of the thermoelectricmaterial, l is the height of thermoelectric leg,S is the cross-section area of thermoelectric leg,$R_c$is the electrical contact resistance, and T_c denotes the cold side temperature.It can be seen that the contact resistance R_c significantly degrades $q_{c,max}$ due to the low l of TFTEC (<100 μm). Therefore, it‘s necessary to optimize the electrical contact at the electrode/TE leg interface of TFTEC.

To date, many methods for optimizing theelectrical contact at the electrode/TE leginterfaces have been studied, mostof which can be concluded into metallization and interlayers design, interface treatment, and heavy doping technique or the combination of them(Kim et al., 2016; Kong et al., 2017; Taylor et al., 2013; Vizel et al., 2016). Among these methods, inserting interlayers is an effective method, which can reduce contact resistivity to lower than 10-11 Ω·m^2(Gupta et al., 2010; Shen et al., 2022b).It's worth noting that researchers found that interfacial compounds inducedby interlayers can result in the decrease of contact resistance.For instance, Shen et al(2019) reported an Ohmic contact for the junction of p-type $Nb_{0.8}Ti_{0.2}FeSb$ and Mo electrode with a low contact resistivity of $<10^{-10}$ Ω·m^2 due to the interfacial compounds FeMo induced by the diffusion of Fe into Mo. The interface carrier transport is dominated by the field emissionand

consequently a strong tunneling electric current is obtained due to the high doping level and relatively low dielectric constant of p-type Nb0.8Ti0.2FeSb semiconductor. Liu etal(2013) found that the formation of Ni_2Te_3 at the interface reduced electrical resistivity in p-type Bi_2Te_3 legs.D. Spataru et al(2019) found that a coherent interface between half-Heusler and full-Heusler compounds can form due to diffusion of transition metal atoms into the vacantsublattice of the half-Heusler lattice. And the prototypicalinterface HfNi2Sn/HfNiSn provides very low contact resistivity and almost ohmic behavior over a wide range of temperatures anddoping levels.The overall values of the contact resistivityare less than 10^{-12} $\Omega \cdot m^2$. However, most of existing studies tend to focus only on the effects of interfacial compounds on contact resistance. The electrical resistance, thermal resistance and possible Seebeck effect of interfacial compounds are not considered, which can also affect the cooling performance.This study aims to establish a sing leg TFTEC model containing interfacial compounds to comprehensively evaluate the effect of interfacial compounds on TFTEC‘s cooling performance. Electrical contact resistance, thermal contact resistance, electrical resistance, thermal resistance and possible Seebeck effect of interfacial compoundswere all considered. The maximum cooling flux$q_{c,max}$and the maximum cooling temperature differenceΔT_{max}were used for evaluation parameters. Two kinds of Bi_2Te_3 with ZT=1.09 and 0.011 were used as thermoelectric material in order to analyse the influence of IFC on TFTEC with different ZT.

2. MODEL DESCRIPTION

In order to investigate the influence of IFC on$q_{c,max}$and ΔT_{max}, two single-leg TFTEC models were established as shown in Figure 1.One is with IFC and the other one is without IFC. The single-leg TFTEC was consisted of AlN substrates, Cu electrodesand N type leg. Geometry parameters ofcomponents are shown in Table 1, which are from Ref.(Shen et al., 2022a). N type leg consists of two IFCs ($Cu_4Ag_3Te_4$ and Ag_2Te), Ag interlayer and N-type Bi_2Te_3 thin film. The total height of N type leg is 6 μm.

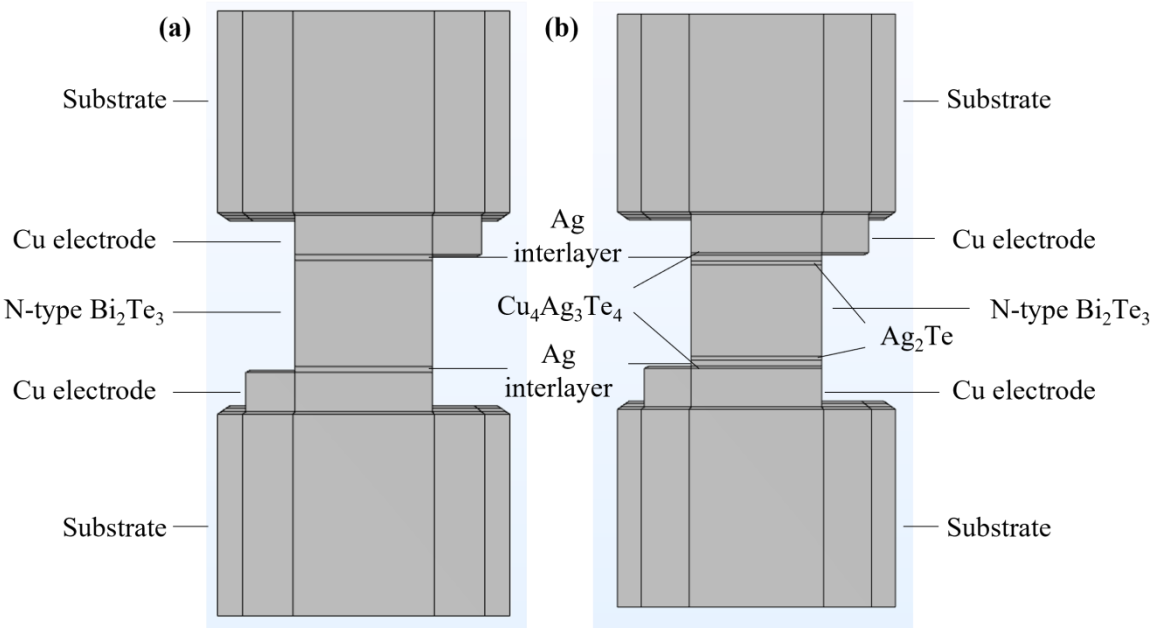

Figure 1:Single leg TFTEC model. (a) without IFC; (b) with IFC.

Table 1. Geometry parameters of components

No.	Components	Length(μm)	Width(μm)	Height(μm)
1	Substrate	14.5	8.5	10
2	Cu electrode	9.5	7	2
3	N-type leg	7	7	6

With the Ag interlayer thickness increasing from 50 nm to 300 nm, the contact resistivity decreased, which was shown in Table 2. Meanwhile, the IFC generated more. Theequivalent thickness of IFCs was calculated

by semi-quantitatively analyzing the XRD pattern. The results are also shown in Table2. Thermal contact resistivity was calculated by Wiedemann–Franz law.

Table 2. Contact resistivity and thickness of interfacial compounds

No.	Aginterlayer thickness(nm)	Contact Resistivity($\Omega \cdot m^2$)	$Cu_4Ag_3Te_4$ Thickness(nm)	Ag_2Te thickness(nm)
1	50	2.940×10^{-10}	0	98.39
2	100	7.477×10^{-11}	23.43	137.08
3	150	2.991×10^{-11}	63.36	146.7
4	200	1.240×10^{-11}	80.36	155.34
5	250	7.205×10^{-12}	97.59	171.78
6	300	3.187×10^{-12}	121.26	206.33

Thematerial property parameters of AlN substrates, Cu electrodes and Ag interlayer came from the built-in database of COMSOL Multiphysics. Thermoelectric property parameters of interfacial compounds were based on the studies of Mukherjee et al. (2020) and Sakakibara et al. (2002), which can be seen in Table 3.

Table 3. Thermoelectric properties of interfacial compounds

No.	Interfacial compounds	Electrical conductivity (S/m)	Thermal conductivity (W/m/K)	Seebeck Coefficient (μV/K)	Ref.
1	$Cu_4Ag_3Te_4$	57608.818	1.40296	4.7577	(Mukherjee et al., 2020)
2	Ag_2Te	57100	1.07298	-122.39	(Sakakibara et al., 2002)

Based on this model, the influence of IFC on cooling performance of two TFTEC made of Bi_2Te_3 thin films with different ZT. ZT values of two Bi_2Te_3 thin films are 0.011 and 1.09, respectively. Electrical conductivity, thermal conductivity and Seebeckcoefficient are shown in Table 4, which are all measured at 350K.

Table 4. Thermoelectric properties of Bi_2Te_3 thin films

No.	Electrical conductivity (S/m)	Thermal conductivity (W/m/K)	Seebeckcoefficient (μV/K)	Temperature	ZT value
1	3228.088744	0.84	-89.2939	350K	0.011
2	109129.2896	0.90	-160.3038	350K	1.09

As for the boundary conditions,maximum cooling flux $q_{c,max}$was calculated by setting the temperature of both sides of TFTEC at a constant 350K. Besides, maximum cooling temperature difference $\Delta T_{max}$was calculated by setting the hot-side temperature at a constant 350K and cooling capacity Q_c=0.

3. RESULTS AND DISCUSSIONS

Basedon the simulation models, maximum cooling flux $q_{c,max}$and maximum cooling temperature difference ΔT_{max}were calculated. The results are shown in Figure 2 and Figure 3. Figure 2(a) and Figure 2(b) was the $q_{c,max}$ and ΔT_{max} simulation results of TFTEC with ZT=1.09.For TFTEC with IFC, $q_{c,max}$ and ΔT_{max} both monotonically increase with the increasing thickness of Aginterlayer. When Aginterlayer thickness increased from 50 nm to 300 nm, the $q_{c,max}$ increased from 2.0607 W/cm^2 to 254.30 W/cm^2, and the ΔT_{max} increased from 4.31 K to 64.18 K. The main reason is that the increasing IFC made the contact resistivity

$\rho_c$decreasefrom $2.940\times10^{-10}\Omega\cdot m^2$to $3.187\times10^{-12}\Omega\cdot m^2$, as shown in Table 2.$q_{c,max}$and ΔT_{max}can be calculated as Eq. (2)(3)

$$q_{c,max} = \frac{\alpha^2 T_c^2}{2\rho l + 4\rho_c} \tag{3}$$

$$\Delta T_{max} = \frac{\alpha^2 T_c^2}{2k(\rho + 2\rho_c / l)} \tag{4}$$

It‘s oblivious that reducing contact resistivity can improve the $q_{c,max}$and $\Delta T_{max}$of TFTEC.

However, if we kept the same contact resistivity and removed the IFC from the model as illustrated in Section 2, the TFTEC without IFC would show better performance than that with IFC. As shown in Figure 2, TFTEC without IFC can achieve maximum $q_{c,max}$of 366.62 W/cm^2 and maximum ΔT_{max} of 82.02 K, which were respectively44.18% and 27.80%higher than that without IFC.It indicated that the IFC degraded the cooling performance of TFTEC in a way. This is because the IFC $Cu_4Ag_3Te_4$ and Ag_2Te have lower electrical conductivity, Seebeckcoefficient and higher thermal conductivity, which resulted in a lower ZT than Bi_2Te_3 thin film. Especially, $Cu_4Ag_3Te_4$ is P-type thermoelectric material rather than N-type thermoelectric material. IFC $Cu_4Ag_3Te_4$ and Ag_2Te would lower the total ZT value of the single-leg TFTEC, leading to degrade the cooling performance of TFTEC.

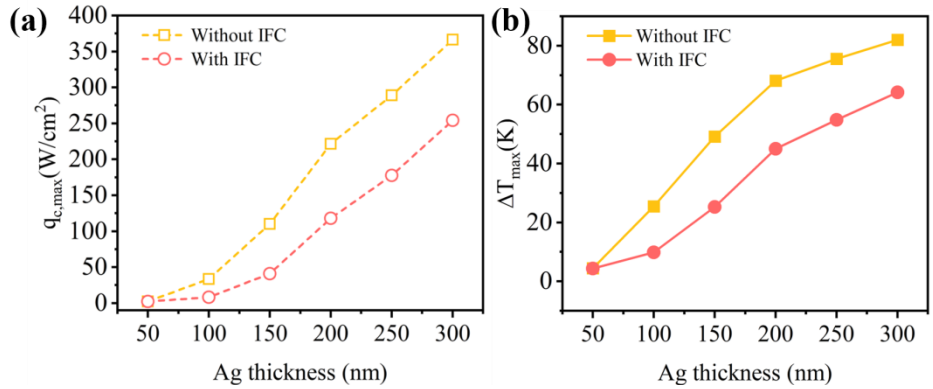

Figure 2: (a)The maximum cooling flux and (b) cooling temperature difference of TFTEC with ZT=1.09

Apart from the TFTEC with ZT=1.09, TFTEC with ZT=0.011 was also modeled. Purpose of this model was to investigate the influence of IFC on TFTEC with relatively lower ZT. The results are shown in Figure 3. For TFTEC with IFC, when Aginterlayer thickness increased from 50 nm to 300 nm, the $q_{c,max}$ increased from 0.40029 W/cm^2 to 4.089 W/cm^2, and the ΔT_{max} increased from 0.85 K to 1.59 K.Unlike that shown in Figure 2, $q_{c,max}$and $\Delta T_{max}$of TFTEC with IFC was higher than that with IFC. As shown in Figure 3, TFTEC without IFC can only achieve maximum $q_{c,max}$of 3.7236 W/cm^2 and maximum ΔT_{max} of 1.49 K, which were only respectively 91.06% and 93.71% of that with IFC. This is because the IFC Ag_2Te have higher electrical conductivity, Seebeck coefficient and lower thermal conductivity, which resulted in a higher ZT than Bi_2Te_3 thin film.As for $Cu_4Ag_3Te_4$, though it‘s P-type thermoelectric material, its thickness was always less than Ag_2Te, so that the negative effect of $Cu_4Ag_3Te_4$ on TFTEC cooling performance would be offset by Ag_2Te.Overall, IFC can improve the total ZT value of the single-leg TFTEC, leading to enhance the cooling performance of TFTEC with ZT=0.011.

That could also explain why $q_{c,max}$and ΔT_{max}didn‘t increasemonotonically with the increasing thickness of Aginterlayer. Because when Ag thickness was 50 nm, the thickness of $Cu_4Ag_3Te_4$ was 0 nm and the thickness of Ag_2Te was 98.39 nm, which meant IFC only had positive effect on the cooling performance of TFTEC. However, when Ag thicknessrose to 100 nm, the thickness of $Cu_4Ag_3Te_4$ also rose to 23.43 nm, starting to havenegative effect on the cooling performance of TFTEC. The decreasing contact resistivity and increasing Ag_2Te were unable to offset the negative effect, leading to degradation of cooling performance.

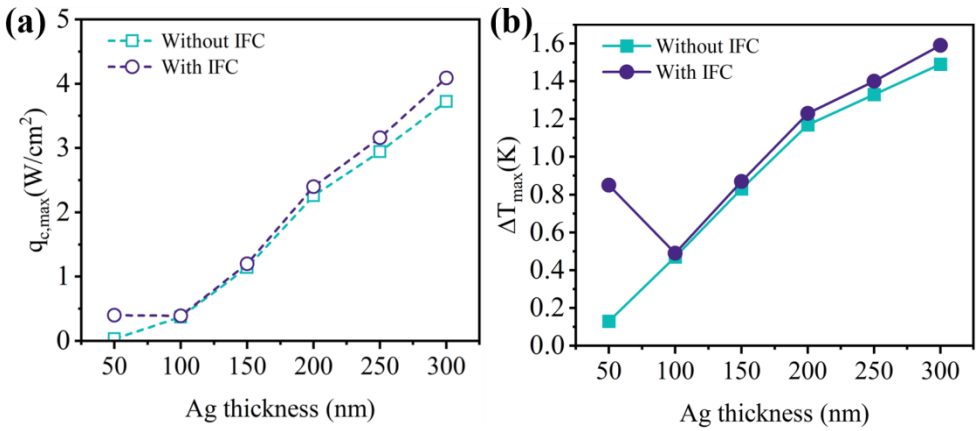

Figure 3: (a)The maximum cooling flux and (b) cooling temperature difference of TFTEC with ZT=0.011

4. CONCLUSIONS

This paper established a single-leg thin film thermoelectric cooler (TFTEC) simulation model for analyzing the influence of interfacial compounds (IFC)$Cu_4Ag_3Te_4$ and Ag_2Te on cooling performance of Bi_2Te_3-based TFTEC. Maximum cooling flux $q_{c,max}$ and maximum cooling temperature difference ΔT_{max} were calculated for TFTEC with ZT=1.09 and 0.011,respectively. The influence of IFC on TFTEC with ZT=1.09was twofold. On the one hand, IFC can optimize the cooling performance due to its optimization on contact resistivity. When IFC increased about 2.33 times, the $q_{c,max}$ increased from 2.0607 W/cm^2 to 254.30 W/cm^2, and the ΔT_{max} increased from 4.31 K to 64.18 K. On the other hand, IFC can also degrade the cooling performance due to its low ZT. By keeping the same contact resistivity and remove IFC layer in simulation model, TFTEC without IFC can achieve maximum $q_{c,max}$of 366.62 W/cm^2 and maximum ΔT_{max} of 82.02 K, which were respectively 44.18% and 27.80% higher than that without IFC. As for TFTEC with ZT= 0.011, IFC can optimize the cooling performance due to its optimization on contact resistivity and higher ZT.when Aginterlayer thickness increased from 50 nm to 300 nm, the $q_{c,max}$ increased from 0.40029 W/cm^2 to 4.089 W/cm^2, and the ΔT_{max} increased from 0.85 K to 1.59 K.

This work provides a single-leg TFTEC simulation model containing IFC and demonstrates that interfacial compounds $Cu_4Ag_3Te_4$ and Ag_2Te have complex effects on cooling performance, which shouldn‘t be neglected while evaluating the performance of TFTEC.It‘s helpful to reduce the error between theoretical calculation and actual performance of TFTEC.

ACKNOWLEDGEMENTS

This work is jointly supported by the National Natural Science Foundation of China (Grant No. 52176007), National Key Research and Development Program of China (Grant No. 2022YFB3803900), Science, Technology and Innovation Commission of Shenzhen Municipality (Grant No. JCYJ20210324115611030).

NOMENCLATURE

IFC	interfacial compound	TFTEC	thin film thermoelectric cooler
$q_{c,max}$	maximum cooling flux (W/cm^2)	ΔT_{max}	maximum cooling temperature difference (K)
α	Seebeck coefficient (V/K)	ρ	electrical resistivity (Ω·m)
k	thermal conductivity (W/m/K)	l	height of thermoelectric leg (m)
S	cross-section area of thermoelectric leg (m^2)	R_c	electrical contact resistance (Ω)
ρ_c	contact resistivity (Ω·m^2)	ZT	figure of merit

REFERENCES

Da Silva, L. W., and M. Kaviany, 2005, Fabrication and measured performance of a first-generation microthermoelectric cooler: Journal of Microelectromechanical Systems, v. 14, p. 1110-1117.

Gupta, R. P., K. Xiong, J. B. White, K. Cho, and B. E. Gnade, 2010, Improvement in Contact Resistivity to thin film Bi2Te3, *in* J. D. Baniecki, G. J. Snyder, J. A. Malen, and H. L. Tuller, eds., THERMOELECTRIC MATERIALS 2010 - GROWTH, PROPERTIES, NOVEL CHARACTERIZATION METHODS AND APPLICATIONS, Symposium DD on Thermoelectric Materials -Growth, Properties, Novel Characterization Methods, and Applications at MRS Spring Meeting.

He, R., G. Schierning, and K. Nielsch, 2018, Thermoelectric Devices: A Review of Devices, Architectures, and Contact Optimization: Advanced Materials Technologies, v. 3.

Kim, S., S. Kim, G. Kim, J. Kim, J. Park, and H. Yu, 2016, Ar Plasma Treatment for III – V Semiconductor-Based Transistor Source/Drain Contact Resistance Reduction: Journal of Nanoscience and Nanotechnology, v. 16, p. 10389-10392.

Kong, X., W. Zhu, L. Cao, Y. Peng, S. Shen, and Y. Deng, 2017, Controllable Electrical Contact Resistance between Cu and Oriented-Bi2Te3 Film via Interface Tuning: ACS Applied Materials & Interfaces, v. 9, p. 25606-25614.

Liu, W., H. Wang, L. Wang, X. Wang, G. Joshi, G. Chen, and Z. Ren, 2013, Understanding of the contact of nanostructured thermoelectric n-type Bi 2 Te 2.7 Se 0.3 legs for power generation applications: JOURNAL OF MATERIALS CHEMISTRY A, v. 1, p. 13093-13100.

Mukherjee, S., S. Ghosh, and K. Chattopadhyay, 2020, Ultralow thermal conductivity and high thermoelectric figure of merit in Cu2Te – Ag2Te composites: Journal of Alloys and Compounds, v. 848, p. 156540.

Sakakibara, T., Y. Takigawa, A. Kameyama, and K. Kurosawa, 2002, Improvement of thermoelectric properties by dispersing Ag 2 Te grains in AgBiTe 2 matrix:: Composition effects in (AgBiTe 2) 1- x (Ag 2 Te) x: JOURNAL OF THE CERAMIC SOCIETY OF JAPAN, v. 110, p. 259-263.

Shen, J., Z. Wang, J. Chu, S. Bai, X. Zhao, L. Chen, and T. Zhu, 2019, Low Contact Resistivity and Interfacial Behavior of p-Type NbFeSb/Mo Thermoelectric Junction: ACS Applied Materials & Interfaces, v. 11, p. 14182-14190.

Shen, L., Y. Chen, B. Niu, Z. Liu, J. Qin, and J. Xie, 2022a, Optimization of Interface Materials between Bi2Te3-Based Films and Cu Electrodes Enables a High Performance Thin-Film Thermoelectric Cooler: ACS Applied Materials & Interfaces, v. 14, p. 21106-21115.

Shen, L., Y. Chen, B. Niu, Z. Liu, J. Qin, and J. Xie, 2022b, Optimization of Interface Materials between Bi2Te3-Based Films and Cu Electrodes Enables a High Performance Thin-Film Thermoelectric Cooler: ACS Applied Materials & Interfaces, v. 14, p. 21106-21115.

Shi, X., J. Zou, and Z. Chen, 2020, Advanced Thermoelectric Design: From Materials and Structures to Devices: Chemical Reviews, v. 120, p. 7399-7515.

Spataru, C. D., Y. He, and F. Leonard, 2019, Atomistic study of an ideal metal/thermoelectric contact: The full-Heusler/half-Heusler interface: APL MATERIALS, v. 7.

Taylor, P. J., J. R. Maddux, G. Meissner, R. Venkatasubramanian, G. Bulman, J. Pierce, R. Gupta, J. Bierschenk, C. Caylor, J. D Angelo, and Z. Ren, 2013, Controlled improvement in specific contact resistivity for thermoelectric materials by ion implantation: Applied physics letters, v. 103, p. 043902.

Vizel, R., T. Bargig, O. Beeri, and Y. Gelbstein, 2016, Bonding of Bi2Te3-Based Thermoelectric Legs to Metallic Contacts Using Bi0.82Sb0.18 Alloy: Journal of Electronic Materials, v. 45, p. 1296-1300.

DOI: 10.18462/iir.thermag.2024.0006

ADVANCED ELASTOCALORIC AIR COOLING BY COIL-BENDING WITH AN ENERGY-EFFICIENT PERFORMANCE

Xueshi Li[(a)], Peng Hua[(a), (b)], Qingping Sun[(a), (b)]

[(a)] Department of Mechanical and Aerospace Engineering, The Hong Kong University of Science and Technology, Kowloon, Hong Kong, 999077, China, penghua@ust.hk (P. Hua), meqpsun@ust.hk (Q. Sun)
[(b)] HKUST Shenzhen-Hong Kong Collaborative Innovation Research Institute, Futian, Shenzhen, Guangdong, 518000, China, penghua@ust.hk (P. Hua), meqpsun@ust.hk (Q. Sun)

ABSTRACT

Elastocaloric cooling is an environment-friendly technology that could supplant greenhouse-gas refrigerants. The pursuit of compact and efficient elastocaloric devices is the cornerstone of its developmental trajectory. In this study, we propose an alternative actuation method called coil-bending to achieve the elastocaloric cooling in lower driving force. Through the implementation of coil-bending, we have developed a compact elastocaloric air cooler with the large specific heat transfer area (12.6 $cm^2 \cdot g^{-1}$) and the constant cold zone of NiTi wires. This innovative design allows continuous cold air output through the constant cold zone. The elastocaloric air cooler outputs a continuous cold airflow with a temperature drop of 10.6 K and achieves a specific cooling power of 2.5 $W \cdot g^{-1}$, all at a low specific driving force of 26 $N \cdot g^{-1}$. Notably, the cooler exhibits a system coefficient of performance of 3.7 (ratio of cooling power to rotated mechanical power). The performance of our coil-bending system, with its efficient and compact design, showcases the viability of elastocaloric cooling technology in the field of air conditioning.

Keywords: Refrigeration, Shape memory alloy, Elastocaloric cooling, Bending, Energy Efficiency.

1. INTRODUCTION

Space cooling is an essential aspect of modern life, with 1.6 billion air conditioners worldwide providing this service. However, air conditioners based on vapor-compression (VC) cooling technology show a significant environmental risk due to leaked refrigerants (e.g., chlorofluorocarbons and hydrochlorofluorocarbons), contributing to 7.8% of all greenhouse-gas emissions. The solid-state elastocaloric cooling has been developed in recent years and considered as the most promising alternative to the VC refrigeration. The binary NiTi shape memory alloy (SMA) with full stress-induced phase transformation shows a large entropy change up to 0.32 $J \cdot cm^{-3} \cdot K^{-1}$ under a maximum tensile stress of 750 MPa, surpassing the entropy change of hydrofluorocarbon-32 refrigerants (0.035 $J \cdot cm^{-3} \cdot K^{-1}$) in VC refrigeration. In commercial air conditioning systems, a compact and stable structure with a small volume is typically required. Among various loading modes (such as tension and compression), bending is a suitable loading mode with advantages of low driving force and high energy efficiency, which facilitates the development of desktop prototypes and enables easy benchmarking with existing products. With a specific driving force of only 5.64 $N \cdot g^{-1}$, bending can induce the phase transformation of NiTi sheets, resulting in a temperature drop of 10 K. This driving force is notably lower than that required for NiTi compression-specific driving force (260 $N \cdot g^{-1}$ at 900 MPa) in recent prototypes. Regarding energy efficiency, NiTi sheets under bending exhibit almost twice the material coefficient of performance (*COP*) compared to the same material under tension with a strain of 8%. Despite its potential, there is limited research in published literature on elastocaloric cooling systems based on bending actuation. Additionally, there are few relevant prototypes available capable of achieving continuous and efficient air cooling.

In this study, we present an alternative actuation method known as coil-bending and develop an elastocaloric air cooling system based on the coil-bending of NiTi wires. Within this system, the coiled wires release latent heat, while the uncoiled wires absorb it. The uncoiled part is intentionally maintained in a constant position to create a cold zone. Ambient air can be channeled through this constant cold zone, enabling the continuous output of cold airflow. Additionally, potential methods for work recovery within the coil-bending system have been discussed to achieve a higher energy efficiency. This desktop and independent elastocaloric air cooler utilizing coil-bending actuation reduces the driving force required and enhances overall energy efficiency.

2. ELASTOCALORIC EFFECT BY COIL-BENDING

2.1. Concept

The coil-bending principle and system design are depicted in Fig. 1(a). When SMA wire was coiled into the grooves of a lead screw, the wire had a bending-induced martensitic transformation, releasing latent heat. Upon uncoiling, the SMA wire reversely transformed into its initial straight shape in the austenite phase, absorbing heat from the ambient environment. Based on this concept, both ends of the SMA wire were initially coiled onto two independent lead screws, which were driven independently by two stepper motors. As the two motors rotated in the same direction, the SMA wire was uncoiled and coiled from one lead screw to the other. Reciprocal coiling/uncoiling was achieved by cyclically changing the rotating direction (forward and reverse). Despite the motion of coiling/uncoiling, the uncoiled part of the SMA wire remained at a constant position. This was achieved by designing the lead screws and motors to move linearly along the rails, compensating for the displacement arising from the rotation of the helical lead screws. The uncoiled part of the SMA wire would also form a cold zone where the temperature was lower than the ambience. The uncoiled part of the SMA wire was insulated in a silicon tube. Consequently, ambient air was pumped through and cooled by the uncoiled SMA wire in the constant cold zone. The released heat of the hot coiled SMA wire was transferred to the lead screw through conduction and to the surrounding still air through natural convection.

2.2. Material

The elastocaloric air cooler utilized ϕ0.50 mm and 325 mm-long round NiTi wires (Kellogg's Research Labs Corporation) with an austenitic finish temperature of 278 K. The lead screw used in the test had a root diameter of 9 mm and was fabricated through steel machining. The maximum tensile strain at the surface of the coil-bent wires on the lead screw was 7%. For comparison, a ϕ0.50 mm and 325 mm-long round NiTiCu wire (Kellogg's Research Labs Corporation) was also used in the test.

2.3. Elastocaloric effect of SMA wire under coil-bending

A thermographic photo (Fig. 1(b)) illustrates that the coiled part of the NiTi wire formed a hot zone while the uncoiled part formed a constant cold zone. During the test, the wire was uncoiled from the lead screw and coiled onto another one in 0.5 s, then held in position for 100 s. The surface temperature of the NiTi wire in operation was captured by an infrared camera (FLIR SC7700M), with an adiabatic temperature jump (ΔT_{jump}) of 14.7 K and a temperature drop (ΔT_{drop}) of 12.8 K. The cyclic stability is important in the elastocaloric refrigerator, which impacts the serve life and quality of the commercial product. Thus, the cyclic functional stability of the SMA wire was investigated. The adiabatic temperature changes of the NiTi wire under the coil-bending were recorded at different cycles shown in Fig. 1(c). The NiTi wire initially showed a temperature rise and drop of nearly 16 K in the first cycle. However, the temperature changes decreased with subsequent cycles, stabilizing after 200 cycles. A small and acceptable decrease in the elastocaloric effect of the NiTi wire was observed from 200 cycles to 400 cycles. The temperature rise of the NiTi wire demonstrated a 12.5% decrease (16 K to 14 K) from the initial state to the stabilized state, while the temperature drop showed an 18.8% decrease (16 K to 13 K). Subsequently, a comparative test was conducted to assess the temperature changes and stability of both NiTi wire and NiTiCu wire under the same driving system. Despite the NiTiCu wire showing a lower elastocaloric effect with lower adiabatic temperature changes, its stability (decrease of 6.9%) was better than that of NiTi (decrease of 18.8%). This improved stability of the NiTiCu wire could be attributed to the altered microstructure of the material caused by the presence of copper. The copper atoms might have hindered the mobility of dislocations, reducing the chances of residual martensite and ultimately improving the stability of the material.

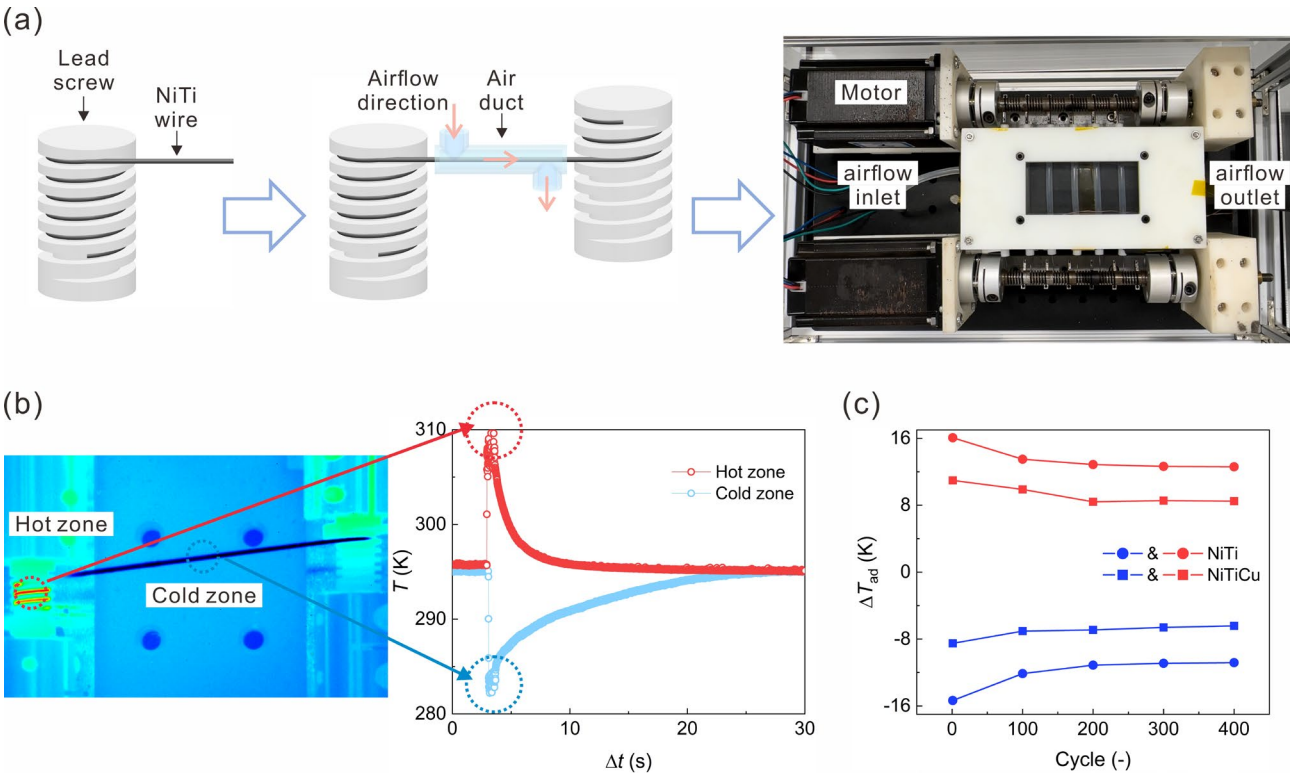

Figure 1: (a) Schematic coil-bending structure. (b) Thermographic image of the NiTi wire subjected to adiabatic coil-bending and corresponding temperature changes. (c) Temperature changes of NiTi and NiTiCu versus the cycles.

3. PEFORMANCE OF ELASTOCALORIC AIR COOLING SYSTEM

3.1. Elastocaloric air cooling system

As shown in Fig. 2(a), The uncoiled part of each NiTi wire was inserted into a silicon tube, with both ends sealed by silicon shims and sponges to prevent air leakage. The effective length of each NiTi wire in the silicon tube for heat transfer was 80 mm. Airflow was pumped into the silicon tubes and cooled by the uncoiled NiTi wires. By increasing the number of tube sections (n), the total length of NiTi wires in the air channel (L_{ht}) was extended to 80n mm. Operating principle of the air cooler in one elastocaloric cooling cycle is comprised of four stages: forward motor rotation, holding for heat transfer between the airflow and NiTi wires, reverse motor rotation, and a second holding for the heat transfer. The motors operated intermittently to save energy, and the air pump worked continuously during the operation. The air channel had an inner diameter of 2 mm. The cooling performance was evaluated at the operating frequencies f of 0.048Hz and 0.286 Hz. Two K-type thermocouples were inserted into the inlet and outlet of the air channel respectively to measure the temperature of airflow. The ambient air with room temperature was pumped into the inlet of the air channel. When the system has an air channel with 6 serially connected tube sections, the outlet airflow can have a 10.6 K temperature drop (Fig.2(b)). Since the two lead screws rotated in the same direction at the same speed, only one of the two motors was required to drive the coiling and uncoiling of NiTi wires during forward and reverse rotation. The torque sensor (JN-DN1) was installed along the axis direction of the shaft. The torque depended on the radius of the lead screw and the mass of the coiled NiTi wire. Six NiTi wires were used in the test at an operational frequency of 0.143 Hz (the middle value of operational frequencies in text). Each cycle consisted of forward rotation for 2.5 s, holding for 1 s, reverse rotation for 2.5 s, and second holding for 1 s. The recorded torque of the motor versus time is shown in Fig. 2(b), showing the periodic pattern. The specific driving force F_{sp} is calculated by Eq. (1). The low specific driving force of NiTi wires under the coil-bending was only 26 $N \cdot g^{-1}$. The average specific required torque $\overline{\Delta\tau_{sp}}$ is calculated by Eq. (2). The specific input mechanical power $\dot{w}_{mech}$ is calculated by Eq. (3).

$$F_{sp} = \frac{\Delta\tau}{r \cdot m_{NiTi}} \quad \text{Eq. (1)}$$

$$\overline{\Delta\tau_{sp}} = \frac{\oint \Delta\tau dt}{\Delta t \cdot m_{NiTi}} \quad \text{Eq. (2)}$$

$$\dot{w}_{mech} = \overline{\Delta\tau_{sp}} \cdot 2\pi \cdot n_{rps} \cdot \frac{P_r}{P} \quad \text{Eq. (3)}$$

Where r is the root radius of lead screw; Δt is duration of the torque applied on the shaft, including two rotation duration and one holding duration (here for 6 s); m_{NiTi} is the total mass of NiTi wires in the air channels, equal to the mass of coiled NiTi wires on the lead screw. where nrps is the number of rotations per second; the angular velocity is $2\pi n_{rps}$; P_r is the sum of duration of the forward rotation and the reverse rotation in each operating cycle; P is the duration of one operating cycle.

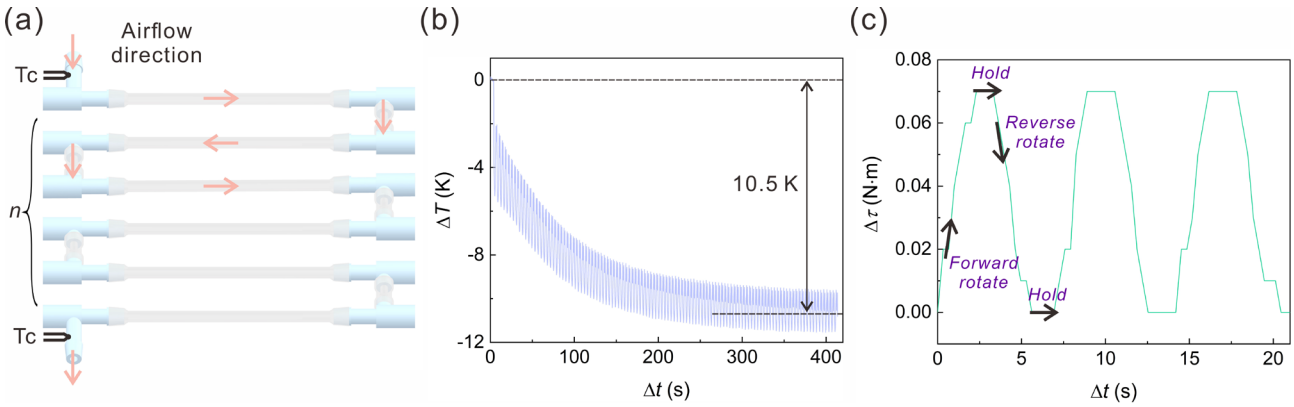

Figure 2: (a) Schematic air channel. (b) Temperature drop of the air versus the operating time at the flow rate of 0.27 L·min^{-1} (c) Recorded torque outputted by one motor at f = 0.143 Hz.

3.2. Cooling performance

The specific cooling power (SCP) of the air cooler was calculated by Eq. (4):

$$SCP = \frac{c_{air} \cdot \rho_{air} \cdot \omega \cdot \Delta T_c}{m_{NiTi}} \quad \text{Eq. (4)}$$

where ρ_{air} = 1.205 kg·m^{-3} is the air density; c_{air} = 1005 J·kg^{-1}·K^{-1} is the specific heat capacity of air; ΔT_c is the average temperature drop of the airflow in the steady state; ω is the flow rate of the outlet airflow.

The coefficient of performance (*COP*) of the air cooler was defined as the ratio of the *SCP* and the specific input mechanical power $\dot{w}_{mech}$. It is important to note that the power of the air pump was not considered when calculating the *COP*. However, it is expected that the inclusion of the pump power would result in a reduction of 10%-20% in the system *COP*. The ϕ0.50 mm NiTi wire has a large specific heat transfer area (12.6 cm^2·g^{-1}), which increases the heat transfer efficiency and results in the good cooling performances. The cooling performances of the elastocaloric air cooling system are shown in Fig.3. In different operating frequency conditions, the system using the air channel with only one tube section shows better performances in *SCP* and *COP* than the system using the air channel with 6 tube sections in serial connection. The elastocaloric air cooling system achieved a high system *COP* of 3.7 at the operating conditions of ω = 4.3 L·min^{-1} and f = 0.048 Hz (Fig. 3(b)). The *SCP* was notably enhanced to 2.5 W·g^{-1} at the operating conditions of ω = 5.1 L·min^{-1} and f = 0.286 Hz (Fig. 3(c)). There is substantial potential to enhance the energy efficiency in elastocaloric prototypes by implementing the recovery of the unloading (uncoiling) work. It is possible to involve converting the rotational mechanical work into electrical energy using electric generators and storing it in batteries. This approach, known as regenerative braking, is widely employed in battery electric vehicles. In general, regenerative braking systems can typically recover around 70-80% of the kinetic energy that would otherwise be lost as heat during traditional braking. Using this method, we can improve the energy efficiency of coil-bending-based elastocaloric air coolers in the future.

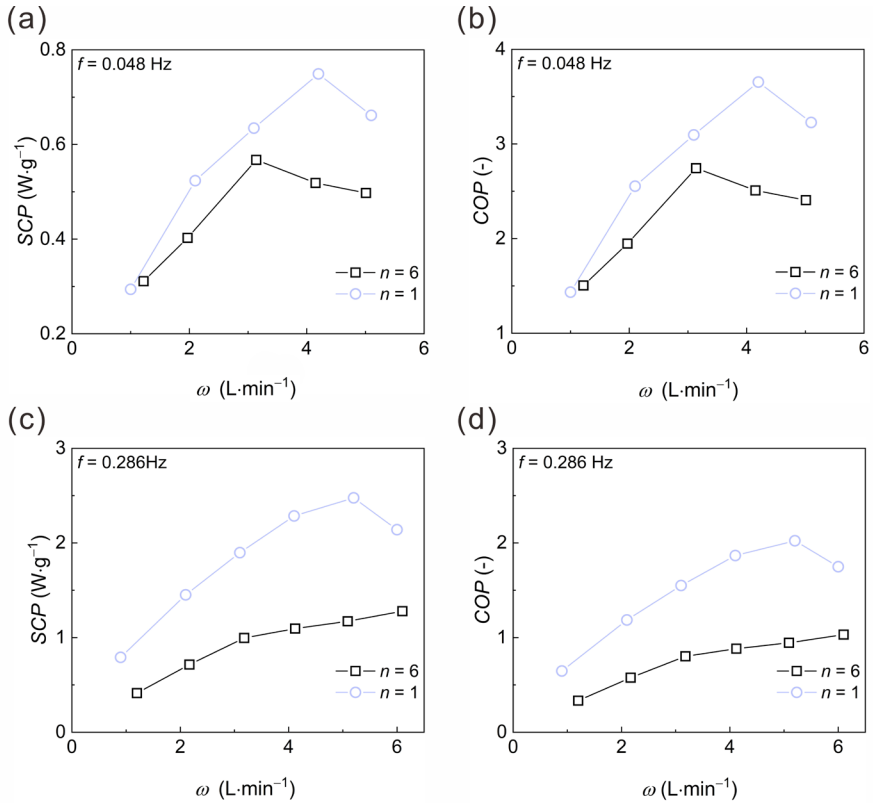

Figure 3: (a) *SCP* of the elastocaloric air cooling system versus ω at f = 0.048 Hz. (b) *COP* of the elastocaloric air cooling system versus ω at f = 0.048 Hz. (c) *SCP* of the elastocaloric air cooling system versus ω at f = 0.286 Hz. (d) *COP* of the elastocaloric air cooling system versus ω at f = 0.286 Hz.

4. CONCLUSIONS

In summary, we have introduced the concept of coil-bending actuation for elastocaloric cooling and developed an elastocaloric air cooling system based on this principle. The low specific driving force of NiTi wires under the coil-bending, at only 26 $N \cdot g^{-1}$, enabled the development of a compact desktop air cooling system with dimensions of 300 x 250 x 200 mm^3. Benefited by the constant cold zone and a large specific heat transfer area of 12.6 $cm^2 \cdot g^{-1}$ of NiTi wire in the system, the elastocaloric air cooling system successfully generated a continuous cold outlet airflow. It demonstrated an average temperature drop of 10.6 K (with an amplitude of temperature fluctuation of 0.95 K), equivalent to 83% of the adiabatic temperature drop of NiTi wires (12.8 K). Additionally, the system achieved a specific cooling power and system coefficient of performance of 2.5 $W \cdot g^{-1}$ and 3.7, respectively, under varying operational conditions. These results underscore the potential of coil-bending actuation in advancing the commercialization of elastocaloric cooling technology.

ACKNOWLEDGEMENTS

This work was financially supported by the Hong Kong Research Grants Council (GRF Project No. 16208420 and No. 16212322) (CRF project No. C6016-20G-A), the National Natural Science Foundation of China (Grant No. 52206224), and the Project of Hetao Shenzhen-Hong Kong Science and Technology Innovation Cooperation Zone (HZQB-KCZYB-2020083).

REFERENCES

Tušek, J., Engelbrecht, K., Eriksen, D., Dall'Olio, S., Tušek, J., & Pryds, N., 2016. A regenerative elastocaloric heat pump. Nat. Energy 1(10), 1-6.

Wu, Y., Ertekin, E., & Sehitoglu, H., 2017. Elastocaloric cooling capacity of shape memory alloys–Role of

deformation temperatures, mechanical cycling, stress hysteresis and inhomogeneity of transformation. Acta Mater. 135, 158-176.

Sharar, D. J., Radice, J., Warzoha, R., Hanrahan, B., Smith, A., 2021. Low-force elastocaloric refrigeration via bending. Appl. Phys. Lett. 118(18).

Hou, H., Simsek, E., Ma, T., Johnson, N. S., Qian, S., Cissé, C., ... & Takeuchi, I., 2019. Fatigue-resistant high-performance elastocaloric materials made by additive manufacturing. Science 366(6469), 1116-1121.

Moya, X., Mathur, N. D., 2020. Caloric materials for cooling and heating. Science 370(6518), 797-803.

Hua, P., Xia, M., Onuki, Y., & Sun, Q., 2021. Nanocomposite NiTi shape memory alloy with high strength and fatigue resistance. Nat. Nanotechnol. 16(4), 409-413.

Hou, H., Qian, S., Takeuchi, I., 2022. Materials, physics and systems for multicaloric cooling. Nat. Rev. Mater. 7(8), 633-652.

Ahčin, Ž., Dall'Olio, S., Žerovnik, A., Baškovič, U. Ž., Porenta, L., Kabirifar, P., ... & Tušek, J., 2022. High-performance cooling and heat pumping based on fatigue-resistant elastocaloric effect in compression. Joule 6(10), 2338-2357.

Qian, S., Catalini, D., Muehlbauer, J., Liu, B., Mevada, H., Hou, H., ... & Takeuchi, I., 2023. High-performance multimode elastocaloric cooling system. Science 380(6646), 722-727.

Zhou, G., Zhu, Y., Yao, S., & Sun, Q., 2023. Giant temperature span and cooling power in elastocaloric regenerator. Joule 7(9), 2003-2015.

Li, X., Hua, P., & Sun, Q. (2023). Continuous and efficient elastocaloric air cooling by coil-bending. Nat. Commun. 14(1), 7982.

DOI: 10.18462/iir.thermag.2024.0007

NUMERICAL AND EXPERIMENTAL STUDY OF A REVERSIBLE THERMOMAGNETIC MOTOR

Michel Risser[(a)], Sergiu Lionte[(a)], Frederic Marrazzo[(a)], Zo é Till[(a)], Christian Muller[(a)]

[(a)] Magnoric
Duppigheim, 67120, France, michel.risser@magnoric.com

ABSTRACT

*Magnoric, evolving from its previous identity as Ubiblue, has been a participant in the magnetocaloric industry since October 2018, utilizing the groundwork formerly laid by Cooltech Applications.

Thermomagnetic (TM) energy conversion is a promising technology for energy harvesting at low temperature span. In this paper we present a theoretical and experimental study of a TM Motor (TMM) built on the base of an existing cascaded gadolinium based Magnetocaloric (MC) cooling system. A numerical model of Active Magnetic Regenerator (AMR) is used to explore the operating range of the device in terms of extracted power density and energy efficiency. The experimental device is connected to a controlled hot source and to a cold thermostatic bath. Magnetic field profile, inside thermal leakages as well as mechanical energy consumption for guidance and for hydraulic distribution are characterized in view of experimental validation. The output mechanical power is investigated for a controlled frequency and the simulation is experimentally validated. The results show that TMM could be used for heat harvesting at low temperature level.

Keywords: Thermomagnetic energy conversion, Reversible thermomagnetic motor, Waste heat harvesting, Magnetocaloric materials.

1. INTRODUCTION

Climate and energy challenges require reducing our energy consumptions, working on the efficiency of energy conversion systems, and stopping the release of greenhouse gases. Wasted heat represent important energy losses that could be harvested. Above 100 °C, vapor-based organic Rankine cycles have significant potential and low cost on a large-scale unit. However, this technology is inefficient for small powers and low temperature differentials due to turbine inefficiencies (Tchanche et al., 2011). 63 % of the world primary energy consumed by the sectors of electricity generation, transportation and industry, is lost as waste heat below 100 °C (Forman et al., 2016). In France, emissions from the industrial sector below 100 °C represent 56.6 Twh×year^{-1}, ie. 52 % of the national wasted heat (ADEME, 2017). Some of these wasted heats cannot be recovered as thermal form directly on site. Their conversion into electricity in view of reinjection into the grid represents an interesting sector for their recovery, despite the limited conversion yields resulting from their low temperature levels.

Several devices‘ configurations have been presented in the past and the potentials of a wide variety of MC Materials (MCM) have been studied by Dzekan et al. (2021) in terms of thermodynamic and economic efficiency. They show that the harvesting of massive waste heat still interesting despite limited conversion efficiency. Oscillating configuration (Ahmim et al., 2019) are well suited for small powers while rotating systems inspired by the Curie wheel seem most interesting for larger powers. Nevertheless, they show limited experimental results. Zeeshan et al. (2021) present a rotating device using Gabolinium (Gd) compact blocks directly sprayed by the heat transfer fluid. The obtained mechanical power is less than 0.5 W and the conversion yield is below 0.2 % for a temperature span around 46 °C. Jiang et al. (2022) present a motionless system exploiting regeneration in order to increase the yield. Hey et al. (2022) present a detailed numerical and experimental study of a rotating system using Mn_2Fe_1Sn alloy, approaching several 10th of Watts of mechanical power for a 2 % conversion yield. Almanza et al. (2017) studies the relative performance of 1st and 2nd order MCMs in the case of a Brayton cycle use. They conclude that 1st order MCMs would present better performances provided they are weakly hysteretic. A MC cooling unit can be converted into TMM, as shown by Deepak et al. (2019) that is presenting a hybrid thermomagnetic oscillator for cooling and direct

heat conversion into electricity. Indeed, other applications than waste or renewable heat conversion can be imagined. A reversible MC machine could be used for the storage of energy into thermal form and the cogeneration of cold and heat, in view of maximizing the machine load rate. There is wide variety of applications, as the smoothing of intermittent renewable energies to match on the demand. That is a key point for the energy transition.

2. THERMOMAGNETIC MOTOR ASSESSMENT

Our MC refrigeration unit constitutes a good experimental tool for TMM assessment despite its limited design. Its typical performances reach 120 W of cooling power at 20 K temperature span. Our interest in this work is also to show the possibility of using these systems in a reversible manner and to validate our simulation tool. We are focused on the fundamental performances because auxiliary systems, as pump and motor, are not optimized.

2.1 Design of the prototype

The rotating MC machine have two magnetically synchronized inner and outer rotors, producing two magnetic field regions and two non-field regions in the cylindrical air gap. The air gap is filled with 12 AMRs of 1.6 cm by 2.6 cm cross section and 15,8 cm length in the fluid motion direction, that is parallel to the rotational axis. The AMRs are composed of a cascade of gadolinium (Gd) and gadolinium-erbium (GdEr) alloys in the form of 0.35 mm thick plates arranged in parallel with the radially oriented magnetic field and separated with 0.13 thick fluids channels. The Curie temperatures (T_C) range of the cascade varies uniformly from 0 to 20 °C by step of 5 °C. A hydraulic distribution made with customized pneumatic distributors ensures the alternative motion of heat transfer coolant inside the AMRs in synchrony with the applied field change to carry out Active Magnetic Regenerative Refrigeration (AMRR) cascaded Brayton cycles. Fluid distributors are placed on the hot side and are controlled by a mechanical cam liked with the rotating magnetic system. Each half cycle phase shifted synchronous AMRs, that are inside and outside of the magnetic field, are forming and hydraulic circuit having its own distributor. A phase shift of the fluid control, relatively to the magnetic field change, can be achieved by setting the angular offset of the cam. The fluid switching times is carried out by different cam profiles. The phase shift of the fluid flow by an half cycle reverses the carried-out magneto-thermodynamic cycles for switching from the cooling mode to the TMM mode. Figure 1 shows a photo (left) and a CAD section (right) of the MC machine. We are focused on the theoretically recoverable mechanical power density because the non-optimized design of the unit lead to significant energy consumption. Indeed, the AMRs of this prototype are positioned in rackable housings for experimental purposes. These housings do not allow the complete filling (less than 50%) of the cylindrical air gap and the frictions of the guidance are also greatly increased by the experimental requirements.

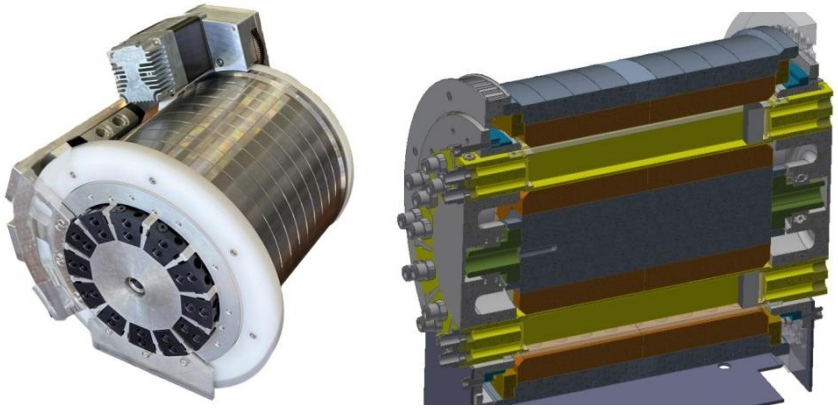

Figure 1: photo (left) and CAD cut (right) of the MC system.

The inner magnetic field profile into the air gap of the magnet assembly is characterized with a commercial gaussmeter, in view of calibrating of the simulations. The figure 2 presents the measurement of the empty air gap magnetic field norm $||B||$ as a function of the angular positions along the circumference and as function of the axial position along the AMR length direction. The maximum magnetic field reach 0.67 T around the middle of the magnetic field region. The minimum magnetic field is lower than 2 mT around the center of the non-field region. The transitions areas represent roughly 35° each between the high magnetic field regions, at over 95% of the maximum magnetic field, and the lower magnetic field regions, at below 5% of the maximum magnetic field.

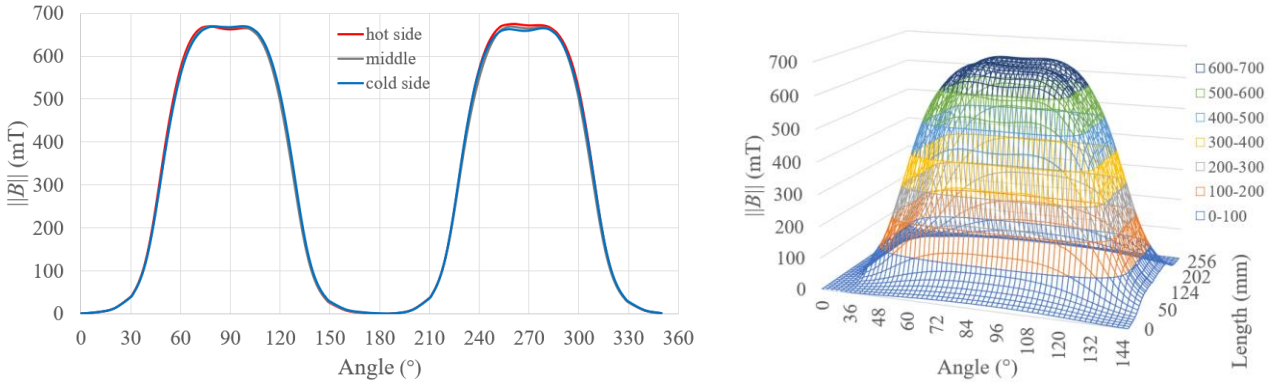

Figure 2: experimental applied magnetic field profile in the empty air gap according to the angular position (left) and spatial distribution of the magnetic field for one magnetic pole (right)

2.2 Thermodynamic simulations

A multiphysics numerical model of parallel plates-based AMR (Risser et al., 2013) is used for behavioral prediction of the TMM. The heat equation for the temperature (T) in the domain (Ω) of the solid MCM (s) that is time (t) dependent, simulated in 2D along the AMR length (x) and along the plate thickness (y) is given by:

$$\rho_s \, c_{H_i,p} \frac{\partial T_s}{\partial t} = \lambda_s \left(\frac{\partial^2 T_s}{\partial x^2} + \frac{\partial^2 T_s}{\partial y^2} \right) + \left(\dot{Q}_{MC} \right)_{\Omega_s} + \left(\dot{Q}_{dep} \right)_{\partial\Omega_s} - \left(\dot{Q}_{HT} \right)_{\Gamma} \qquad \text{Eq. (1)}$$

where ρ is the density, c is the heat capacity at constant internal magnetic field (H_i) and pressure (p) and λ is the thermal conductivity. Q are heat quantities from MC effect (MCE), heat exchange by thermal depletion (dep) and heat transfer (HT) at the fluid interface (Γ). The heat advection in the coolant fluid (f) in 1D is given by:

$$\rho_f \, c_p \left(\frac{\partial T_f}{\partial t} + u \frac{\partial T_f}{\partial x} \right) = \frac{\partial}{\partial x} \left(\lambda_f \frac{\partial T_f}{\partial x} \right) + \left(\dot{Q}_{visco} \right)_{\Omega f} + \left(\dot{Q}_{HT} \right)_{\Gamma} \qquad \text{Eq. (2)}$$

Where u is the velocity of the fluid. The viscous dissipations (visco) and heat transfer are modelled with 1D fluidic correlations related by Bavière et al. (2006) and by Shah and London (1978). The magnetocaloric coupling, function of the internal magnetic field change is correlated with the adiabatic (ad) temperature change and the magnetic (M) entropy (s) change, as it follows :

$$\dot{Q}_{MC} = \rho_s \, c_{H_i,p} \frac{\partial T_{ad}}{\partial H_i} \frac{\partial H_i}{\partial t} = -\rho_s \, T_s \frac{\partial s_M}{\partial H_i} \frac{\partial H_i}{\partial t} \qquad \text{Eq. (3)}$$

A 3D model ensures the computation of H_i as function of the applied magnetic field. The magnetization $J(T,H_i)$, $c_{Hi,p}(T,H_i)$, and all derived materials properties as entropy, magnetic entropy change (Δs_M) and adiabatic temperature change (ΔT_{ad}), are obtained with Bean and Rodbell (1962) magnetic model and Debye model for lattice heat capacity. Theoretical sets of MCM data are correlated with experimental measurements related by Lyubina (2017) for adjusting the free parameters. The data set of Gd and GdEr alloys are obtained by switching the T_C and calibrating the amplitude of the calculated ΔT_{ad} relatively to experimental direct measurements. Figure 3 presents the modelled data for pure Gd as example.

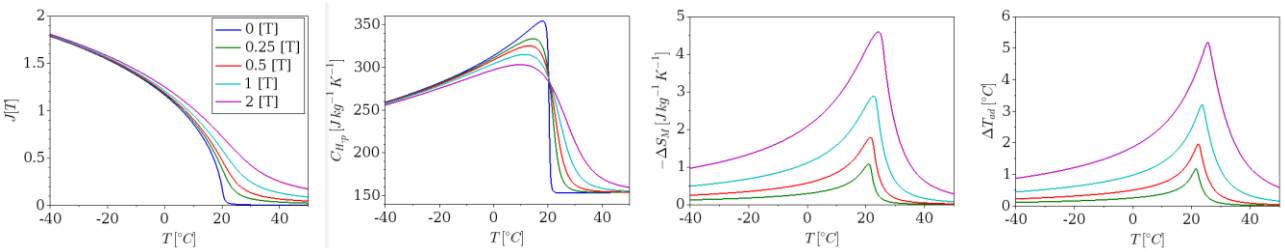

Figure 3: pure Gd data simulated with Bean and Rodbell based magnetic model and Debye model

Figure 4 presents the behavioral simulation of the TMM vs the frequency (f), the flow (q) and the ratio of coolant volume transfer on the AMRR cycle (R_{vol}). It is mapped with an evolutionnary algorithm. The temperature span is optimaly set with respect to the T_C cascade, i.e. -2 °C on the cold side and 24 °C on the hot side. A maximum recoverable mechanical power density ($\dot{W}_r$) of 32 W×dm^{-3} of AMR volume (V) is obtained. $\dot{W}_r$ is deduced from the irreversible magnetic work ($\dot{W}_{mag}$) from which we subtract the viscous dissipations resulting from pumping work ($\dot{W}_{visco}$). The color code represents the product of the AMR recoverable volumic power density by the AMR conversion efficiency (η_{AMR}) relatively to the Carnot limit (η_{Carnot}).

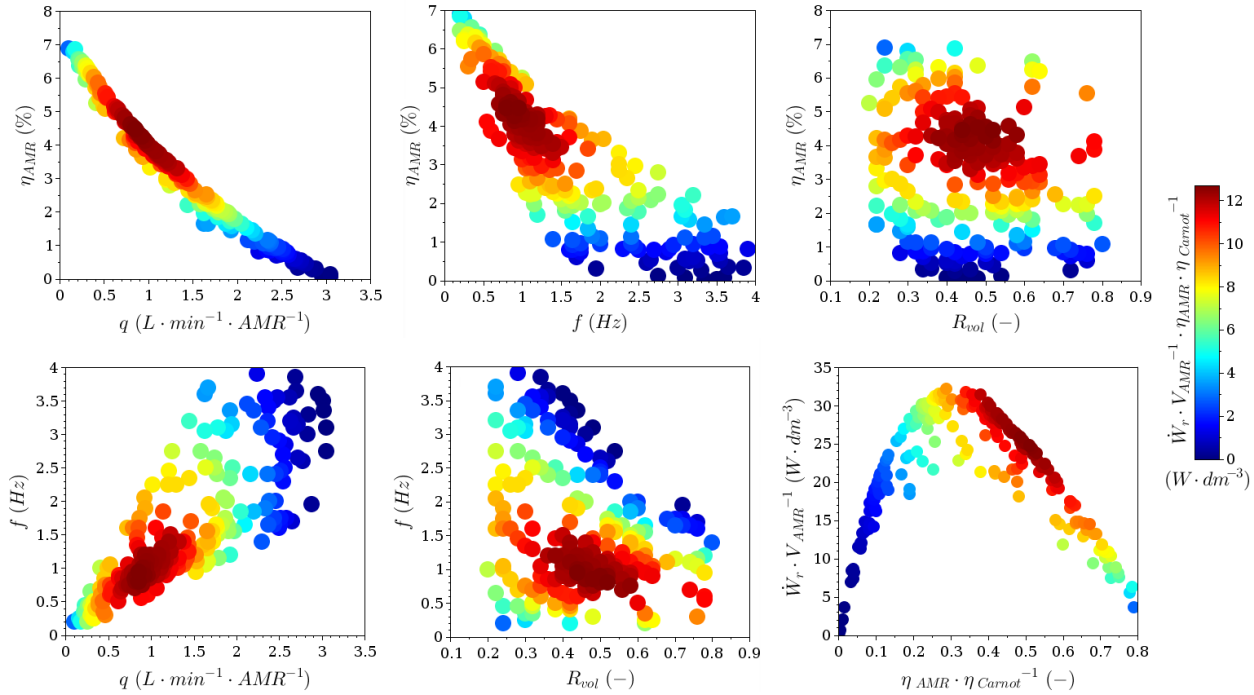

Figure 4: behavior of the TMM mapped with evolutionary algorithm for $T_{cold\ in}$ = -2 ℃ and $T_{hot\ in}$ = 24 ℃

2.3 Experimental bench and characterization

Our objective is the characterization of the fundamental $\dot{W}_r$ at the AMR scale as a function of the hot power supplied to the TMM. Figure 5 shows the experimental bench. In refrigeration mode a submerged electrical heating cartridge simulates the power at the cold source. The thermostatically controlled bath maintains the temperature of the hot source heat exchanger. We use 3 liquid-liquid heat exchangers respectively dedicated to the 3 primary coolant fluid circuits of the synchronous AMR groups. In TMM mode, the thermal sources are reversed. The heating cartridge simulates the hot source with a precisely controlled power ($\dot{Q}_{HC}$). The cold source temperature is maintained by the thermostatic bath across the heat exchangers. PT100 temperature probes measure the machine's inlet and outlet temperatures independently for each of the 3 circuits on the cold side. On the hot side, the inlet and outlet temperature measurement are made at the heating cartridge stage. The heat transfer coolant flow rates (q) are imposed by 3 separate pumps in order to balance the AMR circuits whose the behavior is not perfectly homogeneous. The flow rates are measured by 3 Doppler effect flow meters placed at the pumps outlet and before the distributor creating the alternative flow. The hydraulic circuits are thermally insulated with polyurethane foam tubes that were partially removed for the photo of the figure 5. The heat transfer coolant is a mixture of water, glycol, and corrosion inhibitors.

The magnetic rotors are connected to an electric motor through a reduction belt and a gearbox. The torque meter is placed on the drive shaft between the speed reducer and the belt to obtain the mechanical power $\dot{W}_{mec}$. The motor which allows the rotation in cooling mode is used as a starter and a brake in TMM mode. The starter is necessary to launch the TMM into rotation since its hydraulic distribution is mechanically synchronized with the magnets. Quickly after the beginning of the rotating, the motor become a receiver that allows the control and the limitation of the rotation speed and thus simulates a receiving load at a given operating speed. Maximum Power Point Tracking (MPPT) algorithm based on the torque and the speed can be used to approach the best power. The current motor control does not allow the recovery of the mechanical power into electrical power. Therefore, mechanical power extracted from the TMM is lost into heat at the heatsink of the motor control board.

The thermal leakages ($\dot{Q}_{leak}$) are characterized to obtain the net hot power supplied to the AMRs ($\dot{Q}_{hot\ AMR}$). The heat losses of the pipes and the distribution at the hot side are measured by heating the circuits and bypassing the TMM. A thermal loss of 44 W is obtained for a hot source at 34 °C and an ambient temperature of 21 °C, i.e. a loss of 3.38 W×K^{-1}. Measurements of pressure drop are performed to obtain the viscosity losses into pipes and hydraulic distribution ($\dot{W}_{wisco\ PD}$) that are also converted into heat at the hot side. The heat losses between the hot and cold sides inside the TMM are experimentally measured beforehand, using dummy AMR housings. These dummy AMRs apply to the structure of the machine temperature conditions that are very similar to those seen in the presence of real AMRs with a thermal gradient. The temperature at the cold side inside the AMR housing is imposed by a flow coming from a thermostatic bath while the hot power is dissipated by electrical resistances placed inside each dummy housing on the hot side. The power vs. internal temperature of the housings is characterized as a function of the rotation speed of the magnetic system. A heat flux of approximately 7.5 W for a temperature span of 20 K is obtained for a rotation speed of 30 rpm corresponding to 1 Hz for AMRR cycles. That represents an overall internal thermal leakage of 0.38 W×K^{-1} or 12 W for the experimental span that will be used. Advection measurements of heat provided to the TMM hot side by the mechanical losses and the motor heating of the pumps have a big uncertainty. A very low temperature difference, less than 0.1 K, before and after the pumps is observed. That is corresponding to a power between 0 and roughly 40 W. Assuming most of the heat of the pump is rejected at the heatsink, this heating power is not considered in the TMM heat input.

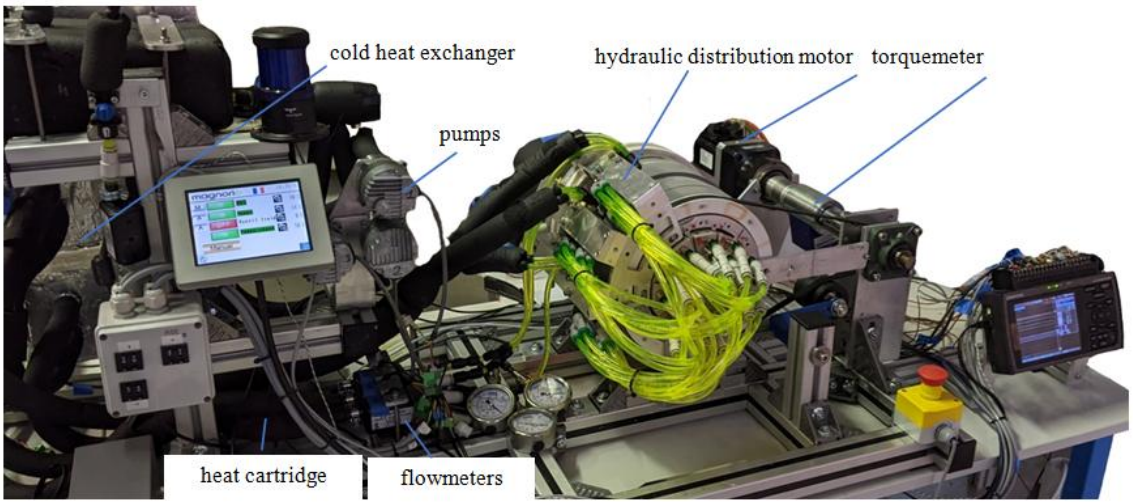

Figure 5: TMM experimental bench with its auxiliary systems, the thermal insulations are removed for the photo

The measurements of one heat conversion test vs time are presented in Figure 6 on the left. The temperature of the hot source is not perfectly stable for the expected fluid flow rates because the thermal power absorbed by the TMM hot side, added to the thermal losses, are slightly higher than the maximum power of the heating cartridge. Furthermore, the thermostatic bath and the cold intermediate heat exchangers allow limited cold power so that we are not able to ideally set cold source temperature with respect to the coldest T_C. The calibrating measurement is therefore made with hot temperature around 34 °C and the cold one around 2 °C. The simulations show an optimal operating frequency close to 1 Hz ie. 30 rpm, as well as sweep rates (R_{vol}) of 0.5 corresponding to flow rates (q) of approximately 1.1 L×min^{-1}×AMR^{-1} ie. 2.2 L×min^{-1}×circuit^{-1}. At the beginning of the test, the TMM is stopped after the setting time of the temperatures that in not represented. The pumps and motors are switched on around the 40th second. The steady state is approached around the 200th second and the net maximum extracted mechanical power at the motor shaft is found as $\dot{W}_{mec}$ = -15 W. The machine is poorly optimized in terms of auxiliary systems. Hydraulic distribution made with market components produces a lot of pressure losses and mechanical friction. The driving of customized air distributors by the cam is also energy consuming and is easily optimizable with dedicated components currently under development. Commercial pumps have limited yield. Likewise, the rotational guidance of magnetic system produces a lot of friction because it is complexified by the experimental need to make the AMR holder easily removable. As we are considering custom auxiliary systems and optimized design, we evaluate the performance of the TMM neglecting the mechanical friction of guidance and hydraulic distribution. These friction consumptions ($\dot{W}_{GD}$) are obtained during a dedicated test presented in Figure 6 on the right. The AMRs are heated close to 36 °C with continuous coolant flow while the cold source is bypassed. This makes it possible to strongly reduce the MCE, and therefore, the consumption resulting from irreversible magnetic work associated with nonadiabatic conditions for the MCM in presence of coolant. An absorbed power $\dot{W}_{mec}$ close to 15.8 W is obtained under these conditions. This consumption is slightly higher that previous measurements with empty AMR holder certainly because of the magnetic attraction forces

applied on the guidance and the remaining MCE for the highest T_C. Therefore, this absorbed power seems to be the higher bound.

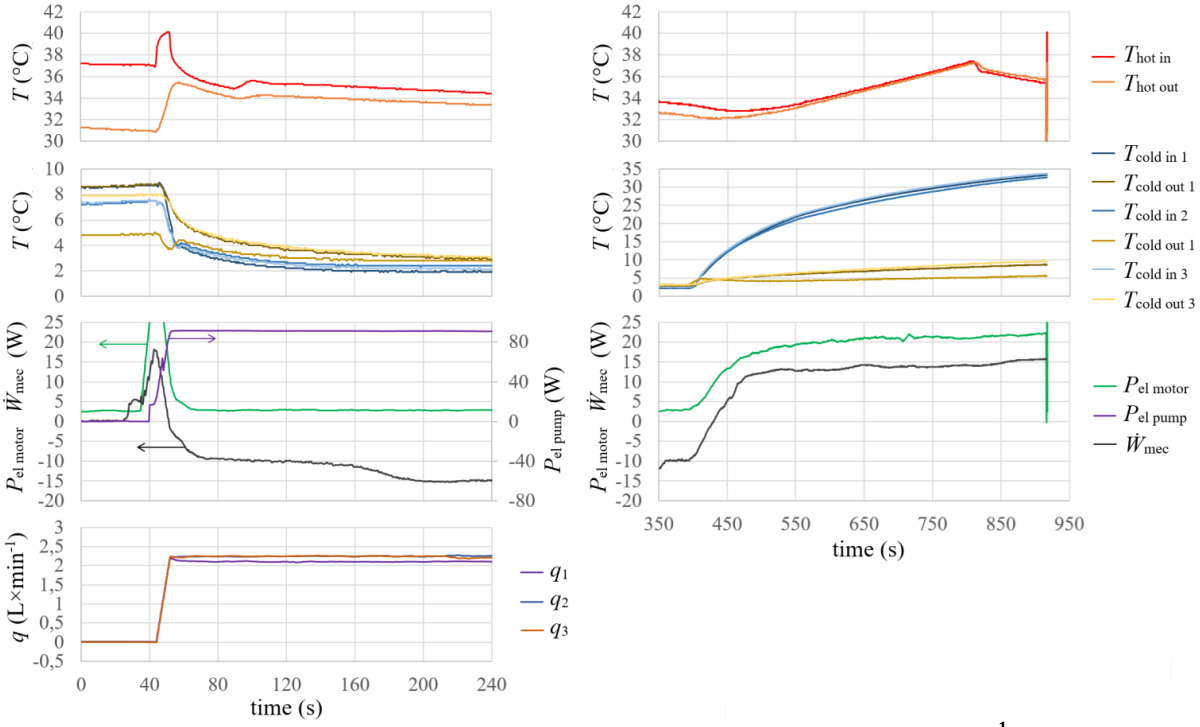

Figure 6: experimental measurement at 1 Hz ie. 30 rpm and total coolant flow = 6.6 L ×min^{-1}. On left, the starting of the test up to the maximum extracted mechanical power. On right, the TMM is disconnected to the cold source. The warming of the AMR is used for assessing the mechanical consumption of the guidance and the flow distribution

The raw power of the magnetic work ($\dot{W}_{mag}$) converted by the AMRs is obtained considering the friction consumption $\dot{W}_{GD}$ that is measured with warmed AMRs and the net maximal mechanical power at the shaft. Electrical consumption of the pumps ($P_{el\ pump}$) is monitored. Nevertheless, we are only using the viscous work resulting from the AMR pressure drop ($\dot{W}_{visco\ AMR}$) to assess the AMR conversion yield (η_{AMR}) that is defined as it follows:

$$\eta_{AMR} = (-\dot{W}_{mag} - \dot{W}_{visco\ AMR}) \times \dot{Q}_{hot\ AMR}^{-1} \qquad \text{Eq. (4)}$$

The validation of the numerical model is done with a specific simulation following these imperfect experimental temperature conditions. Table 1 summarizes the main parameters of the experiment. The sub-table (A) gives the common parameters between simulation and experiment. The sub-table (B) gives the parameters relative to the prototype structure and the experimental bench. The sub-table (C) give the experimental and simulated results obtained at the AMR scale. A TMM with a perfect mechanical design would achieve an efficiency of 3.8 % with these non-optimal temperature conditions with respect to the T_C cascade. The power consumed by the motor controller ($P_{el\ mot}$) remains positive because it does not recover the energy which is then dissipated as heat at the board heatsink. The fundamental magnetic yield ($\eta_{FM} = \dot{W}_{mag.\ AMR} \times \dot{Q}_{hot\ AMR}^{-1}$) obtained without taking into account $\dot{W}_{visco\ AMR}$ is roughly the half of the Carnot limit.

Table 1. main parameters and measurements for the experimental bench and the simulation

A: common parameters			C: TMM internal parameters at AMRs scale			
					Experimental	Simulation
f	(Hz)	1				
$T_{\text{hot in}}$	(°C)	34	q_{system}	(L×min^{-1})	6.6	6.5
$T_{\text{cold in average}}$	(°C)	2.2	$q_{\text{per AMR}}$	(L×min^{-1})	1.1	1.08
			R_{vol}	(-)	0.54	0.53
B: experimental bench			$\dot{Q}_{\text{hot AMR}}$	(W)	550	460.7
$\dot{Q}_{\text{HC}}$	(W)	590	$\dot{W}_{\text{mag}}$	(W)	-31	-23.6
$\dot{Q}_{\text{leak}}$	(W)	-56	η_{FM}	(%)	5.6	5.1
$\dot{W}_{\text{wisco PD}}$	(W)	16.3	$\eta_{\text{FM}} \times \eta_{\text{Carnot}}^{-1}$	(%)	54.5	49.1
$P_{\text{el mot}}$	(W)	2.3	$\dot{W}_{\text{visco AMR}}$	(W)	10.1	9.0
$P_{\text{el pump}}$	(W)	92	$\dot{W}_{\text{r AMR}}$	(W)	-20.9	-14.6
$\dot{W}_{\text{GD}}$	(W)	15.8	η_{AMR}	(%)	3.8	3.3
η_{pump}	(%)	28.7	$\eta_{\text{AMR}} \times \eta_{\text{Carnot}}^{-1}$	(%)	36.7	30.3

Flow correlations for $\dot{W}_{\text{visco AMR}}$ are underestimating the pressure drop. It can be explained by the non-perfect shape of the AMR channels. The extracted magnetic work $\dot{W}_{\text{mag. AMR}}$ is underestimated by the simulation. It can be explained by the calibrating of our theoretical model of MCM data that is performed with experimental measurements of ΔT_{ad}. Therefore, it is expected that the predictive TMM simulation presented in fig. 4 are underestimating the performances in the case with optimal temperature range.

3. CONCLUSIONS

This work demonstrates the possibility of using an MC refrigeration machine in a reversible manner to convert a low temperature differential into work. The maximum magnetic field change applied in the empty air gap is 0.67 T. The source temperatures used for the test are poorly suited to the T_C cascade, due to the experimental problems encountered. The behaviors of the AMR circuits are not perfectly homogeneous. Under these conditions, the net theoretical recoverable mechanical power at the AMR level is close to 21 W. This value is obtained if we ignore the inefficiencies of the customized commercial auxiliary systems which are components not optimized for this application. The conversion efficiency experimentally obtained at the AMR level reaches nearly 37% of the Carnot efficiency. The numerical simulation uses modeled MMC data that are calibrated on experimental ΔT_{ad} measurements. The simulation results underestimate the extractable magnetic work by almost 24%. Viscous dissipations are underestimated by nearly 11% by the model. We can explain these differences by the imperfect nature of the AMR plates channels and the additional coolant pipes length and fluid diffusers on either side of the AMRs, which are not considered in the theoretical model. The numerical model is used to obtain the behavioral map of the TMM. The maximum simulated recoverable power density reaches 32 W×dm^{-3} of AMR with 35 % of the Carnot yield. The maximum simulated conversion efficiency tends towards 80% of the Carnot limit with very limited recoverable power.

REFERENCES

ADEME, 2017. Excess heat. French Agency for ecological transition, ISBN : 979-10-297-0844-2 - April 2018.

Ahmim, S., Almanza, M., Pasko, A., Mazaleyrat, F., LoBue, M., 2019. Thermal energy harvesting system based on magnetocaloric materials. Eur. Phys. J. Appl. Phys. 85 , 10902, doi: 10.1051/epjap/2019180284.

Almanza, M., Pasko, A., Mazaleyrat, F., LoBue, M., 2017. First vs second order magnetocaloric material for thermomagnetic energy conversion. IEEE Trans. on Mag. 2502106, hal-01514750, doi: 10.1109/ TMAG.2017.2697398.

Bavière, R., Favre-Marinet, M., Le Person, S., 2006. Bias effects on heat transfer measurements in microchannel flows. Int. J. of Heat and Mass Transfer (49), 3325-3337, doi: 10.1016/ j.ijheatmasstransfer.2006.03.014.

Bean, C. P., Rodbell, D. S., 1962. Magnetic Disorder as a First-Order Phase Transformation, Phys. Rev. 126, 104, doi: 10.1103/PhysRev.126.104.

Deepak, K., Varma, V.B., Prasanna, G., Ramanujan, R.V., 2019. Hybrid thermomagnetic oscillator for cooling and direct waste heat conversion to electricity. Appl. Energy 233–234, 312–320, doi: 10.1016/j.apenergy.2018.10.057.

Dzekan, D., Waske, A., Nielsch, K., Fähler, S., 2021. Efficient and affordable thermomagnetic materials for harvesting low grade wasteheat. APL Mater. 9, 011105, doi: 10.1063/5.0033970.

Forman, C., Muritala, I.K., Pardemann, R., Meyer, B., 2016. Estimating the global waste heat potential. Renew. Sustain. Energy Rev. 57, 1568–1579, doi: 10.1016/j.rser.2015.12.192.

Hey, J., Repaka, M., Li, T., Tan, J.L., 2022. Design Optimization of a Rotary Thermomagnetic Motor for More Efficient Heat Energy Harvesting. Energies 15(17), 6334, doi: 10.3390/en15176334.

Jiang, C., Zhu, S., Yu, G., Luo, E., Li, K., 2022. Numerical and experimental investigations on a regenerative static thermomagnetic generator for low-grade thermal energy recovery. App. Energy 311, 118585, doi: 10.1016/j.apenergy.2022.118585.

Lyubina, J., 2017. Magnetocaloric materials for energy efficient cooling J. Phys. D: Appl. Phys. 50, 053002, doi: 10.1088/1361-6463/50/5/053002.

Risser, M., Vasile, C., Muller, C., Noume, A., 2013. Improvement and application of a numerical model for optimizing the design of magnetic refrigerators. Int. J. Ref. 36, 950-957, doi: 10.1016/j.ijrefrig.2012.10.012.

Shah, R.K., London, A.L., 1978. Laminar Flow Forced Convection in Ducts: a Source Book for Compact Heat Exchanger Analytical Data. Adv. in Heat Transfer, Academic Press, New York, ISBN-13 978-0120200511.

Tchanche, B. F., Lambrinos, G., Frangoudakis, A., Papadakis, G., 2011. Low-grade heat conversion into power using organic Rankine cycles - A review of various applications. Renew. Sustain. Energy Rev. 15, 3963–3979, doi: 10.1016/j.rser.2011.07.024.

Zeeshan, Mehmood, M. U., Cho, S., 2021. Optimization of a Thermomagnetic Heat Engine for Harvesting Low Grade Thermal Energy. Energies 14(18), 5768, doi: 10.3390/en14185768.

DOI: 10.18462/iir.thermag.2024.0008

LARGE-SCALE MAGNETIC COOLING UNIT FOR INDUSTRIAL APPLICATIONS

Sergiu LIONTE[(a)], Michel RISSER[(a)], Christian MULLER[(a)], Frederic MARRAZZO[(a)]

[(a)] Magnoric
Duppigheim, 67120, France, sergiu.lionte@magnoric.com

ABSTRACT

Amidst growing regulations on refrigerant fluids in the refrigeration and air conditioning sectors, there's a clear shift towards alternative technologies like magnetic cooling. The past decade has witnessed a concerted effort by research institutions and commercial entities in advancing magnetic cooling technologies, which are integral in responding to the changing demands of the market.

In this paper, we discuss the development of a new magnetic cooling unit specifically engineered for industrial applications within a defined temperature range demonstrates our expertise in areas such as mechanical engineering, optimal magnetic field arrangement, Active Magnetic Regenerator (AMR) geometry, and magneto-hydraulic synchronization.

We trace the evolution of this magnetocaloric unit from its conceptualization, guided by an Artificial Evolution-based numerical model, to its realization through detailed CAD designs. The paper goes on to elaborate on the unit's technical specifications and initial operational outcomes. These insights underscore the unit's potential efficacy and applicability in magnetic cooling and the broader context of caloric-based refrigeration technologies.

Keywords: Magnetic cooling, Caloric device, Magnetocaloric materials

1. INTRODUCTION

At the last Conference of the Parties (COP28) held in Dubai in December 2023, at least 60 countries signed a pledge to cut emissions from the cooling sector. This global cooling pledge calls on nations to cut cooling-related emissions by at least 68 per cent from 2022 levels by 2050, as the need for cooling is set to triple in that time period with the planet warming up, as stated in the action plan (COP28 action plan, 2024).

The today’s solutions for the refrigeration market based on natural refrigerants have a series of drawbacks that still require that research has to be done to find the best replacements. Ammonia (R717) is poisonous in high concentrations. Carbon dioxide (R744) works with high pressure values (around 100 bar at the compressor discharge), therefore the system must be substantially reinforced. Hydrocarbons such as propane (R290) and isobutane (R600a) are flammable, require special certifications and are limited to a low charge of maximum 150 g that restricts the application range. All these continuous regulations and limitations in terms of refrigerants lead to an increased interest towards alternatives to existing vapor-compression technologies. Among all the emerging cooling technologies, Magnetic Refrigeration (MR) has been identified as the most promising one (S. Qian, 2016).

This technology exploits the Magnetocaloric Effect (MCE), which is a heat and entropy response of magnetocaloric materials when exposed into a changing magnetic field (Kitanovski et al., 2015). This technology, working with solid-state refrigerants eliminate all risks tied to refrigerant leakage into the atmosphere and it is completely off-regulations in terms of F-Gas.

Most researchers from all scientific research groups concentrated separately either on developing magnetocaloric materials, making magnetic system improvements or dealing with fluid dynamics or heat transfer analysis.

Regarding design solutions, one can mention the prototype operating with a high magnetic flux density of 1.6 T (Dall'Olio et al., 2021), with a large mass flow rate of heat transfer liquid (Masche et al., 2022), with high frequency values (Lozano et al., 2014) or with large quantities of MCM (Peixer et al., 2023b).

Also, important progress has been recorded in recent years, with the development of various prototypes, such as a refrigeration unit (Lionte et al., 2020), a heat pump (Dall'Olio et al., 2021, Masche et al., 2022), a wine cooler (Nakashima et al., 2021), and an air conditioner (Peixer et al., 2023b).

In order to build reliable and efficient industrial cooling units, the entire design of magnetocaloric systems has to be well interconnected and the research has to be completed with mechanical engineering efforts in terms of components assembly in order to increase the performance of the magnetic cooling prototypes. For the MR to successfully be considered as a potential candidate in replacing the actual cooling technology, it has to reach a sufficiently large cooling power value under a real operating-conditions temperature span, together with reduced mass and volume, but also, most important, with a competitive price. So far, only few groups presented prototypes having both a useful temperature span and a sufficient cooling capacity to integrate an industrial application.

This paper presents a novel generation of a magnetic refrigeration unit, built upon an entirely new architecture that we believe is the best compromise in terms of power density and thermodynamic efficiency. This device, designed for a specific industrial application with a fixed temperature span, represents our latest state-of-the-art achievement and includes our latest know-how in terms of mechanics, magnetic field disposal, AMR geometry and magneto-hydraulic synchronization. After presenting the Artificial Evolution-based numerical model used to design this unit, together with the comprehensive engineering efforts to design and build the unit from the CAD files to an existing unit, the characteristics of the unit will be detailed. The preliminary results will also be presented and analyzed.

2. PROTOTYPE DESIGN: FROM SIMULATIONS TO MECHANICAL ASSEMBLY

The numerical modelling process initially started with a relatively large campaign of numerical simulations (containing around 6000 simulation cases), based on the Scope of Work provided by the industrial partner. Several architectures, geometric dimensions and operating points have been identified, based on the purpose of the project, an industrial process with fixed span temperatures. Multiple parameters have been varied such as the T_c layering, material holder's length, magnetic field intensity, operating frequency, flow rate, etc., to identify the most adapted combination of parameters. Choosing the best parameter set is a complex task because it involves a large number of entities in several multi-physics interactions, which are responsible for complex and emergent behaviors.

2.1. Numerical simulations and the Evolutionary Algorithm model

The functioning of a magnetocaloric unit is represented by the use of several operating points obtained by changing the driving parameters such as the frequency and the flow rate value. These operating points represent a behavior map which is traced by a Pareto front. The calculation of a global Pareto's front is also a long and expensive method which implies calculation of irrelevant points of simulation. For this purpose, Roy et al. (2017) introduced the use of a genetic algorithm in order to solve a multiobjective requirement of MC systems.

For the initial numerical simulations part, we used a validated multiphysics numerical model which is in continuous development since the Risser's paper (Risser et al., 2013). It is made of a 3D magnetic - 2D thermal - 1D fluidic modules. Several optimizations were made at the code level to obtain better computation speed and accuracy. Both theoretical sets of material data and numerical methods for multiphysics (magneto-thermics) coupling ensure a good conservation of energy and an accurate computing of the anergy generation.

The magnetization M, the specific heat capacity c_p, and all derived materials properties $(S, \Delta S_M, \Delta T_{ad})$, all internal magnetic field and temperature dependent, are obtained with a Bean & Rodbell - Smart - Debye based model similar to (Piazzi et al., 2016) or with an adapted Weiss - Debye model described in (Risser et al., 2016). Theoretical sets of MCM data are correlated with experimental measurements performed on different samples at the ENSICAEN – CRISMAT, a laboratory of the French National Center for Scientific Research (CNRS).

The 2D model for heat dissipation in the Magnetocaloric Material (MCM) is represented by the following equation:

$$\rho_s c_p \frac{\partial T_s}{\partial t} = \lambda_s \left(\frac{\partial^2 T_s}{\partial x^2} + \frac{\partial^2 T_s}{\partial y^2} \right) + \left(\dot{Q}_{\mathrm{MC}} \right)_{\Omega_s} + \left(\dot{Q}_{\mathrm{dep}} \right)_{\partial \Omega_s} - \left(\dot{Q}_{\mathrm{HT}} \right)_{\Gamma} \quad \text{Eq. (1)}$$

The 1D model for the heat advection in the coolant fluid is represented by the following equation:

$$\rho_f c_p \left(\frac{\partial T_f}{\partial t} + u \frac{\partial T_f}{\partial x} \right) = \frac{\partial}{\partial x} \left(\lambda_f \frac{\partial T_f}{\partial x} \right) + \left(\dot{Q}_{visco} \right)_{\Omega f} + \left(\dot{Q}_{HT} \right)_{\Gamma} \quad \text{Eq. (2)}$$

The magnetocaloric coupling, represented by the Magnetocaloric Effect (MCE) is represented by the following equation:

$$\dot{Q}_{MC} = \rho_s c_p \frac{\partial T_{ad}}{\partial H_i} \frac{\partial H_i}{\partial t} = -\rho_s T_s \frac{\partial s_M}{\partial H_i} \frac{\partial H_i}{\partial t} \quad \text{Eq. (3)}$$

Evolutionary Algorithms (EA) are intended to implement the natural Darwin evolution theory into a virtual environment. These algorithms can be applied on technical systems with reproduction laws not limited to those observed in nature. Extensive literature on this topic was published since Tsutsui and Collet in (2013). We define an entity as a configuration of MC system with a given combination of input parameters.

The behavior of the entity is assessed, and the evolution process is characterized by the size of the initial population, the number of entities (parents) selected for each generation and the number of children each generation has. The evolution laws are a combination of mutations and crossovers from two to many parents, by pair or by group of several entities. At the beginning, the algorithm starts with random entities in the possible space. On each successive generation, the best entities supplant the less efficient ones and will lead to new children. Because the initial entities are random, the evolution process can perform all the possible and relevant branches of the tree of evolution, without being trapped by local optima and by the bias of human judgment.

The following figure shows the process of evolutionary optimization of the population, based on iterative generations of individuals, with the aim of finding the best entities:

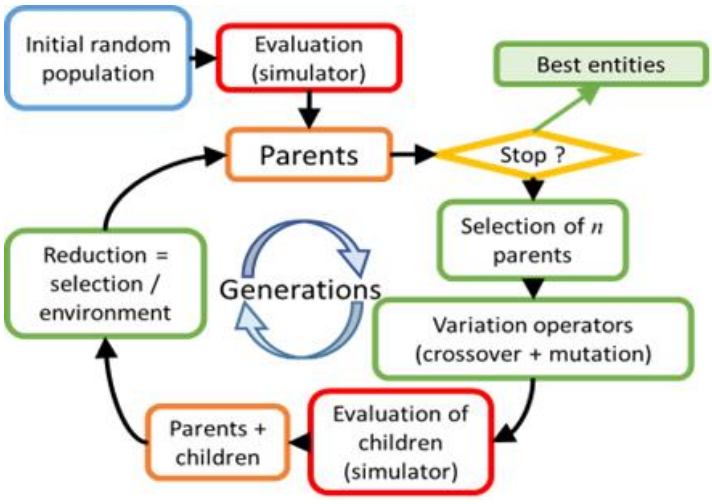

Figure 1: Evolutionary optimization procedure

The selection of the best entities is done based on a weighting function, as presented in the following equation:

$$\chi(x_1, \ldots, x_i, \ldots, x_n) = \left(\frac{\eta}{\eta_{Carnot}}\right)^a \left(\frac{\dot{W}_R}{V_{AMR}}\right)^b \quad \text{Eq. (4)}$$

The process of generating the next generation of children is performed either by crossover, mutation or cloning, depending on the results of the previous equation. The following figure shows the visual representation of the process of generation of a second population, based on the Local Gradient Method (LGM):

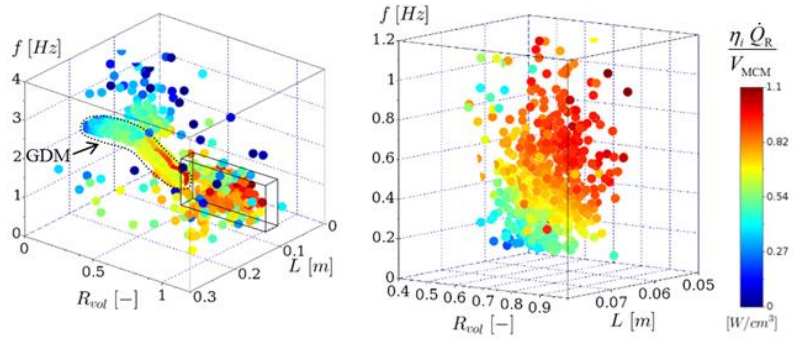

Figure 2: Generation process of a second generation

2.2. Magnetic field simulation

The magnetic assembly has been designed according to a simulation process of the total magnetic field. 3D simulations based on Finite Element Method (FEM) were internally performed with different design's perspectives of the magnetic systems. Two software packages have been used in order to identify the most adapted configurations. Initially, FEMM package has been used for the pre dimensioning of the magnetic system and in a second phase, the magnetic field distribution has been verified with a commercial 3D software, FLUX 3D.

The multi-objective optimization process involving the 3D simulations seeks to maximize the difference of the internal magnetic field (H_i) inside the MCM between high field regions and low field regions of the same volumes.

This process was expected to identify the most adapted topologies for the iron yoke border shape, the segmentation distribution and the magnetization pattern of the PM, the shape of the iron components and the regenerator's geometry and distribution over the entire magnetic surface. The analysis of the resulted magnetic induction values, the cost efficiency, the mechanical and hydraulic connection possibilities, and the weight and size requirements pointed us to using a 4 poles magnetic system with 6 AMRs under the pole.

The results visible in the following figure are obtained with a 3D FEM-based commercial model and are confirmed by a campaign of measurement of the magnetic field values in the air gap of the prototype, which will be presented in the results chapter of this paper.

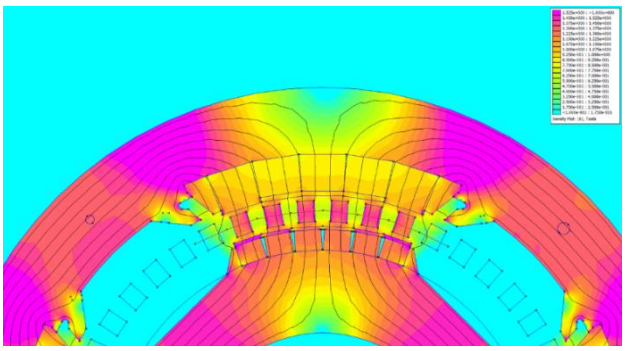

Figure 3: 3D FEM Magnetic induction simulation of the magnetic system assembly used for this application

2.3. CAD design and assembly of the MC cooling unit

The magnetic cooling unit has been designed for an industrial application for a fixed span. It has the following characteristics:

Magnetic system	In-house assembled magnetic system from NdFeB
Temperature span value	20K, from 0°C to 20°C
Magnetic field intensity	B_{max} = 0.86 T
Iron rotors	2 rotors from steel
AMR layering	48 AMRs in total (29.3 kg) - parallel plates of 0.35 mm - microchannels of 0.15 mm - Gd and GdEr, 5 Tcs : 0°C - 20°C
Hydraulic distribution	Mechanical type, in-house tailored One distributor for each AMR

The design of the prototype has been made with a commercially available CAD software and the main components can be seen into the following picture. One can identify into the picture the exterior rotor, the magnet assembly, the interior rotor, the MCM layering with 48 AMRs, the exterior flange, the hydraulic distribution unit, the driving belt and the electric motor.

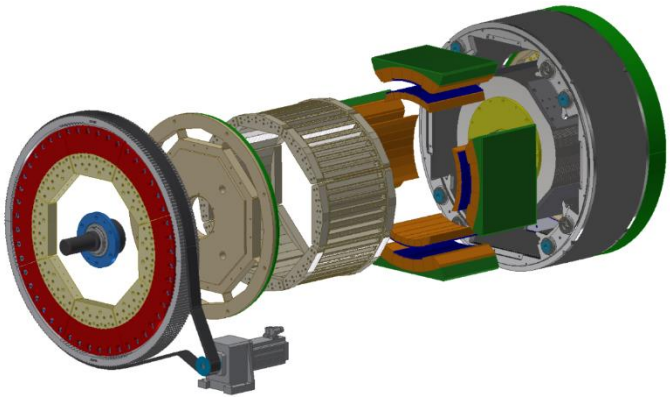

Figure 4: Detailed exploded view of the MC cooling unit

The assembly of the entire components has been realized entirely in-house. Special attention has been paid to the magnetic system as it uses several blocks of magnets which were glued together in order to form the entire magnetic system. The following figure shows the procedure of inserting the magnetic blocks before glueing technique. A sliding device has been used which made it possible to insert the blocks one by one. At the final stage of the assembly, stainless steel screws were used to keep in place the blocks during the drying phase.

Figure 5: sliding process of the magnets during the assembly

After the magnetic assembly, all the other components and peripherals were installed, and the working check-up has been performed first on each sub-system and in the end on the entire cooling unit.

3. RESULTS AND DISCUSSIONS

Before proceeding to the magnetocaloric experimental measurements, it has been decided to proceed to a complete campaign of measurements of the magnetic field. In this way, the experimental magnetic field homogeneity can be verified and compared to the simulations.

The measurement of the magnetic field intensity has been performed with a HGM09S-type Gaussmeter, specially adapted to measure exactly the number of points wanted over the entire 2D space, over the longitudinal position and the angular position of the 4 magnetic poles.

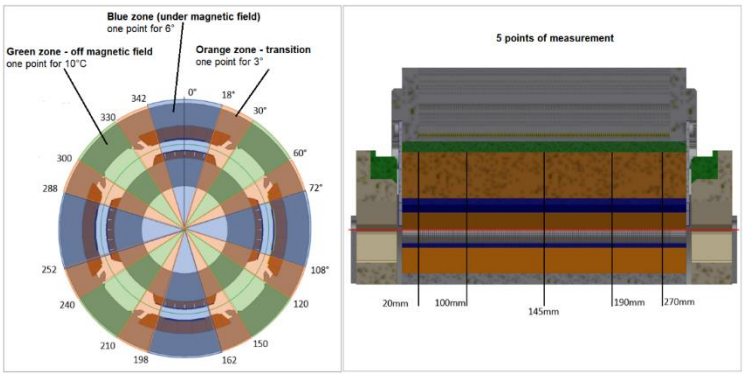

Figure 6: Magnetic field measurement points

The results of the measurements are shown in the following figure. One can observe the 4 poles values over the 5 measurement points, at 20 mm, 100 mm, 145 mm, 190 mm and 270 mm

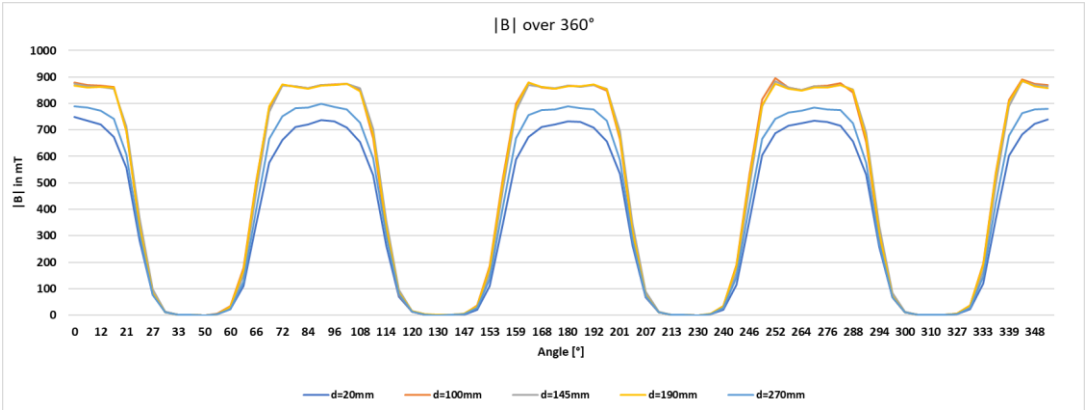

Figure 7: Experimental measurements of the magnetic field for the entire 4 magnetic poles over 5 measurements points

The results show that all 4 poles have identical magnetic field shapes and and that over the 5 measurement points, the difference between the values is around 150 mT, which represents an average of 20%.

In the following figure, the average values of all 4 magnetic poles have been plotted on a single chart and evaluated with the average simulation values.

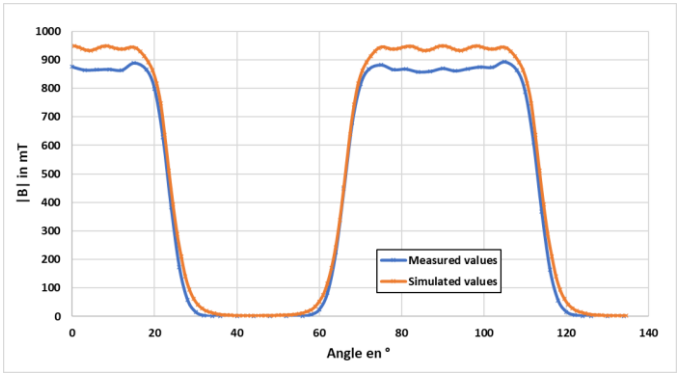

Figure 8: Average experimental measurement values of the magnetic field vs. average simulation points

One can observe the total average values of the magnetic field measurement points around 0.85 T which represent a deviation of 11 % from the total average simulation values. The shape function from minimum to maximum values is very close to a step function, with a transition angle of 12 ° for reaching the maximum value and 14° for reaching the minimum values, which means a total angle of 104° over the 4 poles (104 ° out or 360°).

As the prototype will further enter into a comprehensive and testing campaign, the magnetocalorics test results will be shared with details into a further publication.

4. CONCLUSIONS

This paper presented a novel generation of a magnetic refrigeration unit, built upon an entirely new architecture. This device, designed for a specific industrial application with a fixed temperature span, represents our latest state-of-the-art achievements. We presented the Artificial Evolution-based numerical model used to design this unit, together with the comprehensive engineering efforts to design and build the unit from the CAD files to an existing unit. A total of 29.3 kg of second order phase transition magnetocaloric materials has been used, together with a total quantity if 175 kg of NdFeB magnets. The preliminary results in terms of magnetic field profile and distribution have been presented and analyzed. The further magnetocalorics test results will be shared with details into a further publication.

NOMENCLATURE

p	pressure (kPa)	R	molar gas constant (8.314472 J×mol–1×K–1)
T	temperature (K)	V	molar volume (mol×L–1)
ρ	Density (kg×(m^3) –1)	c_p	heat capacity (J×Kg–1×K–1)
λ	thermal conductivity (W×m–1×K–1)	$\dot{Q}$	Heat flux density (W×(m^2) –1)
χ	Reduced output parameter (-)	η	Efficiency (-)

REFERENCES

Cop28 action plan, Reports on COP28 https://www.thenationalnews.com/climate/cop28/2023/12/08/cop28-action-plan-could-reduce-global-cooling-emissions-by-96, 2024 (accessed in February 2024)

S. Qian, D. Nasuta, A. Rhoads, Y. Wang, Y. Geng, Y. Hwang, R. Radermacher, I. Takeuchi, Not-in-kind cooling technologies: a quantitative comparison of refrigerants and system performance, International Journal of Refrigeration, 2016, 177-192. http://dex.doi.org/10.1016/j.ijrefrig.2015.10.019

A. Kitanovski, J. Tusek, U. Tomc, U. Plaznik, M. Ozbolt, A. Poredos, Magnetocaloric Energy Conversion: From Theory to Applications, Springer 2015, https://doi.org/10.1007/978-3-319-08741-2

S. Dall'Olio, M. Masche, J. Liang, A.R. Insingna, D. Eriksen, R. Bjork, K.K. Nielsen, A. Barcza, H.A. Vieyra, Niels V. Beek, H. Neves Bez, K. Engelbrecht, C.R.H. Bahl, Novel design of a high efficiency multi-bed active magnetic regenerator heat pump, International Journal of Refrigeration, 2021, https://doi.org/10.1016/j.ijrefrig.2021.09.007

M. Masche, J. Liang, K. Engelbrecht, C.R.H. Bahl, Performance assessment of a rotary active magnetic regenerator prototype using gadolinium; Applied Thermal Engineering, 2022, https://doi.org/10.1016/j.applthermaleng.2021.117947

J. Lozano, M. Capovilla, P. Trevizoli, K. Engelbrecht, C.R.H. Bahl, J. Barbosa, Development of a novel rotary magnetic refrigerator, International Journal of Refrigeration, 2016, https://doi.org/10.1016/j.ijrefrig.2016.04.005

S. Lionte, M. Risser, C. Muller, A 15kW magnetocaloric proof-of-concept unit: Initial development and first experimental results, International Journal of Refrigeration, 2020, https://doi.org/10.1016/j.ijrefrig.2020.09.019

A. Nakashima, F. Fortkamp, N. de Sa, V. dos Santos, G. Hoffmann, G. Peixer, S. Dutra, M. Ribeiro, J. Lozano, J. Barbosa, A magnetic wine cooler prototype, International Journal of Refrigeration, 2021, https://doi.org/10.1016/j.ijrefrig.2020.11.015

A. Nakashima, S. Dutra, P. Trevizoli, J. Barbosa, Influence of the flow rate waveform and mass imbalance on the performance of active magnetic regenerators. Part I: Experimental analysis, International Journal of Refrigeration, 2018, https://doi.org/10.1016/j.ijrefrig.2018.07.004

G. Peixer, M. Silva, A. Lorenzoni, G. Hoffmann, D. dos Santos, G. do Rosario, E. Pagnan, H. Teza, P. Silva, S. Dutra, M. Ribeiro, M. Rosa, A. Doring, B. Vieira, A. Nakashima, P. Wendhausen, C. Teixeira, J. Lozano, R. Barbosa, A magnetocaloric air-conditioning system prototype, International Journal of Refrigeration, 2023, https://doi.org/10.1016/j.ijrefrig.2023.03.014

S. Roy, S. Poncet, M. Sorin, Sensitivity analysis and multiobjective optimization of a parallel-plate active magnetic regenerator using a genetic algorithm, International Journal of Refrigeration, 2017, https://doi.org/10.1016/j.ijrefrig.2017.01.005

S. Tsutsui, P. Collet, Massively parallel evolutionary computation on GPGPUs, Springer, Natural Computing Series, 453 p. 2015, ISBN: 978-3-642-37958-1

M. Risser, C. Vasile, C. Muller, A. Noume, Improvement and application of a numerical model for optimizing the design of magnetic refrigerators, International Journal of Refrigeration, 2013, https://doi.org/10.1016/j.ijrefrig.2012.10.012

DOI: 10.18462/iir.thermag.2024.0009

SUCCESSFUL INTEGRATION OF A MAGNETIC REFRIGERATION SYSTEM INTO A REFRIGERATED DISPLAY CABINET: FROM SIMULATIONS TO FIRST EXPERIMENTAL RESULTS

Sergiu LIONTE[(a)], Michel RISSER[(a)], Hugo DU MOULINET D'HARDEMARE [(a)]

(a) **magnoric**

4 Rue de la Gare, Duppigheim, 67120, France, tel. +33 (0)367 476747, sergiu.lionte@magnoric.com

ABSTRACT

This paper discusses a recently developed magnetocaloric unit by magnoric, which features an innovative longitudinal arrangement of Active Magnetic Regenerators. This design enables the MRS unit to be effectively integrated into a commercial refrigerated display cabinet for commercial use.

The prototype incorporates a magnetocaloric system with NdFeB permanent magnets, generating a magnetic field of 0.8 T in the air gap, and employs Gd-based alloys as the magnetocaloric materials.

The focus of this paper is on the detailed steps involved in integrating the unit into a refrigerated display cabinet. The integration process began with a series of numerical simulations using a previously introduced model, enhanced by an Evolutionary Algorithm (EA). This was followed by the CAD design of several essential components. Subsequently, we conducted and analyzed a set of experimental measurements on the complete system. The temperature regulation within the cabinet was achieved using a basic ON-OFF control mechanism.

Keywords: Magnetic cooling, Caloric device, Magnetocaloric materials

1. INTRODUCTION

The cooling sector will again suffer new changes as at least 60 countries signed a pledge to cut emissions at the last Conference of the Parties (COP28) held in Dubai in December 2023 (COP28 action plan, 2024). Today, the cooling sector lies mostly on the vapor compression technology. After more than 100 years of development, this cooling technique is now a mature technology with efficient and compact systems and it uses a reliable supply chain. However, most of the refrigerants currently used in such systems are under different phase-down schedules and are not viable long-term options (R. Gauß, 2017). These continuous regulations towards the refrigerants-based cooling techniques lead to the need for more effective solutions, such as different alternatives to mechanical vapor compression in terms of energy efficiency but also environmental footprint.

Among several candidates, Magnetic Refrigeration (MR) stands out as one of the most promising cooling technologies. The advantages that this technology possesses, and which attract the industry's main players are the followings: the use of solid refrigerants and an inoffensive water-based heat transfer fluid instead of harmful gases, the high thermodynamic efficiency and the great recyclability of the main components, such as the magnetocaloric materials (MCM) and the permanent magnets (PM).

This technology exploits the Magnetocaloric Effect (MCE), which is a heat and entropy response of magnetocaloric materials when exposed into a changing magnetic field (Kitanovski et al., 2015). This technology, working with solid-state refrigerants eliminate all risks tied to refrigerant leakage into the atmosphere and it is completely off-regulations in terms of F-Gas.

Most researchers from all scientific research groups concentrated separately either on developing magnetocaloric materials, making magnetic system improvements or dealing with fluid dynamics or heat transfer analysis. Regarding design solutions, one can mention the prototype operating with a high magnetic flux density of 1.6 T (Dall'Olio et al., 2021), with a large mass flow rate of heat transfer liquid (Masche et al., 2022), with high frequency values (Lozano et al., 2014) or with large quantities of MCM (Peixer et al., 2023b).

Also, important progress has been recorded in recent years, with the development of various prototypes, such as a refrigeration unit (Lionte et al., 2020), a heat pump (Dall'Olio et al., 2021, Masche et al., 2022), a wine cooler (Nakashima et al., 2021), and an air conditioner (Peixer et al., 2023b).

In order to build reliable and efficient industrial cooling units, the entire design of magnetocaloric systems has to be well interconnected and the research has to be completed with mechanical engineering efforts in terms of components assembly in order to increase the performance of the magnetic cooling prototypes. For the MR to successfully be considered as a potential candidate in replacing the actual cooling technology, it has to reach a sufficiently large cooling power value under a real operating-conditions temperature span, together with reduced mass and volume, but also, most important, with a competitive price. So far, only few groups presented prototypes having both a useful temperature span and a sufficient cooling capacity to integrate an industrial application.

This paper presents a successful integration process of a Magnetic Refrigeration System (MRS) from the numerical simulation phase, through the CAD integration design of all main prototype components into the refrigerated display cabinet system's compartment and up to a detailed discussion and analysis of the first experimental results.

2. NUMERICAL SIMULATIONS AND TECHNICAL DESIGN

This unit has been entirely designed and developed by our multidisciplinary team with expertise in magnetic systems, material science, heat transfer, hydraulics, complex mechanics and mechatronics. The development of the entire project started with a feasibility study followed by a complex multiphysics numerical simulations campaign and a CAD technical design of both the main components of the system as well as the integration of the entire unit into the technical volume of the refrigerated display cabinet.

The numerical modelling process involved a relatively large campaign of numerical simulations (containing around 6000 simulation cases), were performed with an Evolutionary Algorithms (EA). Several architectures, geometric dimensions and operating points have been identified, based on the purpose of the project. Multiple parameters have been varied such as the T_c layering, material holder's length, magnetic field intensity, operating frequency, flow rate, etc., to identify the most adapted combination of parameters. Choosing the best parameter set is a complex task because it involves a large number of entities in several multi-physics interactions, which are responsible for complex and emergent behaviors. Evolutionary Algorithms are intended to implement the natural Darwin evolution theory into a virtual environment. These algorithms can be applied on technical systems with reproduction laws not limited to those observed in nature. Extensive literature on this topic was published since 2013 (Tsutsui and Collet, 2013) and out algorithm is explained in detail in (Risser et al. 2018). We define in the end an entity as a configuration of MC system with a given combination of input parameters.

2.1. Magnetic field simulation

Simulation, design and optimization of a magnetic circuit is a compromise between the volume of the air gaps, the volume of the AMR under the magnetic field, and the volume of Permanent Magnets (PM). The limitation of the weight and the cost of such systems are also possible by modifying the relative position of the AMRs towards the PM.

Since 2005 (Zimm et al. 2005) and continuing lately in 2016 and further (Trevizoli et al. 2016) numerous papers present different design studies to reach the best magnetic configuration for a rotating MC system. 3D Finite Element Methods (FEM) simulations were performed at magnoric over the last few years on several new designs of magnetic systems, based on a longitudinal architecture. Our multi-objectives optimization process is inspired from the numerical methods given in (Lee et al., 2018), and seeks to maximize the difference of the internal

magnetic field (H_{int}) inside the MCM between high field regions and low field regions of the same volumes. This process is attending to reach the bests topologies for the borders, the segmentation and the pattern of magnetization directions for the PM, for the shape of iron parts and for the AMR distribution and geometry. The combination of cost, AMR hydraulic connections, weight and size requirements have oriented us to complex designs in which the magnetic interactions are exacerbated between the AMRs and between the MCM of different TC inside the AMR.

The magnetic assembly has been designed according to a simulation process of the total magnetic field. 3D simulations based on Finite Element Method (FEM) were internally performed with different design's perspectives of the magnetic systems. Two software packages have been used in order to identify the most adapted configurations. Initially it was used FEMM package for the pre dimensioning of the magnetic system and in a second phase, the magnetic field distribution has been verified with a commercial 3D software, FLUX 3D.

This process was expected to identify the most adapted topologies for the iron yoke border shape, the segmentation distribution and the magnetization pattern of the PM, the shape of the iron components and the regenerator's geometry and distribution over the entire magnetic surface. The analysis of the resulted magnetic induction values, the cost efficiency, the mechanical and hydraulic connection possibilities, and the weight and size requirements pointed us to using a 2 poles magnetic system with 3 AMRs under the pole. The following figure presents the simulation of the magnetic induction (B) for the designs of magnetic circuits developed for this unit. These results are obtained with the 3D FEM-based commercial model.

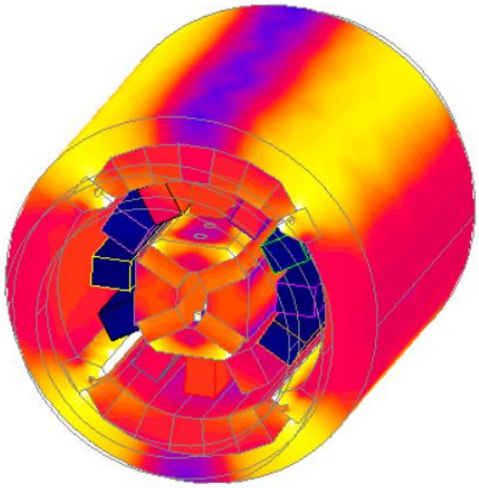

Figure 1: Simulation of the magnetic induction (B) of the longitudinal type of architecture, obtained with a 3D FEM-based commercial software

The results visible in the previous figure are confirmed by a campaign of measurement of the magnetic field values in the air gap of the prototype, which will be presented in the results chapter of this paper.

For this commercial magnetocaloric unit to function at best performance, apart from the magnetic system, several parameters have been properly identified. The geometric dimensions describe the architecture and the size of the unit. The materials of which the unit is built (MCM, PM, iron and aluminum) are characterized in terms of physical properties as magnetization, Tc, specific heat capacity and thermal conductivity. The operating parameters such as the flow rate, the magnetocaloric frequency or the phase shift manage the thermodynamic cycles have been investigated properly to be easily changed during the system's operation.

In general, identifying the optimal design and the most adapted driving strategies regarding given specifications is a long, complex and expensive task. During last few years, we performed internally numerous optimization methods. The prototype design, manufacturing and testing has been identified as not the most suitable method for

such complex and interacting systems. The simulation of a global envelope curve of points (Pareto front's method) is also a long and expensive method which implies calculation of many irrelevant points of simulation.

For this purpose, after performing the initial numerical simulations campaign, the use of a bio-inspired method to solve a multi-objective requirement (power density and efficiency) of the MC system has been implemented. The selection of the most adapted parameters has been made with an Evolutionary Algorithm (EA) associated with massively parallelized computing capabilities.

The algorithm associates a single evaluation parameter (χ), defined in equation 1, to the complete group of n input parameters (x_i) ; V_{MCM} and V_{PM} being the volume of materials and α and β the material cost indices per unit volume, respectively for the MCM and the PM.

$$\chi(x_1,...,x_i,...,x_n) = \frac{\eta_i \, \dot{Q}_R}{(\alpha \, V_{MCM} + \beta \, V_{PM})} \qquad \textit{Eq. (1)}$$

The evolution process of the EA, combined with the temperature span requirement of the application, resulted in a combination of parameters for the most adapted configurations.

The MRS device uses the following configuration of parameter values, as presented in the following table:

Table 1: MRS parameters values

Regenerator type:	Parallel plates	
Magnetocaloric materials:	Gd (*Tc 20°C*) and Gd-Er (*Tc 0 to 15°C*)	
Tc layering:	20 / 15 / 10 / 5 / 0 °C	
Regenerator dimensions: L x l x h	160 x 20 x 26	mm x mm x mm
MCM plates thickness: a	0.35	mm
Microchannel thickness: a	0.15	mm
Magnetic field intensity value: B	0.65	T
Heat transfer fluid:	CLOGEL 15 (freezing point at -5°C)	
Operating magnetocaloric frequency:	0.5 - 2	Hz
Operating fluid displacement value Rvol:	0.15 – 0.5	[-]

3. DESIGN OF ADDITIONAL COMPONENTS USING CAD SOFTWARE

This particular cooling application implies a technical volume in the bottom part of the refrigerated display cabinet, with limited space and volume. The commercial display cabinet (EPTA 9C02106) has been stripped of the elements of the classic cooling solution such as the compressor and the auxiliary parts and the bottom compartment has been used to place the MRS and all the auxiliary components. The compartment is a confined space and the front and rear walls are made from perforated steel plate to create air circulation. The design and placement of the complete system is challenging, as the prototype is no longer used as a research prototype, but with restrictions on weight, volume and noise levels. The additional components such as the hydraulic pump, the heat transfer liquid tank and the electric motor have been placed as shown in figure 2, with additional reserved space for the ventilation duct connecting the hot heat exchanger and its fan to the perforated steel plate wall, to expel the residual heat. The cold heat exchanger and its fan are connected via a duct system to the beverage cooler's main compartment. Other small additional components such as the hydraulic connections and the electric wires have not been represented, as they do not require dedicated space.

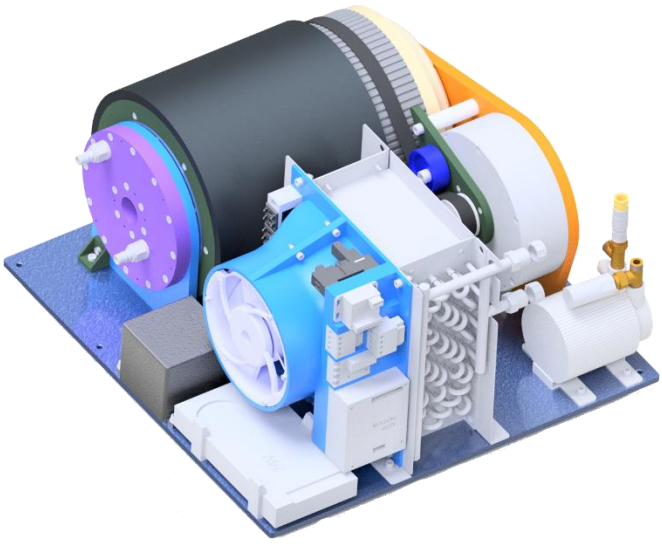

Figure 2: CAD design of the MRS and additional components into the bottom compartment of the display cabinet

The design has been realized with a common CAD commercial software and most of the components have been specially designed for this type of application. Several arrangement possibilities have been analyzed and only the most adapted configuration, which satisfies most of the limitations, has been presented and further used for manufacturing.

4. RESULTS AND DISCUSSIONS

Before proceeding to the magnetocaloric experimental measurements, it has been decided to proceed to a complete campaign of measurements of the magnetic field. In this way, the experimental magnetic field homogeneity can be verified and compared to the simulations. The measurement of the magnetic field intensity has been performed with a HGM09S-type Gaussmeter, specially adapted to measure exactly the number of points wanted over the entire 2D space, over the longitudinal position and the angular position of the 2 magnetic poles, as represented in the following figure.

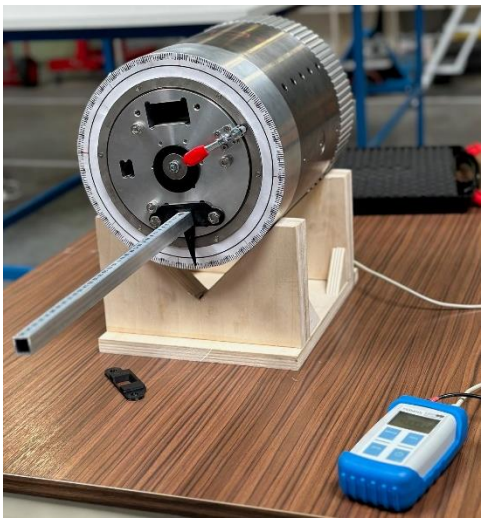

Figure 3 : Measurement of the magnetic field homogeneity at different measurement points

The results of the measurements are shown in figure 4. The measurements have been performed over 3 zones of magnetic field: the green zone (off magnetic field) with one measuring point for every 10° of angle, the blue

zone (under magnetic field) with one measuring point for every 6° of angle and the orange zone (transition) with one measuring point for every 3° on angle.

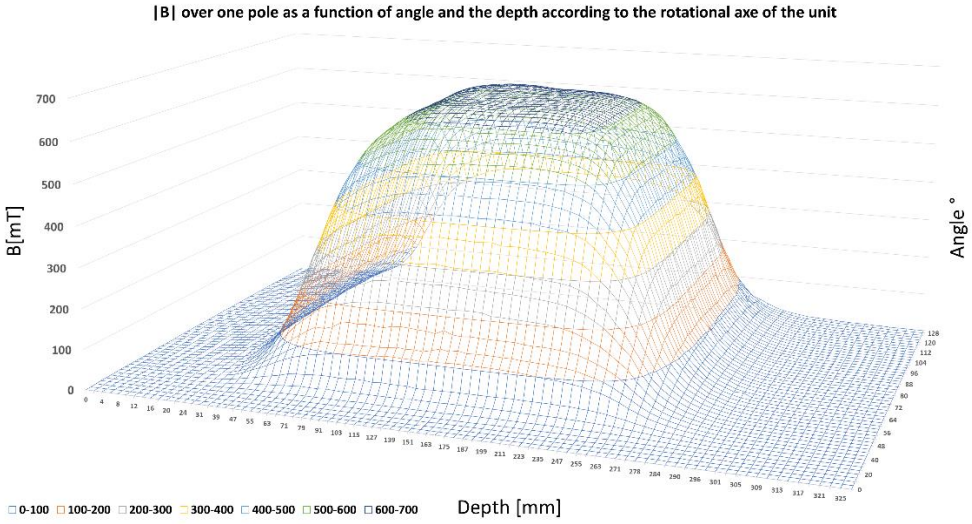

Figure 4: 3D representation of the magnetic induction values over one pole

In the figure 4 one can see the homogenous curve of the magnetic field values, over the entire surface of the magnetic pole. The maximum value of the magnetic field intensity is around 0.65 T and the transition zone is present over the entire surface. From the 3D figure above, the middle values have been extracted into the following picture in order to identify the differences between the simulations and the measurements as well as the length of the transition zone, over one magnetic pole.

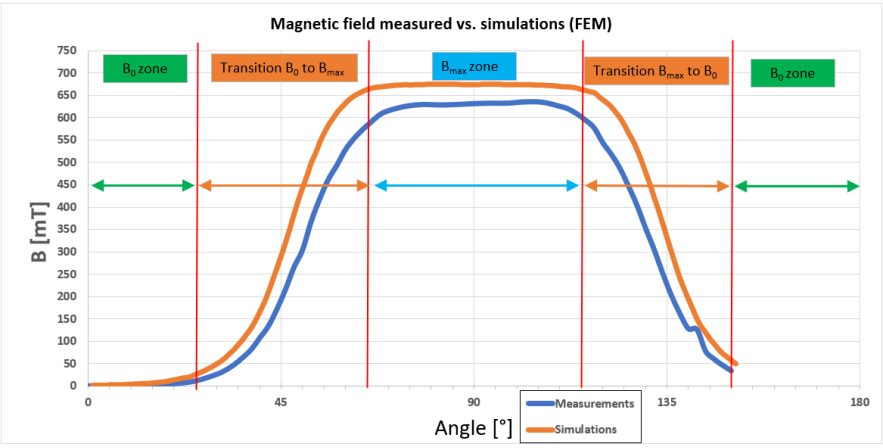

Figure 5: 2D representation of the magnetic field values over one magnetic pole: simulations vs. measurements

One can observe the maximum value of the magnetic field simulation point around 0.67 T and the maximum value of the magnetic field measurement point around 0.63 T which represent a deviation of 6.3 % from the maximum simulation value. The shape function from minimum to maximum values has a relatively important slope angle, with a transition angle of 40 ° for reaching the maximum value and 35° for reaching the minimum values, which means a total angle of 150° over the 2 poles (150 ° out or 360°).

As the prototype will further enter into a comprehensive and testing campaign, the magnetocalorics test results will be shared with details either during the oral presentation at the conference or will be drafted into a further publication.

5. CONCLUSIONS

A series of numerical simulations have been performed in order to identify the most adapted parameters for a Magnetic Refrigeration System (MRS) to work on a display cabinet unit. The selection of the most adapted parameters has been made with an Evolutionary Algorithm (EA) associated with massively parallelized computing capabilities. The prototype and the additional components' design have been realized with the most common CAD commercial software and most of the components have been specially designed for this type of application. The prototype integration had to fit the technical compartment of the display cabinet, with limitations on dimensions, weight and noise levels. In order to have higher energy efficiency, the prototype uses a specific working schedule based on 3 different variable operating points, based on the environment and loading scenario.

The preliminary results in terms of magnetic field profile and distribution have been presented and analyzed. The further magnetocalorics test results will be shared with details either during the oral presentation at the conference or will be drafted into a further publication.

NOMENCLATURE

p	pressure (kPa)	R	molar gas constant (8.314472 J×mol–1×K–1)
T	temperature (K)	V	molar volume (mol×L–1)
ρ	Density (kg×(m^3) –1)	c_p	heat capacity (J×Kg–1×K–1)
λ	thermal conductivity (W×m–1×K–1)	$\dot{Q}$	Heat flux density (W×(m^2) –1)
χ	Reduced output parameter (-)	η	Efficiency (-)

REFERENCES

Cop28 action plan, Reports on COP28 https://www.thenationalnews.com/climate/cop28/2023/12/08/cop28-action-plan-could-reduce-global-cooling-emissions-by-96, 2024 (accessed in February 2024)

R. Gauß, G. Homm, O. Gutfleisch, The resource basis of magnetic refrigeration, J. Ind. Ecol. 21, 1291-1300, 2017, https://doi.org/10.1111/jiec.12488

A. Kitanovski, J. Tusek, U. Tomc, U. Plaznik, M. Ozbolt, A. Poredos, Magnetocaloric Energy Conversion: From Theory to Applications, Springer 2015, https://doi.org/10.1007/978-3-319-08741-2

S. Dall'Olio, M. Masche, J. Liang, A.R. Insingna, D. Eriksen, R. Bjork, K.K. Nielsen, A. Barcza, H.A. Vieyra, Niels V. Beek, H. Neves Bez, K. Engelbrecht, C.R.H. Bahl, Novel design of a high efficiency multi-bed active magnetic regenerator heat pump, International Journal of Refrigeration, 2021, https://doi.org/10.1016/j.ijrefrig.2021.09.007

M. Masche, J. Liang, K. Engelbrecht, C.R.H. Bahl, Performance assessment of a rotary active magnetic regenerator prototype using gadolinium; Applied Thermal Engineering, 2022, https://doi.org/10.1016/j.applthermaleng.2021.117947

J. Lozano, M. Capovilla, P. Trevizoli, K. Engelbrecht, C.R.H. Bahl, J. Barbosa, Development of a novel rotary magnetic refrigerator, International Journal of Refrigeration, 2016, https://doi.org/10.1016/j.ijrefrig.2016.04.005

S. Lionte, M. Risser, C. Muller, A 15kW magnetocaloric proof-of-concept unit: Initial development and first experimental results, International Journal of Refrigeration, 2020, https://doi.org/10.1016/j.ijrefrig.2020.09.019

A. Nakashima, F. Fortkamp, N. de Sa, V. dos Santos, G. Hoffmann, G. Peixer, S. Dutra, M. Ribeiro, J. Lozano, J. Barbosa, A magnetic wine cooler prototype, International Journal of Refrigeration, 2021, https://doi.org/10.1016/j.ijrefrig.2020.11.015

A. Nakashima, S. Dutra, P. Trevizoli, J. Barbosa, Influence of the flow rate waveform and mass imbalance on the performance of active magnetic regenerators. Part I: Experimental analysis, International Journal of Refrigeration, 2018, https://doi.org/10.1016/j.ijrefrig.2018.07.004

G. Peixer, M. Silva, A. Lorenzoni, G. Hoffmann, D. dos Santos, G. do Rosario, E. Pagnan, H. Teza, P. Silva, S. Dutra, M. Ribeiro, M. Rosa, A. Doring, B. Vieira, A. Nakashima, P. Wendhausen, C. Teixeira, J. Lozano, R. Barbosa, A magnetocaloric air-conditioning system prototype, International Journal of Refrigeration, 2023, https://doi.org/10.1016/j.ijrefrig.2023.03.014

M. Risser, P. Collet, J. Chaudron, S. Lionte, C. Muller, Optimization of a layered regenerator inside a magnetocaloric cooling system using an evolutionary algorithm, 8th IIF-IIR International Conference on Caloric Cooling, Thermag VIII, Darmstadt, Germany, September 16th-20th 2018

C. Zimm, A. Boeder, J. Chell, A. Sternberg, A. Fujita, S. Fujieda, K. Fukamichi, Design and performance of a permanent magnet rotary refrigerator, Proceedings of the 1st International Conference on Magnetic Refrigeration at Room Temperature, Thermag 1, (2005) 367-373.

P. Trevizoli, T. Christiaanse, P. Govindappa, I. Niknia, R. Teyber, J. Barbosa Jr., A. Rowe, Magnetic heat pumps: An overview of design principles and challenges, Science and Technology for the Built Environment, Pages 507-519, 2016, https://doi.org/10.1080/23744731.2016.1171632

J. Lee, M. Yoon, T. Nomura, E. M. Dede, Topology optimization for design of segmented permanent magnet arrays with ferromagnetic materials. J. of Mag. and Mag. Mater. 449, 2018, 571-581. https://doi.org/10.1016/j.jmmm.2017.10.109

DOI: 10.18462/iir.thermag.2024.0010

INFLUENCE OF THE INDIUM THERMAL INTERFACE ON THE HEAT TRANSFER IN MECHANICAL THERMAL SWITCH AT CRYOGENICS TEMPERATURE AND EXTERNAL MAGNETIC FIELD

Konstantin KOLESOV[(a)], Alexey MASHIROV[(a)], Alexandr KUZNETSOV[(a)], Akhmed ALIEV[(b)], Vladimir SHAVROV[(a)]

[(a)] Kotelnikov Institute of Radioengineering and Electronics (IRE) of Russian Academy of Sciences
Moscow, 125009, Russia, kolesovkka@gmail.com
[(b)] Amirkhanov Institute of Physics, Daghestan Scientific Center, Russian Academy of Sciences
Makhachkala, 367003, Russia, lowtemp@mail.ru

ABSTRACT

The aim of this work is to evaluate the influence of indium thermal interface 100 μm thick on the thermal contact resistance between copper cylindrical samples with a diameter and height of 15 mm. These copper samples (moving and stationary) represent a model of a mechanical thermal switch for use in magnetic cooling. The experiment was carried out inside a cryostat in a temperature range from 15 to 140 K and an ambient pressure of 1.1×10^{-2} – 4.5×10^{-3} Pa and external magnetic field up to 3 T. The contact force of pressing copper samples with an indium thermal interface was 300 kPa.

Keywords: Cryogenic mechanical thermal switch, thermal contact resistance, indium thermal interface.

1. INTRODUCTION

To create a refrigeration machine Kamiya et.al., (2022), Kamran, Ahmad, Shen (2020) based on a working body with a magnetocaloric effect Koshkid'ko et.al., (2023), in the cryogenic temperature range, it is necessary to use thermal switches Klinar and Kitanovski (2020), Klinar ea.al., (2021). Thermal switches are usually used to control the heat flow between the working body, the heat sink and the cooling object. Mechanical thermal switches are the easiest to manufacture and operate in a wide temperature range. Shu, Demko, Fesmire (2017). In these thermal switches, heat transfer occurs between contacting surfaces. However, when real bodies come into contact, due to the presence of micro-irregularities, roughness, etc., resistance to heat flow arises at the interface, which is called thermal contact resistance (TCR) Clausing and Chao (1965). Real contact occurs only at some points, while the actual contact area becomes smaller than the nominal one, Siddappa and Tariq (2020) thus the heat flow lines are contracted to the actual contact spots (Fig. 1).

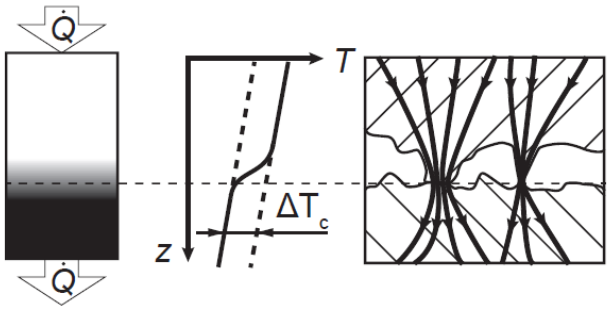

Fig. 1: Thermal transfer mechanism in real contact Frekers et.al., (2017)

Determining the TCR is a complex task, it covers problems associated with the geometry of the contact surface, the mechanics of contact, as well as heat transfer between surfaces Yovanovich (2005). There are many works devoted to determining the TCR Swartz and Pohl (1989), Gmelin (1999), Dhuley (2019), Pan et. al., (2020), Ludwick et. al., (2022). However, despite a large number of studies, both theoretical and experimental, the data obtained do not always agree. This is due to the fact that the authors do not always indicate the parameters at which the experiment was carried out (roughness, pressing force, etc.). Siddappa and Tariq (2023) as a result of which the TCR values cannot always be used in applied problems. Theoretical

models have limitations in applicability or become too complex due to the large number of different parameters included in the equation Lambert and Fletcher (1997). Therefore, the most accurate method remains the experimental determination of the TCR. There are various experimental methods for measuring TCR depending on the size of the objects being measured, temperature levels, etc. Xian et. al., (2018).

2. EXPERIMENTAL METHOD

Copper samples were attached to the upper (movable) and lower (fixed) sample holders (Fig. 2) through fluoroplastic rings to reduce heat gain. A movable holder was attached to the rod of a linear electric motor for reciprocating movement. The stationary one was attached to the end of a stainless-steel pipe immersed in a cryostat. Each copper sample has grooves for «Cernox» temperature sensors and holes drilled to the axis of rotation for T-type differential thermocouples, as well as a recess for a nichrome wire heater. The distance between the «Cernox» sensor and the end of the differential thermocouple is 3 mm.

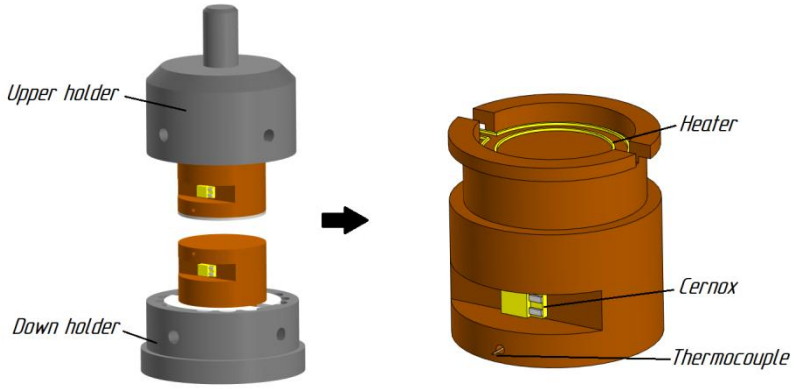

Fig. 2: Fastening elements and measurements

Due to the linear electric motor, the upper holder moves reciprocating with the sample, the thermal switch opens and closes, and the pressing force is controlled. The thickness of the indium layer was 100 μm and covered the entire contact surface. The experiment was carried out on the basis of a cryomagnetic system with the ability to turn on a superconducting magnet and create a magnetic field up to 10 Tesla inclusive. To evaluate the influence of the magnetic field, the experiment was carried out both without action to an external magnetic field and under action to an external magnetic field of 3 T. Cooling of both the superconducting magnet and the working area of the cryostat is carried out using the «SHI Cryogenics RDK-415D» cryocooler. Measurement from «Cernox» temperature sensors is carried out using a «Lakeshore 336» thermal controller, and readings from differential thermocouples are taken using a «Keithley 2182» nanovoltmeter.

The experimental determination of the TCR in this work is based on the ASTM D5470 standard Buliński et. al., (2019), taking into account the transient thermal regime described in Popov (1971). Fig. 3 shows the definition of the main parameters of the described method.

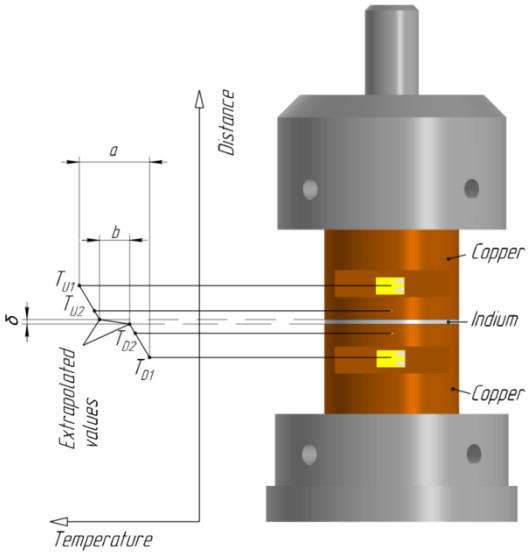

Fig. 3: Method for determining TCR

In this method, thermal contact conductance α_c at a specific time is determined as:

$$\alpha_c = R_c^{-1} = (a-b)\times(b\times(R_u + R_d))^{-1} \quad \text{Eq. (1)}$$

Where a is the rate of temperature rise at the boundaries of the samples, K/min, b is the change in the rate of temperature increase in the contact zone, K/min, R_u and R_d are the thermal resistances of the material of the upper and down samples at a given time, respectively, R_c is the TCR, as shown in Eq. (1). To find the parameters a and b, the change in temperature over time is plotted in relative coordinates (relative to the parting plane) at the temperature reading points along the length of the samples. This change is then extrapolated to the parting plane. Thermal resistances R_u and R_d along the length of the sample are calculated based on the relative coordinates and the avverage thermal conductivity at a given temperature at given points.

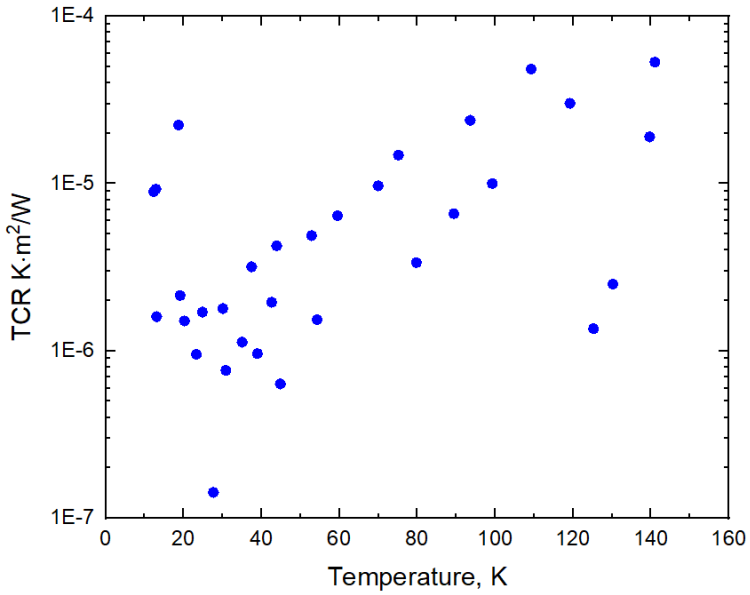

Fig. 4: TCR values in the studied temperature range

Based on measurement method Popov (1971) described above, the TCR of the copper-indium-copper contact were calculated in the temperature range from 15 to 140 K (Fig. 4). As we can see from fig. 4 TCR ranges from 10^{-6} at lower temperatures to 10^{-5} with increasing temperatures. At the same time, the time until the thermal equilibrium was measured at an initial temperature span of copper samples of 5 K and 10 K. At 20 K is 2.5 - 3 sec., then there is an increase at 60 K – 8 sec., at 120 K – 14-15 sec. The obtained values compared with Gmelin (1999) several orders of magnitude greater at 20 – 60 K and coincide with the range of about 100 K. In the theoretical «flat model» Yovanovich (1981) proposed by Yovanovich, presented in workse Phelan and Zhang (2004) the order of values in the temperature level under study coincides with the values presented in this work. Compared with gas-gap thermal keys, the on/off time of a thermal key, for example in a passive gas thermal key, can take several hours Catarino and Paine (2011). There are works in which the transfer time is about a minute DiPirro and Shirron (2014), however, heat transfer occurs faster using the contact method of mechanical thermal switch, thereby increasing the frequency of operation in a magnetic refrigerator.

3. CONCLUSIONS

In this work, the TCR of a copper-copper contact pair with a thermal interface made of indium foil with a thickness of 100 microns was investigated. The TCR values were obtained based on the transient heat flow model described above in the text of this work. The calculated TCR values are in the range 1×10^{-6} – 5×10^{-5}. The time until the thermal equilibrium was also estimated at an initial temperature difference of copper samples of 5 K and 10 K, which varied from 2.5 - 3 sec at an initial temperature of 20 K to 14 - 15 sec at an initial temperature of 120 K. The magnetic field did not have a significant effect on the measured values. Thus, indium foil shows its applicability in a mechanical thermal switch as a thermal interface in the cryogenic temperature range.

ACKNOWLEDGEMENTS

The study was supported by the Russian Science Foundation Grant No. 20-79-10197, https://rscf.ru/project/20-79-10197/.

NOMENCLATURE

α_c	thermal contact conductance (W×m -2×K-1)	R_u	Thermal resistance of the upper sample (W-1×m2×K)
R_c	thermal contact resistance (W-1×m2×K)	R_d	Thermal resistance of the down sample (W-1×m2×K)
a	rate of temperature rise at sample boundaries (K×min-1)	b	magnitude of change in the rate of temperature increase in the contact boundary (K×min-1)

REFERENCES

Buliński, Z., Pawlak S., Krysiński T., Adamczyk W., Białecki R., 2019. Application of the ASTM D5470 standard test method for thermal conductivity measurements of high thermal conductive materials. J. Achiev. Mater. Manuf. Eng. 95 (2), 57-63.

Catarino I. Paine C., 2011. 3He gas gap heat switch. Cryogenics 51 (1), 45-48.

Clausing A.M., Chao B.T., 1965. Thermal Contact Resistance in a Vacuum Environment. J. Heat Transfer 87(2), 243-250.

Dhuley R.C., 2019. Pressed copper and gold-plated copper contacts at low temperatures – A review of thermal contact resistance. Cryogenics 101, 111-124.

DiPirro M.J., Shirron P.J., 2014. Heat switches for ADRs. Cryogenics 62, 172-176.

Frekers Y., Helmig T., Burghold E.M., Kneer R., 2017. A numerical approach for investigating thermal contact conductance. Int. J. Therm. Sci. 121, 45-54.

Gmelin E., 1999. Thermal boundary resistance of mechanical contacts between solids at sub-ambient temperatures. J. Phys. D: Appl. Phys. 32, R19-R43.

Kamiya K., Matsumoto K., Numazawa T., Masuyama S., Takeya H., Saito A.T., Kumazawa N., Futatsuka K., Matsunaga K., Shirai T., Takada S., Iida Y., 2022. Active magnetic regenerative refrigeration using superconducting solenoid for hydrogen liquefaction. Appl. Phys. Express 15, 053001.

Kamran M.S., Ahmad H.O., Shen H., 2020. Review on the developments of active magnetic regenerator refrigerators – Evaluated by performance. Renew. Sust. Energ. Rev. 133, 110247.

Klinar K., Kitanovski A., 2020. Thermal control elements for caloric energy conversion. Renew. Sust. Energ. Rev. 118, 109571.

Klinar K., Swoboda T., Rojo M.M., Kitanovski A., 2021. Fluidic and Mechanical Thermal Control Devices. Adv. Electron. Mater. 7, 2000623.

Koshkid‘ko Yu.S., Dilmieva E.T., Kamantsev A.P., Mashirov A.V., Cwik J., Kol‘chugina N.B., Koledov V.V. Shavrov V.G., 2023. Magnetocaloric Materials for Low-Temperature Magnetic Cooling. J. Commun. Technol. Electron. 68, 379-388.

Lambert M.A., Fletcher L.S., 1997. Review of Models for Thermal Contact Conductance of Metals. J. Thermophys. Heat Transfer 11 (2), 129-140.

Ludwick J., Hernandez N., Tripathi G., Cahay M., Back T., Jensen K.L., 2022. Influence of thermal contact resistance on the field emission characteristics of a carbon nanotube. J. Vac. Sci. Technol. 40 (4), 042804.

Pan X., Cui X., Liu S., Jiang Z., Wu Y., Chen Z., 2020. Research Progress of Thermal Contact Resistance. J. Low Temp. Phys. 201, 213-253.

Phelan P.E., Zhang M., 2004. The thermal conductance of indium-filled contacts at cryogenic temperatures. Proceedings of ASME International Mechanical Engineering Congress and Exposition, Anaheim, California USA, 753-758.

Popov V M., 1971. Heat exchange in the contact zone of detachable and permanent connections. Energiya, Moscow.

Shu Q.S., Demko J.A., Fesmire J.E., 2017. Heat switch technology for cryogenic thermal management. IOP Conf. Ser.: Mater. Sci. Eng. 278, 012133.

Siddappa P.G., Tariq A., 2020. Contact area and thermal conductance estimation based on the actual surface roughness measurement. Tribol. Int. 148, 106358.

Siddappa P.G., Tariq A., 2023. Experimental estimation of thermal contact conductance across pressed copper–copper contacts at cryogenic-temperatures. Appl. Therm. Eng. 219, 119412.

Swartz E.T., Pohl R.O., 1989. Thermal boundary resistance. Rev. Mod. Phys. 61(3), 605-668.

Xian Y., Zhang P., Zhai S., Yuan P., Yang D., 2018. Experimental characterization methods for thermal contact resistance: A review. Appl. Therm. Eng. 130, 1530-1548.

Yovanovich M.M., 1981. New contact and gap correlations for conforming rough surfaces. AIAA 16th Thermophysics Conference. Palo Alto, California, AIAA-81-1164, 1-6.

Yovanovich M.M., 2005. Four Decades of Research on Thermal Contact, Gap, and Joint Resistance in Microelectronics. IEEE Transactions On Components And Packaging Technologies 28(2), 182-206.

DOI: 10.18462/iir.thermag.2024.0011

EXPERIMENTAL RESEARCH ONCOMPRESSION-DRIVEN MULTI-LAYER TUBULAR ELASTOCALORIC REGENERATOR

ZhouGuoqu[(a)], Yanliang Chen, WangYao[(a)], YuJianlin[(a)], QianSuxin[(a)*]
(a) Department of Refrigeration and Cryogenic Engineering, Xi'an Jiaotong University
Xi'an, 710049, P.R. China, qiansuxin@xjtu.edu.cn

ABSTRACT

Elastocaloric refrigeration has attracted widespread attention due to its high energy density,andnumerous elastocaloric cooling prototypes have been developed. However, when stacking multiple regenerator layers for scaling up, the dead volume between layers will have a significant impact on the performance of the regenerators. In this study, we conducted experimental research on tubular elastocaloric regeneratorsdriven by compression. Firstly, we constructed an31-tube regenerator with a temperature span of 18.2K.Subsequently, by stacking two 31-tube regenerators, we developed a double-layer regenerator with 62 tubes, and its maximumtemperature span reached 25.2K. To reveal the contribution of dead volume, we used 59 tubes to form a single-layer regenerator as a comparison, which featureda maximum temperature span of 27.2K. It means that the dead volume between layers had at least 8% impact on the system's cooling performance.

Keywords: Elastocaloric cooling, Dead volume, Regenerator, Compressing tubes, Nickel-titanium alloy

INTRODUCTION

The elastocaloric effect refers to the isothermal entropy change or adiabatic temperature change produced by the stress field in a solid material(Bonnot et al., 2008), and such materialsare known as elastocaloric materials(eC materials). This effect was first discovered by British physicists in natural rubber(Holme, 1806). However, natural rubber exhibits low excitation stress, low fatigue life, and low elastocaloric effects, which prevent them from practical applications(Qian et al., 2016). On the contrary, shape memory alloys (SMAs) have demonstrated longer fatigue life(Porenta et al., 2020). The elastocaloric effect of SMAs comes fromthe solid-state crystal transformation, which is similar to the gas-liquid phase change in a vapor compression refrigeration cycle. Taking the binary Ni-Ti alloy as an example, the material's crystal can transform from high entropy austenite to low entropy martensite under adriving stress, releasing heat to the surroundings, as shown as Figure 1. Conversely, removing the stress can cause the material to transform fromlow entropy martensite back to high entropy austenite, absorbing heat from the surroundings.

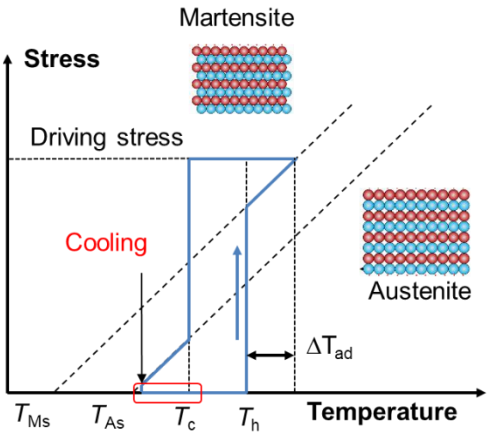

Figure 1: Cooling cycle with solid-solid phase change in SMAs

1. PRINCIPLEOF ELASTOCALORIC REGENERATOR

Similar to thevapor compression refrigeration cycle, we can utilize the reverse Brayton cycle to utilize the latent heat of the solid-solid phase change in SMA:

①Applying a driving stress greater than the martensitic phase transition starting stress (σ_{Ms}). After reaching the critical stress, theaustenite begins the phase transition, releasing latent heat until the SMA completes the martensite phase transition (stress >σ_{Mf}). Then cool down the high-temperature martensitic state SMA by a heat sink.

②Unloading the stress.Below the austenite phase transformation stress (σ_{As}), the martensite begins to transform back to austenite, absorbing latent heatuntil the SMA completes the austenite phase transformation(stress <σ_{Af}). Then cool downthe heat source by the low-temperature austenite state SMA.

In the two steps mentioned above, the methods of exchanging the heat/cold generated by the SMA with the heat sink/source include direct contact heat transfer, and heat transfer using a heat transfer fluid (HTF).For the former, outstanding work primarily involves the direct contact heat transfer scheme of stretching SMA sheets/wires, first pioneered by Saarland University through stretching NiTi sheets and moving the heat source/heat sink with motors to make contact with the NiTi sheets, achieving a 7K temperature span(Schmidt et al., 2015). Subsequently, Karlsruhe Institute of Technology achieved cooling temperature spans of 9.4K(Ossmer et al., 2016) and 15K(Bruederlin et al., 2019) by modifying the layout of the heat source and heat sink and improving materials. Furthermore, Xi'an Jiaotong University obtained a 9.2 K temperature span by stretching NiTi wires with a compact tilted motor(Chen et al., 2022).For the latter, its advantage lies in the greater freedom of SMA geometries, suitable for generating large cooling capacities. As early as 2015, the University of Maryland developed the first compressive elastocaloric prototype with stretched NiTi wires, benefiting from multiple NiTi tubesto achieve a cooling power of 65W(Qian et al., 2015). In 2016, the Technical University of Denmark first utilized the principle of active regeneration in atensile-driven regeneratorconsisting of NiTi sheets, achieving a cooling temperature span of 15.3K(Tušek et al., 2016).Following this, due to the short lifespan issue of SMA under repeated stretching, the academic started focusingonthe compression mode. In 2022, the Technical University of Denmark reported a compressive-drivenbundled-tube regenerator, achieving a temperature span of 5K(Ianniciello et al., 2022); In the same year, the University of Maryland reportedmultiple compressive bundled-tube regenerators that achieved a temperature span of 16.6 K in asingle-stage regenerator, 20.2 K in a double-stage regenerator, and 27.4 K in atriple-stage(Emaikwu et al., 2023); the University of Ljubljana developeda four-stage compressed bundled-tube regenerator realizing a temperature span of 31K(Ahčin et al., 2022).

The regenerator in this article uses HTF for heat transfer. In the flow direction, the latent heat generated by the SMA in the front portion is transferred to the SMA in the rear portion through the HTF, creating a temperature gradientalongthe SMAin the flow direction, as shown in Figure 2.

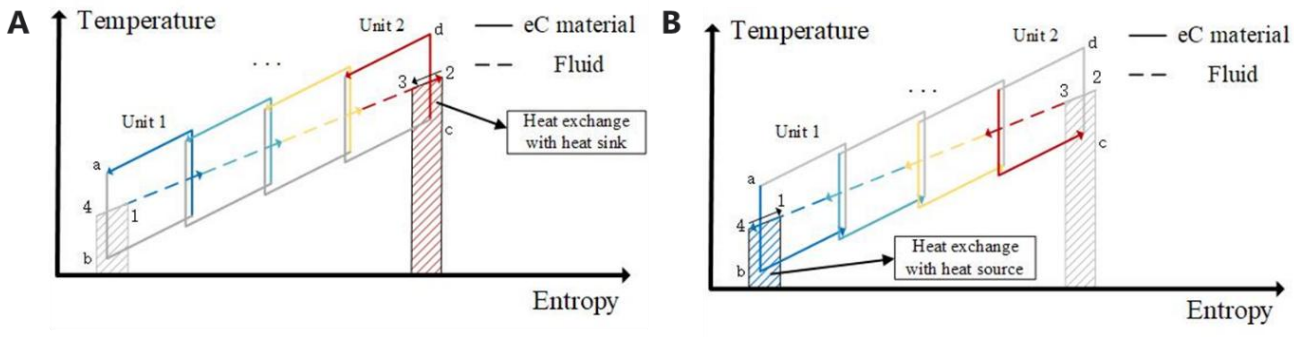

Figure 2: Principle of active regeneration (A) Process ①, (B) Process ②

Essentially, active regeneration benefits from the fact that SMA can undergo phase transformations over a wide temperature range. The active regenerationis so beneficial to the systemperformance that, in cases wherepumping power and driving stress are not limited, we should always strive to extend the flow-wise length as much as possible.

2. RESULT AND DISCUSSION

In the regenerator, we used NiTi tubes with a length of 15mm, an outer diameter of 3mm, and an inner diameter of 2mm as the eC material, which balances performance and durability, as shown in Figure 3 (A). Based on the analysis of active regeneration in section 1.1, we arranged these NiTi tubes in a staggered layout to achieve high heat transfer performance, as shown in Figure 3 (B).

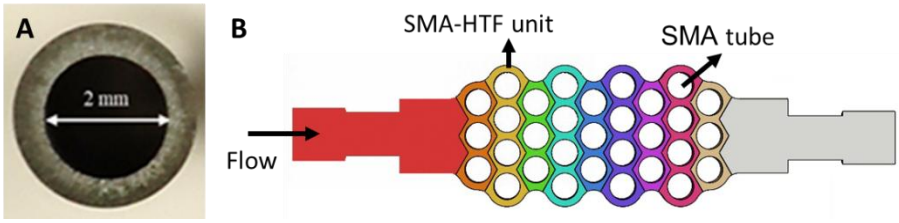

Figure 3: Active regeneration in regenerator (A) SMA tubes, (B) Staggeredtube flow channel

From Figure 4, it can be seen that when the loading/unloading strain rate is greater than 3% s^{-1}, the measured material temperature change can be considered adiabatic temperature change. Therefore, the adiabatic temperature rise of the SMA tubes used in this study can reach 17 K at a strain of 5%, and the adiabatic temperature drop can reach 14 K at a strain of 5%.

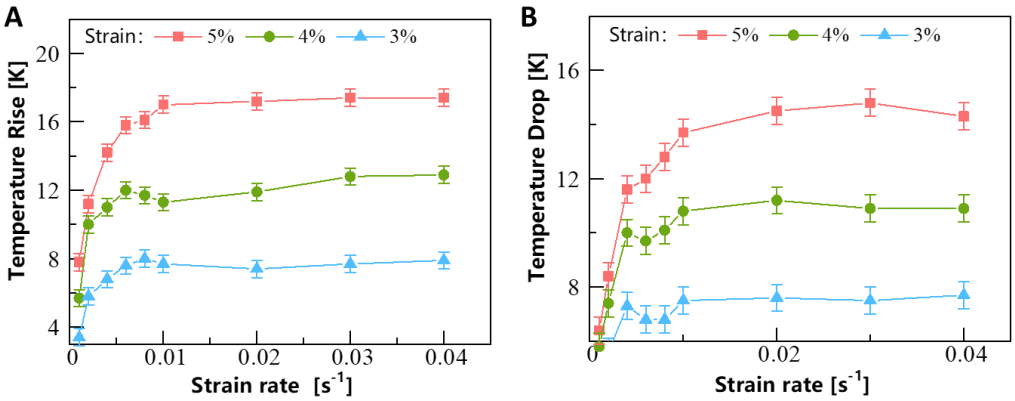

Figure 4: eC effect of a single SMA tube (A) Temperature rise during loading, (B) Temperature drop during unloading

Silicone was used to make the flow channels, and complementary metal parts were used to fitand seal the flow channels.The overall design of the 31-tuberegenerator with 9 unitsis shown in Figure 5B. Furthermore, PU tubesand check valves were used to complement the refrigeration system, as shown in Figure 5A.

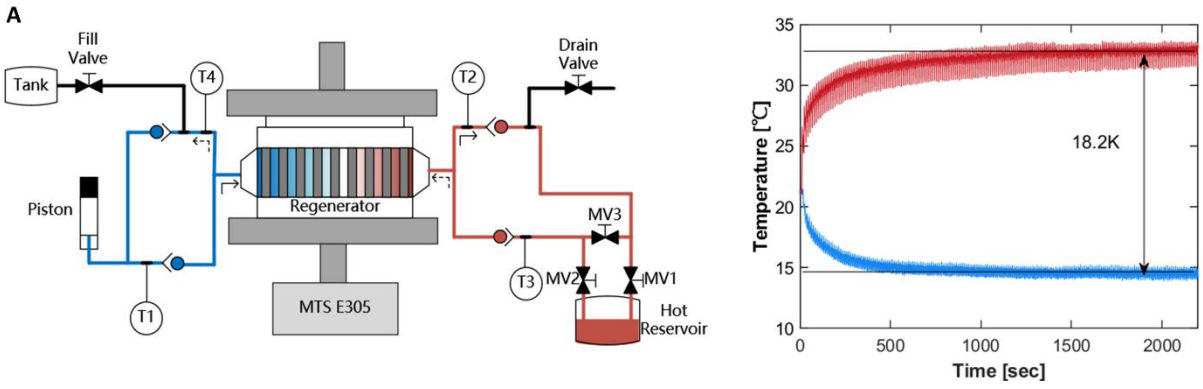

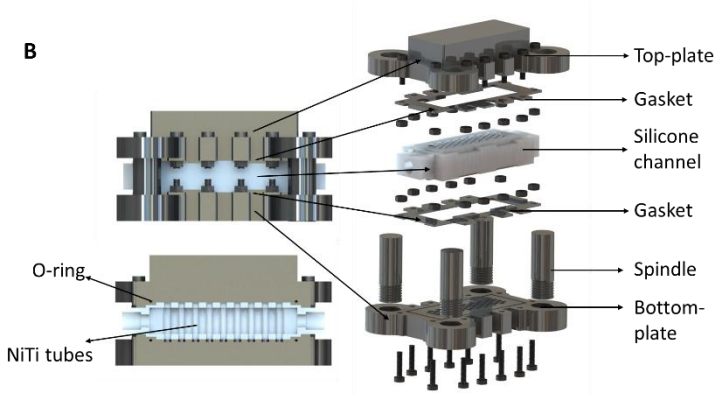

Figure 5: (A) The structure and the performance of the refrigeration system with single-stage eC regenerator with 9 units and 31 tubes, (B) The structure of the single-stageeCregenerator.

As shown in Figure 5A, the single-stage regeneratorwith 9 units and 31 tubes generated a load-free temperature spanof 18.2 K, which exceeds the eC effect of the NiTi tubes. To enhance the performance of the regenerator, as mentioned in section 1, the flow-wise length should be increased. Thus, two different approaches are shown in Figure 6. As shown in Figure 6 (A),there is a U-bend that connects the fluid between two stages in the first regenerator. The fluid in this U-bedcyclically neutralizes the cooling from the top stage and heating from the bottom stage, otherwise known as the dead volume. The presence of dead volumes clearly poses a detrimental effect on the system‘s temperature span.

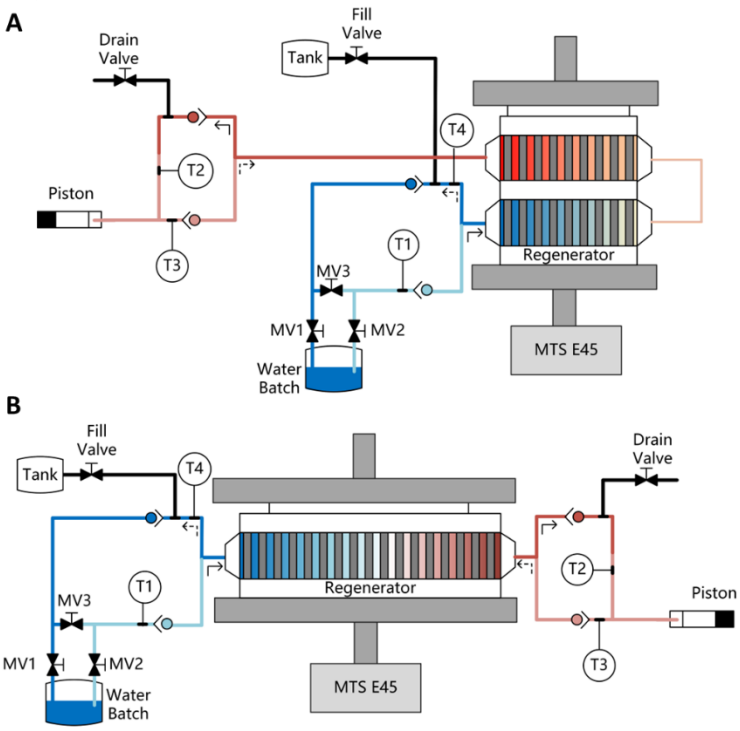

Figure 6: Two designs to enhance active regeneration (A) Cascaded two-stage regenerator, (B) Regenerator with increased flow-wise length.

Toquantify sucha detrimental effectdue to the dead volume, a 59-tuberegenerator with 17 unitswas built, as shown in Figure 6 (B). At the load-free condition without active heat rejection to ambient, after 300-500 cycles, the system's temperature spanstabilized. The averagetemperature spanin the last 10 cycles was then taken as the system's load-freetemperature span.The results are shown in Figure 7:

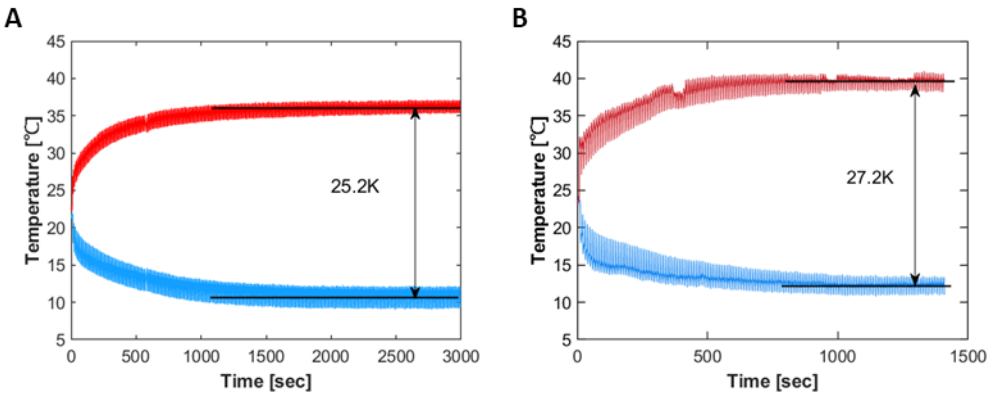

Figure 7: Test results of regenerators (A)Two-stage regenerator with 18 units and 62 tubes, (B) Single-stage regenerator with 17 units and 59 tubes.

From Figure 7, it can be seen that the two-stage cascaded regeneratordemonstrateda load-free temperature span of 25.2 K, representing a close to 50% improvement compared to the single-stage recuperator. The number ofSMA tubes in the59-tuberegenerator wasslightly fewer than the 62-tube two-stage cascaded regenerator, however, it produced a load-free temperature span of 27.2 K, confirming at least 2 Kimprovement by eliminating the dead volume.

3. CONCLUSIONS

This paper introduces an elastocaloric regenerator based on compressing NiTi tubes with external flow. Three different regenerators were tested on the same platform. The single-stage regenerator with 31tubes produced a free-load temperature span of 18.2 K, the two-stage regenerator with 62tubes produced a free-load temperature spanof 25.2 K, and the single-stage regenerator with 59tubes produced a free-load temperature span of 27.2 K.This demonstrates that, increasing the number of SMA-HTF units (without changing the scale of each single SMA-HTF unit) can significantly increase the free-load temperature span produced by the regenerator. It also shows that the inter-stage dead volume in cascaded multi-layer regenerators has a negative impact on their performance (nearly 10%).

ACKNOWLEDGMENT

This work was financially supported by the National Natural Science Foundation of China (NSFC) under grant No. 52376015.

REFERENCES

Ahčin, Ž., Dall'Olio, S., Žerovnik, A., Baškovič, U.Ž., Porenta, L., Kabirifar, P., Cerar, J., Zupan, S., Brojan, M., Klemenc, J., Tušek, J., 2022. High-performance cooling and heat pumping based on fatigue-resistant elastocaloric effect in compression. Joule 6, 2338–2357.

Bonnot, E., Romero, R., Mañosa, L., Vives, E., Planes, A., 2008. Elastocaloric effect associated with the martensitic transition in shape-memory alloys. Phys Rev Lett 100, 125901.

Bruederlin, F., Bumke, L., Quandt, E., Kohl, M., 2019. Cascaded SMA-Film Based Elastocaloric Cooling, in: 2019 20th International Conference on Solid-State Sensors, Actuators and Microsystems and Eurosensors XXXIII, TRANSDUCERS 2019 and EUROSENSORS XXXIII. pp. 1467–1470.

Chen, Y., Wang, Y., Sun, W., Qian, S., Liu, J., 2022. A compact elastocaloric refrigerator. The Innovation 3, 100205.

Emaikwu, N., Catalini, D., Muehlbauer, J., Hwang, Y., Takeuchi, I., Radermacher, R., 2023. Experimental investigation of a staggered-tube active elastocaloric regenerator. International Journal of Refrigeration 153, 370–377.

Holme, 1806. VII. A description of a property of caoutchouc, or indian rubber; with some reflections on the cause of the elasticity of this substance. In a letter to Dr. Holme. The Philosophical Magazine 24, 39–43.

Ianniciello, L., Bartholome, K., Fitger, A., Engelbrecht, K., 2022. Long life elastocaloric regenerator operating under compression. Appl ThermEng 202, 117838.

Ossmer, H., Wendler, F., Gueltig, M., Lambrecht, F., Miyazaki, S., Kohl, M., 2016. Energy-efficient miniature-scale heat pumping based on shape memory alloys. Smart Mater Struct 25, 085037.

Porenta, L., Kabirifar, P., Žerovnik, A., Čebron, M., Žužek, B., Dolenec, M., Brojan, M., Tušek, J., 2020. Thin-walled Ni-Ti tubes under compression: ideal candidates for efficient and fatigue-resistant elastocaloric cooling. Appl Mater Today 20, 100712.

Qian, S., Geng, Y., Wang, Y., Ling, J., Hwang, Y., Radermacher, R., Takeuchi, I., Cui, J., 2016. A review of elastocaloric cooling: Materials, cycles and system integrations. International Journal of Refrigeration 64, 1-19.

Qian, S., Wu, Y., Ling, J., 2015. Design, development and testing of a compressive thermoelastic cooling system. Proceedings of the 24th IIR International Congress of Refrigeration: Yokohama, Japan 92–100.

Schmidt, M., Schütze, A., Seelecke, S., 2015. Scientific test setup for investigation of shape memory alloy based elastocaloric cooling processes. International Journal of Refrigeration 54, 88–97.

Tušek, Jaka, Engelbrecht, K., Eriksen, D., Dall'Olio, S., Tušek, Janez, Pryds, N., 2016. A regenerative elastocaloric heat pump. Nat Energy 1, 16134.

DOI: 10.18462/iir.thermag.2024.0012

COMPARISON BETWEEN SIMULATION AND MEASUREMENTS OF AN APPARATUS FOR A THERMOMAGNETIC MOTOR

Guilherme Hitoshi Kaneko [a], Alisson Cocci de Souza[b,c], Tsuyoshi Kawanami[d]

[a] Department of Mechanical Engineering, Graduate School of Sci. and Tech., Meiji University, Kawasaki, Tama-ku, Higashimita, 1-1-1, 214-8571, Japan, ghkaneko@meiji.ac.jp

[b] Cabo de Santo Agostinho Academic Unit, Federal Rural University of Pernambuco, Cabo de Santo Agostinho, PE, 54518-430, Brazil

[c] Technology Center, Federal University of Pernambuco, Recife, PE, 50670-901, Brazil

[d] Department of Mechanical Engineering Informatics, School of Sci. and Tech., Meiji University, Kawasaki, Tama-ku, Higashimita, 1-1-1, 214-8571, Japan

ABSTRACT

Thermomagnetic motors can generate power using low-grade thermal waste as heat source. These motors are based on the phase transition on magnetic materials (MM) around their Curie Temperature through heating and cooling under a magnetic field. MM and the magnetic circuit (MC) are the main components for the operation of the thermomagnetic motor. The MC is responsible to generate the magnetic field which is going to interact with the MM. The main objective of the present work is the assembly and experimental characterization of a double-C shaped MC to be used in thermomagnetic motors in the future. A double C-shaped MC was designed using permanent magnets of NdFeB arranged in a Halbach configuration using commercially available blocks. It is expected that this MC would enable the utilization of an amount of MM of around 100g per magnetic heat exchanger and at least 4 heat exchangers could be installed.

Keywords: Thermomagnetic Motor, Tesla Motor, Magnetic Circuit, Magnetic Heat Exchangers

1. INTRODUCTION

The concept of the linear thermomagnetic motor was initially conceived by Nikola Tesla (1889), the basic working principle is based on the transition ferro-paramagnetic around Curie Temperature (T_C) of MM, a permanent magnet is used to create a high magnetic field region (B_{high}), while the MM serves both as the heat exchanger and the moving component. Fig. 1 presents a schematical representation of the cycle of the linear thermomagnetic motor, the red blocks are the permanent magnets, the circle indicated by MM is the magnetic heat exchanger (MHE) packed with the MM, the spring on the left side of the MM if pulling the MHE out of the high magnetic field region and is responsible to move the MM, and the thermal bathes illustrated in (2) and (4) represents the heat source and heat sink respectively.

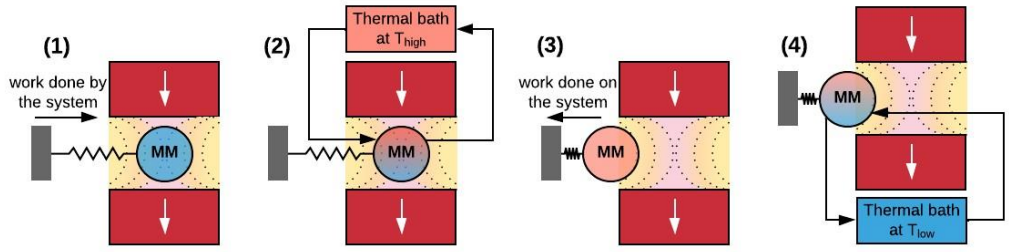

Figure 1: Schematic diagram of the Ericson cycle of a thermomagnetic motor. The red blocks with the white arrows represent the magnetic circuit; the color gradient in the magnetic field volume represents the iso-magnetic field lines; MM is the magnetic material; and the magnetic force is counterbalanced by a traction spring.

The thermodynamic cycle is illustrated in Fig. 2, and it is based on the Ericson cycle (Christiaanse and Brück, 2013) which operates through two isothermal and two isomagnetic-field transitions.

Isofield heating 1 → 2: The MM is in the high field region (B_{high}) and the temperature is increasing from

low ($T < T_C$) to high temperature ($T > T_C$);

Isothermal demagnetization 2 → 3: At this stage the temperature of the MM is higher than its Curie Temperature ($T > T_C$). Consequently, the spring force surpasses the magnetic force, prompting the MM to transition from high field region (B_{high}) to low field region (B_{low});

Isofield cooling 3 → 4: The MM is in the low field region (B_{low}) and the temperature is decreasing from high ($T > T_C$) to low temperature ($T < T_C$).

Isothermal magnetization 4 → 1: At this stage the temperature of the MM is lower than its Curie Temperature ($T < T_C$). Consequently, the magnetic force surpasses the spring force, prompting the MM to transition from low field region (B_{low}) back to high field region (B_{high}), thus restarting the cycle.

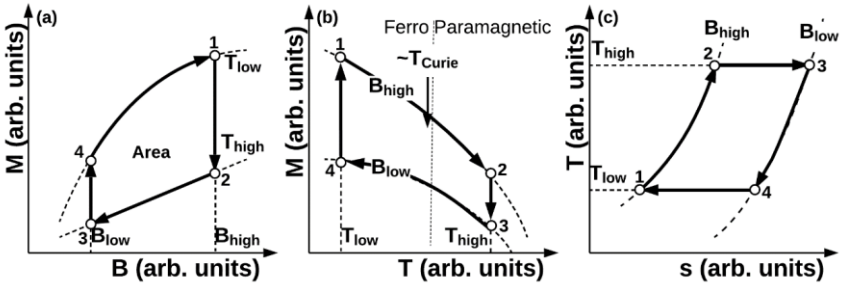

Figure 2: Thermomagnetic motor (Ericson) Cycle (a) M vs. B; (b) M vs. T; (c) T vs. s. Adapted from Christiaanse and Bruck (2013).

The present work presents an experimental apparatus for a linear thermomagnetic motor that operates independently of springs or gravitational force. This study is based on Kaneko et.al. (2021) where some improvements were made in order to allow the utilization of more MHE, and it is expected that it could generate more power with a similar MC.

2. METHODOLOGY

2.1. Magnetic Circuit Assembly

The magnet was designed based on Shäfer (2016), which consists in a double-C shaped MC configuration using commercially available blocks of NdFeB permanent magnets in a Halbach array, and steel alloys as soft magnetic materials. Fig. 3 presents in (a) the superior view of the bottom half of the MC (Plan X0Z) and in (b) the frontal cut view of the MC (Plan XY0).

In Fig. 3, the red blocks represent the NdFeB permanent magnets, the white arrows indicate the remanence direction. The dark gray blocks represent the soft ferromagnetic materials which is responsible to guide the magnetic flux lines between the two poles, for this assembly was used SS400 steel alloy. The light gray blocks are made of non-magnetic materials for structural purposes only.

The selected permanent magnet blocks are outlined in Table 1, three different sizes were selected for the assembly. In Fig. 3(a) the larger central blocks indicated by North Pole and South Pole are the **Main magnets**. The 3 thin blocks flanking the main magnets on each side designated as **Side magnets**. Additionally, positioned above and below the main blocks are the **Frontal magnets**.

Table 1. Selected NdFeB permanent magnets properties

Used as	Size (mm)	Flux Density (mT)	Attractive Force (kgf)
Main	60x30x20	398.6	44
Frontal	30x20x10	358.2	12.3
Side	50x20x5	190.6	13.7

This permanent magnet design includes the capability to adjust the GAP size through two bolts that holds the upper plate, for the present study a GAP of 22mm was chosen.

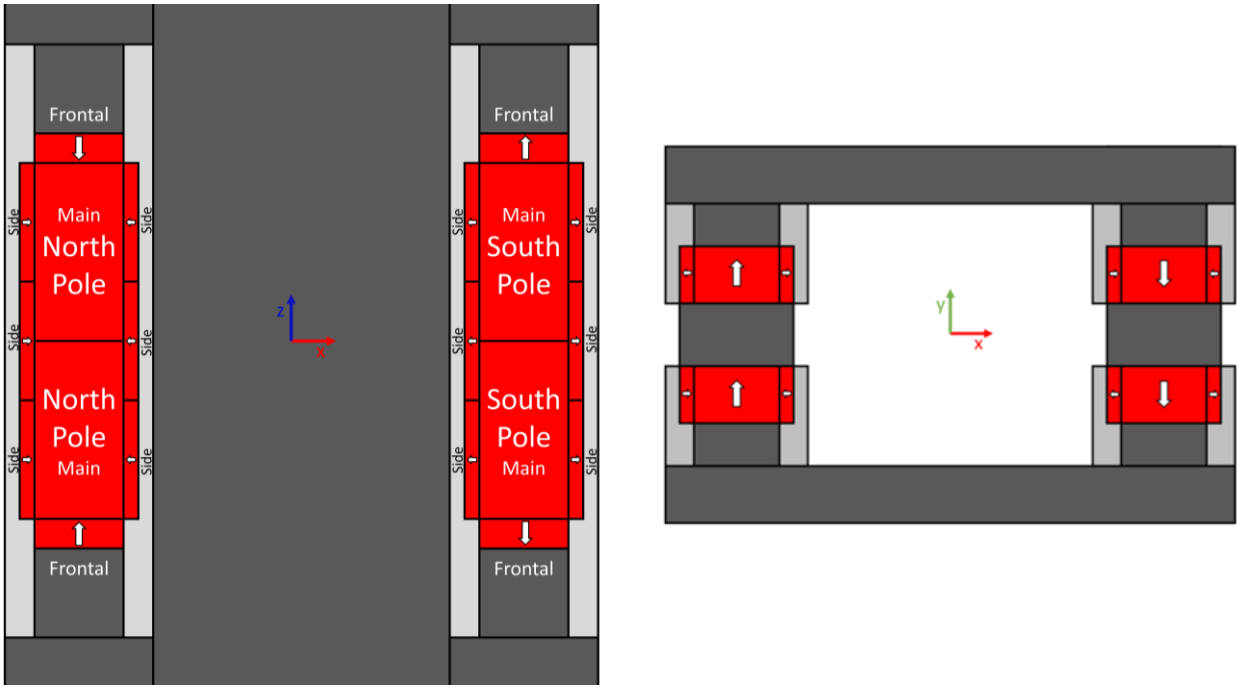

(a) (b)

Figure 3: Magnetic Assemble details (a) Superior view of the bottom part of the Magnetic Circuit (Plan X0Z) (b) Frontal cut view of the Magnetic Circuit (Plan XY0).

2.2. Magnetic Heat Exchanger

The Magnetic Heat Exchanger (MHE) consists of an acrylic tube with an external diameter of 20mm and an inner diameter of 16mm, packed with Gadolinium spheres as the MM within a porous bed of spheres (Trevizoli et.al., 2016).

The Gadolinium region spans a length of 100mm, with a total mass of approximately 99.3g and a porosity (ε) of 37.5%. Fig. 4 provides a representative illustration of the MHE, with the blue region indication the location of the MM.

Figure 4: Magnetic Heat Exchanger.

2.3. Magnetic Flux Density

The magnetic flux density was simulated according to Kaneko (2019). The magnetostatic formulation is modeled using the following equations:

$$H = -\nabla V_m \quad \text{Eq. (1)}$$

$$\nabla \cdot (\mu_0 \mu_r H + B_r) = 0 \quad \text{Eq. (2)}$$

$$B = \mu_0 \mu_r H + B_r \quad \text{Eq. (3)}$$

where H is the magnetic field, Vm is the magnet scalar potential, μ is the magnetic permeability, Br is the remanence, B is the magnetic flux density, and the subscribes r - relative, and 0 - in the vacuum. An air cube of 500 x 500 x 500mm was created around the MC and using the relative permeability (μ_r) of SS400 at room temperature described by Morishita et.al. (2011).

The Magnetic Flux Density was measured using a Gauss-meter with a Hall probe attached to two linear guides for moving on the axis X and Z according to the mesh illustrated in the Fig. 5. The measurement was made along the plan X0Z from -90 to 90mm on the Z axis and from -105 to -40 and from 40 to 105mm on the X axis in steps of 5mm.

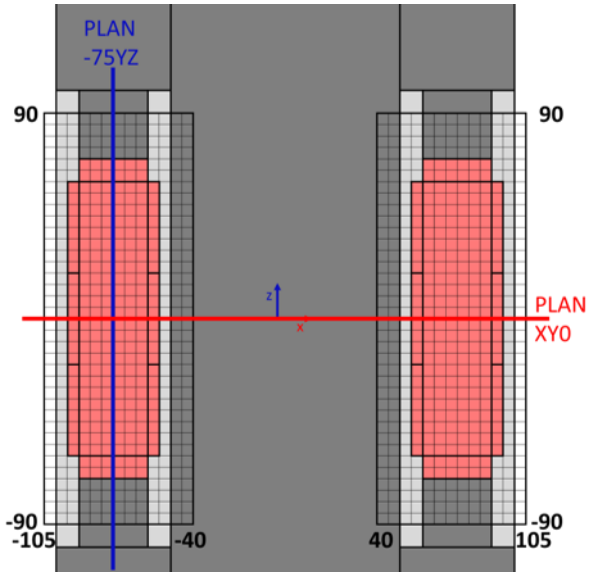

Figure 5: Mesh for Measurement of the Magnetic Flux Density.

2.4. Static Magnetic Force

The simulation of the static force $\vec{F}_m$ is calculated by the following equation (Gama et.al., 2016):

$$\vec{F}_m = M(T, H_{res})V\frac{dB}{dx} \quad \text{Eq. (4)}$$

Where $M(T,H_{res})$ is the Magnetization in function of the Temperature T and the Resulting internal field H_{res}, V is the Volume of MM, and dB/dx is the gradient of the applied magnetic field.

The values of the magnetization were calculated using the Mean Field Theory (MFT) (Morrish, 2001) using the experimental data for the magnetic flux density (B) and the H_{res} is calculated considering the demagnetizing field (Sato and Ishii, 1989) using the following equation:

$$H_{res} = H_{ap} - H_{dem}(H_{ap}, T) \quad \text{Eq. (5)}$$

$$H_{dem} = NM(H_{ap}, T) \quad \text{Eq. (6)}$$

$$N = N_{geo} + (1 - \varepsilon)(N_{hous} - N_{geo}) \quad \text{Eq. (7)}$$

Where H_{ap} is the applied magnetic field generated by the MC, H_{dem} is the demagnetizing field, N is the demagnetizing factor, which combines the demagnetizing factor of the matrix geometry (spheres: N_{geo} = 1/3) and the demagnetizing factor of the MHE housing (cylinder: N_{hous}) calculated by Sato and Ishii (1989) correlation. Also, ε is the porosity of the MHE.

For this simulation a numerical approximation was used in the form of the equation bellow:

$$\vec{F}_m = \sum_{i=1}^{n} M_i(T, H_{res})V_i\left(\frac{dB}{dx}\right)_i \quad \text{Eq. (8)}$$

Fig. 6 presents a representation of the numerical approximation utilized, for this simulation the MHE was divides in 16 parts of Δx=1mm each.

The simulation was conducted within the temperature range of 278 K to 323 K, with increments of 5 K, and spanned from -97 mm to -45 mm along the x-axis, with increments of 1 mm.

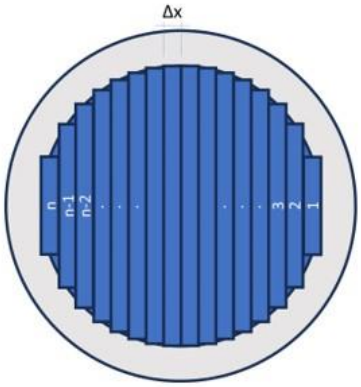

Figure 6: MHE view for simulation of the Static Force.

Fig. 7 presents the schematical view of the setup for Static Force measurement. Due to the change in the force direction at the center of the magnetic pole (x = -75mm for the illustrated left magnetic pole) the experimental static force measurement was conducted in two phases for each magnetic pole, as shown in Figure 7 (a) and (b) for the left magnetic pole measurement. In (a), measurements were taken for -105 < x < -75 mm, while in (b), the range covered was -75 < x < -45 mm.

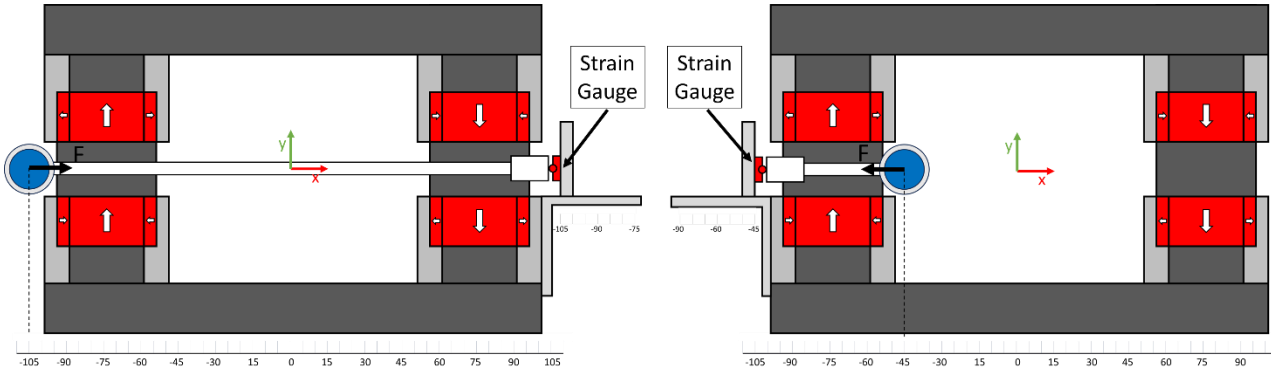

(a) (b)

Figure 7: Static Force Measurement Setup (a) Measurement from -75mm to -105mm (b) Measurement from -45mm to -75mm.

The temperature was incrementally varied from 278 K to 303 K in increments of 5 K. Temperature variation was achieved by circulation water at controlled temperature using a thermal bath. The force itself was measured using 3 strain gauges of model LCCU21N100, with a range of 100N ± 0.5% of R.O.

3. RESULTS AND DISCUTION

3.1. Magnetic Flux Density

The results of the Magnetic Flux Density, *B*, for the Plan X0Z (the same plan illustrated in Fig. 3(a)) are presented in Fig. 8, featuring the theoretical (3D simulation) in (a) and the experimental measurement in (b). The results span approximately -90 < x < 90 mm and -105 < z < 105 mm.

In the regions of high magnetic field intensity (indicated by the red region in Fig. 8(a) and the blue region in Fig. 8(b)), *B* measures around 0.6T for both (a) and (b). Notably, the sizes and positioning of these high magnetic field regions exhibit a good agreement between the theoretical results of the simulation and experimental measurement.

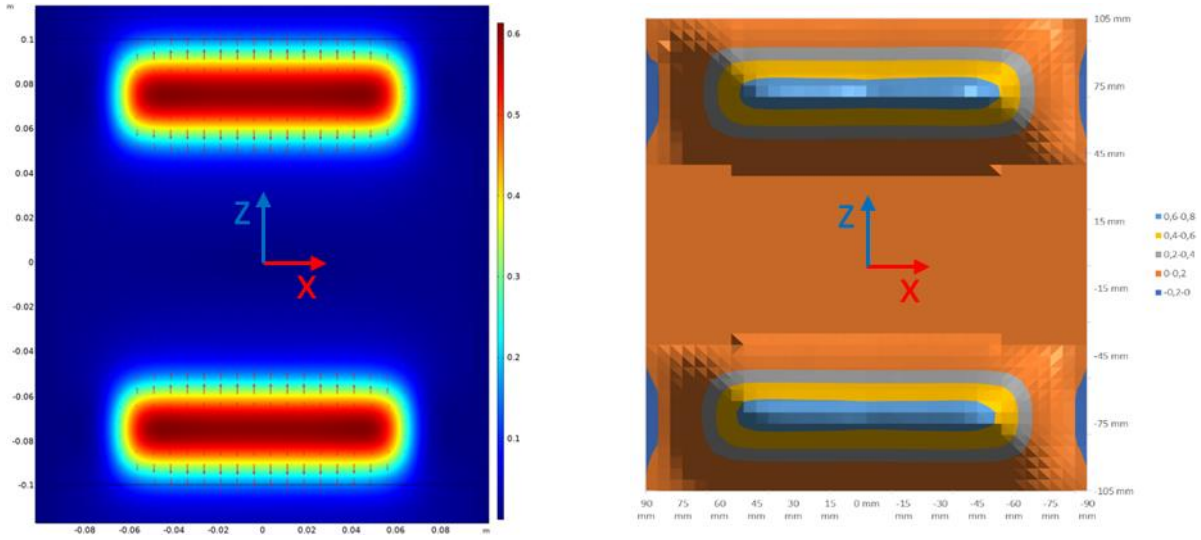

(a) (b)

Figure 8: Magnetic Density Flux in the Plan X0Z (a) Simulation (b) Experimental Measurement.

Fig. 9 presents the results of the magnetic flux density for the plans -75YZ and XY0 (illustrated in Fig. 5). The lines represent the theoretical (3D simulations) results and the * indicates de experimental measurements. The expanded uncertain of the measurements was estimated at ± 0.03T, following the uncertainty evaluation procedure in Holman (2006).

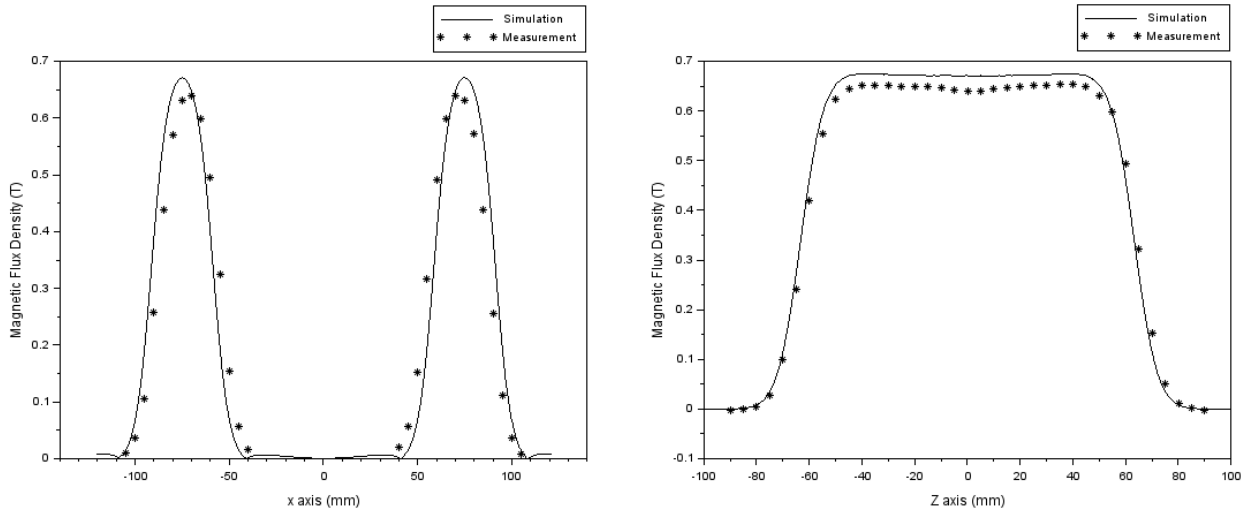

(a) (b)

Figure 9: Magnetic Flux Density Comparison between Simulation (lines) and Experimental (Symbols) Measurement (a) XY0 Plan (b) -75YZ Plan.

Both plots exhibit a good similarity between the experimental measurement and theoretical simulation, indicating a consistency in terms of curve trend and ranges for the magnetic flux density.

3.2. Static Magnetic Force

Fig. 10 presents the results for the static force. The lines represent the theoretical (simulation) and the symbols represent the experimental measurement. As the two poles are symmetrical, only the results of one pole are presented. The uncertain of the measurements was estimated at ± 1.5 N for the static magnetic force and ± 2 mm for the position in the x-axis.

The theoretical and experimental results exhibit a good correlation in trend, both in terms of shape and values, with the maximum force reaching around 250N in both cases. However, it is important to note a small but noticeable discrepancy in the peak position, approximately 5mm apart.

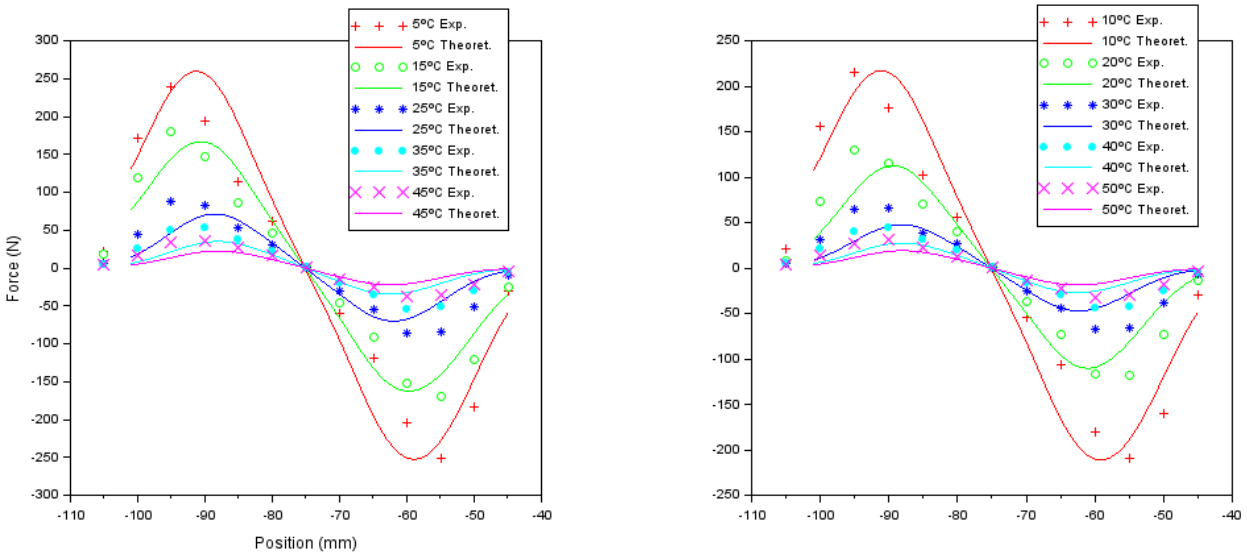

(a) (b)

Figure 10: Magnetic Static Force - Comparison between Simulation (lines) and Experimental Measurement (symbols) as function of Temperature (T) and the position along x-axis.

4. CONCLUSIONS

The present manuscript presented the preliminary results for the apparatus intended for constructing a linear thermomagnetic motor. The main components for the motor, were initially characterized through simulations and experimental measurements. The behavior of the experimental data was aligned to the theoretical results. The Magnetic Flux density is around 0.65T on the high magnetic field's region for a GAP of 22mm, and the magnetic static force for the temperature of 278 K is around 250N for a MHE of approximately 100g of Gd. The next steps of this research involve investigating the variation in peak position for the force. As the peak distance serves as a crucial parameter to define the spacing between MHEs. Subsequently, the motor will be finalized.

ACKNOWLEDGEMENTS

I gratefully acknowledge the support of the Japan International Cooperation Agency (JICA) for providing the scholarship, which has enabled my studies at Meiji University.

NOMENCLATURE

Roman		M	Magnetization (A×m-1)
B	Magnetic flux density (T)	T	Temperature (K)
B_{high}	High magnetic field region (-)	T_C	Curie Temperature (K)
B_{low}	Low magnetic field region (-)	V	Volume (m3)
B_r	Remanence (T)	V_m	Magnet scalar potential (A)
dB/dx	Applied magnetic field gradient (T/m)	**Greek**	
F_m	Magnetic Force (N)	ε	Porosity (-)
H	Magnetic field (A×m-1)	μ_0	Vacuum magnetic permeability (Wb×A-1xm-1)
H_{ap}	Applied magnetic field (A×m-1)	μ_r	Relative magnetic permeability (Wb×A-1xm-1)
H_{dem}	Demagnetizing field (A×m-1)	Δx	Increments of x(mm)
H_{res}	Resulting magnetic field (A×m-1)	**Subscript**	
N	Total demagnetizing factor (-)	*MC*	*MC*
N_{geo}	Geometric demagnetizing factor (-)	*MHE*	*MHE*
N_{hous}	Housing demagnetizing factor (-)	*MM*	*MM*

REFERENCES

Christiaanse, T., Brück E., 2013. “Proof of concept Static Thermomagnetic Generator Experimental Device”, Metallurgical and Materials Transactions E, 1, 36-40.

Corrêa, L. S., Rowe, A., Trevizoli, P.V., Thermodynamic optimization of a linear thermomagnetic motor. Applied Thermal Engineering 219 (2023) 119344.

Gama, S., Ferreira, L.D., Bessa, C.V., Horikawa, O., Coelho, A.A., Gandra, F.C., Araujo, R., Egolf, P.W., Analytic and experimental analysis of magnetic force equations, IEEE Trans. Magn. 52 (7) (2016) 1–4.

Holman JP (2006) Experimental methods for engineers, 8th ed. McGraw-Hill, New York

Kaneko, G.H., Conceição, W.A.S., Colman, F.C., Cocci, A.S., Alves, C.S., Pupim, G.C., Kubota, G.H., Oliveira, V.C., Trevizoli, P.V., 2021. Design and experimental evaluation of a linear thermomagnetic motor using gadolinium: Preliminary results. Applied Thermal Engineering 186 (2021) 116472.

Kaneko, G.H., Souza, A.C., Moro, F., Colman, F.C., Conceição, W.A.S., Alves, C.S., Trevizoli, P.V., Design and assembling of a magnetic circuit for a thermomagnetic motor apparatus. Journal of the Brazilian Society of Mechanical Sciences and Engineering 2019.

Morishita, M., Takahashi N., Miyagi, D., Nakano, M., 2011. Examination of Magnetic Properties of Several Magnetic Materials at High Temperature. Electrical Review, R. 87 No 9b

Morrish, A., “The Physical Principles of Magnetism”. The Institute of Electrical and Electronics Engineers, Inc., 2001. ISBN 9780470546581.

Sato, M., Ishii, Y., 1989. Simple and approximate expressions of demagnetizing factors of uniformly magnetized rectangular rod and cylinder. Journal of Applied Physics 66 (2) 983-985.

Schäfer B., 2016. *Development of a Magnetocaloric test apparatus.* Master Thesis, Faculty of Mechanical Engineering, Munich.

Tesla, N., 1889. “Termo-magnetic motor”. US Patent 396121.

Trevizoli, P.V., Peixer, G.F., Barbosa Jr., J.R., Thermal–hydraulic evaluation of oscillating-flow regenerators using water: Experimental analysis of packed beds of spheres, Int. J. Heat Mass Transfer 99 (2016) 918–930.

DOI: 10.18462/iir.thermag.2024.0013

INFLUENCE OF VELOCITY PATTERN OF HEAT EXCHANGE MEDIUM FLOW ON ENHANCEMENT OF TEMPERATURE SPAN FOR AN ACTIVE MAGNETIC REGENERATOR

Ren Matsushita[(a)], Tsuyoshi Kawanami[(b)], Guilherme Hitoshi Kaneko[(a)]

[(a)] Graduate School of Science and Technology, Meiji University
1-1-1 Higashimita, Tama-ku, Kawasaki 214-8571, Japan
[(b)]Department of Mechanical Engineering Informatics, Meiji University
1-1-1 Higashimita, Tama-ku, Kawasaki 214-8571, Japan, kawanami@meiji.ac.jp

ABSTRACT

A magnetic heat pump has several advantages, such as not carrying any greenhouse gases and generating potential energy savings, over conventional vapor compression heat pumps. Several studies have been conducted to evaluate the performance of magnetic heat pumps operated in an active magnetic regeneration (AMR) cycle. Most of those studies evaluated the capability of AMR cycles using flow rate and average flow velocity as variables. In contrast, the refrigeration performance of the AMR magnetic heat pump is strongly influenced by the flow pattern during one cycle, besides these typical flow conditions. In this study, the effect of the flow pattern of the heat exchange medium during the AMR cycle on the temperature change behavior of the magnetic refrigeration system was investigated. As a result, it was found that the temperature span generated by the AMR depends on the pattern of flow velocity variations of the heat exchange medium.

Keywords: Magnetocaloric effect, Active magnetic regenerator, Heat pump, Refrigeration cycle, Heat exchange medium.

1. INTRODUCTION

Vapor compression heat pumps used for air conditioning and refrigeration employ F-gases as refrigerants. Most gas refrigerants currently in use have a significant global warming effect and may have a negative impact on the global environment. Therefore, magnetic heat pump systems have attracted attention as potential replacements for conventional heat pump systems that use gas refrigerants. Magnetic heat pump systems utilize magnetocaloric materials and magnetocaloric effect (MCE), in which heat is generated and absorbed due to changes in the external magnetic field. This technology has a higher theoretical coefficient of performance (COP) than a conventional vapor compression heat pump using a gas refrigerant. In addition, it offers the benefit of not emitting any greenhouse gases due to the usage of a solid-state type refrigerant. Several studies evaluated the performance of magnetic heat pumps operated in an active magnetic regeneration (AMR) cycle. Most of these studies evaluated the capability of AMR cycles using flow rate, average flow velocity, and utilization factor as variables. In contrast, the refrigeration performance of the AMR magnetic heat pump is strongly influenced by the flow pattern during one cycle, besides these typical flow conditions. However, there is limited research on varying flow velocities within one cycle. In this study, the effect of the flow pattern of the heat exchange medium during the AMR cycle on the temperature change behaviour of the magnetic heat pump system was investigated.

2. ACTIVE MAGNETIC REGENERATOR AND ITS HEAT PUMP CYCLE

When magnetocaloric materials (MCMs) are magnetized, their temperature increases. Conversely, when demagnetized, their temperature decreases. This phenomenon is called the magnetocaloric effect. In the room temperature range, the temperature change caused by a single MCE is small. Consequently, the AMR cycle is utilized to expand this temperature span between the hot and cold ends. Fig.1 shows the fundamental process of the AMR cycle. The AMR consists of an MCM bed, a heat exchange medium, a magnetic circuit, and a displacer. The side that becomes hot to the AMR cycle is the hot end while the side that becomes cool is the cold end. This AMR cycle operates through four processes: (i) magnetization process, (ii) fluid flow process, (iii) demagnetization process, and (iv) fluid flow process. Since the temperature gradient in the packed bed becomes steeper with each repetition of the cycle, the temperature span between the hot and cold ends increases gradually.

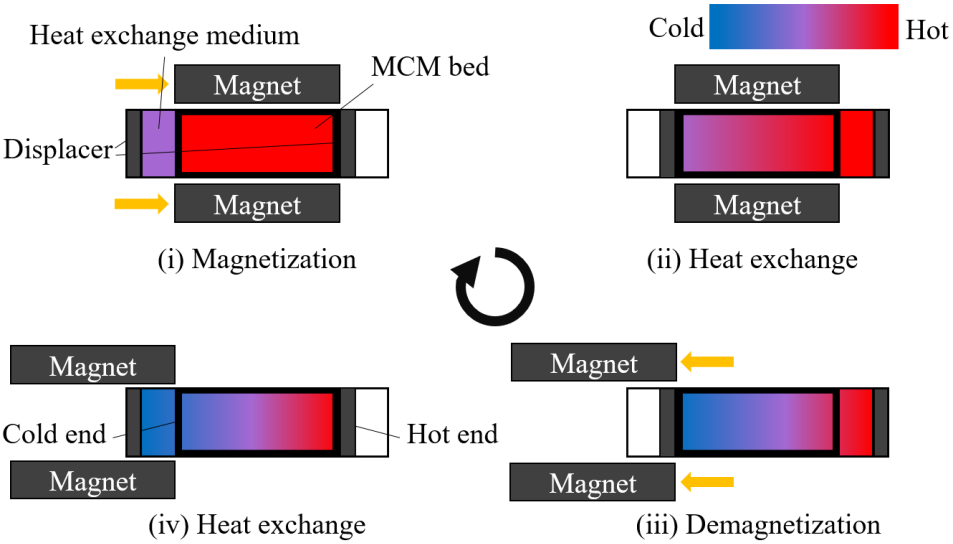

Fig.1: Process of AMR cycle

3. EXPERIMENTAL APPARATUS AND CONDITIONS

3.1 Experimental Apparatus

Fig.2 shows the experimental apparatus used in this study. The experimental apparatus for this study consisted of the AMR packed bed containing MCM, a rodless cylinder for moving the heat exchange medium, a flow channel connecting the acrylic pipe and rodless cylinder, resistance temperature detectors (RTDs) for measuring the temperatures at the cold end and hot end, and a data logger for recording these temperatures. The flow channel was filled with distilled water as a heat exchange medium. The magnetic circuit, which consists of two opposing permanent magnets that are placed 12 mm apart and a yoke, is a closed circuit for protecting the magnetic field from external leakage. The maximum concentration of magnetic fluxes is at a central point between the permanent magnets and is equal to 0.89 Tesla.

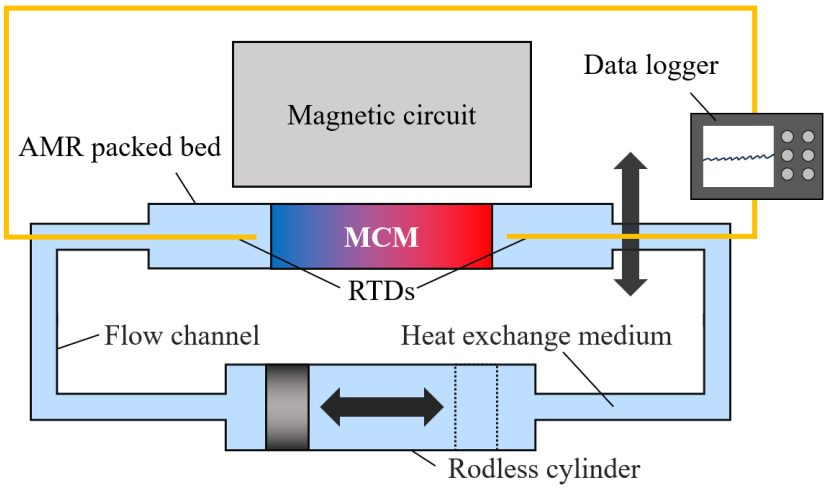

Fig.2: Schematic of experimental set up

Fig.3 shows the details of the AMR bed that the MCM is packed in an acrylic pipe. The inner diameter of the acrylic pipe was 6mm. Gadolinium was packed into the acrylic pipe as the MCM. The filling length of the material was 80mm. The particle diameter of gadolinium is around 0.55mm, and the total packing weight is 10.1g. The RTDs were placed 5mm from both ends of MCM.

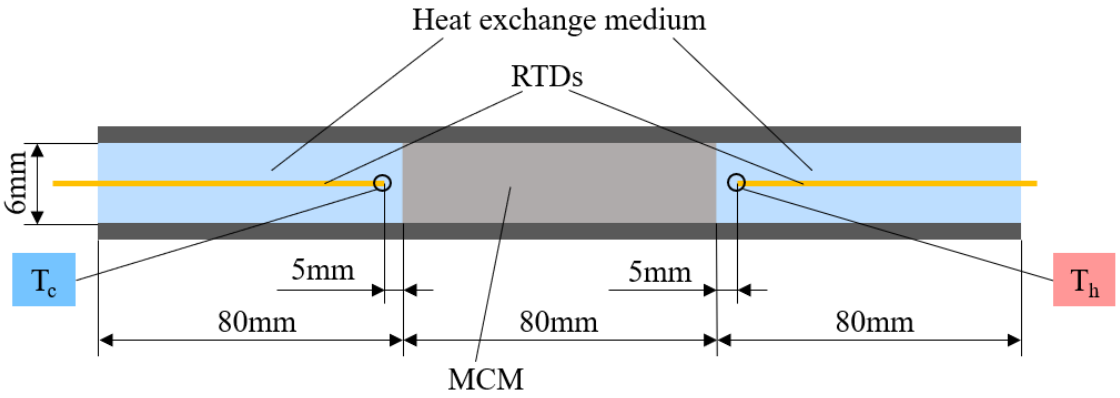

Fig.3: Details of the AMR bed

3.2 Experimental Conditions

The temperature measurement interval of the data logger was set as 0.5s. Once temperature changes stabilized, the temperature difference ΔT between the hot and cold ends was defined as follows:

$$\Delta T = T_h - T_c \qquad \text{Eq.(1)}$$

Where T_h [°C] and T_c [°C] indicate the temperatures at the hot and cold ends, respectively. The varied parameters of the experiment are the frequency of the AMR cycle f, the utilization factor UF, and the ratio of the stopping time of the heat exchange medium in one cycle st.

The utilization factor (UF) is used as a measure of how much heat is transferred to the heat exchange medium by the MCM. Equation 2 shows the UF [-], which is defined as

$$UF = \frac{m_w c_w}{m_s c_s} \qquad \text{Eq.(2)}$$

where c_w [kJ/(kgK)], c_s [kJ(kgK)], m_w [kg], m_s [kg], are the specific heat of the heat exchange medium, the specific heat of the MCM, the mass of the heat exchange medium delivered by the pump during one displaced process, the mass of the MCM, respectively.

Fig.4 shows the variation in flow velocity of the heat exchange medium in this experiment. The vertical axis shows the flow velocity of the heat exchange medium v [m/s], and the horizontal axis shows the measure time t[s]. In this experiment, the flow velocity of the heat exchange medium follows the pattern shown in this graph.

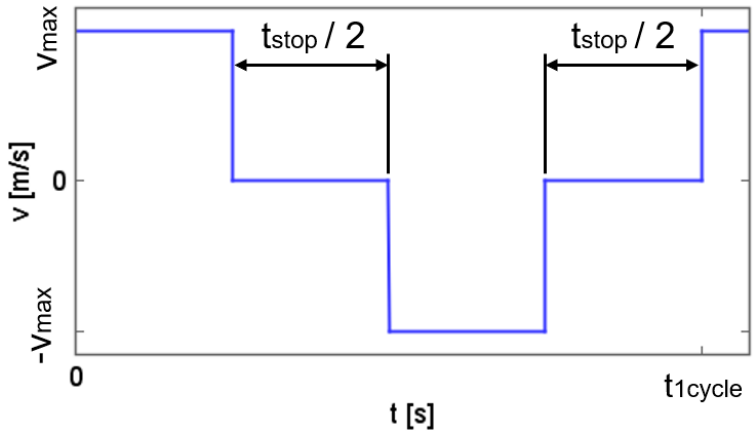

Fig.4: Flow velocity of the heat exchange medium

The *st* [-] is defined as

$$st = \frac{t_{stop}}{t_{1cycle}} \quad \text{Eq.(3)}$$

where t_{stop} [s], t_{1cycle} [s] and the stopping time of the heat exchange medium in one cycle, the time for one AMR cycle, respectively. Increasing *st* requires moving the same distance in a shorter time, leading to a higher v_{max}. Equation 4 shows the v_{max} [m/s], which is defined as

$$v_{max} = \frac{l}{t_{1cycle}(1 - st)} \quad \text{Eq.(4)}$$

where *l* [m] is the displacement of the heat exchange medium in one cycle.

In the present study, the frequency of the AMR cycle, *f*, is varied from 0.6 to 1.4 Hz. The utilization factor *UF*, is varied from 0.75 to 1.25. Furthermore, the ratio of stopping time of the heat exchange medium in one cycle *st*, varied from 0.0 to 0.8. The initial temperature of the experiment was set to 21 ℃ , which is the Curie temperature of gadolinium (Dan'kov et al., 1998). The experimental parameters are listed in Table 1.

Table1. Experimental parameters

Parameters	Symbols [Unit]	Values
Particle size of gadolinium	d_s [m]	0.55×10^{-3}
Porosity	ε [-]	0.43
Mass of MCM	m_s [kg]	10.1×10^{-3}
Specific heat capacity of MCM	c_s [J kg^{-1} K^{-1}]	343
Specific heat capacity of fluid	c_w [J kg^{-1} K^{-1}]	4182
Magnetic flux density at the center of gap	*B* [T]	0.89
Initial temperature	T_i [℃]	21

4. RESULT AND DISCUSSION

Fig.5 shows the relation between the elapsed time and the temperatures at the hot and cold ends for *f*=1.0, *UF*=1.0, *st*=0.0. The horizontal axis shows the elapsed time [s] from the start of the experimental. The vertical axis represents the temperature [℃]. From this figure, it was revealed that the temperature span expanded as soon as the experiment began. After 600 second, the temperatures at the hot and cold ends were achieved at 27.2°C and 14.5°C, respectively. The maximum temperature span between the hot and cold end of 12.7K was obtained. From this figure, it was revealed that the temperature span expanded as soon as the experiment began. After 600 second, the temperatures at the hot and cold ends were achieved at 27.2°C and 14.5°C, respectively. The maximum temperature span between the hot and cold end of 12.7K was obtained.

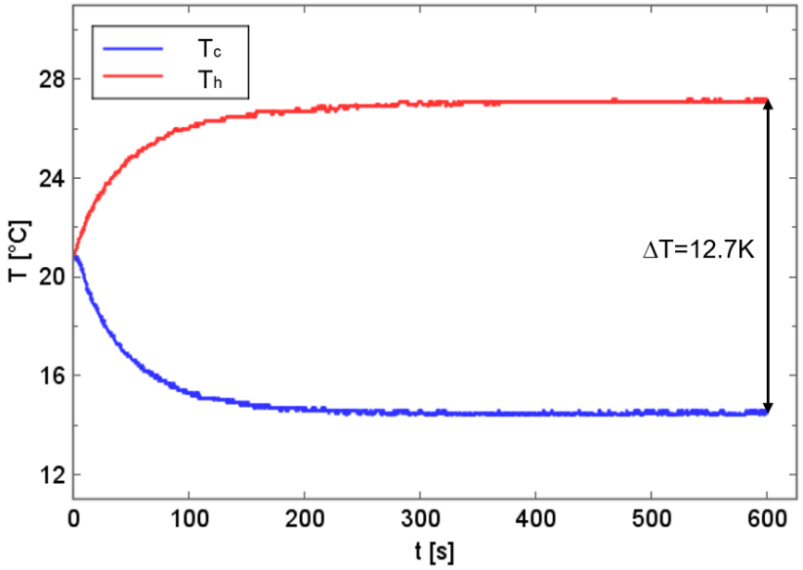

Fig.5: Relation between the elapsed time and temperature for *f*=1.0, *UF*=1.0, *st*=0.0

Fig.6 shows the relation between the elapsed time and the hot end temperature and cold end temperature for *f*=1.0, *UF*=1.0, *st*=0.8. After 600 second, the temperatures at the hot and cold ends were achieved at 27.1°C and 15.7°C, respectively. The maximum temperature span between the hot and cold end of 11.4K was obtained, and this is smaller than the temperature span for *st*=0.0.

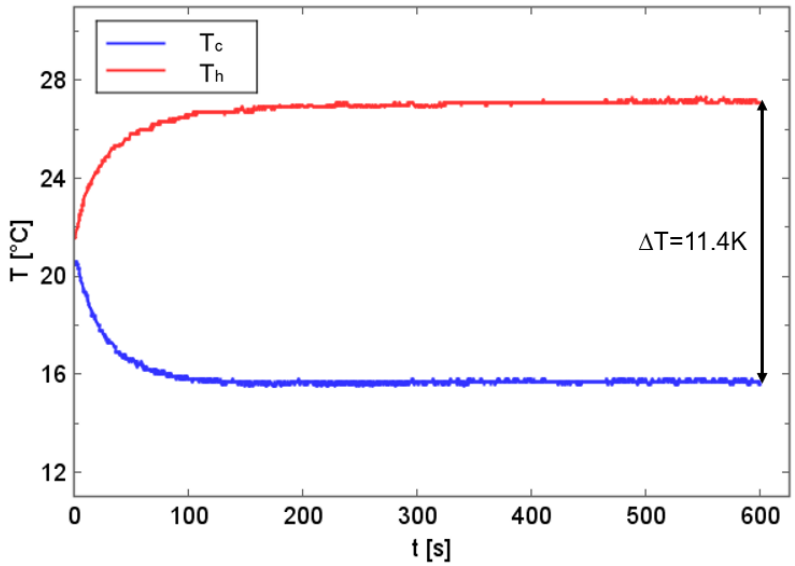

Fig.6 Relation between the elapsed time and temperature for *f*=1.0, *UF*=1.0, *st*=0.8

Fig.7, 8 and 9 shows the relationship between *st* and the final temperature span for *f*=0.6, 1.0, and 1.4. The horizontal axis shows *st* [-]. The vertical axis represents the temperature span [K]. The maximum temperature span, 13.4 K, was obtained when *f*=1.0, *UF*=0.75, and *st*=0.0. These graphs show that as *st* increases, the final temperature span becomes smaller, and this tendency is consistently observed across all graphs. When *st* increases, the flow velocity increases, resulting in a higher heat transfer coefficient. However, it is thought that increasing *st* leads to a decrease in the time of the heat exchange process, resulting in these experimental results.

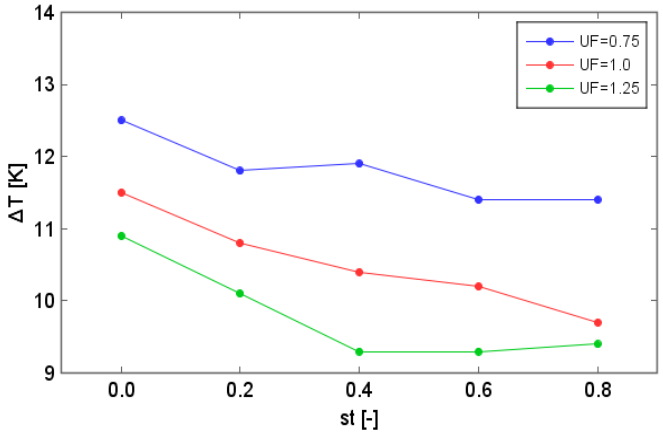

Fig.7: Relation between *st* and the final temperature span for *f*=0.6

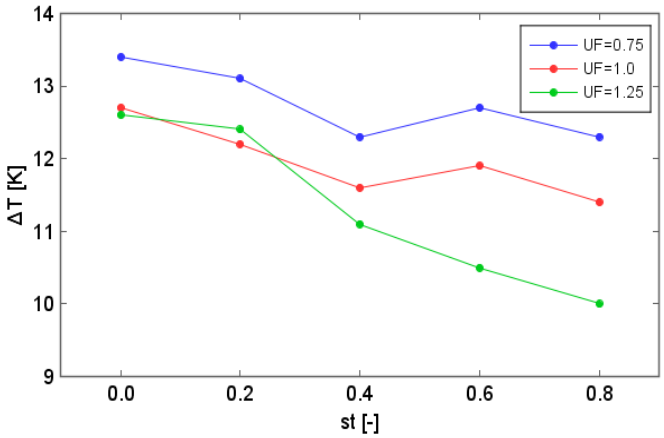

Fig.8: Relation between *st* and the final temperature span for *f*=1.0

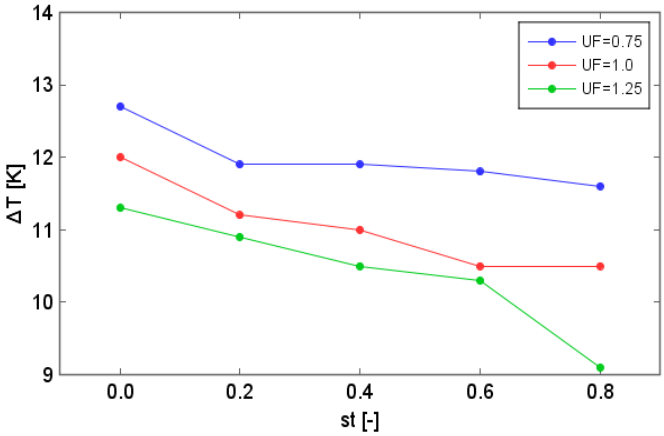

Fig.9: Relation between *st* and the final temperature span for *f*=1.4

CONCLUSIONS

In this study, experiments were conducted to investigate the influence of the ratio of the stopping time of the heat exchange medium in one cycle, *st*, on the temperature difference generated by AMR. As a result, it was observed that increasing the *st* resulted in a smaller temperature span generated by the magnetic heat pump. The maximum temperature span, 13.4 K, was obtained when *f*=1.0, *UF*=0.75, and *st*=0.0.

NOMENCLATURE

B	magnetic flux at the center of gap (T)	T_c	temperature of cold end (℃)
c_s	specific heat of MCM (J kg^{-1} K^{-1})	T_h	temperature of cold end (℃)
c_w	specific heat of water (J kg^{-1} K^{-1})	T_i	initial temperature (℃)
d_s	particle size of MCM (m)	t	time (s)
f	frequency of the AMR cycle (Hz)	t_{1cycle}	the time for one AMR cycle (s)
l	displacement of the heat exchange medium in one cycle (m)	t_{stop}	the stopping time of the heat exchange medium in one cycle (s)
m_s	mass of MCM (kg)	UF	utilization factor
m_w	mass of water (kg)	v_{max}	Maximum velocity of the heat exchange medium (m s^{-1})
st	the ratio of the stopping time of the heat exchange medium in one cycle	ΔT	temperature span (K)
T	temperature (℃)	□	Porosity

REFERENCES

Dan‘kov, S.Y., Tishin, A.m., 1998. Magnetic phase transitions and the magnetothermal properties of gadolinium. Physical Review B, Vol.57, Number 6.

DOI: 10.18462/iir.thermag.2024.0014

STUDY ON THE ELASTIC THERMAL EFFECT OF NATURAL RUBBER UNDER SIMPLE HARMONIC CYCLE

Yunzhao Zhang[(b)], Yumei Wang[(b)], Xinru Niu[(b)], Bin Liu[(a) (b)]

[(a)] Tianjin Key Laboratory of Refrigeration Technology, Tianjin 300134, China, lbtjcu@tjcu.edu.cn (Bin Liu)
[(b)] Tianjin University of Commerce, Tianjin 300134, China, lbtjcu@tjcu.edu.cn (Bin Liu)]

ABSTRACT

As a new and efficient refrigeration technology, elastothermal refrigeration with high refrigeration efficiency and specific refrigeration power is considered to be a promising alternative to traditional vapor compression technology. Compared with shape memory alloys, elastomers require much lower applied stresses to produce elastocaloric effect. In this paper, Elastocaloric effects of cylindrical natural rubber under 4 strains and 4 tensile rates were studied on a self-made experimental bench. The results showed that the elastocaloric effect was almost constant under the periodic strain force of simple harmonic cycle, and the greater the strain, the more obvious the influence of tensile rate on elastocaloric effect. Furthermore, when the strain of cylindrical natural rubber was 250%, the entropy of the stretch-shrink cycle increased with the increase of the tensile rate, but did not change with the ambient temperature.

Keywords: Solid-state refrigeration, Elastocaloric effect, Natural rubber, Entropy.

1. INTRODUCTION

Cooling is essential to modern life, while seriously pollutes environment. (Coulomb et al., 2017, Bhatia et al., 2018; Kishore et al., 2019; Liu et al., 2021). Current refrigeration technology is almost entirely dependent on vapour compression refrigeration technology, in which hydrofluorocarbons (HFCS) are the most commonly used conventional refrigerants, but with a global warming potential (GWP) 1,000 times that of CO_2. Amendments under the Montreal Protocol (Boukai et al., 2008) require that HFCS must be phased out by 2047 and replaced only with natural refrigerants. In the past two decades, elastothermal refrigeration using rubber elastocaloric effect (ECE) was proven to have great application potential (Holzapfel et al.,1999), after conducting lots of researches on new refrigeration technologies such as magnetothermal, electrothermal, elastothermal, and pressure thermal (Fahler et al., 2018, Moya et al., 2020, Hou et al., 2022, Shi et al., 2019, Lloveras et al., 2021). Elastothermal refrigeration refers to the technology of using elastothermal materials to produce temperature changes and entropy changes when subjected to external mechanical stress.

Refrigeration using the thermal effect of natural rubber bullets can be traced back to 1925，when W. B. Wiegand (1978) proposed the design of two elastomer cyclic heat engines, providing inspiration for other scholars. Up to now, many experts have studied the elastothermal cooling effect of natural rubber. For example, Wang Run et al. (2019) found that the twisting and untwisting processes of natural rubber fibers could produce cooling effect and the maximum torsional specific cooling capacity was 19.4 J/g under 100% strain and medium twist density. J. R. Samaca Martinez et al. (2013) found that polymer chains would crystallize under tension, resulting in temperature increase of natural rubber, and the crystallization of rubber occurred during the stress relaxation process. Y. Miyamoto et al. (2003) found that under certain stress and temperature conditions, the melting temperature of crystalline rubber increased in an approximate linear relationship with the nominal stress. A. N. Gent et al. (1995) studied the kinetics of low-temperature crystallization of natural rubber by using the expansion agent method, and found that the maximum crystallization rate of unstretched natural rubber occurred at -25 °C. JJ. M. Chenal et al. (2007) found that the molecular weight between physically entangled states in natural rubber was the key parameter of stress-induced crystallization, with high-vulcanization and weak-vulcanization natural rubber as experimental materials. S. Toki et al. (2013) found that stress-induced crystallization of unvulcanized natural rubber increased with stress at 25 °C with synchrotron radiation X-ray measurement. With *in-situ* wide-angle X-ray scattering measurement, N. Candau et al. (2014) measured the average size and crystallinity index of grains in three main directions during loading and unloading processes at low strain rate (10^{-3} s^{-1}) and room temperature, and found that there was a memory effect in the chain involved in crystallization slowing down the nucleation process of the crystal. Xie Zhongjian et al. (2015) found that pre-tensile deformation would make natural rubber skip the region of low elastic heat coefficient and directly enter the region of high elastic

heat coefficient caused by stress-induced crystallization. G. Sebald et al. (2016) studied the fatigue influence on elastocaloric effect of natural rubber, and found that the cycle number of natural rubber breaking was limited (about 800 cycles), showing a very short fatigue life.

At present, there are many researches on the mechanical properties of natural rubber, but few researches on elastocaloric effects in the stretching-retraction (harmonic cycle) cycle of natural rubber. Therefore, the crystallization phenomena of natural rubber samples at different temperatures were studied by differential scanning calorimeter. The surface morphologies of natural rubber in different states were studied by electron scanning microscope. The elastocaloric effects of cylindrical natural rubber under 4 strains and 4 tensile rates were studied on a self-made experimental bench, and the entropy change of the simple harmonic cycle was analyzed when strains was 250%. The results of this paper provide reference for the follow-up researches on elastocaloric effects of natural rubber.

2. EXPERIMENTAL MATERIALS AND METHODS

The main body of the paper will consist of one or more main sections describing experimental designs, test procedures, theoretical consideration, and results. Sections with appropriate subtitles should describe the test equipment, measurements, observations, and mathematics needed to perform the experiments. Case histories, systems descriptions or applications should contain original aspects, out-of-standard performances or noteworthy details that should be clearly identified and described. Discussion of the results, qualifications, limits to the accuracy of tests, and calculations should also be included in this part.

2.1 Experimental Materials

The main structure of natural rubber used in this experiment is cylindrical (Figure 1). The two ends are flat and have a cylindrical structure with a diameter of 5 mm and a length of 50 mm. The characteristics of natural rubber were shown in Table 1, The shape and dimensions of NR were shown in Figure 1.

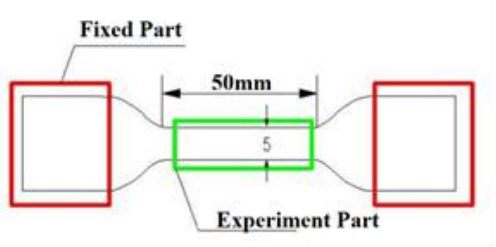

Figure 7: Cylindrical natural rubber dimensions

Table 1. Properties of Nature Rubber

Position Density ρ(kg/m^3)	Tensile strength MPa	Elongation %	Temperature range °C
1177	22.6	1000	-75~90

2.2 Experimental device and scheme

A self-built test bench was used in the experiment, as shown in Figure 2. Linear stretching was controlled by AMC 4030 programming software. The distance, speed and number of movements could be set through software programming, which could reduce the experimental error. During the experiment, infrared thermal imager was used as temperature measuring equipment. The simple harmonic cycle experiments of cylindrical natural rubber were carried out at room temperature under different strains and different tensile rates. The elastocaloric effect of natural rubber was studied by recording the temperature change curve with time during the simple harmonic cycle in 300 s.

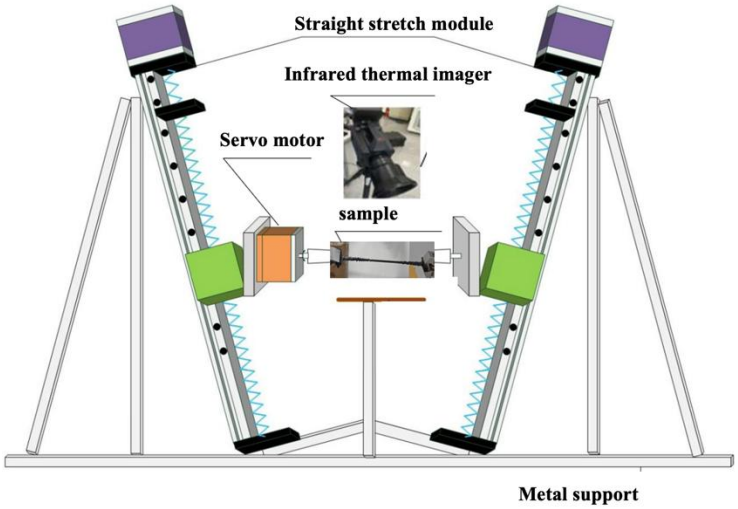

Figure 2: Test device diagram

3. RESULT AND ANALYSIS

3.1 Elastocaloric effect of natural rubber at different tensile rates

Unlike metallic functional materials (reversible strain of a few percent or a few hundred), rubber has a reversible strain of several hundred percent, which provides more precise study for elastocaloric effect.

With entropy elasticity, rubber sample was heated during stretching while was cooled during compression process. When external forces were applied, the polymer chain stretched and obtained a low-probability energy state with low entropy (Cadwell et al., 1940), resulting in rapid reversible changes for sample temperature under near-adiabatic conditions of rapid tension-compression cycle.

The temperature changes versus time under harmonic cycles with strain of 150%、200%、250%、300% and tensile speeds of 10, 20, 30, 40 mm/s, respectively, were shown in Figure 3. 5 MPa stress was applied to the sample. The sample temperature showed reversible change synchronizing with sample strain change. ECE decreased sharply with the increase of harmonic cyclic tensile speed.

As shown in Figure 3a, when the strain was 150%, the temperature changes of natural rubber in the harmonic cycle process changed with the tensile speed changes. When the drawing speed was 10 mm/s, the average temperature difference was 0.2 ℃, and the temperature of natural rubber increased with the increase of the number of cycles. When the stretching speed was 20 mm/s, the average temperature difference was 0.18 ℃, and the temperature of natural rubber decreased with the increase of the number of cycles. When the stretching speed was 30 mm/s, the average temperature difference was 0.15 ℃, and the temperature of natural rubber increased with the increase of the number of cycles. When the drawing speed was 40 mm/s, the average temperature difference was 0.14 ℃, and the temperature of natural rubber was rising with the increase of the number of cycles.

As shown in Figure 3b, when the strain was 200% and the tensile speed was 10 mm/s, the average temperature difference was 1.03 ℃. When the drawing speed was 20 mm/s, the average temperature difference was 0.8 ℃. When the drawing speed was 30 mm/s, the average temperature difference was 0.61 ℃. When the drawing speed was 40 mm/s, the average temperature difference was 0.57 ℃. With the increase of tensile speed, the temperature difference of natural rubber in the harmonic cycle process decreased sharply. This showed that the elastothermal properties of natural rubber decreased with the increase of tensile rate when the strain was 200%.

As shown in Figure 3c, when the strain was 250%, the tensile length of natural rubber was 75 mm. The temperature difference of natural rubber decreased with the increase of the drawing rate. When the strain was 200% and the tensile speed was 10 mm/s, the average temperature difference was 1.36 ℃. When the drawing speed was 20 mm/s, the average temperature difference was 1.2 ℃. When the drawing speed was 30 mm/s, the average temperature difference was 1.1 ℃. When the drawing speed was 40 mm/s, the average temperature difference was 1 ℃. With the increase of tensile speed, the temperature difference of natural rubber in the harmonic cycle process showed a downward trend.

As shown in Figure 3d, when the strain was 300%, the tensile length of natural rubber was 100 mm. The temperature difference of natural rubber decreased with the increase of the drawing rate. When the strain was 200% and the tensile speed was 10 mm/s, the average temperature difference was 2.38 ℃. When the drawing speed was 20 mm/s, the average temperature difference was 2.1 ℃. When the drawing speed was 30 mm/s, the average temperature difference was 1.93 ℃. When the tensile speed was 40 mm/s, the average temperature difference was 1.7 ℃. With the increase of the tensile speed, the temperature difference of natural rubber in the harmonic cycle process showed a downward trend. This showed that the elastothermal properties of natural rubber decreased with the increase of tensile rate when the strain was 300%.

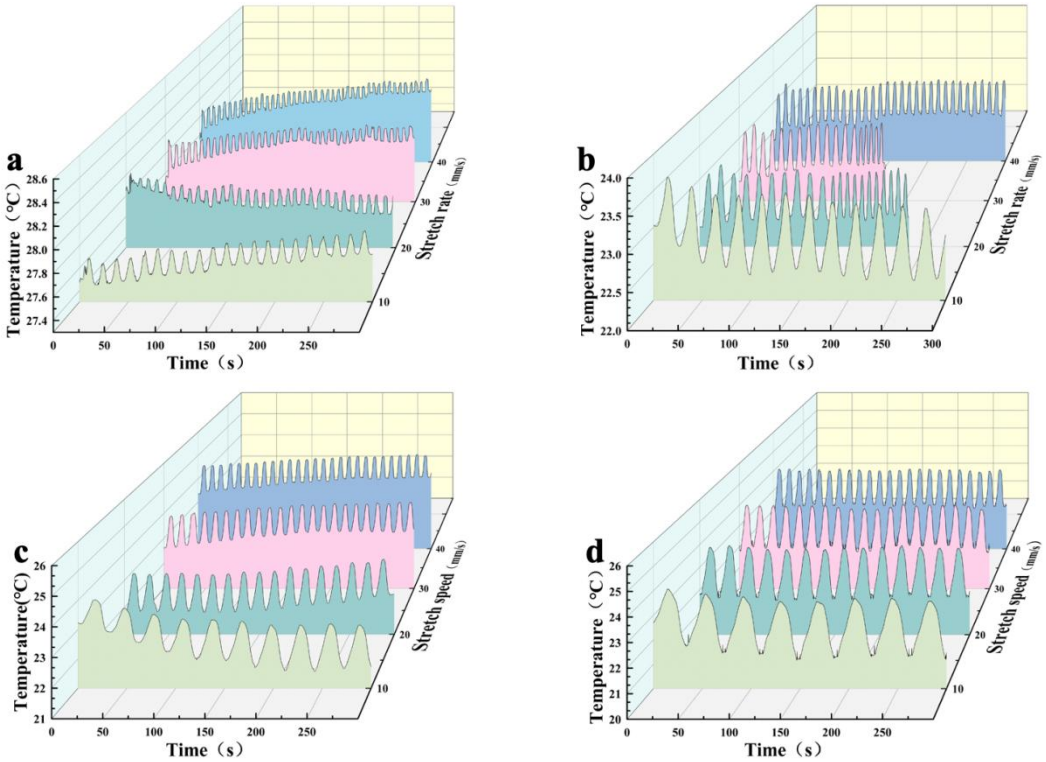

Figure 3: Temperature changes versus time under harmonic cycles for different tensile speeds under strain of 150% (a)、200% (b)、250% (c)、300% (d)

As shown in figure 4, the elastothermal effect remained almost unchanged under the force of periodic strain, and the larger the strain, the more obvious the effect of tensile rate on the elastothermal effect. The elastothermal effect decreased with the increase of the tensile rate. The rubber consists of polymer chains connected by cross-linking bonds. When the elastomer was stretched, the polymer chain was stretched, and the cross-bond changed during reverse compression and reached the initial state. At higher rates, the network of polymer chains and crosslinked bonds changed during stretching, but the recovery time during compression was too short to produce elastothermal effect.

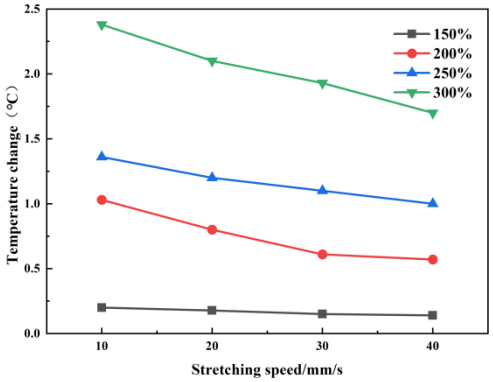

Figure 4: The variation of sample temperature difference with stretching speed during periodic strain action

The strain dependence of ECE at different tensile rates was shown in figure 5. It is known that the strain dependence of temperature for solid materials at low strain was linear (Buckley et al.,2010). But from a classical point of view, natural rubber was not a solid and could withstand huge reversible relative

deformation, so we observed the nonlinear strain dependence of elastothermal effect. The elastothermal effect decreased with the increase of the stretching rate under the simple harmonic cycle (figure 5). When the strain was 150%, the tensile rate had the least influence on the elastothermal effect; when the strain was 300%, the tensile rate had the greatest influence on the elastothermal effect. At the same time, figure 5 also showed that there was an inverse correlation between the deformation temperature change and the stretching rate, and the higher the stretching rate was, the smaller the temperature change was. Because the temperature change caused by conformational entropy is only a function of strain and has nothing to do with the tensile rate. The relationship is as follows:

$$\Delta T = -\frac{T}{cm}\int_0^l \left(\frac{\partial S}{\partial l}\right)_T dl \qquad \text{Eq. (1)}$$

where, $\left(\frac{\partial S}{\partial l}\right)_T$ is the change value of deformation entropy, $J/(K\cdot m)$; c is the specific heat capacity, $J/(kg\cdot K)$. The temperature rise caused by friction loss is a function of the tensile rate, which also proves that rubber has obvious inelastic behavior during deformation.

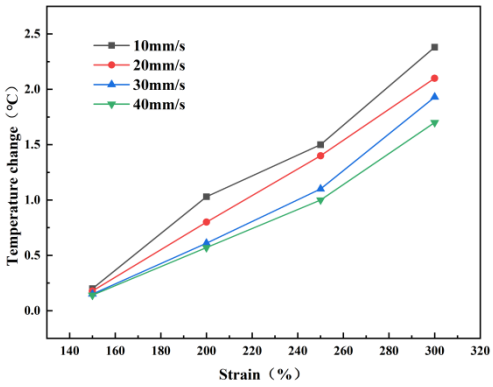

Figure 5: Elastocaloric effect in natural rubber samples

Through the change of temperature in different cycles, it could be noted that the temperature change of natural rubber had the following characteristics: (1) The endothermic and exthermic processes in the initial stretch-retraction process were irreversible. And there was a temperature accumulation at the end of the cycle. (2) After the initial stretch-retraction cycle, the subsequent cycle process showed a certain reversibility. (3) The temperature change in the initial cycle was higher than that in the subsequent cycle. Conformational change, crystallization enthalpy and frictional loss were the main causes of temperature change during deformation. Among them, conformational change, crystallization enthalpy and friction loss showed their own characteristics. The conformational entropy heat and crystallization enthalpy of cyclic deformation were completely reversible, while the friction loss of rubber in the process of stretch-retraction was irreversible. This would inevitably produce a temperature accumulation phenomenon, which was the main reason for the temperature accumulation of natural rubber at the end of the cycle. In addition to the conformational entropy heat generated in the stretch-retraction process, the heat generated by friction cannot be ignored. In some cases, the temperature changes during the subsequent stretch-retraction process were almost identical. This also proved that during the subsequent stretch-shrink cycle, the temperature change of natural rubber elastomer was mainly caused by conformational change. This rule was also consistent with the Mullins effect in the mechanical behavior of rubber (Buckley et al.,2010).

3.2 Entropy changes analysis of thermal effect of natural rubber bullets

Entropy is a state parameter closely related to the second law of thermodynamics, which provides a criterion for determining the direction of the actual process, whether it is reversible, and whether the process can be realized. Starting from Clausius method of Carnot cycle and Carnot theorem, entropy is analyzed and calculated.

The definition of entropy can be written as:

$$\Delta S = \int_1^2 dS = \int_1^2 \frac{\delta Q_{rev}}{T} \qquad \text{Eq. (2)}$$

Where: S represents entropy; δQ_{rev} represents the heat transfer of a reversible process; T represents the working medium temperature; 1 and 2 are the two states in a reversible process.

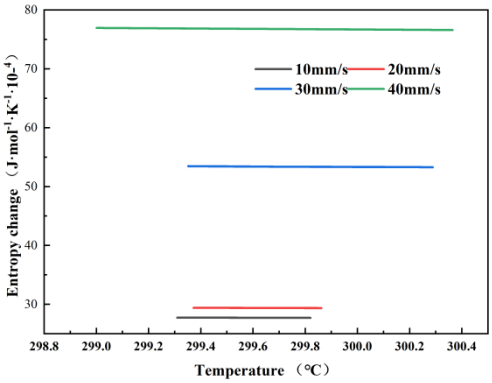

Figure 6: Changes in entropy change of tension contraction cycle with temperature under different environmental temperatures at a strain of 250%.

The stretch-shrink cycle of natural rubber is an irreversible process in practice. Because natural rubber in the stretching process, there will be a break or reorganization between the molecular chains, cannot be restored to the original state. However, the temperature of natural rubber with the elimination of Mullins effect tends to be stable during the stretch-shrink cycle, which can be approximately considered as a reversible process. All the natural rubbers used in this experiment have eliminated the Mullins effect. The heat transfer mode of natural rubber in the process of stretch-retraction is mainly heat convection, and thermal radiation is ignored. Newton's cooling formula is used to calculate the heat transfer of natural rubber during the stretch-retraction process:

$$Q_{rev} = cm\Delta T \qquad \text{Eq. (3)}$$

Where, c is the specific heat capacity of natural rubber, the specific heat capacity of natural rubber; m is the quality of natural rubber; ΔT is the temperature change of natural rubber during the cycle. Fig. 6 showed the change of entropy of the stretch-shrink cycle with ambient temperature at different stretching rates when the strain is 250%. The entropy change was linear with the ambient temperature, and the maximum entropy change was 0.0078J / (mol K) when the stretching rate was 40 mm/s.

4. CONCLUSIONS

The coupling between the externally applied stress and lattice of the material resulted the elastocaloric effect. Natural rubber could stretch to hundreds of percent, but once the external stress was removed, it quickly shrank back to its original shape. In this paper, DSC test, surface morphology characterization and elastocaloric effect of cylindrical natural rubber under simple harmonic cycle were carried out. We reached the following conclusions：

(1)Under the periodic strain force of simple harmonic cycle, the elastic-thermal effect remained almost constant. The larger the strain, the more obvious the effect of the tensile rate on the elastic-thermal effect. The elastocaloric effect decreasd with the increase of the tensile rate.

(2)Under the simple harmonic cycle, the temperature changes in different cycles of natural rubber elastomers were mainly caused by conformational changes.

(3)When the strain of cylindrical natural rubber was 250%, the entropy change had a linear relationship with the ambient temperature. When the drawing rate was 40 mm/s, the maximum entropy change was 0.0078J / (mol K).

REFERENCES

Bhatia B, Leroy A, Shen Y, et al. Passive directional sub-ambient daytime radiative cooling[J]. Nature communications, 2018, 9(1): 5001.

Boukai A I, Bunimovich Y, Tahir-Kheli J, et al. Silicon nanowires as efficient thermoelectric materials[J]. nature, 2008, 451(7175): 168-171.

Buckley C P, Prisacariu C, Martin C. Elasticity and inelasticity of thermoplastic polyurethane elastomers: Sensitivity to chemical and physical structure[J]. Polymer, 2010, 51(14): 3213-3224.

Cadwell S M, Merrill R A, Sloman C M, et al. Dynamic fatigue life of rubber[J]. Rubber Chemistry and Technology, 1940, 13(2): 304-315.

Candau N, Laghmach R, Chazeau L, et al. Strain-induced crystallization of natural rubber and cross-link densities heterogeneities[J]. Macromolecules, 2014, 47(16): 5815-5824.

Chenal J M, Chazeau L, Guy L, et al. Molecular weight between physical entanglements in natural rubber: A critical parameter during strain-induced crystallization[J]. Polymer, 2007, 48(4): 1042-1046.

Coulomb D, Dupont J L, Morlet V. The impact of the refrigeration sector on climate change-35. Informatory note on refrigeration technologies[J]. 2017.

Fähler S, Pecharsky V K. Caloric effects in ferroic materials[J]. MRS Bulletin, 2018, 43(4): 264-268.

Gent A N. Crystallization in natural rubber. IV. Temperature dependence[J]. Journal of Polymer Science, 1955, 18(89): 321-334.

Holzapfel G A, Simo J C. Entropy elasticity of isotropic rubber-like solids at finite strains[J]. Computer Methods in applied mechanics and engineering, 1996, 132(1-2): 17-44.

Hou H, Qian S, Takeuchi I. Materials, physics and systems for multicaloric cooling[J]. Nature Reviews Materials, 2022, 7(8): 633-652.

Kishore R A, Nozariasbmarz A, Poudel B, et al. Ultra-high performance wearable thermoelectric coolers with less materials[J]. Nature communications, 2019, 10(1): 1765.

Liu X, Wu Z, Guan T, et al. Giant room temperature electrocaloric effect in a layered hybrid perovskite ferroelectric: [(CH3) 2CHCH2NH3] 2PbCl4[J]. Nature Communications, 2021, 12(1): 5502.

Lloveras P, Tamarit J L. Advances and obstacles in pressure-driven solid-state cooling: A review of barocaloric materials[J]. MRS Energy & Sustainability, 2021, 8: 3-15.

Martinez J R S, Le Cam J B, Balandraud X, et al. Mechanisms of deformation in crystallizable natural rubber. Part 1: thermal characterization[J]. Polymer, 2013, 54(11): 2717-2726.

Miyamoto Y, Yamao H, Sekimoto K. Crystallization and melting of polyisoprene rubber under uniaxial deformation[J]. Macromolecules, 2003, 36(17): 6462-6471.

Moya X, Mathur N D. Caloric materials for cooling and heating[J]. Science, 2020, 370(6518): 797-803.

Mullen J G, Wasserstein R, Burmeister L. On optimizing an Archibald rubber-band heat engine[J]. American Journal of Physics, 1978, 46(11): 1107-1110.

Sebald G, Xie Z, Guyomar D. Fatigue effect of elastocaloric properties in natural rubber[J]. Philosophical Transactions of the Royal Society A: Mathematical, Physical and Engineering Sciences, 2016, 374(2074): 20150302.

Shi J, Han D, Li Z, et al. Electrocaloric cooling materials and devices for zero-global-warming-potential, high-efficiency refrigeration[J]. Joule, 2019, 3(5): 1200-1225.

Toki S, Che J, Rong L, et al. Entanglements and networks to strain-induced crystallization and stress–strain relations in natural rubber and synthetic polyisoprene at various temperatures[J]. Macromolecules, 2013, 46(13): 5238-5248.

Wang R, Fang S, Xiao Y, et al. Torsional refrigeration by twisted, coiled, and supercoiled fibers[J]. Science, 2019, 366(6462): 216-221.

Xie Z, Sebald G, Guyomar D. Elastocaloric effect dependence on pre-elongation in natural rubber[J]. Applied Physics Letters, 2015, 107(8).

DOI: 10.18462/iir.thermag.2024.0015

RESEARCH ON THE CORROSION AND MAGNETIC PROPERTIES OF LA(FE, SI)$_{13}$H$_Y$/10CO4CR-WC COMPOSITE PREPARED BY PLASMA SPRAYING

Juan Cheng[(a, b)], Cuilan Liu[(a)], Zhaojie Li[(a)], Jiaohong Huang[(a)], Caiyin You[(b)], Peiyu Jin[(a)], Yingde Zhang[(a)], Yaru Guo[(a)], Mohan Dai[(a)], Lei Gao[(a)], Pengyu Wang[(a)], Hao Pei[(a)]

[(a)] State Key Laboratory of Baiyunobo Rare Earth Resource Researches and Comprehensive Utilization, Baotou Research Institute of Rare earths, Baotou, 014030, China, jchengre@163.com

[(b)]School of Materials Science and Technology, Xi'an University of Technology, Xi'an, 710048, China, caiyinyou@xaut.edu.cn

ABSTRACT

La(Fe, Si)$_{13}$H$_y$ has been regarded as one of the most promising magnetocaloric materials near room temperature. However, the corrosion resistance is poor result from the large corrosion potential difference of the multiphase coexisted in La(Fe, Si)$_{13}$H$_y$. In this work, the 10Co4Cr-WC coated La(Fe, Si)$_{13}$H$_y$ composites were prepared by plasma spraying. The corrosion behavior, microstructure and magnetic properties were investigated. The corrosion resistance improves with the increase of 10Co4Cr-WC coating thickness. The corrosion potential (E_{corr}) is -21 mV and corrosion current (I_{corr}) is 4.01×10^{-7} A/cm^2 for the sample with the coating thickness of 90 μm. The Curie temperature T_C decrease from 290 K to 262 K with the coating thickness increase from 20 μm to 90 μm caused by partial dehydrogenation during the plasma spraying process. The maximum magnetic entropy change ΔS_m is 9.76-11.5 J/kg·K for the La(Fe, Si)$_{13}$H$_y$/10Co4Cr-WC composite under the magnetic field of 0-2 T. The composite shows good corrosion resistance and large magnetocaloric effect, which represents plasma spraying is a competitive way to improve the corrosion resistance.

Keywords: corrosion resistance, plasma spraying, magnetocaloric effect.

1. INTRODUCTION

In addition to high thermal conductivity and good mechanical properties, good corrosion resistance is also needed for the magnetocaloric materials should be immersed in the heat exchange fluid when they are applied in magnetic refrigerator. Water is often used as a heat exchange fluid in magnetic refrigeration systems due to its high thermal conductivity and specific heat. However, the corrosion resistance of La(Fe, Si)$_{13}$ alloy is poor in water for the coexistence of multi-phases in the alloy. Corrosion inhibitor was adopted, such as sodium benzoate inhibitor solution[1], Na_2WO_4 water solution and benzotriazole/sodium benzoate mixed solution[2]. However, these corrosion inhibitors cause pollution to the environment usually. It is an effective way to improve corrosion resistance by coating on the surface. La(Fe,Si)$_{13}$ hydride thin-plates coated with Ni-P by electroless plating technology shows a large magnetic entropy change of about 12 J/kg K (0-2 T). The charge transfer resistance was increased to 6-17 times and the corrosion current density was reduced to 5-7 times compared to the uncoated samples[3]. FeNi films were hot pressed with $LaFe_{11.6}Si_{1.4}$/Sn powder to prepare FeNi-$LaFe_{11.6}Si_{1.4}$/Sn-FeNi compound with a sandwich structure, and the corrosion resistance voltage of the compound was increased to -0.2455 V, which improved the corrosion resistance significantly[4]. The core-shell La(Fe, Si)$_{13}$/Cu composite powders with 1 wt.% Cu were fabricated through magnetron sputtering, accompanied with the spark plasma sintering. Polarisation curve tests showed a decrease in the corrosion resistance current for the La(Fe, Si)$_{13}$/Cu composite, providing better corrosion resistance[5].

The common ways to coat materials include chemical plating, electroplating, vacuum plating and spraying. The coating thickness of electroless plating is difficult to control. The waste water and gas generated in the electroplating process are easy to pollute the environment. The disadvantages for vacuum plating are expensive, low film-forming rate and long preparation time. Plasma spray coating technology has been widely used because of non-pollution, short processing time, optional choice of spray materials, and a wide

range of controllable spraying parameters. WC-Co Cemented Carbide has good thermal conductivity, high bending strength and corrosion resistance. The corrosion resistance of WC-Co can be significantly improved by addition of Cr elements, the bonding strength between the WC-Co particles and substrate can be strengthened, which is an ideal corrosion-resistant coating[6]. In this work, the corrosion behaviors and magnetocaloric effects of $La_{0.8}Ce_{0.2}Fe_{11.51}Mn_{0.19}Si_{1.3}H_y$ plates coated with 10Co4Cr-WC by plasma spray were investigated.

2. EXPERIMENTAL

The synthesis of $La_{0.8}Ce_{0.2}Fe_{11.51}Mn_{0.19}Si_{1.3}H_y$ plates (hot pressed for 30 min) has been described in our previous research[7]. The commercial WC-10Co4Cr spherical powder with the diameter of 15-45 μm prepared by atomisation method was selected for plasma spraying. $La_{0.8}Ce_{0.2}Fe_{11.51}Mn_{0.19}Si_{1.3}H_y$ plates with the size of Φ20×1 mm were plasma sprayed by WC-10Co4Cr powder at the voltage of 60 V, current of 600 A. The thickness of WC-10Co4Cr coating was adjusted by changing spraying numbers (15, 45 and 75 times). The crystal structure was analyzed by X-ray diffraction (XRD, Philips PW-1700). The magnetic properties were tested by VersaLab (HAC 900, Quantum Design). The galvanic corrosion were researched by electrochemical workstation (Autolab PGSTAT302N). Saturated calomel electrode and rectangle platinum electrode were used as reference and auxiliary electrode, respectively.

3. RESULTS AND DISCUSSION

$La_{0.8}Ce_{0.2}Fe_{11.51}Mn_{0.19}Si_{1.3}H_y$ (LFSH) samples sprayed with 15, 45 and 75 times of WC-10Co4Cr coatings were named W1, W2 and W3, respectively. Figure 1 is the XRD patterns of LFSH samples before and after plasma spraying. The crystal structure of LFSH before spraying is cubic $NaZn_{13}$-type $La(Fe, Si)_{13}$ phase. The crystal structure of samples remained unchanged after spraying, but the diffraction peaks of the 1:13 phases shifted slightly towards higher diffraction angles with the increase of spraying number, which indicated the decrease of lattice parameter. The dehydrogenation is more pronounced as the surface temperature of sample increases with the spraying numbers.

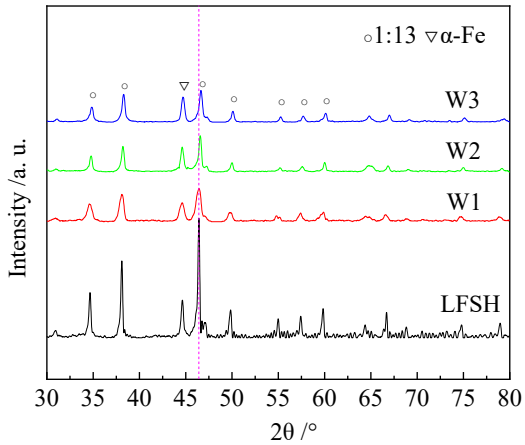

Figure 1: XRD patterns of LFSH samples before and after plasma spraying

Figure 2 shows EDS line scan results of coating cross-section for the samples sprayed with different times. The elements W, C, Co and Cr were analysed by EDS line scanning in the direction from the outside of the coating to the LFSH substrate. The thicknesses of WC-10Co4Cr coating increase significantly with the spraying numbers. The coating thicknesses of the samples sprayed different times were about 20 μm (W1), 50 μm (W2) and 90 μm (W3).

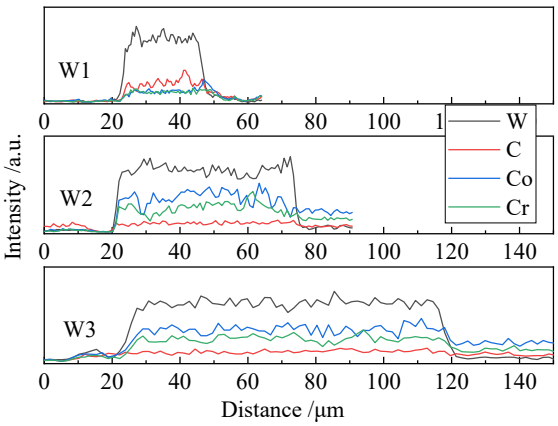

Figure 2: EDS line scan results of coating cross-section for W1, W2 and W3

Temperature dependences of magnetization curves (0.05 T) and the magnetic entropy change curves (0-2 T) for the samples before and after plasma spraying are shown in Figure 3. The Curie temperature (T_C) of the sprayed LFSH samples decrease significantly compared to initial LFSH sample result from partial dehydrogenation during the plasma spraying process. The surface temperature of LFSH substrate increased rapidly when the high temperature molten WC-10Co4Cr droplets came into contact with the surface of LFSH, which resulted in partial of interstitial H atoms escaping from the 1:13 phase. With the increase of spraying numbers, the surface temperature of LFSH substrate rise continuously result in dehydrogenation accelerating, leading to T_C of the samples decrease significantly. Figure 3(b) shows the magnetic entropy change curves of the samples calculated from the isothermal magnetization curves under a magnetic field of 0-2 T. The maximum magnetic entropy change $-\Delta S_m$ of the sprayed samples are all lower than that of the initial LFSH sample. The $-\Delta S_m$ decrease slightly with the increase of spraying number, which are 11.49 J/kg·K (W1), 11.5 J/kg·K (W2) and 9.76 J/kg·K (W3), respectively. Due to the partial dehydrogenation during the spraying process the hydrogen-poor $La(Fe, Si)_{13}H_y$ phase is formed, whose temperature corresponding to the maximum magnetic entropy change decrease, leading to the deterioration of $-\Delta S_m$. On the other hand, non-working media WC-10Co4Cr coating bring in the diluted effect to $La(Fe, Si)_{13}H_y$. With the increase of coating thickness, the $-\Delta S_m$ also decrease.

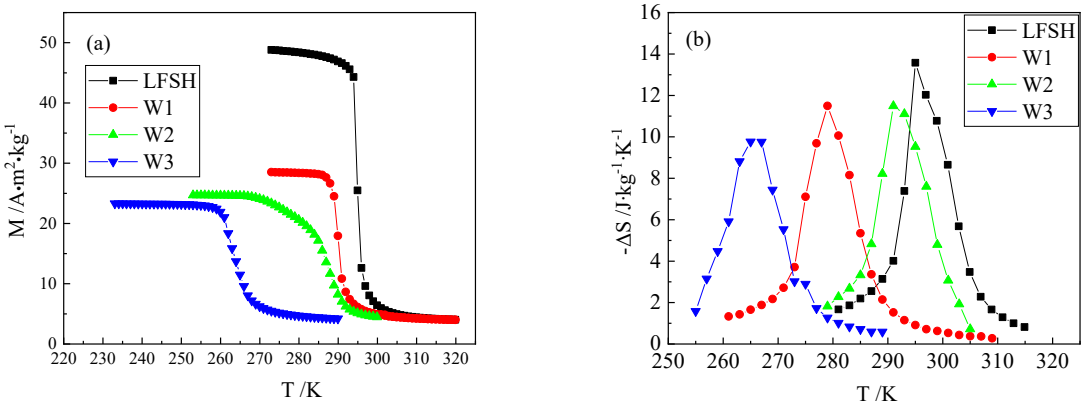

Figure 3: Temperature dependences of magnetization (0.05 T) (a) and the magnetic entropy change (0-2 T) (b) of the samples before and after plasma spraying WC-10Co4Cr

The potentiodynamic polarization curves of the samples before and after plasma spraying WC-10Co4Cr in deionized water are shown in Figure 4. The curves have similar cathodic branches, indicating similar cathodic reduction reactions for all the samples. The corrosion potential E_{corr} increase from -533 mV(LFSH) to -524 mV (W1), and the corrosion current density I_{corr} decrease from 1.19×10^{-5} A/cm^2 to 5.31×10^{-7} A/cm^2 (W1). With the increase of sprays numbers to 75 the E_{corr} of the sample increased to -21 mV and the I_{corr} further decreased to 4.01×10^{-7} A/cm^2, indicating the corrosion resistance of the sample is improved with the increase in the number of sprays.

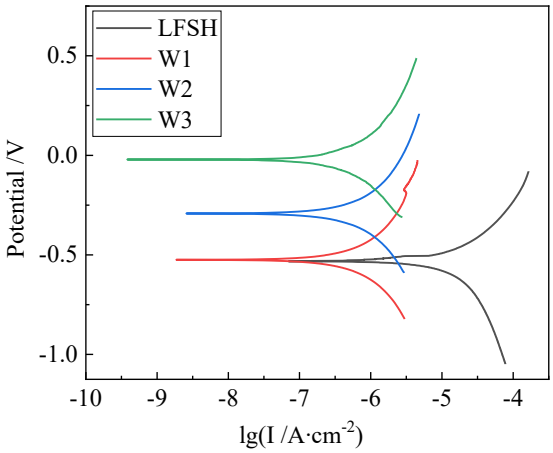

Figure 4: Potentiodynamic polarization curves of the samples before and after plasma spraying WC-10Co4Cr in deionized water

4. CONCLUSION

In conclusion, WC-10Co4Cr coating with high corrosion resistant has been successfully sprayed on the hot-pressed $La_{0.8}Ce_{0.2}Fe_{11.51}Mn_{0.19}Si_{1.3}H_y$ plates by employing a simple and widely applied plasma spraying technology. The Curie temperature and the maximum magnetic entropy change of the sprayed samples decrease compared to initial LFSH sample result from partial dehydrogenation during the plasma spraying process. The $-\Delta S_m$ is 11.49, 11.5 and 9.76 J/kg·K for the samples with the coating thickness of 20, 50 and 90 μm, respectively, which show large magnetocaloric effect. The E_{corr} increase to -21 mV and I_{corr} decrease to 4.01×10^{-7} A/cm^2 for the sprayed sample with the coating thickness of 90 μm, which showed a remarkable corrosion resistant effect.

[1]Zhang, E.Y., Chen, Y.G., Tang, Y.B., 2011, Investigation on corrosion and galvanic corrosion in $LaFe_{11.6}Si_{1.4}$ alloy, Materials Chemistry and Physics, 127: 1-6.

[2]Tang, Y.B., Chen, Y.G., Zhang, E.Y., 2012, The corrosion behavior of $LaFe_{11.6}Si_{1.4}$ alloy in inorganic and organic water solution, C.V. Muller, 5th International Conference on Magnetic Refrigeration at Room Temperature, Grenoble: International institute of refrigeration, 187-192.

[3]Sun, N.K., Zhao, X.G., Song, Y.W. et al., 2021, Electroless plating Ni-P coatings on $La(Fe, Si)_{13}$ hydride bulks for room-temperature magnetic-refrigeration application, Journal of Magnetism and Magnetic Materials, 525: 167685.

[4]Zhao, X., Fang, P., Tang, Y.B. et al. 2019, Corrosion behavior and magnetocaloric effect of FeNi (1J85) coated $LaFe_{11.6}Si_{1.4}$/Sn composites, Journal of Rare Earths, 37: 633-637.

[5]You, C.Y., Wang, S.P., Zhang, J. et al. 2016, Improvement of magnetic hysteresis loss, corrosion resistance and compressive strength through spark plasma sintering magnetocaloric $LaFe_{11.65}Si_{1.35}$/Cu core-shell powders, AIP Advances, 6: 055321.

[6]Xie, X.M., Zhang, S.H., Li, M.X. et al. 2012, High temperature wear resistance of HVOF sprayed Cr3C2-25NiCr coating, Transactions of Materials and Heat Treatment, 23 (S2): 129-133.

[7]Cheng, J., C.Y. You, B., Li, et al. 2023, Simultaneously realizing good volumetric entropy change and mechanical strength of $La_{0.8}Ce_{0.2}Fe_{11.51}Mn_{0.19}Si_{1.3}H_y$ plates, Journal of Rare Earths, 41:1568-1573.

DOI: 10.18462/iir.thermag.2024.0016

STUDY ON MATERIAL ARRANGEMENT OF MULTI-LAYERED ACTIVE MAGNETIC REGENERATOR WITH LANTHANUM COMPOUND MATERIALS

Yusuke HANAOKA[(a)], Daito MATSUBAYASHI[(a)], Tsuyoshi KAWANAMI[(b)], Guilherme Hitoshi KANEKO[(a)],Junya FUKUDA[(c)], Tetsuya KUME[(c)]

[(a)] Graduate School of Science and Technology, Meiji University

1-1-1 Higashimita, Tama-ku, Kawasaki 214-8571, Japan

[(b)]Department of Mechanical Engineering Informatics, Meiji University

1-1-1 Higashimita, Tama-ku, Kawasaki 214-8571, Japan

[(c)] Magnetic Materials Research Center, Shin-Etsu Chemical Co., Ltd.

1-5, Kitago 2-chome, Echizen-shi, Fukui 915-8515, Japan

Corresponding author: E-mail : kawanami@meiji.ac.jp

ABSTRACT

In recent years, there has been much development and research on solid refrigerant heat pumps as a refrigeration technology placing a low environmental impact. Among them, a magnetic heat pump technology is known to have a higher theoretical COP than conventional vapor compression heat pump using gas refrigerant, and to have advantages in energy conservation. The challenges for the practical application of the magnetic heat pump are the expansion of the temperature spangenerated and the improvement of the refrigeration capacity. To solve these problems, the most crucial element of the magnetic heat pump cycle, the Active Magnetic Regenerator (AMR), must be improved in performance. The AMR has a packed structure filled with a magnetocaloric material that generates temperature changes. The magnetocaloric material filled in the AMR has the characteristic of generating peaks in a narrow temperature range, and as the temperature span increases, the AMR tends to shift out of the applicable temperature range of the material. Therefore, a multi-layered AMR structure was designed in which magnetocaloric materials with different operating temperature ranges are arranged sequentially according to the temperature range. The multi-layered structure allows each material to exhibit its characteristics of entropy change in different temperature ranges, and it is believed that a large temperature span and refrigeration capacity can be obtained. In this study, La-Fe-Si magnetocaloric materials with different Curie points were first prepared. Moreover, layered AMRs were fabricated using these materials. The effects of the packing amount and number of each material on the temperature span generation as well as the refrigeration capacity of the AMRs were investigated for these multi-layered AMRs. As a result, it was found that the generated temperature span was the largest when the multi-layered structure was under the condition of 1-1-1 of the volume ratio. On the other hand, the refrigeration capacity was found to be the highest when the multi-layer structure was under the condition of 3-1-3 of the volume ratio.

Keywords: Magnetocaloric material, Magnetic heat pump, Multi-layered active magnetic regenerator, Utilization factor.

1. INTRODUCTION

Gas refrigerants are used in heat pumps in air conditioning and refrigeration fields. The problem with the use of gas refrigerants is that they are emitted into the atmosphere. Alternatives to CFCs have a significant greenhouse effect compared to carbon dioxide and may have a negative impact on the global environment. Therefore, magnetic heat pump systems have attracted attention as potential replacements for conventional heat pump systems that use gas refrigerants. Magnetic heat-pump systems utilize the magnetocaloric effect of magnetocaloric materials, in which heat is generated and absorbed owing to changes in the external magnetic field. A magnetic heat pump technology is known to have a higher theoretical COP than conventional vapor compression heat pumps using gas refrigerants, and to have advantages in energy conservation. However, magnetic heat pump systems have not been put to practical use because of their lower refrigeration capacity compared with that of conventional vapor compression heat pumps. For practical use, it is necessary to improve the performance of magnetic refrigeration and magnetic heat pump systems and further increase the

efficiency of the systems.In recent years, various research and developments of multi-layered magnetic heat pumps(Tušek et al., 2014,Navickaitéet al., 2018, Balli et al.,2012, Steven et al.,2013, Govindappa et al., 2018) have been conducted.In this study, a multi-layered AMR was used to expand the temperature difference and the refrigeration capacity, as a single-layered AMR using one type of material have low refrigeration capacity. When multiple materials are arranged side by side, they are called the multi-layered magnetic heat pump. A multi-layered material can receive heat from the temperature ranges of multiple materials. Therefore, its temperature difference and its refrigeration capacity are said to be expanded. In this study, the effects of the packing amount and number of each material on the temperature span generation as well as the refrigeration capacity of the AMRs were investigated for these multi-layered AMRs.

2. EXPERIMENTAL APPARATUS AND PROCEDURE

2.1 AMR Cycle

Figure 1 shows each process of the AMR. The side that becomes hot to the AMR cycle is the hot end and the side that becomes cool is the cold end. The AMR consists of theAMRbed filled with magnetocaloric material. There are gaps between materials, and both ends of the AMR bed are filled with a heat-exchange medium (distilled water). Then, the displacers move the heat exchange medium to the high- and low-temperature end sides. It also comprises permanent magnets that provide an external magnetic field. The AMR cycle has four processes, as shown in Figure 1. These four processes are sequentially repeated.

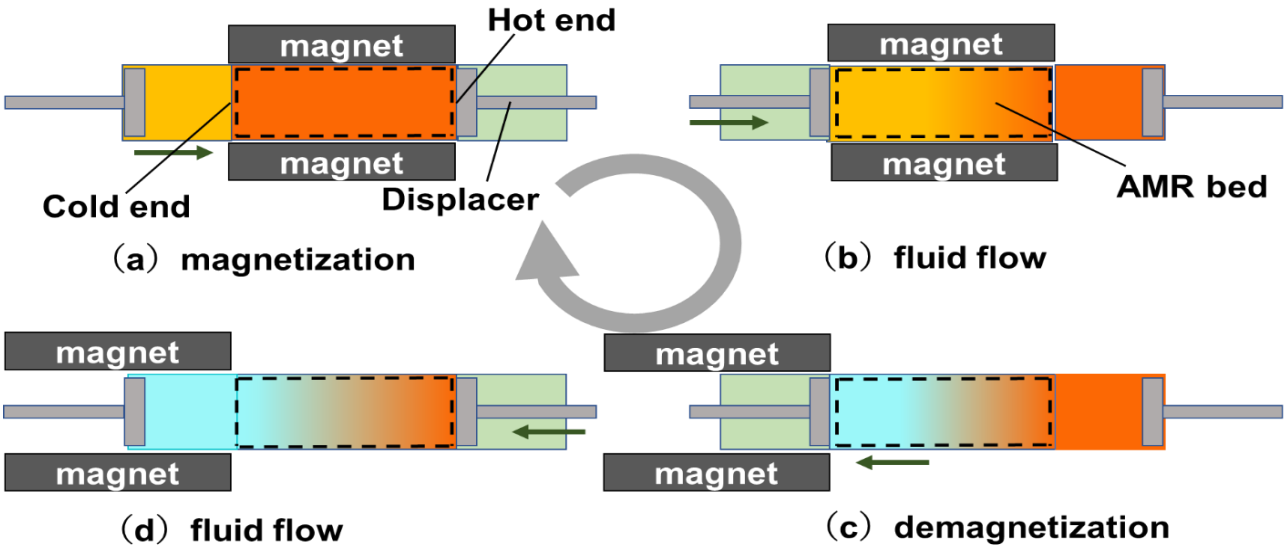

Figure1: AMR cycle

2.2 Comparison of singlelayer and multi-layered compositions of materials

Figure. 2shows the relationship between the amount of change in magnetic entropy and the temperature before the magnetic flux density change for the three Ln-based magnetic materials used in this study when the magnetic flux density change is applied from 0 T to 1 T.The Curie temperatures of the three magnetocaloric materials used in this study are 25°C, 29°C, and 33°C. The three magnetocaloric materials are defined as La25, La29, and La33 defined based on their compositional formula and Curie temperature,as determined in this study. From Figure. 2, A single layer is affected by the temperature range of one type of material, whereas a multi-layered material can be affected by multiple temperature ranges. Therefore, theoretically, a larger temperature difference and refrigeration capacity can be obtained with multi-layered AMR than with singlelayer AMR.

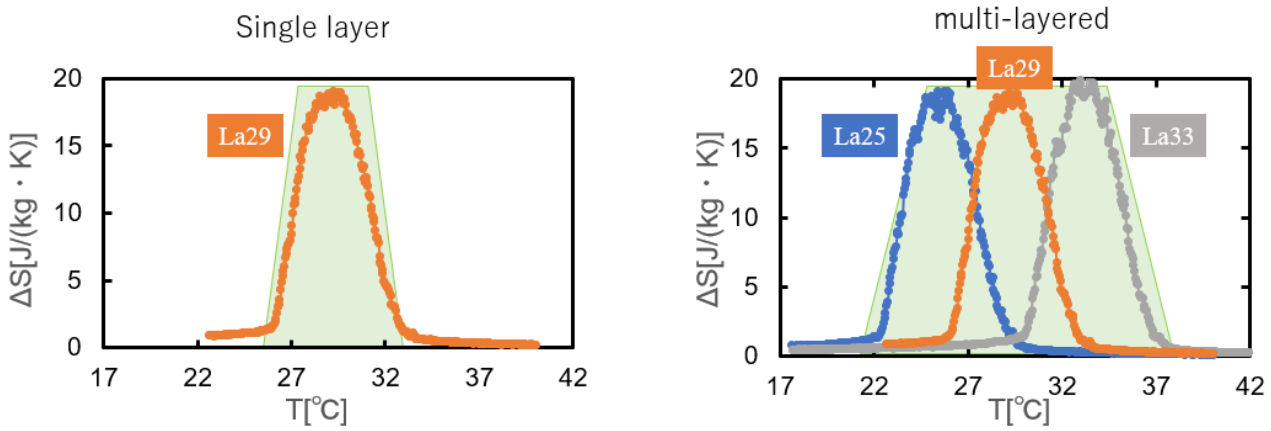

Figure2:Comparison of single layer and multi-layered compositions

3. EXPERIMENTAL APPARTUES AND PROCEDURE

3.1 Apparatus

Figure 3 shows the experimental apparatus used in this study. The experimental apparatus consists of a magnetic circuit for imparting a magnetic field to the magnetocaloric material, an AMRbed filled with magnetocaloric material, a displacer for driving the heat exchange medium in the AMR back and forth, a PC for controlling their

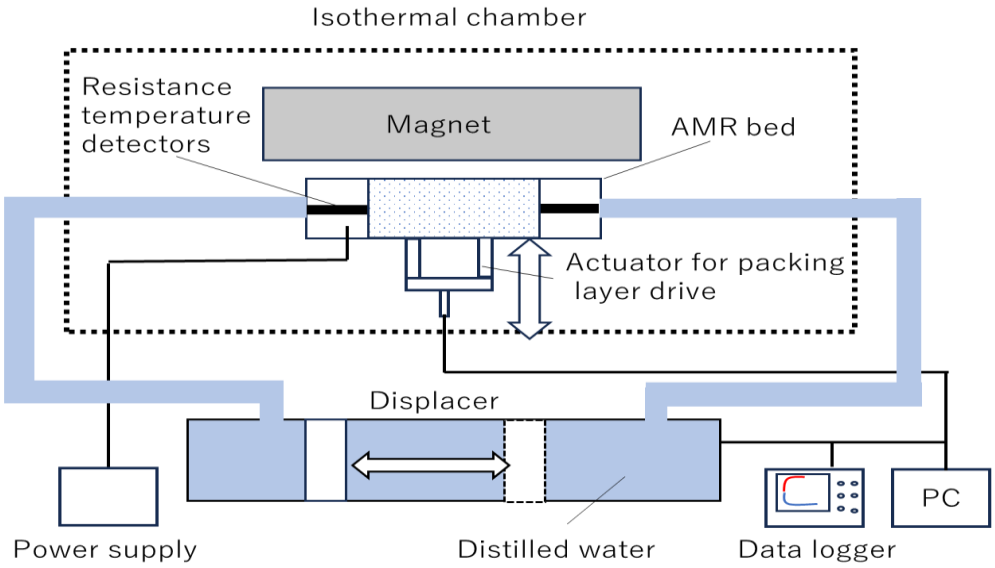

Figure 3: Schematic of experimental apparatus

movement, and a data logger for recording temperature data.The AMR test section and magnetic circuit are placed in an isothermal chamber to maintain a constant ambient temperature. The temperatures at the hot and cold ends of the AMR are measured by a resistance temperature detector. The magnetic circuit used in the experiment is a C-type magnetic circuit consisting of two NdFeB magnets, centered at a gap distance of 20 mm and generating a magnetic flux density of 0.8 T. The magnetic circuit is placed at the center of the test section.

Figure 4 shows the details of the AMR bed. The sample tube section consists of a double coaxial pipe for the thermal insulation. The outer diameter of each pipe was 18 mm for the outer pipe and 8 mm for the inner pipe,respectively. Pipes with an outside diameter of 18 mm are used to prevent external heat input. The magnetocaloric materials were packed in the inner pipe which has 6mm of inner diameter. The filling length of the material was 63 mm. The resistance temperature detectors were placed 2 mm from the magnetocaloric material. Subsequently, the temperature at this location was measured. The mesh was used to keep the magnetocaloric materials from mixing and to keep the magnetocaloric materials in place.The heater is

located at the cold end with a length of 20 mm. The heatergenerates heat using Joule heat with the power supply.

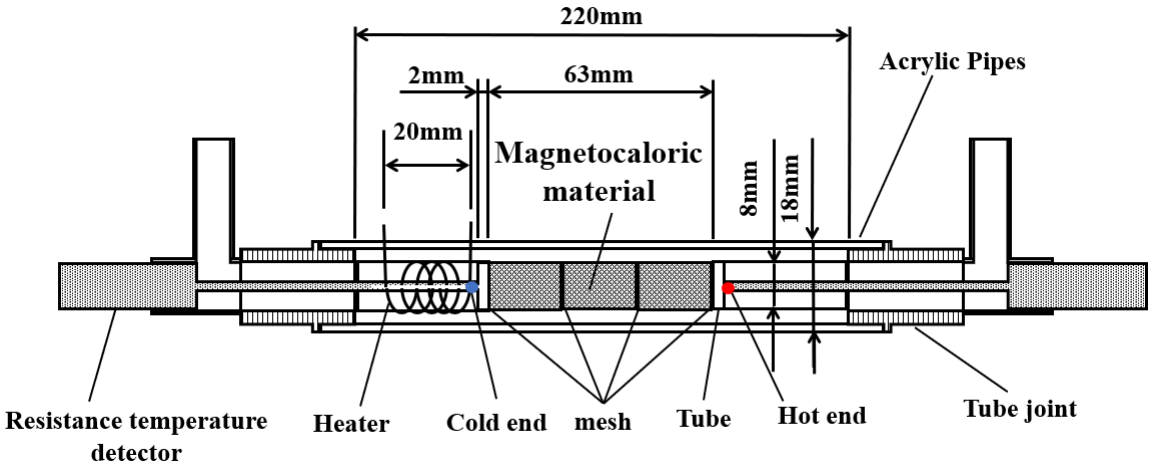

Figure4: Details of AMR bed

Figure 5 shows the material composition used in this study. In this study, the magnetocaloric material was packed and tested using the five patterns shown in Figure 4. Pattern (a) is filled with only La29;pattern (b) is filled with La25 at the cold end half and La29 at the hot end half; pattern(c) is filled with La25, La29, and La33 in 1 1 1 of the volume ration; pattern(d) is filled with La25, La29, La33 in 2 3 2 of the volume ration; pattern(e) is filled with La25, La29, La33 in 3 13 of the volume ration.

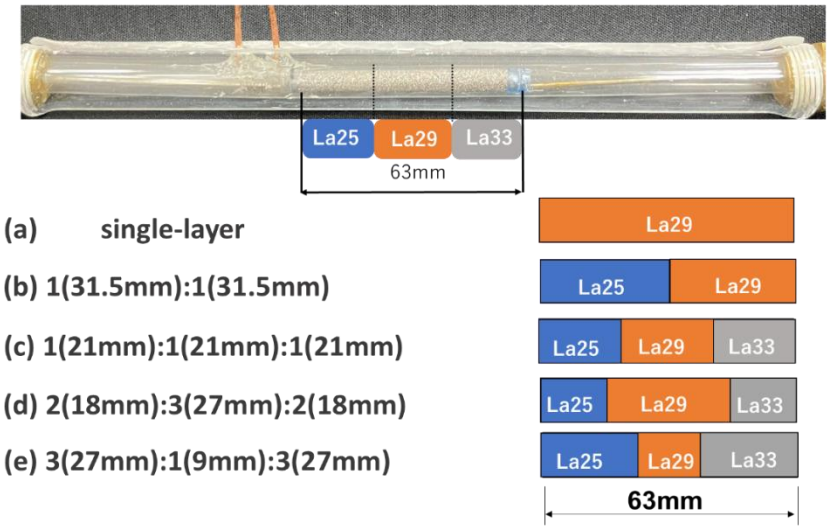

Figure 5: The material composition used in this study.

The masses of (a), (b), (c),(d) and (e) in each bed are presented in Table 1.

Table 1:The masses of (a), (b),(c),(d) and (e)

Material composition	La25 [g]	La29 [g]	La33 [g]	Total [g]
(a)	0	6.932	0	6.932
(b)	3.467	3.454	0	6.921
(c)	2.205	2.537	2.302	7.044
(d)	2.051	3.095	1.979	7.125
(e)	2.88	1.144	2.302	6.95

In the present study, the velocity of water flowing through the filling bed, U_w is 50×10^{-3}m/s.In the case of a single-layered structure, the initial temperatureT_i is set by the Curie temperature of the material used. In the case of a multi-layered structure with two types of materials, the initial temperature $T_i$is set by the average Curie temperature of each material. Furthermore, when three types of materials are used in the multi-layered structure, the initial temperature $T_i$is set at the Curie temperature of the middle of the three types of materials. The experimental and analytical parameters are listed in Table 2.

Table 2: Parameters

Parameters	Values
Fluid	Distilled water
Velocity of water flowing through the filling bed, U_w	50×10^{-3} m/s
Time required for magnetization or demagnetization	0.3 s
Time required for fluid flow process	0.1-0.2 s
Initial temperature,T_i	29℃(a), 27℃(b), 29℃(c),(d),(e)
Magnetic field	0.8Tesla (at the center of the gap)

3.2 Experimental conditions and properties

T_H [°C] and T_L [°C] indicate the temperatures at the hot and cold ends, respectively. The temperature measurement interval of the data logger was set as 1 s. The temperature difference ΔT between the hot and cold ends was defined as follows:

$$\Delta T = T_H - T_L \quad \text{Eq.(1)}$$

The maximum temperature differenceΔT_{max} is defined as the temperature difference when the temperature change becomes steady.

V [V] indicate voltage and I [A]indicate current.The refrigeration capacity Q is the multiplication of the current and voltage when a heat load is applied at the cold end.

$$Q = VI \quad \text{Eq.(2)}$$

The maximum refrigeration capacity$Q_{max}$is defined as the multiplication of the current and voltage when the temperature differenceΔT is zero.

3.3 Utilization Factor

The Utilization Factor (UF) is used as a measure of how much heat is transferred to the heat exchange medium by the magnetocaloric material. Equation 2 shows the utilization factor UF [-], which is defined as

$$UF = \frac{C_W V_W \rho_W}{m_s C_s} \quad \text{Eq.(3)}$$

where C_w [KJ/kgK], C_s [KJ/kgK], m_s [kg],ρ_w [kg/m³],and V_w[m³] are the specific heat of the heat exchange medium, the specific heat of the magnetocaloric material, the mass of the magnetocaloric material, the density of the heat exchange medium and the volume of the heat exchange medium delivered by the pump during one displaced process, respectively.

The physical properties of the magnetocaloric materials and heat exchange medium used in this study are shown in Table 3.

Table 3:physical properties of the magnetocaloric materials and distilled water(Matsubayashi, 2023)

Thermophysical properties	Values
ρ_w [kg /m^3]	998.233
C_w[kJ/ kgK]	4.182
C_s [kJ/ kg K]	0.46

4. EXPERIMENTAL RESULTS

Figure 6 shows the experimental results for *UF* 0.5, as shown (e) in Figure 5. The vertical axis shows the temperature *T*[°C], and the horizontal axis shows the measure time *t*[s]. The line extending upward was the hot end, whereas the line extending downward was the cold end. Figure 6 shows that the temperature difference increased as soon as the experiment began. When *Q* was zero, the temperatures at the high and low ends were 34.17°C and 24.65°C, respectively. The maximum temperature difference occurred 9.52K. When *ΔT* was zero, the voltage was 1.4V and the current was 0.39A. The maximum refrigeration capacity obtained was 0.546W.

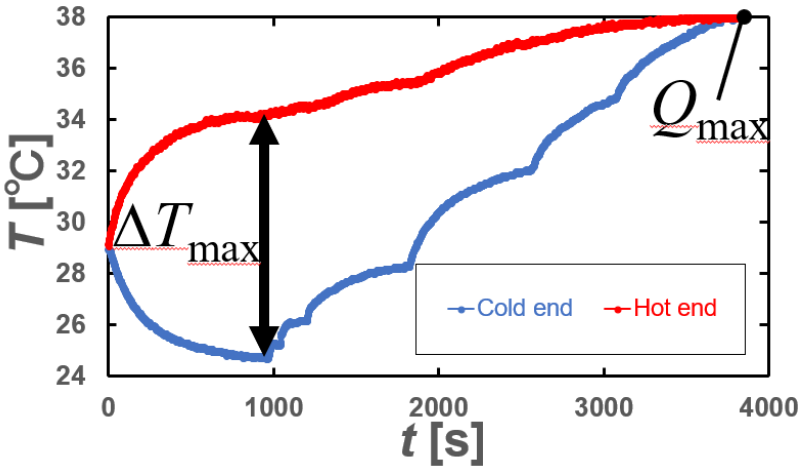

Figure 6: Experimental results for UF 0.5, asshown (d)in Figure 5

Figure 7 showsthe Relationship between the maximum temperature difference and each structure. The vertical axis shows the maximum temperature difference ΔT_{max}[K], while the horizontal axis shows *UF*. The maximum temperature difference, 11.25 K, was obtained at *UF* 0.5 of the multi-layered material in Figure 5 (c), which consists of three types of materials. If the volume ration of the materials is not equal, the characteristics of the smaller amount of material may not be fully utilizedlimitating the potential increase in temperature difference. The largest temperature differences are taken at *UF*0.5 and 0.75 for all material compositions in this study.Flow rates of UF 0.5 and 0.75 were optimal at the flow rates of this experiment. When *UF* is 1, the temperature difference is smaller for all material compositions, indicating that *UF* has a significant effect on temperature difference generation.

Figure 8 showsthe Relationship between the maximumrefrigeration capacity span and each structure. The vertical axis shows the maximum refrigeration capacity Q_{max}[K], and the horizontal axis shows *UF*.The maximum refrigeration capacity, 0.771W, was obtained at *UF* 1.0 of the multi-layered material in Figure 5 (e), which contained three types of materials (Figure 5 (e)). As the heat input on the cold end increases, the magnetocaloric material on the hot end, which was not contributing to the AMR function, starts to contribute to the AMR function, resulting in muti-layered with a large refrigeration capacity. Among the material compositions in this study, the multi-layered structure with a volume ration of 3-1-3 of the volume ration, which had a large proportion of magnetocaloric effect material on the high-temperature end, is considered to have the largest refrigeration capacity.

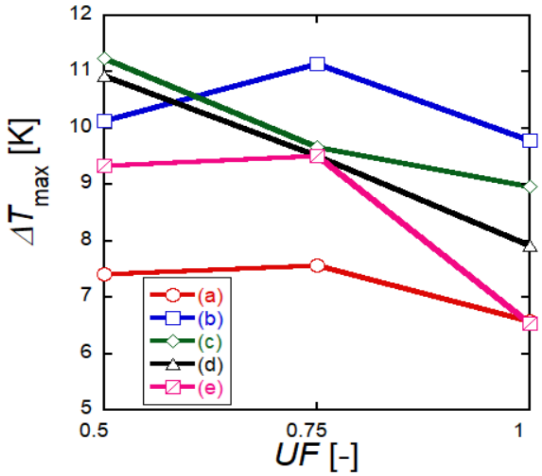

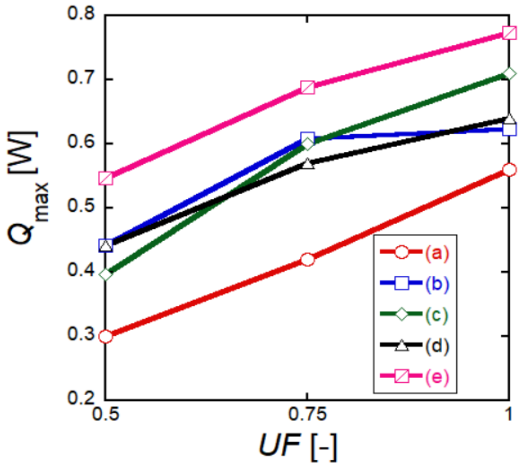

Figure 7:Relationship between maximum temperature difference and each structure
Figure 8:Relationship between maximum refrigeration capacity and each structure

CONCLUSION

A comparison between single- and multi-layered AMR configurations revealed that the multi-layered AMR exhibited the larger temperature difference. It was found that when the proportion of material in the muti-layered structure is equal, the temperature difference can be expanded. It was also found that a material composition with more material on the hot end in a muti-layered structure can obtain a large refrigeration capacity.

NOMENCLATURE

T_c	curie temperature(℃)	*UF*	the utilization factor
T_H	hot end temperature (℃)	*V*	volume (m)
T_L	cold end temperature (℃)	*C*	specific heat (J/kg K)
T	temperature (℃)	*W*	water
t	time (s)	*D*	difference
m	mass (kg)	*Ds*	entropy change (J/kg K)
U_w	velocity of water flowing (m/s)	T_i	initial temperature(℃)
s	solid	*DT*	temperature difference(K)
Q	refrigeration capacity(W)	DT_{max}	max temperature difference(K)
Q_{max}	max refrigeration capacity(W)	*r*	density (kg/m$^{3)}$
V	voltage(V)	*I*	current (A)

REFERENCES

Balli, M., Sari, O., Zamni, L., Mahmed, C., Forchelet, J., 2012. Implementation of $La(Fe,Co)_{13-x}Si_x$ materials in magnetic refrigerators: Practical aspects. Materials Science and Engineering B, vol.177: p.629-634.

Govindappa, P., Trevizoli, P. V.,Niknia, I., Christiaanse, T. V., Teyber, R., Rowe, A., 2018, Experimental characterization of multilayered active magnetic regenerators using first order materials: Multiple points of equilibrium. Journal of applied physics, vol.124: p134901-134901-7.

Matsubayashi, D.,Kawanami, T., Fukuda, J., Kume, T., 2023, Study on the Configuration of Multi-layered Active Magnetic Regenerator with Lanthanum Compound Materials for Magnetic Heat Pump Devices, Proceedings of the 26th IIR International Congress of Refrigeration – ICR2023, Paris, France, (2023-8).

Navickaité, K., Neves Bez, H., Lei, T., Barcza, A., Vieyra, H., Bahl, C.R.H., Engelbrecht, K.,2018, Experimental and numerical comparison of multi-layered $La(Fe,Si,Mn)_{13}H_y$ active magnetic regenerators. International Journal of refrigeration, vol.86: p322-330.

Steven,J, Steven,R, Jon,A,Andre,B, Jeremy,C, Lenny,K, John,L, Carl,Z,2013, The Performance of Rotary Magnetic Refrigerator with Layered Beds of LaFeSiH. Journal of the Japan AEM society, Vol.21 No.1: p.21-27.

Tušek,J., Kitanovski,A., Tomc,U., Favero,C., Poredoš,A.,2014,Experimental comparison of multi-layered La-Fe-Co-Si and single-layered Gd active magnetic regenerators for use in a room-temperature magnetic refrigerator. International journal of refrigeration, vol.37: p117-126.

DOI: 10.18462/iir.thermag.2024.0017

THE EFFECT OF THERMAL CYCLING ON MAGNETOCALORIC PROPERTIES OF $FE_{48}RH_{52}$ ALLOY

Alexander Kamantsev[a,b], Adler Gamzatov[b], Akhmed Aliev[b]

[a] Kotelnikov Institure of Radioengineering and Electronics of RAS
Moscow, 125009, Russia, kaman4@gmail.com
[b] Amirkhanov Institute of Physics of Dagestan Federal Research Centre of RAS,
Makhachkala, 367003, Russia, gamzatov_adler@mail.ru, lowtemp@mail.ru

ABSTRACT

The effect of thermal cycling on the magnetic and magnetocaloric properties of the $Fe_{48}Rh_{52}$ alloy was studied. It was found that the 2000 cycles of rapid heating/cooling through the temperatures of the metamagnetic isostructural phase transition (PT) leads to the decrease of the magnetocaloric effect (MCE) value and the shift of the MCE's peak down to low temperatures. The maximum MCE value is ΔT_{ad} = -7.4 K at T_{peak} = 308.7 K in the magnetic field of 1.8 T before thermal cycling, and both the absolute MCE value and the peak temperature decrease on 0.5 K after thermal cycling. The temperature dependence of ΔT_{ad} shows a deviation from a monotonic change. The special thermal procedure was performed after thermal cycling and then the magnetization and the MCE value were measured again. The repeated measurements showed that the original properties of the $Fe_{48}Rh_{52}$ alloy completely recovered.

Keywords: Magnetocaloric Effect, Iron Rhodium, Thermal Cycling

1. INTRODUCTION

The solid-state magnetic refrigeration (SMR) technology is considered an alternative to traditional vapor compression technology, which is now used in air conditioners and refrigerators both in industry and in everyday life. The great interest is the search for magnetic materials with the MCE and the study of their properties, so far as the SMR technology is based on their use as the working body. Currently, one of the main requirements for these materials is their ability to exhibit the giant MCE in the required temperature range (Gomez, 2013). Whereas the working body in the SMR device is experiences the cyclic changes of the external magnetic fields and the temperatures, when the material is periodically heated above and subsequent cooling below PT temperatures. It is necessary to study the magnetocaloric properties of the materials under frequent cyclic exposure of them (magnetic or thermal), because they can differ significantly from initials for a number of reasons. First of all, this applies to materials with the first-order PT, due to the processes that usually accompany these PTs, such as temperature and magnetic-field hysteresis, PT irreversibility, giant changes in lattice volume and, accordingly, giant magnetostriction values. For example, the MCE values in the first and subsequent cycles of applying a magnetic field in these materials will differ significantly (Basso, 2011, Liu, 2012, Skokov., 2013, Kamantsev, 2015, Zverev, 2016). Thus, one of the requirements for the materials of the working body is a large value of the MCE during magneto- and thermal cycling. The materials exhibiting magnetostructural PTs, known as the materials with giant MCE, are considered the most promising for developing the SMR technology (Pecharsky, 1997, Hu, 2001, Wada, 2001, Tegus, 2002, Fujita, 2003, Krenke, 2005, Sandeman, 2006, Trung, 2010).

In this work, the studies on the magnetic and magnetocaloric properties of samples of the binary alloy $Fe_{48}Rh_{52}$ were carried out. This alloy is characterized by the 1st order metamagnetic isostructural PT from the antiferromagnetic (AFM) to the ferromagnetic (FM) state with transition temperatures about 320 K (Zakharov, 1964, Shirane, 1964). This PT is accompanied by a sharp (about 1% in volume) expansion of the crystal lattice, which has the *bcc* structure of the CsCl type. The maximum known value of the inverse MCE in magnetic field change of 1.95 T: ΔT_{ad} = -13 K was observed in an alloy with a similar composition $Fe_{49}Rh_{51}$ (Nikitin, 1990).

2. MAIN SECTION

2.1 Experimental Methods

The $Fe_{48}Rh_{52}$ alloy sample was prepared by an induction melted technique under an argon atmosphere. The sample was homogeneously annealed at about 1300 K under vacuum over 72 h and then was quenched in water. Such properties of the $Fe_{48}Rh_{52}$ alloy as the latent heat of PT and the electrical resistance in high magnetic fields were studied by the authors in (Batdalov, 2020). The dependence of the magnetization of $Fe_{48}Rh_{52}$ alloy samples on temperature was measured on a vibrating magnetometer in the heating and cooling regimes with a temperature change rate of 1 K/min.

The procedure described in (Aliev, 2014, Aliev, 2016) was used to study the magnetocaloric properties of $Fe_{48}Rh_{52}$ samples in cyclic magnetic fields. The samples had a plate form with dimensions 2.5x2.5x0.4 mm^3. The magnetic field source with a magnitude up to 1.8 T and a field frequency of 0.2 Hz was used for magnetocaloric experiments. The temperature change rate of the sample was maintained at 1 K/min., The chromel-constantan microthermocouple with the measuring end thickness of ~3 μm was used for the adiabatic MCE measuring in cyclic magnetic fields. The signal from the microthermocouple, which passed through the transformer preamplifier SR554, was measured by the Lock-in amplifier SR830.

Previously, the authors have already established that the cycling in alternating magnetic fields leads to degradation of the magnetocaloric properties of the $Fe_{48}Rh_{52}$ alloy (Aliev, 2016), the Heusler $Ni_{49.3}Mn_{40.4}In_{10.3}$ alloy (Aliev, 2020), and the MnAs compound (Aliev, 2021). We need to make sure that we are dealing with a sample with initial magnetocaloric properties before studying the effect of thermal cycling on the MCE in the $Fe_{48}Rh_{52}$ alloy. It was found that, first a sample of the FeRh alloy must be heated above the Curie temperature ($T_C \approx 700$ K) in order to restore the original properties.

The thermal cycling of $Fe_{48}Rh_{52}$ alloy samples was carried out as follows. The sample was manually placed into hot water with a temperature of 360 K, and then placed into an ice/water mixture with the temperature of 273 K. A total of 2000 such cycles were carried out.

2.2 Results and Discussion

Fig. 1 shows the temperature dependences of the $Fe_{48}Rh_{52}$ sample magnetization in a magnetic field of 0.02 T in the initial state (circles) and after thermal cycling (triangles). The direct PT from FM to AFM phase at the cooling regime begins at the temperature A_S = 314.5 K and ends at A_F = 313 K, the reverse PT from AFM to FM phase at the heating regime begins at the temperature F_S = 320 K and ends at F_F = 321 K in the initial sample state. Thus, the metamagnetic isostructural PT in alloy occurs in a narrow 313–321 K temperature range with width Δ = 8 K. The magnetization of the FM phase does not change in absolute value after 2000 thermal cycling cycles (Fig. 1), but the direct PT begins at a temperature A_S = 312.5 K and ends at A_F = 310.5 K, the reverse PT begins at a temperature F_S = 319 K and ends at F_F = 320 K. Thus, the PT temperatures shift by 1.0–2.5 K towards the low temperatures and the PT region expands to Δ = 9.5 K. Also, the PT‘s curves after thermal cycling becomes smoother then initial.

Fig. 2 shows the results of MCE measurements at the heating regime in a magnetic field of 1.8 T with a frequency of 0.2 Hz. The MCE maximum ΔT_{ad} = -7.4 K is observed at the temperature of peak T_{peak} = 308.7 K in the sample of the initial state (green dots). The MCE maximum is ΔT_{ad} = - 6.9 K at the T_{peak} = 308.2 K in the sample after thermal cycling (black dots). In addition, the deviation from a monotonic change appears after thermal cycling on the temperature dependence of ΔT_{ad} (indicated by an arrow).

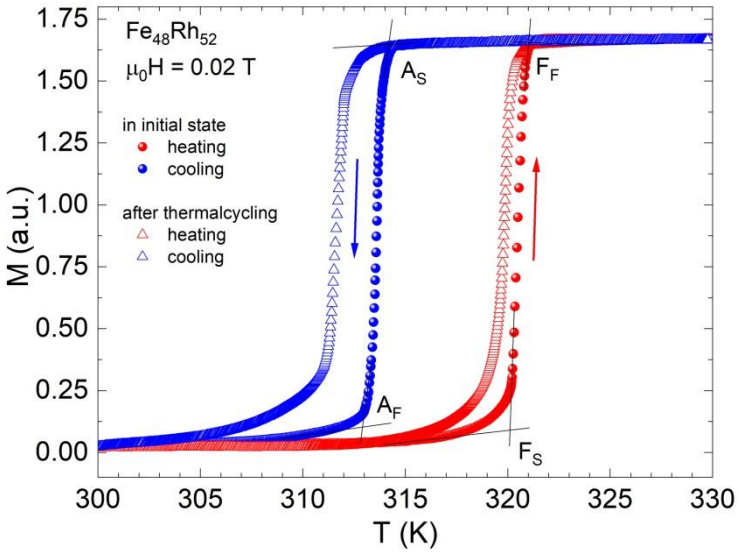

Fig. 1. Temperature dependences of the magnetization of $Fe_{48}Rh_{52}$ alloy in the magnetic field of 0.02 T at heating and cooling regimes (1 K/min): the filled circles – the sample in the initial state, the empty triangles – the sample after thermal cycling.

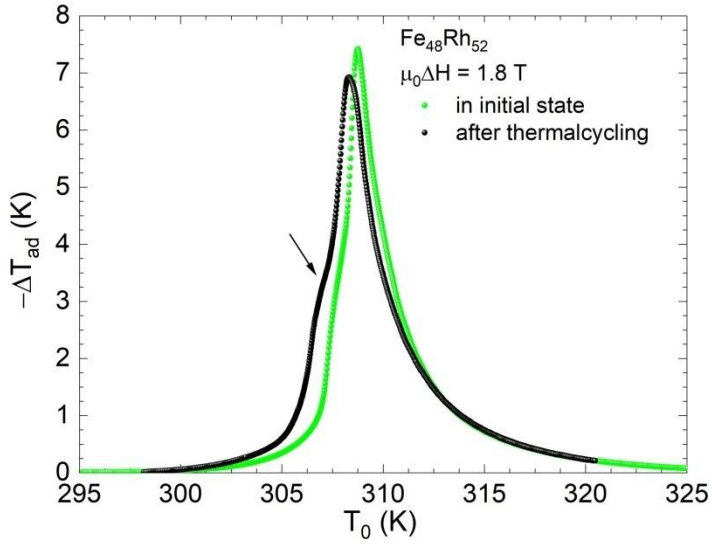

Fig. 2. Dependence of the MCE on the initial temperature of $Fe_{48}Rh_{52}$ alloy in the magnetic field of 1.8 T at the heating regime: the green dots – the sample in the initial state, the black dots – the sample after thermal cycling.

The obtained results can be explained as follows. The movement of FM and AFM domain boundaries is initiated due to sharp thermal expansion/compression (Taaev, 2022), which accompanies each heating/cooling cycle through the metamagnetic isostructural PT. This process may ultimately lead to a decrease in domain sizes, as well as an increase in the role of domain walls from cycle to cycle. It leads to a decrease in the number of magnetic spins in domains, a decrease in magnetostriction, and an increase in coercive force (Fig. 3). All these effects lead to a decrease in magnetization caused by the applied magnetic field.

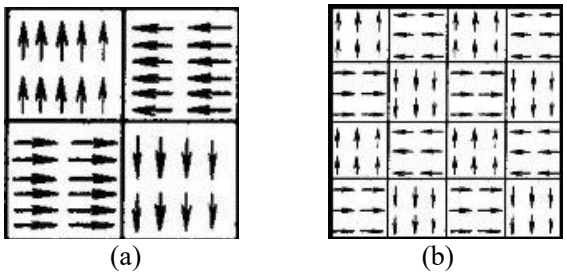

Fig. 3. Schematic representation of FM domains in $Fe_{48}Rh_{52}$ alloy in the absence of a magnetic field: (a) the sample in the initial state, (b) the sample after thermal cycling.

The process of the interaction between domain walls can lead to a change in the PT temperature of each domain, which will lead to an overall smoothing of the magnetization curves at the PT (Fig. 1). Therefore, the special thermal procedure is required to restore the original properties of the $Fe_{48}Rh_{52}$ alloy – the heating of the sample above the Curie temperature ($T_C \approx 700$ K) followed by its cooling to form a new pattern of the FM domains (Fig. 3). As mentioned above, we carried out exactly this procedure to restore the original properties of the material. This procedure was also carried out after thermal cycling, and the magnetization and the MCE were measured again. The obtained results show that the original properties of the $Fe_{48}Rh_{52}$ alloy were completely recovered.

3. CONCLUSIONS

The effect of thermal cycling on the magnetic and magnetocaloric properties of the $Fe_{48}Rh_{52}$ alloy was studied. It was found that 2000 thermal cycles of rapid heating/cooling through the temperatures of the metamagnetic isostructural PT leads to decrease of the MCE value and the shift of the MCE‘s peak towards to the low temperatures. The maximum MCE value is ΔT_{ad} = -7.4 K at T_{peak} = 308.7 K in the magnetic field of 1.8 T before thermal cycling, and both the absolute MCE value and the peak temperature decrease on 0.5 K after thermal cycling. In addition, the temperature dependence of ΔT_{ad} shows the deviation from a monotonic change.

The obtained results can be explained as follows. The movement of FM and AFM domain walls is initiated by the sharp thermal expansion/compression at passing through the PT. It leads to decrease of the magnetic domains sizes and to increase of the role of their walls from each cycle, which leads to decrease of the saturation magnetization of the alloy. The interaction between domain walls leads to a change of the PT temperature of each domain, which leads to a general smoothing of the magnetization curves at the PT.

The special thermal procedure – the heating above T_C – is required for the recover of the original properties of the alloy. This procedure was performed after thermal cycling, and the magnetization and the MCE were measured again. The original properties of the $Fe_{48}Rh_{52}$ alloy were completely recovered.

The significant MCE values are observed in the $Fe_{48}Rh_{52}$ alloy. However, the effect of the MCE degradation during thermal cycling that we discovered in this study, as well as the previously discovered effect of the MCE degradation during cycling in alternating magnetic fields (Aliev, 2016), indicate that such materials are not promising for use in the SMR technology. The establishing of the nature of the MCE degradation mechanism allows us to hope that it is possible to synthesize new materials with giant MCE, that are not subject to the phenomenon of the MCE degradation.

ACKNOWLEDGEMENTS

This work was supported by Russian Science Foundation, project № 24-43-00156.
https://rscf.ru/project/24-43-00156/

REFERENCES

Aliev, A.M., 2014. Direct magnetocaloric effect measurement technique in alternating magnetic fields. arXiv preprint arXiv:1409.6898.

Aliev, A.M., Batdalov, A.B., Khanov, L.N., Koledov, V.V., Shavrov, V.G., Tereshina, I.S., Taskaev, S.V., 2016. Magnetocaloric effect in some magnetic materials in alternating magnetic fields up to 22 Hz. J. Alloy. Comp. 676, 601-605.

Aliev, A.M., Batdalov, A.B., Khanov, L.N., Kamantsev, A.P., Koledov, V.V., Mashirov, A.V., Shavrov, V.G., Grechishkin, R.M., Kaul', A.R., Sampath, V., 2016. Reversible magnetocaloric effect in materials with first order phase transitions in cyclic magnetic fields: $Fe_{48}Rh_{52}$ and $Sm_{0.6}Sr_{0.4}MnO_3$. Appl. Phys. Lett. 109(20).

Aliev, A.M., Batdalov, A.B., Khanov, L.N., Mashirov, A.V., Dil‘mieva, E.T., Koledov, V.V., Shavrov, V.G., 2020. Degradation of the magnetocaloric effect in $Ni_{49.3}Mn_{40.4}In_{10.3}$ in a cyclic magnetic field. Phys. Solid State. 62, 837-840.

Aliev, A.M., Khanov, L.N., Gamzatov, A.G., Batdalov, A.B., Kurbanova, D.R., Yanushkevich, K.I., Govor, G.A., 2021. Giant magnetocaloric effect in $MnAs_{1-x}P_x$ in a cyclic magnetic field: Lattice and magnetic contributions and degradation of the effect. Appl. Phys. Lett., 118(7).

Basso, V., 2011. The magnetocaloric effect at the first-order magneto-elastic phase transition. J. Phys.: Cond. Mat. 23, 226004.

Batdalov, A.B., Aliev, A.M., Khanov, L.N., Kamantsev, A.P., Mashirov, A.V., Koledov, V.V., Shavrov, V.G., 2020. Specific heat, electrical resistivity, and magnetocaloric study of phase transition in $Fe_{48}Rh_{52}$ alloy. J. Appl. Phys. 128(1), 013902.

Fujita, A., Fujieda, S., Hasegawa, Y., Fukamichi, K., 2003. Itinerant-electron metamagnetic transition and large magnetocaloric effects in $La(Fe_xSi_{1-x})_{13}$ compounds and their hydrides. Phys. Rev. B. 67(10), 104416.

Gómez, J.R., Garcia, R.F., Catoira, A.D.M., Gómez, M.R., 2013. Magnetocaloric effect: A review of the thermodynamic cycles in magnetic refrigeration. Renew. Sust. Energ. Rev. 17, 74-82.

Hu, F.X., Shen, B.G., Sun, J.R., Wu, G.H. 2001. Large magnetic entropy change in a Heusler alloy $Ni_{52.6}Mn_{23.1}Ga_{24.3}$ single crystal. Phys. Rev. B. 64(13), 132412.

Kamantsev, A.P., Koledov, V.V., Mashirov, A.V., Dilmieva, E.T., Shavrov, V.G., Cwik, J., Los, A.S, Nizhankovskii, V.I., Rogacki, K., Tereshina, I.S., Koshkid'ko, Yu.S., Lyange, M.V., Khovaylo, V.V., Ari-Gur, P., 2015. Magnetocaloric and thermomagnetic properties of $Ni_{2.18}Mn_{0.82}Ga$ Heusler alloy in high magnetic fields up to 140 kOe. J. Appl. Phys., 117, 163903.

Krenke, T., Duman, E., Acet, M., Wassermann, E. F., Moya, X., Mañosa, L., Planes, A., 2005. Inverse magnetocaloric effect in ferromagnetic Ni–Mn–Sn alloys. Nat. Mater. 4(6), 450-454.

Liu, J., Gottschall, T., Skokov, K. P., Moore, J. D., Gutfleisch, O., 2012. Giant magnetocaloric effect driven by structural transitions. Nat. Mater. 11(7), 620-626.

Nikitin, S.A., Myalikgulyev, G., Tishin, A.M., Annaorazov, M.P., Asatryan, K.A., Tyurin, A.L., 1990. The magnetocaloric effect in $Fe_{49}Rh_{51}$ compound. Phys. Lett. A. 148(6-7), 363-366.

Pecharsky, V.K., Gschneidner Jr., K.A., 1997. Giant magnetocaloric effect in $Gd_5(Si_2Ge_2)$. Phys. Rev. Lett. 78(23), 4494-4497.

Pecharsky, V. K., Gschneidner Jr, K.A. 1997. Tunable magnetic regenerator alloys with a giant magnetocaloric effect for magnetic refrigeration from 20 to 290 K. Appl. Phys. Lett. 70(24), 3299-3301.

Sandeman, K.G., Daou, R., Özcan, S., Durrell, J.H., Mathur, N.D., Fray, D.J., 2006. Negative magnetocaloric effect from highly sensitive metamagnetism in $CoMnSi_{1-x}Ge_x$. Phys. Rev. B. 74(22), 224436.

Shirane, G., Nathans, R., Chen, C.W., 1964. Magnetic moments and unpaired spin densities in the Fe-Rh alloys. Phys. Rev. 134(6A), A1547.

Skokov, K.P., Müller, K.H., Moore, J.D., Liu, J., Karpenkov, A.Y., Krautz, M., Gutfleisch, O., 2013. Influence of thermal hysteresis and field cycling on the magnetocaloric effect in $LaFe_{11.6}Si_{1.4}$. J. Alloy. Comp. 552, 310-317.

Taaev, T.A., Amirov, A.A., Aliev, A.M., Chirkova, A., Soldatov, I.V., Schäfer, R., 2022. Kerr microscopy study of magnetic phase transition in $Fe_{49}Rh_{51}$. Phys. Met. Metallogr. 123(4), 402-406.

Tegus, O., Brück, E., Buschow, K.H.J., De Boer, F.R., 2002. Transition-metal-based magnetic refrigerants for room-temperature applications. Nature. 415(6868), 150-152.

Trung, N.T., Zhang, L., Caron, L., Buschow, K.H.J., Brück, E., 2010. Giant magnetocaloric effects by tailoring the phase transitions. Appl. Phys. Lett. 96(17), 172504.

Wada, H., Tanabe, Y. 2001. Giant magnetocaloric effect of $MnAs_{1-x}Sb_x$. Appl. Phys. Lett. 79(20), 3302-3304.

Zakharov, A.I., Kadomtseva, A.M., Levitin, R.Z., Ponyatovskii, E.G., 1964. Magnetic and magnetoelastic properties of a metamagnetic iron-rhodium alloy. Sov. Phys. JETP 19, 1348-1353.

Zverev, V.I., Saletsky, A.M., Gimaev, R.R., Tishin, A.M., Miyanaga, T., Staunton, J.B., 2016. Influence of structural defects on the magnetocaloric effect in the vicinity of the first order magnetic transition in $Fe_{50.4}Rh_{49.6}$. Appl. Phys. Lett. 108, 192405.

DOI: 10.18462/iir.thermag.2024.0018

OPTIMIZATION RESEARCH OF SALT PILL IN AN ADIABATIC DEMAGNETIZATION REFRIGERATOR

Wenshuai Zheng[(a)], Jun Shen[(a,b,c,d,*)], Ya'nan Zhao[(a,*)], Zhuo Chen[(a)], Zhenxing Li[(a)]

[(a)] Beijing Institute of Technology
Beijing 100081, China, 3120225271@bit.edu.cn
[(b)] Technical Institute of Physics and Chemistry, Chinese Academy of Sciences
Beijing 100190, China
[(c)] University of Chinese Academy of Sciences
Beijing 100049, China
[(d)] Ganjiang Innovation Academy, Chinese Academy of Sciences
Jiangxi 341000, China

ABSTRACT

As an important refrigeration technology in the temperature range of sub-Kelvin, the adiabatic demagnetization refrigeration is widely used to cool bolometric infrared detectors and cryogenic X-ray detectors for low background astronomy because of its high efficiency, gravity independence, and high reliability. The adiabatic demagnetization refrigerator (ADR) mainly consists of the salt pill, superconducting magnet and thermal switch. In the salt pill, the magnetocaloric materials used are mainly hydrated salts, such as $CrK(SO_4)_2 \cdot 12H_2O$, $CrCs(SO_4)_2 \cdot 12H_2O$ and $Fe(SO_4)_2NH_4 \cdot 12H_2O$. In the salt pill, due to the low thermal conductivity of the hydrated salt in the sub-Kelvin temperature range, an efficient heat-conducting structure, called thermal bus, is necessary to transport the heat generated by the magnetocaloric materials. However, an increase in the volume of thermal buses will lead to a decrease in the theoretical entropy capacity of the magnetocaloric materials, so the volume ratio of magnetocaloric materials and thermal buses in the salt pill needs to be optimized. In this paper, a numerical model of salt pill was established to optimize the cooling performance of the ADR. The performance parameters including the volume ratio of magnetocaloric materials and the diameter of thermal buses were optimized. The results show that there were optimal volume ratios and copper wire diameters in the salt pill.

Keywords: Magnetocaloric material, Adiabatic demagnetization refrigerator, Salt pill, Cooling performance, Optimization.

1. INTRODUCTION

Adiabatic demagnetization refrigeration is a significant refrigeration method to achieve ultra-low temperatures*(Li et al., (2023))*. Due to its irreplaceable advantages, such as no moving parts, independence from gravity, and no use of the scarce refrigerant ^{3}He, it is frequently employed in space applications, particularly for cooling in tasks like infrared detection*(Hagmann and Richards, (1994); Serlemitsos, SanSebastian, Kunes and Behr, (1999); P. J. Shirron, (2014); P. J. Shirron et al., (2016))*. The fundamental principle of adiabatic demagnetization refrigeration relies on the magnetocaloric effect (MCE), wherein magnetic materials release heat during the magnetization process and absorb heat during the demagnetization process*(Zheng et al., (2023))*. In adiabatic demagnetization refrigerator (ADR), the commonly used refrigeration cycle is the reverse Carnot cycle, as illustrated in Figure 1. It comprises four main processes*(Peter J. Shirron and McCammon, (2014))*: I) Adiabatic magnetization A→B: The magnetic field increases from 0, causing the temperature of the magnetic material to gradually rise to the heat sink temperature T_H. II) Isothermal magnetization B→C: The magnetic field continues to increase, the heat generated by the magnetic material is entirely rejected to the heat sink, and the magnetocaloric material maintains the temperature T_H. III) Adiabatic demagnetization C→D: The magnetic field gradually decreases, leading to a gradual decrease in the temperature of the magnetic material to the cooling temperature T_C. IV) Isothermal demagnetization D→A: The magnetic field continues to decrease, the cold energy generated by the magnetic material is entirely used for refrigeration, and the magnetocaloric material maintains at T_C.

From the Figure 1, it can also be observed that the area enclosed by process IV and the *s*-axis represents the theoretical refrigeration capacity Q_C of the magnetic material at the cooling temperature.

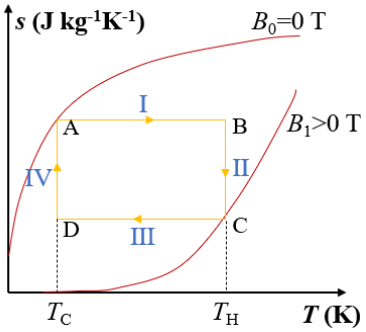

Figure 1: Refrigeration cycle for ADR.

The ADR mainly consists of the salt pill, superconducting magnet and heat switch, as shown in Figure 2. In the salt pill, in addition to magnetocaloric materials, mainly hydrated salts (such as $CrK(SO_4)_2 \cdot 12H_2O$ (CPA)*(P. Shirron, (2014))*, $CrCs(SO_4)_2 \cdot 12H2O$ (CCA)*(Hagmann and Richards, (1995))*, and $Fe(SO_4)_2NH_4 \cdot 12H_2O$ (FAA))*(P. Shirron et al., (2001))* or rare metal oxides*(P. J. Shirron, (2014); P. J. Shirron et al., (2016))*, an efficient heat-conducting structure, called thermal bus*(Peter J. Shirron and McCammon, (2014))*, is usually used to transport the heat generated by the magnetocaloric materials. This is due to the low thermal conductivity of hydrated salts in the sub-Kelvin temperature range*(Peter J. Shirron and McCammon, (2014))*. Theoretically, the larger the volume proportion of the thermal bus made of copper/gold wires in the salt pill, the better the heat transfer in the salt pill. However, with the volume of the thermal bus increases, although the heat transfer of the salt pill is enhanced, the mass proportion of the magnetocaloric material is reduced, which may lead to a reduction in the theoretical cooling capacity of the ADR. So, the volume ratio of magnetocaloric materials and thermal bus in the salt pill needs to be optimized. Given the complexity and time-consuming nature of experimental design and testing in ADR, relying solely on experimental optimization seems impractical. Therefore, the development of a comprehensive and reliable simulation model for the salt pill becomes essential. In 2014, Peter et al. investigated the effects of parasitic heat, eddy current heat, and conductive heat leakage on the cooling performance of ADR through numerical models *(Peter J. Shirron and McCammon, (2014))*. Subsequently, after the optimization of the salt pill, the cooling performance of the ADR system was also tested*(P. Shirron, (2014))*. In 2015, to achieve rapid thermal response in salt pills, Bartlett et al simulated the eddy current heat in the thermal bus and external metal end caps*(Bartlett, Hardy and Hepburn, (2015))*. In 2022, a numerical model was also established by Vivek to study the impact of various parameters, including heat switch closing rate, area-to-length ratio of the heat switch, magnetization rate, and area-to-length ratio of the support structure, on the cooling performance of ADR*(Kumar Singh, Balaji C and Vora, (2022))*. Nevertheless, the majority of existing reports concentrates on the optimization of individual components and the overall performance of the ADR, with limited research on the magnetothermal material and thermal bus within the salt pill. Consequently, it is necessary to establish a numerical model of the salt pill to study the impact of the magnetocaloric material and thermal bus on the cooling performance of ADR.

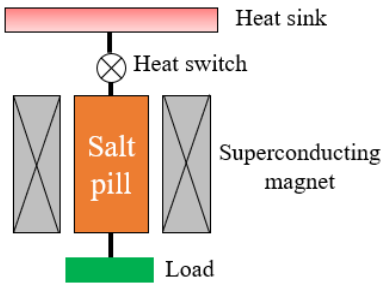

Figure 2: Schematic diagram of ADR

In this paper, based on COMSOL Multiphysics, a numerical model of salt pill has been established to optimize the cooling performance of an ADR operating in the range of 1 K to 0.2 K. With the holding-time of ADR at 0.2 K as the evaluation parameter, the effects of the volume ratio and the wire diameter of thermal buses were investigated. Additionally, in this salt pill model, the volume ratio of and the number of thermal buses were also optimized.

2. SIMULATION MODEL

2.1 Geometry of the salt pill

An ADR operating in the temperature range of 1 K to 0.2 K is planned to be built. As the core of the ADR, the salt pill will directly affect the cooling performance of system. As shown in Figure 3, the salt pill is mainly composed of the magnetocaloric material (CPA), thermal buses, two copper rods, and a cylindrical shell (not shown in Figure 3) used for packaging. Thermal buses are composed of many copper wires with the same diameter, which are evenly distributed inside the magnetocaloric material to transport the heat/cold generated by the magnetocaloric material to the end of copper rods.

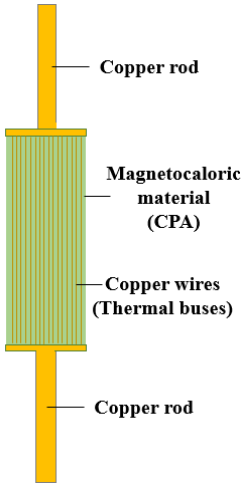

Figure 3: Geometry of salt pill

In salt pill, the temperature difference of the CPA in the radial direction is smaller due to the thermal bus. Therefore, to simplify the computational effort in the constructed simulation model, the thermal conductivity of the magnetocaloric material in the radial direction could be assumed to be infinite, allowing all the fine copper wires to be equivalently represented by a thick copper rod, which was called the equivalent thermal bus, as shown in Figure 4. The heat sink (The temperature is about 1 K) was in contact with the copper rod on the left side of the salt pill, and the heat load (The temperature is about 0.2 K) was in contact with the copper rod on the right side of the salt pill. The geometry and operating parameters of the salt pill model were shown in Table 1.

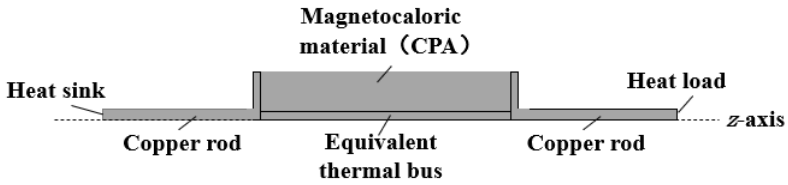

Figure 4: Two-dimensional axisymmetric geometric model of the salt pill

Table 1. Geometrical and operational parameters of the salt pill

Parameter	Value	Parameter	Value
Diameter of salt pill (D_{salt})	32 mm	Volume ratio of thermal buses (f)	1% – 10%
Length of salt pill (L_{salt})	58 mm	Magnetic field (B)	0 - 2 T
Diameter of copper rod (D_{rod})	10 mm	Heat sink temperature (T_H)	1 K
Length of copper rod (L_{rod})	50 mm	Cooling temperature (T_C)	0.2 K
Diameter of copper wire (d_{wire})	0.1 - 0.4 mm		

2.2 Governing equations for the salt pill

To simplify the model, it was assumed that the magnetic field applied to CPA is uniform. Demagnetization effects and eddy current losses of magnetocaloric materials are ignored in salt pill. In addition, in the model, the magnetocaloric effect of CPA was simplified to an internal heat source with magnetic field *B* and temperature *T* as variables. Then, based on these simplifying assumptions, the governing equations of the salt pill were established in COMSOL Multiphysics. The energy equation is expressed as follows：

$$\rho c \frac{\partial T}{\partial t} = \nabla \cdot k \nabla T + Q_{\mathrm{MCE}} \qquad \text{Eq. (1)}$$

where *T*, ρ, *c* and *k* are the temperature, density, specific heat, and thermal conductivity of CPA or copper, respectively. The internal heat source Q_{MCE} can be calculated by*(Nielsen et al., (2011))*:

$$Q_{\mathrm{MCE}} = -\rho T \frac{\partial M}{\partial T}\frac{\partial B}{\partial t} = -\rho T \frac{\partial s}{\partial B}\frac{\partial B}{\partial t} = -\rho T \frac{\partial s}{\partial B}\dot{B}_{\mathrm{t}} \qquad \text{Eq. (2)}$$

where *M* is the magnetization intensity and B_{t} is the magnetic field change rate.

For the magnetocaloric material CPA, the specific heat capacity *c* and entropy *s* are functions of magnetic field *B* and temperature *T*, which can be calculated by*(P. Shirron, (2014); P. J. Shirron, (2014))*:

$$c = \frac{\mathrm{R}}{M}\left(\frac{x^2}{\sinh^2(x)} - \frac{\sinh\left(x(2J+1)\right)}{\sinh(x)}\right) \qquad \text{Eq. (3)}$$

$$s = \frac{n\mathrm{R}}{M}\left(x\coth(x) - (2J+1)x\coth\left(x(2J+1)\right) + \ln\left(\frac{\sinh\left(x(2J+1)\right)}{\sinh(x)}\right)\right) \qquad \text{Eq. (4)}$$

$$x = \frac{\mu_{\mathrm{B}} g B_{\mathrm{eff}}}{2k_{\mathrm{B}}T} = \frac{(0.336\ \mathrm{K/T})\, g B_{\mathrm{eff}}}{T} \qquad \text{Eq. (5)}$$

$$B_{\mathrm{eff}} = \sqrt{B^2 + b^2} \qquad \text{Eq. (6)}$$

where u_{B}, k_{B} and *g* are Bohr magneton, Boltzmann's constant and Lande *g*-factor for the magnetic ion. The factor 2*J*+1 represents the number of possible values for the *z*-component of the magnetic moment*(P. J. Shirron, (2014))*. *b* is the background field generated by each ion‘s nearest neighbors, which can calculated by:

$$b = b_0\left(1 - e^{-\left(\frac{T}{T_0}\right)^{\alpha}}\right) \qquad \text{Eq. (7)}$$

Table 2 summarizes some physical properties of CPA*(P. Shirron, (2014); P. J. Shirron, (2014))*. At the same time, some physical properties of copper are also listed.

Table 2. The physical properties of CPA and copper in the model*(P. Shirron, (2014); P. J. Shirron, (2014))*

Properties of CPA	Value	Property of copper	Value
Density (ρ_{CPA})	1830 kg·m^{-3}	Density (ρ_{Cu})	9028 kg·m^{-3} @ 4 K
Specific heat (c_{CPA})	Equation (3)	Specific heat (c_{Cu})	0.013 J·kg^{-1}K^{-1} @ 1 K
Entropy (s_{CPA})	Equation (4)	Thermal conductivity (k_{Cu}))	488 W·mK^{-1} @ 1 K
Thermal conductivity (k_{CPA})	0.072 W·mK^{-1} @ 260 mK		

During the operation of ADR, isothermal magnetization and isothermal demagnetization need to be achieved, as shown in Figure 1. Therefore, in order to achieve isothermal control in the model, a PID controller in COMSOL Multiphysics was used, which could automatically control the temperature of the salt pill to remain constant. The real-time temperature T_t at the load position was used as the input of the PID controller, and the change rate of the magnetic field $\dot{B}_t$ is used as the output. The control equation is shown as follows:

$$\dot{B}_t = K_P\left(T_t - T_{set}\right) + K_I\int_0^t\left(T_t - T_{set}\right)dt + K_D\frac{d\left(T_t - T_{set}\right)}{dt} \quad \text{Eq. (8)}$$

where T_{set} is the holding temperature set during the isothermal process. K_P, K_I, and K_D are the proportional gain, integral gain and derivative gain in the control equation respectively, which were set to 0.8, 0.5, and 2 respectively in this model.

2.3 Boundary conditions and output parameters

In the model, the initial temperature of the salt pill was set to the heat sink temperature T_H. Several temperature boundaries existed simultaneously in the salt pill model, including heat leakage of the heat switch in the "off" state (disconnected state), heat load, and other heat leakage (including suspension heat leakage, radiation heat leakage, and metal eddy flow heat, etc.). the leakage heat of the heat switch and heat load were respectively applied to the left and right round surfaces of copper rods in the salt pill, as indicated by the heat sink and heat load in Figure 4. According to the reported work*(Hagmann and Richards, (1994); P. J. Shirron et al., (2016); Wang, (2022))*, the leakage thermal conductance of the thermal switch could be set to 2 uW·K^{-1}, while the heat load and other total heat leakage were set to 110 uW and 25 uW respectively. In addition, in the ultra-low temperature range, the effect of surface thermal resistance is large enough*(Peter J. Shirron and McCammon, (2014))*, so the surface contact thermal resistance between copper wires (thermal buses) and CPA needs to be considered. In the salt pill model, in order to consider the effect of surface contact thermal resistance, the contact surface between the equivalent thermal bus and the CPA was simplified as an equivalent thin thermal resistance layer. The thermal conductivity k_{layer} of the equivalent thin thermal resistance layer could be calculated by the following equation*(Peter J. Shirron and McCammon, (2014); Wang, (2022))*:

$$k_{layer} = \frac{T^3}{30[\mathrm{K^4cm^2W^{-1}}]}\frac{N_{wire}r_{wire}}{\sqrt{N_{wire}r_{wire}{}^2}} \quad \text{Eq. (9)}$$

where N_{wire} and r_{wire} were the number and radius of copper wires in the salt pill respectively.

In the model, to further reduce computational complexity, only demagnetization processes (including the adiabatic demagnetization process and the isothermal demagnetization process) in the refrigeration cycle were considered. To assess the impact of the thermal bus on the cooling performance of the ADR, the holding-time of the ADR at the cooling temperature T_C during isothermal demagnetization process was considered as the output parameter. The longer the holding-time, the better the cooling performance of ADR.

3. RESULTS AND DISCUSSION

Figure 5 illustrates the changes in temperature and magnetic field at the heat load during the demagnetization process. It could be observed that within 0 - 848 s, as the magnetic field gradually decreased from the initial value of 2 T, the temperature of the salt pill decreased due to the magnetocaloric effect. During this period,

the salt pill was in the demagnetization cooling process, and the demagnetization rate is relatively fast. Once the temperature of the salt pill was lowered to 0.2 K, the demagnetization rate of the magnetic field was automatically reduced by the PID controller. This adjustment ensured that the heat produced by the magnetothermal effect just compensated for the heat leakage and heat load, allowing the temperature of the salt pill to be maintained at 0.2 K until the magnetic field was reduced to zero.

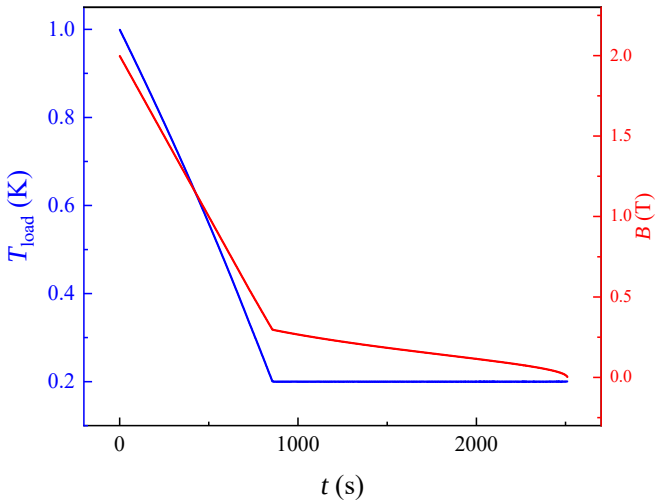

Figure 5: Temperature and magnetic field curves of the salt pill during the demagnetization process. (The blue line represents temperature and the red line represents magnetic field)

Figure 6 shows the temperature cloud diagram of the salt pill at 1000 s. During refrigeration process, the difference between the minimum and maximum temperatures of the salt pill was small (about 1.5 mK), which means that the heat transfer performance of the thermal bus in the salt pill was sufficiently excellent. In addition, it could also be seen from Figure 6 that the minimum and maximum temperatures were at the center of the CPA and the heat load, respectively.

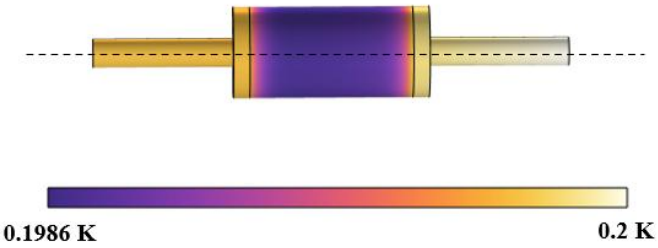

Figure 6: Temperature distribution of the salt pill

In order to ensure that the thermal bus efficiently transfers the heat generated by the magnetocaloric material without significantly occupying the volume of the salt pill, the volume ratio f and the wire diameter d_{wire} of thermal buses in the salt pill were both optimized. As shown in Figure 7, the holding-time t_{hold} of the ADR at the cooling temperature T_C changed with the volume ratio f of thermal buses. Under the same thermal bus diameter, it could be observed that the holding-time of the ADR decreased (With the thermal bus diameter of 0.1 - 0.15 mm) or increased (With the thermal bus diameter of 0.2 - 0.4 mm) slowly with the volume ratio f of thermal buses in the range of 1% - 2%. This was because the number of thermal bus wires was too small (For thermal bus wire diameters ranging from 0.2 - 0.4 mm). Consequently, the thermal buses are unable to extract all the heat/cold generated by the magnetocaloric material. As the volume ratio of thermal buses continued to increase, the holding-time of the ADR decreased rapidly with the volume ratio of thermal buses in the range of 2% - 10%. This was because, within the range of 2% - 10%, the number of thermal buses in the salt pill was already sufficient to extract all the heat/cold generated by the magnetocaloric material. It could be also seen from Figure 7 that when the diameter of the thermal bus was in the range of 0.2 - 0.4 mm, the optimal volume ratio of thermal buses was 2%, which could be a choice of the salt pill, but it was worth noting that the corresponding optimal number of thermal buses was different. The optimal numbers of thermal buses corresponding to different wire diameters were listed in Table 3. It could be observed that when the diameter of the thermal bus was 0.2 mm, the maximum holding-time of ADR at 0.2 K was 1713 s, and the corresponding number of thermal buses in the salt pill was 525.

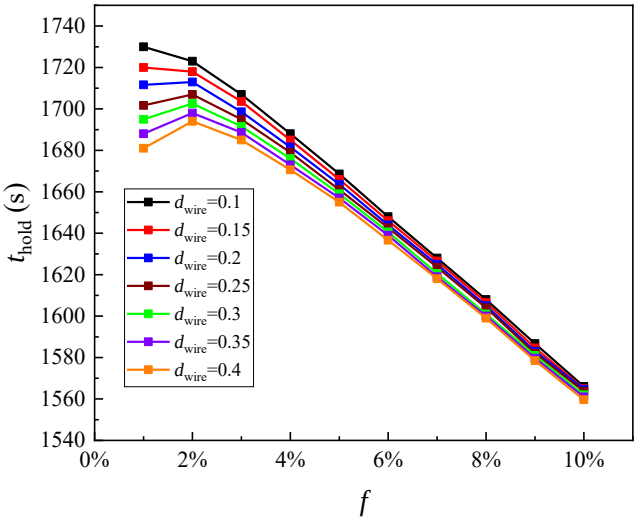

Figure 7: Holding-time of ADR changes with the volume ratio of thermal buses under different wire diameters.

Table 3. Corresponding numbers of thermal buses for different wire diameters

Wire diameters (mm)	Number of thermal buses (-)	Wire diameters (mm)	Number of thermal buses (-)
0.1	1050	0.3	233
0.15	467	0.35	171
0.2	525	0.4	131

The variation of the ADR holding-time with the thermal bus wire diameter was shown in Figure 8. At the same volume ratio of thermal buses, the holding-time of ADR gradually decreased with increasing wire diameter. This was because as the wire diameter increases, the number of thermal buses gradually decreased, resulting in less contact heat exchange area between the thermal buses and the magnetocaloric material. Furthermore, it could be seen that the lower the volume ratio, the more sensitive the holding-time was to the thermal bus wire diameter. For example, at a volume ratio of 1%, the holding-time of the ADR decreased most rapidly with an increase in wire diameter.

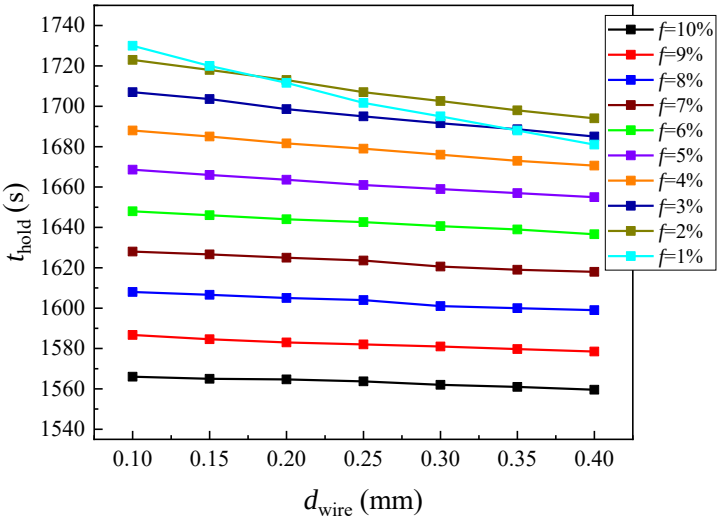

Figure 8: Holding-time of ADR changes with the wire diameter of thermal buses.

4. CONCLUSION

In this paper, in order to optimize the cooling performance of ADR operating in the range of 1 K to 0.2 K, a two-dimensional axisymmetric model of salt pill was established. In the model, the contact thermal resistance between the magnetocaloric material (CPA) and the thermal bus was considered. Through the simulation model, the influence of the volume ratio and the wire diameter of the thermal bus was revealed. As the

volume ratio of thermal buses increased, the holding-time of ADR initially decreased (With the thermal bus diameter of 0.1 - 0.15 mm) or increased (With the thermal bus diameter of 0.2 - 0.4 mm) slowly, then decreased rapidly. When the diameter of the thermal bus was 0.2 mm, the ADR holding time at 0.2 K could reach 1713 s, and the corresponding optimal number of thermal buses was 525. In addition, when the volume ratio of thermal buses was the same, the holding-time of ADR decreased as the wire diameter increased due to the reduction in the contact area between the thermal bus and the magnetocaloric material. The holding time of ADR has different sensitivities to the wire diameter at different volume ratios of thermal buses. In this article, it was worth mentioning that both the volume ratio and wire diameter of the thermal bus in the salt pill were optimized through the model, which could provide crucial insights for the later design and fabrication of the salt pill in ADR.

ACKNOWLEDGEMENTS

This work was supported by the National Key Research and Development Program of China (Grant No. 2022YFB3505100), and the National Natural Science Foundation of China (Grant No. 51925605, 52206034 and 52201036).

REFERENCES

Bartlett, J., Hardy, G., & Hepburn, I. D. 2015. Design and performance of a fast thermal response miniature Chromium Potassium Alum (CPA) salt pill for use in a millikelvin cryocooler. Cryogenics, 65, 26-37.

Hagmann, C., & Richards, P. 1994. Two-stage magnetic refrigerator for astronomical applications with reservoir temperatures above 4 K. Cryogenics, 34(3), 221-226.

Hagmann, C., & Richards, P. 1995. Adiabatic demagnetization refrigerators for small laboratory experiments and space astronomy. Cryogenics, 35(5), 303-309.

Kumar Singh, V., Balaji C, H., & Vora, A. P. 2022. Numerical modelling of a single stage adiabatic demagnetization refrigerator (ADR). Journal of Magnetism and Magnetic Materials, 564.

Li, K., Wang, Y.-N., Liu, P., Yu, F.-Q., Dai, W., & Shen, J. 2023. Experimental research of a 50 mK multi-stage adiabatic demagnetization refrigerator. Acta Physica Sinica, 0(0), 0-0.

Nielsen, K. K., Tusek, J., Engelbrecht, K., Schopfer, S., Kitanovski, A., Bahl, C. R. H., . . . Poredos, A. 2011. Review on numerical modeling of active magnetic regenerators for room temperature applications. International Journal of Refrigeration-Revue Internationale Du Froid, 34(3), 603-616.

Serlemitsos, A. T., SanSebastian, M., Kunes, E. S., & Behr, J. 1999. Performance of the XRS/ASTRO-E engineering model ADR. Cryogenics, 39(4), 399-404.

Shirron, P. 2014. Optimization strategies for single-stage, multi-stage and continuous ADRs. Cryogenics, 62, 140-149.

Shirron, P., Canavan, E., DiPirro, M., Jackson, M., King, T., Panek, J., & Tuttle, J. 2001. A compact, high-performance continuous magnetic refrigerator for space missions. Cryogenics, 41(11), 789-795.

Shirron, P. J. 2014. Applications of the magnetocaloric effect in single-stage, multi-stage and continuous adiabatic demagnetization refrigerators. Cryogenics, 62, 130-139.

Shirron, P. J., Kimball, M. O., James, B. L., Muench, T., DiPirro, M. J., Letmate, R. V., . . . Kelley, R. L. 2016. Operating Modes and Cooling Capabilities of the 3-Stage ADR Developed for the Soft-X-ray Spectrometer Instrument on Astro-H. Cryogenics (Guildf), 74, 2-9.

Shirron, P. J., & McCammon, D. 2014. Salt pill design and fabrication for adiabatic demagnetization refrigerators. Cryogenics, 62, 163-171.

Wang, C. 2022. System Construction and Experimental Study of Adiabatic Demagnetization Refrigerator for Ultra-Low Temperature Region. University of Chinese Academy of Sciences,

Zheng, W., Shen, J., Li, Z., Huang, H., Hai, P., Liu, J., . . . Mo, Z. 2023. Numerical simulation of a multistage magnetic refrigeration system in the temperature range of liquid hydrogen. International Journal of Hydrogen Energy.

DOI: 10.18462/iir.thermag.2024.0019

RESEARCH ON STAGES MATCHING OF TWO-STAGE ADIABATIC DEMAGNETIZATION REFRIGERATOR

Zhuo Chen[(a)], Jun Shen[(a,b,c,d),*], Ya'nan Zhao[(a),*] Wenshuai Zheng [(a)] Zhenxing Li [(a)] Jun Liu [(a)]

[(a)] Beijing Institute of Technology
Beijing, 100081, China, 3120215289@bit.edu.cn
[(b)] Technical Institute of Physics and Chemistry, Chinese Academy of Sciences,
Beijing, 100190, China
[(c)] University of Chinese Academy of Sciences,
Beijing, 100049, China
[(d)] Ganiiang Innovation Academy, Chinese Academy of Sciences,
Jiangxi, 341000, China

ABSTRACT

As one of the most popular ultra-low temperature refrigeration methods, adiabatic demagnetization refrigerators (ADR) are widely used in space exploration projects. In order to obtain lower refrigeration temperature and larger refrigeration capacity, multi-stage ADRs are often adopted. Besides the choice of suitable magnetocaloric materials according to the different refrigeration temperatures at each stage, optimization between stages is also important. In this paper, a double-stage ADR in which GGG and CPA are used as refrigerants is taken as an example, to study the effects of the matching mass of magnetocaloric materials used and the initial temperature of demagnetization operation for the cold stage on the cooling capacity of the refrigerator.

Keywords: Ultra-low Temperature, ADR, Stages Matching, Cooling capacity, Salt pill

1. INTRODUCTION

Ultra-low temperature refers to temperatures below 1 K. Common ultra-low temperature refrigeration technologies include dilution refrigeration, adsorption refrigeration, and adiabatic demagnetization refrigeration. Among these technologies, adiabatic demagnetization refrigerators (ADR) are gaining traction in space exploration projects and ground laboratories due to several advantages: it doesn't rely on gravity, doesn't require the rare material ^{3}He, has intrinsic high efficiency and uses a solid refrigerant that prevents leakage. Research on ADRs has been conducted and reported by many researchers such as Shirron (2001, 2004, 2006, 2012) and Serlemitsos (1999) of NASA, Bartlett (2015) of UCL, Jiang (2023) of Tsinghua University, and Wang (2021) of Technical Institute of Physics and Chemistry. The current leading achievement is continuous refrigeration with approximately about 5~10 μW@50 mK.

Achieving cooling from 4 K down to 50 mK with a single-stage ADR presents challenges due to limitations in material properties. It's difficult to achieve both a wide temperature span and high cooling capacity in commonly used magnetocaloric materials. Additionally, practical constraints such as the weight and volume of the ADR limit the magnetic field, typically kept under 4 T. Therefore, a multi-stage structure is often employed to achieve larger temperature spans. In a two-stage ADR, for instance, the first stage (S1) cools from 4 K to around 1 K, with the second stage (S2) providing further cooling to reach a final temperature of 50 mK, achieving a stepwise cooling process.

Current research and design effort on multi-stage ADRs primarily focus on independently optimizing each stage. However, exploring stages matching is equally crucial. It's evident that by increasing the amount of magnetocaloric material in S2 and lowering the initial cooling temperature, a larger cooling capacity can be achieved, allowing for a longer holding time of the working temperature under a specific load. When considering both stages together, increasing the amount of magnetocaloric material in S2 can make it harder for S1 to cool S2 to a lower temperature. This means S2 will have to start cooling from a relatively high temperature. One solution is to increase the cooling frequency of S1, so after several cooling cycles, S2 reaches the preset initial temperature. However, this approach significantly extends the preparation time

before S2 begins its refrigeration. Further increasing the amount of magnetocaloric material in S1 will inevitably result in increased volume and weight of the ADR. Therefore, it becomes crucial to optimize the quantity of magnetocaloric materials for each stage and select a suitable initial temperature for S2. This optimization process aims to balance cooling capacity with practical considerations such as size, weight, and requirement for the cooling capacity of the pre-cooling system.

A simulation model using COMSOL Multiphysics simulation software is established for a two-stage ADR in this article, and the aim is to investigate the issue of stage matching. While maintaining a constant quantity of magnetocaloric material in S1, the refrigeration performance achieved by S2 at different amounts of magnetocaloric material and initial temperatures are calculated.

2. SIMULATION MODEL

In a single-stage ADR, a superconducting magnet, a salt pill, a heat switch (HS), and a heat sink are typically included. Among these components, the salt pill serves as the source of cooling capacity. An ideal ADR cycle comprises four processes: isothermal magnetization, adiabatic demagnetization, isothermal demagnetization, and adiabatic magnetization. Only the isothermal demagnetization process can provide a certain amount of cooling capacity at the cooling temperature. During the adiabatic demagnetization, isothermal demagnetization, and adiabatic magnetization processes, the heat switch is in an OFF state, and it switches to an ON state during the isothermal magnetization process. For a two-stage ADR, its basic structure is similar with single-stage ADR, as shown in Fig. 1.The heat switch between S1 and 4 K sink is HS1, and the heat switch between S1 and S2 is HS2.

The operation of a two-stage ADR is complex. Typically, the first stage (S1) and the second stage (S2) are firstly magnetized to their full magnetic fields with the two heat switches remain in the ON state. After that the two stages are cooled down to 4 K. Then the heat switch HS1 is turned to the OFF state, while HS2 is in the ON state. When HS1 is completely disconnected, S1 begins to be demagnetized, and S2 is cooled to a certain temperature. During this period, S2 is not demagnetized. When S2 is cooled to the target initial temperature, HS2 is turned to the OFF state, and the S2 is demagnetized to cool down and hold at the working temperature. In the demagnetization process of S2, even if the magnetic field of S1 is exhausted, in order to give S2 a lower temperature heat guard, S1 is only heated up naturally by the heat leakage, and will not be magnetized until the magnetic field of S1 is exhausted.

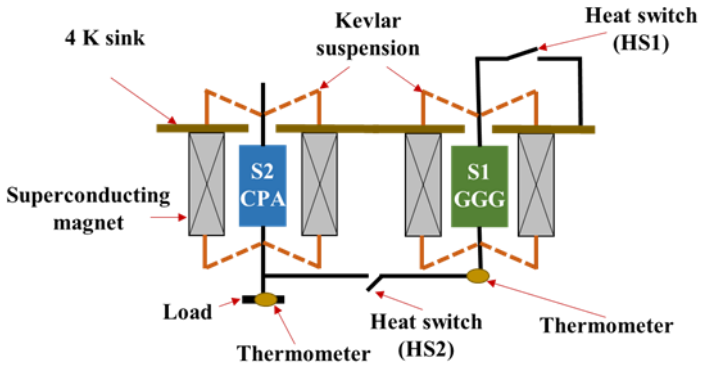

Figure 1: Structure map of a two-stage ADR

In the planned design of a two-stage ADR, S1 operates at approximately 0.7 K ~ 1.1 K, cooling S2 to its initial temperature. A gadolinium gallium garnet (GGG) crystal, measuring 30 mm in diameter and 50 mm in height, will be employed in S1. S2 operates at 0.05 K using a chromic potassium alum (CPA) salt pill, and optimizing the mass of paramagnetic salt is necessary to extend the holding time of the refrigeration at 0.05 K.

2.1 Geometry of the model

In order to study the stages matching in a two-stage ADR, COMSOL Multiphysics is employed to create a simplified simulation model to conserve computational resources. This two-dimensional axisymmetric model is depicted in Fig. 2. The model encompasses three distinct components: a GGG salt pill, a CPA salt pill, and a pair of virtual heat switches.

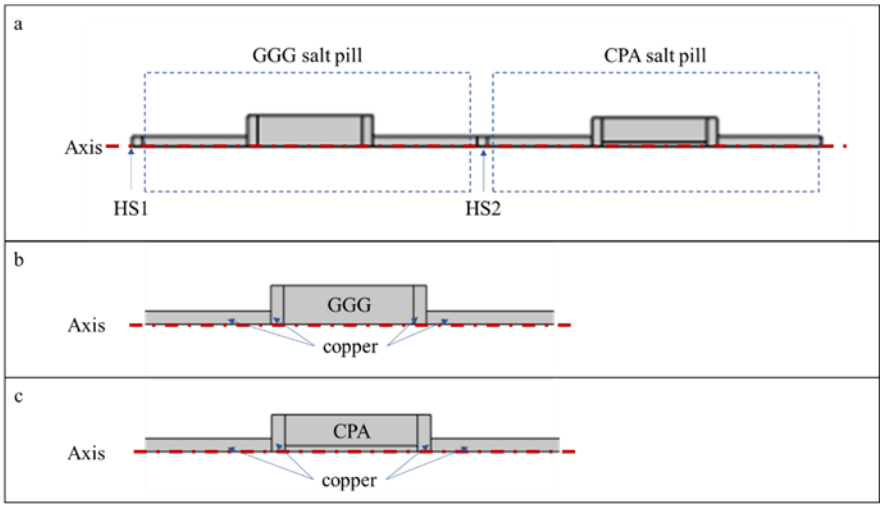

Figure 2: (a) 2D axisymmetric simulation model. (b) GGG salt pill model. (c) CPA salt pill model.

The GGG and CPA salt pills both consist of paramagnetic salt and thermal bus. The CPA salt pill includes a copper wire bundle inside, which is considered as a whole in this model. In a single calculation, magnetization is conducted first from zero magnetic fields at the heat sink temperature, followed by demagnetization after reaching the maximum magnetic field and returning to the heat sink temperature. This setup circumvents convergence issues stemming from poor initial value settings in the model. The heat switches in the model serve to achieve ON/OFF states of heat exchange between the salt pills and the heat sink during transient calculations. Given the intricate structure of actual heat switches and other heat conductivity structures between the salt pills and the heat sink, a simplified model of the heat switches and other thermal conductivity structures is implemented to ensure their thermal conductivity matches that of the actual heat switches.

2.2 Governing equation

The calculation model involves the solid heat transfer. Due to slow changes in magnetic field and the well insulation of GGG, the eddy current can be ignored, the control equation for heat transfer in solid is.

$$\rho c_p \frac{\partial T}{\partial t} + \nabla \cdot \vec{q} = Q \qquad \text{Eq. (1)}$$

Where ρ and c_p are the density and the heat capacity at constant pressure of metals used in the model, $\boldsymbol{q}$ is the heat flux vector and Q is provided by an internal heat source. In this model Q is the magnetocaloric effect Q_{MCE}.

The internal heat source of magnetocaloric effect is given by

$$Q_{MCE} = \frac{\partial S(B,T)}{\partial B} \frac{dB}{dt} T \rho \qquad \text{Eq. (2)}$$

Where B and T are the magnetic flux density and the temperature, S is the entropy of the magnetocaloric material and t is the time.

2.3 Boundary condition and parameters setting

Due to the coupling of two stages, it is necessary to set thermal boundary conditions and magnetic flux density separately for each stage. The specific parameters are shown in Table. 1. The application position of the thermal boundary is shown in Fig. 3.

Table. 1 Parameters of the two-stage ADR model

Parameters	Values	Description
$\boldsymbol{B}_{S1}$	4.0 T	Maximum magnetic flux density of S1
$\boldsymbol{B}_{S2}$	2.0 T	Maximum magnetic flux density of S2
$d\boldsymbol{B}_{S1}/d\boldsymbol{t}$	0.04 T/s	magnetic flux density change rate of S1
$D\boldsymbol{b}_{S2}/d\boldsymbol{t}$	0.01 T/s	magnetic flux density change rate of S2

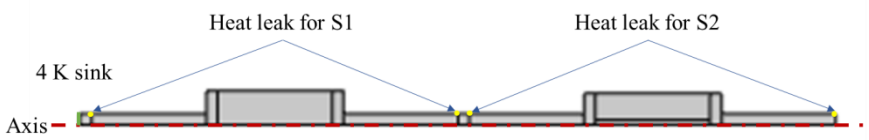

Figure 3. The applied position of thermal boundary condition

The heat leaks of salt pills mainly include the following aspects: radiation heat leak from 4 K, the OFF thermal conductivity of the heat switches, heat leak of support structure and sensor wires, eddy current heat and so on. To simplify the model, all the heat leaks are applied at the end of the salt pills in form of heat flux expect the heat switches' OFF mode. The values for S1 and S2 are assumed as 120 μW/K and 20 μW/K.

The thermal conductivity of the heat switch refers to the UCL's heat switch reported by Bartlett (2015), and the axial thermal conductivity of the equivalent heat switch in the modeling is equal to the actual heat switch's thermal conductivity through the equation. Considering that the heat capacity of the thermal conductivity structure is much smaller than that of salt pills at ultra-low temperature, the heat capacity and density of the equivalent heat switch part are set to a minimum non-zero value. The thermal conductivity, heat capacity and density of GGG and CPA are obtained from Wikus (2014), Shirron (2014) and Hornung (1974). The remaining physical parameters are based on the default values provided by the COMSOL Multiphysics material library.

2.4 Assumptions of the model

The following assumptions are made in this simulation model:

1) The temperature of the heat sink is stable without fluctuations.

2) The contact thermal resistance between solids is ignored.

3) Neglecting the heat capacity and density of thermal conductivity structures.

4) The magnetic field is uniform.

5) The heating of the eddy current heat is ignored.

6) Neglecting the switching time between conduction and disconnection of the heat switches.

3. SIMULATION RESULTS AND DISCUSSION

In order to verify the effect of different ratios of magnetocaloric materials and initial temperatures on the performance of S2, three parameters including the holding time t_{hold}, the total time t_{total} and the duty ratio t_{hold}/t_{total} are introduced. The t_{hold} refers to the time experienced by S2 from the time it reaches the working temperature of 50 mK until its magnetic field is exhausted. The t_{total} refers to the time spent to complete the cooling at 50 mK, from the state that the two stages are at a state of zero magnetic field at 4 K, to the state that the magnetic field of S2 is exhausted. It is worth mentioning that if S1 doesn‘t cool S2 to the target initial temperature after a single cooling cycle, HS2 is turned OFF and the magnetization-demagnetization process of S1 is experienced again until S2 is cooled to the target initial temperature.

Once the size of the S1 salt pill and the height of the S2 salt pill are determined, and different volume ratios are obtained by changing the diameter of the S2 salt pill. The maximum, minimum and initial salt pills for S2 are shown in Fig. 4. The thermal bus changes with the salt pill to hold the volume proportion of CPA at 0.9.

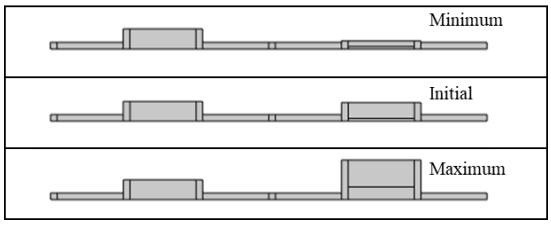

Figure 4. Change of the S2 salt pill

3.1 Analysis of the holding time

The calculation results of holding time at 0.05 K are quantitatively presented in Fig 5. At different initial temperatures of 0.7, 0.8, 0.9, 1.0, and 1.1 K for S2 to begin demagnetization, it is obvious that as the mass of CPA salt used increases and the initial temperature of S2 decreases, the holding time of S2 at working temperature becomes longer. This is consistent with the understanding of ADR, that is, the lower the initial temperature and the more paramagnetic salt is used, usually it is easier to obtain a larger cooling capacity at a suitable working temperature.

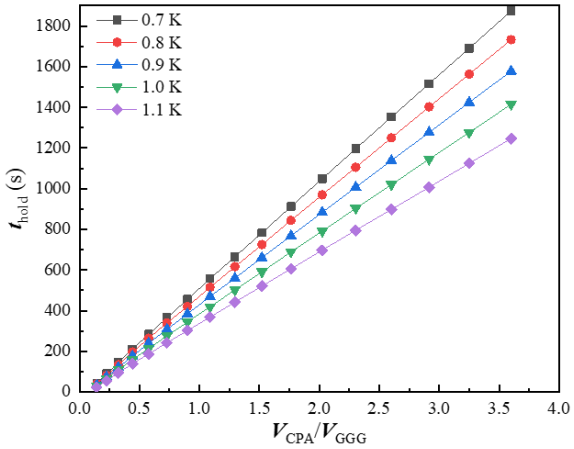

Figure 5: Holding time varies with the volume ratio of CPA and GGG at different initial temperature

3.2 Analysis of the total time

When the total time is considered, the situation becomes special in some cases. The calculation results of total time are shown in Fig. 6, it is obvious that the total time becomes longer with a lower initial temperature and a larger volume ratio of CPA and GGG. But at some points, for example, the initial temperature is 0.7 K and the volume ratio is about 0.32 and 0.44, this trend of change is faster than elsewhere.

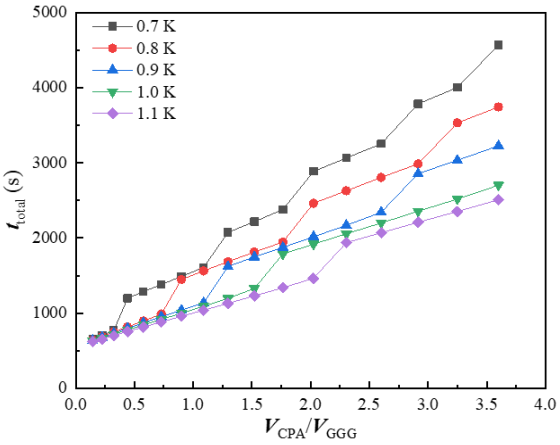

Figure 6: Total time varies with the volume ratio of CPA and GGG at different initial temperature

By observing the corresponding demagnetization process, as shown in Fig. 7, when the volume ratio is 0.44, S1 needs to undergo two cooling cycles to cool S2 to the set initial temperature, which is 0.7 K. When the volume ratio is 0.32, S1 only needs one cooling cycle to cool S2 to 0.7 K. Therefore, when the volume of CPA used in S2 increases to a certain extent, an additional cooling process of S1 will be added to make sure S2 can reach the preset temperature, which will lead to a significant increase in the total time.

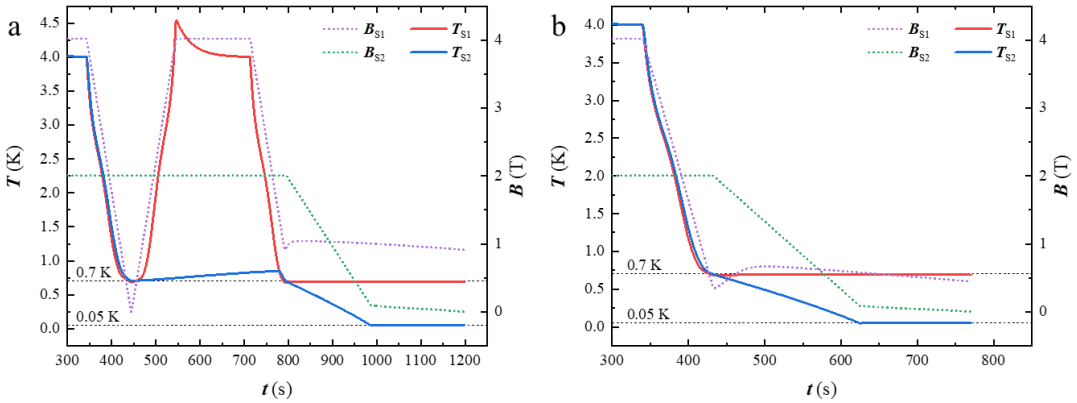

Figure 7: Demagnetization process at initial temperature of 0.7 K. (a) the volume ratio is 0.44(b) the volume ratio is 0.32

3.3 Analysis of the duty ratio

Considering the working time ratio per unit time is another important target, the duty ratio of holding time and total time t_{hold}/t_{total} is introduced. The results are shown in the Fig. 8 and Fig. 9. As shown in the figures, the parameter t_{hold}/t_{total} does not vary monotonically. When the volume of CPA is very small, a starting temperature of 0.7 K is more advantageous than other higher starting temperatures. However, the duty ratio with small volume of CPA is generally low, which refers to a short holding time corresponding to a certain total time. As the volume of CPA increases, the duty ratio will increase in the very beginning and then present a different situation. For example, as shown in Fig. 9 (a), the duty ratio increases gradually with the initially temperature of 0.8 K when the volume ratio is lower than 0.73. With the volume ratio increasing to 0.9, the duty ratio begins to decrease. In the volume ratio range from 0.15 to 3.6, the maximum proportion of holding time occurs at a volume ratio of 3.6 and an initial temperature of 1 K, exceeding 50%. At this volume ratio, the proportion of holding time with an initial temperature of 0.7 K is only 41%. In other words, it is not the case that the lower the initial temperature, the larger the t_{hold}/t_{total}. This is because achieving a lower initial temperature requires more preparation time, which increases a significant amount of non-working time within a refrigeration cycle, leading to a decrease in the proportion of holding time.

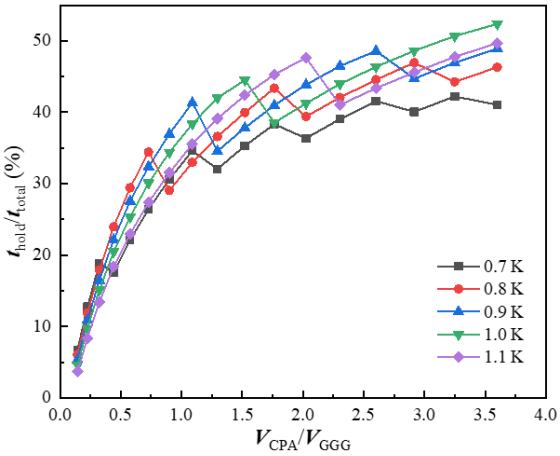

Figure 8 t_{hold}/t_{total} varies with V_{CPA}/V_{GGG} at different initial temperature

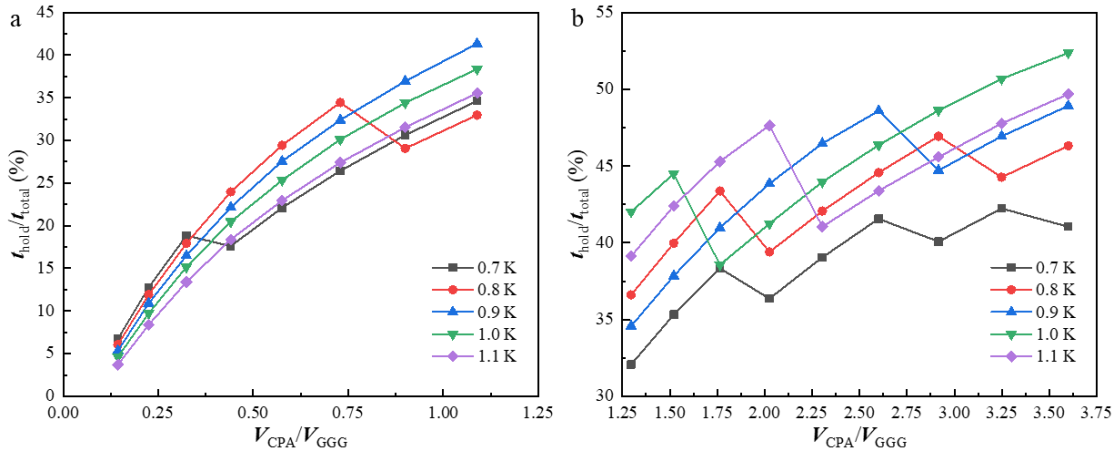

Figure 9: Segmented display of Fig. 8. (a) The range of V_{CPA}/V_{GGG} is 0~1.25 (b) The range of V_{CPA}/V_{GGG} is 1.25~3.75

It is worth noting that in some cases, such as with an initial temperature of 1 K and a volume ratio of 1.5 and 2.3, the time ratios of the two points are very close. Moreover, with an initial temperature of 0.7 K, the t_{hold}/t_{total} fluctuates and rises slowly when the volume ratio is larger than 1.75. These are also because although the holding time increases, the preparation time before S2 begins its refrigeration also increases, which results in much higher increase for the total time than the hold time. Therefore, increasing the volume of CPA does not always improve the time proportion.

4. CONCLUSION

A two-stage ADR is designed and investigated operating at 50 mK in this article. GGG is utilized for the first stage, and CPA is employed for the second stage. The holding time of the second stage and the proportion of holding time at 50 mK in relation to varying initial temperature and different amounts of CPA used in the second stage are examined, while keeping the amount of GGG constant. With the increase of the CPA used in the second stage and the decrease of the initial temperature, the holding time at 50 mK is monotonically increasing. Therefore, for application that only pursue maximum cooling time, the amount of the second stage material should be increased as much as possible, provided that the volume and weight of the system meet the requirements. However, in terms of the proportion of holding time, its variation pattern is relatively complex. When the volume ratio of CPA is lower, the proportion of refrigeration time also monotonically changes with the amount of CPA and the initial temperature. When the volume ratio of CPA is higher, for example, with an initial temperature of 0.7 K, the proportion of holding time fluctuates and rises slowly as the volume ratio gets higher, and a small volume ratio is more suitable to reduce the size of the system. Therefore, it is important to note that simply increasing the amount of the second stage or reducing the initial temperature may not necessarily increase the proportion of refrigeration time, but may lower this value.

ACKNOWLEDGEMENTS

This work was supported by the National Key Research and Development Program of China (Grant No. 2022YFB3505100), and the National Natural Science Foundation of China (Grant No. 51925605, 52206034 and 52201036).

REFERENCES

Shirron, P., D. Wegel and M. Dipirro., 2006. A Continuous Adiabatic Demagnetization Refrigerator for Cooling to 10 mK and Below. Low Temperature Physics: Part B (AIP Conference Proceedings Volume 850). 850, 1573-1574.

Shirron, P., et al., 2001. A compact, high-performance continuous magnetic refrigerator for space missions. Cryogenics (Guildford). 41(11), 789-795.

Shirron, P., et al., 2004. Development of a cryogen-free continuous ADR for the constellation-X mission. Cryogenics (Guildford). 44(6), 581-588.

Serlemitsos, A.T., et al., 1999. Performance of the XRS/ASTRO-E engineering model ADR. Cryogenics (Guildford). 39(4), 399-404.

Shirron, P.J., et al., 2012. Design and predicted performance of the 3-stage ADR for the Soft-X-ray Spectrometer instrument on Astro-H. Cryogenics (Guildford). 52(4-6), 165-171.

Bartlett, J., G. Hardy and I.D. Hepburn., 2015. Design and performance of a fast thermal response miniature Chromium Potassium Alum (CPA) salt pill for use in a millikelvin cryocooler. Cryogenics (Guildford). 65, 26-37.

Bartlett, J., G. Hardy and I.D., 2015.Hepburn, Performance of a fast response miniature Adiabatic Demagnetisation Refrigerator using a single crystal tungsten magnetoresistive heat switch. Cryogenics (Guildford). 72, 111-121.

Jiang, C., et al., 2023. Development of adiabatic demagnetization refrigerator for the HUBS mission. Sci Bull (Beijing).68(22), 2709-2711.

Wang, Chang., et al., 2021. Ultra-low temperature adiabatic demagnetization refrigerator for sub-Kelvin region. Acta Physica Sinica. 70(9): 257-263.

Wikus, P., et al., 2014. Magnetocaloric materials and the optimization of cooling power density. Cryogenics (Guildford). 62, 150-162.

Shirron, P.J. and D. McCammon, 2014.Salt pill design and fabrication for adiabatic demagnetization refrigerators. Cryogenics (Guildford). 62, 163-171.

Hornung, E. W., et al., 1974. Magnetothermodynamics of gadolinium gallium garnet. II. Heat capacity, entropy, magnetic moment from 0.5 to 4.2°K, with fields to 90 kG, along the [111] axis. J. Chem. Phys. 61, 282.

DOI: 10.18462/iir.thermag.2024.0020

EXPLORING THE TRADEOFF BETWEEN MAGNETIC FORCE AND THERMAL PROCESSES IN A THERMOMAGNETIC DEVICE

Alisson Cocci de Souza [a,b]*, Guilherme Hitoshi Kaneko [c], William Imamura [d,e] Nadège Bouchonneau [b], José Ângelo Peixoto Costa [b,f], Alvaro Antonio Villa Ochoa [b,f]

[a] Unidade Acadêmica do Cabo de Santo Agostinho, Universidade Federal Rural de Pernambuco, 54518-430, Cabo de Santo Agostinho, PE, Brazil

[b] Centro de Tecnologia, Universidade Federal de Pernambuco, 50670-901, Recife, PE, Brazil

[c] Department of Mechanical Engineering, Graduate School of Sci. and Tech., Meiji University, 214-8571, Kawasaki, Japan

[d] Centro de Tecnologia, Universidade Federal de Alagoas, 57072-970, Maceió, AL, Brazil

[e] Departamento de Engenharia Mecânica, Universidade Estadual de Maringá, 87020-900, Maringá, PR, Brazil

[f] Instituto Federal de Educação, Ciência e Tecnologia de Pernambuco, 50740-545, Recife, PE, Brazil

*alisson.cocci@ufrpe.br

ABSTRACT

Thermomagnetic devices output power harness the influence of a magnetic field and thermal processes period. In this context, our study aims to conduct a theoretical investigation into the correlation between the amount of magnetic material in the permanent magnet gap and the thermal exchange time between the material and the flowing fluid. A parametric analysis of the magnetic and thermal processes was conducted using COMSOL software, employing a flat plate and cylinder geometries for the magnetic material. Our findings reveal a direct proportionality between the magnetic field and the magnetic force applied to the material, resulting in a higher magnetic energy density with an increased amount of magnetic material in the gap. Concerning thermal exchange processes, a greater quantity of magnetic material leads to an extended duration of thermal exchange. Therefore, a tradeoff was observed between the period of the thermal process and the magnetic energy density supported by the magnet gap.

Keywords: Permanent magnet, Thermomagnetic device, Magnetic field, Thermal processes.

1. INTRODUCTION

Thermomagnetic motors utilize the interaction between heat and the magnetic properties of magnetic or magnetocaloric materials (MCMs) (Alves et al., 2013; Trapanese et al., 2015). Through controlled temperature and magnetic field variations, these motors facilitate the conversion of thermal energy into mechanical power. This technology presents potential applications within the industrial sector for the recovery of low-grade heat, serving as effective energy harvesters (Ahmed et al., 2021).

In a simplified thermomagnetic power device cycle, the magnetic heat exchanger (MHE) performs two heat exchange processes within a constant magnetic field: heating in the high magnetic field region and cooling in the low magnetic field region. Additionally, it undergoes two displacement processes at constant temperature: from the low magnetic field region to the high magnetic field region and vice versa (Bessa et al., 2018). Several studies have been dedicated to analyzing the cycle and power output of these devices. Efficiency and power of a thermal

energy harvesting thermodynamic cycle using MCMs were evaluated in a study (Almanza et al., 2017) evaluated the efficiency and power of a thermal energy harvesting thermodynamic cycle using MCMs. Another study focused on the design and experimental evaluation of a linear thermomagnetic motor utilizing gadolinium (Gd) as a magnetic material (Kaneko et al., 2021). The concept proposed by the authors employs a double-C shaped permanent magnet magnetic circuit to convert thermal energy into mechanical energy. The motor design involved two MHEs operating at different magnetic phases, generating linear motion due to the imbalance of forces. Another study explores the mathematical modeling and simulation results of a linear thermomagnetic motor with gravity return (Evaristo et al., 2022). The motor design utilized gadolinium as the magnetic material and incorporates a C-shape magnetic circuit and a prismatic-shaped MHEs. Numerical simulations investigated various factors affecting motor performance, revealing a dependence of produced power on the temperature difference.

The power output of power devices is governed by torque and cycle frequency. In thermomagnetic motors, torque — being proportional to the magnetic field's force of attraction —, increases with higher magnetic field strengths in the heat exchanger. Typically, this region coincides with a gap in the magnetic circuit, introducing reluctance and diminishing the magnetic field strength. However, enlarging this gap accommodates more magnetic material, enhancing the force of attraction. Nevertheless, increased material mass may prolong the cycle period due to extended thermal exchange time required for reaching a specified temperature.

In this context, this work aims to conduct a numeric-theoretical study on the relationship between magnetic force and the thermal exchange period of a thermomagnetic device. To achieve this goal, we performed a parametric analysis of the mass accommodated in the gap of the magnetic circuit, varying it according to the opening in the circuit. Through this analysis, we observed the relationship between this mass and the magnetic force exerted on the material, as well as the thermal exchange time with the system's thermal exchange fluid.

2. METODOLOGY

2.1. Magnetic Circuit Modeling and Magnetic Heat Exchanger

To conduct this study, a C-shaped permanent magnet model was adopted to generate the magnetic field necessary for exerting magnetic attraction force on the MCM. This magnet model produces an effective magnetic field and its construction is relatively straightforward., making it widely utilized in these applications (de Souza et al., 2024). The magnet structure consists of magnetized blocks of NdFeB, grade N54, serving as the magnetic field source, and AISI 1020 as the soft magnetic material for conducting the field (*Spacemagnets Europe GmbH*, n.d.)]. The properties of the NdFeB grade used are listed in Table 1. The magnetic permeability of AISI 1020 was determined based on its B-H curve (*Spacemagnets Europe GmbH*, n.d.).

Table 1. Magnetic properties of NdFeB N54 grade

B_{rem}	1.49 T
H_{cj}	876 kA/m

Fig.1 illustrates a representative schematic of the system. In Fig. 1(a), The NdFeB blocks are depicted in green (arrows indicate the direction of the magnetic field), while the AISI 1020 blocks are shown in gray. The region of high magnetic field is generated within the magnet gap, and the magnetic flux density in this region is inversely proportional to the gap height in the magnetic circuit. For comparative analysis, five different gap size were utilized, and simulations of the magnetic field produced by the magnet were conducted for each value. The surface area was maintained constant at 101.6 mm × 101.6 mm for all gap values. The specific gap size, the corresponding average magnetic flux density in the gap region and the total mass of Gd used in each case are presented in Table 2.

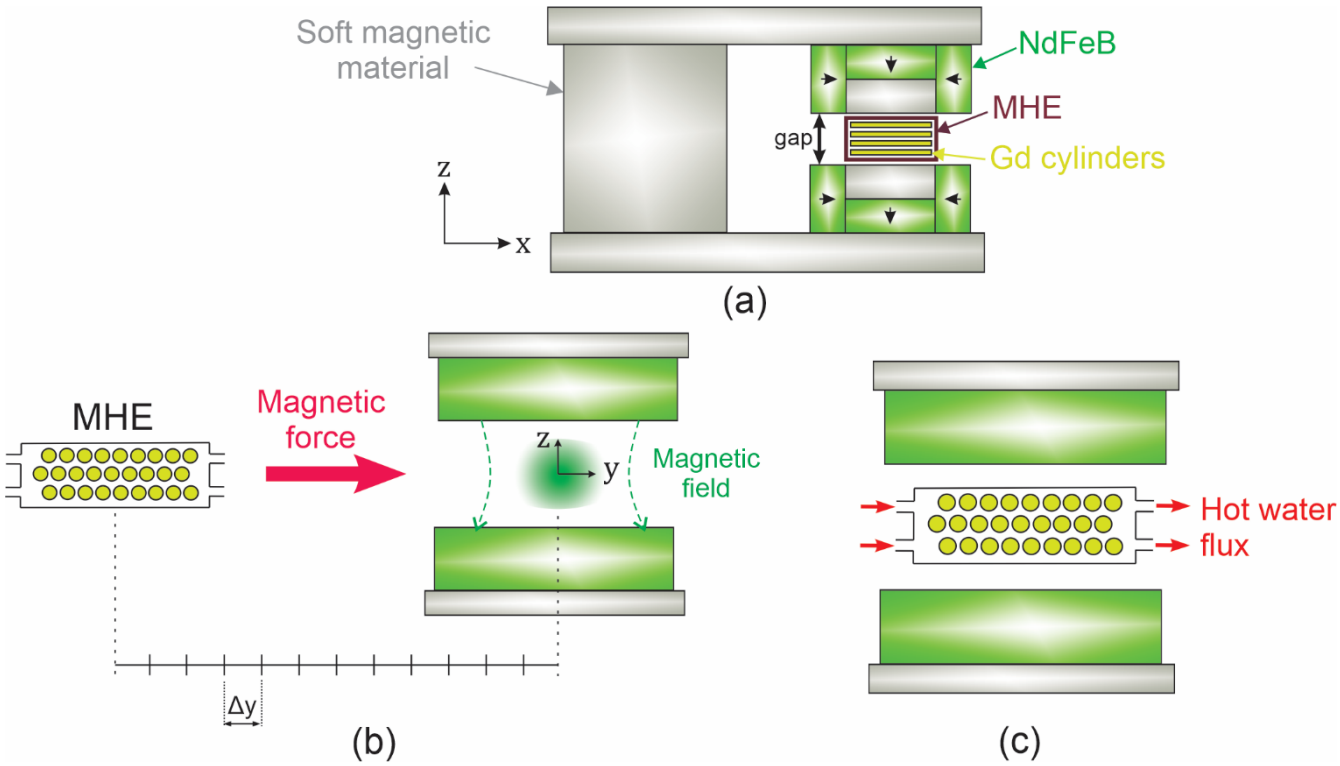

Figure 1: System representative scheme. (a) System components; (b) MHE displacement toward the gap due to the action of magnetic force; (c) Hot water flux through the MHE positioned in the gap of the permanent magnet

Table 2. Average magnetic field and Gd mass for each gap size

Gap size (mm)	Average magnetic flux density (T)	Total mass of Gd (kg)
20	1.2155	0.1396
25	1.0742	0.2783
30	0.9620	0.4188
35	0.7682	0.5542
40	0.6213	0.6980

The amount of MCM that can be accommodated in the gap region depends on its dimensions. Larger gaps allow for a greater mass of material, while smaller gaps accommodate lessGd was selected as the MCM for the MHE, adopting a cylindrical geometry with each cylinder having a diameter of 5 mm and a length of 100 mm, with a center spacing of 10 mm.

As the gap size increases, the number of cylinders supported by the MHE also increases. For instance, with a gap size of 20 mm, a total of 9 parallel cylinders can be accommodated in the MHE. Subsequently, with each increment in the gap value, an additional row of 9 cylinders is added to the MHE. In each case, a 5 mm gap is left at each end of the gap to account for the wall thickness of the MHE, as well as to keep a safe distance between the MHE and the magnet.

In these setting, the magnetic attraction force and heating time for each gap size were evaluated.

2.2. Modeling of thermal and magnetic processes

The magnetic force acting on the set of Gd cylinders during their path to the gap region was directly calculated using Maxwell tensors within the COMSOL software (*COMSOL Multiphysics*, n.d.). In addition to the magnetic field gradient, the calculation required estimation of the magnetic permeability of Gd, which was determined based on B-H curves obtained from (Pecharsky et al., 1999).

The distance traveled by the MHE between the high and low magnetic field regions is 120 mm. This interval was discretized into 13 equidistant points, each separated by Δy = 10 mm, as illustrated in Fig. 1(b). Magnetic modeling and simulation in COMSOL were performed using the Magnetic Fields, No Currents (mfnc) physics module, utilizing 3D dimensions and steady-state conditions, as described by Eq. (1).

$$-\nabla.\left(\mu_0\mu_r\nabla V_m - \vec{B}_{rem}\right) = 0 \qquad \text{Eq. (1)}$$

For each gap size, the material contained in the MHE exchanges heat with the fluid from the hot thermal reservoir (Fig. 1(c)). Water was chosen as the heat exchange fluid, with a constant inlet temperature of 303 K serving as a boundary condition, and the initial temperature of the system was 283 K. To ensure efficient heat transfer, water is pumped through the MHE using a pump with a capacity of 13 L in all cases.

As the gap size varies, the amount of Gd accommodated by the MHE changes. Consequently, to facilitate better flow distribution, the number of fluid inlets was adjusted accordingly, as detailed in Table 3. Each inlet has a diameter of 5 mm.

Table 3. Water inlet velocity for each gap size

Gap size (mm)	Number of heat exchanger inlets	V_{inlet} (m ×s^{-1})
20	3	0.5
25	3	0.5
30	6	0.25
35	6	0.25
40	9	0.167

The thermal properties of Gd were assumed to be constant, with k = 8.8 W.m^{-1}.K^{-1} and c_p = 230 J.kg^{-1}.K^{-1} (Glorieux et al., 1995). The total simulated time was set to 8 s, with a time step of 0.05 s. The heat exchange process was modeled using the Conjugate Heat Transfer, Turbulent Flow, κ-ε, 2D dimension module, under transient regime conditions, as described by Eq. (2). For simplification purposes, a 2D simulation was conducted in the midsection of the MHE, specifically in the yz plane at x = 0.

$$d_z\rho c_p\frac{\partial T}{\partial t} + d_z\rho c_p\vec{u}.\nabla T = d_z Q + q_0 \qquad \text{Eq. (2)}$$

In all cases, the mesh consisted of tetrahedral elements (for 3D geometries) and triangular elements (for 2D geometries). For magnetic simulations, the maximum element size in the region of interest was set to 10^{-3}, while it was 10^{-4} for thermal simulations. A stopping criterion of 10^{-3} was adopted for all simulations.

3. RESULTS AND DISCUSSION

Fig. 2a illustrates the variation in the average magnetic force acting on the set of Gd cylinders along the path of the MHE from the low magnetic field region to the high magnetic field region (gap), considering all gap values. It is evident that, as the gap increases, the magnetic force also increases along the path for all points, despite the reduction in the magnetic field produced by the permanent magnet. This highlights a stronger dependence of the magnetic force on the mass of the material rather than solely on the applied magnetic field. Comparatively, the average force along the path for the 20 mm gap was measured at 45.43 N, while it escalated to 98.88 N for the 40 mm gap, representing a notable increase of 117.65%. Employing the same comparison with the mass of Gd utilized in each scenario, the increase is 400%. Thus, it is evident that there exists a directly proportional nonlinear relationship between the mass of the MCM and the magnetic force.

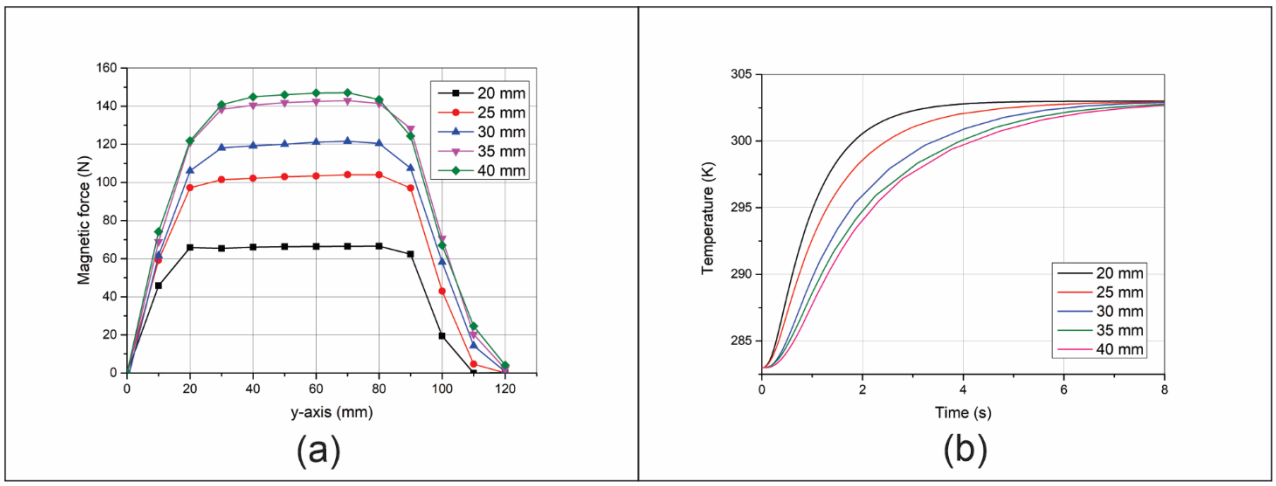

Figure 2: (a) Variation of magnetic force acting on the cylinder assembly along the MHE route toward gap for each gap size; (b) Variation in the average temperature of the cylinder assembly.

Fig. 2b illustrates the variation in the average temperature of the set of Gd cylinders over time for each gap value. At the initial time (t = 0 s), all curves exhibit a temperature of 283 K, while the temperature closely approaches 303 K at the final time (t = 8 s). However, it is evident that the time required for the set of Gd cylinders to approach the asymptote of 303 K varies for each case. Table 4 presents the time taken in each scenario for the average temperature of the cylinders to reach 99.5% of the water inlet temperature value.

Table 4. Thermal exchange time for the Gd set to reach 99.5% of the reference temperature

Gap size (mm)	Time (s)
20	2.4
25	3.35
30	4.55
35	5.15
40	5.5

Based on the time values listed in Table 4, the time required for the set of cylinders to reach the reference temperature in the case of a 40-mm-gap represents an increase of 129.17% compared to the case of a 20-mm-gap. Comparing this value with the percentage increase in magnetic force for these same cases, it is observed that the thermal exchange still represents a higher percentage increase than the increase in force. However, it is important to highlight that optimization of the thermal exchange process is possible through improvements in the geometry

of the MHE or the MCM, aiming to enhance the contact area between the fluid and the material.

Fig. 3 presents a temperature color map of the cylinder assembly for the 3- mm-gap case. In this configuration, the cross section of cylinders bank consists of three rows, each containing nine cylinders, totaling twenty-seven cylinders. In Fig. 3a, it can be observed that the water flow has not yet reached the MHE outlet, and the cylinders remain at a temperature close to the initial value (283 K). As the flow develops, the temperature of the assembly increases (Fig. 3b and 3c); however, a temperature gradient is evident in the cylinders in the direction of flow, as expected, since water tends to reduce the intensity of thermal exchange as it flows through the cylinder assembly. At the final time (Fig. 3d), the cylinder bank is close to the water inlet temperature the temperature gradient along the flow direction is practically negligible.

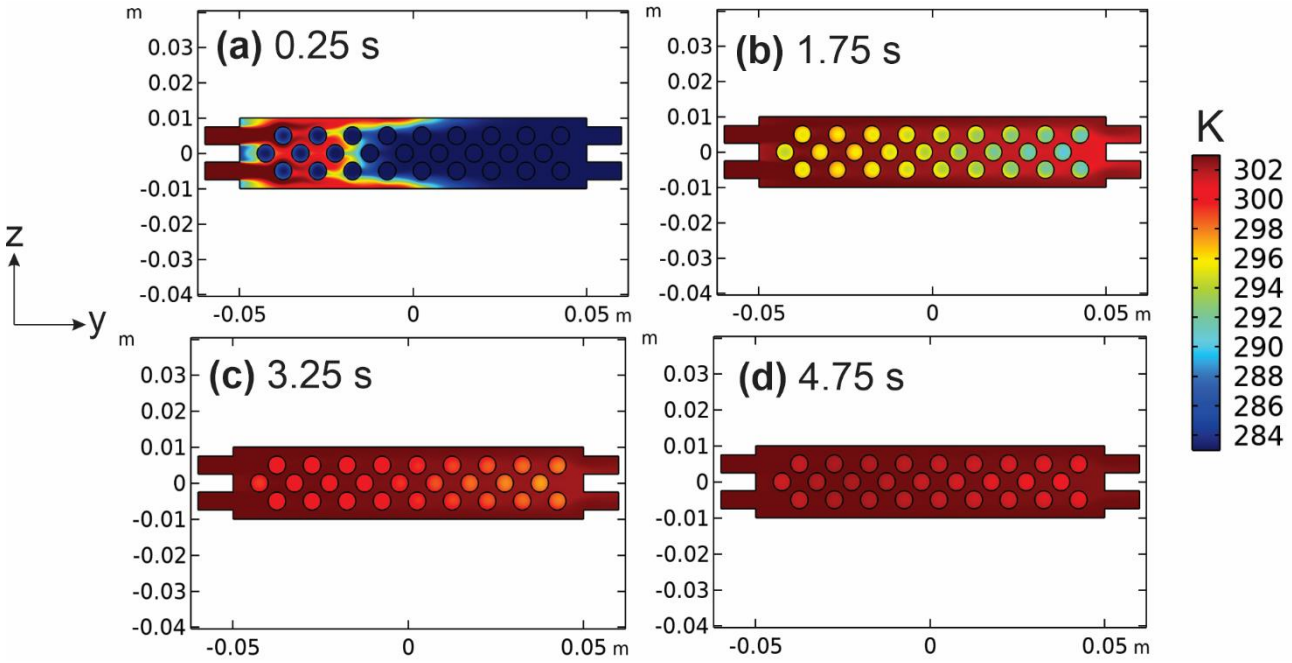

Figure 3: Temperature colormap during the heating process for the case of a 30-mm-gap at four different times.

4. CONCLUSIONS

In this study, a numerical theoretical investigation was conducted to explore the relationship between magnetic force and thermal exchange time in a thermomagnetic device using COMSOL software. To achieve this, variations in the size of the magnetic circuit gap and the amount of magnetic material accommodated in the magnetic heat exchanger were considered, and the magnetic force and thermal exchange period were evaluated for each case.

The analysis of the results revealed that both magnetic force and thermal exchange period are influenced by the increase in the amount of magnetic material. Despite the reduction in the magnetic field produced by the permanent magnet, the magnetic force exhibited a percentage increase with the expansion of the gap and the amount of material. This trend was similarly observed in relation to the thermal exchange time. However, a more substantial percentage increase in thermal exchange time compared to magnetic force was noted when comparing the same cases.

ACKNOWLEDGEMENTS

The authors acknowledge financial support from Universidade Federal de Pernambuco, Universidade Federal Rural de Pernambuco, Instituto Federal de Educação e Tecnologia de Pernambuco, Fundação de Amparo à Ciência e Pesquisa de Pernambuco, and Conselho Nacional de Desenvolvimento Científico e Tecnológico.

NOMENCLATURE

B	magnetic induction (T)	Q	heat source (W×m^{-3})
B_{rem}	remanence (T)	q_0	inward heat flux (W×m^{-2})
c_p	specific heat at constant pressure (J×kg^{-1}×K^{-1})	$\vec{u}$	fluid velocity vector (m×s^{-1})
d_z	thickness of domain in the out-of-plane direction (m)	t	time (s)
H_{ci}	magnetic coercivity (A×m^{-1})	T	temperature (K)
k	thermal conductivity (W×m^{-1}×K^{-1})	V_m	magnetic scalar potential (A)

Greek symbols

μ_0	vacuum magnetic permeability (N×A^{-2})	∇	gradient operator
μ_r	relative magnetic permeability (-)	$\nabla.$	divergent operator
ρ	density (kg×m^{-3})		

REFERENCES

Ahmed, R., Park, J. C., Zeeshan, Mehmood, M. U., Lim, S. H., Lee, J., & Chun, W. (2021). Optimization of a cylindrical thermomagnetic engine for power generation from low-temperature heat sources. *Energy Research*, *45*, 8606–8619. doi: 10.1002/er.6396

Almanza, M., Pasko, A., Mazaleyrat, F., & LoBue, M. (2017). Numerical study of thermomagnetic cycle. *Journal of Magnetism and Magnetic Materials*, *426*, 64–69. doi: 10.1016/j.jmmm.2016.11.058

Alves, C. S., Colman, F. C., Foleiss, G. L., Vieira, G. T. F., & Szpak, W. (2013). Numerical simulation and design of a thermomagnetic motor. *Applied Thermal Engineering*, *61*(2), 616–622. doi: 10.1016/j.applthermaleng.2013.07.053

Bessa, C. V. X., Ferreira, L. D. R., Horikawa, O., & Gama, S. (2018). On the relevance of temperature, applied magnetic field and demagnetizing factor on the performance of thermomagnetic motors. *Applied Thermal Engineering*, *145*, 245–250. doi: 10.1016/j.applthermaleng.2018.09.061

COMSOL Multiphysics. (n.d.). Retrieved from www.comsol.com

de Souza, A. C., Imamura, W., Kaneko, G. H., Bouchonneau, N., da Costa, J. Â. P., Leite, G. N. P., & Ochoa, A. A. V. (2024). A parametric and comparative study of a permanent magnet structure. *Applied Physics A: Materials Science and Processing*, *130*(3). doi: 10.1007/s00339-024-07361-6

Evaristo, E. H. G., Colman, F. C., Alves, C. S., & Trevizoli, P. V. (2022). Mathematical modelling and simulation results of a linear thermomagnetic motor with gravity return. *Journal of Magnetism and Magnetic Materials*, *544*. doi: 10.1016/j.jmmm.2021.168668

Glorieux, C., Thoen, J., Bednarz, G., White, M. A., & Geldart, D. J. W. (1995). Photoacoustic investigation of the temperature and magnetic-field dependence of the specific-heat capacity and thermal conductivity near the Curie point of gadolinium. *Physical Review B*, *52*(17), 12770–12778. doi: 10.1103/PhysRevB.52.12770

Kaneko, G. H., Conceição, W. A. S., Colman, F. C., Cocci, A. S., Alves, C. S., Pupim, G. C., Kubota, G. H., Oliveira, V. C., & Trevizoli, P. V. (2021). Design and experimental evaluation of a linear thermomagnetic motor using gadolinium: Preliminary results. *Applied Thermal Engineering*, *186*. doi: 10.1016/j.applthermaleng.2020.116472

Pecharsky, V. K., & Gschneidner, K. A. (1999). Magnetocaloric effect from indirect measurements: Magnetization and heat capacity. *Journal of Applied Physics*, *86*(1), 565–575. doi: 10.1063/1.370767

Spacemagnets Europe GmbH. (n.d.). Retrieved from https://www.spacemagnets.de/de/

Trapanese, M., Cipriani, G., Di Dio, V., Franzitta, V., & Viola, A. (2015). Optimization of a thermomagnetic motor. *Journal of Applied Physics*, *117*(17). doi: 10.1063/1.4919231

DOI: 10.18462/iir.thermag.2024.0021

SPECTROSCOPY AND LASER-INDUCED COOLING CHARACTERISTICS OF 4%YB^{3+}: YAG CRYSTALS

Jiayi Zhang[(a, b)], Jiajin Xu[(a)], Ziheng Zhang[(a)], Chaoyu Wang[(a)], Biao Zhong[*(a, b)]

[(a)]State Key Laboratory of Precision Spectroscopy, East China Normal University, Shanghai, 200062, China

[(b)]Key Laboratory of Cryogenics, Technical Institute of Physics and Chemistry, Chinese Academy of Sciences, Beijing, 100190, China,bzhong@mail.ipc.ac.cn

ABSTRACT

Radiation-balanced lasers (RBLs) represent a significant application of solid-state laser cooling. Yb^{3+}-doped YAG crystals have been recognized for their dual role in laser technology as a superior gain medium for lasers and as a medium for laser cooling, which make them widely used in the development of high-power RBLs. Here, we focus on the laser cooling properties of 4% Yb^{3+}-doped YAG crystals. We have measured the relative parameters which affect the laser cooing efficiency, including the mean fluorescence wavelength, the resonant absorption coefficient, the external quantum efficiency, and the background absorption coefficient. We explore the cooling efficiency as a function of temperature and wavelength with fixed background absorption coefficient and external quantum efficiency. This comprehensive study has allowed us to obtain the minimum achievable temperature of the sample, which iscalculated to be 231 K. Our work is helpful for the cooling of YAG crystals and the development of RBLs.

Keywords: Optical Cooling, Laser Cooling, Yb^{3+}: YAG Crystal, Radiation-balanced Lasers

1. INTRODUCTION

Laser cooling of solids, achieved by the process of anti-Stokes fluorescence(ASF), has the potential to be widely used in a variety of field. In 1995, net laser cooling was observed in Yb^{3+}-doped ZBLANP glass(Epstein et al., 1995), confirming the feasibility of using anti-Stokes fluorescence for cooling solid, an idea initially proposed by P. Pringsheim(Pringsheim, 1929). Since then, with the progresses in laser technology and advancements in material processing, research in solid-state laser cooling has made greatachievements, particularly in the cooling of Yb^{3+}-doped crystals. The laser cooling of Yb^{3+}:YLF and Yb^{3+}:LLF crystals has reached temperatures below 123 K(Melgaard et al., 2016 , Lei et al., 2022). Yb^{3+}:YAG crystals, which play a crucial role in the development of high-power radiation-balanced lasers (RBLs)(Bowman, 1999), are also widely used in various laser applications(Demirkhanyan, 2006), and have reached the lowest cooling temperature of 218.9 K(Zhong et al., 2021). In this work, we focus on the laser cooling properties of the 4% Yb^{3+}:YAG crystal, employing spectroscopy and the laser induced temperature modulation spectrum (LITMoS) to assess its cooling performance parameters and estimate the minimum achievable temperature (MAT).Our work willbeuseful for the developments of radiation-balanced lasers (RBLs).

2. METHOD

This section outlines the fundamental principles of solid-state laser cooling, presents the experimental setup, and elaborates on the parameters associated with cooling efficiency, including their measurement and calculation methods.

2.1 Experimental principle

Laser cooling of solid relies on ASFprocessing. In this process, electrons at the top of the ground state absorb photons with energy $h\nu$, transitioning to the bottom of the excited state. Once there, they absorb phonon energy, which prompts them to move to the higher levels within the excited state, to reach quasi-thermal equilibrium. These electrons then emit fluorescence photons with energy $h\nu_f$, returning to the bottom of the

ground state. Subsequently, the electrons in the ground state reabsorb phonon energy to reestablish thermal equilibrium. This repetitive cycle facilitates the cooling of the solid.

The presence of the matrix material lattice field induces the Stark effect, leading to the splitting of both the ground and excited states of the rare-earth ions. As depicted in Fig.1(a), the Stark energy level distribution in the Yb^{3+}:YAG crystal shows that the ground state $^2F_{7/2}$ and the excited state $^2F_{5/2}$ of the Yb^{3+} ions are split into four and three sublevels, respectively, due to the crystal field.

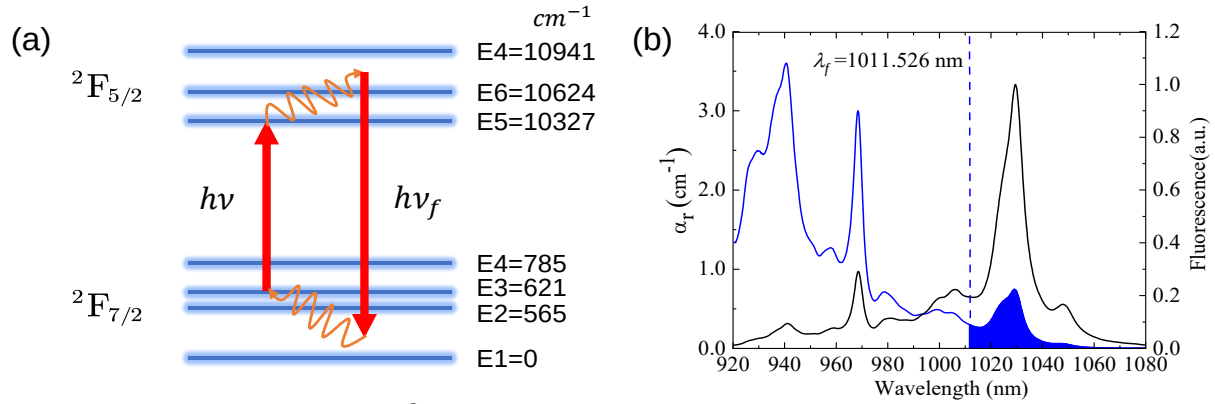

Figure 1: (a) Energy diagram of the Yb^{3+} in YAG crystals. (b) Absorption(blue) and fluorescence spectra (black) for the 4% Yb^{3+}:YAG crystal at 300 K. The blue dashed line indicates the mean fluorescence wavelength at 300 K, and the blue-filled region is the cooling tail.

The cooling efficiency of the crystal is commonly characterized using a four-level model(Sheik-Bahae and Epstein, 2007):

$$\eta_c = \eta_{ext}\eta_{\text{abs}}\frac{\lambda}{\lambda_f} - 1 \qquad \text{Eq.(1)}$$

where λ_f is the mean fluorescence wavelength,The external quantum efficiency, η_{ext}, is calculated as $\eta_e W_r/(\eta_e W_r + W_{nr})$, where η_e represents the fluorescence escape efficiency, and W_r and W_{nr} are the radiation and non-radiationdecay rate, respectively. The absorption efficiency, denoted as η_{abs}, is calculated by $\alpha_r/(\alpha_r + \alpha_b)$. Here, α_r represents the resonant absorption coefficient, while α_b signifies the background absorption coefficient.

The parameters that define the cooling efficiency of the sample include the mean fluorescence wavelength λ_f, the resonant absorption coefficient α_r, the external quantum efficiency η_{ext}, and the background absorption coefficient α_b. Fig.1(b) presents the absorption and fluorescence spectra of the Yb^{3+}:YAG crystal at 300 K. In the absorption spectrum, the region where the pump laser wavelength is longer than the mean fluorescence wavelength is referred to as the "cooling tail".It is crucial for the ASF cooling of the Yb^{3+}:YAG crystal.

2.2 Experimental setup

Fluorescence spectra were obtained using a laser with a wavelength of 914 nm to pump the samples, which were housed in a vacuum liquid nitrogen cryostat (JANIS VPF-100). The spectra were recorded with a calibrated spectrometer (Ocean Optics Maya2000 Pro-NIR) over a temperature range of 80K to 300K.

The mean fluorescence wavelength can be determined using the following equation(Melgaard, 2013):

$$\lambda_f = \frac{\int \lambda S(\lambda,T)\,d\lambda}{\int S(\lambda,T)\,d\lambda} \qquad \text{Eq.(2)}$$

where $S(\lambda,T)$ is the temperature-dependent fluorescence spectra of the sample.

The absorption spectra can be obtained from $S(\lambda,T)$using the McCumber relation(McCumber, 1964):

$$\alpha(\lambda,T) \propto \lambda^5 S(\lambda,T) e^{hc/\lambda k_B T} \quad \text{Eq.(3)}$$

wherek_B is the Boltzmann constant.$\alpha(\lambda,T)$is the temperature-dependent absorption spectra, and its absolute value can be obtained using the Lambert-Beer law: $I = I_0 e^{-\alpha L}$, where I and I_0 are the incident and attenuated light intensities, respectively, and L denotes the length of the sample.

LITMoS test is a standard technique used for characterizing laser cooling media. Fig. 2 illustrates the experimental setup, where a high-power tunable laser serves as the pumping source. The sample is enclosed in a high-finesse optical cavity, stabilized by two optical fibers (diameter 100 mm). A thermal camera (FLIR A300) is used for non-contact temperature measurements of the sample by monitoring pixel changes. The temperature change, denoted as ΔT, is correlated with the variation in pixel changes.The emitted fluorescence spectrum is captured to calculate the absorbed power using the integral $P_{abs} = k \int S(\lambda_P)\, d\lambda$, with k as a constant scaling factor.Cooling efficiency can be obtained by thermal load analysis:

$$\eta_c^{\exp} = K \cdot \Delta T / P_{\text{abs}} \quad \text{Eq.(4)}$$

where K is the thermal loading parameter.Consequently, the external quantum efficiency η_{ext} and the background absorption coefficient α_b can be determined by fitting Eq. (1) to the experimentally measured cooling efficiency η_c^{exp}.

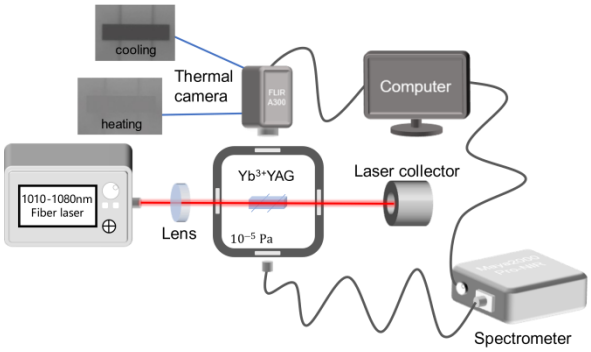

Figure 2: Experimental setup of the LITMoS.

3. RESULT

Spectra were collected from 4% Yb^{3+}:YAG crystals with dimensions of $2 \times 2 \times 10\ \text{mm}^3$. As displayed in Fig. 3(a), the fluorescence spectrum shows distinct peaks at 1030 nm and 1048 nm, corresponding to the transitions E3-E5 and E4-E5, respectively. The absorption spectrum as shown in Fig. 3(b) indicates that the absorption intensity of the crystal increases with temperature, with notable peaks around 970 nm, 1030 nm, and 1048 nm.Fig. 3(c) displays the mean fluorescence wavelengths at different temperatures, indicating a red-shift with decreasing temperature as electrons move to lower energy levels. The mean fluorescence wavelength in relation to temperature is linearly fitted with the equation $\lambda_f = -0.065 \cdot T + 1030.88\ \text{nm}$. What is more, we perform the LITMoS test, as shown in Fig. 3(d), result in an external quantum efficiency of 98.7% and a background absorption coefficient of $3.4 \times 10^{-4}\ \text{cm}^{-1}$, derived from the fitting procedure.

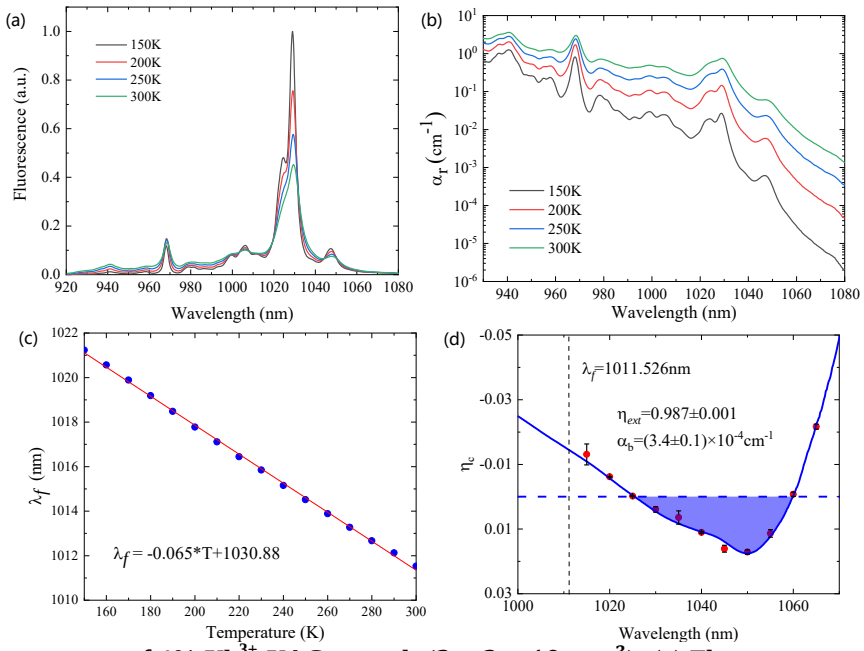

Figure 3: Cooling parameters of 4% Yb^{3+}:YAG crystals ($2 \times 2 \times 10$ mm^3): (a) Fluorescence spectra from 150K-300K. (b) Absorption spectra from 150K-300K. (c)The mean fluorescence wavelength versus the temperature, with the red solid line indicating the fitted curve. (d) Results of the LITMoS test,$\eta_{ext} = 0.987(\pm 0.001)$, $\alpha_b = 3.4(\pm 0.1) \times 10^{-4}$ cm^{-1} .

Compared to other Yb^{3+}-doped crystals used for laser cooling, such as Yb^{3+}:YLF and Yb^{3+}:LLF, Yb^{3+}:YAG crystals show a lower external quantum efficiency. This can be attributed to its higher refractive index, which impedes the emission of fluorescence photons. Additionally, the background absorption coefficient is affected by impurity ions present in the crystal, including Cu^{2+}, Fe^{3+}, and Co^{2+}. The presence of these impurities can create extra energy levels that absorb photon energy, resulting in non-radiative decay and the production of heat, both of which negatively impact the efficiency of the laser cooling process.

Considering the external quantum efficiencyand the background absorption coefficientas parameters independent of temperature(Melgaard et al., 2013), the cooling efficiency is plotted against both temperature and wavelength to form the "cooling window", as depicted in Fig. 4. In this representation, the blue area indicates regions of cooling, while the red area signifies heating. The temperature at which the cooling efficiency is zero represents the minimum achievable temperature (MAT). This temperature demarcates the boundary between cooling and heating zones, with the global minimum of MAT denoted as g-MAT. It is observed that the two cooling peaks within the cooling window at wavelengths of 1031.3 nm and 1047.8 nm align with the two resonance absorption peaks found in the "cooling tail". For the 4% Yb^{3+}:YAG crystal utilized in this study, g-MAT is estimated to be 231 K.

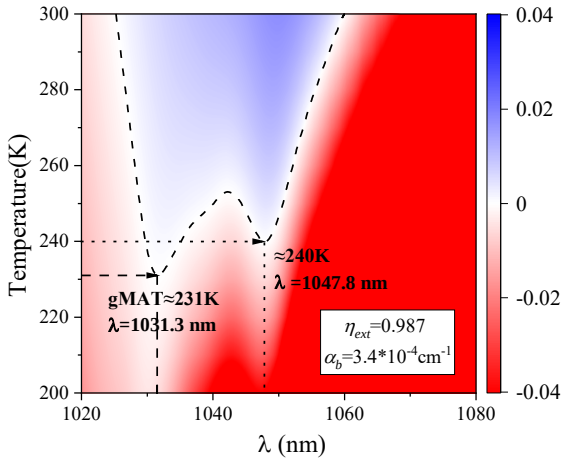

Figure 4: The cooling window of the 4% Yb^{3+}:YAG crystal with $\eta_{ext} = 0.987$, $\alpha_b = 3.4 \times 10^{-4}$ cm^{-1}. The dotted lines representing $\eta_c = 0$.

4. CONCLUSIONS

Using LITMoS test andcombining with spectrumofthe 4% Yb^{3+}:YAG crystal with dimensions of $2 \times 2 \times 10\ mm^3$, we obtain the cooling performance parameters of the sample: the mean fluorescence wavelength λ_f, the resonance absorption coefficient α_r, the external quantum efficiency η_{ext}, and the background absorption coefficient α_b. Using these parameters, we constructed the cooling window to gain an intuitive understanding of the cooling properties of the 4% Yb^{3+}:YAG crystal and get its g-MAT to be 231K. Our method is versatile and can be extended to study other laser-cooled crystals, such as Yb^{3+}:YLF and Yb^{3+}:LLF. Our results will serve as valuable references for the cooling processes of Yb^{3+}-doped crystals and for the advancement of radiation-balanced lasers.

ACKNOWLEDGEMENTS

This research was supported by the NationalNatural Science Foundation of China (Grant Nos. 11604100), the Special Financial Grant fromthe China Postdoctoral Science Foundation (Grant No. 2016T90346).

NOMENCLATURE

η_c	cooling efficiency	η_{ext}	external quantum efficiency
η_e	fluorescence escape efficiency	η_{abs}	absorption efficiency
λ_f	mean fluorescence wavelength (nm)	λ	wavelength (nm)
α_r	resonant absorption coefficient (cm^{-1})	α_b	background absorption coefficient (cm^{-1})
W_r	radiationdecay rate	W_{nr}	non-radiation decay rate
S	fluorescence spectra	α	absorption spectra
I	incidentlight intensity	I_0	attenuated light intensity
L	length of the sample	P_{abs}	absorbed power
η_c^{exp}	measured cooling efficiency	K	thermal loading parameter
k	constant scaling factor	T	temperature (K)
k_B	Boltzmann constant (1.3806×10^{-23} J/K)	ΔT	temperature change (K)

REFERENCES

Bowman, S.R., 1999. Lasers without internal heat generation. IEEE journal of quantum electronics, 35(1), 115-122.

Demirkhanyan, G.G., 2006. Intensities of inter-Stark transitions in YAG-Yb3+ crystals. Laser Physics, 16(7), 1054-1057.

Epstein, R.I., Buchwald, M.I., Edwards, B.C., et al., 1995. Observation of laser-induced fluorescent cooling of a solid. Nature, 377(6549), 500-503.

Lei, Y., Zhong, B., Yang, T., et al., 2022. Laser cooling of Yb3+:LuLiF4 crystal below cryogenic temperature to 121 K. Applied Physics Letters, 120(23).

McCumber, D., 1964. Einstein relations connecting broadband emission and absorption spectra. Physical Review, 136(4A), A954.

Melgaard, S.D., 2013. Cryogenic optical refrigeration: Laser cooling of solids below 123 K. The University of New Mexico.

Melgaard, S.D., Albrecht, A.R., Hehlen, M.P., et al., 2016. Solid-state optical refrigeration to sub-100 Kelvin regime. Scientific Reports, 6(1), 20380.

Melgaard, S.D., Seletskiy, D.V., Di Lieto, A., et al., 2013. Optical refrigeration to 119 K, below National Institute of Standards and Technology cryogenic temperature. Optics Letters, 38(9), 1588-1590.

Pringsheim, P., 1929. Zwei bemerkungen über den unterschied von lumineszenz-und temperaturstrahlung. Zeitschrift für Physik, 57, 739-746.

Sheik-Bahae, M., Epstein, R.I., 2007. Optical refrigeration. nature photonics, 1(12), 693-699.

Zhong, B., Lei, Y., Duan, X., et al., 2021. Optical refrigeration of the Yb3+-doped YAG crystal close to the thermoelectric cooling limit. Applied Physics Letters, 118(13).

DOI: 10.18462/iir.thermag.2024.0022

HIGH FREQUENCY MAGNETOCALORIC COOLING

Urban Tomc[(a)],Simon Nosan[(a)],Katja Klinar[(a)], Nada Petelin[(a)], Blaž Velkavrh[(a)], Katja Vozel[(a)], Jakob Perne[(a)], Simon Bogić[(a)], Andrej Kitanovski[(a)]

[(a)]University of Ljubljana, Faculty of Mechanical Engineering, Laboratory for Refrigeration and District Energy, Slovenia

Ljubljana, Slovenia, andrej.kitanovski@fs.uni-lj.si

ABSTRACT

Magnetocaloric cooling represents one of the most promising alternatives to vapour-compression. Despite that this technology has made substantial progress over last two decades, there are still unsolved challenges regarding the use of rare-earth materials, energy efficiency, and the competitive cost of potential future devices. State-of-the-art devices are based on the so-called Active Magnetic Regeneration, which is moderately efficient at low operating frequencies (up to 5 Hz). To achieve considerable cooling power and magnetic fields at such low frequencies, significant amounts of magnetocaloric and permanent magnet materials are required. A new research direction has emerged in recent years where researchers are trying to develop devices that operate efficiently at much higher frequencies (up to 50 Hz or more). We present a high-energy efficiency electro-permanent magnetic field source, which is able to oscillate relatively high magnetic fields without moving parts and at operating frequencies up to 50 Hz with energy efficiency above 80%.

Keywords: magnetic field source; magnetocaloric; refrigeration; energy conversion; energy recovery

1. INTRODUCTION

The global energy demand for refrigeration and air conditioning is growing rapidly (Coulomb et al., 2015) and could triple by 2050 (OECD/IEA, 2018) without major improvements in energy efficiency. Widely used vapour-compression suffers from environmental problems of refrigerants (McLinden et al., 2017 and Bell et al., 2019) and moderate energy efficiency (Domanski et al., 2014). Among the alternative refrigeration technologies (Brown and Domanski, 2014), solid-state caloric cooling, heat pumping and air conditioning are at the forefront of future substitutes for vapour-compression (Goetzler et al., 2016). Enormous research efforts in the last twenty years have resulted in much-improved knowledge on caloric materials (Moya et al., 2014 and Griffith et al., 2018) and numerous conceptual devices (Greco et al., 2019 and Kitanovski et al., 2015a), especially for magnetocaloric energy conversion (Qian et al., 2016). Despite proven examples of high-energy efficiency (Kitanovski et al., 2015b), going beyond conceptual devices requires a high degree of innovation in connection with considerable increases in power density (Kitanovski, 2020). This is directly related to a high operating frequency or, in other words, the ability to perform the greatest possible number of thermodynamic cycles per unit of time.

In addition to the requirements for new and improved magnetocaloric materials (MCMs) (Gottschall et al., 2019 and Zarkevich et al., 2018) and the reduced use of rare-earth materials (Skokov and Gutfleisch, 2018), future magnetocaloric devices will need to incorporate highly efficient and fast heat transfer principles (Wehmeyer et al., 2017) in a form of thermal control devices (thermal diodes and switches). These solutions are also needed for problems involving high viscous losses in hydraulics (Klinar and Kitanovski, 2020). An experimental study (Maier et al., 2020) presented an alternative solution to existing active magnetocaloric regeneration by utilizing thermal diodes in a form of active magnetocaloric heat pipes. They showed experimentally for the first time that it is possible to achieve an efficient heat transfer with an order higher power density and operating frequency than the state-of-the-art.

Finally, the magnetic field source (Figure 1), which is the heaviest and most expensive part of the magnetocaloric device (Teyber et al., 2018), must provide magnetic energy with the highest possible energy efficiency—preferably with no moving parts—and should offer the highest possible operating frequency. Apart from the efficient thermal control at high frequencies, the magnetic field source therefore represents an equally important element to be substantially improved and optimized by going far beyond the state-of-the-art with new approaches in the design concept and operation.

Most prototype magnetocaloric devices use assemblies based on rare-earth permanent magnets (PMs) (Kitanovski et al., 2015b and Kitanovski, 2020). The supply of the time-varying magnetic energy to a magnetocaloric material is usually provided via a motor and a gear drive, which heavily affect the energy efficiency of the device. Such magnet assemblies do not have capabilities for fast rotation required by the goal of very high power density. Until recently, research on magnetic field sources has focused mainly on the topography optimization of PM assemblies (Kitanovski et al., 2015b and Kitanovski, 2020). Few studies have reported the use of superconducting magnets (SMs) (Gimaev et al., 2019) for the characterization of magnetocaloric materials or magnetocaloric regenerators. For similar reasons, conventional electromagnetic field sources (EMs) (Bahl et al., 2008, Gao et al., 2006 and Elamalayil et al., 2015) were used. However, their exploitation in prototype devices is strongly restricted by excessive energy losses, substantial Joule (resistance) heating, and prohibitively slow time variation of the magnetic field.

A recent study on static EMs with magnetic energy recovery revealed its potential for application in magnetocaloric devices (Klinar et al., 2019). Another study demonstrated the successful combination of PMs and electric coils in static thermomagnetic power generation (Waske et al., 2019). By keeping this in mind, we made further research efforts to overcome most of the existing barriers in magnetic field sources for magnetic refrigeration: noise and vibrations related to moving parts, lack of time-variable control and fast switching of the magnetic field, limited energy efficiency, and large content of rare-earth materials. This was achieved by combining the best features of PMs and windings in an electro-permanent static magnetic field source (EPM) with magnetic energy recovery, which enables highly efficient operation at operating frequencies of an order higher than that of state-of-the-art.

Our primary hypothesis is that static EPMs with magnetic energy recovery can successfully replace moving PM assemblies in magnetic refrigeration or heat pump applications. The main objective of this paper is to report on a numerical and experimental study in which such EPM was designed, built and tested. An extensive numerical investigation of the proposed design was carried out in terms of various geometrical and operating parameters. The design is optimized for the minimum mass of the iron yoke and PM, since they significantly affect the cost of the magnetic field source. One of the variations of the design was built and experimentally evaluated. An energy efficiency of such magnets of over 80% and operation with frequencies up to 50 Hz is demonstrated. To clearly represent the characteristics of the EPM itself, as well as to provide a common basis for any kind of magnetocaloric system, we avoided any consideration of the magnetocaloric thermodynamic cycles, related heat transfer or fluid flow principles.

2. EPM FOR MAGNETOCALORIC REFRIGERATION

The energy efficiency and slow magnetization of the conventional EM can be improved by magnetic energy recovery (Klinar et al., 2019). For the same magnetic flux density, a further increase in the energy efficiency can be provided by increasing the mass of windings, which is undesired. On the other hand, the introduction of a PM into the EM assembly can decrease the electric current required for magnetization. Consequently, the energy efficiency of the magnetic field source can be increased due to reduced Joule heating.

Figure 1 shows the operation of equivalent PM-, EM- and EPM-based magnetic assemblies. Here, the magnetic flux inside air gaps containing a magnetocaloric material changes with the rotary motion of the magnetic assembly (PM) or by switching the electric current through the windings (EM and EPM). Processes 1 and 2 in Figure 1 denote the alternating magnetisation/demagnetisation in two air gaps (the location of the magnetocaloric regenerator). In the EPM, the air gaps are magnetised/demagnetised (B_{max}/B_{min}) when the electric current is $I=I_{max}/2$, which corresponds to the design feature of the EPM assembly in Figure 1. However, the magnetic flux density in both air gaps is B_{aver} when $I=0$ A (Figure 1 bottom EPM).

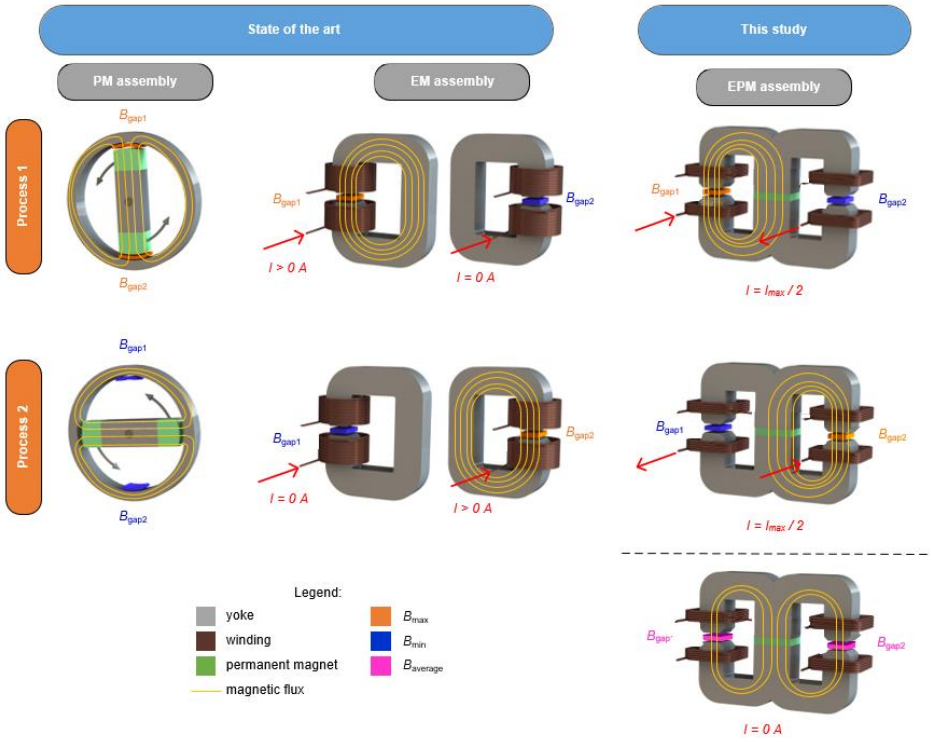

Figure 1. Example operation of equivalent magnetic assemblies. Examples show magnetic field (*B*) inside two air gaps (i.e., gap_1 and gap_2)in permanent magnet (PM), electromagnetic (EM), and electro-permanent magnet (EPM) assemblies. Two processes show the different situations of magnetized/demagnetized air gaps, while EPM also has third option, where both air gaps have average magnetic field. The MCM inside the air gap is only shown for clearer understanding of magnetic cycling and was not included in this study. (adapted from Tomc et al., 2022)

The proposed EPM concept (Figure 2a and 2b) consists of a two-part iron yoke with three iron pillars, of which the two outer pillars have an air gap. Two windings are positioned near each air gap, which reduces the fringing flux. The PM is embedded in the central iron pillar. Figure 2c shows the electric circuit to control the oscilation of the EPM with magnetic energy recovery.

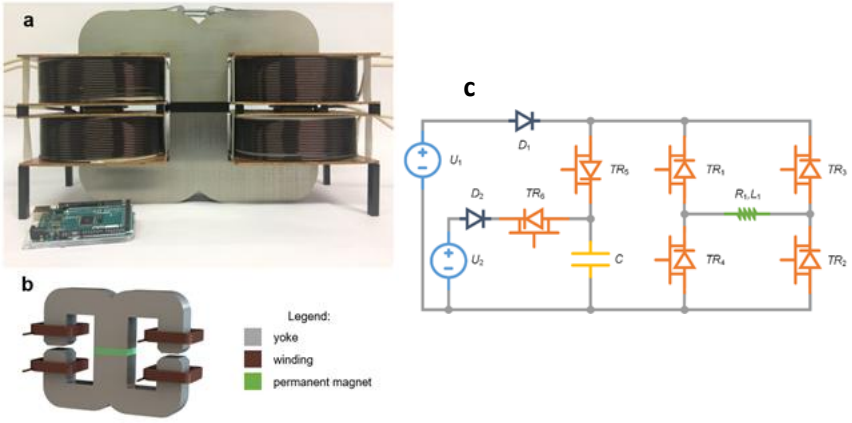

Figure 2. Proposed EPM design. a) Constructed proof-of-concept (Arduino Mega 2560 for scale). B) 3D-model of the proposed EPM design. c) Schematics of the electric circuit. The electric circuit controls the operation of the electro-permanent magnet EPM (denoted with resistance *R* and inductance *L*) with magnetic energy recovery (*TR* – transistor, *D* – diode, *C* – capacitor, *U* – voltage source). (adapted from Tomc et al., 2022)

2.1 Theoretical methods

The theoretical approach consisted of four main steps as follows: basic design of concepts, analytical modelling, numerical simulations and experimental validation of our EPM concept. The numerical simulations were carried out with varying magnetic flux between 0 T and 1 T inside the air gap. The iron

yoke was considered to be a laminated sheet M270 (Voestalpine, 2018) with a stacking factor of 0.95. The copper windings had the cross-sections of 55x50 mm. The PM properties were provided by Bakker Magnetics for neodymium sintered magnets (Bakker Magnetics, 2020), grade N45. The EPM design concept was first analytically evaluated using a Python-based model. The EPM concept was described using an equivalent reluctance circuit, which included the reluctances of the air gaps, PM and yoke segments. The PM and windings were considered to be magnetic flux sources. Through multi-parametric analysis for different dimensions of PM and yoke, different geometries that achieved targeted magnetic flux density in the air gap were obtained. Among these, the design with the minimum total mass of the magnetic structure was further numerically analysed. The numerical investigation was performed with the FEM program ANSYS Maxwell 3D. The aim of the numerical simulation was to obtain the dependence of the magnetic flux density in the air gap related to the ampere-turns of the EM. The geometry of the EPM was confirmed using the obtained dependency after the following two conditions were met. The first was that the contributions of magnetic flux density in the air gap due to the PM and EM were equal. The second was that the total magnetic flux density in the air gap reached the target value (i.e. B_{min}<0.005 T, and B_{max}=1T). The magnetic energy recovery was assumed to be 0.918 (experimentally determined). For more detail numerical procedures please refer to the publication Tomc et al. (2022).

2.2 Experimental methods

We constructed our EPM concept (Figure 2a-b) and control circuit (Figure 2c) as follows. The yoke was made of M270-35A(Voestalpine, 2018) backlack sheet metal. We used a Bakker Magnetics N45-grade PM. The four windings with 4×240 turns of 3 mm in diameter wire were powered via an adjustable DC power supply (Velleman LABPS3020). To achieve magnetic field of 1 T inside the air gap, an electric current of approximately 3.75 A had to flow through each winding. This contributed to 0.5 T, while the other 0.5 T was contributed by PM, cumulatively achieving 1 T inside the air gap. To achieve 0 T inside the air gap, the electric current of approximately 3.75 A had to flow in counter direction through windings, which opposed the 0.5 T provided by PM. The time variation in magnetic flux density inside the gap was regulated by transistors, which were controlled by an Arduino Mega. The measurements were conducted by a Hall probe (Magnet-Physik Gauss-/Teslameter FH 54) measuring the magnetic flux density in the air gap, current clamps (Chauvin Arnoux AC/DC 10 A/1 V 100 A/1 V E3N) measuring the electric current through the EM winding, and a Keysight EDUX1002A oscilloscope. The experiments were repeated at frequencies of 1, 2.5, 5, 10, 15, 25 and 50 Hz. The temperature of the EPM operation was measured using FLIR A6750sc infrared camera with an absolute accuracy of ±2% of the reading, equipped with the lens of 50 mm focal length and 640 × 512 pixel IR sensor with a spatial resolution of 15 μm. The yoke and windings were coated with a thin layer of LabIR paint for standard applications with an emissivity of 0.92.

2.3 Equations for magnetic energy recovery, power input and energy efficiency

Duetomagneticenergyrecovery,themagneticstructurenotonlyachievesahigherefficiencyinoperationbutalsoenablesfastmagnetisationanddemagnetisationandthusoperationathigheroperatingfrequencies (Klinar et al., 2019).The energy efficiency of theactualmagneticenergyrecovery was calculated by the following relation:

$$\boldsymbol{\eta}_{\text{recovery}} = \frac{\boldsymbol{E}_{\text{C,full}} - \boldsymbol{E}_{\text{C,par}}}{\boldsymbol{E}_{\text{C,full}}} \qquad \text{Eq. (1)}$$

where the energy of the fully charged capacitor is:

$$\boldsymbol{E}_{\text{C,full}} = \frac{\boldsymbol{C} \cdot \boldsymbol{U}_{\text{C,full}}^{\boldsymbol{2}}}{\boldsymbol{2}} \qquad \text{Eq. (2)}$$

and the energy of the partially charged capacitor is:

$$\boldsymbol{E}_{\text{C,par}} = \frac{\boldsymbol{C} \cdot \boldsymbol{U}_{\text{C,par}}^{\boldsymbol{2}}}{\boldsymbol{2}} \qquad \text{Eq. (3)}$$

$U_{C,full}$stands for the capacitor voltage (V) at full charge, $U_{C,par}$ is the capacitor voltage (V) at partial charge, and C stands for the capacitance of the capacitor and in our case is 100 μF. The energy of the partially charged capacitor $E_{C,par}$ actually represents the energy losses that occur during the energy transfer between windings and the capacitor during the (de)magnetisation process. These losses account for losses in electronic circuit, Joule heating, hysteresis losses and eddy currents.

Taking into account Eq. (2) and Eq. (3), the efficiency of the magnetic energy recovery can be defined as:

$$\boldsymbol{\eta}_{\text{recovery}} = \frac{\boldsymbol{U}^{\mathbf{2}}_{\text{C,full}} - \boldsymbol{U}^{\mathbf{2}}_{\text{C,par}}}{\boldsymbol{U}^{\mathbf{2}}_{\text{C,full}}} \quad \text{Eq. (4)}$$

Inthisway,themagneticenergyrecoverywasexperimentallydeterminedtobe0.918 onaverage and was implemented in numerical analyses.

Furthermore, the EPM total energy loss E_{EPM} during one cycle of operation may be determined by:

$$\boldsymbol{E}_{\text{EPM}} = \boldsymbol{E}_{\text{Joule}} + \mathbf{2} \cdot \boldsymbol{E}_{\text{C,par}} \quad \text{Eq. (5)}$$

E_{Joule} contains the Joule (resistance) losses in the windings during both constant magnetic flux density phases (B_{max} and B_{min}):

$$\boldsymbol{E}_{\text{Joule}} = \boldsymbol{R}_{\text{windings}} \cdot \boldsymbol{I}^{\mathbf{2}} \cdot \mathbf{2} \cdot \boldsymbol{t}_{\text{B,cons}} \quad \text{Eq. (6)}$$

where:

- R_{windings} is the electric resistance of the windings (Ω)

- I is the electric current through the windings (A)

- $t_{\text{B,cons}}$ is the time interval of the constant magnetic flux density phase (s)

Considering Eq. (5), the average quasi-steady-state EPM power input P_{EPM} can be expressed as:

$$\boldsymbol{P}_{\text{EPM}} = \left(\boldsymbol{E}_{\text{Joule}} + \mathbf{2} \cdot \boldsymbol{E}_{\text{C,par}}\right) \cdot \boldsymbol{f} \quad \text{Eq. (7)}$$

where the operating frequency f is:

$$\boldsymbol{f} = \left(\mathbf{2} \cdot \boldsymbol{t}_{\text{de/mag}} + \mathbf{2} \cdot \boldsymbol{t}_{\text{B,cons}}\right)^{-\mathbf{1}} \quad \text{Eq. (8)}$$

and $t_{\text{de/mag}}$ is the time interval of the de/magnetisation phase (in our case 5 ms each).

Finally, the EPM energy efficiency η can be calculated by the following equation:

$$\boldsymbol{\eta} = \frac{\boldsymbol{E}_{\text{gap}}}{\boldsymbol{E}_{\text{gap}} + \boldsymbol{E}_{\text{EPM}}} \quad \text{Eq. (9)}$$

where E_{gap} is the magnetic energy in the air gap:

$$\boldsymbol{E}_{\text{gap}} = \frac{\boldsymbol{B}_{\text{max}}{}^{\mathbf{2}} \cdot \boldsymbol{h}_{\text{gap}} \cdot \boldsymbol{l}_{\text{gap}} \cdot \boldsymbol{w}_{\text{gap}}}{\mathbf{2} \cdot \boldsymbol{\mu}_{\mathbf{0}}} \quad \text{Eq. (10)}$$

where:

- h_{gap} is the air gap height (m)

- l_{gap} is the air gap length (m)

- w_{gap} is the air gap width (m)

- μ_0 is the permeability of free space ($4\pi \times 10^{-7}$ H m^{-1}).

2.4 Estimation of energy efficiency of state-of-the-art PM assemblies

Table 1 presents estimations of energy efficiencies of six most prominent rotary PM assemblies utilized in magnetocaloric refrigeration prototypes. The efficiencies of the induction and DC motors were assumed to be 0.81 and 0.85, respectively, and were accounted for in cases where only torque measurements are reported. Torque measurements account for PM rotation, as well as all the other mechanical losses, such as gear, belt

drive and bearings. However, torque measurements do not account for the losses within electric motors. Therefore, the induction motor efficiency was accounted for in energy efficiency η estimation in Nakashima et al. (2021), while DC motor efficiency was accounted for in Aprea et al. (2014, 2016) and Eriksen et al. (2015). The rest of the research papers report on the plug-in power delivered to the magnet assemblies, therefore it is assumed that all the losses were accounted for. The two frequencies are defined: f_{AMR} denotes the operating frequency regarding the magnetocaloric thermodynamic cycle and f_{shaft} denotes operating frequency of the PM shaft itself. P_{gap} denotes the magnetic power inside the air gap and may be calculated as:

$$\boldsymbol{P}_{\text{gap}} = \boldsymbol{E}_{\text{gap}} \cdot \boldsymbol{f}_{\mathbf{shaft}} \quad \text{Eq. (11)}$$

where E_{gap} is the magnetic energy (Eq. (10)) regarding all the air gaps within a given prototype.

P_{input} represents the power input to rotate PMs within the assembly. Where only the torque was reported, P_{input} was calculated according to the next equation:

$$\boldsymbol{P}_{\text{input}} = \frac{\mathbf{2} \cdot \boldsymbol{\pi} \cdot \boldsymbol{f}_{\mathbf{shaft}} \cdot \boldsymbol{\tau}}{\boldsymbol{\eta}_{\mathbf{mot}}} \quad \text{Eq. (12)}$$

where τ is the reported measured torque on the PM assembly‘s shaft, while the η_{mot} is the electric motor efficiency.

Finally, the PM assembly energy efficiency is calculated as:

$$\boldsymbol{\eta} = \frac{\boldsymbol{P}_{\text{gap}}}{\boldsymbol{P}_{\text{gap}} + \boldsymbol{P}_{\text{input}}} \quad \text{Eq. (13)}$$

Table 1. Overview of estimated energy efficiencies η for state-of-the-art rotary PM assemblies.

Reference	Type of PM	Available data	τ (Nm)	f_{AMR} (Hz)	f_{shaft} (Hz)	P_{gap} (W)	P_{input} (W)	η (-)
Okamura *et al.* (2007)	Rotating two pole assembly	Plug-in power	/	0.42	0.21	66.8	150.0	**0.308**
Tura and Rowe (2007)	Rotary two concentric Halbach cylinders	Plug-in power	/	2.00	2.00	78.0	45.5	**0.632**
			/	3.00	3.00	117.0	64.1	**0.646**
			/	4.00	4.00	156.0	83.4	**0.652**
Aprea *et al.* (2014, 2016)	Rotating two pole assembly	Torque	19	0.38	0.19	91.5	37.7	**0.708**
			19	0.46	0.23	110.7	45.6	**0.708**
			19	0.56	0.28	134.8	55.5	**0.708**
			19	1.08	0.54	260.0	107.1	**0.708**
			19	1.79	0.90	430.9	177.5	**0.708**
Eriksen *et al.* (2015)	Rotating two pole assembly	Torque	/	0.61	0.31	16.4	10.4	**0.612**
Lozano *et al.* (2016)	Rotating two pole assembly	Plug-in power	/	0.40	0.20	6.0	87.6	**0.064**
			/	0.80	0.40	11.9	100.3	**0.106**
			/	1.40	0.70	20.8	145.0	**0.126**
Nakashima *et al.* (2021)	Rotating two pole assembly	Torque	2.83	0.50	0.25	5.7	6.1	**0.483**
			2.23	0.75	0.38	8.6	7.3	**0.542**
			1.93	1.00	0.50	11.5	8.4	**0.578**

2.5 Results

We demonstrated that such an EPM can operate with high energy efficiency, especially at higher operating frequencies (Figure 3-left). For example, at operating frequency of 10 Hz the EPM achieved energy efficiency of 64.7%, while at 50 Hz the energy efficiency increased up to 82.9%. Additionally, Figure 3-left shows also energy efficiencies of the state-of-the-art rotary PM assemblies in comparison to our static EPM. Some of the authors show the whole energy input to rotate their magnet assemblies (considering also the electric motor and gear efficiencies). Others show measurements of the torque at the shaft of the drive system, which is a completely standard procedure. However, in those cases we had to account for the maximum electric motor efficiency, since the actual efficiencies are not known. In reality the electric motor efficiency highly depends on the mechanical load. In other words, if the electric motor is not specifically optimized for the given mechanical load of the magnet assembly, its efficiency may drastically deteriorate, which in turn may profoundly decrease the energy efficiency of the magnet assembly. On the other hand, it is known (Bjørk et al., 2011) that mechanical load of the PM assembly increases when the MC material (magnetocaloric regenerator) is present in the air gap, especially if the temperature of the MC material is in a ferromagnetic phase. Where it was possible, we accounted for energy input data, which was measured without the MC material present in the air gap or at least when the MC material was at room temperature (in paramagnetic phase).

Another important operation parameter of the EPM is also the power input. In Figure 3-right we show our EPM‘s power input in relation to the operating frequency. As it is clear, the power input increases with higher operating frequency, which is expected due to the larger number of magnetic cycles per unit of time. However, on account of the high energy efficiency at higher operating frequencies, the EPM‘s power input increases proportionally to the operating frequency with the proportionality constant lower than 1. For example, the energy input at 1 Hz is about 18.4 W. Whereas, at operating frequency of 50 Hz the power input is only about 43.4 W and not fifty times larger than at 1 Hz.

In spite of the high energy efficiency, especially at higher operating frequencies, there remains the question of additional heating of the EPM due to Joule heating, hysteresis losses and eddy currents. In this manner we conducted temperature measurements of EPM during thermal steady state operation at different operating frequencies up to 50 Hz. Figure 4 shows measured temperature difference above ambient temperature of EPM‘s windings and yoke under natural cooling conditions and operating at thermal steady state and operating frequencies up to 50 Hz. It is clear that the windings operated at approximately constant temperature difference of 5-6 K above ambient temperature at all the operating frequencies. This may be contributed to the Joule heating, especially during the constant electric current flow through windings (constant B_{min} and B_{max}). On the other hand, the yoke temperature increased from about 2 K (5 Hz) to about 10 K (50 Hz) above ambient temperature, which may be contributed to the increasing eddy currents and hysteresis losses in yoke‘s metal sheets with increasing operating frequency.

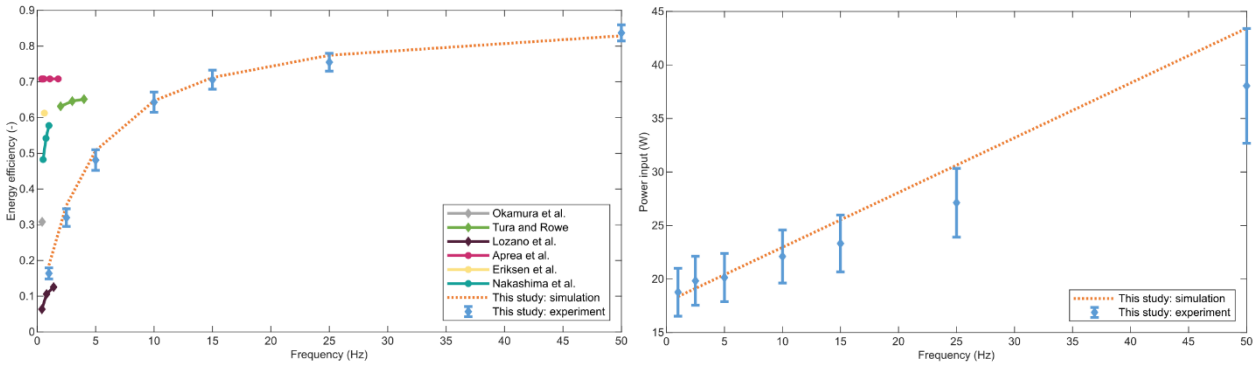

Figure 3. left: EPM energy efficiency vs. operating frequency compared to the state-of-the-art. Validation of the simulated energy efficiencies by energy efficiency measurement of the EPM (this study); additional comparison of energy efficiencies of state-of-the-art rotary PM assemblies (diamond – actual energy efficiency, circle – estimated energy efficiency). right: EPM power input vs. operating frequency. Validation of the simulated power input by power input measurement of the EPM. (adapted from Tomc et al., 2022)

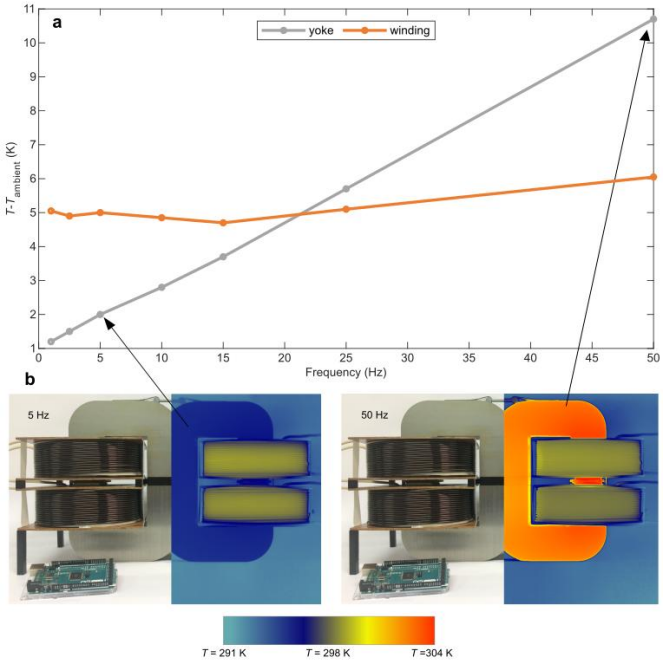

Figure 4. Temperatures of yoke and windings during EPM operation. a) Diagram of measured temperature difference between yoke/windings and ambient of EPM operating at different operating frequencies. b) Photographs and IR camera images of our experimental EPM. IR camera image shows the temperature distribution during operation at 5 and 50 Hz in a thermal-steady-state.

3. CONCLUSIONS

We have demonstrated that static electro-permanent magnets with magnetic energy recovery have the potential to replace moving PM assemblies in future magnetocaloric devices. We found that the reduction in the electric current magnitude can be achieved by analysing the equivalent magnetic circuits of the magnetic assemblies in connection with the design of the windings and the PMs. By experimentally testing our EPM**,** we demonstrated that energy efficiencies at higher operating frequencies can be increased (over 80% at 50 Hz), which is an important finding, especially for future high-power-density and high-frequency magnetocaloric devices utilizing highly efficient and fast heat transfer principles with thermal switches or thermal diodes. Another important improvement concerns the reduction in Joule heating, as this heating is one of the main problems of electrically generated magnetic fields. By combining EM with PM in one EPM, the electric current required for the same magnetic field was halved compared to only EM concept, since half of the magnetic flux is contributed by PM. In turn, this reduced the amount of Joule heating of the windings (it is proportional to I^2). The developed EPM allows operation with no moving parts, a high power density due to the high operating frequency, and the reduced use of rare-earth materials. Although the temperature in the experimentally evaluated solution is relatively low, it still represents an undesirable heat source for a magnetocaloric material. By implementing other design features for windings or the iron yoke, the problem of heat gains can be reduced. This aim can be further achieved by active or passive cooling, by introducing extended surfaces or heat pipes, and, most importantly, by the further reduction in the electric current magnitude. At low frequencies of operation, which are common for moving PMs in the state-of-the-art, the low energy efficiency of the EPM restricts its application. However, the low frequency is not desired due to the very low power density, which restricts the realistic use of present magnetocaloric devices. By implementing the above mentioned changes and by considering a high operating frequency (and thus high power density) such EPMs allow for miniaturization, making them a viable option for future compact magnetocaloric devices.

ACKNOWLEDGEMENTS

The authors acknowledge the financial support of the Slovenian Research Agency for the projects Multicaloric cooling (No. J2-9253), MagBoost: Magnetocaloric booster micro-heat pump for district heating system (No. L2-2610) and the research core fundings (No. P2-0223 and P2-0422). Furthermore, the authors also acknowledge the financial support from the transnational consortium M-ERA.NET for the project Cool

BatMan: Battery Thermal Management System Based on High Power Density Digital Microfluidic Magnetocaloric Cooling (No. 9400).

REFERENCES

Aprea, C., Greco, A., Maiorino, A., Mastrullo, R., Tura, A., 2014. Initial experimental results from a rotary permanent magnet magnetic refrigerator. *Int. J. Refrig*. 43, 111–122.

Aprea, C., Greco, A., Maiorino, A., Masselli, C., 2016. The energy performances of a rotary permanent magnet magnetic refrigerator. *Int. J. Refrig.* 61.

Bahl, C. R. H., Petersen, T. F., Pryds, N., Smith, A., 2008. A versatile magnetic refrigeration test device. *Rev. Sci. Instrum.* 79, 093906.

Bakker Magnetics, 2020. Neodyum sintered–standard grade datasheet. Accessed in May 2020. https://bakkermagnetics.com/en/magnetic-technology-assemblies/#downloads.

Bell, I. H., Domanski, P. A., McLinden, M. O. & Linteris, G. T., 2019. The hunt for nonflammable refrigerant blends to replace R-134a. *Int. J. Refrig.* 104, 484–495.

Bjørk, R., Bahl, C. R. H., Smith, A., Pryds, N., 2011. Improving magnet designs with high and low field regions. *IEEE Trans. Magn*. 47, 1687–1692.

Brown, S., Domanski, P. A., 2014 Review of alternative cooling technologies. *Appl. Therm. Eng.* 64, 252–262.

Coulomb, D., Dupont, J.-L. & Pichard, A., 2015. *The Role of Refrigeration in the Economy* (International Institute of Refrigeration).

Domanski, P. A., Steven Brown, J., Heo, J., Wojtusiak, J. & McLinden, M. O., 2014. A thermodynamic analysis of refrigerants: performance limits of the vapor compression cycle. *Int. J. Refrig.* 38, 71–79.

Elamalayil Soman, D. *et al.,* 2015. Development of power electronics based test platform for characterization and testing of magnetocaloric materials. *Adv. Electr. Eng.* 2015, 1–7.

Eriksen, D. et al., 2015. Design and experimental tests of a rotary active magnetic regenerator prototype. *Int. J. Refrig*. 58, 14–21.

Gao, Q. *et al.,* 2006. Experimental investigation on refrigeration performance of a reciprocating active magnetic regenerator of room temperature magnetic refrigeration. *Int. J. Refrig.* 29, 1274–1285.

Gimaev, R. *et al.,* 2019. Review on magnetic refrigeration devices based on HTSC materials. *Int. J. Refrig.* 100, 1–12.

Goetzler, W., Guernsey, M., Young, J., Fuhrman, J. & Abdelaziz, O., 2016. *The Future of Air Conditioning for Buildings: Executive Summary* (U.S. Department of Energy, Office of Energy Efficiency and Renewable Energy, Building Technologies Office).

Gottschall, T. *et al.,* 2019. Magnetic refrigeration: making a cool choice: the materials library of magnetic refrigeration (Adv. Energy Mater. 34/2019). *Adv. Energy Mater.* 9, 1970130.

Greco, A., Aprea, C., Maiorino, A., Masselli, C., 2019. A review of the state of the art of solid-state caloric cooling processes at room-temperature before 2019. *Int. J. Refrig.* 106, 66–88.

Griffith, L. D., Mudryk, Y., Slaughter, J., Pecharsky, V. K., 2018. Material-based figure of merit for caloric materials. *J. Appl. Phys.* 123, 034902.

International Energy Agency, 2018. *The Future of Cooling* (OECD/IEA).

Kitanovski, A., Plaznik, U., Tomc, U., Poredoš, A., 2015a. Present and future caloric refrigeration and heat-pump technologies. *Int. J. Refrig.* 57, 288–298.

Kitanovski, A.*, Tušek, J., Tomc, U., Plaznik, U., Ožbolt, M., Poredoš, A.,* 2015b. *Magnetocaloric Energy Conversion* (Springer).

Kitanovski, A., 2020. Energy applications of magnetocaloric materials. *Adv. Energy Mater.* 10, 1903741.

Klinar, K., Tomc, U., Jelenc, B., Nosan, S., Kitanovski, A., 2019. New frontiers in magnetic refrigeration with high oscillation energy-efficient electromagnets. *Appl. Energy* 236, 1062–1077.

Klinar, K., Kitanovski, A., 2020. Thermal control elements for caloric energy conversion. *Renew. Sustain. Energy Rev.* 118, 109571.

Lozano, J. A. et al., 2016. Development of a novel rotary magnetic refrigerator. *Int. J. Refrig.* 68, 187–197.

Maier, L. M. *et al.,* 2020. Active magnetocaloric heat pipes provide enhanced specific power of caloric refrigeration. *Commun Phys 3*, 186.

McLinden, M. O., Brown, J. S., Brignoli, R., Kazakov, A. F. & Domanski, P. A., 2017. Limited options for low-global-warming-potential refrigerants. *Nat. Commun.* 8, 14476–14476.

Moya, X., Kar-Narayan, S. & Mathur, N. D., 2014. Caloric materials near ferroic phase transitions. *Nat. Mater.* 13, 439–450.

Nakashima, A. T. D. et al., 2021. A Magnetic Wine Cooler Prototype. *Int. J. Refrig*. 122, 110–121.

Okamura, T., Yamada, K., Hirano, N., Nagaya, S., 2007. Improvement of 100w class room temperature magnetic refrigerator. In *Proceedings of the 2nd International Conference of Magnetic Refrigeration at Room Temperature* 377–382.

Qian, S. *et al.,* 2016. Not-in-kind cooling technologies: a quantitative comparison of refrigerants and system performance. *Int. J. Refrig.* 62, 177–192.

Skokov, K. P., Gutfleisch, O., 2018. Heavy rare earth free, free rare earth and rare earth free magnets-vision and reality. *Scr. Mater.* 154, 289–294.

Teyber, R., Trevizoli, P. V., Christiaanse, T. V., Govindappa, P., Rowe, A., 2018. Topology optimization of reduced rare-earth permanent magnet arrays with finite coercivity. *J. Appl. Phys.* 123, 193903.

Tomc, U., Nosan, S., Klinar, K. Kitanovski, A., 2022. Towards powerful magnetocaloric devices with static electro-permanent magnets, Journal of Advanced Research.

Tura, A., Rowe, A., 2007. Design and testing of a permanent magnet magnetic refrigerator. In *Proceedings of the Second International Conference on Magnetic Refrigeration at Room Temperature* 363–370.

Voestalpine, 2018. Isovac 270-35 A datasheet. Accessed in May 2020. https://www.voestalpine.com/division_stahl/content/download/33125/351203/file/DB_isovac_270-35A_E_280715.pdf.

Waske, A. *et al.,* 2019. Energy harvesting near room temperature using a thermomagnetic generator with a pretzel-like magnetic flux topology. *Nat. Energy* 4, 68–74.

Wehmeyer, G., Yabuki, T., Monachon, C., Wu, J., Dames, C., 2017. Thermal diodes, regulators, and switches: physical mechanisms and potential applications. *Appl. Phys. Rev.* 4, 041304.

Zarkevich, N. A., Johnson, D. D., Pecharsky, V. K., 2018. High-throughput search for caloric materials: the CaloriCool approach. *J. Phys. D* 51, 024002.

DOI: 10.18462/iir.thermag.2024.0023

PROGRESS ON POWER ELECTRONICS FOR ELECTROCALORIC HEAT PUMP SYSTEMS

Stefan Mönch[a,b], Richard Reiner[a], Michael Basler[a], Kareem Mansour[a], Daniel Grieshaber[a], Patrick Waltereit[a], Rüdiger Quay[a,c], Kilian Bartholomé[d]

[a] Fraunhofer Institute for Applied Solid State Physics (IAF)
Freiburg, 79110, Germany, stefan.moench@iaf.fraunhofer.de

[b] University of Stuttgart, Institute of Electrical Energy Conversion (IEW), Stuttgart, 70569, Germany

[c] Albert Ludwig University of Freiburg, Department for Sustainable Systems Engineering (INATECH)
Freiburg, 79110, Germany

[d] Fraunhofer Institute for Physical Measurement Techniques (IPM)
Freiburg, 79110, Germany

ABSTRACT

This work gives an overview on power electronics for charging and discharging electrocaloric capacitors, which aim to increase the system coefficient of performance (COP) of electrocaloric heat pumps towards the higher material performance limit. The electrical charging efficiency (which is either characterized for electrocaloric capacitors, or often only for ideal capacitive loads) is reviewed for resonant-circuits (up to 70%), two-level half-bridge converters (around 99.2%) and multi-level or partial-power processing converters (up to 99.75%, power-stage only, without control, gate drive and sensing losses). Alternative stepwise capacitor charging circuits with up to 240 levels and up to 95% electrical efficiency are also reviewed. The importance of high electrical charging efficiency is discussed. While the work focuses mainly on electrocaloric ceramics, which often require ultra-high external electrical charging efficiencies, electrocaloric polymers (with different permittivity and dissipation factor characteristics) are also discussed. Efficient power electronics contributes to solid-state, emission-free and efficient electrocaloric heat pumps.

Keywords: Refrigeration, COP, energy efficiency, heat pumps, electrocalorics, power electronics, converters

1. INTRODUCTION

Electrocaloric cooling or heating is an emerging solution for emission-free energy conversion with high efficiency, potentially outperforming vapor compression systems [1]. Several electrocaloric materials [2–4] with material coefficient of performance over 80% of the Carnot-limit have been demonstrated and calculated [5–9]. However, the system coefficient of performance (COP) of actual prototypes (examples and reviews in [10–16]) is additionally limited by external losses from the electrical charging circuit and control system [5, 17], such that state-of-the-art electrocaloric systems (as of early 2024) have not yet achieved competitive high system COPs.

Sec. 2 reviews the importance of efficient electrical energy recovery during charging/discharging of electrocaloric capacitors, which are essential components of electrocaloric heat pump systems; in additional to the electrocaloric capacitors and materials. Sec. 3 reviews published power electronics, which was designed for efficient electrocaloric capacitor charging, focusing of the works by Fraunhofer IAF during the Fraunhofer lighthouse project ElKaWe until early 2024, and including so far unpublished circuits. Also, the application of the converters to actual electrocaloric capacitors or electrocaloric heat pump systems are reviewed. Sec. 4 concludes.

2. ELECTROCALORIC MATERIAL AND SYSTEM COEFFICIENT OF PERFORMANCE

Figure 1 illustrates a simplified electrocaloric heat pump system from the perspective of the driving and external power electronics: The power electronics (for example a two-level half-bridge converter or resonant circuit) charges and discharges the electrocaloric capacitive load, which is often build as multilayer ceramic capacitors

(MLCCs) [18] that contain electrocaloric dielectric materials. Figure 1 visualizes two parts of electrocaloric components in an electrical series connection, where the midpoint is driven by the power electronics. This configuration (also used e.g. in [19–21]) enables to transfer energy from the one to the other part, which minimizes the required external energy buffers (for example by non-electrocaloric dc-link capacitors). The electrocaloric effect [22], an almost fully reversible temperature change of below 1 K up to over 5.5 K [4] (ceramic) or even beyond 10 K [23] (polymers) in the electrocaloric material, is caused by the change of electrical field in the material, which is generated by applying a varying voltage to the MLCCs. By separating the heating and cooling phases, a heat pump system can be created. Figure 1 does not show this required thermal system. From literature, different approaches for such thermal system approaches are known, for example using solid-solid (e.g. [24, 25]), solid-liquid (e.g. [26–32]), or solid-liquid/vapor (electrocaloric heat-pipe [14]) thermal control systems. The challenge is to control the heat flow from the electrocaloric component to the hot and cold site by thermal control devices [33], and to ensure the heat flow in the components [34, 35] does not limit the system frequency or power.

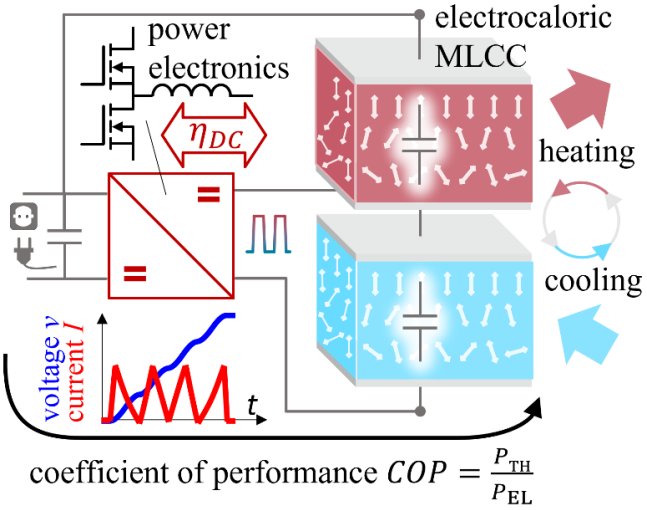

Figure 1: Simplified electrocaloric heat pump system focusing on electronics (thermal system not shown).

2.1. Importance of electrical charging efficiency for high system coefficient of performance

From thermal cycle analysis (see e.g. [6, 7, 12, 36–38]), the best-case relative system coefficient of performance $COP_{\mathrm{R,SYS}}$ can be estimated as

$$COP_{\mathrm{R,SYS}} = \begin{cases} \dfrac{1}{1 + 4\left(\dfrac{\varepsilon_{\mathrm{TR}} T E_{\mathrm{MAX}}^2}{\rho c_{\mathrm{P}} \Delta T_{\mathrm{AD,MAX}}}\right)\left(\dfrac{\pi}{4} DF_{\mathrm{TR}} + (1 - \eta_{\mathrm{DC}})\right)}, & \text{Carnot-like cycle for } T_{H-C} = \tfrac{1}{2}\Delta T_{\mathrm{AD,MAX}} \\ \dfrac{1}{1 + 1\left(\dfrac{\varepsilon_{\mathrm{TR}} T E_{\mathrm{MAX}}^2}{\rho c_{\mathrm{P}} \Delta T_{\mathrm{AD,MAX}}}\right)\left(\dfrac{\pi}{4} DF_{\mathrm{TR}} + (1 - \eta_{\mathrm{DC}})\right)}, & \text{regenerative cycle for } T_{H-C} = \Delta T_{\mathrm{AD,MAX}}. \end{cases}$$

In addition to the electrocaloric material parameters, which include the effective time-related permittivity $\varepsilon_{\mathrm{TR}}$, operation temperature T, electric field change E_{MAX}, density ρ and heat capacity c_{P}, partly lumped to a material figure-of-merit in [12], mainly the dissipation factor (as defined in [6] to represent all hysteresis losses) and the external electrical charging efficiency η_{DC} (see Figure 1) is relevant for the COP. The external charging loss reduces an initially high $COP_{\mathrm{R,MAT}}$ to a lower relative system COP. Especially for electrocaloric ceramics, which have high permittivity but low dissipation factor, high (99%) or ultra-high (> 99.7%) charging efficiencies are required to maintain a competitive high system COP (beyond 50% of the Carnot limit on the system level is considered a milestone still being aimed for at the time of this publication). For electrocaloric polymers, which have lower permittivity but higher hysteresis loss or dissipation factor), the sensitivity of the COP to the external charging efficiency is much lower [17], such that less efficient power electronics might be sufficient, but at the same time polymer-based electrocaloric materials can also have lower material COP limits. The choice of thermal

cycle [7] also influences the achievable system COP. Figure 2 shows the calculated best-case relative system COPs for Carnot-like cycles and cycles with ideal heat regeneration, for different electrocaloric materials, as already shown in [17]. Especially for electrocaloric ceramics, high electrical efficiencies are desired for high heat pump system COPs, and thus in this work's scope.

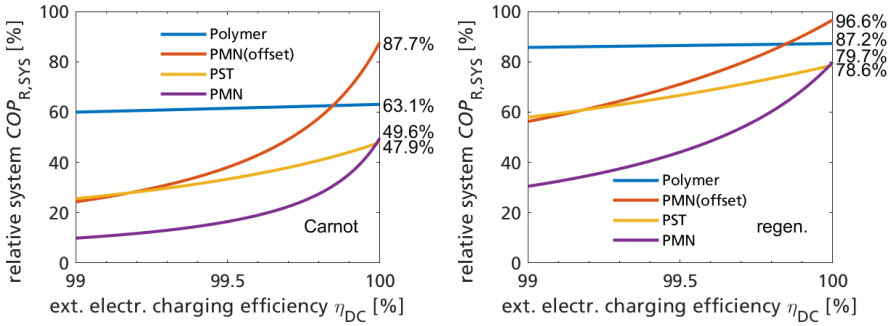

Figure 2: Best-case relative system COP for Carnot-like and regenerative thermal cycles. Calculated as in [17].

3. REVIEW OF EFFICIENT ELECTROCALORIC LOAD CHARGING CIRCUITS

Table 1 reviews charging electronics reported in literature, sorted by publication time, which were designed for or already applied to electrocaloric loads. It should be mentioned that there exists further literature on driving circuits for similar capacitive-load applications such as piezoelectric actuators [39] or energy harvesters [40], and the efficient electrical energy recovery approaches reported for those applications can also be applied to electrocaloric loads. This work later reviews the circuits from Table 1 which were (partly) designed by Fraunhofer IAF.

Table 1 Reported charging electronics for (electrocaloric) capacitive loads.

Year	Institution	Approach	Electrical efficiency	Cap. load material	Ref.
2018	LIST	2 level resonant circuit	≈ 70%	$BaTiO_3$	[20]
2020	UCLA	2 level resonant circuit	≈ 70%	PVDF	[21]
2021	Fraunhofer IAF/ INATECH	4 level GaN/Si partial power processing	99.66% [a]	ideal cap.	[41] and this work
2022	Fraunhofer IAF	2 level GaN half-bridge	99.2% [a]	PMN	[6]
2022	Fraunhofer IAF	2 level GaN half-bridge	99.3% [a]	PMN-2PT	[42]
2022	Fraunhofer IAF	2 level GaN half-bridge	≈ 99% [a]	$BaTiO_3$	[19]
2022	CPES	2 level half-bridge	n/a	n/a	[43]
2022	ENS Paris-Saclay	24 level Marx modulator	≈ 88%	ideal cap.	[44]
2023	Fraunhofer IAF	6 level GaN/Si partial power processing	99.74% [a]	ideal cap.	[45]
2023	Fraunhofer IAF	7 level GaN multilevel π-type converter	99.75 [a]	ideal cap.	[46]
2024	Fraunhofer IAF	6 level GaN multilevel π-type converter (with low-power gate driver)	n/a	n/a	[47]
2024	Fraunhofer IAF	6 level GaN multilevel π-type converter (with low-power gate driver)	99.75% [a] 99.71% [b]	ideal cap.	[48]
2024	Fraunhofer IAF	240 level stepwise capacitor charging	≈ 95% [a]	ideal cap.	this work
2024	Fraunhofer IAF	2 level GaN half-bridge (low-power driver)	≈ 99% [b]	ideal cap.	this work

[a] power stage efficiency only (no driving and control circuit or sensors included)
[b] power stage (with gate drivers) efficiency (no control circuit or sensors included)

The “importance of electric-energy recovery and heat regeneration” was discussed in [5]. In 2018, a resonant circuit was proposed [20] and applied to electrocaloric ceramics ($BaTiO_3$ MLCCs) in a mechanically actuated small-scale electrocaloric heat pump demonstrator. Such circuits were previously used only for “piezoelectric actuation [39], piezoelectric harvesting [49], and pyroelectric harvesting [50]” as stated in [20]. In 2020, a related, but higher-voltage resonant circuit was applied to electrocaloric polymers [21]. Both works report around 70% electrical charging efficiency. Switched-mode power converters [51] and stepwise-adiabatic capacitor charging circuits [52] are known to enable significantly higher electrical efficiencies than resonant circuits, and were then developed and tailored especially for electrocaloric applications: A 24 level Marx modulator published in [44] achieved around 88% electrical efficiency, and in the same year a 2 level half-bridge circuit using state-of-the-art gallium nitride (GaN) power transistors was built and applied to electrocaloric ceramics (PMN-based material). With a hysteretic current control (the control loop [42] is shown in Figure 3) and zero-voltage switching between 99.2% [6] and 99.3% [42] electrical efficiency was achieved when charging real electrocaloric (PMN and PMN-2PT) and ideal loads. This kind of two-level half-bridge was also applied to an electrocaloric heat pump demonstrator in [19], were with arbitrary field variation [53] both Carnot-like and Brayton cycles were demonstrated in a cascaded solid-solid heat pump prototype. Figure 4 show the first generation half-bridge from [6] and a second generation (published in this work) which has improved gate drivers and gate driver supplies that achieve ultra-low additional power consumption in the gate driver stage compared to the first generation.

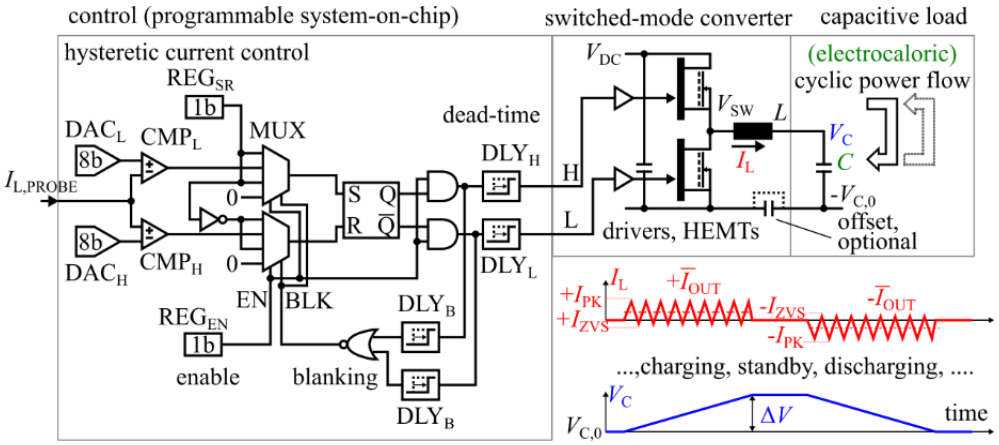

Figure 3: Hysteretic current control loop for two-level half-bridge power converters. Reprinted from [42] with permission, © 2022 VDE VERLAG GMBH.

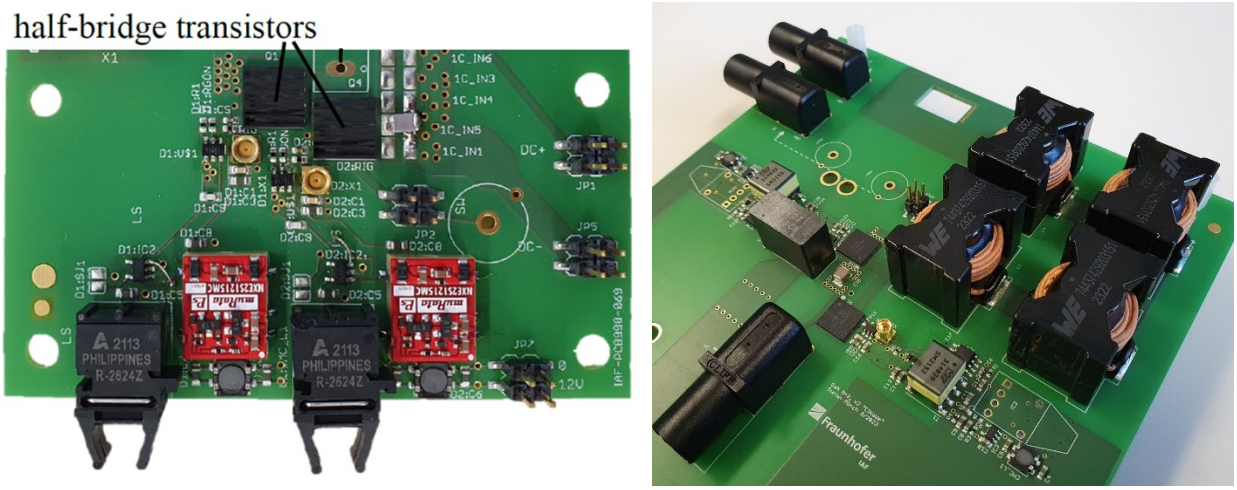

Figure 4: 1st generation (left, modified from [6], CC-BY) and 2nd generation (right) two-level GaN half-bridges.

Already 2021, the concept of partial power processing [54] was implemented for electrocalorics: Based on a two

level GaN half-bridge power converter and two 4 level silicon (Si) transistor-based multiplexers, an ideal capacitive load (lossless, linear and non-electrocaloric) was charged with 99.66% efficiency (power-stage only). This 4 level partial power processing power converter was developed in a Master's thesis [41] and is now also published in this work, shown in Figure 5. The photo shows only the Si-based input and output multiplexers, the complete board was connected to a GaN two-level converter from Figure 4 to form the complete circuit. This converter had two input stage multiplexers, but later it was found just one input stage is sufficient and also the circuit can be functionally merged to a similar E-type (π-type) multilevel converter. The initial partial power processing converter was also extended by an output multiplexer (5 phases) which allows the time multiplexed charging and discharging of five (electrocaloric) capacitive loads. With an odd number of output phases, the high hard-switching loss when switching between phases is avoided. By rearranging the series connection of the Si-and GaN-based converter and load, the partial power processing converter from Figure 6 was derived, and after adding more levels (6-level), 99.74% charging efficiency (power stage) was measured with ideal capacitive loads [45].

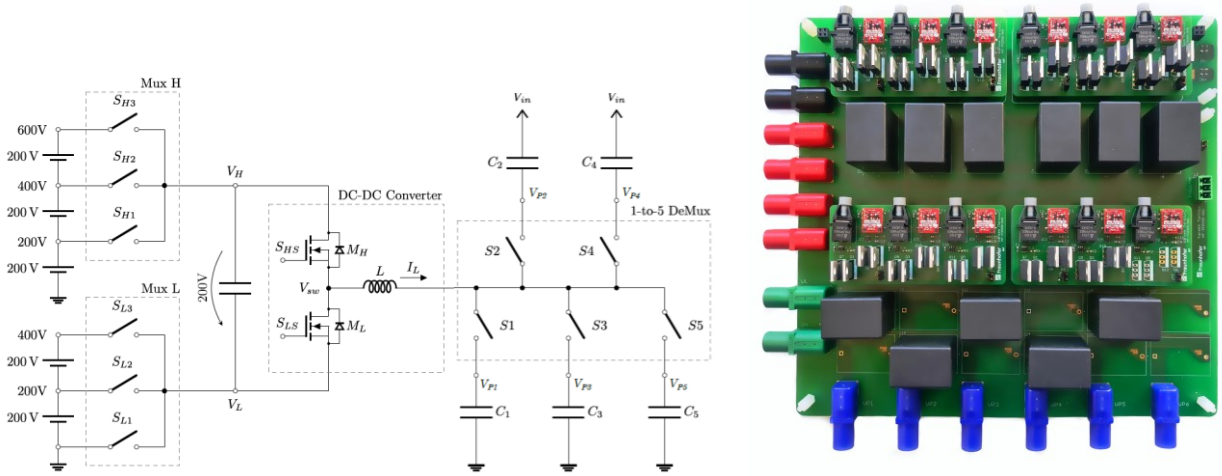

Figure 5: 4-level (input) partial power processing and 5-phase (output) converter (photos reprinted from [41]).

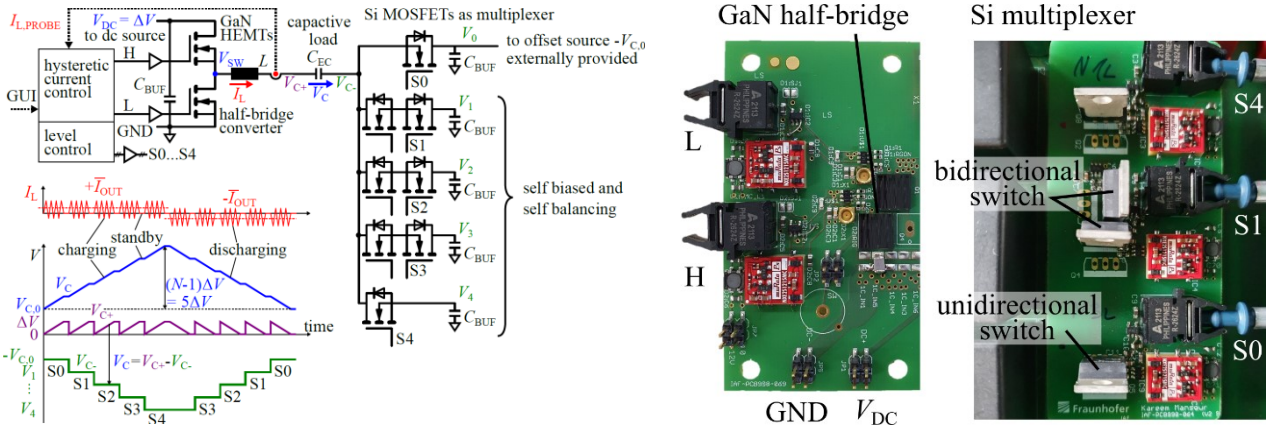

Figure 6: Partial power processing 6-level hybrid GaN/Si converter (right, reprinted from [45], CC-BY).

Then, an all-GaN multilevel converter in E-type (also called π-type) was built with 7 levels, achieving 99.75% charging efficiency (power stage only) when charging ideal capacitors [46]. This converter was redesigned with ultra-low loss gate drivers (similar to the improvement in half-bridge generations), and by further optimization also up to 99.75% power stage efficiency was achieved already for 6 levels [47, 48]. Thanks to the efficient gate driver, the efficiency reduced just slightly to 99.71% when including the gate driver losses. Both E-type multilevel converters are shown in Figure 7: Multilevel ***π***-type converters: 7-level (left, reprinted from [46], © Fraunhofer IAF) and 6-level (middle/right, reprinted from [47, 48] with permission, © 2024 VDE VERLAG GMBH). Efficient voltage balancing of the multilevel converters was not yet investigated, but will be required for lossy electrocaloric loads, and is part of ongoing research.

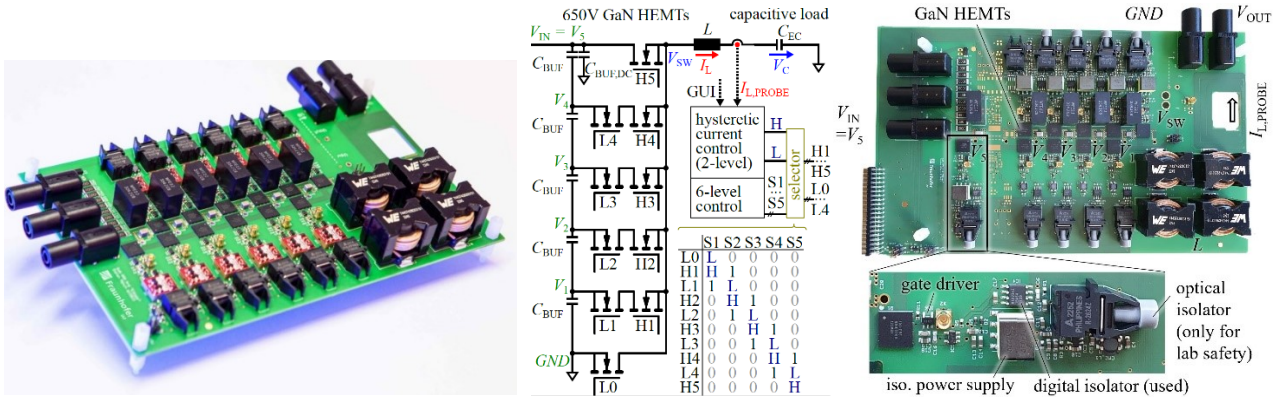

Figure 7: Multilevel π-type converters: 7-level (left, reprinted from [46], © Fraunhofer IAF) and 6-level (middle/right, reprinted from [47, 48] with permission, © 2024 VDE VERLAG GMBH).

Another research direction is stepwise capacitor charging [44, 52]. An array of bidirectional blocking optocoupler switches was assembled as 240-level charging circuit (Figure 8), which is now published in this work. Such circuits do not necessary require inductive components or switched-mode operation. Theoretically, by stepwise charging using the circuit from Figure 8 with more and more levels N, the charging efficiency can be increased, since the voltage drop across the charging resistor gets smaller and smaller. Thereby, a loss reduction to $1/(N\text{-}1)$ of the 2-level ($N = 2$) charging loss is theoretically possible. Using 10 nF buffer capacitors and a 10 nF load, the number of steps was varied experimentally, and the measured efficiency is shown in Figure 8. The efficiency is only the power stage efficiency, and does not include the high required driving power to drive the optocouplers. A maximum power stage efficiency of around 95% was measured at 81 levels. Since more levels also require more time and introduce additional switching and leakage current loss, the efficiency reduced for more levels. For 25 levels, the Figure 8 shows time-domain voltage measurements with visible voltage steps.

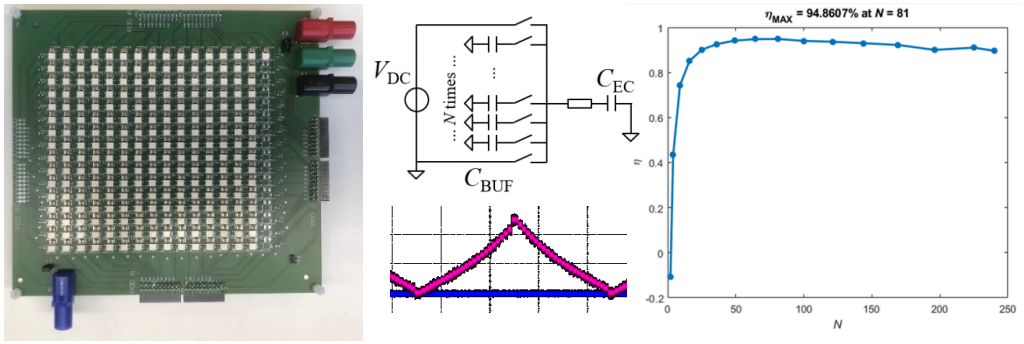

Figure 8: Up to 240-level stepwise capacitor charging circuit and measurements.

4. CONCLUSIONS

Efficient charging and discharging by means of external electronics are decisive to transfer the initially high electrocaloric material coefficient of performance to a still sufficiently high system performance. While on the one hand the choice of electrocaloric material and thermal cycles significantly influences the achievable performance, on the other hand, an external charging efficiency as high as possible is always worthwhile to increase the system performance. After initial attempts to recover electrical energy from electrocaloric capacitors capacitive by resonant circuits, this work now reviewed switched-mode power electronics circuits which achieve even higher electrical efficiencies of 99% and beyond.

ACKNOWLEDGEMENTS

This work was supported by the Fraunhofer Society in the Fraunhofer lighthouse project “ElKaWe - Electrocaloric Heat Pumps” (www.ElKaWe.org).

REFERENCES

[1] J. Shi *et al.,* "Electrocaloric Cooling Materials and Devices for Zero-Global-Warming-Potential, High-Efficiency Refrigeration," *Joule*, vol. 3, no. 5, pp. 1200–1225, 2019, doi: 10.1016/j.joule.2019.03.021.
[2] A. S. Mischenko, "Giant Electrocaloric Effect in Thin-Film PbZr0.95Ti0.05O3," *Science*, vol. 311, no. 5765, pp. 1270–1271, 2006, doi: 10.1126/science.1123811.
[3] B. Neese, B. Chu, S.-G. Lu, Y. Wang, E. Furman, and Q. M. Zhang, "Large Electrocaloric Effect in Ferroelectric Polymers Near Room Temperature," *Science*, vol. 321, no. 5890, pp. 821–823, 2008, doi: 10.1126/science.1159655.
[4] B. Nair *et al.,* "Large electrocaloric effects in oxide multilayer capacitors over a wide temperature range," *Nature*, vol. 575, no. 7783, pp. 468–472, 2019, doi: 10.1038/s41586-019-1634-0.
[5] U. Plaznik, M. Vrabelj, Z. Kutnjak, B. Malič, A. Poredoš, and A. Kitanovski, "Electrocaloric cooling: The importance of electric-energy recovery and heat regeneration," *EPL*, vol. 111, no. 5, p. 57009, 2015, doi: 10.1209/0295-5075/111/57009.
[6] S. Moench *et al.,* "Enhancing Electrocaloric Heat Pump Performance by Over 99% Efficient Power Converters and Offset Fields," *IEEE Access*, vol. 10, pp. 46571–46588, 2022, doi: 10.1109/ACCESS.2022.3170451.
[7] D. E. Schwartz, "Thermodynamic Cycles and Electrical Charge Recovery in High-Efficiency Electrocaloric Cooling Systems," *International Journal of Refrigeration*, 2021, doi: 10.1016/j.ijrefrig.2021.02.003.
[8] E. Defay, S. Crossley, S. Kar-Narayan, X. Moya, and N. D. Mathur, "The Electrocaloric Efficiency of Ceramic and Polymer Films," *Advanced Materials*, vol. 25, no. 24, pp. 3337–3342, 2013, doi: 10.1002/adma.201300606.
[9] Y. Nouchokgwe *et al.,* "Giant electrocaloric materials energy efficiency in highly ordered lead scandium tantalate," *Nature Communications*, vol. 12, no. 1, p. 3298, 2021, doi: 10.1038/s41467-021-23354-y.
[10] A. Torelló and E. Defay, "Electrocaloric Coolers: A Review," *Adv Elect Materials*, p. 2101031, 2022, doi: 10.1002/aelm.202101031.
[11] A. Greco and C. Masselli, "Electrocaloric Cooling: A Review of the Thermodynamic Cycles, Materials, Models, and Devices," *Magnetochemistry*, vol. 6, no. 4, p. 67, 2020, doi: 10.3390/magnetochemistry6040067.
[12] J. Schipper *et al.,* "On the efficiency of caloric materials in direct comparison with exergetic grades of compressors," *Journal of Physics: Energy*, vol. 5, no. 4, p. 45002, 2023, doi: 10.1088/2515-7655/ace7f4.
[13] Y. Wang *et al.,* "A high-performance solid-state electrocaloric cooling system," *Science*, vol. 370, no. 6512, pp. 129–133, 2020, doi: 10.1126/science.aba2648.
[14] J. Metzdorf *et al.,* "Electrocaloric cooling system utilizing latent heat transfer for high power density," *Communications Engineering*, vol. 3, no. 1, p. 55, 2024, doi: 10.1038/s44172-024-00199-z.
[15] Y. D. Wang, S. J. Smullin, M. J. Sheridan, Q. Wang, C. Eldershaw, and D. E. Schwartz, "A heat-switch-based electrocaloric cooler," *Applied Physics Letters*, vol. 107, no. 13, p. 134103, 2015, doi: 10.1063/1.4932164.
[16] R. Ma *et al.,* "Highly efficient electrocaloric cooling with electrostatic actuation," *Science*, vol. 357, no. 6356, pp. 1130–1134, 2017, doi: 10.1126/science.aan5980.
[17] S. Mönch *et al.,* "How highly efficient power electronics transfers high electrocaloric material performance to heat pump systems," (in En;en), *MRS Advances*, pp. 1–10, 2023, doi: 10.1557/s43580-023-00670-7.
[18] C. Molin, P. Neumeister, H. Neubert, and S. E. Gebhardt, "Multilayer Ceramics for Electrocaloric Cooling Applications," *Energy Technol.*, vol. 6, no. 8, pp. 1543–1552, 2018, doi: 10.1002/ente.201800127.
[19] S. Moench *et al.,* "GaN Power Converter Applied to Electrocaloric Heat Pump Prototype and Carnot Cycle," in *2022 IEEE 9th Workshop on Wide Bandgap Power Devices & Applications (WiPDA)*, 2022, pp. 186–191.

[20] E. Defay *et al.,* "Enhanced electrocaloric efficiency via energy recovery," *Nature Communications*, vol. 9, no. 1, 2018, doi: 10.1038/s41467-018-04027-9.
[21] Y. Meng *et al.,* "A cascade electrocaloric cooling device for large temperature lift," *Nat Energy*, vol. 5, no. 12, pp. 996–1002, 2020, doi: 10.1038/s41560-020-00715-3.
[22] G. G. Wiseman and J. K. Kuebler, "Electrocaloric Effect in Ferroelectric Rochelle Salt," *Phys. Rev.*, vol. 131, no. 5, pp. 2023–2027, 1963, doi: 10.1103/PhysRev.131.2023.
[23] Q. Li *et al.,* "Low-k nano-dielectrics facilitate electric-field induced phase transition in high-k ferroelectric polymers for sustainable electrocaloric refrigeration," *Nature Communications*, vol. 15, no. 1, p. 702, 2024, doi: 10.1038/s41467-024-44926-8.
[24] T. Zhang, X.-S. Qian, H. Gu, Y. Hou, and Q. M. Zhang, "An electrocaloric refrigerator with direct solid to solid regeneration," *Applied Physics Letters*, vol. 110, no. 24, p. 243503, 2017, doi: 10.1063/1.4986508.
[25] Y. Jia and Y. Sungtaek Ju, "A solid-state refrigerator based on the electrocaloric effect," *Applied Physics Letters*, vol. 100, no. 24, p. 242901, 2012, doi: 10.1063/1.4729038.
[26] H. Cui *et al.,* "Flexible microfluidic electrocaloric cooling capillary tube with giant specific device cooling power density," *Joule*, vol. 6, no. 1, pp. 258–268, 2022, doi: 10.1016/j.joule.2021.12.010.
[27] K. Klinar, K. Vozel, T. Swoboda, T. Sojer, M. Muñoz Rojo, and A. Kitanovski, "Ferrofluidic thermal switch in a magnetocaloric device," *iScience*, vol. 25, no. 2, p. 103779, 2022, doi: 10.1016/j.isci.2022.103779.
[28] D. Sette, A. Asseman, M. Gérard, H. Strozyk, R. Faye, and E. Defay, "Electrocaloric cooler combining ceramic multi-layer capacitors and fluid," *APL Materials*, vol. 4, no. 9, p. 91101, 2016, doi: 10.1063/1.4961954.
[29] D. Guo *et al.,* "Design and modeling of a fluid-based micro-scale electrocaloric refrigeration system," *International Journal of Heat and Mass Transfer*, vol. 72, pp. 559–564, 2014, doi: 10.1016/j.ijheatmasstransfer.2014.01.043.
[30] J. Li *et al.,* "High cooling performance in a double-loop electrocaloric heat pump," *Science*, vol. 382, no. 6672, pp. 801–805, 2023, doi: 10.1126/science.adi5477.
[31] P. Lheritier *et al.,* "Large harvested energy with non-linear pyroelectric modules," *Nature*, vol. 609, no. 7928, pp. 718–721, 2022, doi: 10.1038/s41586-022-05069-2.
[32] A. Torelló *et al.,* "Giant temperature span in electrocaloric regenerator," *Science*, vol. 370, no. 6512, pp. 125–129, 2020, doi: 10.1126/science.abb8045.
[33] K. Klinar and A. Kitanovski, "Thermal control elements for caloric energy conversion," *Renewable and Sustainable Energy Reviews*, vol. 118, p. 109571, 2020, doi: 10.1016/j.rser.2019.109571.
[34] R. Faye *et al.,* "Heat flow in electrocaloric multilayer capacitors," *Journal of Alloys and Compounds*, vol. 834, p. 155042, 2020, doi: 10.1016/j.jallcom.2020.155042.
[35] C. Molin and S. Gebhardt, "PMN-8PT device structures for electrocaloric cooling applications," *Ferroelectrics*, vol. 498, no. 1, pp. 111–119, 2016, doi: 10.1080/00150193.2016.1169062.
[36] G. Suchaneck and G. Gerlach, "Lead-free Relaxor Ferroelectrics for Electrocaloric Cooling," *Materials Today: Proceedings*, vol. 3, no. 2, pp. 622–631, 2016, doi: 10.1016/j.matpr.2016.01.100.
[37] N. Zeggai, B. Dkhil, M. LoBue, and M. Almanza, "Cooling efficiency and losses in electrocaloric materials," *Applied Physics Letters*, vol. 122, no. 8, p. 81903, 2023, doi: 10.1063/5.0138887.
[38] T. Hess *et al.,* "Thermal hysteresis and its impact on the efficiency of first-order caloric materials," *Journal of Applied Physics*, vol. 127, no. 7, p. 75103, 2020, doi: 10.1063/1.5132897.
[39] D. Campolo, M. Sitti, and R. S. Fearing, "Efficient charge recovery method for driving piezoelectric actuators with quasi-square waves," *IEEE Transactions on Ultrasonics, Ferroelectrics and Frequency Control*, vol. 50, no. 3, pp. 237–244, 2003, doi: 10.1109/tuffc.2003.1193617.
[40] K. Uchino, "Piezoelectric Energy Harvesting Systems—Essentials to Successful Developments," *Energy Technol.*, vol. 6, no. 5, pp. 829–848, 2018, doi: 10.1002/ente.201700785.
[41] K. Mansour, "Design and Implementation of a Highly Efficient Bidirectional DC-DC Converter for Multi-Phase Control of Capacitive Loads: Masterarbeit," INATECH, Universität Freiburg (extern: Fraunhofer IAF), 2021.
[42] S. Moench *et al.,* "A GaN-based DC-DC Converter with Zero Voltage Switching and Hysteretic Current Control for 99% Efficient Bidirectional Charging of Electrocaloric Capacitive Loads," in *PCIM Europe*

2022; International Exhibition and Conference for Power Electronics, Intelligent Motion, Renewable Energy and Energy Management.
[43] Le Wang, *Power Converter for Electrocaloric Refrigeration: (CPES Nuggets).* [Online]. Available: https://cpes.vt.edu/library/viewnugget/1041
[44] M. Almanza, T. Martinez, M. Petit, Y. Civet, Y. Perriard, and M. LoBue, "Adaptation of a Solid-State Marx Modulator for Electroactive Polymer," *IEEE Trans. Power Electron.*, vol. 37, no. 11, pp. 13014–13021, 2022, doi: 10.1109/TPEL.2022.3183437.
[45] S. Mönch *et al.,* "A 99.74% Efficient Capacitor-Charging Converter using Partial Power Processing for Electrocalorics," *IEEE Journal of Emerging and Selected Topics in Power Electronics*, vol. 11, no. 4, pp. 4491–4507, 2023, doi: 10.1109/JESTPE.2023.3270375.
[46] Fraunhofer IAF, *Leistungselektronik für neuartige Wärmepumpen erzielt Wirkungsgrad von über 99,7 Prozent*, 2023. [Online]. Available: https://www.iaf.fraunhofer.de/de/medien/pressemitteilungen/leistungselektronik-im-projekt-elkawe.html
[47] S. Mönch, R. Reiner, M. Basler, P. Waltereit, and R. Quay, "Voltage-Sensorless Control and GaN Multilevel Converter for Charging Non-Linear and Lossy Electrocaloric Capacitors," *13th International Conference on Integrated Power Electronics Systems (CIPS 2024)*, pp. 202–207, 2024.
[48] S. Mönch, R. Reiner, M. Basler, K. Bartholomé, P. Waltereit, and R. Quay, "Over 99.7% Efficient GaN-based 6-Level Capacitive-Load Power Converter," *PCIM Europe 2024; International Exhibition and Conference for Power Electronics, Intelligent Motion, Renewable Energy and Energy Management*, 2024.
[49] A. Badel, D. Guyomar, E. Lefeuvre, and C. Richard, "Efficiency Enhancement of a Piezoelectric Energy Harvesting Device in Pulsed Operation by Synchronous Charge Inversion," *Journal of Intelligent Material Systems and Structures*, vol. 16, no. 10, pp. 889–901, 2005, doi: 10.1177/1045389X05053150.
[50] G. Sebald, E. Lefeuvre, and D. Guyomar, "Pyroelectric energy conversion: Optimization principles," *IEEE Transactions on Ultrasonics, Ferroelectrics and Frequency Control*, vol. 55, no. 3, pp. 538–551, 2008, doi: 10.1109/tuffc.2008.680.
[51] L. Corradini, *Digital Control of High-Frequency Switched-Mode Power Converters,* 1st ed. Hoboken: John Wiley & Sons Incorporated, 2015. [Online]. Available: https://ebookcentral.proquest.com/lib/kxp/detail.action?docID=4040610
[52] L. J. Svensson and J. G. Koller, "Driving a capacitive load without dissipating fCV/sup 2," in *1994 IEEE Symposium on Low Power Electronics: Digest of technical papers*, San Diego, CA, USA, 2011, pp. 100–101.
[53] S. Crossley, B. Nair, R. W. Whatmore, X. Moya, and N. D. Mathur, "Electrocaloric Cooling Cycles in Lead Scandium Tantalate with True Regeneration via Field Variation," *Phys. Rev. X*, vol. 9, no. 4, 2019, doi: 10.1103/PhysRevX.9.041002.
[54] C. Li, Y. E. Bouvier, A. Berrios, P. Alou, J. A. Oliver, and J. A. Cobos, "Revisiting "Partial Power Architectures" from the "Differential Power" Perspective," in *2019 IEEE 20th Workshop on Control and Modeling for Power Electronics (COMPEL): University of Toronto, Toronto, Canada, June 17-20, 2019*, Toronto, ON, Canada, 2019, pp. 1–8.

DOI: 10.18462/iir.thermag.2024.0024

Oscillating Gadolinium thermal switch

N PETELIN[(a)], B PEČAR[(b)], D VRTAČNIK[(b)], J PERNE[(a)], U TOMC[(a)], A KITANOVSKI[(a)]*

[(a)] University of Ljubljana, Faculty of Mechanical Engineering
Ljubljana, 1000, Slovenia, andrej.kitanovski@fs.uni-lj.si
[(b)] University of Ljubljana, Faculty of Electrical Engineering
Ljubljana, 1000, Slovenia, danilo.vrtacnik@fe.uni-lj.si

ABSTRACT

Thermal control devices such as thermal switches, thermal diodes and thermal regulators are two-terminal devices used to passively or actively control the intensity and direction of heat flow, which has proven useful in various thermal management applications, including caloric technologies. Here, a millimetre-scale oscillating gadolinium thermal switch is constructed using commercially available materials, with steady-state switching ratio of r_{switch} = 2,3. The thermal switch uses electrostatic forces for actuation and makes thermal contact between the heat source and the heat sink when in the ON state, and breaks contact when in the OFF state. In the ON state when the thermal switch is oscillating the Gd plate transfers heat, while in the OFF state, the Gd plate does not oscillate and heat is transferred via parasitic conduction through air gap and device's housing. The thermal conductance is $2{,}42 \cdot 10^{-1}$ W/K in the ON state and $1{,}22 \cdot 10^{-1}$ W/K in the OFF state. The thermal switch exhibits consistent and repeatable actuation over more than > 10^5 oscillation cycles and can be used to actively route heat flows in thermal management applications. Our proof-of-concept device has a convenient geometry and can be easily implemented in various thermal management system where implementation and/or operation of conventional thermal management methods are not suitable.

Keywords: thermal control elements, thermal switch, thermal management, magnetocaloric cooling/heating.

1. INTRODUCTION

Efficient thermal management is crucial for improving energy efficiency and ensuring optimal performance, reliability and safety of systems. Conventional thermal management methods such as large-scale heat exchangers, thermal resistors and thermal capacitors struggle to meet the requirements of modern, particularly compact systems with high power density and varying temperature gradients. In response to these challenges, a new concept of thermal control devices has emerged that includes thermal switches, diodes and capacitors. These devices provide non-linear, switchable and active heat control, similar to the way their electrical counterparts control electric current, and are suitable for a wide range of sizes, from sub-micrometre to larger systems of over 100 mm.

Thermal switches are active thermal devices in which the steady-state thermal conductance denoted as $G = Q/\Delta T$, can be toggled between an ON and an OFF state [1,2]. Ideally, the thermal conductance is infinitely high in the ON state and zero in the OFF state. A figure of merit for a thermal switch is the switching ratio r between the highest archived thermal conductance G_{on} (the ON state) and the lowest achievable thermal conductance G_{off} (the OFF state). Thermal control devices can be used in a wide range of applications, from solid-state cooling [3–7] to thermal regulation of buildings [8,9], electronics, batteries[10,11] and solar thermal energy storage [12,13].

Similar to their electrical counterparts, thermal switches rely on a non-thermal control parameter, such as electric fields, magnetic fields, or pressure, to modulate thermal conductance. The devices with the highest thermal switching ratio utilise electrostatic actuation to make and break thermal contacts between hot and cold spots [3,14–16]. Electrostatic actuation is characterized by its compactness, quiet operation and energy efficiency [17]. However, unlike magnetic actuation [18–21] or external electromotor-driven actuation, which offer larger actuation strokes [7,22–25], it requires precise engineering to achieve small contact gaps between hot and cold spots.

In this study, we present an electrostatic millimetre-scale oscillating thermal switch that can be used to influence the heat flow between the hot spot and the heat sink. First, the performance of the device is predicted theoretically using the online simulation tool TCC builder. Later, we experimentally investigated the behavior and switching ratio of the thermal switch under different conditions and demonstrated its ability to actively control the heat flux in low power density applications at room temperature.

1.1 Thermal switch concept

The main part of the device consists of an oscillating 161 µm thick Gd plate (Heeger Materials) and two Si plates (MicroChemicals GmbH) with a thickness of 516 um, which serve as hot and cold heat exchangers. The Gd plate was polished to create an optically reflective surface and to reduce the thermal contact resistance associated with surface asperities. The gold electrode was sputtered onto the Gd surface, while the graphite electrodes (Chemie Graphit 33) were spray-coated onto the heat exchangers. A 32 µm thick polyamide film (CAPLINQ, PIT0.5S) with a one-sided silicone adhesive (16 µm polyamide, 16 µm silicone adhesive) was attached to the graphite electrode, creating a structure of Si/graphite layer/ polyamide film on the side of the hot heat exchanger (HHEX). The same structure was also applied to the cold heat exchanger (CHEX). The polyamide film prevents a short circuit when the Gd plate moves between the cold and hot heat exchanger. The Si wafer with the corresponding layers is inserted into a housing printed with a 3D printer, which serves as a spacer. The thickness of the air gap is 310 µm. The Gd plate is freely movable and not attached to the spacer structure. To reduce heat loss through the spacers, the housing is printed from a material with low thermal conductivity. The total mass of the device with housing is 10.31 g, the mass of the thermal switch is 2.18 g. The electrodes were connected to an amplifier (TREK 2220) using thin copper wires. In order to generate a time-varying voltage at the electrodes, the voltage signal at the rectifier (Dr.meter PS-3010DF) was controlled by an Arduino (Uno) control system. According to the control signal, the Gd plate oscillated between the cold and hot heat exchanger. The size of cold and hot heat exchangers is 55.11 mm × 40.11 mm, but the active area is smaller, measuring 34.8 mm × 53 mm. This area corresponds to the size of the Gd plate, which serves as a thermal switch in our case. Figure 1 shows a cross-section of the device with the positions of the thermocouples marked in purple. The entire housing of the device was insulated with 30 mm thick thermal insulation (Armaflex) to reduce heat loss to the surroundings (not shown in figure 1). The heat source was simulated by a flexible electric thin-film heater (KLC, 8.17 W). The electric heater was attached to the hot heat exchanger on one side and insulated with thermal insulation (Armaflex) on the other side. By adjusting the electrical power of the electric heater, different temperatures were generated on the surface of the hot heat exchanger.

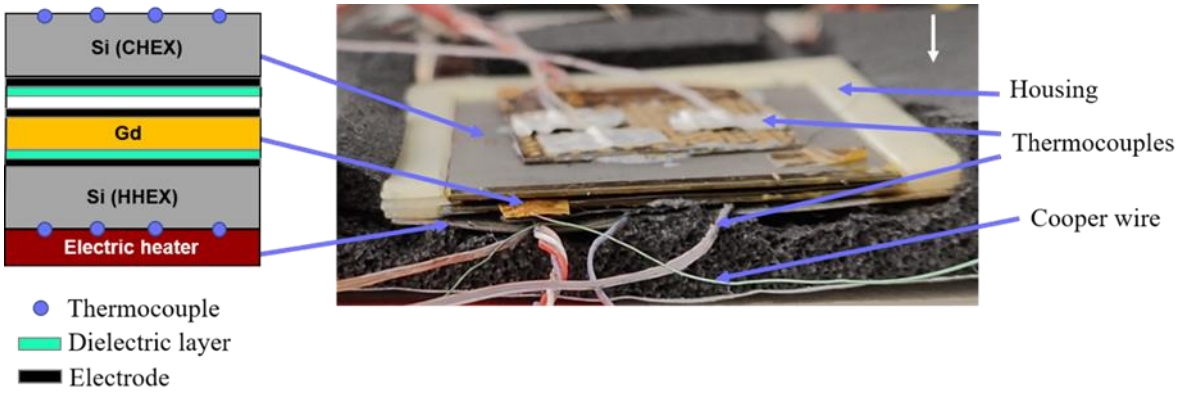

Figure 1: Cross section of the thermal switch device.

2. TCC BUILDER

First, we evaluated the performance of the device with the TCC builder. The TCC builder is an online tool for designing thermal control elements and thermal control circuits with a user-friendly interface and an associated library of materials and thermal control elements. A schematic representation of the device in TCC builder is shown in Figure 2 and consists of six main components: Hot Heat Exchanger (HHEX), Polyamide, air, Gd, Polyamide and Cold Heat Exchanger (CHEX). The Gd and air change position according to the operating frequency that dictate the heat transfer time. The electrodes are not included in the simulations as they are only a few nanometers thick and are also made of highly conductive material. The

selected boundary conditions were: Heat input on the HHEX side, which represents the electrical power of the electric heater, and on the CHEX side the adiabatic wall was chosen as boundary condition. The power density of the electric heater was 95 W/m^2. The thermal switch is ON, with high thermal conductance G_{on}, when it is in contact with the cold heat exchanger, and is OFF with low thermal conductance G_{off} when it is in contact with the hot heat exchanger. The thermal conductance in the ON state G_{on} is primarily affected by the thermal contact resistance between Gd and the Si heat exchangers. Thermal contact resistance depends mainly on the contact pressure, the surface roughness, the ambient pressure (air pockets trapped between the surface asperities) and the choice of materials in contact (presence or absence of thermal interface materials). In addition to the factors mentioned above, convection heat losses at higher operating frequencies also have a significant influence on G_{on} [166]. In the OFF state, the thermal conductance G_{off} is affected by the heat conduction through the housing of the spacer $G_{housing}$, the heat conduction through the air gap G_{air} and the heat transfer by radiation G_{rad} between Gd and the polyamide film. The Gd moves between HHEX and CHEX with an operating frequency of 0.25 Hz, where the time for each heat transfer process is 2 s and the time for the Gd position change is 6.25 ms, which was determined experimentally. The thermal contact resistance between Si and polyamide in contact was 8.4 m²K/W and between Gd and polyamide was 9.1 m²K/W. These values were taken from reference [26]. In the TCC builder, the user can switch between different scales in the program, which determine how much real length can be placed on the TCC-Builder canvas. We have chosen a scale of 100 um so that a 10 mm thermal control circuit fits on the canvas. If the thickness of one of the elements of the thermal control circuit is too large or too small to fit on the canvas, the thickness and therefore the effective thermal conductivity must be changed, as the thermal resistance must remain unchanged. This applies if the thermal mass of the element does not significantly affect the operation of the device. Therefore, the polyamide with a thickness of 32 µm was instead modelled with a thickness of 100 µm to fit the circuit on the canvas. For this reason, the thermal conductivity of the polyamide was changed from 1.25 W/mK to 3.906 W/mK. Since the Gd oscillates between HHEX and CHEX due to electrostatic forces, Joule heating is also included in the simulation as volumetric heat gain. The current and voltage for the electrostatic actuation were 0,1 mA and 800 V. The results show that the thermal conductance is 1.05 W/K when the thermal switch is on and 0.428 W/K when it is off. The corresponding switching ratio r is 2.5.

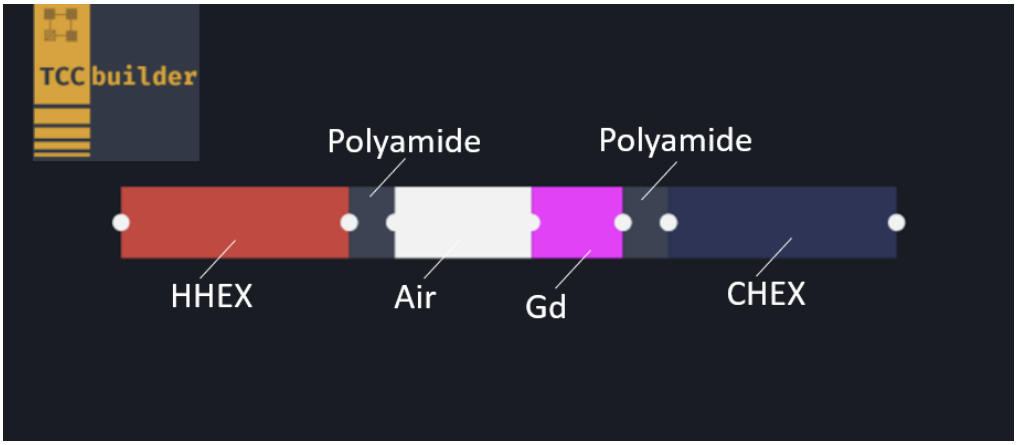

Figure 1: Device with thermal switch as presented in TCC builder.

3. EXPERIMENTAL RESULTS

Figure 2 shows the experimentally determined thermal conductance of the thermal switch in the ON (blue colour) and OFF state (black colour) as a function of the power of the electric heater. In the OFF state, the thermal switch has a low thermal conductance G_{off}, which ranges from 0,8 $\cdot 10^{-1}$W/K to 1,7$\cdot 10^{-1}$ W/K. In the ON state, however, the thermal conductance G_{on} is higher and reaches values of 1,2$\cdot 10^{-1}$ W/K to 4,0$\cdot 10^{-1}$ W/K at an operating frequency of 0.5 Hz.

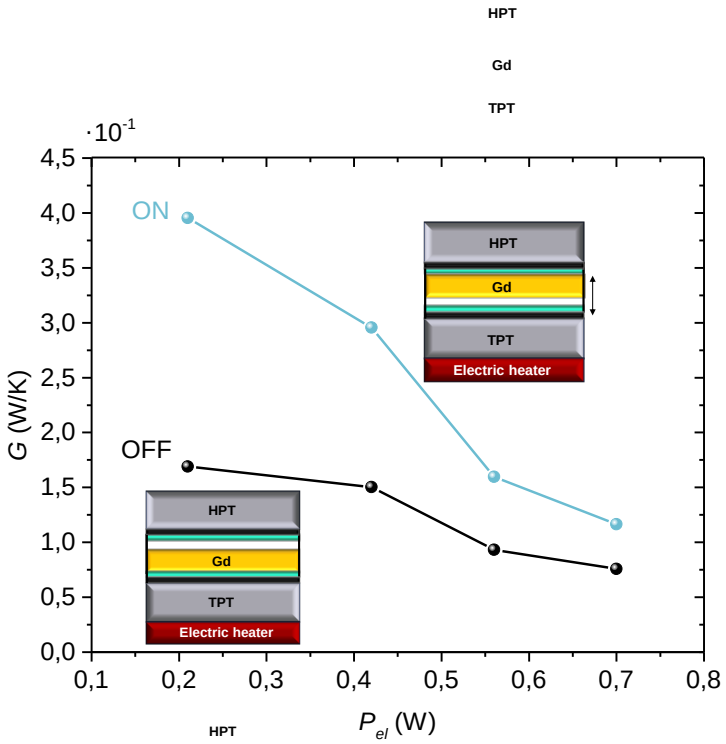

Figure 2: Thermal conductance G in ON and OFF state at different electrical power P_{el}.

The switching ratio is defined as $r_{switch} = G_{on} / G_{off}$ and is the primary metrics for evaluating thermal switch performance. Measurements were made at four different heating powers: 0.7 W, 0.56 W, 0.42 W and 0.21 W. As the heating area has a size of 55.11 mm × 40.11 mm, these values correspond to 316.7 W/m^2, 253.3 W/m^2,190 W/m^2, 95 W/m^2.

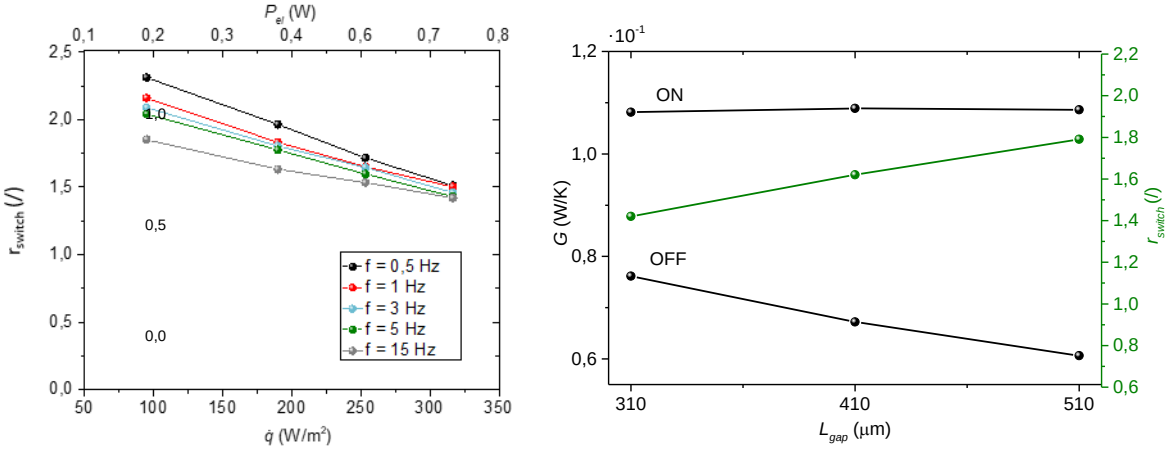

Figure 3: (a) Switching ratio r_{switch} as a function of the operating frequency and the electrical power of the electric heater P_{el}. (b) Different air gap sizes and their influence on the thermal conduction of the thermal switch.

Figure 3(a) shows that the maximum switching ratio r_{switch}= 2.3 achieved was at an operating frequency of 0.5 Hz and a minimum heating power of 0.21 W. As the frequency increases, the convection losses that occur during the movement of the Gd plate increase, which is particularly noticeable at low operating powers. The convection losses could be reduced by closing the entire device with a thermal switch and thus preventing the exchange with the surrounding (colder) air. Figure 3 (b) shows the influence of the air gap size on the thermal conductance when switched ON and OFF at an operating frequency of 15 Hz. The measurements were carried out with three different air gap sizes: 310 µm, 410 µm, 510 µm, with a heating power of 0.7 W. As the air gap increases, the thermal conductance G_{off} decreases in the OFF state, while the air gap size in the ON state does not significantly affect the thermal conductance G_{on}. By increasing the air gap size, the switching ratio also increases, as the OFF state the device has better thermal insulation properties. Increasing the air gap from 310 µm to 510 µm increased the switching ratio by 26%, from r_{switch} =

1.4 to r_{switch} = 1.8. It should be noted that the electrostatic field decreases as the air gap increases, which plays an important role in operation if the air gap is increased further. If the device were in a vacuum, heat transfer by conduction through the air gap would not occur and the only heat transfer mechanism in the OFF state would be heat conduction through the housing and heat transfer by radiation. This would increase the switching ratio as the thermal conductivity in the OFF state G_{off} would be significantly lower. In a similar design using magnetic forces for actuation, the switching ratio increased from 2,1 in air to 34 in vacuum [27]. In addition, the thermal contact resistance is lower in vacuum than in air, as the air trapped in the irregularities on the surface acts as a thermal insulator and reduces the transferred heat flux [28]. Heat transfer by radiation plays only a minor role, as the temperature difference between the hot and cold heat exchanger is relatively small (< 6 K). If we compare the result from 1D numerical simulation in TCC builder for 310 μm air gap and 95 W/m^2 heating power, we can see that in the ON state the experimentally determined thermal conductance is $G_{on,exp}$ = 0.108 W/K, while the numerical predicted thermal conductance is 10 times higher and is $G_{on,num}$ = 1.05 W/K. One of the main reasons are the heat losses to the environment, which were not considered in the numerical model, and the second reason is that in the experimental setup the thermocouples on the surfaces create small bumps that increase the thermal contact resistance when Gd oscillates between the hot and cold heat exchanger. In the OFF state, the experimental thermal conductance value is $G_{off,exp}$ = 0.077 W/K, while the numerically predicted value is 5 times higher and is $G_{off,num}$ = 0.428 W/K.

During the OFF state in the numerical simulations, heat gains from the electric heater to the cold heat exchanger occur only through heat conduction within the air gap. Conversely, in the experimental set-up heat gains extend towards the ambient surroundings, consequently resulting in a reduced amount of heat leakage towards the cold heat exchanger. Therefore, the experimentally determined switching ratio is $r_{switch,exp}$ = 1.4 and the numerical determined switching ratio is $r_{switch,num}$ = *2.5*.

4. CONCLUSIONS

In summary, we have numerically simulated in experimentally demonstrated a millimetre-scale thermal switch that uses electrostatic forces to make and break thermal contact between the Gd surface and the heat exchangers. Our experimental results show that the switching ratio is r_{switch}= 2.3 at a heating power of 95 W/m^2 (0.21 W). The thermal switch has a rigid stationary frame that could be enclosed, which would reduce convection losses and also allow operation in a vacuum. Operating in a vacuum would reduce heat conduction through the air gap in the OFF state, which could significantly improve the switching ratio. Another way to improve the switching ratio would be to increase the electric field between the electrodes, which would reduce the thermal contact resistance between the thermal switch and the heat exchanger. This could be achieved simply by increasing the voltage amplitude, but the maximum voltage for the same dielectric layer thickness is limited by the dielectric strength of the chosen material and its ability to withstand a voltage before breakdown occurs. The device is constructed using commercially available materials and can be easily incorporated into existing devices that operate at room temperature. The thermal switch has demonstrated consistent and repeatable actuation over more than 500 thermal cycles.

ACKNOWLEDGEMENTS

The authors acknowledge the financial support of the Slovenian Research Agency for the projects TCCbuilder: An open-source simulation tool for thermal control circuits J7-3148, MagBoost: Magnetocaloric booster micro-heat pump for district heating system L2-2610, MHD-magcool: Novel MHD-thermal switch essential for nonconventional magnetic cooling system BI-DE/21- 22-008, and the research core funding no. P2-0223. This work was also financially supported by the Slovenian Research Agency as part of the Young Researcher PhD program.

REFERENCES

[1] Wehmeyer G, Yabuki T, Monachon C, Wu J and Dames C 2017 Thermal diodes, regulators, and switches: Physical mechanisms and potential applications *Appl. Phys. Rev.* **4**

[2] Klinar K and Kitanovski A 2020 Thermal control elements for caloric energy conversion *Renew. Sustain. Energy Rev.* **118**

[3] Ma R, Zhang Z, Tong K, Huber D, Kornbluh R, Ju Y S and Pei Q 2017 Highly efficient electrocaloric cooling with electrostatic actuation *Science (80-.).* **357** 1130–4

[4] Bo Y, Zhang Q, Cui H, Wang M, Zhang C, He W, Fan X, Lv Y, Fu X, Liang J, Huang Y, Ma R and Chen Y 2021 Electrostatic Actuating Double-Unit Electrocaloric Cooling Device with High Efficiency *Adv. Energy Mater.* **11** 1–8

[5] Bradeško A, Fulanović L, Vrabelj M, Matavž A, Otoničar M, Koruza J, Malič B and Rojac T 2021 Multifunctional Cantilevers as Working Elements in Solid-State Cooling Devices *Actuators* **10**

[6] Meng Y, Zhang Z, Wu H, Wu R, Wu J, Wang H and Pei Q 2020 A cascade electrocaloric cooling device for large temperature lift *Nat. Energy* **5** 996–1002

[7] Wang Y, Schwartz D E, Smullin S J, Wang Q and Sheridan M J 2017 Silicon Heat Switches for Electrocaloric Cooling *J. Microelectromechanical Syst.* **26** 580–7

[8] Varga S, Oliveira A C and Afonso C F 2002 Characterisation of thermal diode panels for use in the cooling season in buildings *Energy Build.* **34**

[9] Booten C, Rao P, Rapp V, Jackson R and Prasher R 2021 Theoretical Minimum Thermal Load in Buildings *Joule* **5**

[10] Hao M, Li J, Park S, Moura S and Dames C 2018 Efficient thermal management of Li-ion batteries with a passive interfacial thermal regulator based on a shape memory alloy *Nat. Energy* **3** 899–906

[11] Zeng Y, Zhang B, Fu Y, Shen F, Zheng Q, Chalise D, Miao R, Kaur S, Lubner S D, Tucker M C, Battaglia V, Dames C and Prasher R S 2023 Extreme fast charging of commercial Li-ion batteries via combined thermal switching and self-heating approaches *Nat. Commun.* **14**

[12] Muhumuza R, Zacharopoulos A, Mondol J D, Smyth M and Pugsley A 2019 Experimental study of heat retention performance of thermal diode Integrated Collector Storage Solar Water Heater (ICSSWH) configurations *Sustain. Energy Technol. Assessments* **34**

[13] Pugsley A, Zacharopoulos A, Deb Mondol J and Smyth M 2019 Theoretical and experimental analysis of a horizontal planar Liquid-Vapour Thermal Diode (PLVTD) *Int. J. Heat Mass Transf.* **144**

[14] Jahromi A E and Sullivan D F 2014 A piezoelectric cryogenic heat switch *Rev. Sci. Instrum.* **85** 85–8

[15] Keum H, Seong M, Sinha S, Kim S, Keum H, Seong M, Sinha S and Kim S 2012 Electrostatically driven collapsible Au thin films assembled using transfer printing for thermal switching *Appl. Phys. Lett.* **100**

[16] Beasley M A, Firebaugh S L, Edwards R L, Keeney A C and Osiander R 2004 MEMS Thermal Switch for Spacecraft Thermal Control *Proc. SPIE 5344, MEMS/MOEMS Components and Their Applications* vol 5344 p 4

[17] Meng Y, Zhang Z, Wu H, Wu R, Wu J, Wang H and Pei Q 2020 A cascade electrocaloric cooling device for large temperature lift *Nat. Energy* **5** 996–1002

[18] Ahmim S, Almanza M, Pasko A, Mazaleyrat F and Lobue M 2018 Study of the energy conversion chain in a thermomagnetic generator *Thermag VIII, Darmstadt, Ger.* 197–201

[19] Bulgrin K E, Lavine A S and Ju Y S 2009 Magnetomechanical thermal diode with tunable switching *Mater. Sci.*

[20] Chong Tai Y and Wright J A 2001 Fabrication and using a micromachined magnetostatic relay or switch, Patent US 6320145 B1

[21] Tai C Y, Wong Y, Rodenbush A J, Joshi C H and Shirron P J 2010 A High Conductance Detachable Heat Switch for ADRs *AIP Conf. Proc.* **710** 443–50

[22] Smullin S J, Wang Y and Schwartz D E 2015 System optimization of a heat-switch-based electrocaloric heat pump *Appl. Phys. Lett.* **107**

[23] Ossmer H, Miyazaki S and Kohl M 2015 Elastocaloric heat pumping using a shape memory alloy foil device *Transducers* pp 726–9

[24] Ossmer H, Wendler F, Gueltig M and Lambrecht F 2016 Energy-efficient miniature-scale heat pumping based on shape memory alloys *Smart Mater. Struct.* **25**

[25] McCarty R 2007 Experimental Verification of Thermal Switch Effectiveness in Thermoelectric Energy Harvesting *J. Thermophys. Heat Transf.* **21**

[26] Petelin N, Kalin M and Kitanovski A 2023 A conceptual design of a thermal switch capacitor in a magnetocaloric device: experimental characterization of properties and simulations of operating characteristics *JPhys Energy* **5**

[27] Castelli L, Garg A, Zhu Q, Sashital P, Shimokusu T J and Wehmeyer G 2023 A thermal regulator using passive all-magnetic actuation *Cell Reports Phys. Sci.* **4**

[28] Madhusudana C V 2014 *Thermal Contact Conductanc,* (New York: Springer) 25-77

DOI: 10.18462/iir.thermag.2024.0025

RESEARCH ON THE SPRING-LOADED GGG SALT PILL FOR ADIABATIC DEMAGNETIZATION REFRIGERATORS

Peng Zhao [a,b], Jun Shen [a,b,c]*, Ke Li[a],Ping Liu [a,b], Zhenxing Li[c], Wei Dai[a,b]*

[a] Key Laboratory of Cryogenic Science and Technology, Technical Institute of Physics and Chemistry, Chinese Academy of Sciences,
Beijing 100190, China, jshen@mail.ipc.ac.cn, cryodw@mail.ipc.ac.cn
[b] University of Chinese Academy of Sciences,
Beijing 100049, China
[c] School of Mechanical Engineering, Beijing Institute of Technology,
Beijing 100081, China

ABSTRACT

Adiabatic demagnetization refrigerators (ADR), as a sub-Kelvin refrigerator, has been widely studied for its advantages of high efficiency, gravity independence and high temperature control accuracy, and is especially suitable for space applications. Crystals represented by GGG, owing to their excellent performance in cooling power and thermal conductivity, are often fabricated into salt pills for ADR in the temperature range of 1 K. Heat transfer between the crystal and other components usually relies on copper fingers. Reliable and efficient connection between copper fingers and crystal is an important issue. This paper compares different crystal salt pill structures and proposes a spring-loaded salt pill structure. With GGG as the salt pill, the experiments show that the single stage ADR can obtain a cooling temperature of 800.4mK when starting from an initial temperature of 4K.

Keywords: Adiabatic demagnetization refrigerators, Sub-Kelvin, Salt pill

1. INTRODUCTION

By harnessing materials with low specific heat characteristics under these ultra-low temperature environments, detectors of high sensitivity can be developed, simultaneously, the ultra-low temperature can reduce thermal noises, thereby facilitating the observation of weak cosmic signals (Wang Chang et al., 2021; WANG Chang et al., 2019) , such as X-rays. The primary methods for achieving sub-Kelvin temperatures include dilution refrigeration, adsorption refrigeration, and adiabatic demagnetization refrigeration (Pobell, 2007). Among these approaches, ADR stands out due to its inherent high efficiency, no moving parts, and particularly its insensitivity to gravity (Li Ke et al., 2023; Wang Chang, 2022). Consequently, ADR has become the main cooling method to provide the sub-Kelvin temperature for space observation (Bartlett, 2010; DiPirro et al., 2012; Duval et al., 2020; Kanao et al., 2017; Shirron et al., 2010, 2016, 2015, 2012), such as PIXIE (Primordial Inflation Explorer) to study the cosmic microwave background (DiPirro et al., 2012; Shirron et al., 2012), and Astro-H astronomical satellite carrying SXS (Soft X-ray Spectrometer) (Kanao et al., 2017; Shirron et al., 2010, 2016, 2015).

The adiabatic demagnetization refrigeration system is schematically shown in Figure 1(a) and consists of a precooling system and an ADR system. Due to the large temperature span between the room temperature region and the ultra-low temperature region, a mechanical refrigerator is typically used to pre-cool the ADR from room temperature down to the liquid helium temperature. The basic structure of the ADR is shown in Figure 1 (b), which includes heat sink, superconducting magnet, heat switch (HS) and salt pill. The heat sink provides pre-cooling for the ADR system and absorbs the heat released from the salt pill and the load; the superconducting magnet provides the magnetic field required for magnetization/demagnetization of the salt pill; the HS controls the ON/OFF of the heat transfer circuit between the heat sink and the salt pill; and the salt pill is the source of cooling power for the ADR.

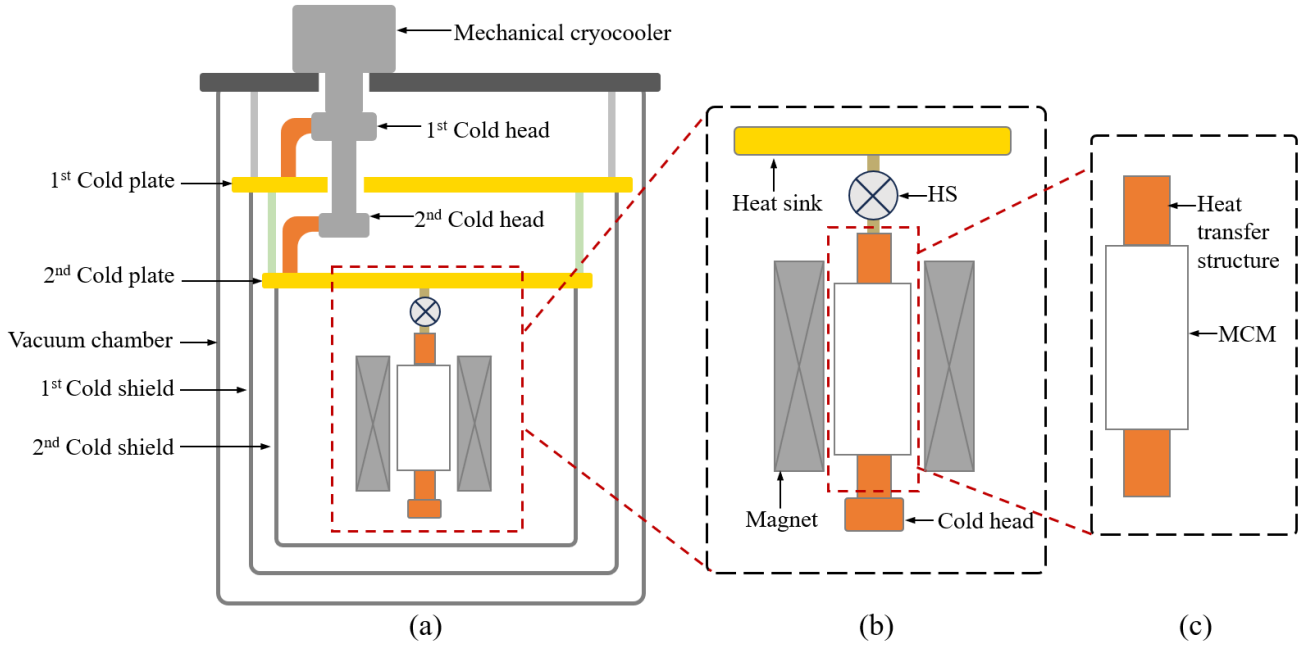

Figure 1:Schematic diagram of adiabatic demagnetization refrigerator system. (a) whole machine system (b) ADR part (c) Salt pill

2. CRYSTAL SALT PILL STRUCTURES

The salt pill, depicted in Figure 1(c), serves as the pivotal component within the ADR setup and wields a profound influence on the cooling efficiency. For ADR operating at temperatures above 0.3K, crystals are generally used as magnetocaloric materials (MCM) (Shirron and McCammon, 2014), and the commonly used ones are GGG (Gadolinium Gallium Garnet, GGG), GLF (Gadolinium Lithium Fluoride, GLF), and DGG (Dysprosium Gallium Garnet, DGG).

For the crystal salt pill, achieving efficient heat transfer between the MCM and the heat transfer structure is crucial. Several approaches have been reported for this, including gas conduction, bonded conduction and pressure-contact heat transfer methods (Shirron and McCammon, 2014).

The gas conduction salt pill refers to a structure in which the MCM is sealed, utilizing helium to conduct heat between the MCM and the heat transfer structure, suitable for both single-crystals and poly-crystals. Figure 2(a) shows the gas conduction salt pill reported by James Tuttle et al. (Tuttle et al., 2017), which is used for cooling from 10 K to 4 K. GGG is employed as the MCM, placed inside a copper shell serving as a thermal bus, and sealed with an outer stainless steel shell. Helium gas is injected through a designated inflation port and sealed thereafter. This gas conduction mechanism enhances heat transfer between the salt pill and the copper thermal bus. Figure 2 (b) shows a gas conduction salt pill designed for the Astro-H, reported by Peter Shirron et al. (Shirron et al., 2010). Pressed GLF disks with a diameter of 20 mm and a thickness of 3 mm are stacked in a copper can, which is filled with ^{4}He and sealed. Heat transfer is carried out through superfluid helium at low temperatures. At 0.8K, the thermal conductivity between the bolt surface of the copper can and the GLF is greater than 40 mW/K, and at temperatures of 1.3K and above, the thermal conductivity is greater than 100 mW/K. The gas conduction salt pill has the advantage of being able to provide a large heat flux while the necessity of sealing introduces complexity to the structure.

The bonded conduction salt pill refers to the formation of a thermal conduction path by bonding a single crystal to a thermal transfer structure using adhesive materials. Figure 2 (c) illustrates the bonded conduction salt pill reported by Peter J. Shirron et al. (Shirron and McCammon, 2014), employing GGG as the MCM. Due to significant differences in thermal expansion coefficients between GGG and copper at low temperatures, direct bonding between them is prone to fracture. However, tungsten exhibits a thermal expansion coefficient similar to

GGG, and high-purity tungsten demonstrates preferable thermal conductivity at low temperatures(Antyukhov et al., 1987; Pobell, 2007; Shirron and McCammon, 2014; Touloukian et al., 1975; Ventura and Perfetti, 2014). Therefore, bonding between GGG and tungsten is employed. Figure 2 (d) showcases a bonded conduction salt pill crafted by Wang Chang (Wang Chang, 2022), wherein copper disks are vacuum brazed to tungsten disks, and the copper fingers are thread-connected to the copper disks. Finally, GGG is bonded to the tungsten disks using Stycast 2850. The bonded conduction salt pill demonstrates effective thermal transfer; however, due to disparities in crystal and metal thermal expansion coefficients, there exists a risk of bond fracture. Our laboratory once faced fracture issues during the experiments, resulting in the inability of the ADR to operate normally. Peter J. Shirron has also noted that the long-term stability of this structure poses a challenge (Shirron and McCammon, 2014).

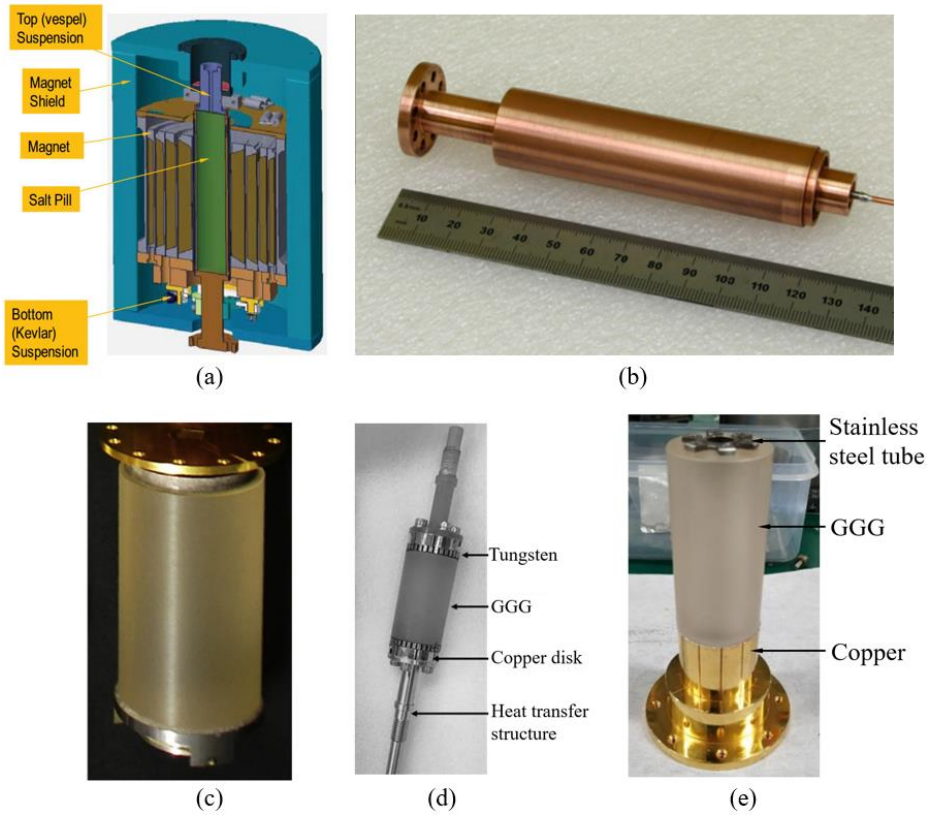

Figure 2 Salt pills of different structures. (a) Gas conduction salt pill reported by James Tuttle et al(Tuttle et al., 2017). (b) Gas conduction salt pill reported by Peter Shirron(Shirron et al., 2010).(c) Bonded conduction salt pill reported by Peter J. Shirron et al(Shirron and McCammon, 2014). (d) Bonded conduction salt pill reported by Wang Chang(Wang Chang, 2022).(e) Pressure-contact salt pill reported by Jin Hai et al (Jin et al., 2022)

The pressure-contact salt pill creates an effective heat transfer interface by applying pressure to the contact surface between the single crystal and the heat transfer structure. The structure of this salt pill is simple and stable, facilitating the change of MCM. In comparison to gas conduction salt pill, this approach offers simplicity in both production and utilization. And pressure-contact salt pills exhibit enhanced stability, devoid of any potential joint surface failures, rendering them well-suited for prolonged usage. As shown in Figure 2(e), Jin et al. presented a design for pressure-contact salt pill (Jin et al., 2022). They drilled a hole through the GGG crystal, then used a thin-walled stainless steel tube to tighten the GGG end face against the copper sheet. N-grease was applied to enhance heat transfer efficiency at the contact surface between GGG and copper. With an initial temperature of 4 K, a no-load temperature of 768.4 mK was achieved after demagnetization.

To fully harness the benefits of pressure-contact salt pill, meticulous investigation into pressing methodologies is imperative. Current literatures lack sufficient coverage on pressure-contact salt pills. Based on this, the present study proposes a novel pressure-contact salt pill employing springs to provide contact pressure. GGG single

crystal is utilized as the MCM for the design and experimentation of this salt pill.

3. SALT PILL DESIGN

The pressure-contact salt pill, which utilizes springs to provide pressure, is depicted in Figure 3. It consists of a GGG crystal, a heat transfer copper finger, an aluminum alloy finger, springs, gaskets, and a nut. The heat transfer copper finger and aluminum alloy finger are threaded together to form a single unit, and the perforated GGG is pressed against the upper plate of the heat transfer copper finger by springs, gaskets, and nut.

According to Figure 4, it can be observed that in this ADR, GGG exchanges heat or cold with the external parts through the copper finger placed underneath. The metallic finger situated above the GGG primarily serve a supportive role, thus the heat transfer capacity of the upper metallic finger is not critical. For the purpose of lightweight design and reducing eddy currents, 6061 aluminum alloy is utilized to manufacture the upper metallic finger of the GGG, which is designed with a hollow structure. The other design details include adjusting the preload force of the springs by installing nuts on the aluminum alloy finger; enhancing heat transfer between the GGG and the copper finger interface using indium sheet, with the other contact areas treated with N-grease for improved heat exchange. To prevent radial displacement of the GGG due to clearance between the perforations and the radial dimensions of the aluminum alloy finger, aluminum foil is wrapped around the aluminum alloy finger to ensure a snug fit. Similarly, to prevent radial displacement of the springs, spring grooves are machined on the gaskets to secure the springs position. Notches are made on the upper plate of the lower copper finger to facilitate surface temperature monitoring of the GGG when necessary.

For the springs, two different sizes of 304 stainless steel springs are selected and nested together for use. As shown in Figure 4, the presence of the springs occupies some space, causing the center of GGG to be positioned slightly lower than the center of the magnetic field.

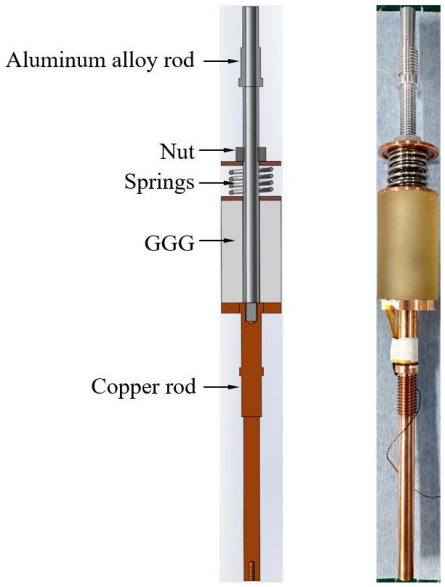

Figure 3 Design and physical diagram of salt pill

4. EXPERIMENTAL SYSTEM AND RESULTS

4.1. Experimental system

The experimental setup employs a pulse tube cryocooler (0.9 W @ 4.2 K) for precooling and a superconducting magnet capable of generating magnetic fields ranging from 0 to 4 T. As depicted in Figure 4, the salt pill is

suspended within the cavity of the magnet by two Kevlar suspensions positioned at the top of the heat sink and at the bottom of the magnet. Given that the upper aluminum alloy finger of the salt pill extends beyond the heat sink, a copper cover is used to shield it, preventing radiation heat leakage from the high-temperature region to the salt pill.

The heat switch employed in the experiment is a custom-made active gas-gap heat switch from Chase Research Cryogenics. While at the ON state, it exhibits a stronger heat transfer capability compared to the standard heat switch, there is also a larger heat leakage when at the OFF state. For the magnet system, the Model 625 superconducting magnet power supply from Lake Shore Cryotronics is utilized as the power supply for the superconducting magnet. Temperature measurements are conducted using temperature sensors from Lake Shore Cryotronics, with temperature data collected using their Model 224 temperature monitor and Model 372 AC resistance bridge. The error of the Model 372 AC resistance bridge, when using a ruthenium oxide temperature sensor in the 1 K temperature range, is influenced by the following factors (Lake Shore Cryotronics, Inc, 2019, n.d.): a measurement resolution of 50.2 mΩ (143 μK); electronic accuracy of 0.9 Ω (2.6 mK); calibration accuracy of ±4 mK; interpolation error of ±0.2 mK; and self-heating error of 1.2 μK. The overall precision is 4.78mK.

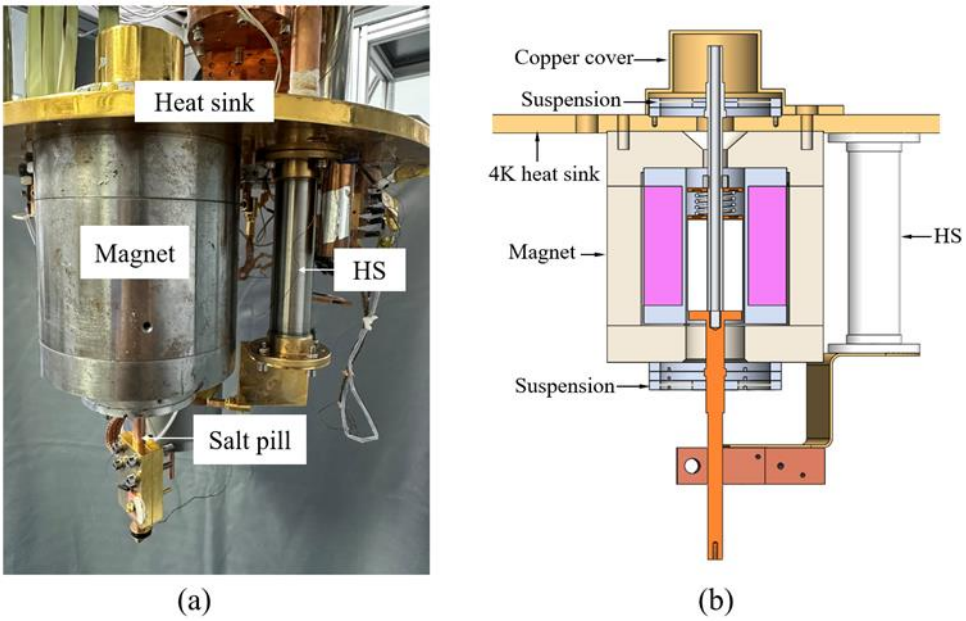

Figure 4 Experimental apparatus. (a) Physical diagram. (b) Structural diagram

4.2. Experimental results

The thermometer is set on the heat transfer copper finger of the salt pill shown in Figure 4. Since it is not necessary to consider the temperature difference between the salt pill and the heat sink during the magnetization process, and to shorten the cycle time, the heat switch remains ON throughout the magnetization process, allowing the GGG to quickly dissipate the generated heat to the heat sink. The demagnetization rate is 7.27 mT/s, and the no-load demagnetization process is shown in Figure 5(a). At the onset of demagnetization, the thermometer on the salt pill exceeds its calibrated range, hence the temperature of the salt pill is not depicted in Figure 5(a). Since the heat switch has only been OFF for a short time, the temperature of the heat sink is considered to be the demagnetization starting temperature. At the end of demagnetization, the salt pill can obtain a minimum temperature of 800.4mK. Testing the salt pill by varying the demagnetization rate, as shown in Figure 5(b), revealed that the demagnetization rate has a weak effect on the minimum temperature. Additionally, isothermal demagnetization of the salt pill at 1 K was conducted, but the salt pill could only maintain a constant temperature for 24 minutes under conditions where only heat switch leakage was present.

For the isothermal demagnetization time is too short possible reasons are: first, the end of the experiment found

that Kevlar suspension line broken, it is inferred that may be the stainless steel springs and GGG are subjected to the force of the magnetic field, so that the salt pill and the 4 K components may be in contact with each other, resulting heat leakage. Secondly, the force applied by the spring may not be appropriate; Thirdly, the change in spring stiffness during the process from room temperature to 4 K is not clear, it is possible that changes in spring stiffness result in variations in contact pressure, thereby affecting the heat transfer effectiveness. These factors can result in high no-load temperatures and short isothermal demagnetization times.

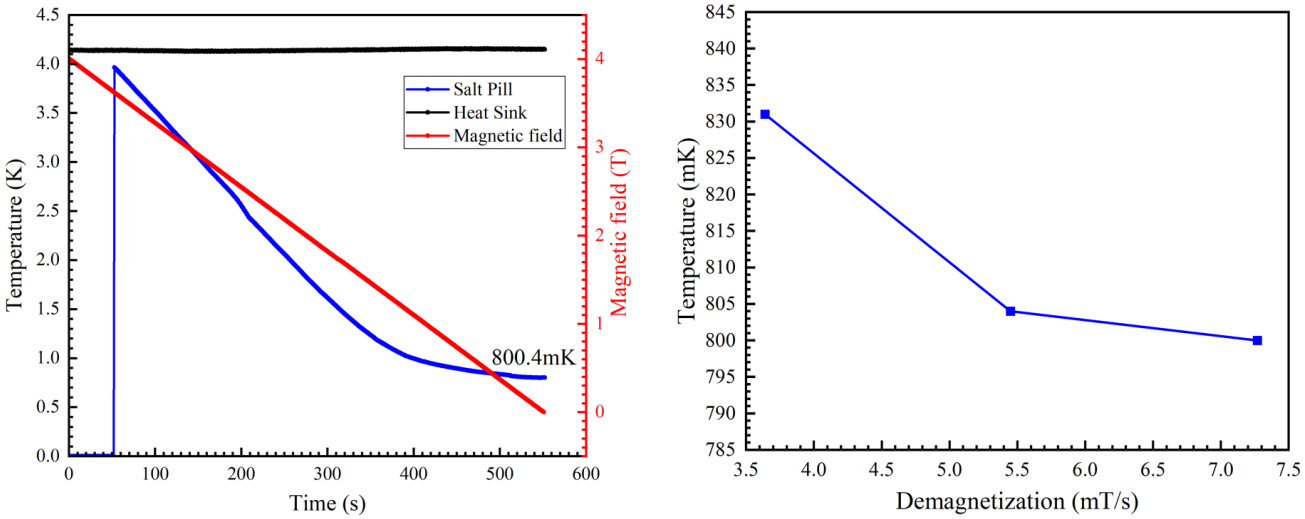

(a) (b)

Figure 5 (a) No-load cool-down curve of salt pill. (b) The change of the minimum temperature of salt pill with the demagnetization rate

5. CONCLUSIONS

To further enhance the structural stability and cooling performance of crystal salt pill, we present the spring-loaded GGG salt pill, two different sizes of stainless steel springs are selected and nested together for use. The experiments achieved a minimum temperature of 800.4 mK. However, the isothermal demagnetization times was only 24 minutes at a cooling temperature of 1 K. Herein, we probe the possible causes of this phenomenon. The pressure-contact salt pill offers structural stability, ease of use, and facilitates the change of MCM, thereby providing a new approach for developing salt pill. Future research will focus on reducing the minimum temperature and extending the isothermal demagnetization times of this salt pill.

ACKNOWLEDGEMENTS

This work is financially supported by the National Key Research and Development Program of China (Grant No. 2021YFC2203303), the Scientific Instrument Developing Project of the Chinese Academy of Sciences (Grant No. GJJSTD20190001), and the National Natural Science Foundation of China (Grant No.51925605).

NOMENCLATURE

ADR	Adiabatic demagnetization refrigerators	MCM	Magnetocaloric materials
GGG	Gadolinium Gallium Garnet	GLF	Gadolinium Lithium Fluoride
HS	Heat switch	DGG	Dysprosium Gallium Garnet

REFERENCES

Antyukhov, A.M., Sidorov, A.A., Ivanov, I., Antonov, A.V., 1987. Thermal expansion of gadolinium gallium garnet. Sov Phys Solid State 29.
Bartlett, J., 2010. Improved performance of an engineering model cryogen free double adiabatic demagnetization refrigerator 9.
DiPirro, M., Fixsen, D., Kogut, A., Li, X., Marquardt, J., Shirron, P., 2012. Design of the PIXIE cryogenic system. Cryogenics, 2011 Space Cryogenics Workshop 52, 134–139. https://doi.org/10.1016/j.cryogenics.2012.01.017
Duval, J.-M., Prouvé, T., Shirron, P., Shinozaki, K., Sekimoto, Y., Hasebe, T., Vermeulen, G., André, J., Hasumi, M., Montier, L., Mot, B., 2020. LiteBIRD Cryogenic Chain: 100 mK Cooling with Mechanical Coolers and ADRs. J. Low Temp. Phys. 199, 730–736. https://doi.org/10.1007/s10909-020-02371-z
Jin, H., Shen, J., Li, C.Z., Wang, C., Yu, F.Q., Zu, H.Y., Liu, P., Ding, J., Li, K., Wang, Y.N., Dai, W., Zhou, Y., Cui, W., 2022. Development of Adiabatic Demagnetization Refrigerator for Future Astronomy Missions. Iop Conf. Ser.: Mater. Sci. Eng. 1240, 012027. https://doi.org/10.1088/1757-899X/1240/1/012027
Kanao, K., Yoshida, S., Miyaoka, M., Tsunematsu, S., Otsuka, K., Hoshika, S., Narasaki, K., Mitsuda, K., Yamasaki, N., Takei, Y., Fujimoto, R., Sato, Y., Okamoto, A., Noda, H., DiPirro, M.J., Shirron, P.J., 2017. Cryogen free cooling of ASTRO-H SXS Helium Dewar from 300 K to 4 K. Cryogenics 88, 143–146. https://doi.org/10.1016/j.cryogenics.2017.10.018
Lake Shore Cryotronics, Inc, 2019. Model 372 AC Resistance Bridge and Temperature Controller User's Manual.
Lake Shore Cryotronics, Inc, n.d. Model 372 AC resistance bridge [WWW Document].
Li Ke, Wang Ya-Nan, Liu Ping, Yu Fang-Qiu, Dai Wei, Shen Jun, 2023. Experimental research on a 50 mK multi-stage adiabatic demagnetization refrigerator. Acta Phys. Sin. 72, 37–44.
Pobell, F., 2007. Matter and methods at low temperatures, 3rd, rev.expanded ed ed. Springer, Berlin ; New York.
Shirron, P., Kimball, M., Wegel, D., Miller, F., 2010. ADR design for the Soft X-ray Spectrometer instrument on the Astro-H mission. Cryogenics 50, 494–499. https://doi.org/10.1016/j.cryogenics.2010.02.018
Shirron, P.J., Kimball, M.O., DiPirro, M.J., Bialas, T.G., 2015. Performance Testing of the Astro-H Flight Model 3-stage ADR. Phys. Procedia 67, 250–257. https://doi.org/10.1016/j.phpro.2015.06.083
Shirron, P.J., Kimball, M.O., Fixsen, D.J., Kogut, A.J., Li, X., DiPirro, M.J., 2012. Design of the PIXIE adiabatic demagnetization refrigerators. Cryogenics 52, 140–144. https://doi.org/10.1016/j.cryogenics.2012.01.009
Shirron, P.J., Kimball, M.O., James, B.L., Muench, T., DiPirro, M.J., Letmate, R.V., Sampson, M.A., Bialas, T.G., Sneiderman, G.A., Porter, F.S., Kelley, R.L., 2016. Operating modes and cooling capabilities of the 3-stage ADR developed for the Soft-X-ray Spectrometer instrument on Astro-H. Cryogenics 74, 2–9. https://doi.org/10.1016/j.cryogenics.2015.10.013
Shirron, P.J., McCammon, D., 2014. Salt pill design and fabrication for adiabatic demagnetization refrigerators. Cryogenics 62, 163–171. https://doi.org/10.1016/j.cryogenics.2014.03.022
Touloukian, Y.S., Kirby, R.K., Taylor, R., Desai, P.D., 1975. Thermophysical Properties of Matter - the TPRC Data Series. Volume 12. Thermal Expansion Metallic Elements and Alloys.
Tuttle, J., Canavan, E., DeLee, H., DiPirro, M., Jahromi, A., James, B., Kimball, M., Shirron, P., Sullivan, D., Switzer, E., 2017. Development of a space-flight ADR providing continuous cooling at 50 mK with heat rejection at 10 K. Iop Conf. Ser.: Mater. Sci. Eng. 278, 012009. https://doi.org/10.1088/1757-899X/278/1/012009
Ventura, G., Perfetti, M., 2014. Thermal Properties of Solids at Room and Cryogenic Temperatures, International Cryogenics Monograph Series. Springer Netherlands, Dordrecht. https://doi.org/10.1007/978-94-017-8969-1
Wang Chang, 2022. System Construction and Experimental Study of Adiabatic Demagnetization Refrigerator for Ultra-Low Temperature Region. Chinese Academy of Sciences.
Wang Chang, Li Ke, Shen Jun, Dai Wei, Wang Ya-Nan, Luo Er-Cang, Shen Bao-Gen, Zhou Yuan, 2021. Ultra-low temperature adiabatic demagnetization refrigerator for sub-Kelvin region. Acta Phys. Sin. 70, 263–269.
WANG Chang, WANG Yanan, LIU Yuanwei, DAI Wei, SHEN Jun, 2019. Heat Switches in Ultralow-temperature Adiabatic Demagnetization Refrigeration System. Vacuum & Cryogenics 25, 317–323.

DOI: 10.18462/iir.thermag.2024.0026

MACHINE LEARNING AND HIGH-THROUGHPUT SCREENING ALGORITHMS FOR OPTIMIZATION OF MAGNETOCALORIC EFFECT IN ALL-D METAL HEUSLER ALLOYS

Danil Baigutlin, Vladimir Sokolovskiy, Vasiliy Buchelnikov, Sergey Taskaev

Faculty of Physics, Chelyabinsk State University
Chelyabinsk, 454001, Russia, d0nik1996@mail.ru

ABSTRACT

This paper examines the application of regression models using active machine learning techniques to predict the structural and magnetic properties, as well as to estimate the magnetocaloric effect of all-d metal Heusler alloys. The accuracy of the model was determined by cross-validation using the coefficient of determination R^2 and the root mean square error RMSE. The model predictions were compared with experimental data and the results of density functional theory (DFT) calculations. The resulting regression model exhibits high accuracy for structural properties, although difficulties in predicting magnetic moments are noted due to the limited representation of magnetic states in the training dataset. The model is capable of qualitatively predicting martensitic transition stoppages for Ni-Co(Fe)-Mn-Ti systems. An improvement of the model could be achieved by extending the training data set to include other possible magnetic states and types of structural disorder.

Keywords: Machine Learning, Heusler Alloys, Magnetocaloric Effect, Magnetic Phase Transitions, Martensitic Transition.

INTRODUCTION

The significance of refrigeration technology is on the rise in modern society, with applications in food storage, maintaining comfortable indoor temperatures, and numerous other purposes. According to the International Energy Agency, total energy consumption for cooling has doubled in the last 50 years. For instance, air conditioning accounts for almost 20% of the total electricity consumed in buildings around the world today [1]. In industrial processes, cooling consumes approximately 10% of the total energy [2]. In contrast to liquefaction-based technologies, caloric cooling does not emit harmful substances into the environment, making it an environmentally friendly technology. One of the promising materials in this field is Heusler alloys. However, traditional X_d-Y_d-Z_{sp} type alloys (e.g., Ni_2MnGa) exhibit high brittleness due to *p-d* covalent hybridization, which leads to material degradation and significantly reduced effect in cyclic phase transitions [3, 4]. A recently proposed method to address this problem is to replace the Z_{sp} element with a transition metal, thereby replacing strong *p-d* covalent hybridization with metallic bonding between elements. This results in enhanced mechanical properties associated with the martensitic transition [5]. In such systems, elastocaloric [5, 6], barocaloric [7] and magnetocaloric [8] effects are observed near room temperature, comparable or even exceeding those of Heusler alloys with *p* and *d* elements. However, the number of possible compositions of all-*d* metal Heusler alloys is vast, and when non-stoichiometric compositions are considered, infinite. The identification of suitable materials among the multitude of possible compositions is a laborious and time-consuming process. Only a limited number of compositions within this series have been investigated in recent years, with the majority being Ni-Mn-Ti [5] with the addition of fourth Co [5, 9], Fe [10], and fifth element Cu [11]. An alternative to traditional random search is the use of machine learning algorithms. The authors of [12] employed machine learning methods to address the optimization of the magnetocaloric effect in Heusler alloys. This approach enabled the identification of several promising new materials for magnetic cooling from complete Heusler alloys. However, the training set used by the authors [12] included exclusively classical Heusler alloys, so the problem of brittleness remains relevant. In the context of Heusler alloys, the optimization of mechanical properties, such as the Pugh coefficient, was carried out using artificial intelligence methods [13]. The objective of this study is to develop a model for predicting the volume, tetragonality parameter, and

magnetization of austenitic and martensitic phases, as well as an algorithm for optimizing the difference in magnetization for a given atomic composition of all-*d* metal Heusler alloys.

MAIN SECTION

Computational methodology and feature engineering

A regression model was constructed for each of the four predicted properties. The prediction of the cell volume was conducted using linear regression, while the Random Forest Regression method was selected for the tetragonality parameter and magnetic moments of the austenitic and martensitic phases. This decision was made due to the presence of complex nonlinear dependencies in the input data. A descriptor, X=(x_1, x_2, ... x_n), was created, where x_i is the value of the feature. Composition-based features were selected to predict the volume of cells, as well as chemical disorder, which was estimated based on Shannon entropy. Composition-based features, Shannon entropy, and the cell volume obtained in the previous step were also used to predict the tetragonal ratio. Finally, the features for predicting magnetic moments included all the previous ones, as well as the tetragonality parameter. The Python matminer module was used to calculate all the features except the Shannon entropy [14].

To avoid the problem of retraining and reduce the required DFT calculations, an active learning technique was employed. The calculations were conducted according to the following scheme: a random atomic composition of three 3*d* elements was generated, and then, based on it, one stoichiometric composition, ten non-stoichiometric compositions with random coefficients, and ten compositions with the addition of a random concentration of the fourth atom were created. Subsequently, density functional theory (DFT) calculations were conducted with the PBE functionality [15], implemented in the VASP software package [16], for both austenitic and martensitic structures using a complete structural optimization procedure. This yielded reference values for the volume, tetragonality parameter, and magnetic moments of the austenitic and martensitic phases. The type of structure was selected in accordance with the established classical rule for conventional Heusler alloys. It should be noted, however, that this is a simplification, and in all-*d* metal alloys, the *Z* atom must also be taken into account (see reference [17]). Subsequently, the generated compositions were descriptorized, and a regression model was compiled in the Scikit-learn Python module [18]. The predictions of the regression model were compared with DFT calculations, and only those compositions for which the deviation of the DFT prediction and the model was > 5% were added to the training dataset. This procedure was performed iteratively until an average deviation of < 5% was obtained over ten iterations.

Evaluation of the regression models

Cross-validation was used to assess the stability and generalizability of the model. The test set consisted of 1,000 samples that were not included in the training set. This separation enabled the evaluation of the model's performance on a large number of independent data sets and the determination of its accuracy in predicting the structural and magnetic properties of all-*d* metal Heusler alloys.

Two metrics are used to determine the accuracy of regression models in this paper. The first is the coefficient of determination R^2, which is determined by the proportion of the variance in the dependent variable that can be predicted from the independent variables the closer this coefficient is to one, the better description is given by the model.

$$R^2 = 1 - \frac{SS_{res}}{SS_{tot}} = 1 - \frac{\sum_{i=1}^{n}(y_i - \hat{y}_i)^2}{\sum_{i=1}^{n}(y_i - \bar{y})^2}, \qquad \text{Eq. (1)}$$

where SS_{res} represents the sum of squared residuals and SS_{tot} represents the total sum of squares and y_i is the actual value, $\hat{y}_i$ is the predicted value.

The second metric is root mean square error (RMSE), which quantifies the root of average squared

difference between the actual and predicted values. It provides a measure of the model's precision, with lower RMSE values indicating a closer fit of the model to the data points.

$$RMSE = \sqrt{\frac{1}{n}\sum_{i=1}^{n}(y_i - \hat{y}_i)^2}, \qquad \text{Eq. (2)}$$

where y_i is the actual value, $\hat{y}_i$ is the predicted value, and n is the number of data points.

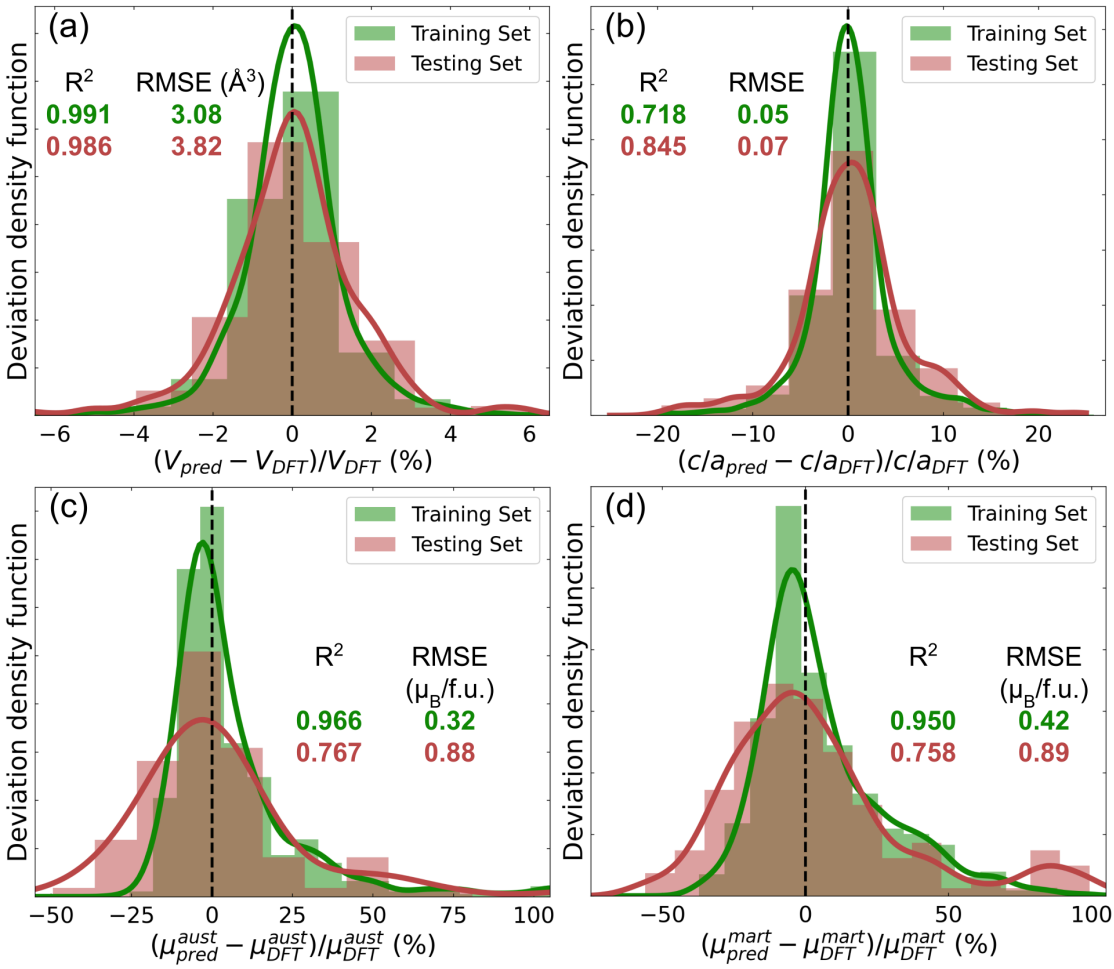

Figure 1: Distribution density of the regression prediction results and the R^2 and RMSE metrics for the training and test sets for (a) volume of cell, (b) tetragonal ratio and (c, d) magnetic moment of austenitic and martensitic phase of all-*d* metal Heusler alloy

Fig. 1 shows the distribution density of the regression prediction results and the R^2 and MSE metrics for the training and test sets for volume, tetragonality parameter and total magnetic moment for austenitic and martensitic phases. The cell volume is fully described by the model and is the average between the volumes of the elementary cells of its constituent elements, which is in good agreement with the results of the work [17]. The tetragonality parameter is primarily influenced by the atomic mass of the alloy (≈ 20%), the magnetic moment of the elements composing the alloy in their ground state (≈ 10%) and the cell volume (≈ 5%). The absolute error in determining the tetragonality parameter is approximately 0.07 and thus makes it possible to reliably predict the geometry of the martensitic phase in all-*d* metal Heuslers, which are characterized by a large *c*/*a*. Finally, for the prediction of magnetic moments in the case of austenite, the main influence (≈ 35%) is

exerted by the magnetic moment of the constituent elements of the alloy in their ground state, electronegativity (≈ 5%), as well as atomic mass, volume and structural disorder (≈ 3%), for the martensitic structure the situation is almost the same, but a significant influence the tetragonality ratio (≈ 5%) also has an effect. The R^2 and RMSE values for magnetic moment differ more significantly between the test and training samples, which indicates an increase in the problem of retraining. In addition, the distribution profile becomes asymmetric with a slope towards a higher estimate of the model relative to the DFT. Both of these factors are most likely related to the overwhelming presence of ferromagnetic phases in the training set, whereas other magnetic states, such as AFM, are experimentally known [5].

Predictions for the all-d metal half-Heusler alloys

In order to test the model, it is necessary to compare the results with those available in the literature. At the first stage, the magnetic moments of the ground state of several all-*d* metal Heusler alloys were first predicted. Fig. 2 shows the results of predictions of magnetic moments in comparison with those calculated in [19]. The values obtained from the regression model follow the trends calculated using DFT. The maximum deviation of the magnetic moment is 33%, while the average deviation from the DFT values is 15%, which is consistent with the results shown in Fig. 1. The largest deviation is observed for Mn_2TiZn, Ni_2CoFe, and Ni_2FeCu. This is likely due to the fact that these all-*d* metal alloys, depending on the concentration of the constituent elements, have a complex magnetic structure, including ferromagnetic, antiferromagnetic, and non-magnetic configurations that are not sufficiently represented in the training dataset.

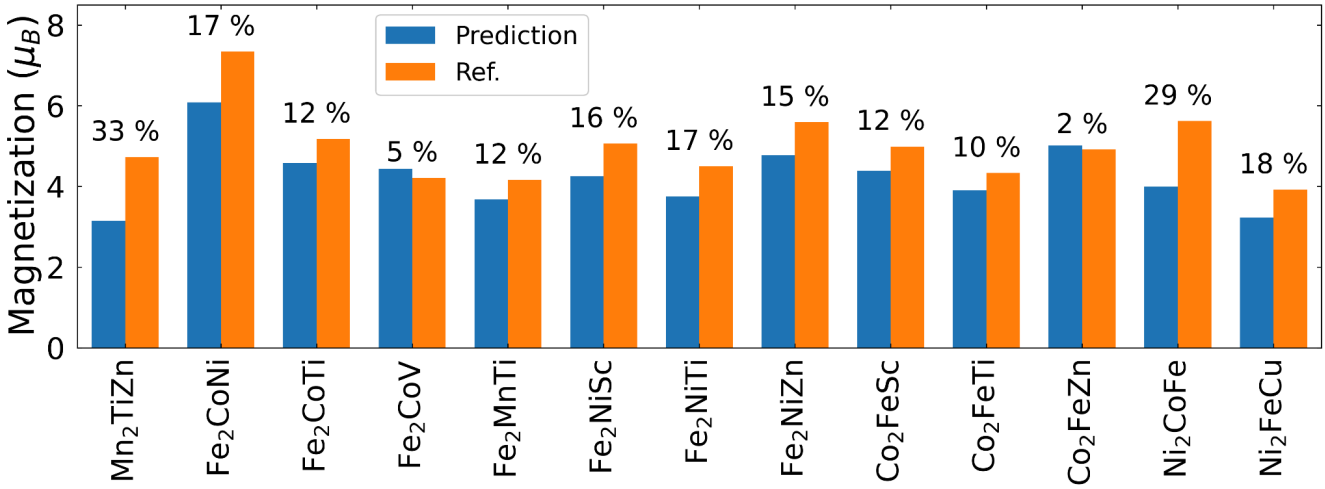

Figure 2: The magnetization of the ground state for a number of all-*d* metal Heusler alloys. Reference values (Ref.) correspond to the values from the work [19]. The numbers above the bars show the deviations between the magnetization of the obtained DFT and the regression model

An indirect indicator of the magnitude of the magnetocaloric effect can be the difference in magnetic moments between the austenitic and martensitic phases Δμ. Fig. 3 shows the Δμ for the Ni-Mn-Ti system with Fe and Co substitution. According to the experimental data [13], there is no martensitic transition to a Fe concentration of 17% for $Ni_{50-x}Fe_xMn_{35}Ti_{15}$. Further, martensitic transformation is possible, and the difference in magnetization between the austenitic and martensitic phases increases with increasing Fe concentration. The regression model, the results of which are presented in Fig. 3(a), qualitatively replicates the results indicating a pronounced increase in magnetization at a Fe concentration of 15%. However, the model is currently unable to predict the complete absence of the martensitic phase at Fe concentrations up to 15%. The results presented in Fig. 3(b) demonstrate similar trends for $Ni_{35}Co_{15}Mn_{50-x}Ti_x$ and $Ni_{33}Co_{17}Mn_{50-x}Ti_x$ Heusler alloys series. The authors of [12] experimentally and theoretically predicted that the martensitic transformation would cease at low and high Ti concentrations, which are marked by shaded areas on the boundaries of the martensitic transition.

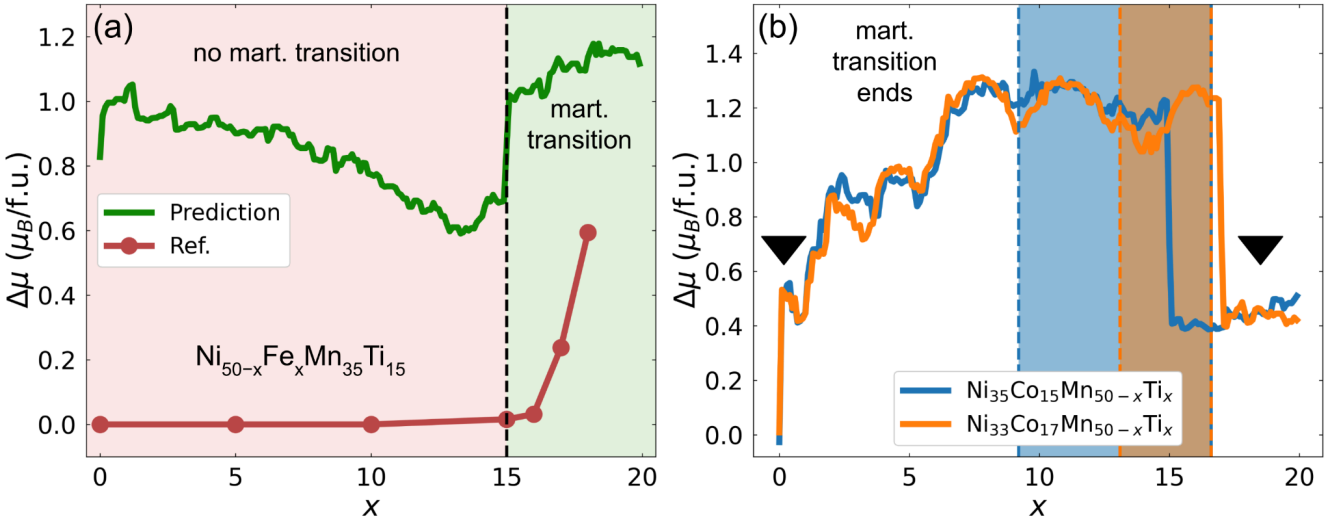

Figure 3: The difference in magnetization between the austenitic and martensitic phases Δμ for (a) $Ni_{50-x}Fe_xMn_{35}Ti_{15}$ and (b) $Ni_{35}Co_{15}Mn_{50-x}Ti_x$ (blue) and $Ni_{33}Co_{17}Mn_{50-x}Ti_x$ (orange), depending on the concentration of the additional element. The experimental values are taken from the works [12, 13]. Black triangles indicate areas where the martensitic transition is stopped

The regression model is able to quantitatively predict the cessation of the transition at high concentrations, which is expressed by a sharp decline in the difference Δμ. At low Ti concentrations, a reduction in the difference in magnetization is also observed, although the concentrations are far from those observed experimentally. The absence of a martensitic transition is predicted for the Ni-Co-Mn system.

CONCLUSIONS

A regression model is constructed to estimate the difference in magnetization between the austenitic and martensitic phases of al-d Heusler alloys. The highest accuracy is obtained for structural properties, while magnetic moments are the most challenging for regression models. Inaccuracies in the prediction of magnetic properties are most likely related to complexity in determining the basic magnetic state of the compositions used for training, since only ferromagnetic and nonmagnetic states were considered. The constructed models were used to predict the magnetization of several systems based on Fe, Co, and Ni-Co(Fe)-Mn-Ti. In the case where the system has a ferromagnetic ordering, a quantitative agreement of the results with the DFT calculations is observed. For the Ni-Fe-Mn-Ti system, the appearance of a martensitic transformation and the subsequent nonlinear increase in the magnetization difference between the austenitic and martensitic phases with an increase in Fe doping are qualitatively shown. For the Ni-Co-Mn-Ti system, the qualitative agreement of the suppression of martensitic transformation with an increase and decrease in Ti concentration with experimental results is shown. To improve the predictions of the regression model, it will be necessary to add other basic magnetic states as well as structural disorder, such as B2, to the training set.

ACKNOWLEDGEMENTS

The research was supported by the RSF - Russian Science Foundation project No. 24-12-20016.

REFERENCES

[1] IEA (2018), The Future of Cooling, IEA, Paris https://www.iea.org/reports/the-future-of-cooling, License: CC BY 4.0

[2] Pezzutto, S., Quaglini, G., Riviere, P., Kranzl, L., Novelli, A., Zambito, Bottecchia L., Wilczynski, E., 2022. Space cooling market in Europe: assessment of the final energy consumption for the year 2016. Sustainability, 14(5), 2667.

[3] Gamzatov, A. G., Aliev, A. M., Ghotbi Varzaneh, A., Kameli, P., Abdolhosseini Sarsari, I., Yu, S. C., 2018. Inverse-direct magnetocaloric effect crossover in Ni47Mn40Sn12.5Cu0.5 Heusler alloy in cyclic magnetic fields. Applied Physics Letters, 113(17).

[4] Law, J. Y., Moreno-Ramírez, L. M., Díaz-García, Á., Franco, V., 2023. Current perspective in magnetocaloric materials research. Journal of Applied Physics, 133(4).

[5] Wei, Z. Y., Liu, E. K., Chen, J. H., Li, Y., Liu, G. D., Luo, H. Z., et al., 2015. Realization of multifunctional shape-memory ferromagnets in all-d-metal Heusler phases. Applied Physics Letters, 107(2).

[6] Wei, Z. Y., Sun, W., Shen, Q., Shen, Y., Zhang, Y. F., Liu, E. K., Liu, J., 2019. Elastocaloric effect of all-d-metal Heusler NiMnTi(Co) magnetic shape memory alloys by digital image correlation and infrared thermography. Applied Physics Letters, 114(10).

[7] Aznar, A., Gràcia-Condal, A., Planes, A., Lloveras, P., Barrio, M., Tamarit, J. L., et al., 2019. Giant barocaloric effect in all-d-metal Heusler shape memory alloys. Physical Review Materials, 3(4), 044406.

[8] Liu, K., Ma, S., Ma, C., Han, X., Yu, K., Yang, S., et al., 2019. Martensitic transformation and giant magneto-functional properties in all-d-metal Ni-Co-Mn-Ti alloy ribbons. Journal of Alloys and Compounds, 790, 78-92.

[9] Beckmann, B., Koch, D., Pfeuffer, L., Gottschall, T., Taubel, A., Adabifiroozjaei, E., et al., 2023. Dissipation losses limiting first-order phase transition materials in cryogenic caloric cooling: A case study on all-d-metal Ni(-Co)-Mn-Ti Heusler alloys. Acta Materialia, 246, 118695.

[10] Zeng, Q., Shen, J., Zhang, H., Chen, J., Ding, B., Xi, X., et al., 2019. Electronic behaviors during martensitic transformations in all-d-metal Heusler alloys. Journal of Physics: Condensed Matter, 31(42), 425401.

[11] Zhang, F., Westra, K., Shen, Q., Batashev, I., Kiecana, A., van Dijk, N., Brück, E., 2022. The second-order magnetic phase transition and magnetocaloric effect in all-d-metal NiCoMnTi-based Heusler alloys. Journal of Alloys and Compounds, 906, 164337.

[12] Court, C. J., Jain, A., Cole, J. M., 2021. Inverse design of materials that exhibit the magnetocaloric effect by text-mining of the scientific literature and generative deep learning. Chemistry of Materials, 33(18), 7217-7231.

[13] Liu, H. X., Yan, H. L., Jia, N., Tang, S., Cong, D., Yang, B., et al., 2022. Machine-learning-assisted discovery of empirical rule for inherent brittleness of full Heusler alloys. Journal of Materials Science and Technology, 131, 1-13.

[14] Ward, L., Dunn, A., Faghaninia, A., Zimmermann, N. E., Bajaj, S., Wang, Q., et al., 2018. Matminer: An open source toolkit for materials data mining. Computational Materials Science, 152, 60-69.

[15] Perdew, J. P., Burke, K., Ernzerhof, M., 1996. Generalized gradient approximation made simple. Physical review letters, 77(18), 3865.

[16] Kresse, G., Joubert, D., 1999. From ultrasoft pseudopotentials to the projector augmented-wave method. Physical review b, 59(3), 1758.

[17] Li, G., Liu, E., Wang, W., Wu, G., 2023. Theoretical investigations on elastic properties, phase stability, and magnetism in Ni_2Mn-based all-d− metal Heusler compounds. Physical Review B, 107(13), 134440.

[18] Pedregosa, F., Varoquaux, G., Gramfort, A., Michel, V., Thirion, B., Grisel, O., et al., 2011. Scikit-learn: Machine learning in Python. The Journal of machine Learning research, 12, 2825-2830.

[19] Marathe, M., Herper, H. C., 2023. Exploration of all-d Heusler alloys for permanent magnets: An ab initio based high-throughput study. Physical Review B, 107(17), 174402.

DOI: 10.18462/iir.thermag.2024.0027

EXPERIMENTAL STUDY ON LONG-DISTANCE HELIUM PULSATING HEAT PIPES

Rendong Guo [a,b], Yaran Shi [a,b],Li Shi[a], Peng Jia [a,*] , Dong Xu [a,*], Chuanjun Huang [a], Laifeng Li [a,b]

[a] Key Laboratory of Cryogenics, Technical Institute of Physics and Chemistry, Chinese Academy of Sciences
Beijing 100190, China
[b] University of Chinese Academy of Sciences
Beijing 100049, China E-mail: xudong@mail.ipc.ac.cn, jiapeng@mial.ipc.ac.cn

ABSTRACT

Superconducting magnets are typically maintained in a cryogenic environment to sustain their superconducting state. The use of cryocoolers for conductive cooling of these magnets has emerged as a cost-effective and operationally simple cooling trend. However, achieving an efficient heat connection between cryocoolers and low-temperature superconducting magnets has become a key concern. Vibrations and electromagnetic interference from the cold head can impact magnet performance, while the leakage field from high-field magnets can affect cryocooler efficiency. Furthermore, the integration of coolers and cooled objects necessitates efficient heat transfer units for long-distance heat conduction. Pulsating heat pipes have shown remarkable advantages in this aspect.

This study aims to experimentally investigate the heat transfer characteristics of long-distance liquid helium pulsating heat pipes. Specifically, it seeks to explore the relationship between the effective heat transfer coefficient of these heat pipes and the length of heat transfer while providing theoretical explanations.

Keywords: Superconducting magnet quenching; pulsating heat pipe (PHP); cryogenic; Two-phase helium; filling ratio.

1. INTRODUCTION

Superconducting magnets are typically maintained in a superconducting state under low-temperature conditions. The use of a cryocooler for conductive cooling of superconducting magnets is a new cooling trend due to its simplicity and low operational cost[1,2]. However, the efficient heat transfer between the cryocooler and the low-temperature superconducting magnet has become an increasingly important issue. On one hand, the vibration and electromagnetic interference of the cryocooler can affect the performance of the superconducting magnet[3]. On the other hand, the leakage magnetic field of high-field magnets can impact the performance of the cryocooler. Furthermore, the integration of cooling components with the cooled objects necessitates an efficient heat transfer unit to meet the demands of long-distance cryogenic conduction.

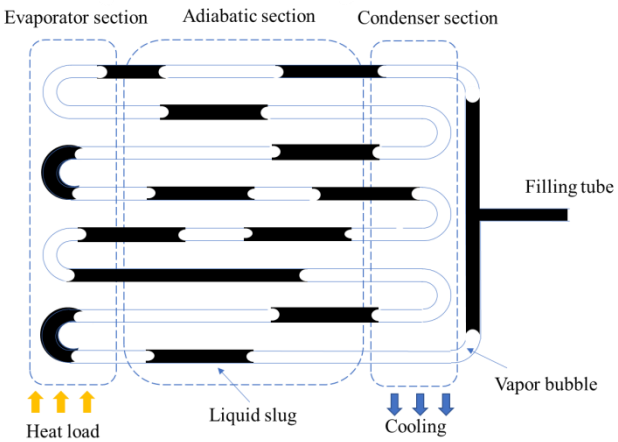

Fig. 1.Schematic of a typical closed-loop PHP.

Pulsating heat pipes (PHPs), as highly efficient heat transfer devices, have a structure as shown in the Fig. 1[4]. In the capillary network, the working fluid operates in a saturated state, where alternating plugs of gas and liquid form randomly under the influence of surface tension. In the evaporator section, the working fluid absorbs heat and rapidly expands, generating bubbles, which then increase the pressure and propel the working fluid towards the condenser section. In the condenser section, the bubbles cool down, contract, and burst, leading to a pressure drop and creating a pressure difference between the two ends and among adjacent tubes. This pressure imbalance drives the oscillatory motion of the working fluid, enabling heat transfer. The unique heat transfer mechanism of PHPs theoretically ensures that their thermal resistance does not increase with the length of heat transfer. Therefore, PHPs exhibit outstanding advantages in long-distance cryogenic conduction. The objective of this study is to experimentally investigate the heat transfer characteristics of a long-length liquid helium pulsating heat pipe and explore the relationship between the effective thermal conductivity of the pipe and the heat transfer length, along with providing a mechanistic explanation.

2. EXPERIMENTAL APPARATUS AND PHP TYPES

2.1 Experimental apparatus

Fig. 2 shows that the experimental apparatus for heat transfer performance of cryogenic PHPs, which is mainly composed of cooling system, vacuum insulation system, helium filling system, cryogenic PHP, and data acquisition system. The working fluid of PHPs is helium.

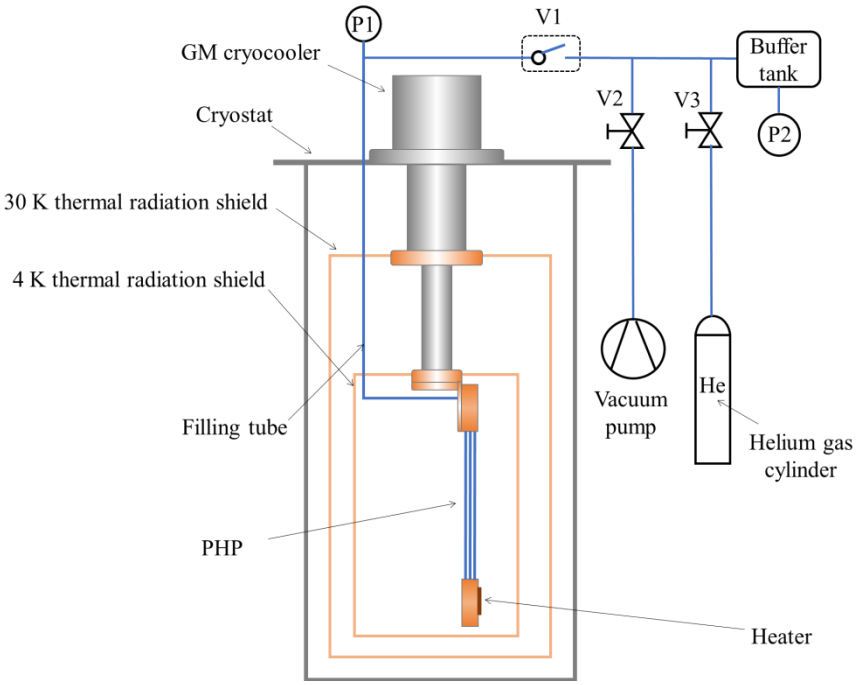

Fig. 2.Schematic of the experimental apparatus.

The cooling system adopts a two-stage GM cryocooler as the cold source. The rated cooling power is as follows: the first stage cold head 35 W@50 K, and the second stage cold head 1.5 W@4.2 K. The lowest temperature is lower than 3.5 K. To reduce heat leakage, the GM cryocooler and the PHP were both placed in the vacuum insulation system, and two layers of radiation shield were set up to eliminate the environmental thermal radiation. The working medium in the PHP was injected from a helium cylinder, and a buffer tank was provided.

The helium filling system incorporates a buffer tank, a gas cylinder, a vacuum pump, two pressure transducers, and three valves. One of the pressure transducers (P1) was fixed in the filling tube to monitor the pressure oscillations of the PHP, another transducer (P2) was installed in the buffer tank to control the filling ratio of the working fluid. The heater installed on the evaporator was powered by a precise variation of current through a DC power supply (Keithley® model 2231A) and the heat load was calculated by the product of voltage and current. The temperatures, the heat load, and the pressures were acquired by a data acquisition system (Keithley® model 3706) connected with the computer and it was out by developing virtual instrumentation.

The condenser section of the PHP was fixed by copper plate and connected to the secondary cold head of the GM cryocooler. The contact surface was tightened by indium sheet and thermal vacuum grease to reduce thermal contact resistance. The evaporator of the PHP was equipped with a manganese-copper resistance wire as a heater. Temperature measurements were conducted using multiple Rhodium-Iron resistance thermometers. Each first and second stage cold head had a single thermometer, while the evaporator and condenser sections of the PHP had two thermometers. The specific locations of the thermometers were visually indicated in Fig. 2 (a), Fig. 3 (a), and Fig. 4 (a), with red markers highlighting their spatial coordinates. For the series-parallel PHP configuration, the exact positions of the thermometers in both the evaporator and condenser sections were depicted in Fig. 6 to provide reference and clarity. All temperature measurements were carried out using a 4-wire configuration, and the lead wires were secured near the thermal anchor using varnish (GE-7031) to ensure thermal stability. To connect the PHP with the helium filling system outside the cryostat, a stainless-steel filling tube with an inner diameter of 0.3 mm was utilized. This small diameter was chosen to minimize heat loss through heat conduction.

2.2 PHP types

The experiment employed four different lengths of liquid helium pulsating heat pipes, with evaporator and condenser sections both utilizing copper plates measuring 100 mm in length and 50 mm in width. The lengths of the adiabatic sections varied at 100 mm, 300 mm, 400 mm, and 500 mm. Each pulsating heat pipe was labeled based on the lengths of its evaporator section, adiabatic section, and condenser section.

The above four types of PHP were made of capillary stainless-steel tubes with an outer diameter of 0.8 mm and an inner diameter of 0.5 mm, which were bent back and forth between the evaporator section and the condenser section. When helium is selected as the working medium, the inner diameter of the PHP satisfies Equation (1), and the working medium is controlled by surface tension to maintain the alternating distribution of vapor bubble and liquid plug[30]. The structure of the evaporator section and the condenser section is similar. The groove with width slightly larger than the outer diameter of PHP was milled on the copper plate, and then the copper plate and PHP were welded together by TIG welding. The above three types of PHPs have the same geometrical dimensions, including the pipe diameter, the size of the copper plate, etc.

$$D_{crit} \leq 2\sqrt{\frac{\sigma}{g(\rho_l - \rho_v)}}\# \tag{1}$$

3. PARAMETERS AND EXPERIMENTAL PROCEDURE

3.1 Parameters

3.1.1 Liquid filling rate

The filling ratio of the helium PHP is defined as the ratio of the volume of liquid helium to the volume of PHP at 4.215 K. The filling ratio of the PHP was calculated from the difference between the pressure indication of the buffer tank at the beginning of cooling and the pressure indication of the buffer tank at the end of PHP intake. The specific calculation process is as follows.

The filling ratio, FR, can be calculated by Equation (2):

$$\mathrm{FR} = \frac{\mathrm{V_l}}{\mathrm{V_{PHP}}} \times 100\%\# \tag{2}$$

where V_{PHP} and V_l are respectively the volume of PHP and the volume of liquid helium in the pipe, in m^3. V_{PHP} is calculated by the PHP specification. V_l is the volume of saturated liquid helium. According to the law of mass conservation, the mass can be calculated by Equation (3):

$$\mathrm{m_t} = \rho_\mathrm{l}\mathrm{V_l} + \rho_\mathrm{v}(\mathrm{V_{PHP}} - \mathrm{V_l})\# \tag{3}$$

where, ρ_V and ρ_L is the density of saturated helium and saturated liquid helium at 4.215 K, in kg/m^3.According to the ideal gas state equation, the mass m_t, which means the helium mass in PHP, in kg, can be calculated by Equation (4):

$$\frac{P_0 V_{BT}}{R_g T_{amb}} = \frac{P_1 V_{BT}}{R_g T_{amb}} + \frac{P_1 V_{FT}}{R_g T_{FT}} + m_t \# \quad (4)$$

where P_0 and P_1 are the initial pressure and final pressure of the buffer tank at the beginning and end of the filling process, respectively, in Pa; V_{FT} and V_{BT} are the volume of helium filling pipe (the part from valve V1 to PHP) and buffer tank, respectively, in m^3; T_{FT} and T_{BT} are the average temperatures of the helium filling pipe and buffer tank, respectively, in K; T_{amb} is the ambient temperature of the experimental setup, in K; and R_g is the gas constant of helium, Rg=2077 J/(kg · K) .

According to the initial and final pressure of the buffer tank, the filling ratio of the PHP can be determined. The calculation formula of the filling ratio considers the influence of the volume of the helium filling pipe, and the volume of the rest of the pipes of the helium filling system is considered as a part of the volume of the buffer tank.

3.1.2 Effective thermal conductivity

The effective thermal conductivity of cryogenic PHPs is usually used to evaluate their heat transfer performance. The effective thermal conductivity of PHPs is calculated by the data after they reach a stable state under each heating power. The calculation formula is as follows:

$$K_{eff} = \frac{L}{A} \cdot \frac{Q}{T_E - T_C} \#(5)$$

where, Keff is the effective thermal conductivity of the PHP, expressed in W/(m·K). TC and TE are the average temperatures in the condenser and evaporator sections of the PHP, respectively, expressed in K. Q is the heat load, and the unit is W; A is the cross-sectional area of the PHP (unit: m2); L is the length of the adiabatic section of the PHP (unit: m).

3.1.3 Heat transfer limits

The maximum heat load that the PHP can transmit before drying out is defined as the heat transfer limit of the PHP. At a low filling ratio, when the PHP reaches the heat transfer limit, that is, the temperature of the evaporator section of the PHP keeps rising, while the temperature of the condenser section suddenly drops, which means that the PHP stops running after the heating power increases and cannot transfer heat normally. As the heat transferred from the evaporator section to the condenser section of the PHP decreases, the temperature of the condenser section decreases.

Khandekar et al.[5] found in the visualization experiment that with the increase of heat load, the flow pattern of the working medium in the pipe changed from bubble flow to plug flow, and then to semi-annular flow and annular flow. Wang et al. [6]showed that the thermal resistance of PHPs decreased with the increase of heat load. Hu and Jia [7]reached the same conclusion. However, the heat load cannot be infinite, and there is a heat transfer limit. Once the maximum heat load is exceeded, the PHP fails.

The heat transfer limit is a parameter which characterizes the maximum heat load to the PHP. However, when the heating power is higher than the rated power of the cryocooler, even if the heat transfer limit is reached, the system could reach a stable state. As the temperature of evaporator section increases, the temperature of condenser section increases, and the temperature of secondary cooling head also increases. This will cause the temperature of the condenser section to stabilize rather than drop suddenly. Therefore, when the heating power exceeds 1.5 W, the heat transfer limit measured in the experiment may be higher than the actual heat transfer limit of PHP. The cryocooler used in this experiment is common in practical applications, so the heat transfer limit measured in the experiment can provide reference value for practical application scenarios.

3.2 Experimental steps

After the cooling process, the temperatures in the evaporator and condenser sections of the PHP were reduced to the operating temperature range of liquid helium. Subsequently, a power progressive experiment was conducted. Initially, a heating power of 0.2 W was generated by the heating resistance wire in the evaporator section to monitor and record the temperatures of both the evaporator and condenser sections. Once the temperature and pressure in both sections stabilized, the heating power was increased to 0.4 W until the temperature and pressure reached a steady state again. This process was repeated, increasing the heating power by 0.2 W each time. When the heat load exceeded 2 W, the increase in heating power was changed to

2 W. Furthermore, when the heat load exceeded 10 W, the increase in heating power was adjusted to 3 W. The heat load increment was stopped when the PHP could no longer effectively transfer heat.

4. RESULTS AND DISCUSSION

4.1 Effective thermal conductivity

The experimental findings demonstrate that the PHP with a 0.5 m adiabatic section achieves the highest effective thermal conductivity, reaching up to 70,000 W/(m·K). In contrast, the PHP with a 0.1 m adiabatic section exhibits a consistent and stable trend in effective thermal conductivity. However, the PHP with a 0.5 m adiabatic section displays relatively larger fluctuations in its thermal conductivity trend.

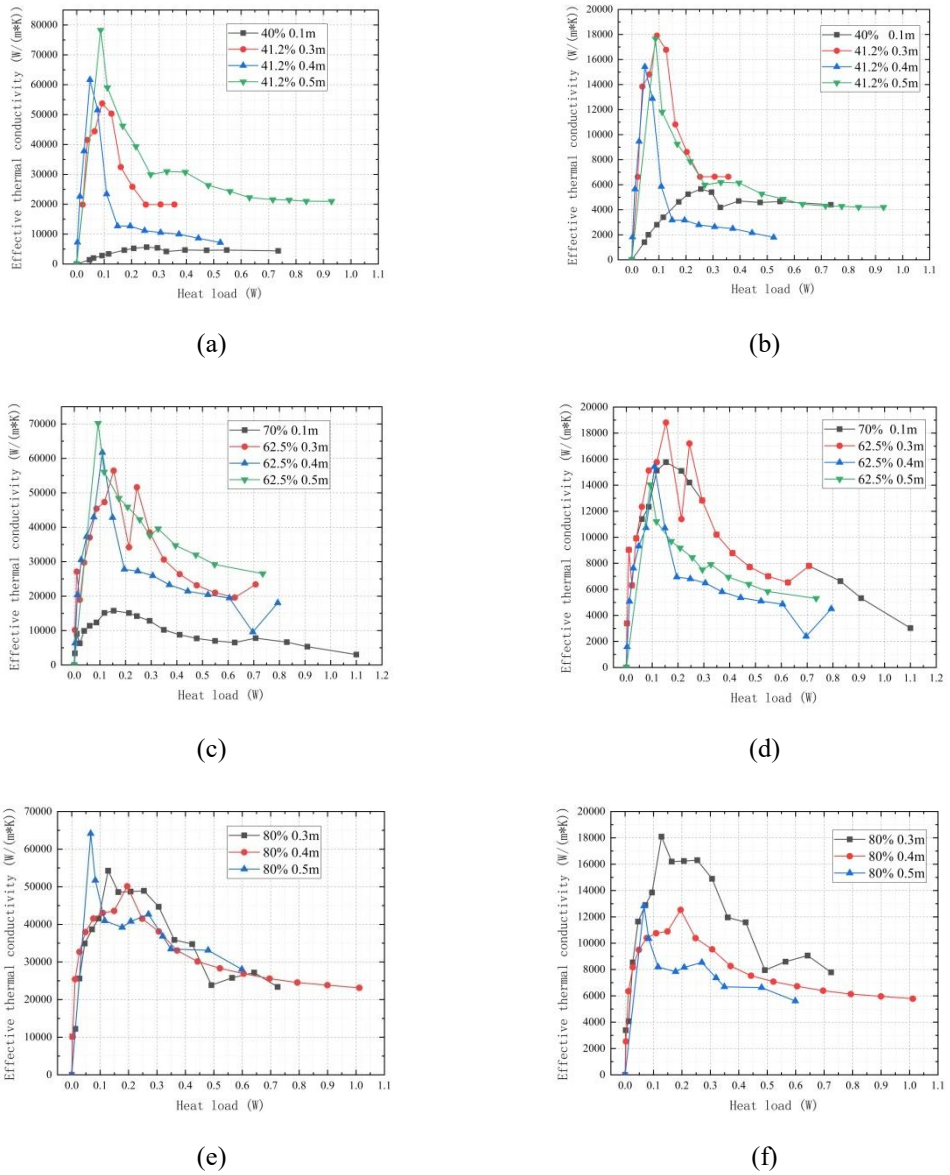

Figure 3 The effect of adiabatic sectionlength on effective thermal conductivity(a) 41.2% of the initial data, (b) 41.2% of the post-processing data, (c) 62.5% of the initial data, (d) 62.5% of the post-processing data, (e) 80% of the initial data, (f) 80% of the post-processing data

At the same structural configuration and different filling ratios, a PHP with a 60 % filling ratio exhibits superior heat transfer performance. This may be attributed to the appropriate filling ratio ensuring a uniform distribution of gas-liquid plugs, minimizing the occurrence of long gas or liquid plugs that impede pulsation. At high filling ratios, prolonged liquid plugs are prone to form within the capillary structure, increasing resistance to pulsatile motion. Conversely, at low filling ratios, extended gas plugs within the capillary

structure similarly hinder the pulsation of two-phase flow. Additionally, at low filling ratios, PHPs are more susceptible to reaching the heat transfer limit at low power levels, leading to dry-out and failure.

It can be observed that there is a significant difference in the effective thermal conductivity of PHPs of different lengths, making direct comparisons challenging. The fundamental trend is that the effective thermal conductivity increases with an increase in the adiabatic section length. This phenomenon arises from the fact that the thermal resistance of PHPs does not vary proportionally with length. As the adiabatic section length increases, the driving force for PHP operation remains unaffected, resulting in minimal weakening of the fluid's pulsating motion. Therefore, the temperature difference between the evaporation and condensation sections does not exhibit a significant change compared to shorter distances. However, the calculated effective thermal conductivity utilizes a heat transfer distance that doubles with the adiabatic section length increment. Consequently, the basic principle is that the effective thermal conductivity increases with the extension of the adiabatic section length. This aspect represents an advantage of PHPs over high-thermal-conductivity metals like copper.

The purpose of this exercise was to examine the relationship between the adiabatic section length and the effective thermal conductivity of the PHPs. By systematically altering the adiabatic section lengths and observing the resulting changes in the effective thermal conductivity, it becomes possible to discern any correlation or patterns between these variables. In order to investigate whether the changes in the two are positively correlated, the effective thermal conductivity of an adiabatic section with a length of 0.3 m was reduced to one-third, and the effective thermal conductivity of an adiabatic section with a length of 0.5 m was reduced to one-fifth. These values were then compared to each other.

Under low-power conditions, the heat transfer performance of the adiabatic section with a length of 0.3 m is superior to that of the adiabatic section with a length of 0.1 m, while the heat transfer performance of the adiabatic section with a length of 0.5 m is weakened. This may be due to the existence of an optimal length that maximizes the effective thermal conductivity in PHPs. When the adiabatic section length is below this value, the heat transfer performance of the PHP continuously improves with increasing length. However, when the adiabatic section length exceeds this value, the flow resistance becomes too high due to the excessive length, and the limited driving force cannot overcome the resistance brought by the long distance, resulting in inefficient operation of the PHP.

Under the same heating power condition, the driving force of the three types of PHPs is the same, while the flow resistance differs due to the different adiabatic section lengths. There exists a specific length value at which the PHP can achieve optimal heat transfer performance, enabling efficient long-distance heat transfer. Experimental results indicate that the optimal adiabatic section length is around 0.3 m.

The purpose of this study was to investigate the relationship between adiabatic section length and heat transfer performance in PHPs. It was found that there is an optimal length value that maximizes the effective thermal conductivity. The heat transfer performance improves with increasing adiabatic section length up to a certain point, after which it starts to decline due to excessive flow resistance. This is because the driving force remains constant while the flow resistance increases with longer adiabatic sections. The optimal adiabatic section length is a crucial parameter for achieving efficient and effective long-distance heat transfer in PHPs.

The progression of heat transfer performance in the three types of PHPs can be attributed to the interplay of slug flow characteristics, heat transfer mechanisms, and the effects of increasing heating power. The enhancement of sensible heat transfer due to increased oscillation amplitudes and gas-liquid slug motion reflects the initial response to rising driving forces. However, the degradation in heat transfer performance occurs when the heat transfer capacity of slug flow lags behind the escalating power input. Subsequently, the intensification of boiling action and the dominance of phase-change heat transfer contribute to the transition towards directed circulation or annular flow patterns, resulting in improved thermal conductivity until the occurrence of dry-out phenomena.

4.2 Heat tansfer limit

In terms of heat transfer limits, the PHPs of 0.3 m, 0.4 m, and 0.5 m exhibit similar heat transfer limits, all around 0.7 W, while the 0.1m PHP shows a significantly higher heat transfer limit of 1.3 W. This disparity can be attributed to the excessively long adiabatic section in longer PHPs, limiting the amount of heat that can be transferred. As the heating power increases, the resulting temperature rise inevitably leads to a higher proportion of gas slugs in the PHP, often causing the formation of long gas slugs that impede the pulsating

motion of the working fluid. Conversely, shorter PHPs experience fewer instances of long gas slugs, which do not hinder pulsating motion under the same power input, enabling more effective heat transfer.

The increase in adiabatic section length results in higher flow resistance within the PHP, leading to an earlier onset of the heat transfer limit and accelerating the failure of the PHP. This phenomenon underscores the critical role of adiabatic section length in determining the heat transfer performance and overall efficiency of PHPs, highlighting the need for optimal design considerations to mitigate flow resistance and enhance heat transfer capabilities.

Despite the significant difference in length between the 0.3m and 0.5m PHPs, their heat transfer limits are quite similar. This similarity arises from the fact that at the same heating power, the temperature rise has already caused the working temperature range of the PHP to depart from the liquid helium temperature zone. While the temperature range of the evaporation section and the condensation section can still remain stable, the PHP has essentially reached a state resembling dryout, rendering it unable to continue effective operation.

Under the same filling ratio conditions, the heating power at which the 0.3m and 0.5m PHPs reach this dryout-like state is similar, leading to a comparable heat transfer limit. This underscores the critical influence of the working temperature range on the heat transfer limit of PHPs, highlighting the need for careful consideration of operating temperatures and their impact on overall performance.

5. CONCLUSION

Based on experimental testing of the heat transfer characteristics of liquid helium pulsating heat pipes (PHPs) with different adiabatic section lengths, the following conclusions can be drawn:

1. The effective thermal conductivity increases with an increase in the adiabatic section length. As the adiabatic section length increases, the driving force for PHP operation remains unaffected, and the weakening of the pulsating motion of the working fluid is relatively minor. Consequently, the temperature difference between the evaporator and condenser sections shows no significant change compared to shorter distances. Therefore, the fundamental trend is that the effective thermal conductivity increases with the adiabatic section length.

2. There exists an optimal length at which a PHP exhibits its best heat transfer performance. Below this length, the heat transfer performance of the PHP improves continuously with increasing length. However, beyond this optimal length, the excessively long adiabatic section leads to increased flow resistance. The limited driving force is unable to overcome the resistance associated with longer distances, thereby hindering the efficient operation of the PHP.

3. Increasing the length of the PHP accelerates the dryout phenomenon and reduces the power range. The excessively long adiabatic section of a long-distance PHP limits the amount of heat that can be transferred. As the heating power increases, the resulting temperature rise inevitably leads to a higher proportion of gas blocking within the PHP, making it highly susceptible to extended gas blocks that impede the pulsating motion of the working fluid.

These findings highlight the intricate relationship between adiabatic section length and the heat transfer performance of PHPs, emphasizing the importance of optimizing the length to achieve efficient and stable operation.

NOMENCLATURE

σ	surface tension (kg/s^2)	m_t	the mass of the working fluid in the PHP (kg)
ρ_l	liquid density (kg/m^3)	T_{FT}	the average temperature of the filling tube (K)
ρ_v	vapor density (kg/m^3)	V_l	the volume of the liquid helium in the PHP (m^3)
g	gravitational acceleration (m/s^2)	V_{PHP}	the volume of the PHP (m^3)
D_{crit}	critical diameter of the capillary tube (m)	R_g	gas constant (J/(kg·K))
FR	filling ratio (%)	k	effective thermal conductivity (W/(m·K))

P_1	the pressure of buffer tank after charge process (Pa)	T_E	the temperature of the evaporator of PHP (K)
P_0	the pressure of buffer tank before charge process (Pa)	T_C	the temperature of the condenser of PHP (K)
V_{BT}	the volume of the buffer tank (m^3)	S	the cross-sectional areaof the PHP (m^2)
V_{FT}	the volume of the filling tube (m^3)	L	length of the adiabatic section (m)
T_{amb}	the temperature of the buffer tank (K)		

REFERENCES

[1] Weijun Shen, Coffey M, McGhee W. Development of 9.5 T NbTi cryogen-free magnet. IEEE Trans AppiledSupercond2001;11:2619–22. https://doi.org/10.1109/77.920405.

[2] Choi YS, Kim DL, Shin DW. Cool-down characteristic of conduction-cooled superconducting magnet by a cryocooler. Phys C Supercond Its Appl 2011;471:1440–4. https://doi.org/10.1016/j.physc.2011.05.212.

[3] Chandratilleke R, Hatakeyama H, Nakagome H. Development of cryogenic loop heat pipes. Cryogenics 1998;38:263–9. https://doi.org/10.1016/S0011-2275(97)00128-8.

[4] Akachi H. Structure of a heat pipe. US Pat 1990;No. 4921041.

[5] Charoensawan P, Khandekar S, Groll M, Terdtoon P. Closed loop pulsating heat pipes. Appl Therm Eng 2003;23:2009–20. https://doi.org/10.1016/S1359-4311(03)00159-5.

[6] Wang XH, Zheng HC, Si MQ, Han XH, Chen GM. Experimental investigation of the influence of surfactant on the heat transfer performance of pulsating heat pipe. Int J Heat Mass Transf2015;83:586–90. https://doi.org/10.1016/j.ijheatmasstransfer.2014.12.010.

[7] Hu C, Jia L. Experimental study on the start up performance of flat plate pulsating heat pipe. J Therm Sci 2011;20:150–4. https://doi.org/10.1007/s11630-011-0450-0

DOI: 10.18462/iir.thermag.2024.0028

B-SITE DOPED AL MODULATION OF MAGNETIC AND MAGNETOCALORIC PROPERTIES OF RARE EARTH-BASED MANGANESE OXIDES $LA_{0.65}CA_{0.35}MNO_3$

Qi Li [(a)], Huaijin Ma [(a, b)], Lei Gao [(b)], Xiang Jin [(a, c)], Jing Zhao [(a)], Jiawei Xu [(a)], Jianjun Zhao [(a)*], Jiaohong Huang [(b)*]

School of Physical Science and Technology, Baotou Teachers' College, Key Laboratory of Magnetism and Magnetic Materials for Higher Education in Inner Mongolia Autonomous Region

Baotou, 014030, China

National Key Laboratory of Baiyunobo Rare Earth Resource Research and Comprehensive Utilization, Baotou Research Institute of Rare Earths

Baotou, 014030, China

School of Physics and Electronic Information, Inner Mongolia Normal University

Hohhot, 010020, China

ABSTRACT

In this work, the modulation of the magnetic and magnetocaloric properties of the classical $La_{0.65}Ca_{0.35}MnO_3$ system by B-site doping with the non-magnetic element Al has been investigated. Structural studies of $La_{0.65}Ca_{0.35}Mn_{1-x}Al_xO_3$ (x=0.0 and 0.1) show that the substitution of the small ionic radius Al^{3+} by Mn^{3+} leads to a decrease in cell volume. Based on the Density functional theory (DFT), the Total Density of States (TDOS) and the Partial Wave Density of States (PDOS) of the system are calculated using the Vienna ab initio Simulation Package (VASP). It is found that the doped system weakens the O-2p orbitals and the Mn-3d crossover, which in turn directly affects the double-exchange interactions of the system. The Curie temperature (T_C) is effectively controlled from 261 K to 98 K. The magnetocaloric effect studies show that the doped samples exhibit a wider full width at half-maximum temperature region (ΔT_{FWHM}), increased from 30.89 K to 50.65 K (at 5 T magnetic field). It showed superior relative cooling capacity (*RCP* = 239.44 $J \cdot kg^{-1}$ (x=0.0, $\mu_0 H$=5T); 281.45 $J \cdot kg^{-1}$ (x=0.1, $\mu_0 H$=5T)) and refrigerant capacity (*RC*= 186.82 $J \cdot kg^{-1}$ (x=0.0, $\mu_0 H$=5T); 229.76 $J \cdot kg^{-1}$ (x=0.1, $\mu_0 H$=5T)). The high overlap between *TEC* (4K) and $|-\Delta S_M{}^{max}|$ at the same magnetic field of the sample after doping suggests good utility. Based on the Landau theory and the magnetocaloric effect, it was found that this series of materials belongs to the type of first-order phase transition and the continuity of the phase transition is enhanced after doping. The B-site doping of Al has been demonstrated to optimize the magnetocaloric properties of the $La_{0.65}Ca_{0.35}MnO_3$ system. The possibility of cryogenic magnetic refrigeration applications for this material is provided.

Keywords: Perovskite, Double-Exchange Interactions, Density Functional Theory, Magnetocaloric Effect, Phase Transition

1. INTRODUCTION

The magnetocaloric effect (MCE) is a phenomenon in which a magnetic material releases heat when magnetized and absorbs heat when demagnetized during the adiabatic process. Magnetic refrigeration technology has been extensively studied in recent decades due to its effect [1-5]. Compared to traditional gas compression refrigeration technology, magnetic refrigeration is more environmentally friendly and has a higher theoretical Carnot cycle efficiency[4]. Magnetic refrigeration technology utilizes a solid magnetic refrigerant as the refrigerant and a specific liquid as the heat exchanger, which is environmentally friendly. This technology avoids the use of harmful refrigerants that can damage the environment. Traditional gas compression refrigeration technology can only achieve 5-10% of the Carnot cycle due to high heat loss. In contrast, magnetic refrigeration technology has a theoretical energy efficiency of 50-70% of the Carnot cycle. Magnetic refrigerants exhibit large MCE in the vicinity of the phase transition due to the strong interactions between charge, spin, and orbital degrees of freedom, as well as significant changes in structure at the phase transition. The evaluation of a material's MCE involves the following coefficients: isothermal magnetic entropy change ($|\Delta S_M|$), relative cooling power (*RCP*), refrigerant capacity (*RC*), and temperature-averaged entropy change (*TEC*) [2] . Magnetic refrigerants can be classified into first-order and second-order phase

transition materials based on the first derivative of the magnetic free energy at the temperature point of the phase transition. [6]。Second-order phase transition materials exhibit a smaller maximum magnetic entropy change compared to first-order phase transition materials due to the absence of a significant structural transition at the phase transition point. This limits their applications [6]. Therefore, researchers have focused on developing new materials for first-order phase transition magnetic refrigeration.

Several first-order phase transition magnetic refrigerants have been developed, such as $Gd_5(Si_{1-x}Ge_x)_4$, $MnFeP_{0.45}As_{0.45}$, and $La(Fe_xSi_{1-x})_{13}$, etc [7-9]. However, achieving these material properties requires high purity of raw materials, which can be difficult to obtain. Additionally, the preparation process is complex and may involve the use of toxic elements, which can be a disadvantage. It is important to note these potential drawbacks when considering the use of these materials. Perovskite manganese oxides are commonly synthesized using metal oxides and carbonates as raw materials through a low-cost, solid-state reaction method at high temperatures. This process is simple and efficient. Perovskite manganese oxides exhibit lower hysteresis and thermal hysteresis in comparison to conventional first-order phase transition magnetic refrigerants in terms of performance [10,11].Therefore, this material compensates for the limitations of traditional first-order phase transition magnetic refrigerants and is presently the primary material under development in the field of magnetic refrigeration [12,13]. Rare earth elements possess large magnetic moments because of the significant number of unpaired electrons in their 4f layer and the electromagnetic shielding effect of the outermost electrons on the electrons in the 4f layer. Rare earth-based perovskite manganese oxides typically exhibit a large MCE. Rare-earth-based perovskite manganese oxides with a cubic ABO_3-type structure contain trivalent rare-earth ions (such as La^{3+} and Pr^{3+}) or doped divalent alkaline-earth-metal ions (such as Ca^{2+}, Sr^{2+}, and Ba^{2+}) at the A-site located at the top corners of the cubes[14, 15]. B-site at the center of the cube is occupied by manganese ions (Mn^{3+} and Mn^{4+}) or doped ions of other transition group metals such as Fe, Co, Ni, and Cr [15]. The six adjacent oxygen ions O^{2-} occupy the cubic center and form a coordination octahedron with the B-site [15]. The system exhibits rich spin-orbit properties due to mutual coupling and interactions between spin, orbital, and lattice degrees of freedom [15, 16]. Jeong et al. [17] discovered that decreasing Sr^{2+} in the $La_{1-x}Sr_xMnO_3$ system can increase the maximum magnetic entropy change $|\Delta S_M^{max}|$. The values for $|\Delta S_M^{max}|$ were found to be 1.10 $J\cdot kg^{-1}K^{-1}$ (x=0.35; $\mu_0 H$=1T), 1.14 $J\cdot kg^{-1}K^{-1}$ (x=0.3; $\mu_0 H$=1T), and 1.42 $J\cdot kg^{-1}K^{-1}$ (x=0.2; $\mu_0 H$=1T). Tonozlis et al. [18] discovered that the maximum magnetic entropy change, $|\Delta S_M^{max}|$, of the $La_{1-x}Ba_xMnO_3$ system effectively increases from 1.51 $J\cdot kg^{-1}K^{-1}$ (x=0.1; $\mu_0 H$=2T) to 2.61 $J\cdot kg^{-1}K^{-1}$ (x=0.3; $\mu_0 H$=2T) with the increase of Ba^{2+} content.

$LaMnO_3$ is a rare-earth-based perovskite manganese oxide that exhibits an antiferromagnetic state resulting from the super-exchange interaction between Mn^{3+} - O^{2-} - Mn^{3+}. Replacing La3+ with a divalent alkaline-earth-metal ion results in the formation of a mixed Mn3+/Mn4+ valence state. This promotes a ferromagnetic double exchange interaction between Mn^{3+} - O^{2-} - Mn^{4+} [19-21]. The structural phase transition in rare-earth-based perovskite manganese oxides causes changes in the $\theta_{Mn\text{-}O\text{-}Mn}$ bond angles and $d_{Mn\text{-}O}$ bond lengths, resulting in an abrupt change in magnetization strength[22]. In contrast, structural phase transitions in such materials are typically driven by an applied magnetic field, which can result in significant MCEs. Compounds in the (La-Ca)MnO_3 system, where Ca^{2+} is used as a doping element, have a stable perovskite structure and exhibit an excellent MCE [23-28]. The MCE of the (La-Ca)MnO_3 system is especially significant when the La:Ca elemental ratio is approximately 7:3 [6]. Most of the experiments have shown that the (La-Ca) sites are doped for good modulation of the magnetic properties and MCE of this system [29-35]。However, most of the above studies on secondary doping lead to disappearance of the first-order phase transition characteristics, which drastically reduces the maximum magnetic entropy change. Moreover, there are few reports on the doping of (La-Ca) MnO_3 system with non-magnetic elements at the Mn site. Therefore, we choose the $La_{0.65}Ca_{0.35}MnO_3$ (parent sample) system with a small amount of Mn doped with Al to prepare the $La_{0.65}Ca_{0.35}Mn_{0.9}Al_{0.1}O_3$ sample. The structure, magnetic properties, magneto-thermal effects and phase transitions were investigated.

2. EXPERIMENTAL

$La_{0.65}Ca_{0.35}Mn_{1-x}Al_xO_3$ (x=0.0 and 0.1) polycrystalline samples were prepared by solid-state reaction method at high temperatures. Firstly, high purity La_2O_3、$CaCO_3$、Al_2O_3 and MnO_2 powdered raw materials (Alfa Aesar) with purity greater than 99.99 wt% according to stoichiometric ratios were dried and placed in a ball mill (Omni-Directional Planetary Ball Mill QM-QX04) for 6h of grinding and mixing. 12h of sintering at 900°C by chamber sintering furnace (TM KSL-1700X Chamber Sintering Furnace). Then, secondary grinding was carried out and finally 24h of sintering at 1350°C completed the preparation. The powder samples were examined for their microstructure and composition using a field emission microscope (SIGMA500) equipped with an energy dispersive spectroscopy (Bruker EDS QUANTAX). The crystal

structure was analyzed using an X-ray diffractometer (X-pertpowder). The density functional theory (DFT) calculation by the Vienna ab initio Simulation Package (VASP) was performed for the high-pressure samples according to the obtained lattice information. In the calculation, we used a generalized gradient approximation +U(GGA+U) of the Pardew–Burke–Brinkerhoff (PBE) method. The truncation energy of the plane wave was set to 520 eV. The k-points used in the Brillouin zone were generated using the Monkhorst–Pack method, and the k-point grid was 9 × 9 × 1 in electron self-consistent calculations. The process was terminated when the energy acting was $<1 \times 10^{-6}$ eV/Å. The temperature-dependent variation of magnetization intensity (M-T) and isothermal magnetization curves (M-H) were measured using a vibrating sample magnetometer (P525 type VSM) in a multifunctional physical property measurement system (Quantum Design PPMS-9).

3. RESULTS AND ANALYSIS

3.1 Composition and Structure

Determination of each element of $La_{0.65}Ca_{0.35}Mn_{1-x}Al_xO_3$ (x=0.0 and 0.1) polycrystalline samples using SEM piggybacked EDS is shown in Fig. 1 (a, b). To assess the homogeneity of the prepared samples, we tested the elemental contents and average values of La, Ca, Mn, Al, and O at a serie of points. The elemental content's proximity at each point confirms the samples' excellent homogeneity. As depicted in Fig. 1 (a, b), the average value of each element is near the design value, with a maximum difference of only 0.28%. This indicates successful synthesis of the $La_{0.65}Ca_{0.35}Mn_{1-x}Al_xO_3$ (x=0.0 and 0.1) polycrystalline sample. The XRD pattern of the $La_{0.65}Ca_{0.35}Mn_{1-x}Al_xO_3$ (x=0.0 and 0.1) polycrystalline powder samples are presented in Fig. 2a. Table 1 lists the lattice parameters and the computational error χ^2 obtained from the GSAS software refinement, where the smaller χ^2 reflects the reliability of the refinement results. The results indicate that the polycrystalline powder samples are a single phase with a space group of *Pbnm*. Compared to the parent phase, Al doping exhibits a smaller cell volume. This is due to the fact that the ionic radius of Al is smaller than that of Mn (The radii of Al ion is 0.535 Å and the Mn ion is 0.645 Å)。To provide a clearer visual representation and confirm the crystal structure and atomic occupancy, we utilized the refined diffraction data and VEST software to construct a ball-and-stick model diagram of a 1 × 1 × 1 cell, as depicted in Fig. 2d.

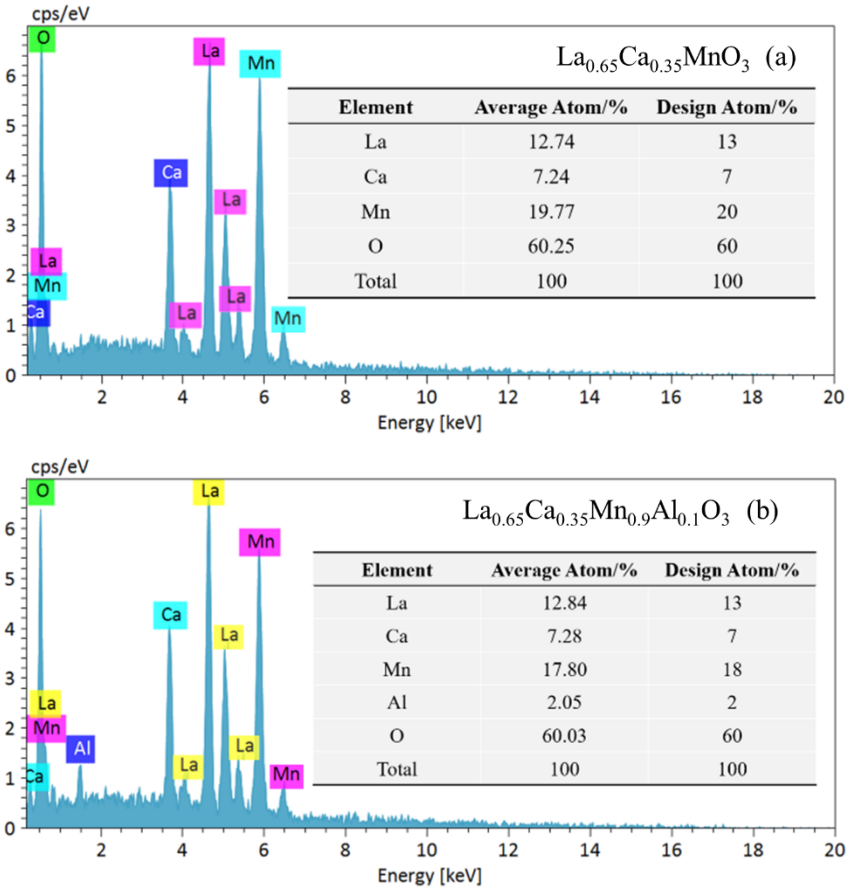

Fig. 1 EDS spectrums of $La_{0.65}Ca_{0.35}Mn_{1-x}Al_xO_3$ (x=0.0 and 0.1) polycrystalline powder samples

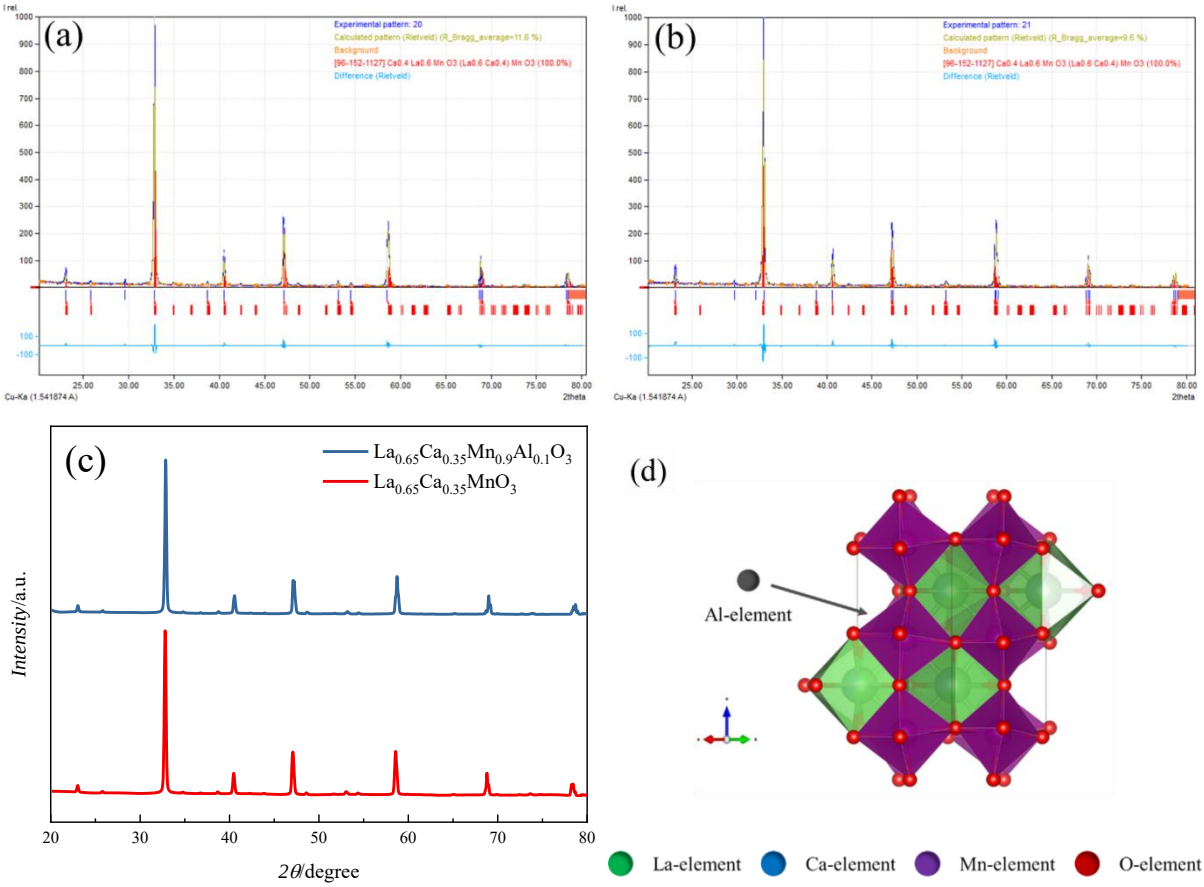

Fig. 2 (a, b) XRD refinement process, (c) XRD refinement results (d) ball and stick structural (green: La element; blue: Ca element; grizzly: Al element; purple: Mn element; rad: O element) of $La_{0.65}Ca_{0.35}Mn_{1-x}Al_xO_3$ (x=0.0 and 0.1) polycrystalline powder samples

Tab. 1 Lattice parameters and structural parameters after refinement of $La_{0.65}Ca_{0.35}Mn_{1-x}Al_xO_3$ (x=0.0 and 0.1) polycrystalline powder samples

Sample	X=0.0	X=0.1
a/Å	5.44980	5.43350
b/Å	5.46200	5.45460
c/Å	7.69910	7.67400
V/Å^3	229.1776	227.4387
Space group	*Pbnm*	*Pbnm*
$<d_{Mn-O}>$/Å	1.94883	1.94249
$<\theta_{Mn-O-Mn}>$/degree	161.9777	161.9729
χ^2	1.25	1.84

3.2 Magnetic properties

The magnetization versus temperature (*M*-*T*) curves for $La_{0.65}Ca_{0.35}Mn_{1-x}Al_xO_3$ (x=0.0 and 0.1) samples under 0.05T magnetic field can be categorized into zero-field-cooled and field-cooled (ZFC&FC) curves (Fig. 3a). The samples demonstrate a distinct ferromagnetic-paramagnetic phase transition as evidenced by the variation of magnetization with temperature [37]. The minimum value of the dM_{FC}/d*T*-*T* curve (Fig. 3b) allows defining the phase transition temperature (i.e. Curie temperature T_C) as $T_{C\ (x=0.0)}$ = 261 K and $T_{C\ (x=0.1)}$ = 98 K, respectively. When the temperature is higher than T_C the sample exhibits a paramagnetic phase where the ZFC and FC curves overlap [38]. With decreasing temperature below T_C, the ZFC and FC curves exhibit an obvious divergence, which is often observed in perovskite manganites or cobaltites and can be assigned to

the local anisotropic field generated from FM clusters due to the magnetic inhomogeneity[39-41]. The comparison reveals that the magnetization intensity and T_C of the Al doped system appear to be significantly reduced. The decrease of M and T_C with Al substitution is mainly due to the local cutoff of magnetic interaction between the spins of the t_{2g} electrons [42].

The magnetic properties of this sample were further analyzed by a series of isothermal magnetization curves (i.e., M-$\mu_0 H$ curves) measured near the T_C (Fig.4). The samples exhibit a linear behavior in the high temperature region, displaying a typical paramagnetic phase. In the low temperature region, there is a typical ferromagnetic phase as M increases sharply with $\mu_0 H$ and tends to saturate [44]. Interestingly, the M-$\mu_0 H$ curve near T_C shows S-shape this is due to fluctuations originating from a competing mode coupled to the magnetic system [45] or to a discontinuous transition between polaronic and extended charge carriers [46].

Tab. 2 shows the total ground state energy (E_{tot}) calculations for $La_{0.65}Ca_{0.35}Mn_{1-x}Al_xO_3$ (x=0.0 and 0.1) in the paramagnetic (PM), ferromagnetic (FM), and antiferromagnetic (AFM) states to determine the magnetic interactions. The FM state had the lowest energy, indicating that both samples were in a ferromagnetic ground state. Using VASP software and the GGA+U method, the TDOS and PDOS were calculated for both samples in the FM states. The results in Fig. 5 show that the 3d electrons in Mn is the primary contributors to the magnetic properties of both samples. In addition, the 3*d* orbitals of Mn and the 2*p* orbitals of O appear to overlap considerably, so that the mode of magnetic interaction of the system may be predominantly an exchange interaction between Mn and O. There was no energy gap between the valence and conducting states, indicating that the crystals were metallic. Al^{3+} does not contribute to the magnetism of the magnet since it does not have a magnetic moment. Besides, we found that the doped system weakens the O-2*p* orbitals and the Mn-3*d* crossover, which in turn directly affects the double-exchange interactions of the system.

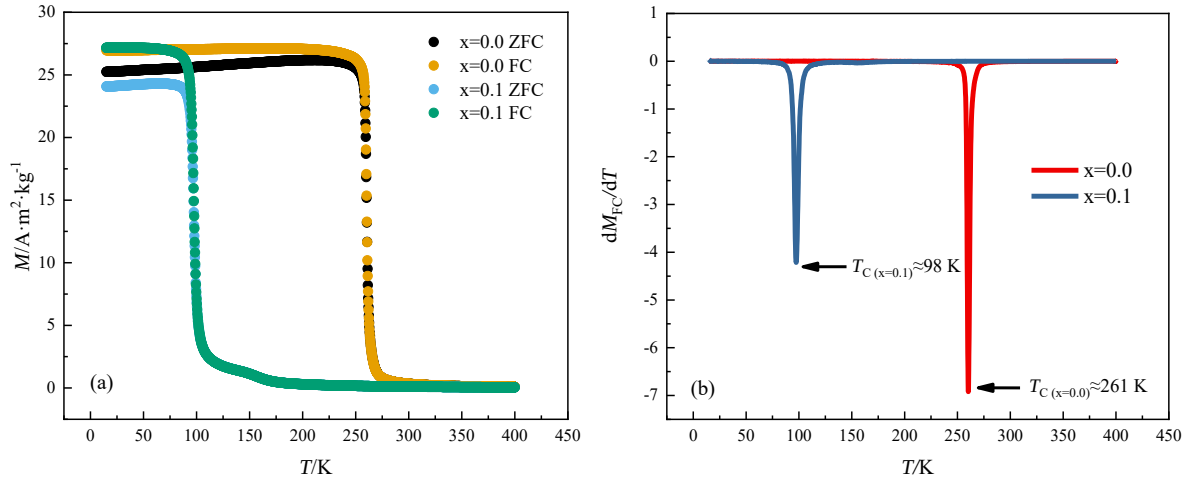

Fig. 3 (a) Temperature dependence of M_{FC} and M_{ZFC} curves under an applied magnetic field of 0.05 T, (b) the dM/dT curves of $La_{0.65}Ca_{0.35}Mn_{1-x}Al_xO_3$ (x=0.0 and 0.1) polycrystalline powder samples

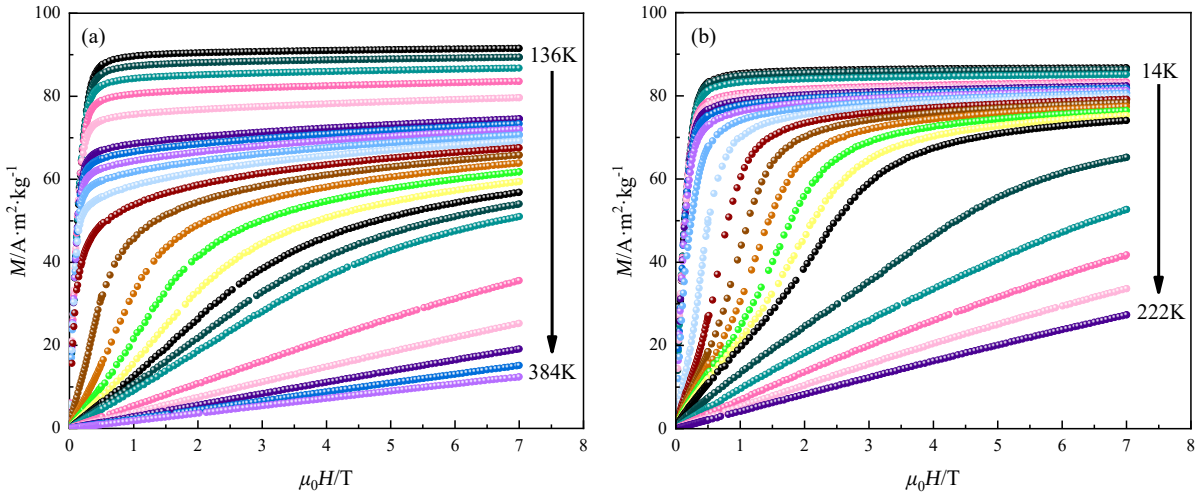

Fig. 4 (a, b) Isothermal magnetization curves of $La_{0.65}Ca_{0.35}Mn_{1-x}Al_xO_3$ (x=0.0 and 0.1) polycrystalline powder samples

Tab. 2 Total ground state energy (E_{tot}) at PM, FM, and AFM states of $La_{0.65}Ca_{0.35}Mn_{1-x}Al_xO_3$ (x=0.0 and 0.1) polycrystalline powder samples

samples	$E_{tot\text{-}PM}$ ($\times 10^3$eV)	$E_{tot\text{-}FM}$ ($\times 10^3$eV)	$E_{tot\text{-}AFM}$ ($\times 10^3$eV)
x=0.0	-0.31399406456 eV	-0.32310244856 eV	-0.32289470731 eV
x=0.1	-0.31268696571 eV	-0.32072929276 eV	-0.32055228190 ev

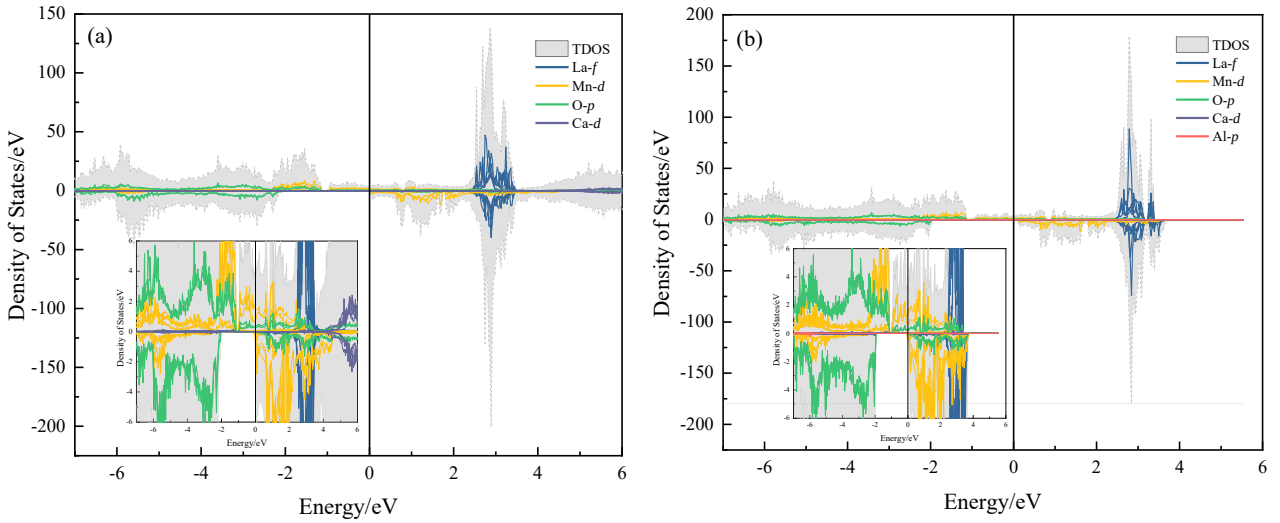

Fig. 5 (a, b) Total DOS, partial DOS for La, Ca, Mn, Al, and O from the ab initio calculations of $La_{0.65}Ca_{0.35}Mn_{1-x}Al_xO_3$ (x=0.0 and 0.1) polycrystalline powder samples

3.3 Magnetocaloric effects

Isothermal magnetic entropy change $|\Delta S_M|$ as a thermodynamic response of a magnetic material, which is a better measure for the material's MCE. According to Maxwell's thermodynamic equation, $|\Delta S_M|$ can be calculated using M-$\mu_0 H$ data and the following relation [47-49]:

$$\Delta S_M(T, \mu_0 H) = S_M(T, \mu_0 H) - S_M(T, 0) = \int_0^{\mu_0 H} \left(\frac{\partial M}{\partial T}\right)_{\mu_0 H} d\mu_0 H \quad (1)$$

Fig. 6 demonstrates the variation of $|\Delta S_M|$ with temperature (under 1-7 T magnetic field) for $La_{0.65}Ca_{0.35}Mn_{1-x}Al_xO_3$ (x=0.0 and 0.1) polycrystalline powder samples. The sample exhibited a large $|\Delta S_M|$ and peaked ($|\Delta S_M^{max}|$) near T_C. The $|\Delta S_M^{max}|$ of the samples with x=0.0 and 0.1 were 8.77 and 5.98 J·kg-1·K^{-1}, respectively, under a 7 T magnetic field. It is interesting to note that the Al doping significantly broadened the $|\Delta S_M|$-T peak of the image, with ΔT_{FWHM} of 39.95 and 67.61 K at 7 T magnetic field, respectively

Generally, besides the values of $|\Delta S_M|$, there are several other vital and efficient figures of merit, namely, the refrigerant capacity (*RC*), relative cooling power (*RCP*) and temperature-averaged entropy change (*TEC*) are always used to check the magnetocaloric performances of materials.

The *RC* and *RCP* are two interrelated parameters that can provide rough estimates of the energy transferred during the ideal magnetic refrigeration cycle. These parameters can be evaluated using the following equations[50-52],

$$RC = \int_{T_{Cold}}^{T_{Hot}} |-\Delta S_M(T)| dT \quad (2)$$

$$RCP = |\Delta S_M^{max}| \cdot \Delta T_{FWHM} \quad (3)$$

where ΔT_{FWHM} denotes he full width at half-maximum temperature region of $|\Delta S_M^{max}|$ and $T_{Hot\ (Cold)}$ denote the temperature points at ΔT_{FWHM}. We calculated the *RC* and *RCP* at different magnetic fields as shown in Fig. 7. The samples with x = 0.0 and 0.1 had *RC* of 271.55 and 327.96 J·kg^{-1} and *RCP* of 350.18 and 404.42 J·kg^{-1} at 7 T magnetic field, respectively. Tab. 4 lists the T_C, ΔT_{FWHM}, $|\Delta S_M^{max}|$, *RC* and *RCP* for $La_{0.65}Ca_{0.35}Mn_{1-x}Al_xO_3$ (x=0.0 and 0.1) and common magnetic refrigeration materials in the references at an applied magnetic field of 5 T. Comparison shows that this sample has outstanding magnetic refrigeration capacity. Interestingly,

sample $La_{0.65}Ca_{0.35}Mn_{0.9}Al_{0.1}O_3$ exhibits a better magnetocaloric effect than the parent sample $La_{0.65}Ca_{0.35}MnO_3$. This is because the *RC* and *RCP* are due to the joint determination of $|\Delta S_M^{max}|$ and ΔT_{FWHM}, and the introduction of Al is a dominant factor in the broadening of the peaks of the $|\Delta S_M|$-*T* image, which effectively enhances the MCE of the sample.

The *TEC* was recently introduced as an important parameter for determining the potential working temperature range of magnetocaloric materials, which can be evaluated using the following relation[52],

$$TEC(\Delta T_{H-C}) = \frac{1}{\Delta T_{H-C}} max\left\{\int_{T_{mid}-\frac{\Delta T_{H-C}}{2}}^{T_{mid}+\frac{\Delta T_{H-C}}{2}} |\Delta S_M| dT\right\} \quad (4)$$

where T_{mid} denotes the value of the average temperature. The *TEC* (4K) is calculated for $La_{0.65}Ca_{0.35}Mn_{1-x}Al_xO_3$ (x=0.0 and 0.1) and compared with $|\Delta S_M^{max}|$ (at same magnetic fields), as shown in Fig. 7. Both samples exhibit $|\Delta S_M^{max}|$ greater than *TEC* (4K) at the same magnetic field, but Al doping significantly reduces this trend. Calculation of the average overlap between $|\Delta S_M^{max}|$ and *TEC* (4K) at 1-7 T magnetic fields reveals an increase from 93.8% to 98.1% after Al doping. These high percentages demonstrated that sample could be good candidate materials with a 4 K working temperature range.

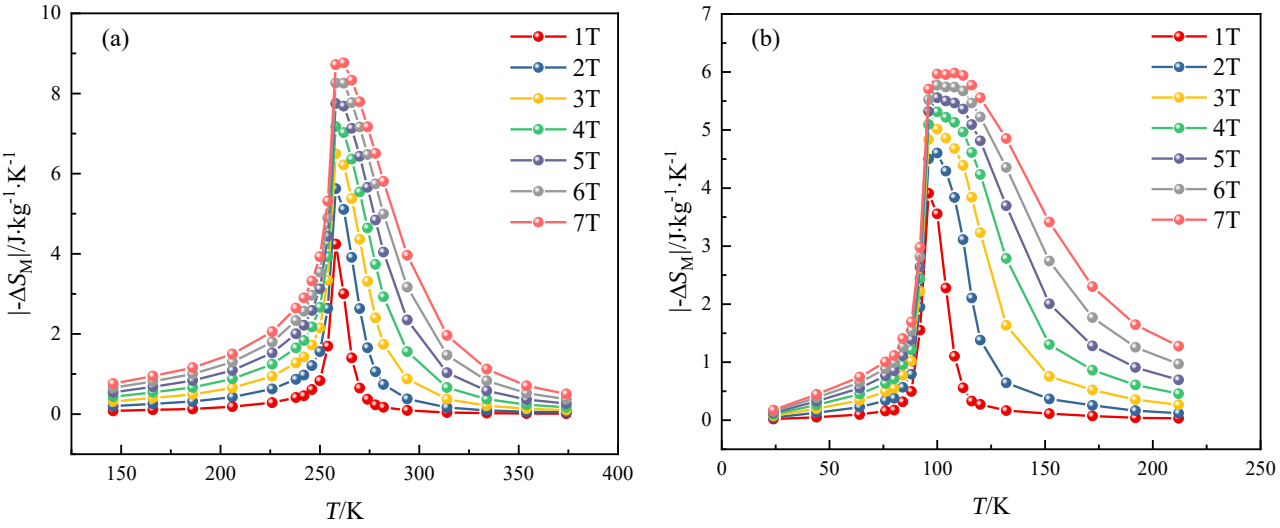

Fig. 6 (a, b) Magnetic entropy change as a function of temperature under an applied magnetic field of 1-7 T for $La_{0.65}Ca_{0.35}Mn_{1-x}Al_xO_3$ (x=0.0 and 0.1) polycrystalline powder samples

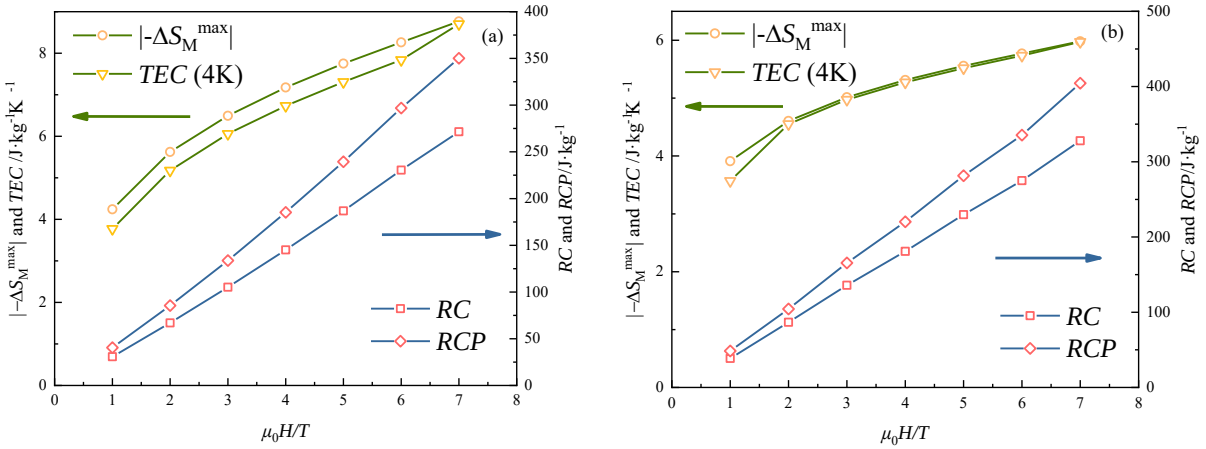

Fig. 7 (a, b) Magnetic field dependence of $|-\Delta S_M^{max}|$, *TEC*, *RC*, and *RCP* of $La_{0.65}Ca_{0.35}Mn_{1-x}Al_xO_3$ (x=0.0 and 0.1)

polycrystalline powder samples

Tab. 3 T_C, ΔT_{FWHM}, $|\Delta S_M^{max}|$, *RC* and *RCP* of $La_{0.65}Ca_{0.35}Mn_{1-x}Al_xO_3$ (x=0.0 and 0.1) polycrystalline powder samples, and some representative work at 5 T and 7 T applied magnetic field.

Compounds	T_C/K	ΔT_{FWHM}/K	$\lvert\Delta S_M^{max}\rvert$/ J·kg^{-1}K^{-1}	*RC*/ J·kg^{-1}	*RCP*/ J·kg^{-1}	$\Delta\mu_0 H$/T	Ref
$La_{0.65}Ca_{0.35}MnO_3$	261	39.95	8.77	271.55	350.18	7	This work
$La_{0.65}Ca_{0.35}MnO_3$	261	30.89	7.75	186.82	239.44	5	This work
$La_{0.65}Ca_{0.35}Mn_{0.9}Al_{0.1}O_3$	98	67.61	5.98	327.96	404.42	7	This work
$La_{0.65}Ca_{0.35}Mn_{0.9}Al_{0.1}O_3$	98	50.65	5.56	229.76	281.45	5	This work
$LaMnO_3$	124	84.00	2.69	170.00	207.31	5	[53]
$La_{0.7}Ca_{0.3}MnO_3$	264	-	7.7	187	-	5	[54]
$La_{0.67}Ba_{0.33}MnO_3$	292	108.78	1.48	132.02	161.00	5	[55]
$La_{0.7}Sr_{0.3}MnO_3$	365	40.09	4.44	145.96	178.00	5	[56]
$La_{0.5}Ca_{0.5}MnO_3$	220	42.00	3.00	132.84	126.00	5	[57]

3.4 Magnetic phase transitions

The Banerjee criterion was developed in the framework of the Landau-Lifshitz theory for magnetic phase transitions. An Arrott plot (i.e., an isotherm of M^2- $\mu_0 H \cdot M^{-1}$) can be produced. According to the Banerjee criterion, if a negative slope region (approaching T_C) appears on the plot, it corresponds to a magnetic first-order phase transition, and vice versa, it implies a second-order phase transition[58]. As can be seen in Fig. 8, according to this criterion, first-order phase transitions occur for both $La_{0.65}Ca_{0.35}Mn_{1-x}Al_xO_3$ (x=0.0 and 0.1). However, the negative slope trend in the Arrott plots is significantly weakened after Al doping, and this phenomenon is attributed to the introduction of the nonmagnetic ion Al which weakens the magnetic interactions leading to the enhancement of the continuity of the phase transition. This phenomenon is effective for magnetic refrigeration to reduce the loss caused by hysteresis and thermal stagnation, and to enhance the cooling temperature region.

In addition, the phase transition of the system can also be judged from the MCE. The dependence of the magnetic entropy change on the magnetic field can be expressed as follows [62]:

$$n = \frac{dln(\Delta S_M)}{dln(\mu_0 H)} \tag{5}$$

where n is determined by the magnetic state of the sample, n tends to be close to "2" in the paramagnetic state ($T >> T_C$) , n tends to be close to "1" in the ferromagnetic state ($T << T_C$), and n is independent of the magnetic field in the paramagnetic-ferromagnetic phase transition ($T = T_C$) [62,63]. In addition, the type of phase transition of the system can be verified as a first order phase transition if $n > 2$ exists after the phase transition temperature. [64]. The relationship of n with temperature in a 1-7 T magnetic field (Fig. 9a, b) and the Heatmap characterizing the distribution of n (Fig. 9c, d) were plotted by isothermal magnetic entropy change as in Eq. 5. The analysis reveals that n converges to "1" at low temperature and to "2" at high temperature. The magnetic properties mirror those of the M-T and M-$\mu_0 H$ curves. Moreover, the collapse of the curve at T_C in Fig. 9a, b and the emergence of the deep blue region between 1 and 7 T in Fig. 9c, d confirm the stability of the n value at T_C. It was also found that there is a region above T_C with n greater than "2" (black region in Fig. 9c, d), confirming the first-order phase transition characteristic of the system. And the reduction of the black region after Al doping also verifies the enhancement of phase transition continuity.

The study points out that the recalibration curves of the magnetic entropy change at different magnetic fields show a high degree of recalibration for the first-order phase transition regime; the first-order phase transition regime shows a discrete distribution with magnetic field [65]. $|\Delta S_M^{max}|$ normalized to $|\Delta S_M|$ gets the longitudinal axis, and scaling of T on both sides of T_C gives the longitudinal axis θ, i.e:

$$\theta = \begin{cases} (T_C - T)/((T_{r1} - T_C) , & T \le T_C \\ (T - T_C)/((T_{r2} - T_C) , & T > T_C \end{cases} \tag{6}$$

where T_{r1} and T_{r2} are the reference temperatures at the half-height width in the $|\Delta S_M(T)|$ curve. As shown in Fig. 10, the data clearly depend on the variation of $\mu_0 H$ at θ less than "0" and show a discrete distribution behavior. From this, it can be further determined that the ferromagnetic-paramagnetic phase transition characteristic of the $La_{0.65}Ca_{0.35}Mn_{1-x}Al_xO_3$ (x=0.0 and 0.1) sample belongs to the first-order phase transition. Compared to the parent sample, the secondary doped sample still retain the first-order phase transition characteristics. Thus, the enhancement of MCE for Al-doped samples can be attributed to the following two points: i) Effective broadening of ΔT_{FWHM} after doping carries a larger *RC* and *RCP*. ii) Large MCE due to the first-order phase transition characterized by a structural phase transition [66-69].

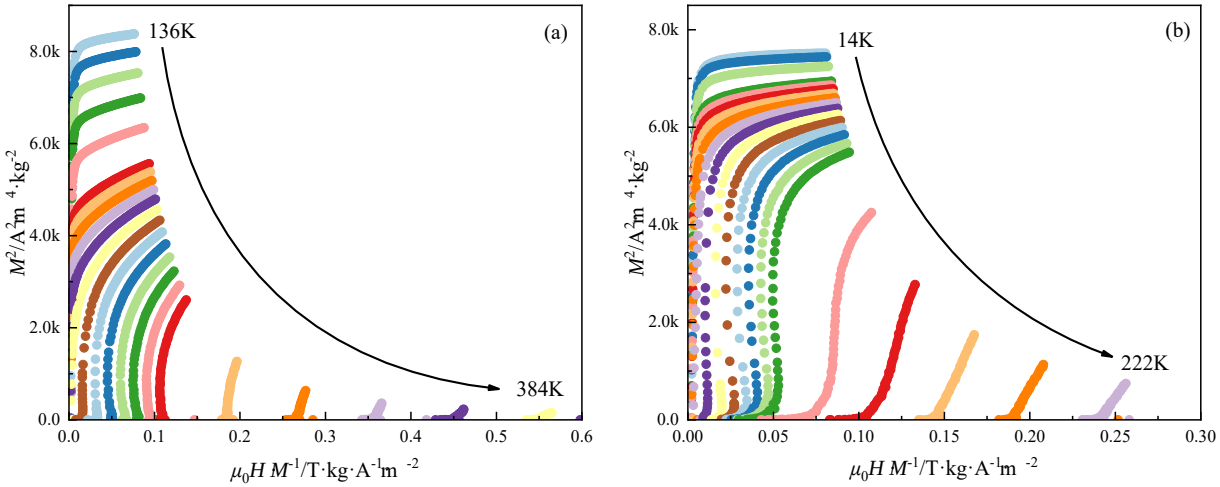

Fig. 8 (a, b) Isothermal Arrott plots of $La_{0.65}Ca_{0.35}Mn_{1-x}Al_xO_3$ (x=0.0 and 0.1) polycrystalline powder samples

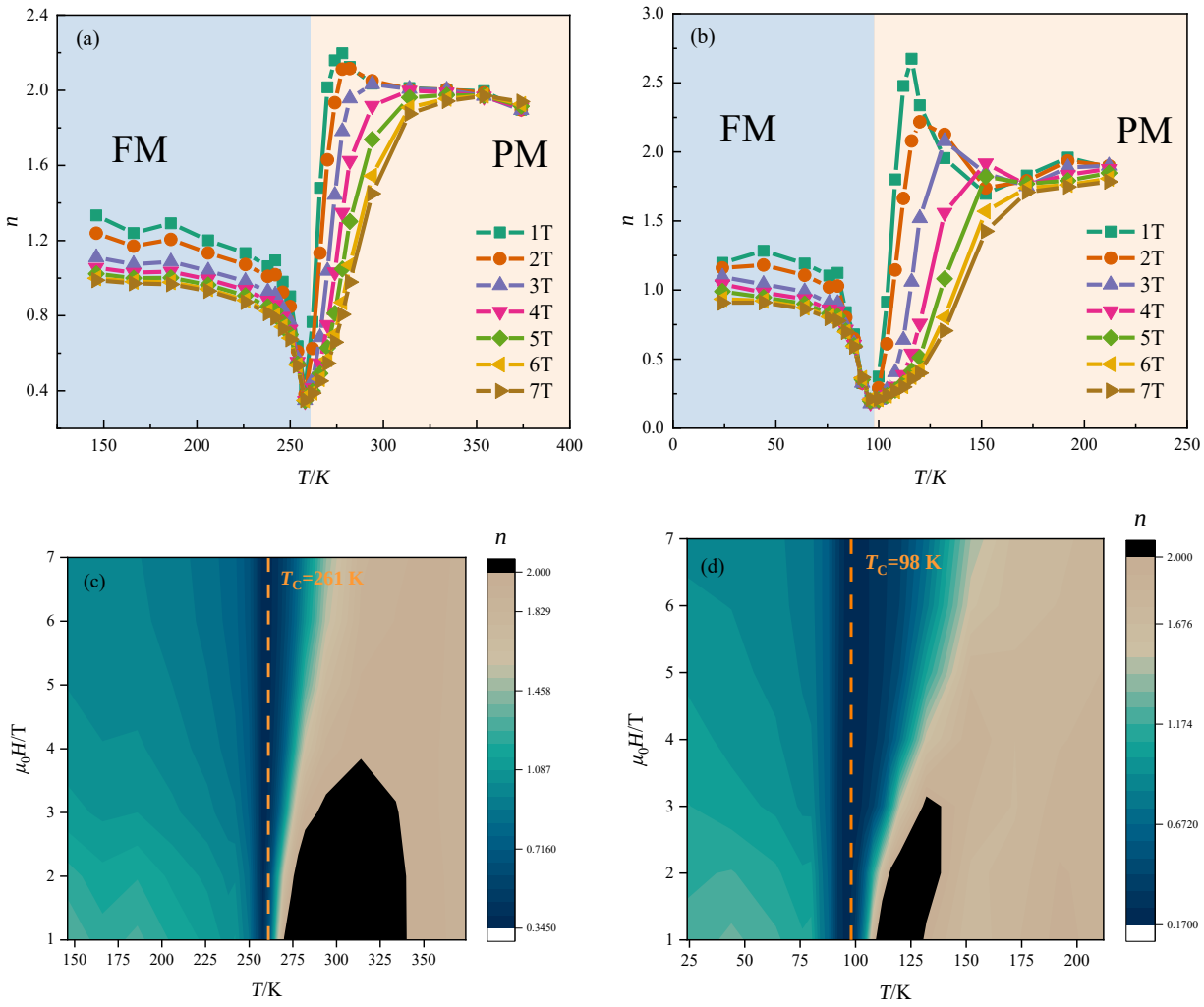

Fig. 9 (a, c and b, d) Temperature dependence of the *n* at different magnetic fields from 1 to 7 T of $La_{0.65}Ca_{0.35}Mn_{1-x}Al_xO_3$ (x=0.0 and 0.1) polycrystalline powder samples

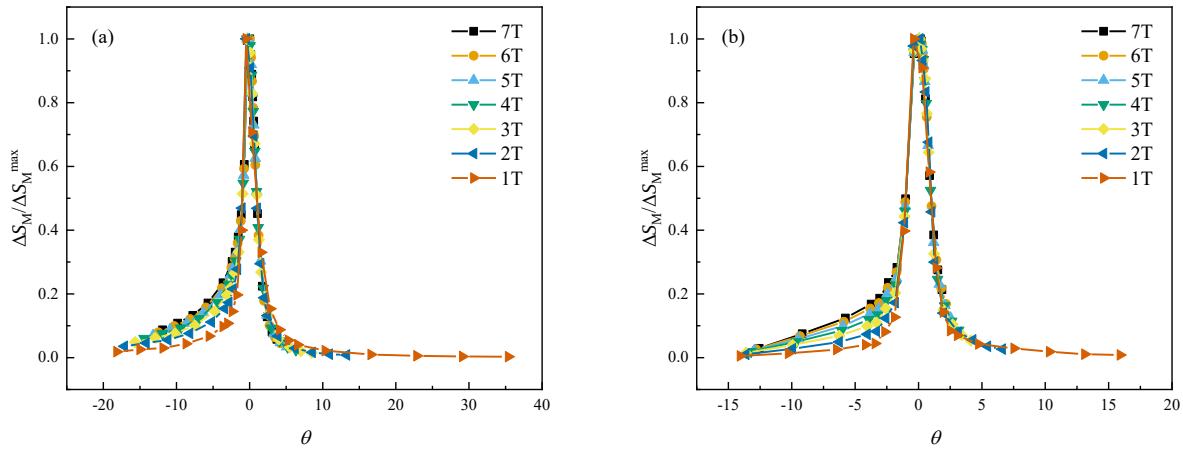

Fig. 10 Universal curve plot of normalized entropy change versus θ from 1 to 7 T of $La_{0.65}Ca_{0.35}Mn_{1-x}Al_xO_3$ (x=0.0 and 0.1) polycrystalline powder samples

4. CONCLUSIONS

In this work, $La_{0.65}Ca_{0.35}Mn_{1-x}Al_xO_3$ (x=0.0 and 0.1) polycrystalline samples were prepared by solid-state reaction method at high temperatures. The EDS and XRD results show that the samples are pure and have good single-phase properties. The analysis shows that the sample belongs to the *Pbnm* space group perovskite structure. The weakening of the magnetic interaction due to the substitution of Al for Mn reduces T_C and $|\Delta S_M|$. However, this is significant for the enhancement of the phase transition continuum, greatly broadening ΔT_{FWHM} and leading to a better MCE for the Al-doped samples. The maximum isothermal magnetic entropy changes x=0.0 and 0.1of the sample at 7T magnetic field reaches 8.77 and 5.98 J·kg-1·K^{-1}; the *RC* are 271.55 and 327.96 J·kg^{-1} and *RCP* are 350.18 and 404.42 J·kg^{-1}, respectively. Besides, the average overlap between $|\Delta S_M^{max}|$ and *TEC* (4K) at 1-7 T magnetic fields reveals an increase from 93.8% to 98.1% after Al doping. We further characterize the ferromagnetic-paramagnetic first-order phase transition of the samples based on the Landau theory and MCE, which not only verified the enhancement of Al doping for the continuity of the phase transition, but also reveals the excellent magnetocaloric effect of the structural transformation. In conclusion, this study enhances the physical properties of $La_{0.65}Ca_{0.35}Mn_{1-x}Al_xO_3$ (x=0.0 and 0.1) polycrystalline samples and demonstrates their potential for use in magnetic refrigeration.

ACKNOWLEDGEMENTS

This project was supported by the State Key Development Program for Basic Research of China (Grant Nos. 51562032) and the 2023 Inner Mongolia Autonomous Region Master's Graduate Research and Innovation Project (S20231246Z).

REFERENCES

[1]Shen B G, Sun J R, Hu F X, *et al*. Advanced Materials, 2009, 21(45): 4545-4564.

[2]Zhang Y K, Wu B B, Guo D, *et al*. Chinese Physics B, 2021, 30(1): 017501.

[3]Xu P, Ma Z P, Wang P F, *et al*. Materials Today Physics, 2021, 20: 100470.

[4]Gutfleisch O, Willard M A, Brück E, *et al*. Adv Mater, 23 (2011) 821–842.

[5]Franco V, Bl´azquez J S, Ipus J J, *et al*. Prog Mater Sci, 93 (2018) 112–232.

[6]Zhang P, Piao H G, Zhang Y D, *et al*. Acta Physica Sinica, 70(15), 256–271 (2021)

[7]Tegus O, Brück E, Buschow K H J, et al. Nature, 2002, 415(6868): 150-152.

[8]Pecharsky V K, Gschneidner Jr K A. Physical review letters, 1997, 78(23): 4494.

[9]Fujieda S, Fujita A, Fukamichi K. Science and Technology of Advanced Materials, 2003, 4(4): 339-346.

[10]Li S B, Wang C B, Liu H X, et al. Materials Research Bulletin, 2018, 99: 73-78.

[11]Wang H, Su K, Huang S, et al. Journal of Superconductivity and Novel Magnetism, 2019, 32: 3887-3891.

[12]Wang Q W, Yang H F, Luo X Y, *et al*. Ceramics International, 2022, 48(10): 13589-13597.

[13]Phan M H, Yu S C. Journal of Magnetism and Magnetic Materials, 2007, 308(2): 325-340.

[14]Sharma M K, Basu T, Mukherjee K, et al. Journal of Physics: Condensed Matter, 2017, 29(8): 085801.

[15]Su Y T. Harbin Institute of Technology, 2013.

[16]Kumar A, Kumari K, Sharma M K, et al. Journal of Materials Science & Technology, 2022, 124: 232-242.

[17]Jeong Y S, Anwar M S, Ahmed F, et al. Applied Mechanics and Materials, 2013, 378: 225-229.

[18]Tonozlis G, Litsardakis G. physica status solidi (c), 2014, 11(5 - 6): 1133-1138.

[19]Zener C. Physical Review, 1951, 82(3): 403.

[20]Anderson P W, Hasegawa H. Physical Review, 1955, 100(2): 675.

[21]De Gennes P G. Physical Review, 1960, 118(1): 141.

[22]Yadav K, Kaur G, Sharma M K, et al. Physics Letters A, 2020, 384(26): 126638.

[23]Radaelli P G, Cox D E, Marezio M, *et al*. Phys Rev Lett, 75 (1995) 4488.

[24]Alonso J, Herrero E, Gonza´lez-Calbet J M, *et al*. Phys Rev B, 62 (2000)11328.

[25]Sahana M, Hegde M S, Vasanthacharya N Y, *et al*. Appl Phys Lett, 71 (1997) 2701.

[26]Troyanchuk I O, Khalyavin D D, Szymczak H, Phys Sta Sol, (a) 164 (1997) 821.

[27]Troyanchuk I O, Khalyavin D D, Pastushonok S N, J Phys: Condens Matter, 10 (1998) 185.

[28]Araujo J P, Amaral V S, Tavares P B, *et al*. J Magn Magn Mater, 226–230 (2001) 797.

[29]Phan M H, Tian S B, Yu S C, *et al*. J Magn Magn Mater, 256 (2003) 306.

[30]Mira J, Rivas J, Hueso L E, *et al*. J Appl Phys, 91 (2002) 8903.

[31]Phan M H, Yu S C, Hur N H, Appl Phys Lett, 86 (2005) 072504.

[32]Rebello A, Naik V B, Mahendiran R, J Appl Phys, 110 (2011) 013906.

[33]Linh D C, Ha N T, Duc N H, et al. Physica B: Condensed Matter, 2018, 532: 155-160.

[34]Taboada-Moreno C A, Sánchez-De Jesús F, Pedro-García F, et al. Journal of Magnetism and Magnetic Materials, 2020, 496: 165887.

[35]Bouderbala A, Makni-Chakroun J, Cheikhrouhou-Koubaa W, et al. Ceramics International, 2015, 41(6): 7337-7344.

[36]Biesinger M C, Payne B P, Grosvenor A P, et al. Applied Surface Science, 2011, 257(7): 2717-2730.

[37]Chen H W, Li C, Zhao J J, *et al*. Journal of Superconductivity and Novel Magnetism, 2021, 34: 2651-2666.

[38]Khlifi M, Bejar M, Sadek O E L, *et al*. Journal of Alloys and Compounds, 2011, 509(27): 7410-7415.

[39]Nam D N H, Jonason K, Nordblad P, et al. Physical Review B, 1999, 59(6): 4189.

[40]Zhang P, Thanh T D, Yu S C. Journal of Applied Physics, 2014, 115(17).

[41]Zhang Y D, Zhang P, Thanh T D, et al. Journal of Applied Physics, 2012, 112(9).

[42]Sawaki Y, Takenaka K, Osuka A, et al. Physical Review B, 2000, 61(17): 11588.

[43]Romero-Muniz C, Ipus J J, Blazquez J S, *et al*. Appl Phys Lett, 104 (2014), 252405.

[44]Vadnala S, Asthana S. Journal of Magnetism and Magnetic Materials, 2018, 446: 68-79.

[45]Rößler S, Rößler U K, Nenkov K, *et al*. Physical Review B, 2004, 70(10): 104417.

[46]Archibald W, J S Zhou, Goodenough J B. Physical Review B, 1996, 53(21): 14445.

[47]Franco V, Blázquez J S, Ipus J J, *et al*. Progress in Materials Science, 2018, 93: 112-232.

[48]Zhang Y K. Journal of Alloys and Compounds, 2019, 787: 1173-1186.

[49]Li L W, Yan M. Journal of Alloys and Compounds, 2020, 823: 153810.

[50]Biswas A, Samanta T, Banerjee S, *et al*. Applied Physics Letters, 2008, 92(21): 212502.

[51]Xie Q Y, Lv B, Wang P F, *et al*. Materials Chemistry and Physics, 2009, 114(2-3): 636-643.

[52]Griffith L D, Mudryk Y, Slaughter J, *et al*. Journal of Applied Physics, 2018, 123(3): 034902.

[53]Biswas A, Chandra S, Phan M H, *et al*. Journal of alloys and compounds, 2012, 545: 157-161.

[54]Lampen P, Bingham N S, Phan M H, *et al*. Appl. Phys. Lett, 102 (2013) 062414.

[55]Morelli D T, Mance A M, Mantese J V, *et al*. Journal of Applied Physics, 1996, 79(1): 373-375.

[56]Barik S K, Mahendiran R. Journal of Applied Physics, 2010, 107(9): 093906.

[57]Krishnamoorthi C, Barik S K, Siu Z, *et al*. Solid State Communications, 2010, 150(35-36): 1670-1673.

[58]Banerjee B K. Physics letters, 1964, 12(1): 16-17.

[59]Landau L D, Lifshitz E M, Course of Theoretical Physics, vol. 5, 3rd ed., Butterworth-Heinemann, 1980.

[60]Inoue J, Shimizu M. J Phys F: Met Phys, 12 (1982) 1811–1819.

[61]Inoue J, Shimizu M. J Phys F: Met Phys, 18 (1988) 2487–2497.

[62]Kaul S N. J Magn Magn Mater, 1985, 53: 5.

[63]Jaballah H, Bouzidi W, Fersi R, *et al*. Journal of Physics and Chemistry of Solids, 2022, 161: 110438.

[64]Law J Y, Franco V, Moreno-Ramírez L M, *et al*. Nature communications, 2018, 9(1): 2680.

[65]Franco V, Blázquez J S, Conde A. Applied Physics Letters, 2006, 89(22): 222512.

[66]Hong C S, Kim W S, Hur N H. Phys Rev B, 63 (2001) 092504.

[67]Mira J, Rivsa J, Rivadulla F, *et al*. Quintela, Phys Rev B 60 (1999) 2998.

[68]Moutis N, Panagiotopoulos I, Pissas M, *et al*. Phys Rev B, 59 (1999) 1129.

[69]Shin H S, Lee J E, Nam Y S, *et al*. Solid State Commun, 118 (2001) 377.

DOI: 10.18462/iir.thermag.2024.0029

INFLUENCE OF HIGH-PRESSURE HEAT TREATMENT ON MAGNETIC AND MAGNETOCALORIC EFFECTS IN $LA_{0.75}SR_{0.25}MN_{0.9}CO_{0.1}O_3$

Xiang Jin[a, b], Jing Zhao[b], Lei Gao[c], Huaijin Ma[b, c], Luomeng Chao[d], Haiqiang Gao[e], Haschuluu O[a], Hongwei Zhu[b] , Qi Li [b], Jiawei Xu [b], Yang Li[d], Tegus O[a]*, Jianjun Zhao[b]*

[a]School of Physics and Electronic Information, Inner Mongolia Normal University Hohhot, 010020, China

[b]School of Physical Science and Technology, Baotou Teachers' College, Key Laboratory of Magnetism and Magnetic Materials for Higher Education in Inner Mongolia Autonomous Region Baotou, 014030, China

[c]National Key Laboratory of Baiyunobo Rare Earth Resource Research and Comprehensive Utilization, Baotou Research Institute of Rare Earths Baotou, 014030, China

[d]College of Science, Inner Mongolia University of Science and Technology Baotou, 014010, China

China Northern Rare Earth (Group) High-Tech Co.,Ltd Baotou 014030, China

ABSTRACT

The magnetic and magnetocaloric effects of $La_{0.75}Sr_{0.25}Mn_{0.9}Co_{0.1}O_3$ compounds synthesized under ambient pressure and a high pressure of 6 GPa were investigated by experiments combined with first-principles calculations. Lattice distortion was enhanced by high-pressure heat treatment. Furthermore, the application of pressure adjusted the Curie temperature near to room temperature. The density of states and spin density indicate that the magnetization of the compounds mainly originated from the Mn and Co moments. The samples exhibited maximum magnetic entropy changes of 4.96 and 3.95 $J \cdot kg^{-1}K^{-1}$, along with relative cooling powers of 365.50 and 403.92 $J \cdot kg^{-1}$ (at a magnetic field of 7 T). The good overlap of the rescaling curves proves that all samples belong to the ferromagnetic-paramagnetic second-order phase transition. Therefore, high-pressure heat treatment is expected to be a means of modulating magnetocaloric materials. And the samples also provide new options for room-temperature magnetocaloric working materials.

Keywords: perovskite, high-pressure synthesis, magnetic phase transition, magnetocaloric effect

1. INTRODUCTION

Magnetic refrigeration, which leverages the magnetocaloric effect (MCE), is poised as a promising, energy-efficient, and environmentally friendly alternative to traditional gas compression refrigeration technology[1] . In recent years, extensive experimental and theoretical explorations of the MCE across various magnetic materials have been conducted. This interest is driven not only by its potential applications in magnetic refrigeration but also by its contribution to a deeper understanding of the basic physical properties of these materials[2–8]. MCE, a magneto-thermodynamic phenomenon intrinsic to magnetic materials, manifests itself during changes in the external magnetic field, particularly around thermomagnetic phase transitions. It is characterized by an isothermal magnetic entropy change ($|-\Delta S_M|$) and an adiabatic temperature change (ΔT_{ad})[9, 10]. In the context of magnetic refrigeration, the second-order phase transitions associated with the MCE are generally less favorable at higher temperatures[11] . Conversely, the first-order phase transitions tend to yield a larger MCE. However, the latter often has such drawbacks as significant thermal hysteresis, a limited cooling temperature range, and a modest relative cooling power. A pivotal insight, as highlighted by Law et al.[12] , is that the optimal magnetic refrigeration material may reside in a critical state between the first- and second-order phase transitions. Consequently, research on magnetic refrigeration revolves around studying MCEs and modulating phase transitions in magnetic refrigerant materials.

It is well known that the typical broadband La–Sr–Mn–O system exhibits a predominantly second-order phase transition characteristic of the parent phase owing to double-exchange interactions, and that the materials of this system have the potential for magnetic refrigeration near room temperature. Pekala[13] and Guo et al.[14] observed that $La_{0.75}Sr_{0.25}MnO_3$ exhibits a high MCE. However, the Curie temperature (T_C) exceeds room temperature, and the temperature range in which the magnetic entropy change is significant is too limited for practical applications. In our previous study[15] , we synthesized $La_{0.75}Sr_{0.25}Mn_{0.9}Co_{0.1}O_3$

samples under 4 GPa of pressure at 1350 °C. We observed that applying pressure significantly enhanced the refrigeration efficiency, but it also resulted in a lower T_C, which deviated notably from room temperature.

To align the refrigeration temperature more closely with room temperature and to further improve the continuity of phase transitions within the system for enhanced refrigeration efficiency, this study involved synthesizing the samples at an increased pressure of 6 GPa and a lower temperature of 1250 °C. This method provided an opportunity to investigate the magnetically ordered temperature, phase transition properties, and magnetocaloric features of the $La_{0.75}Sr_{0.25}Mn_{0.9}Co_{0.1}O_3$ polycrystalline samples in greater depth.

2. EXPERIMENT AND CALCULATIONS

The $La_{0.75}Sr_{0.25}Mn_{0.9}Co_{0.1}O_3$ perovskite oxide samples were synthesized at ambient pressure by a solid-phase reaction method. La_2O_3, $SrCO_3$, $MnCO_3$, and Co_3O_4 powders (purity &gt: 99.99%) were weighed accurately according to stoichiometric ratios. The powders were mixed thoroughly using a planetary ball mill (QM-QX04) and ground for 6 h. The mixed samples were dried and sintered at 950°C for 12 h in a chamber furnace (KSL-1700X). Afterward, they were removed from the furnace, ground again, and calcined at 1350 °C for 24 h. The samples were then cooled from 1350 °C to 800 °C over 5 h and allowed to cool naturally to room temperature at atmospheric pressure (sample-A). A portion of the $La_{0.75}Sr_{0.25}Mn_{0.9}Co_{0.1}O_3$ sample was sintered at 1250 °C for 25 min under a six-sided top hydraulic pressure of 6 GPa (sample-B). The crystal structures of both samples were analyzed by an X-ray diffractometer (XD-3). The physical properties were also measured, including the magnetization versus temperature, $M(T)$, and magnetization versus applied magnetic field, $M(H)$. These measurements were performed at a magnetic field of 0.05 T and in the range of 0–7 T using a Quantum Design Model PPMS-9 multifunctional measurement system. Density functional theory (DFT) calculations were performed for $La_{0.75}Sr_{0.25}Mn_{0.9}Co_{0.1}O_3$ based on the obtained lattice information. These calculations were carried out by the Vienna Ab initio Simulation Package (VASP)[16] . In the DFT calculations, the generalized gradient approximation +U (GGA+U) method of the Perdew–Burke–Ernzerhof approach was employed. The U-values for La, Mn, and Co atoms were set to 6.0, 3.9, and 3.4 eV, respectively[17–20]. A plane wave truncation energy of 520 eV was employed. K-points within the Brillouin zone were generated by the Monkhorst–Pack method with a 9 × 9 × 1 k-point grid in the electron self-consistent calculations[21] . The calculation process was terminated when the energy convergence was less than 1×10^{-6} eV/Å.

3. RESULTS AND ANALYSIS

3.1 Structure Analysis

Figure 1(a) shows the refined X-ray diffraction patterns of $La_{0.75}Sr_{0.25}Mn_{0.9}Co_{0.1}O_3$ synthesized at ambient pressure and 6 GPa. The peak positions were labeled using MDI Jade 6's card library for the $La_{0.7}Sr_{0.3}MnO_3$ phase. No significant impurity peaks were found, indicating that both samples had a single-phase structure with a trigonal crystal system (space group $R\bar{3}c$). Table 1 lists the unit cell parameters, showing the changes in c/a ratio and cell volume under pressure. In addition, Fig. 1(b) shows crystal structures based on refined parameters. Table 2 shows the total ground state energy (Etot) calculations for $La_{0.75}Sr_{0.25}Mn_{0.9}Co_{0.1}O_3$ in the paramagnetic (PM), ferromagnetic (FM), and antiferromagnetic (AFM) states to determine the magnetic interactions. The FM state had the lowest energy, indicating that both samples were in a ferromagnetic ground state.

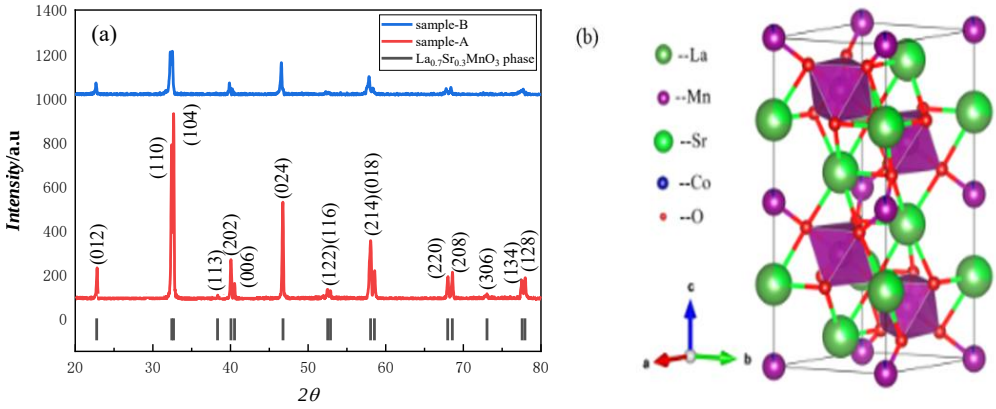

Fig. 1: (a) Refined XRD patterns and (b) crystal structure of $La_{0.75}Sr_{0.25}Mn_{0.9}Co_{0.1}O_3$

Table 1: Lattice parameters of $La_{0.75}Sr_{0.25}Mn_{0.9}Co_{0.1}O_3$

Samples	a (Å)	c (Å)	c/a	V (Å^3)	$\theta_{Mn\text{-}O\text{-}Mn}$ (°)	χ^2	R_{Bragg}
Sample A	5.510	13.340	2.421	404.946	165.764	2.8	9.86
Sample B	5.509	13.341	2.422	404.897	165.753	3.2	9.42

Table 2: Total ground state energy (E_{tot}) of $La_{0.75}Sr_{0.25}Mn_{0.9}Co_{0.1}O_3$ in PM, FM, and AFM states

Samples	$E_{\text{tot-PM}}$ ($\times 10^3$ eV)	$E_{\text{tot-FM}}$ ($\times 10^3$ eV)	$E_{\text{tot-AFM}}$ ($\times 10^3$ eV)
Sample A	−0.47496516	−0.48699209	−0.48699017
Sample B	−0.47446624	−0.48743510	−0.48691497

3.2 Magnetism Analysis

The $M(T)$ curves, including both zero-field-cooled (ZFC) and field-cooled (FC) curves, for $La_{0.75}Sr_{0.25}Mn_{0.9}Co_{0.1}O_3$ in a magnetic field of $\mu_0 H = 0.05$ T are shown in Fig. 2(a). The dM/dT(T) curves are shown in the inset. The temperature sweep rate for the $M(T)$ curve is 4 K/min. In a detailed analysis of the magnetic properties of the samples, it was observed that they undergo a PM–FM transition at $T_{C\,(\text{sample-A})} \approx$ 292 K and $T_{C\,(\text{sample-B})} \approx$ 274 K, respectively. Compared with $La_{0.75}Sr_{0.25}MnO_3$ with a T_C of approximately 310 K, it is evident that both doping and pressurization reduce T_C[22] . The Mn–O–Mn bond angles of the samples were measured, with sample A having an angle of 165.76°, and sample B having an angle of 165.63°. The decrease in these bond angles, which is caused by the pressure during the synthesis process, results in increased lattice distortion. This distortion, in turn, reduced the double exchange interaction between Mn^{3+} and Mn^{4+} through oxygen, leading to a decrease in T_C. In other words, the change in the bond angles affected the magnetic behavior of the samples, causing a reduction in the FM transition temperature. In addition, at temperatures of less than 250 K, the magnetization curves of the samples exhibited bifurcations. This phenomenon was particularly pronounced in sample B and can be attributed to either the domain wall pinning effect[23] or spin reorientation[24] . Using VASP software and the GGA+U method, the TDOS and PDOS were calculated for both samples in the FM states. The results in Figs. 2(b) and (c) show that the 3d electrons in Mn and Co are the primary contributors to the magnetic properties of both samples. There was no energy gap between the valence and conducting states, indicating that the crystals were metallic. To analyze the origin of the magnetism visually at the electronic level, the spin density distributions of the samples are shown in Figs. 2(d) and (e). The total magnetic moment is mainly contributed by Mn and Co electrons.

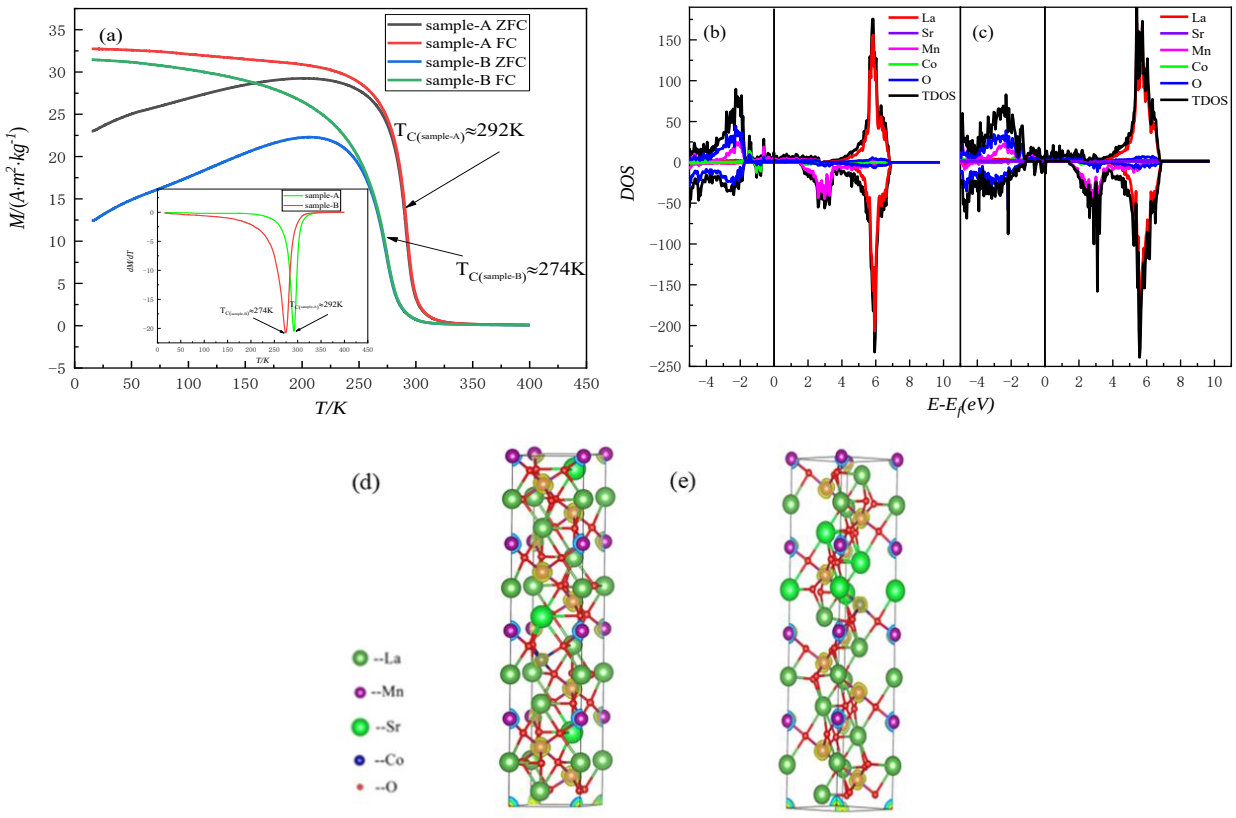

Fig. 2: (a) *M*(*T*) curves for $La_{0.75}Sr_{0.25}Mn_{0.9}Co_{0.1}O_3$ in a magnetic field of 0.05 T—the inset shows *dM/dT*(*T*) curves: sample A (b) and sample B (c), respectively, are total DOS (gray lines) and partial DOS for La, Sr, Mn, Co, and O from the ab initio calculations, and sample A (d) and sample B (e) are spin density distributions

The magnetization of the samples was measured at different temperatures near T_C, and the applied field was determined using $H_{int}=H-N_DM$, where N_D represents the demagnetization factor[25] . Here, N_D was obtained by establishing a tangent line at the origin of the *M*-*H* curve, where the external magnetic field is small. The slope of this tangent line provides the N_D values ($N_{D(sample\text{-}A)}$ = 0.039, $N_{D(sample\text{-}B)}$ = 0.041). Subsequently, *M*–*H* plots were constructed, as depicted in Figs. 3(a) and (b). The data reveal that *M* increased linearly with *H*, indicating a PM state without saturation. Below T_C, the plot shows a rapid increase in *M* with *H*, reaching saturation and exhibiting FM behavior.

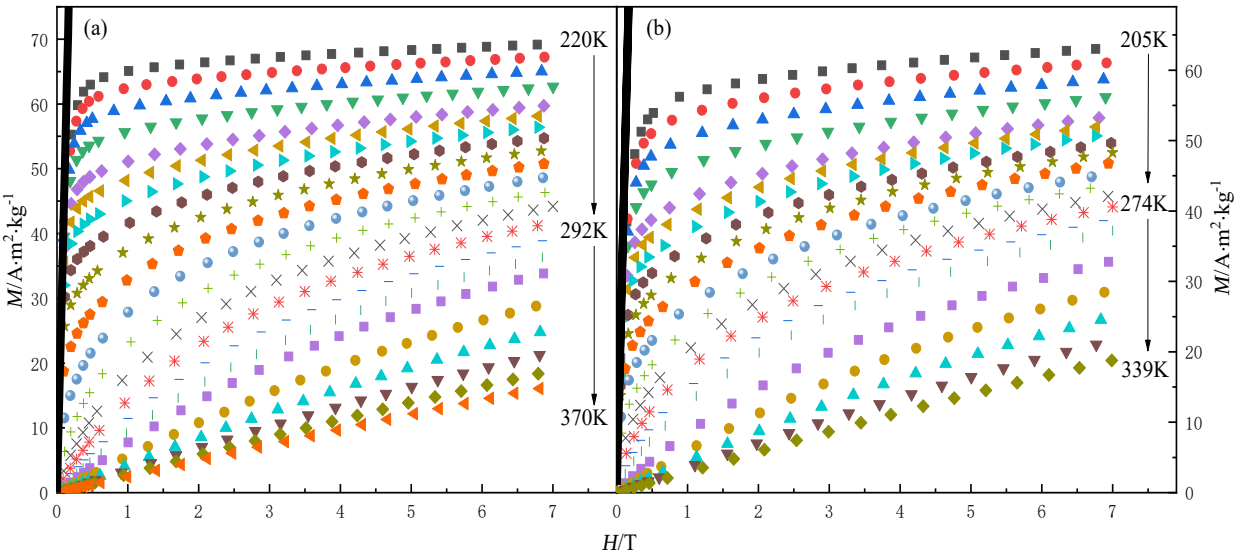

Fig. 3: *M*–*H* curves of $La_{0.75}Sr_{0.25}Mn_{0.9}Co_{0.1}O_3$ for sample A (a) and sample B (b) at different temperatures

3.3 Magnetothermal effect analysis

The thermodynamic Maxwell relation is used to calculate the isothermal $|-\Delta S_M|$, as shown in the following equation[26–28]:

$$|-\Delta S_M| = \int_0^{H_{max}} \left(\frac{\partial M}{\partial T}\right)_H dH. \# \quad (1)$$

Figure 4 shows $|-\Delta S_M|$ versus temperature for $La_{0.75}Sr_{0.25}Mn_{0.9}Co_{0.1}O_3$. The $|-\Delta S_M^{max}|$ peak is broader in sample B than in sample A, although the $|-\Delta S_M^{max}|$ peak value is lower in sample B ($|-\Delta S_M^{max}|$=3.95 $J \cdot kg^{-1}K^{-1}$) than in sample A ($|-\Delta S_M^{max}|$=4.96 $J \cdot kg^{-1}K^{-1}$) for 7 T.

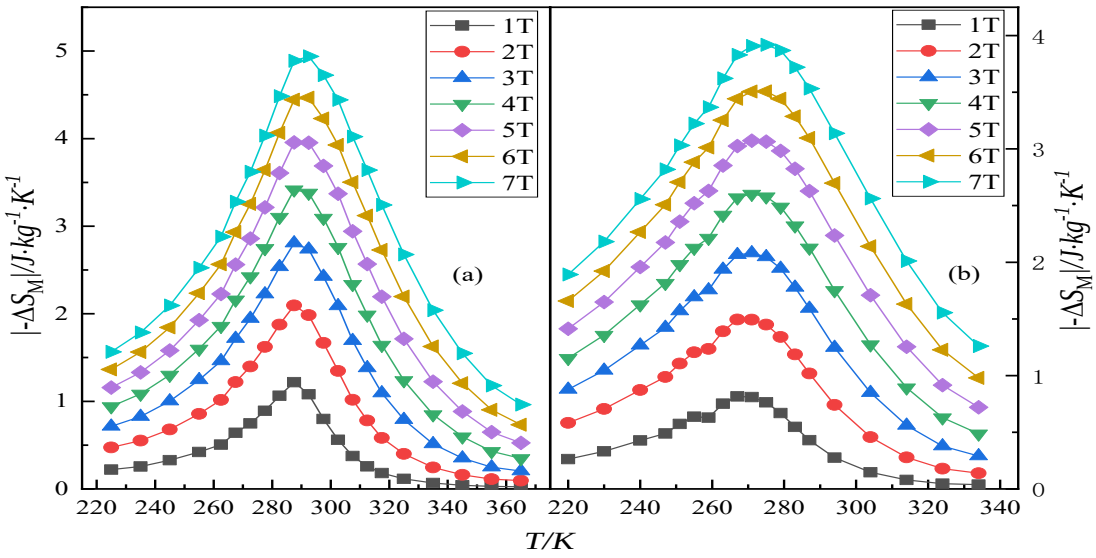

Fig. 4: Isothermal magnetic entropy changes of $La_{0.75}Sr_{0.25}Mn_{0.9}Co_{0.1}O_3$ for sample A (a) and sample B (b), measured in a field change from 0 to 7 T

The maximum values of magnetic entropy change were reduced for samples A and B, while the refrigeration temperature region of both samples increased compared with the $La_{0.75}Sr_{0.25}MnO_3$ atmospheric pressure sample ($|-\Delta S_M^{max}|$=9.23 $J \cdot kg^{-1}K^{-1}$)[22] . This suggests that high-pressure synthesis results in a more continuous magnetic phase transition and that the reduction in the magnetic entropy change peak aligns with the widening of the FM–PM transition[29] . In Fig. 4(b), T_C can be observed to shift slightly toward higher temperatures as the magnetic field increases, which is attributed to the strengthened ferromagnetic double-exchange interaction with the increasing magnetic field.

The refrigeration performance of a material can be measured by its RCP, which is a vital parameter [6, 30]. RCP, defined as RCP = $|-\Delta S_M^{max}|(\Delta T_{FWHM})$, is calculated by multiplying $|-\Delta S_M^{max}|$ by the full width at half-maximum (ΔT_{FWHM}) of the $|-\Delta S_M|(T)$ plot. At a magnetic field of 7 T, the RCP values for the two samples were $RCP_{(sample\text{-}A)}$ = 365.50 $J \cdot kg^{-1}$ and $RCP_{(sample\text{-}B)}$ = 403.92 $J \cdot kg^{-1}$ based on this definition. This shows that the increase in the width of the temperature zone under pressure is greater than the decrease in the value of $|-\Delta S_M^{max}|$, indicating that the refrigeration capacity of the sample under pressure synthesis is enhanced. As Table 3 indicates, the refrigeration efficiency of the sample significantly increases under high pressure. It is worth noting that, compared to the previous 4 GPa sample, although the cooling efficiency of sample-B has slightly decreased, the cooling temperature is closer to room temperature. This further advances the potential of the material as a room-temperature magnetic refrigerant.

Table 3: Comparison of the magnetocaloric parameters of $La_{0.75}Sr_{0.25}Mn_{0.9}Co_{0.1}O_3$ with some other magnetic refrigerants

Samples	T_C / K	$\lvert-\Delta S_M\rvert$ / (J·kg^{-1}K^{-1})	RCP / (J·kg^{-1})	$\mu_0\Delta H$ / T	Ref.
Sample-A	292	4.96	365.50	7	This study
Sample-B	274	3.95	403.92	7	This study
$La_{0.75}Sr_{0.25}Mn_{0.9}Co_{0.1}O_3$ (4 GPa)	243	3.75	404.78	7	[15]
$La_{0.7}Sr_{0.3}MnO_3$	338	1.36	53.00	1.5	[31]
$La_{0.7}Sr_{0.3}Mn_{0.95}Co_{0.05}O_3$	300	1.17	46.80	1.5	[31]
$La_{0.7}Sr_{0.3}Mn_{0.9}Co_{0.1}O_3$	260	0.92	54.30	1.5	[31]
$La_{0.9}Sr_{0.1}MnO_3$	130	2.76+	295	5	[32]
$La_{0.875}Eu_{0.025}Sr_{0.1}MnO_3$	120	2.81	296	5	[32]
$La_{0.67}Sr_{0.33}MnO_3$	275	1.09	133	5	[33]
$La_{0.7}Sr_{0.3}Mn_{0.8}Fe_{0.2}O_3$	94	1.3	168	5	[34]

Recently, temperature-averaged entropy change (TEC) has been employed to assess the effectiveness of magnetic refrigeration materials within a designated temperature range. This is calculated as follows[36–38].

$$TEC(\Delta T_{H-C}) = \frac{1}{\Delta T_{H-C}} max\left\{\int_{T_{mid}-\frac{\Delta T_{H-C}}{2}}^{T_{mid}+\frac{\Delta T_{H-C}}{2}} |\Delta S_M|\, dT\right\} \quad (2)$$

where $\Delta T_{H\text{-}C}$ is the temperature difference between the cold and hot endpoints of the heat exchanger, and T_{mid} is the average central temperature of the $|-\Delta S_M|(T)$ curve. The TEC was calculated for both samples under different magnetic fields with a selection of $\Delta T_{H\text{-}C}$ at 5 and 4 K, respectively. For sample A, the TEC values ranged from 1.15 to 4.83 J/kg·K as the magnetic field increased from 1 to 7 T. Sample B exhibited TEC values ranging from 0.81 to 4.83 J/kg·K across the same range of magnetic fields. Figure 6 displays the relationship curves between $|-\Delta S_M{}^{max}|(H)$ and TEC(H), which show a strong alignment for both samples and various magnetic field strengths. This alignment suggests that these compounds can serve as magnetic refrigerants in active magnetic regenerator cycles, with a functional temperature range of 5 K for sample A and 4 K for sample B. In this operational range, they achieve performances that closely approach their maximum capabilities[27].

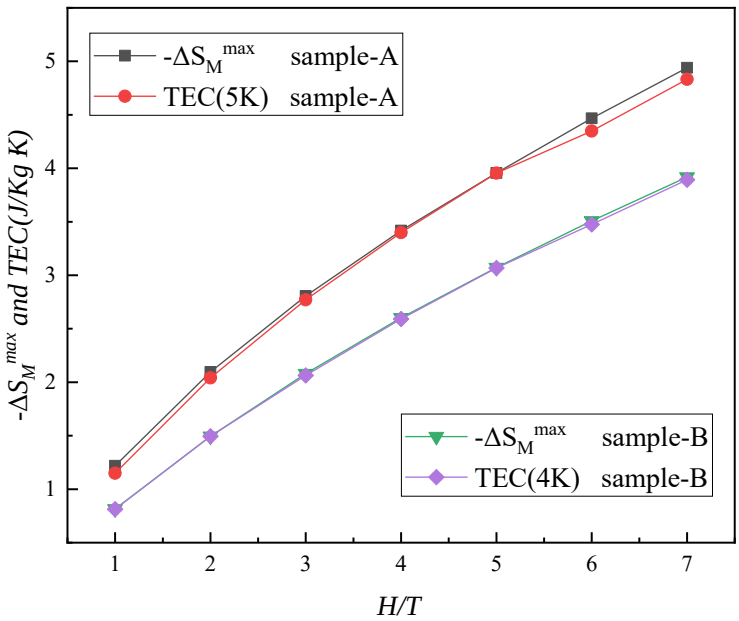

Fig. 5: $|-\Delta S_M{}^{max}|(H)$ and $TEC(H)$ curves for $La_{0.75}Sr_{0.25}Mn_{0.9}Co_{0.1}O_3$ for magnetic fields ranging from 0 to 7 T

The text area is to be 17.0 cm wide by 25.2 cm high. Table 1 presents the margin settings for A4 size paper. It is important to adhere to these margins to ensure that your manuscript prints properly on the paper format from the Conference Proceedings.

3.4 Magnetic phase transition analysis

Figures 6(a) and (b) illustrate the Arrott plots, showing M^2 plotted against $H\,M^{-1}$, which helps determine the nature of the phase transition order. This analysis was conducted at both ambient pressure and 6 GPa. Using Banerjee's criterion[39] , an S-shaped or negative slope of the Arrott curve indicates a first-order phase transition, whereas a positive slope signifies a second-order phase transition. The Arrott plots exhibited positive slopes, strongly indicating the presence of second-order phase transitions in the system induced by the magnetic field at ambient pressure and 6 GPa.

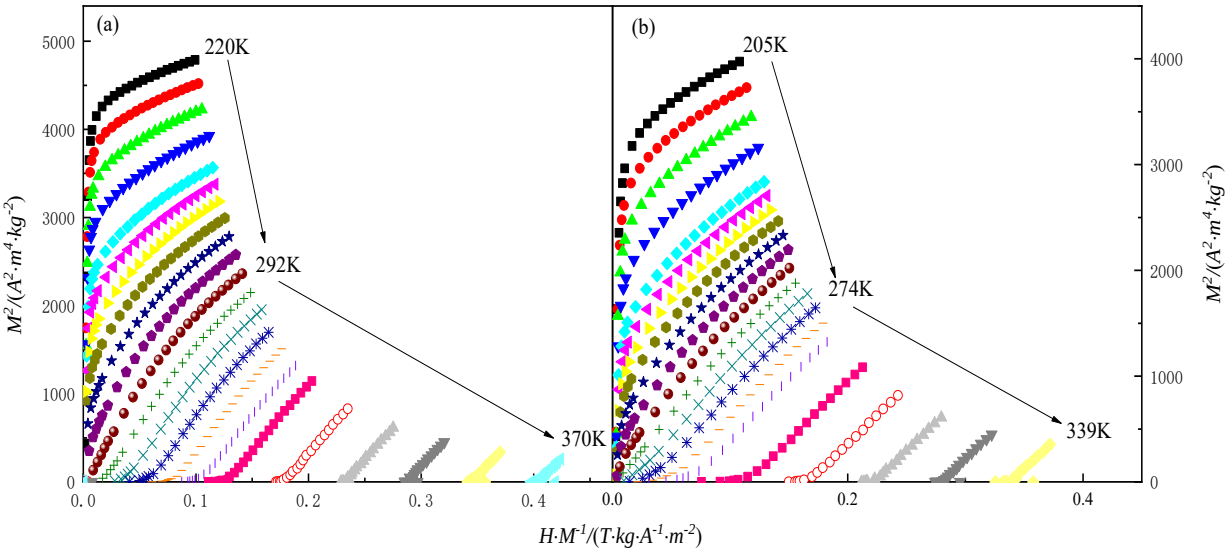

Fig. 6: Arrott curves of $La_{0.75}Sr_{0.25}Mn_{0.9}Co_{0.1}O_3$ for sample A (a) and sample B (b)

The magnetic phase transition mode for a set of samples was determined using the rescaling curve method, which relies on magnetic entropy change. As described by Franco et al.[40] , when a material undergoes a second-order phase transition, its rescaling curves overlap significantly and align closely with the same main line. Conversely, in the case of a first-order phase transition, the rescaling curves do not converge onto a single main line but instead exhibit a scattered distribution. The rescaling curves are presented in Fig. 7 for polycrystalline samples, showing the ratio of $|-\Delta S_M|$ to $|-\Delta S_M{}^{max}|$ on the vertical axis and the corresponding definition of the horizontal axis[41] .

$$\theta = \begin{cases} -\frac{T-T_c}{T_1-T_c} & T \le T_c \\ \frac{T-T_c}{T_2-T_c} & T > T_c \end{cases} \tag{3}$$

where T_1 and T_2 can be derived from $|-\Delta S_M{}^{max}|/2$. Figure 7 shows a large degree of overlap in the rescaling curves at various magnetic fields, essentially aligned on one primary line. This indicates that both samples underwent second-order phase transitions.

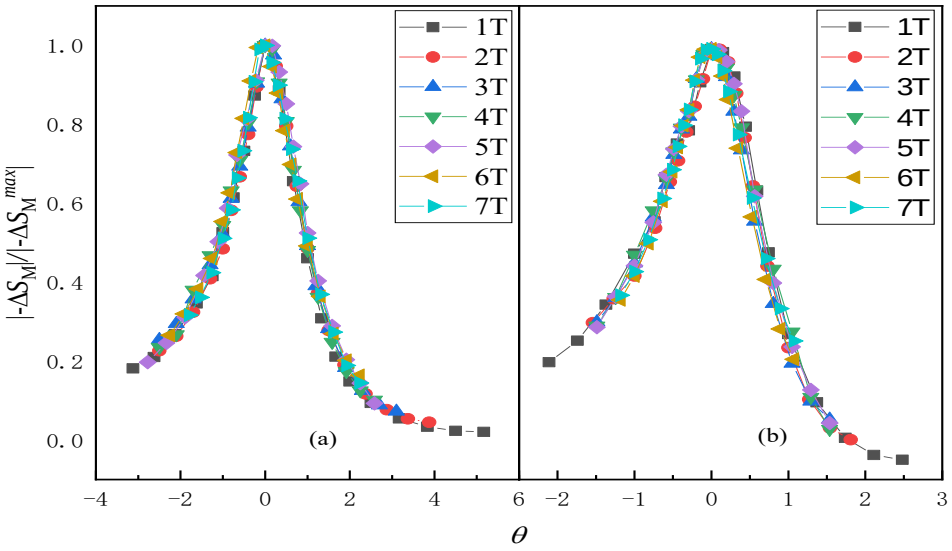

Fig. 7: Rescaling curves of La0.75Sr0.25Mn0.9Co0.1O3 for sample A (a) and sample B (b) at different magnetic fields

4. CONCLUSION

$La_{0.75}Sr_{0.25}Mn_{0.9}Co_{0.1}O_3$ polycrystalline compounds were synthesized at ambient pressure and 6 GPa. $La_{0.75}Sr_{0.25}Mn_{0.9}Co_{0.1}O_3$ polycrystalline undergoes a magnetic phase transition of the PM–FM transition at $T_C \approx 292$ K for sample-A and at $T_C \approx 274$ K for sample-B. The Curie temperatures of these samples are closer to room temperature than that of $La_{0.75}Sr_{0.25}MnO_3$ and $La_{0.75}Sr_{0.25}Mn_{0.9}Co_{0.1}O_3$ under 4 GPa. The total magnetic moments of both the samples are mainly contributed by the electrons from Mn and Co. Pressure synthesis enhanced the lattice distortion of sample B, resulting in a lower Curie temperature and reduced magnetization. The increase in the width of temperature zone under the action of a constant magnetic field is greater than the decrease in the value of $|-\Delta S_M^{max}|$ under pressure synthesis. This leads to an increase in RCP, indicating that the refrigeration capacities of the sample were enhanced after pressurization. Co-doping modulated the Curie temperature of the sample to near room temperature, and further pressurization extended the cooling temperature range of the sample. This modification is useful for practical applications of magnetically driven magnetic refrigeration materials.

ACKNOWLEDGEMENTS

This project was supported by the State Key Development Program for Basic Research of China (Grant Nos. 51562032) and the 2021 Intramural Project - $La_{0.75}Sr_{0.25}Mn_{1-x}Co_xO_3$ (x=0.0~0.2) series polycrystalline samples high-pressure preparation, magnetic and magnetothermal effect study (Grant Nos. 30234013).

REFERENCES

[1]Thiyagarajan R, Muthu S E, Mahendiran R, Arumugam S. Effect of hydrostatic pressure on magnetic and magnetocaloric properties of Mn-site doped perovskite manganites $Pr_{0.6}Ca_{0.4}Mn_{0.96}B_{0.04}O_3$ (B=Co and Cr) [J]. Journal of Applied Physics, 2014, 115(4): 043905.

[2]Gutfleisch O, Willard M A, Brück E, Chen C H, Sankar S G, Liu J P. Magnetic materials and devices for the 21st century: stronger, lighter, and more energy efficient [J]. Advanced materials, 2011, 23(7): 821-842.

[3]De Oliveira N A, Von Ranke P J. Theoretical aspects of the magnetocaloric effect [J]. Physics Reports, 2010, 489(4-5): 89-159.

[4]Fujita A, Fujieda S, Hasegawa Y, Fukamichi K. Itinerant-electron metamagnetic transition and large magnetocaloric effects in $La(Fe_xSi_{1-x})_{13}$ compounds and their hydrides [J]. Physical Review B, 2003, 67(10): 104416.

[5]Li L W, Nishimura K, Hutchison W D, Qian Z H, Huo D X, Namiki T. Giant reversible magnetocaloric effect in $ErMn_2Si_2$ compound with a second order magnetic phase transition [J]. Applied Physics Letters, 2012, 100(15): 152403.

[6]Gschneidner K A, Pecharsky V K, Tsokol A O. Recent developments in magnetocaloric materials [J]. Reports on progress in physics, 2005, 68(6): 1479.

[7]Zhang Y K, Li S, Hu L, Wang X H, Li L W, Yan M. Excellent magnetocaloric performance in the carbide compounds $RE_2Cr_2C_3$ (RE= Er, Ho, and Dy) and their composites [J]. Materials Today Physics, 2022, 27: 100786.

[8]Li L W, Yan M. Recent progress in the development of $RE_2TMTM'O_6$ double perovskite oxides for cryogenic magnetic refrigeration [J]. Journal of Materials Science & Technology, 2023, 136: 1-12.

[9]Li L W, Hu G H, Umehara I, Huo D X, Namiki T, Nishimura K. Pressure effects on magnetic and magnetocaloric properties of $GdCo_2B_2$ [J]. Journal of the Physical Society of Japan, 2012, 81(7): 073701.

[10]Zhang Y K, Zhu J, Li S, Zhang Z Q, Wang J, Ren Z M. Magnetic properties and promising magnetocaloric performances in the antiferromagnetic $GdFe_2Si_2$ compound [J]. Science China Materials, 2022, 65(5): 1345-1352.

[11]Zhang P, Piao H G, Zhang Y D, Huang J H. Research progress of critical behaviors and magnetocaloric effects of perovskite manganites [J]. Acta Physica Sinica, 2021, 70(15): 256-271.

[12]Law J Y, Franco V, Moreno-Ramírez L M, Conde A, Y. Karpenkov D, Radulov I, P. Skokov K, Gutfleisch O. A quantitative criterion for determining the order of magnetic phase transitions using the magnetocaloric effect [J]. Nature communications, 2018, 9(1): 1-9.

[13]Pekala M, Pekala K, Drozd V, Fagnard J F, Vanderbemden P. Magnetocaloric effect in $La_{0.75}Sr_{0.25}MnO_3$ manganite[J]. Journal of Magnetism and Magnetic Materials, 2010, 322 (21): 3460-3463.

[14]Guo Z B, Yang W, Shen Y T, Du Y W. Magnetic entropy change in $La_{0.75}Ca_{0.25-x}Sr_xMnO_3$ perovskites[J]. Solid state communications, 1998, 105(2): 89-92.

[15]Zhao J, Gao L, Zhao J J, Wei W, Yun H Q, Xing R, Ma H J, Jin X, Chao L M. Magnetocaloric effect and phase transition critical behavior of $La_{0.75}Sr_{0.25}Mn_{0.9}Co_{0.1}O_3$ compound synthesized under the high pressure[J]. Tungsten, 2023: 1-12.

[16]Zhang Y K, Tian Y, Zhang Z Q, Jia Y S, Zhang B, Jiang M Q, Wang J, Ren Z M. Magnetic properties and giant cryogenic magnetocaloric effect in B-site ordered antiferromagnetic Gd_2MgTiO_6 double perovskite oxide [J]. Acta Materialia, 2022, 226: 117669.

[17]Perdew J P, Burke K, Ernzerhof M. Generalized gradient approximation made simple [J]. Physical review letters, 1996, 77(18): 3865.

[18]Xu P, Ma Z P, Wang P F, Wang H F, Li L W. Excellent cryogenic magnetocaloric performances in ferromagnetic Sr_2GdNbO_6 double perovskite compound [J], Materials Today Physics, 2021, 20: 100470.

[19]Kresse G, Furthmüller J. Efficient iterative schemes for ab initio total-energy calculations using a plane-wave basis set [J]. Physical Review B, 1996, 54(16): 11169-11186.

[20]Hao W P. DFT+U Study of transitional metal doped Graphene [D]. Xiangtan University, 2013.

[21]Fa-Yun L, Zhi-Xiong Y, Xue C, Li-Ying Z, Fang-Ping O. First-principles study of electronic structure and optical properties of monolayer defective tellurene [J]. Acta Physica Sinica, 2021, 70(16)： 166301.

[22]Kadim G, Masrour R, Jabar A, Hlil E K. Room-temperature large magnetocaloric, electronic and magnetic properties in $La_{0.75}Sr_{0.25}MnO_3$ manganite: Ab initio calculations and Monte Carlo simulations[J]. Physica A: Statistical Mechanics and its Applications, 2021, 573: 125936.

[23]Ćwik J, Koshkid'ko Y, Nenkov K, Mikhailova A, Malecka M, Romanova T, Kolchugina N, De Oliveira N A. Experimental and theoretical analysis of magnetocaloric behavior of $Dy_{1-x}Er_xNi_2$ intermetallics (x= 0.25, 0.5, 0.75) and their composites for low-temperature refrigerators performing an Ericsson cycle[J]. Physical Review B, 2021, 103(21): 214429.

[24]Zhang Y K, Yang Y, Xu X, Geng S H, Hou L, Li X, Ren Z M, Wilde G. Excellent magnetocaloric properties in RE_2Cu_2Cd (RE= Dy and Tm) compounds and its composite materials [J]. Scientific Reports, 2016, 6(1): 1-9.

[25]Romero-Muniz C, Ipus J J, Blazquez J S, Franco V, Conde A. Influence of the demagnetizing factor on the magnetocaloric effect: critical scaling and numerical simulations, Appl. Phys. Lett. 104 (2014), 252405.

[26]Jin X, Zhao J J, Wu H Y, Xu B, Sun Y B, Sun X D, Cao F Z, Wang K, Wang W X, Zhang Y T, Lu Y. Magnetic properties and magnetic entropy change of perovskite manganites $La_{0.9-x}Eu_xSr_{0.1}MnO_3$ (x=0.000, 0.075) by experimental method and numerical fitting [J]. Journal of Rare Earths, 2019, 37(6): 622-627.

[27]Guo D, Moreno-Ramírez L M, Law J Y, Zhang Y K, Franco V. Excellent cryogenic magnetocaloric properties in heavy rare-earth based $HRENiGa_2$ (HRE= Dy, Ho, or Er) compounds [J]. Science China Materials, 2023, 66(1): 249-256.

[28]Ma Z P, Dong X S, Zhang Z Q, Li L W. Achievement of promising cryogenic magnetocaloric performances in $La_{1-x}Pr_xFe_{12}B_6$ compounds [J]. Journal of Materials Science & Technology, 2021, 92: 138-142.

[29]Liu J, Wang W Q, Wu H Y, Tian Y, Cao F Z, Zhao J J. Electromagnetic properties of Co-doped perovskite manganese oxide $La_{0.8}Sr_{0.2}MnO_3$ [J]. Journal of Inorganic Materials, 2018, 33(11): 1237-1247.

[30]Phan M H, Yu S C. Review of the magnetocaloric effect in manganite materials [J]. Journal of Magnetism and Magnetic Materials, 2007, 308(2): 325-340.

[31]Zhang P Y, Yang H F, Zhang S Y, Ge H L, Hua S H. Magnetic and magnetocaloric properties of perovskite $La_{0.7}Sr_{0.3}Mn_{1-x}Co_xO_3$ [J]. Physica B: Condensed Matter, 2013, 410: 1-4.

[32]Chen H W, Li C, Zhao J J, Lu Y, Cao F Z, Wang W X, Zheng L, Jin X. Critical field analysis and magnetocaloric effect of A-Site double-doped manganese oxide $La_{0.9}EuSr_{0.1}MnO_3$ [J]. Journal of Superconductivity and Novel Magnetism, 2021, 34: 2651-2666.

[33]Baaziz H, Tozri A, Dhahri E, Hlil E K. Magnetocaloric properties of $La_{0.67}Sr_{0.33}MnO_3$ tunable by particle size and dimensionality [J]. Chemical Physics Letters, 2018, 691: 355-359.

[34]Barik S K, Krishnamoorthi C, Mahendiran R. Effect of Fe substitution on magnetocaloric effect in $La_{0.7}Sr_{0.3}Mn_{1-x}Fe_xO_3$($0.05\leq x\leq 0.20$) [J]. Journal of Magnetism and Magnetic Materials, 2011, 323(7): 1015-1021.

[35]Su Y T. Study on magnetocaloric effect and critical behavior of perovskite rare earth titanate crystals [D]. Harbin Institute of Technology, 2013.

[36]Zhang Y K, Wu B B, Guo D, Wang J, Ren Z M. Magnetic properties and promising cryogenic magneto-caloric performances of $Gd_{20}Ho_{20}Tm_{20}Cu_{20}Ni_{20}$ amorphous ribbons [J]. Chinese Physics B, 2021, 30(1): 017501.

[37]Xu P, Hu L, Zhang Z Q, Wang H F, Li L W. Electronic structure, magnetic properties and magnetocaloric performance in rare earths (RE) based RE_2BaZnO_5 (RE = Gd, Dy, Ho, and Er) compounds[J]. Acta Materialia, 2022, 236: 118114.

[38]Zhang Y K, Zhu J, Li S, Wang J, Ren Z M. Achievement of giant cryogenic refrigerant capacity in quinary rare-earths based high-entropy amorphous alloy [J]. Journal of Materials Science & Technology, 2022, 102: 66-71.

[39]Banerjee B K. On a generalised approach to first and second order magnetic transitions [J]. Physics Letters, 1964, 12: 16-17.

[40]Franco V, Conde A, Provenzano V, Shull R D. Scaling analysis of the magnetocaloric effect in $Gd_5Si_2Ge_{1.9}X_{0.1}$ (X= Al, Cu, Ga, Mn, Fe, Co) [J]. Journal of Magnetism and Magnetic Materials, 2010, 322(2): 218-223.

[41]Cao F Z, Chen H W, Xie Z K, Lu Y, Zhao J J, Jin X. Magnetic properties and magnetic entropy changes of perovskite manganese oxide $La_{0.8-x}Eu_xSr_{0.2}MnO_3$ (x= 0, 0.075) [J]. Chinese Journal of Physics, 2020, 65: 424-435.

DOI: 10.18462/iir.thermag.2024.0030

COMPARATIVE PERFORMANCE STUDY OF ACTIVE MAGNETIC REGENERATIVE SYSTEM USING MONO/HYBRID NANOFLUIDS

Sumit Kumar Singh[(a)], Jong SukLee[(a)]

[(a)]Department of Mechanical Engineering, Gangneung-Wonju National University,
Wonju, Gangwon 26403, Korea,
e-mail :jslee@gwnu.ac.kr , sumitkrs.rs.mec15@itbhu.ac.in

ABSTRACT

This study conducts a numerical analysis to compare the performance of an active magnetic regenerative system (AMR) using Al_2O_3 nanofluids, multi-walled carbon nanotube (MWCNT) nanofluids, and hybrid nanofluids composed of Al_2O_3(50%) and MWCNT (50%), with volume concentrations ranging from 0-1%. The evaluation focuses on thermophysical propertiesand overall system performance. The results indicate that MWCNT nanofluids, particularly at higher concentrations, outperform other nanofluids, demonstrating superior thermal conductivity and heat transfer rates. MWCNT nanofluids also achieve lower cold-end temperatures and a greater temperature span between the hot and cold ends of the AMR. However, the higher viscosity of MWCNT nanofluids poses challenges by increasing the pumping power required. These findings highlight the significant potential of MWCNT nanofluids to enhance the efficiency of magnetic regenerative systems, suggesting promising advancements for advanced thermal management and sustainable energy applications.

Keywords: Active Magnetic Regenerative, Magnetocalorific Effect, Nanofluids, MWCNT, Gadolinium

1. INTRODUCTION

Conventional vapor compression refrigeration systems, though effective in cooling and heating, are noisy, polluting, and achieve only about 50% of Carnot efficiency, contributing to global warming through emissions of CFCs and HCFCs (Chdil et al., 2024; Choi et al., 2018; Kamran et al., 2020). Magnetic refrigeration, based on the magnetocaloric effect (MCE) of magnetocaloric materials (MCMs), offers a greener alternative with up to 70% of Carnot efficiency and higher COP. However, challenges remain in finding ideal MCMs with high adiabatic temperature change over a broad range. The active magnetic regenerator (AMR) cycle enhances the MCE, creating significant temperature spans through magnetization, adiabatic cooling, demagnetization, and adiabatic heating steps.

Advancements in nanofluid technology offer opportunities to improve heat transfer properties in applications like magnetic refrigeration. Nanofluids, suspensions of nanoparticles in a base fluid, significantly enhance thermal conductivity and heat capacity (Sumit and Sarkar, 2020). These characteristics are crucial for efficient heat transfer in the regenerator and heat exchangers of an AMR system (Chiba et al., 2019; Scarpa and Bianco, 2024). This study compares the performance of an AMR system using Al_2O_3 nanofluids, multi-walled carbon nanotube (MWCNT) nanofluids, and hybrid nanofluids (50-50% Al_2O_3 and MWCNT), investigating their impact on system efficiency and cooling capabilities at varying concentrations (0-1%).

2. OVERVIEW OF THE ACTIVE MAGNETIC REGENERATIVE SYSTEM

Fig. 1 illustrates the schematic diagram of an Active Magnetic Regenerative (AMR) system, which includes two AMR beds: AMR-A and AMR-B. Each bed contains magnetocaloric material that functions both as refrigerant and regenerator. The system is equipped with pumps to ensure efficient circulation of the heat transfer fluid, utilizing both nanofluids and water in this study. AMR-A and AMR-B are connected to cold and hot heat exchangers, respectively, through 3-way valves. This setup facilitates efficient heat transfer during the cooling and heating stages of the cycle.

The AMR cycle comprises four primary steps: isentropic magnetization, hot blow, isentropic demagnetization, and cold blow. These steps are achieved through the application and removal of a magnetic

field, as well as the circulation of the fluid for cooling and heating. Table 1 reports thedefault set of parameters used in the preliminary analysis andin the parametric investigation.

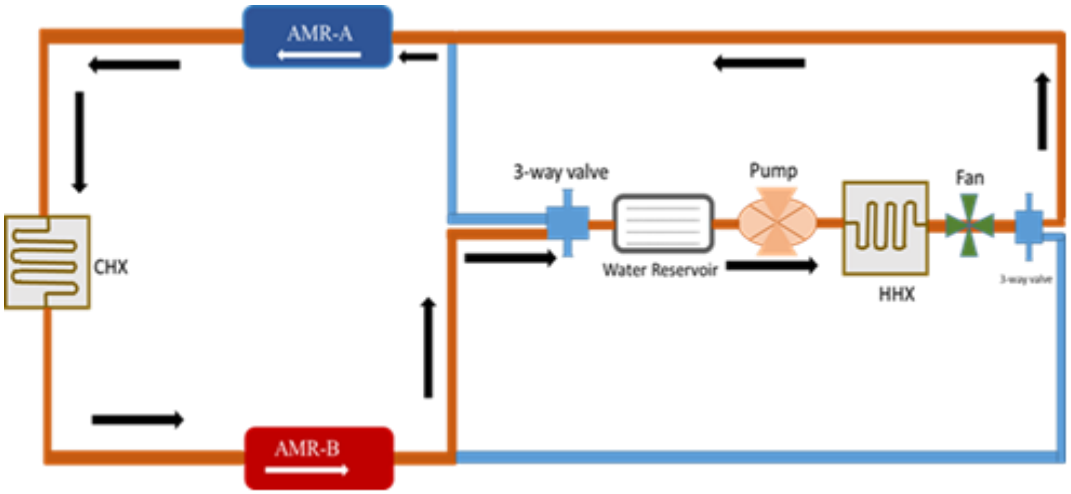

Figure 1: Schematic diagram of magnetic refrigeration system

Table 1. Input parameters

Parameters	Value
Length (m)	0.2
MCM mass (g)	1200
Void fraction	0.35
Flow rate (lpm)	0.6
Hot and Cold blow time (s)	2 and 2
Total time (s)	3600
B_{max}(T)	1.35
B_{min} (T)	0.01
T_{amb} (^{o}C)	20

2.1 Mathematical Modelling for Mono/hybrid nanofluids

Table 2 shows the thermophysical properties of base fluid (water) and nanoparticles (Al_2O_3 and MWCNT) composed of nanofluids. The thermophysical properties of mono/hybrid nanofluids can be measured by using the equations (1-9).

Table2. Thermophysical properties of base fluid and nanoparticles

	ρ (kg/m^3)	c_p (J/kgK)	k (W/m.K)	μ (kg/ms)
Water	998	4183	0.597	0.00089
Al_2O_3	3970	765	36	---
MWCNT	2660	740	3000	---

For Mono nanofluids:

The density, specific heat, thermal conductivity and viscosity of mono nanofluid have been calculated by the correlation:

$$\rho_{nf} = \emptyset\rho_p + (1-\emptyset)\rho_{bf} \quad (1)$$

$$\boldsymbol{c_{p,nf}} = \frac{\emptyset\boldsymbol{\rho_p c_{p,p}} + (\mathbf{1}-\emptyset)\boldsymbol{\rho_{bf} c_{p,bf}}}{\boldsymbol{\rho_{nf}}} \quad (2)$$

$$\frac{\boldsymbol{k_{nf}}}{\boldsymbol{k_{bf}}} = \frac{\boldsymbol{k_p} + 2\boldsymbol{k_{bf}} + 2\emptyset(\boldsymbol{k_p} - \boldsymbol{k_{bf}})}{\boldsymbol{k_p} + 2\boldsymbol{k_{bf}} - \emptyset(\boldsymbol{k_p} - \boldsymbol{k_{bf}})} \quad (3)$$

$$\boldsymbol{\mu_{nf}} = \boldsymbol{\mu_{bf}}(\mathbf{1} + \mathbf{2.5}\emptyset + \mathbf{6.2}\emptyset^{\mathbf{2}}) \quad (4)$$

where, ϕ is the overall volume concentration of nanoparticles dispersed in nanofluid

For Hybrid nanofluids:

The density, specific heat, thermal conductivity and viscosity of hybrid nanofluid have been calculated by**(Sumit and Sarkar, 2018)**:

$$\rho_{hnf} = \emptyset_{p1}\rho_{p1} + \emptyset_{p2}\rho_{p2} + (1-\emptyset)\rho_{bf} \quad (5)$$

$$\boldsymbol{c_{p,hnf}} = \frac{\emptyset_{\boldsymbol{p1}}\boldsymbol{\rho_{p1}}\boldsymbol{c_{p,p1}} + \emptyset_{\boldsymbol{p2}}\boldsymbol{\rho_{p2}}\boldsymbol{c_{p,p2}} + (\mathbf{1}-\emptyset)\boldsymbol{\rho_{bf}}\boldsymbol{c_{p,bf}}}{\boldsymbol{\rho_{hnf}}} \quad (6)$$

$$\frac{\boldsymbol{k_{hnf}}}{\boldsymbol{k_{bf}}} = \frac{\frac{\emptyset_{\mathbf{p1}}\mathbf{k_{p1}} + \emptyset_{\mathbf{p2}}\mathbf{k_{p2}}}{\emptyset} + 2\mathbf{k_{bf}} + 2(\emptyset_{\mathbf{p1}}\mathbf{k_{p1}} + \emptyset_{\mathbf{p2}}\mathbf{k_{p2}}) - 2\emptyset\mathbf{k_{bf}}}{\frac{\emptyset_{\mathbf{p1}}\mathbf{k_{p1}} + \emptyset_{\mathbf{p2}}\mathbf{k_{p2}}}{\emptyset} + 2\mathbf{k_{bf}} - 2(\emptyset_{\mathbf{p1}}\mathbf{k_{p1}} + \emptyset_{\mathbf{p2}}\mathbf{k_{p2}}) + \emptyset\mathbf{k_{bf}}} \quad (7)$$

$$\boldsymbol{\mu_{hnf}} = \frac{\boldsymbol{\mu_{nf,1}}\emptyset_{\boldsymbol{p1}} + \boldsymbol{\mu_{nf,2}}\emptyset_{\boldsymbol{p2}}}{\emptyset} \quad (8)$$

where, ϕ is the overall volume concentration of two different types of nanoparticles (p1 and p2) dispersed in hybrid nanofluid and is calculated as:

$$\emptyset = \emptyset_{\boldsymbol{p1}} + \emptyset_{\boldsymbol{p2}} \quad (9)$$

2.2 Governing Equations for AMR system

The equations governing the temperature distributions in the fluid and solid parts during blows are derived from the application of the energy conservation law to a differential control volume within the AMR bed **(Tagiafico et al., 2010)**.

$$\frac{\partial T_f}{\partial t} = \frac{1}{\rho_f c_{p,f}}\left[\frac{\gamma}{\varepsilon}h_e(T_s - T_f) + k_f\frac{\partial^2 T_f}{\partial x^2} - \frac{m_f c_{p,f}}{\varepsilon A}\frac{\partial T_f}{\partial x}\right] \quad (11)$$

$$\frac{\partial T_s}{\partial t} = \frac{1}{\rho_s c_{p,s}}\left[-\frac{\gamma}{1-\varepsilon}h_e(T_s - T_f) + k_s\frac{\partial^2 T_s}{\partial x^2}\right] \quad (11)$$

where the subscript f and s refer to (nano)fluid and the solid (Gd) respectively. ρ,c_p, and k refer the density, heat capacity and thermal conductivity of the materials respectively. γ and ε refer the exchange surface to volume ratio and void fraction. The convective heat transfer coefficient (h_e) is determined by the heat transfer correlation for flow through porous media in the low Reynolds number flow regime.

$$Nu = \frac{hd_p}{k_f} = 2 + 1.1Re^{0.6}Pr^{1/3} \quad (12)$$

$$h_e = \frac{h}{1 + \frac{hd_p}{2k_s a_o}} \quad (13)$$

where Nu, Re, and Pr, are the Nusselt number, Reynolds number and Prandtl number, respectively. The shape factor a_0 depends on the MCM geometry and has a value of 3 for sphere particles. d_p is the sphere particle diameter.

According to the flow direction, the boundary conditions can be expressed as:

Hot blow ($0 < t < \tau/2$)

$$\frac{\partial T_s}{\partial x}(x=0,t)=0,\quad \frac{\partial T_s}{\partial x}(x=L,t)=0,\quad T_f(x=0,t)=T_c \tag{14}$$

$$m_f(t)=m_{f,}\qquad B(t)=B_{MAX}$$

Cold blow ($\tau/2 < t < \tau$)

$$\frac{\partial T_s}{\partial x}(x=0,t)=0,\quad \frac{\partial T_s}{\partial x}(x=L,t)=0,\quad T_f(x=\mathrm{L},t)=T_h \tag{15}$$

$$m_f(t)=-m_{f,}\qquad B(t)=B_{MIN}$$

The temperature span between the hot and cold ends and the refrigeration capacity are given as:

$$\Delta T_{SPAN}=T_h-T_c \tag{16}$$

3. RESULT AND DISCUSSIONS

Figure 2shows the effect of volume concentration on the density and specific heat of two nanofluids (Al_2O_3, MWCNT) and one hybrid nanofluid (Al_2O_3+MWCNT).As the volume concentration of nanoparticles increases, the density of all three fluids increases. This is because the nanoparticles are denser than the base fluid.The Al_2O_3+MWCNT hybrid nanofluid exhibited a density between that of the Al_2O_3 and MWCNTs nanofluids, and MWCNT showed higher density nanofluid. On the other hand, the specific heat of all nanofluids decrease with increased volume concentrations of the particles.Among all nanofluids, MWCNT nanofluid offers potentially higher specific heat at higher concentrations.

As the volume concentration of nanoparticles increases, the thermal conductivity and the viscosity of all nanofluids increases as shown in Figure 3. MWCNTs have a higher thermal conductivity than Al_2O_3, so the MWCNT nanofluid has the highest thermal conductivity overall. The Al_2O_3+MWCNT hybrid nanofluidhas a thermal conductivity between that of the Al_2O_3 and MWCNT nanofluids.While the viscosity of all nanofluidsincreased because the presence of nanoparticles disrupts the flow of the base fluid. The Al_2O_3 nanofluid has the lowest viscosity and the MWCNT nanofluid has the highest viscosity. The Al_2O_3+MWCNT hybrid nanofluid has a viscosity between that of the two mono nanofluids.

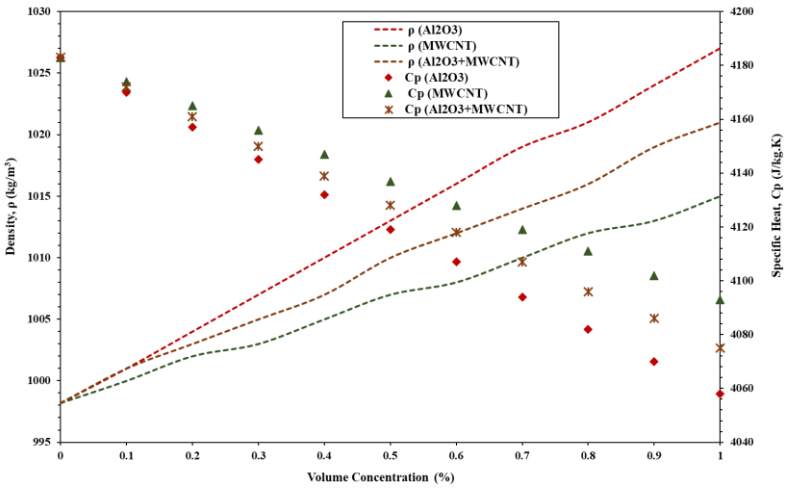

Figure 2: Variation of density and specific heat with respect to volume concentrations

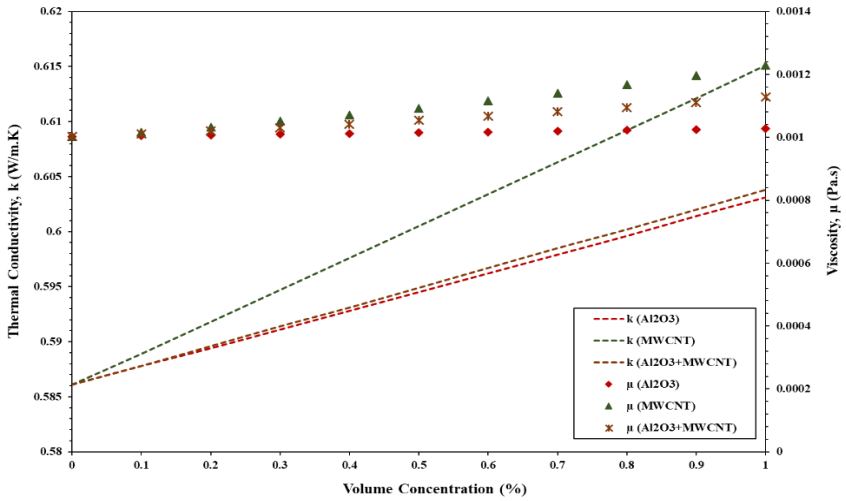

Figure 3: Variation of thermal conductivity and viscosity with respect to volume concentrations

Figure4 illustrates the variation of cold end temperature with respect to the time. This indicates effective cooling within the simulated AMR system.The results found that using both mono and hybrid nanofluids, it shows the significant decrease in temperature than that of using water. Notably, MWCNT nanofluids with a concentration of 1.0% exhibit a significant decrease in temperature. However, it's important to note that as nanoparticle concentration increases, viscosity also rises. Consequently, nanofluids with higher nanoparticle concentrations may necessitate increased pump work to counter the elevated viscosity and maintain optimal flow rates. In Figure5, the variation of temperature span with utilization for both water and nanofluids is depicted over time. Remarkably, MWCNT nanofluids demonstrate a higher temperature span compared to all nanofluids and water, attributable to their significantly enhanced thermal conductivity relative to pure water.

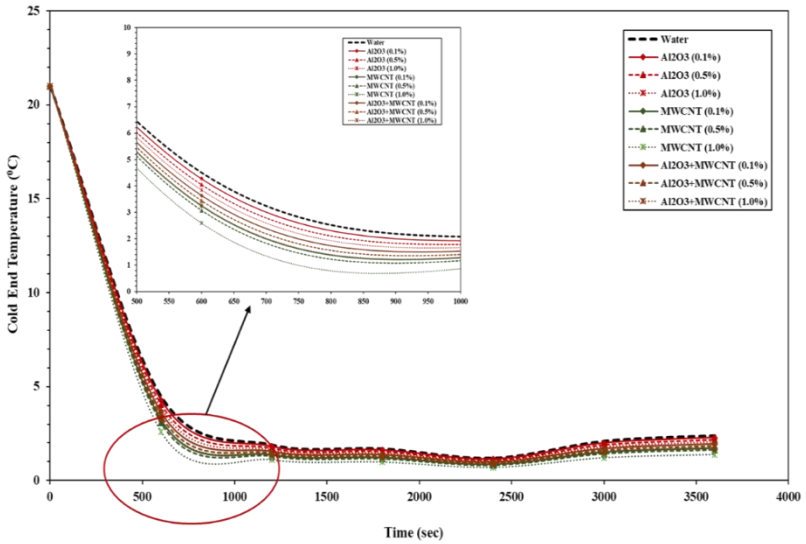

Figure 4: Cold end temperature vs time

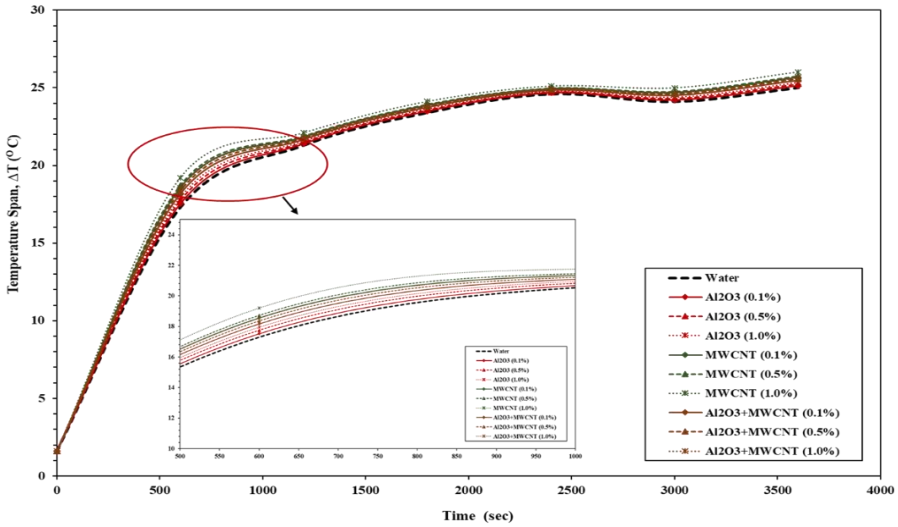

Figure 5: Temperature span vs time

4. CONCLUSIONS

This study presents a comparative numerical analysis of an active magnetic regenerative (AMR) system using Al_2O_3 nanofluids, multi-walled carbon nanotube (MWCNT) nanofluids, and hybrid nanofluids composed of a 50-50% mixture of Al_2O_3 and MWCNT, with volume concentrations ranging from 0-1%. The evaluation focused on the thermophysical properties and overall performance of the AMR system. The results can be concluded as follow:

1. The density increases and specific heat decreases with the volume concentration of nanoparticles for all nanofluids. MWCNT nanofluids exhibit the highest density and specific heat.

2. MWCNT nanofluids have the highest thermal conductivity and viscosity, followed by hybrid and then Al_2O_3 nanofluids.

3. MWCNT nanofluids, particularly at a 1.0% concentration, demonstrate the most significant decrease in cold-end temperature, indicating superior cooling performance. Also, MWCNT nanofluids achieve the highest temperature span between the hot and cold ends of the AMR system, outperforming both Al_2O_3 and hybrid nanofluids, as well as water.

4. Higher nanoparticle concentrations result in increased viscosity, which necessitates greater pumping power to maintain optimal flow rates. This is a critical consideration for system efficiency, particularly for MWCNT nanofluids.

ACKNOWLEDGEMENTS

This study was supported by the Institute of Information & Communications Technology Planning & Evaluation (IITP) grant funded by the Korea government (MSIT) (No.2022-0-00882, Development of eco-friendly active magnetic regenerator and magnetic cooling system for the thermal managements of ICT parts and products to improve energy efficiency and reduce carbon emission).

NOMENCLATURE

ρ	density (kg/m^3)	T	temperature (K)
c_p	specific heat (J/kg.K)	μ	viscosity (Pa.s)
k	Thermal conductivity (W/m.K)	ε	void fraction

REFERENCES

Chdil, O., Bikerrouin, M., Balli, M., Mounkachi, O.,2024. New horizons in magnetic refrigeration using artificial intelligence. Appl. Energy335, 120773.

Choi, S., Han, U., Cho, H., Lee, H., 2018. Recent advances in household refrigerator cycle technologies. Appl ThermEng 132, 560–74.

Kamran, M.S., Ahmad, H.O., Wang, H.S., 2020. Review on the developments of active magnetic regenerator refrigerators–evaluated by performance. Renew Sustain Energy Rev 133, 110247.

Singh, S.K., Sarkar, J., 2020, Improvement in energy performance of tubular heat exchangers using nanofluids: a review, Curr.Nanosci. 16 (2),136-156.

Chiba, Y., Marif, Y., Boukaoud, A.,Sebbar, D., 2019. Performance Enhancement of a Magnetic Refrigeration Device based on TiO_2 used as Secondary Fluid, 7th International Renewable and Sustainable Energy Conference (IRSEC), Agadir, Morocco,1-4.

Scarpa, F., Bianco V., 2024. Improving the performance of room temperature magnetic regenerators using Al_2O_3-water nanofluid. Appl. Therm. Eng. 236,121711.

Singh, S.K., Sarkar, J., 2018. Energy, exergy and economic assessments of shell and tube condenser using hybrid nanofluid as coolant, Int.Commun. Heat Transfer98, 41-48.